Inverse Analysis and Modelling of Unsteady Pipe Flow: Theory, Applications and Experimental Verification

by

John Philipp Vítkovský

March 2001

A Thesis Submitted for the Degree of

Doctor of Philosophy

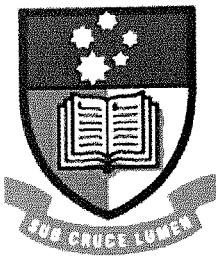

Department of Civil & Environmental Engineering

Adelaide University

Australia

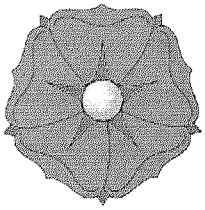

Abstract

A comprehensive study is presented in this thesis for leak detection and calibration using inverse transient analysis. The inverse transient method solves an inverse problem in which system parameters (such as lumped leak coefficients and friction factors) are determined from measured transient pressure head data. The research presented in this thesis falls into three areas: transient model development, inverse analysis improvement and experimental verification. The transient model has been extended to include variable position valves, nodal and non-nodal leaks. The modelling of frictional effects is improved for unsteady pipe flow. New unsteady friction models are proposed and unsteady friction coefficients quantified. Improvements to the inverse transient method are made. The speed of calculation is improved through the formulation of a method that quickly and efficiently calculates the partial derivatives of the pressure heads and flows with respect to parameters, time and space. The optimal number, data length and location of measurement sites are found through the use of genetic algorithms and parameter error estimates. Existing and proposed unsteady friction models are tested against experimental data with good results. Experimental verification of leak detection methods including inverse transient analysis and a first pressure rise method are performed, also with good results.

Statement of Originality

This work contains no material which has been accepted for the award of any other degree or diploma in any university or other tertiary institution and, to the best of my knowledge and belief, contains no material previously published or written by another person, except where due reference has been made in the text.

I give consent to this copy of my thesis, when deposited in the University Library, being available for loan and photocopying.

Signed: Date: 19/9/01

John Philipp Vítkovský

Acknowledgements

I wish to thank my supervisors Dr. Angus Simpson and Dr. Martin Lambert who have always been very supportive and helpful throughout this study. This thesis is as much mine as it is theirs and without their involvement would not have eventuated.

I would like to thank Prof. James Liggett for his great help with the final revisions of this thesis. His comments and suggestions, I believe, have strengthened this thesis and improved my English skills along the way.

I would like to extend my best wishes to Xiaojian Wang who is also supervised by Dr. Simpson and Dr. Lambert and whose research topic is closely associated with mine. His help with experimental testing and discussion was well received.

The assistance of Prof. Liggett of Cornell University in providing in inverse transient analysis computer code is gratefully acknowledged. The use of genetic algorithm source code supplied by Dr. Simpson and Dr. Alexander Anderson from the University of Adelaide and University of Newcastle upon Tyne respectively is greatly appreciated. The use of existing experimental data for fast valve closures from Dr. Anton Bergant and Dr. Simpson is acknowledged. Also, I would like to thank Dr. Bergant for his input at various times in this study.

This project was funded by an Australian Postgraduate Research Award (APRA), a small Australian Research Council (ARC) grant and a Large ARC grant.

Finally, I would like to thank my family and fellow postgraduate students for their friendship and valuable discussion.

List of Publications

Several papers, as a part of this thesis, have been published during this study. They reflect formative ideas for work presented in this thesis. These papers are listed in chronological order:

1. Simpson, A.R., and Vítkovský, J.P. (1997). "A Review of Pipe Calibration and Leak Detection Methodologies for Water Distribution Networks." *17th Federal Convention, Australian Water and Wastewater Association*, March, Vol. 1, 680-687.

2. Vítkovský, J.P., and Simpson, A.R. (1997). "Calibration and Leak Detection in Pipe Networks Using Inverse Transient Analysis and Genetic Algorithms." *Research Report No. R157*, August, Department of Civil & Environmental Engineering, Adelaide University, Australia.

3. Bergant, A., Simpson, A.R., and Vítkovský, J.P. (1999). "Review of Unsteady Friction Models in Transient Pipe Flow." *9th International Meeting of the Work Group on the Behaviour of Hydraulic Machinery Under Steady Oscillatory Conditions*, IAHR, 7-9 September, Brno, Czech Republic.

4. Vítkovský, J.P., Simpson, A.R., and Lambert, M.F. (1999). "Leak Detection and Calibration of Water Distribution Systems Using Transients and Genetic Algorithms." *Preparing for the 21st Century: Proceedings of the 26th Annual Water Resources Planning and Management Conference*, ASCE, Tempe, Arizona, 7-9 June.

5. Vítkovský, J.P., Lambert, M.F., Simpson, A.R., and Bergant, A. (2000). "Advances in Unsteady Friction Modelling in Transient Pipe Flow." *Safe Design and Operation of Industrial Pipe Systems: 8th International Conference on Pressure Surges*, BHR Group, The Hague, The Netherlands, 12-14 April, 471-482.

6. Simpson, A.R, Vítkovský, J.P., and Lambert, M.F. (2000). "Transients for Calibration of Pipe Roughnesses Using Genetic Algorithms." *Safe Design and Operation of Industrial Pipe Systems: 8th International Conference on Pressure Surges*, BHR Group, The Hague, The Netherlands, 12-14 April, 587-598.

7. Vítkovský, J.P., Simpson, A.R., and Lambert, M.F. (2000). "Leak Detection and Calibration Using Transients and Genetic Algorithms." *Journal of Water Resources Planning and Management*, ASCE, 126(4), July/August, 262-265.

8. Bergant, A., Simpson, A.R., and Vítkovský, J.P. (2001). "Developments in Unsteady Pipe Flow Friction Modelling." *Journal of Hydraulic Research*, IAHR, 39(3), 249-257.

9. Wang, X., Lambert, M.F., Simpson, A.R., Liggett, J.A., and Vítkovský, J.P. (2001). "Leak Detection in Pipelines Using the Damping of Fluid Transients." Conditionally accepted by: *Journal of Hydraulic Engineering*, ASCE.

Table of Contents

List of Figures

List of Tables

Nomenclature

Roman Letters

a = wave speed

$\mathbf{a}$, $\{a\}$ = vector of parameters

A = cross-sectional area

$\mathbf{A}$ = vector of the outflow area which acts normal to the control surface

A, B = smooth pipe log law velocity distribution coefficients

a_k, b_k = coefficients from Wang *et al.* (1991)

b = lateral orifice width

B = characteristic impedance

B_R, C_R = rough pipe log law velocity distribution coefficients

C = Daily *et al.* (1956) unsteady friction coefficient

$[C]$ = covariance matrix

C^+, C^- = positive and negative characteristic

C^* = shear decay coefficient of Vardy and Brown (1996)

$C\vartheta$ = control volume

C_β = momentum coefficient (Wiggert, 1968)

C_d = coefficient of discharge

C_dA_L = lumped leak coefficient

C_P, C_M = coefficients for explicit method of characteristics scheme

C_r = Courant number

CS = control surface

C_V = valve coefficient

c_v = volumetric tank constant

D = internal pipe diameter

D_U = exponential unsteady friction decay coefficient

e = internal energy per unit mass, pipe wall thickness

E = objective function, Young's modulus of elasticity of pipe wall

E_A = average of the absolute differences in friction factor

E_B = average head difference at all nodes

E_C = average head difference at measurement nodes

E_{DER} = number of evaluations required for parameter derivatives

E_{TOTAL} = total number of evaluations

f = Darcy-Weisbach friction factor, frequency of oscillation

f_S = steady state component of Darcy-Weisbach friction factor

f_U = unsteady state component of Darcy-Weisbach friction factor

F = force

F_C = cut-off frequency for IIR filter

F_1, F_2 = variables used in method of characteristics

F_1, F_2, F_3 = variables used by Carstens and Roller (1959)

fitness = fitness of a string

g = gravitational acceleration

$[g_a]$ = matrix used in fast analytic parameter derivative method

g_v = velocity distribution function

gene = gene value in string

h = perturbation for divided difference derivative calculation

h_f = steady state friction loss

H = hydraulic head (equal to the sum of the pressure head and elevation)

$\mathbf{H}$ = Hessian matrix

I_{LVMQ} = number of Levenberg-Marquardt iterations

$\mathbf{I}$ = identity matrix

J = total unsteady headloss per metre

$\mathbf{J}, [J]$ = Jacobian matrix

J_M = unsteady headloss per metre due to momentum component

J_S = unsteady headloss per metre due to steady friction component

J_U = unsteady headloss due to unsteady friction component

k_1 = Carstens and Roller (1959) unsteady friction coefficient

k_2 = Golia (1990) unsteady friction coefficient

k_3 = Brunone *et al.* (1991) unsteady friction coefficient

k_A = unsteady friction amplitude coefficient in the k_A & k_P model

k_M = unsteady friction coefficient in the k_3 & k_M model

k_P = unsteady friction phase coefficient in the k_A & k_P model

k_S = sand grain roughness height

K = bulk modulus of elasticity of water, number of repeated measurements

l = chromosome length

L = pipeline length

m = mass of system

m, n = coefficients for weighting function in Zielke (1968)

M = number of measured data points, Savitsky-Golay smoothing filter order

$\mathbf{M}$ = Mach number

$[M]$ = coefficient matrix for implicit method of characteristics scheme

$\mathbf{MCS}$ = performance indicator based on Monte Carlo simulations

$[M_D]$ = coefficient matrix for fast analytic parameter derivative method

M_L = number of measurements for loading condition L

$[M_T]$ = coefficient matrix for time derivatives

$[M_X]$ = coefficient matrix for spatial derivatives

n = exponent in universal power law of velocity distribution, population size

N = an advected extensive fluid property, number of parameters, pressure head peak number

N_I = number of iterations used to resolve nonlinearities

N_L = number of loading conditions

N_{MR} = number of Monte Carlo simulations

N_{MS} = number of measurement sites

N_{MSC} = number of measurement site combinations

N_P = number of parameters, Savitsky-Golay smoothing filter window size

N_{SAM} = number of measurement site configuration samples

N_{TS} = number of time steps

p = pressure

P = maximum likelihood probability

P_A = probability of adjacency mutation

P_C = probability of crossover

P_D = probability used in adjacency mutation

P_M = probability of mutation

P_S = probability of selection

q_L = lateral orifice outflow

Q = flow rate, variable in bivariate distribution

Q_D = nodal demand

Q_H = heat energy

r = distance from the centre of the pipe

r_0 = pipe radius

R = pipe radius, characteristic resistance, relaxation coefficient

$\mathbf{R}$ = Reynolds number

$\mathbf{R}_{ta}$ = time averaged Reynolds number

$\{R\}$ = vector for implicit method of characteristics scheme

$[R_D]$ = total right hand side matrix for fast analytic parameter derivative method

$[R_{DP}]$ = dependent parameter matrix

$\{R_{DP}\}$ = dependent parameter vector

$\{R_{IP}\}$ = independent parameter vector

RND = random number generated from a uniform distribution

$\{R_T\}$ = right hand side vector for time derivatives

$\{R_X\}$ = right hand side vector for spatial derivatives

s = sample standard deviation, tournament size, selection pressure

SAH = performance indicator based on inverse analyses

SE = performance indicator based on gradient

SH = performance indicator based of Jacobian

Step_Size = mutation range

SV = performance indicator based on predicted parameter variance

t = time

t_c = valve closure time

$t_{\Delta z}$ = time taken for change in tank level

T = temperature

T_{DER} = time taken for computation of parameter derivatives

T_{TS} = time taken for computation of transient solver

u = intrinsic energy per unit mass due to molecular spacing and forces dependent upon p, ρ or T

v = axial velocity

$\mathbf{v}$ = vectorial velocity

V = average cross-sectional velocity

$\hat{V}$ = average velocity calculated using the absolute axial velocity

W = weighting function in Zielke (1968), work done by a system

W_L = weight for loading condition L

W_{pr} = work done by the pressure forces

W_S = shaft work

x = distance

x_L = distance to leak, leak position

y = radial distance from the pipe wall

z = elevation

Greek Letters

α = kinetic energy correction factor (also called the Coriolis coefficient), unsteady friction decay coefficient

$[\alpha]$, $\{\beta\}$ = variables used in the Levenberg-Marquardt algorithm

β = momentum correction factor (also called the Boussinesq coefficient)

β_1 = modified momentum correction factor (from Buthaud, 1977)

δ = Heaviside operator used by Golia (1990)

δx = small perturbation in distance

Δt = change in time, characteristic time step

Δt_L = time delay due to leak

Δx = change in distance, characteristic space step

Δz = change in tank level

ε = pipe roughness, ratio between the parameter error and the measured data error

ε_D = relative roughness

η = an advected, extensive fluid property (N) per unit mass, dimensionless radial distance from pipe wall

η_l = smooth pipe dimensionless radial viscous sub-layer distance

η_{lR} = rough pipe dimensionless radial viscous sub-layer distance

η_R = pipe roughness variable using in log law of velocity distribution

ϑ = volume

κ = coefficient used by Vardy and Brown (1996), von Kármán universal constant

λ = method of characteristics multiplier, Levenberg-Marquardt multiplier

μ = Poisson's ratio of pipe wall, mean

ν = kinematic viscosity, number of degrees of freedom

ν^* = friction velocity

$\{\nu\}$ = vector of pressure heads and flows

ξ = parameter derivative calculation efficiency

π = pi

ρ = fluid density, correlation coefficient

σ_x = standard deviation of x

σ_x^2 = variance of x

σ_{xy} = covariance of x and y

τ = dimensionless valve-opening coefficient, dimensionless time in Zielke (1968)

τ_S = axial steady shear stress

τ_U = axial unsteady shear stress

τ_0 = shear stress at pipe wall

τ_{0S} = steady shear stress at the pipe wall

τ_{0U} = unsteady shear stress at the pipe wall

ϕ = dimensionless axial velocity, pipe anchorage variable for wave speed calculation

ϕ_A = acceleration sign operator

ϕ_V = velocity sign operator

ϕ_X = sign operator indicating the sign of X

$[\varphi^*]$ = adjoint matrix

χ^2 = chi-square statistic

χ_ν^2 = reduced chi-square statistic

ψ = weighting factor of Wylie (1984)

$\{\psi^*\}$ = adjoint vector

ω = circular frequency

ω' = dimensionless frequency

∇ = gradient vector

Sub- and Superscripts

$-$ = negative characteristic

$+$ = positive characteristic

$*$ = variable at current time step

$'$	=	linearised variable at current time step
0	=	reference condition, pre-transient condition
BC	=	boundary condition
f	=	faulty (leaking) condition, post-transient condition
L	=	leak, loading condition
m	=	measured value
n	=	non-leaking condition
V	=	valve

Chapter 1

Introduction

Leak detection and calibration in pipe networks has been the focus of research and the concern of water authorities for many years. The amount of leakage in a pipe network can be representative of its overall efficiency to deliver water. A poorly maintained network will often have high leakage. In many countries water is a scarce resource. Any waste due to leakage represents an extra cost to consumers. In pipelines containing hazardous fluids, leakage could have detrimental environmental consequences. Traditional leak detection methods are expensive and time consuming and hardly an exact science. The majority of leak detection in the past was achieved through water audits, listening devices and passive leak control. Water audits use mass balance techniques to measure the difference between the amount of water being supplied to a network and the amount of water being delivered to customers. The water audits do not locate leaks, but rather indicates their existence. This method also depends on the accuracy of meters (which typically have inaccuracies of 15%; Andrés, 1995). Listening devices are a labour intensive method to locate leakage. Personnel systematically work their way around a network with microphones to listen for the characteristic noise generated by a leak. The success of this method depends on the skill of the listener. Passive leak detection is the detection of leakage when its effects are noticeable (e.g. ground-surface water, poor pressure, noise in pipes, etc.). Naturally, this method only finds those leaks with noticeable effects and, therefore, leaves many more (whose effects cannot be noticed) unfound. These leak detection methods are time consuming, expensive, partially effective and are only applied periodically. New

methods must be found that address these shortcomings. Continuous monitoring could be used to locate a leakage when it occurs (rather than later when a leakage audit is performed).

A poorly calibrated pipe network restricts an authority's ability to model that network correctly. Decisions regarding the future of the pipe network cannot be correctly made without adequate models. Traditionally, calibration of pipe networks has been achieved through a trial and error method. Such methods may produce poorly calibrated networks which, although adequately modelled for the particular conditions of the calibration, cannot accurately model the pipe network when subjected to different conditions.

Inverse analysis provides the basis for the location of leakage and calibration in pipe networks. Through the use of observable data (pressure measurements), leakage parameters, such as lumped leakage coefficients, and calibration parameters, such as friction factors, can be estimated through inverse analysis. Previous research has concentrated on steady state methods for leak detection and calibration. These have produced limited success. An innovative way to improve results is to use unsteady state (or transient) methods. This type of technique is referred to as "inverse transient analysis." There are many advantages exhibited by transient analysis over steady state analysis. Some of these include a greater availability in the amount of measured data, the creation of a better posed inverse problem, an increase in the associated confidence of an inverse solution and the prospect of continuous monitoring.

In this thesis, methods are developed for inverse transient analysis and experimentally verified. This research confirms the usefulness of inverse transient analysis for leak detection. Further improvements to the inverse transient method and the transient model are also presented. These improvements are detailed in the scope of the research in Section 1.2.

1.1 Objectives of the Research

The ultimate goal of the research into inverse transient analysis is its successful application in the field. Two main objectives to achieve this goal are (1) improvement of the inverse transient method as applied to leak detection and calibration, including finding optimal measurement site configurations, optimal numbers of measurement sites, optimal lengths of measured data and improvements to the numerical algorithm and (2) perhaps more important, is the application in actual pipe networks. Controlled laboratory experimental and field testing are necessary. To date, there has been little experimental verification of the inverse transient method ever performed. An aim of research presented in this thesis is to provide one of the first ever experimental verifications of the inverse transient method on a well controlled pipeline. First, it is necessary to be able to model accurately the behaviour of fluid in a pipeline under steady and transient conditions without leakage. Because frictional effects of unsteady flow are different than those of steady flow, the transient model must contain an unsteady friction formulation. Such formulations are not well grounded in theory and experiment so a necessary priority is to verify experimentally at least one such model.

1.2 Scope of the Research

The scope of the research presented in this thesis can be best observed through a description of each chapter. Chapter 2 contains a review of current technology for leak detection and calibration. Chapter 3 defines the basic transient simulation model used in this study. Many different formulations are presented concerning the implementation of such a model in pipe networks with and without leakage. Original work is presented for the inclusion of variable position valves in a method of characteristics implicit solution scheme and nodal and non-nodal leakage formulations. Chapter 4 considers many aspects for the solution of the inverse problem. New work presented in Chapter 4 is concerned with enhancing the efficiency of the minimisation algorithm used in the inverse transient technique. The focus is on the calculation of the Jacobian (and hence the gradient and Hessian), which requires the greatest computational effort. Two new methods for the calculation of the Jacobian together with a different derivation of an

adjoint method shows promising results. One method (the fast analytic method) is particularly effective. A new method for calculation of the temporal and spatial derivatives of velocity is formulated. Chapter 5 contains material pertaining to the initial conditions used in the inverse transient method and especially their effect on the calculation. Chapter 6 considers genetic algorithms for leakage detection and calibration. Concepts from that chapter are used elsewhere in this thesis. Genetic algorithms are used to solve the inverse transient problem with the introduction of new genetic operators. Chapter 7 answers many questions concerned with the application of the inverse transient method including: How many measured sites are necessary for effective implementation of the inverse transient method? Where are the best locations for these measurement sites? How much measurement data are necessary? and What confidence is to be associated with the parameters gained from the inverse transient method? These questions are answered using performance indicators and the use of two case studies. Chapters 8 and 9 consider the modelling of advanced frictional effects in unsteady flow, i.e., unsteady friction. A review of previous unsteady friction models is presented in Chapter 8. Chapter 9 contains formulations for improved unsteady friction models. A new methodology is presented for the description of unsteady flow events that is helpful for diagnosis of potential problems in unsteady friction models. These models are extended to low Reynolds numbers in which the initial flow is turbulent and unsteady. An exact solution is presented for these models. Through examination of the velocity profile before a transient event, relationships for the unsteady friction coefficients are derived. Experiments on a laboratory pipeline verify both the unsteady friction models and the inverse transient method. Chapter 10 is a basis for future experimental analysis. It defines the layout of the experimental pipeline. Various aspects, including measurement, calibration, data filtering and boundary condition usage are considered. Chapters 11 and 12 present results for the experimental verification of unsteady friction models and the inverse transient method. The verification of the unsteady friction models is important because any verification of the inverse transient method relies on it. Chapter 11 presents verification of unsteady friction models for initially laminar and turbulent flows, fast and slow valve closures and different types of events. That verification indicates where various unsteady friction models are valid. Chapter 12 contains experimental verification of inverse transient analysis for leak detection. Leakage is detected for three different leak sizes for three different valve closure speeds. Various aspects relating to the behaviour of

leakage, modelling of leakage and leak detection strategies are discussed. Finally, conclusions and recommendations of the research presented in this thesis are made in Chapter 13.

Chapter 2

Review of Leak Detection and Calibration Techniques

2.1 Introduction

Leak detection and calibration in pipelines and pipe networks has been the focus of research for over a hundred years. The efficiency of a pipe network can be defined in terms of the amount of fluid it leaks. Although water loss due to leakage is a waste of a precious and scarce resource, the extra water needed to satisfy demands (to replace the lost water due to leakage) is often required to be pumped as well as treated. The extra pumping and treatment costs can be large. Leaks can often be a precursor to catastrophic pipe failure. For pipelines carrying fluids such as oil, early detection and location of leakage can lessen environmental consequences. Not all of the effects of leakage are detrimental to a water pipeline or pipe network. An example is the decrease in water age causing improved water quality, however the negative effects outweigh the positive effects. This chapter provides a review of previous methods of leak detection and calibration in pipe networks.

2.2 Previous Methods of Leak Detection

In most countries, water is a finite resource and leaks deplete that store, which usually results in a higher cost of water to the consumers. The detection of leaks can also find unauthorised use of water whereby people are stealing this valuable resource. In pipe networks that transport potentially hazardous fluids, the detection of leaks can stop or minimise contamination of the environment. Leaks can be a precursor to failure of pipes which can cause loss of supply and, in some cases, property. Many different techniques exist to discover leaks and find their locations; most come from the field of oil and gas where the consequences of leaks are the most severe.

Preventative measures can be applied so that leaks (and bursts) do not occur in the first place. It is widely known that regions of higher pressure in a pipe network experience higher leakage rates and numbers of leaks (Vela *et al.*, 1991 and 1995). Some researchers have focused their attention towards the minimisation of pressure in pipe networks while still complying with consumer demands using such methods as variable speed pumps (Wood and Reddy, 1995), and the setting of PRV's (Germanopoulos, 1995). Other methods look at replacing pipes before they break. The bursts and background method (Lambert, 1994) can provide probabilities on whether certain pipes are likely to break. Another probabilistic method listens to tendons breaking in prestressed concrete pipes to gauge the likelihood of failure (Rasmussen, 1997).

The Asian Development Bank (1993) has estimated that water leakage in distribution networks in Asia range from 8% in Singapore to 62% in Dhaka, Bangladesh. The average loss for a water network is 36%, which is large and is unacceptable in any country.

Due to the nature of this research the main emphasis of the literature survey, with regards to leak detection, is on transient techniques for leak detection and location.

2.2.1 Traditional and Hydrostatic Methods

The traditional method for the detection and location of leaks is to test each length of pipe as it is laid. Testing involves pressurising the pipe with a low-cost liquid, usually water. Pressure sensors are then positioned in the pipe to see if there is any reduction of pressure that could result from the presence of a leak. The method cannot easily be performed with existing pipe networks because it is hard to isolate sections of the network, the pipes are buried and due to disruptions to the consumers.

Another traditional technique is the mass balance technique. Here the inflow to the network and the outflow from the network are measured and compared. If there are differences, there must be leaks. Mass balance is a cost effective way to show the existence of leaks. A drawback is that the number and location of leaks remain unknown, thus tracking them down can be a problem. Another drawback is that flow meters are not usually accurate (Laverty, 1979). The mass balance technique has been reformulated for unsteady state conditions by Liou (1994), who concluded that leakage could not be accurately detected when the flow was not steady.

A good indicator of the presence of leakage, that is commonly in use, is minimum night flows (Campbell, 1970). By comparing minimum night flows to day flows, a simple notion of how the network is functioning can be deduced. Theodoulides *et al.* (1995) suggested that the minimum night flow is the maximum bound for leakage in a network. Cole (1979) states that when the ratio between night flows and day flows is 30% or less, serious leakage in a network is unlikely. For ratios of 50% and higher leakage is probable and may be a serious concern.

Currently, the most popular methods of leak detection use flow direction indicators, tracer gases (Heim, 1979), subsurface radar, earth resistivity changes, infrared thermography (Weil *et al.*, 1994), listening devices or geophones (Waller *et al.*, 1969) and odorant and radioactive tracers. These methods are both expensive and time consuming. Recently a refinement to the use of listening devices has increased their effectiveness. Fantozzi and Villa (1992) used a cross-correlator that can pin-point the location of leakage along a pipeline. Listening devices are set up at either end of the

pipe then use mathematical cross-correlation procedures (using acoustic properties) that can determine where the leak is located.

2.2.2 Inverse Steady State Leak Detection

Pudar and Liggett (1992) carried out the use of inverse steady state analysis to find leaks. The objective of their work was to see if leaks could be found using a minimal amount of steady state pressure and flow data measured in a network. The approach behind the analysis was to set up the steady state equations and include a leak area at certain nodes. An orifice equation was applied to calculate flow from each leak due to pressure difference across the leak area. An objective function was created that was equal to the sum of the squares of the differences between measured and calculated pressures and flows. Then a minimisation process was used to determine the leak areas, which was adjoint-based, that also simultaneously found the sensitivities for all leak parameters in the network.

Pudar and Liggett (1992) also saw the need to test if the amount of data made the problem underdetermined or overdetermined, a major consideration if the practical implementation of steady state calibration is possible. A small network and then a larger network were analysed using this method with the results showing that inverse steady state analysis was not well posed for the leak detection problem. Pudar and Liggett (1992) concluded that inverse steady state leak detection would only be well posed if there were massive, accurate data for a system. If accurate knowledge of the friction factors was not known, leaks could not be determined.

Baghdadi and Mansy (1988) presented an approach for locating leaks based on steady state conditions and Bernoulli's equation. Experimental results were presented using different shaped leak orifices (circular and rectangular) and different leak locations. The results were mixed with only small errors present in the location of a leak. The effect of leak orifice geometry was found to be small.

Carpentier and Cohen (1991) used an approach not unlike Pudar and Liggett (1992) and applied it to an actual water distribution network in France. After first calibrating the

system they then searched for leaks that were created by opening fire mains. After intensive testing, the detection of leaks was not acceptable with most of the leaks being hidden through lack of data measuring stations. Their results reinforce the view of Pudar and Liggett (1992) that enormous data sets were needed if steady state analysis was going to viable for leak detection in real networks.

Liou (1994) presented an unsteady state method where a mass imbalance between nodal points could be inferred from the governing unsteady state equations. This technique is related to steady state mass balance that has been used to determine whether or not a leak is occurring between two points. Unfortunately, Liou (1994) concluded that this technique was not accurate enough to find leaks under water hammer conditions.

2.2.3 Acoustical Leak Detection

The acoustical method uses the correlation between acoustic velocity and pressure in a liquid filled pipeline to detect leaks. It has been used to test the integrity of pipelines in the oil and gas field (Hough, 1988). The manner in which this technique is applied is to position at one end of the pipeline a pressure gauge and a few metres apart from it a sound transmitter. The sound transmitter generates signals in the range of 2 to 1,000 Hz with an amplitude of about 1 kPa. The signal travels down the pipe to a transducer that detects and records the signal. Using the time difference between the outgoing and incoming signals, the acoustic velocity can be calculated. Readings of both pressure and acoustic velocity are then taken at about half hour intervals so a graph can be drawn. If there are no leaks, the acoustic velocity curve will mimic the pressure curve, if there is a leak, the acoustic velocity curve will kink, and not correlate with the pressure curve. The leakage rate can also be estimated based on the difference between the acoustic velocity and the pressure and the measured pressure change.

The advantage in using this technique is that no temperature measurement is needed, unlike other hydrostatic methods (especially for gas pipelines) where multiple temperature readings are needed to check if the pressure drops can be attributed to temperature drops. Also, the equipment can be set up at just one end of the pipeline meaning that data telemetry is not needed for long pipes and pipes do not need to be

excavated to install sensors. Disadvantages of this technique are few, but some are important. One of the most important is that the presence of air in a pipeline creates gross error. Air reduces the bulk modulus of elasticity and density of the liquid and can cause large reductions in the acoustic velocity. Another disadvantage is that suspended solids in the liquid increase the density of the liquid and cause a decrease in the acoustic velocity. This decrease in the acoustic velocity can be initially interpreted as leakage. The final problem is that noise detected by the transducer (which may be generated from the environment or the electrical equipment) can also be interpreted as leakage. While this method detects the presence of a leak, the location cannot be determined.

2.2.4 Point Analysis

Point analysis technology is a process that compares the statistical properties of a series of pressure and velocity measurements before and after the occurrence of a leak. An analyser accumulates these sets of measurements then executes a series of mathematical tests to prove or disprove the hypothesis that a leak has occurred. This technique has been successfully implemented on a fuel transfer pipeline by Farmer *et al.* (1988) with promising results.

Point analysis has many advantages, one is that the leak detection can be performed in real time; thus continuous monitoring can decrease the time taken to discover a leak. A reduced number of pressure and velocity measurements are required and these can be acquired using standard industry instrumentation, hence this technique can be implemented at low cost. A disadvantage of the technique is that noise seriously inhibits the statistical process and, in field tests, some leaks were not discovered.

2.2.5 Transient Analysis Method for Leak Detection

The transient analysis method is associated with the response generated by the existence of a leak somewhere in a pipeline. It deals with the measurement and associated interpretation of pressure waves that reflect off the leak. The key lies in initiating a pressure wave by closing a valve and then recording the changes in pressure at a

position just downstream from that valve. Jönsson (1995) identified three effects that a leak has on the resultant pressure response. The first is when the initial negative pressure wave reaches the leak. The leak will produce a reflection that can be seen when the pressure wave arrives back at the valve. The time required for the wave to travel to the leak and back to the valve can be measured and the location of the leak calculated as

$$x_L = \frac{a\Delta t_L}{2} \qquad (2.2.1)$$

where a = the wave speed, x_L = distance to the leak from the valve and Δt_L = time difference between the generation of the initial wave and the reflected wave

The second effect is the distortion in the shape of the oscillatory pressure peaks and troughs that occur after the main pressure rise has occurred. This distortion is due to the interaction of the leak with the pressure wave (and secondary waves) and can be used to find the location of the leak based on the shape of the distortion. The third and last effect is a reduction in the amplitude of the oscillatory pressure response after the main pressure rise has occurred, due to the leakage.

Experimental results have been obtained using this method (Jönsson, 1995), and the technique has had reasonable success in locating the position of a leak. Jönsson (1995) is continuing studies with proposed experiments in the laboratory and in the field.

2.2.6 Transient Simulation Approach

The occurrence of a leak produces an effect on the pressures in a pipeline. The difference between the pressures with and without the leak is called a discrepancy pattern, which is specific to that leak. If a leak's discrepancy pattern can be recognised, then the occurrence of that leak can be detected. Liou and Tian (1995) proposed two algorithms for the identification of such a pattern.

The first method is called an initial value problem or a Cauchy algorithm. The initial value problem uses the characteristic grid (Figure 2.1) but, rather than analyse from the bottom to the top of the grid (increasing time), the analysis is performed from the sides

of the grid. The pressure values at the ends of the pipe are known but initial values along the pipe are unknown. It is possible to calculate across the grid (i.e. points E and G are used to calculate F in Figure 2.1) thus avoiding the problem of having to know the initial conditions along the pipe. This method uses continuous measurements at each end of a pipe to set up a basis for calculation of the future flows and pressures. Actual measurements of pressure head and flow are continuously taken at some time after these previous measurements. If these actual measurements are not the same as the calculated ones a discrepancy arises and a leak has occurred.

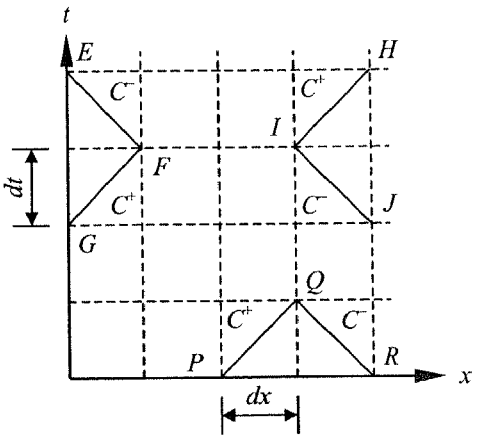

Figure 2.1 Characteristic *x*-*t* Plane Grid

Discrepancies in pressure due to leaks have certain patterns that distinguish them from discrepancies due to other sources. Liou and Tian (1995) concluded, after numerous numerical simulation runs, that there are four main effects that predict the onset of a leak. These are:

1. Immediate and simultaneous rise in the discrepancies (measured values minus calculated ones) of inlet head and inlet flow.
2. Immediate rise in the discrepancy of outlet head and immediate and simultaneous falls in the discrepancy of outlet flow.
3. The timing of sudden changes of discrepancy traces at the pipe ends must indicate the location of the leak.
4. The sum of the number of consecutive time steps with discrepancies at the pipe ends equals the number of computational reaches (i.e. the length of the discrepancy must last longer than L/a—must traverse the length of the pipe).

However, a single discrepancy might be due to measurement error rather than a leak. The problem of unexplained noise in experimental trials makes the identification of discrepancies harder, causing the fourth effect never to be satisfied. To solve this problem the fourth step can be replaced with:

4. The rise and fall for all three discrepancy traces must persist for a number of consecutive time steps.

Using larger numbers of consecutive time steps improves the reliability of this technique. One problem, although, is the amplification of false discrepancy patterns (noise).

The second method of Liou and Tian (1995) is a time-marching algorithm, which avoids the noise amplification problem. The second method varies from the first algorithm in that the initial boundary values are known. Thus, points forward in time can be calculated by the usual method of characteristics (i.e. points P and R are known in Figure 2.1, point Q can be calculated from P and R). Measurements are made of the steady state flow and pressures before any leak has occurred. All of the future flows and pressures can be calculated using the method of characteristics. After subsequent numerical trials, a number of conditions can be characterised that show a leak discrepancy pattern:

1. An inlet head discrepancy fall and simultaneous inlet flow discrepancy rise.
2. An outlet head discrepancy fall and a simultaneous outlet flow discrepancy fall.
3. The timing of the occurrence of discrepancies at the pipe ends should indicate the location of the leak.

The nature of the time-marching method reduces the build up of the discrepancies because noise does not propagate backwards in time. As a result, leakage detection requires a longer time to identify compared to using the Cauchy algorithm. Field data was used from a 225 km petroleum product pipeline in which a leak was simulated at a distance of 98 km downstream from the inlet. The pipeline was divided into twelve computational reaches. After the implementation of the two techniques (including the

application of a noise filter to the raw data), the leak was found to be in the computational reach corresponding to a distance from the inlet of between 93 km and 113 km. Liou and Tian (1995) concluded that the time-marching and Cauchy algorithms could detect leaks with noisy data and large pipe friction factors.

There are inherent problems with the use of measured boundary conditions in the Cauchy algorithm that were not addressed by Liou and Tian (1995). Section 10.6 demonstrates the problems of transient analysis when using measured boundary conditions.

2.2.7 The Inverse Transient Method for Leak Detection

The inverse transient technique, which is the focus of research presented in this thesis, is new in many ways, but old in others. The main focus of the method is to back calculate leak parameters and leak locations using data gathered from a pipe network under transient conditions. This approach is much like the inverse steady state leak detection and calibration techniques. An advantage over steady state methods is that a greater amount of data can be found in a smaller amount of time. Also, rather than just a mass imbalance being used for leak location determination, the interaction of a leak with a pressure wave under unsteady conditions is used. Liggett and Chen (1994) were the first to develop the inverse transient technique for simultaneous leak detection and calibration. The most common tool used to achieve results was a nonlinear solver (such as the Levenberg-Marquardt algorithm) in conjunction with a transient solver. Given measurement data, these algorithms could solve for unknown parameters. The leakage was described in terms of a lumped discharge coefficient and leaks were assumed to occur only at nodal positions in the modelled network. Koelle *et al.* (1996) considered non-nodal leaks modelled by the transient solver. Non-nodal leak location has also been studied by Wang *et al.* (1991) who showed close links to work by Koelle *et al.* (1996). Their method of transient analysis was based upon the pole method of analysis (rather than the MOC), but the method that was used to find a non-nodal leak is applicable regardless of the computational algorithm. A relationship for determining where a leak occurs (shown at position x_L in Figure 2.2) was formulated.

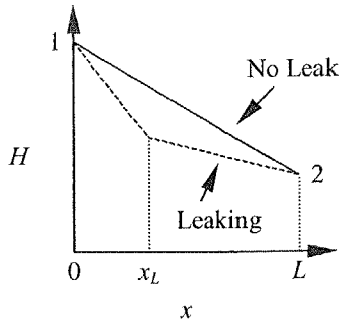

Figure 2.2 Pressure Distribution Along a Pipeline, Wang *et al.* (1991)

A leak location is found by the comparison of the partial derivatives of pressure head with respect to displacement between conditions with and without leakage. The leak location is given by

$$x_L = \frac{\sum_{k=1}^{N_{TS}} a_k b_k}{\sum_{k=1}^{N_{TS}} a_k^2} \qquad (2.2.2)$$

where k = the time step number, N_{TS} = maximum number of time steps, L = the pipe length, x_L = leak location and the parameters a_k and b_k are defined as following

$$a_k = \left(\left.\frac{\partial H_k}{\partial x}\right|_f^1 - \left.\frac{\partial H_k}{\partial x}\right|_n^1 \right) - \left(\left.\frac{\partial H_k}{\partial x}\right|_f^2 - \left.\frac{\partial H_k}{\partial x}\right|_n^2 \right) \qquad (2.2.3)$$

$$b_k = \left(\left.\frac{\partial H_k}{\partial x}\right|_n^2 - \left.\frac{\partial H_k}{\partial x}\right|_f^2 \right) L \qquad (2.2.4)$$

The superscript position markers 1 and 2 refer to ends of the pipe, and the subscript position markers n and f refer to the normal condition and the faulty (leaking) condition respectively. There appears to be promise in these methods, although they are far from developed for commercial use.

2.3 Previous Methods of Calibration

For many years, many people have put forward various methods for calibrating a pipe network. The majority of this work has been based on steady state analysis. Recently,

extended period steady state analysis and inverse steady state analysis has improved results.

What does calibration mean? Shamir and Howard (1977) stated that "calibration consists of determining the physical and operational characteristics of an existing system and determining the data that when input to the computer model will yield realistic results." Walski (1983) defined calibration as "a two step process consisting of: (1) Comparison of pressures and flows predicted ... with observed pressures and flows for known operating conditions, i.e. pump operation, tank levels, pressure reducing valve (PRV) settings; and (2) adjustment of the input parameters for the model to improve agreement between observed and predicted values."

The next issue is how do you calibrate models and what are the most important parameters to calibrate? The AWWA Research Committee on Water Distribution Systems (1974) stated that "... the major source of error in simulation of contemporary performance will be in the assumed loadings distributions and their variations." Whereas Eggener and Polkowski (1976) stated "... the weakest piece of input information is not the assumed loading condition, but the pipe friction factor." Cesario (1980) remarked that data on pump lifts, valve positions, and pressure reducing valve settings should be modified first (being more important), while water demand loadings and pipe friction factors should be the last variables to be changed. The answer is that they are all important, and a model is only calibrated if all parameters are close to their true values; otherwise the model will not perform adequately under different water demand loading conditions or circumstances (given that the model is adequate).

Current calibration techniques use optimisation methods, such as genetic algorithms, to search for optimum pipe friction values that fit measured data readings (Savic and Walters, 1995). Transient analysis has recently been found to yield superior results for calibrated values (Liggett and Chen, 1994).

2.3.1 Traditional Calibration Methods

In industry, a typical method for the estimation of pipe friction factors, if measurement data are not available, is to use standard tables and manufacturer's data. Pipes are often characterised by age, type and size. Estimates of pipe friction factors are determined using pressure testing where pressure gauges and flow meters are used in conjunction with steady state analysis to calculate the friction factor for an individual pipe. This information may then be used to make informed estimates for the other pipes that share similar age, type and size characteristics. The problem with this approach is that two similar pipes (having similar age, type and size) may still not have similar friction factors. A reason for this difference is that all pipes are subjected to different flows, pressures, water quality and usage characteristics that affect the diameters (tuberculation) or friction factors at different rates with long term usage. Because of these non-uniform factors, assembling pipes into groups will generally not lead to a well calibrated model that adequately reproduces the actual network responses for different water demand loading conditions.

2.3.2 Inverse Steady State Calibration

Walski (1983) used inverse steady state analysis for automated pipe friction calibration. He proposed an implicit method that does not rely on trial and error to obtain good estimates of parameters. In considering previous attempts, different formulations of the steady state equations were used to enhance their solution. Donachie (1974) and Shamir and Howard (1968) adopted a nodal formulation of the pipe network equations, whereas Gofman and Rodeh (1981) used loop equations. The solution of the equations was for unknown headlosses for each pipe element and hence the friction factors could be inferred.

Ormsbee and Wood (1985) linearised the nonlinear friction term in the steady state equations and solved for new estimates of the friction factors to obtain improved estimates of the linearised friction terms. The linearisation of the friction term (thus creating an explicit solution) and use of better friction factor estimates improved pipe network calibration. In his 1989 paper, Ormsbee also included extended period analysis

from different tank levels with good results. This approach depended on the initial guesses of the friction factors with an iterative method subsequently used to find them. The results were acceptable but Ormsbee noted that "due to the complex nature of the calibration problem and the large number of decision variables, many solutions are possible." He meant that there may not be a unique solution to the calibration problem, thus the "solution" might be dependent upon initial guesses. The non-uniqueness of the solution is one major reason why steady state analysis is not a particularly successful method for calibration.

Walski (1983) used fire flows for calibration. The basic formulation was performed using the nodal method of the steady state pipe network equations. Walski (1983) used lumped groups of pipes to skeletonise real networks to reduce the number of pipe friction factors to be determined. Initial guesses were put forward, then a better set of estimates for the parameters were found using the analysis. Only one such iteration was done; results using this method were poor.

Walski (1986) continued his research into calibration with field tests of his method where he calibrated a complicated water distribution network with 271 nodes, 307 pipes and 9 pressure reducing valves. His results were mixed, as were many other studies based on a similar approach, such as those by Rahal *et al.* (1980), Bhave (1988), Ormsbee and Chase (1988) and Boulos and Wood (1990).

The major problems encountered by researchers were the non-uniqueness of solution and the insensitivity of the headloss equations near the solution. Due to the large number of calibration parameters and the low numbers of measurements, the calibration problem was ill posed. In an attempt to overcome these problems Lansey (1988) and Lansey and Basnet (1991) minimised the sum of the squares of the differences between calculated and measured flows, pressures, and tank levels at nodes over a number of different demand loading cases. Constraining the parameters between some minimum and maximum values reduced the feasible solution space. Examples of parameters included the roughness coefficients, valve coefficients, pressure reducing valve coefficients and the nodal demands. The minimisation technique was an adaptation of nonlinear programming based on the generalised reduced gradient method. Iteration concluded when the Kuhn-Tucker optimality conditions were reached. Lansey and

Basnet (1991) applied this technique to three different networks, a 21 pipe network, a system taken from KYPIPE User's Manual (Wood, 1980) and an example from Ormsbee (1989). The objective of these examples was to test how this technique would perform for underdetermined cases, measurement errors in field data and lumping of parameters. The conclusions of this research were that the techniques performed well with little error caused by the initial guesses. However, some systems still required around 100 iterations to converge to the final solutions. Lansey and Basnet (1991) concluded with this view: "... even a stable calibration model algorithm cannot overcome the lack of good or sufficient data. There can be numerous alternate optima, even in comparatively simple systems, and a wide variation of values of parameters that have a significant impact on the system." The extension of the method of least squares was explored by Carpentier and Cohen (1991), and then and Datta and Sridharan (1994). The use of sensitivity analysis and the weighting of the least squares greatly improved the speed of convergence and accuracy for locating an optimal solution. The objective function (the weighted sum of the squares of the differences) used by Datta and Sridharan (1994) is

$$E = \sum_{L=1}^{N_L} \sum_{i=1}^{M_L} W_L(i) \left[\nu_L^m(i) - \nu_L(i) \right]^2 \quad \text{.....(2.3.1)}$$

where $W_L(i)$ = weight associated with i^{th} observation for water demand loading condition L, $\nu_L^m(i)$ = observed value of variable i for loading condition L, $\nu_L(i)$ = computed value of variable i for loading condition L, M_L = number of measurements for L^{th} loading condition and N_L = number of loading or operating conditions. The weighting for each squared difference is

$$W_L(i) = \left[\frac{1}{\nu_L^m(i)} \right]^2 \quad \text{.....(2.3.2)}$$

The weighted least squares method was applied to a network of principal water transmission mains of Bangalore in Southern India. In this network there were 87 nodes and 94 elements. Also, there were three operating conditions to be analysed. The results of the analysis confirmed that the objective function had indeed found a set of parameters that could match the computed values of pressure and flow to the actual values. The weighted least squares approach took about 50 iterations compared with the Lansey and Basnet (1991) algorithm, which took about 100 iterations. The problem

still existed that the computed parameters may be a local optimum solution rather than a global solution.

The application of genetic algorithms to the calibration problem is a new approach to an old problem. In any calibration of a network there is a need to find optimal parameters that when used in simulation yield results that model network behaviour accurately. The approach taken by Savic and Walters (1995) was to minimise the sum of the squares of the measured and predicted flows and pressures in a network under steady state conditions using genetic algorithms. The genetic algorithm technique is a powerful search tool that uses evolutionary based principles to find optimal solutions. Like the evolution of a species, the genetic algorithm initially starts out with a population of potential solutions. Each solution is represented as a string of bits analogous to a human chromosome. The fitness of each member of the population is calculated to determine how good a particular solution is. Three main operators are used to generate a new population of solutions. The operators are reproduction, crossover and mutation, each having an analogy with population genetics. Through the evolution of many generations, the population will tend towards an optimal solution. The power of this algorithm is in its ability to search though large search spaces without having to enumerate completely every solution within the entire search space (in fact only a tiny portion of the search space needs to be evaluated). This property is well suited to the calibration problem in large water distribution systems.

In 1995 Savic and Walters undertook a case study of a network for Pynes Water Treatment Works in the Danes Castle Zone of Exeter City (Devon, UK). The network consisted of 197 nodes and 242 elements. Three loading cases were used in the hydraulic analysis of networks, including a peak demand, average (day) demand, and minimum (night) demand. As with any real network, the actual friction values were not precisely known, thus no comparison of predicted and actual friction factors could be made. The only comparison made was the difference between friction factors as estimated by an engineering consulting firm and the friction factors calculated from the genetic algorithm. The differences were large, which meant that the traditional method of calibration was over and under estimating the magnitudes of friction factors. Another measure of comparison was the fit was between the predicted and measured

flows and pressures. That comparison showed that the genetic algorithm did indeed improve the fit to the data.

Genetic algorithms have recently been incorporated into software packages for the sole purpose of calibration of water networks. The University of Kentucky offers an auxiliary module named KYCAL (network calibration module; Wood, 1996) that can be used as a supplement to their KYPIPE3 (steady state network tool) program. This package allows the use of genetic algorithms to find an optimal set of pipe friction factors, valve settings, tank levels, demand distribution, and other data that better represents the performance of actual networks.

2.3.3 The Inverse Transient Technique for Calibration

The field of steady state calibration has been routinely considered over the years, with most of the opinion suggesting that it will never result in an entirely satisfactory calibration. Steady state flow rarely exists in a water distribution network, so the question may be posed as to why calibrate using steady state relationships when solving for friction factors?

An alternative approach to this problem is to use unsteady state or transient analysis to calibrate pipe networks. The method of characteristics can be used in conjunction with measured data to find pipe friction factors. Liggett and Chen (1994) have outlined a theoretical framework for this technique. An objective function was used to test the fit of calculated data to artificially generated measured data containing no error. Root finding and optimisation methods were implemented to solve iteratively for the pipe friction parameters. The sensitivity of various properties of the pipe network can also be found to show which known parameters (pipe length, pipe diameter, valve setting, etc.) affect the discovery of the unknown parameters (that may also include leak areas and wave speeds in addition to friction factors). Results showed that the computation time for a solution of pipe friction factors by inverse transient calculations was faster, and the uniqueness of this solution was much improved compared to steady state analysis. For a complete explanation of the inverse transient technique see Chapter 4.

2.4 Summary

A number of different techniques for leak detection and calibration have been presented in this chapter. Both steady state and transient based techniques have been discussed. It is the opinion of the author that steady state methods can never really yield confident solutions for either leak detection or calibration of pipe networks due to the non-uniqueness of the solution and low sensitivity of parameters combined with inherent errors in the data. Transient techniques, with a wealth of data at their disposal, display the prospect of greater certainty in parameter calibration and leak detection.

2.5 Direction of Study

The objective of the research presented in this thesis is to investigate a number of different aspects of calibration and leak detection techniques. Inverse transient analysis is one of the most promising methods for calibration and leak detection. The use of transient data is expected to outperform methods that use steady state data alone. A number of questions arise with respect to the successful application of inverse transient analysis. These include how many measurement sites are adequate, what length (in time) of measured data is required and where the measurement sites should be located. This thesis provides methods to answer these questions. The inverse transient method requires a transient model that is able to simulate transient conditions for a specified amount of time. Research in this thesis provides new ideas and models for the simulation of turbulent unsteady pipeline flow. These models are called unsteady friction models. An experimental program for the verification of these unsteady friction models and leak detection using the inverse transient method is also presented. These methods constitute an important step for the eventual application of the inverse transient method in the field.

Chapter 3

Network Transient Analysis Including Leakage

3.1 Introduction

Douglas *et al.* (1985) define unsteady (i.e. transient) flow as "...a state in which flow parameters are time-dependent, governed by partial differential equations requiring, in their complete form, numerical methods of solution...." The objective of this Chapter is to develop an accurate simulation model for transient events in pipe networks with leakage. Previous transient simulation models are extended using valve and non-nodal leak formulations implemented both explicitly and implicitly.

3.2 Governing Unsteady Equations

Unsteady state flow in a closed conduit can be described by equations derived from the principles of conservation of mass and linear-momentum. Both of these principles can be expressed as control volume integrals (Eq. 3.2.1). Eq. 3.2.1 is also known as the Reynolds transport theorem for an extensive fluid property (e.g. mass, momentum, energy). Although not shown in this section, a detailed derivation of this equation can be found in Streeter and Wylie (1983).

$$\frac{dN}{dt} = \frac{\partial}{\partial t}\int_{C\vartheta} \eta\rho \, d\vartheta + \int_{CS} \eta\rho \mathbf{v} \cdot d\mathbf{A} \quad \text{.....(3.2.1)}$$

where N = any advected, extensive fluid property (such as mass, momentum or energy), η = N per unit mass, ϑ = volume, ρ = fluid density, $\mathbf{v}$ = velocity vector and $\mathbf{A}$ = outflow area in the form of a vector that points in the direction of the outward normal to the control surface. The integrals are taken over the control volume ($C\vartheta$) and the boundary of the control volume, the control surface (CS). The dot product of $\mathbf{v}$ and $d\mathbf{A}$ is equal to zero when there is no inflow or outflow of property N.

Eq. 3.2.1 is described in words by Streeter and Wylie (1983) as: "... the time rate of increase in N within a system is just equal to the time rate of the property N within the control volume (fixed relative to a set of co-ordinate axes xyz) plus the net rate of efflux of N across the control volume boundary."

3.2.1 The Equation of Continuity

The first of the two equations that describe unsteady state flow is the equation of continuity. This equation is formed by applying the principle of conservation of mass to the integral control volume equation (Eq. 3.2.1). In this case, let N be the total mass of the system (m) and therefore η equals 1, thus forming

$$0 = \frac{dm}{dt} = \frac{\partial}{\partial t}\int_{C\vartheta} \rho d\vartheta + \int_{CS} \rho \mathbf{v} \cdot d\mathbf{A} \quad \text{.....(3.2.2)}$$

Eq. 3.2.2 is applied to the control volume shown in Figure 3.1. The result is the one-dimensional expression Eq. 3.2.3.

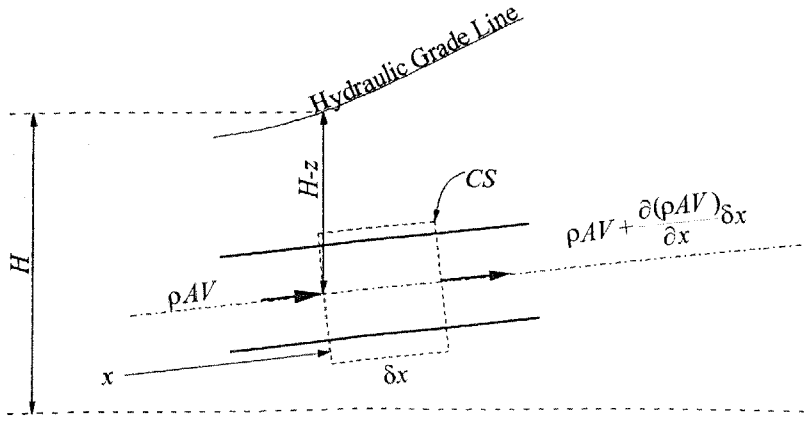

Figure 3.1 Control Volume for Continuity Equation

The integral along the control surface can be evaluated as

$$0 = \frac{\partial}{\partial t}\int_A \rho \delta x dA + \left(\int_A \rho v dA + \frac{\partial}{\partial x}\int_A \rho v dA \delta x \right) - \int_A \rho v dA \quad \text{.....(3.2.3)}$$

Simplification of Eq. 3.2.3 produces

$$0 = \frac{\partial}{\partial t}\int_A \rho \delta x dA + \frac{\partial}{\partial x}\int_A \rho v dA \delta x \quad \text{.....(3.2.4)}$$

Using the definition of average velocity, $V = \frac{1}{A}\int_A v dA$, the integrals are evaluated forming a partial differential equation

$$0 = \frac{\partial(\rho A \delta x)}{\partial t} + \frac{\partial(\rho A V)}{\partial x}\delta x \quad \text{.....(3.2.5)}$$

In the first term, δx is not a function of t and can be cancelled from both terms on the right hand side of Eq. 3.2.5 forming

$$0 = \frac{\partial(\rho A)}{\partial t} + \frac{\partial(\rho A V)}{\partial x} \quad \text{.....(3.2.6)}$$

The equation of continuity has been derived but is not in a form to provide a numerical solution. The partial derivatives are expanded and divided by $A\rho$ yielding

$$\frac{1}{A}\left(\frac{\partial A}{\partial t} + V\frac{\partial A}{\partial x}\right) + \frac{1}{\rho}\left(\frac{\partial \rho}{\partial t} + V\frac{\partial \rho}{\partial x}\right) + \frac{\partial V}{\partial x} = 0 \quad \text{.....(3.2.7)}$$

The general expression for the decomposition of a total derivative into its partial components is shown in Eq. 3.2.8. The derivative of displacement with respect to time is replaced with the velocity.

$$\frac{d}{dt} = \frac{\partial}{\partial t} + \frac{dx}{dt}\frac{\partial}{\partial x} = \frac{\partial}{\partial t} + V\frac{\partial}{\partial x} \quad \text{.....(3.2.8)}$$

The definition of the total derivative d/dt is arbitrary. Eq. 3.2.8 is sometimes called a substantial or full derivative, however a directional derivative is a more accurate description. In Eq. 3.2.8, d/dt may be thought of as a directional derivative along the line $dx/dt = V$. Although the term "directional" is more accurate, the term "total" is more commonly used and is hereby used in this thesis. The partial derivatives of the cross-sectional area and density in Eq. 3.2.7 can be reduced to

$$\frac{1}{A}\frac{dA}{dt} + \frac{1}{\rho}\frac{d\rho}{dt} + \frac{\partial V}{\partial x} = 0 \quad \text{.....(3.2.9)}$$

in which the *d*/*dt* are total derivatives defined by Eq. 3.2.8. The bulk unit modulus is defined as

$$K = \frac{dp}{d\rho/\rho} \quad \text{.....(3.2.10)}$$

Eq. 3.2.10 is rearranged to find an expression relating pressure to the density.

$$\frac{1}{\rho}\frac{d\rho}{dt} = \frac{1}{K}\frac{dp}{dt} \quad \text{.....(3.2.11)}$$

The stress-strain relationship of the pipe wall can relate the term containing the derivative of the cross-sectional area to the pressure within the pipe. The term containing the derivative of the pipe area defines the following relationship (Street and Wylie, 1983):

$$\frac{dA}{dt} = \frac{D}{2eE}\frac{dp}{dt}\frac{D}{2}\pi D \quad \text{.....(3.2.12)}$$

where D = pipe diameter, e = pipe wall thickness and E = Young's modulus of elasticity of the pipe wall material. If the cross-sectional area (in terms of the diameter) is the moved to the other side of the equation, it becomes

$$\frac{1}{A}\frac{dA}{dt} = \frac{D}{eE}\frac{dp}{dt} \quad \text{.....(3.2.13)}$$

Substituting Eqs. 3.2.11 and 3.2.13 into Eq. 3.2.9 yields a relationship containing only variables of pressure and velocity,

$$\frac{1}{K}\frac{dp}{dt}\left(1+\frac{K}{E}\frac{D}{e}\right)+\frac{\partial V}{\partial x} = 0 \quad \text{.....(3.2.14)}$$

It is convenient to express this equation in terms of the wave speed, a, where the wave speed is defined as

$$a^2 = \frac{K/\rho}{1+(K/E)(D/e)} \quad \text{.....(3.2.15)}$$

Thus, the expression becomes

$$\frac{1}{\rho}\frac{dp}{dt}+a^2\frac{\partial V}{\partial x} = 0 \quad \text{.....(3.2.16)}$$

The derivative of pressure is expanded into its component partial derivatives according to Eq. 3.2.8 and the equation is divided by the gravitational acceleration (g). The final form of the one-dimensional continuity equation is

$$\frac{1}{g\rho}\left(\frac{\partial p}{\partial t}+V\frac{\partial p}{\partial x}\right)+\frac{a^2}{g}\frac{\partial V}{\partial x} = 0 \quad \text{.....(3.2.17)}$$

3.2.2 The Equation of Motion

In a similar procedure to the formation of the equation of continuity, the equation of motion is formed using the integral control volume equation (Eq. 3.2.1). In this case, Newton's second law is implied with N being the momentum of the system and η equalling the velocity. The result is Eq. 3.2.18 where the derivative of the momentum equals the sum of forces acting on the control volume in the x-direction.

$$\sum F = \frac{dN}{dt} = \frac{\partial(\rho AV\delta x)}{\partial t} + \frac{\partial(\rho AV^2)}{\partial x}\delta x \quad \text{.....(3.2.18)}$$

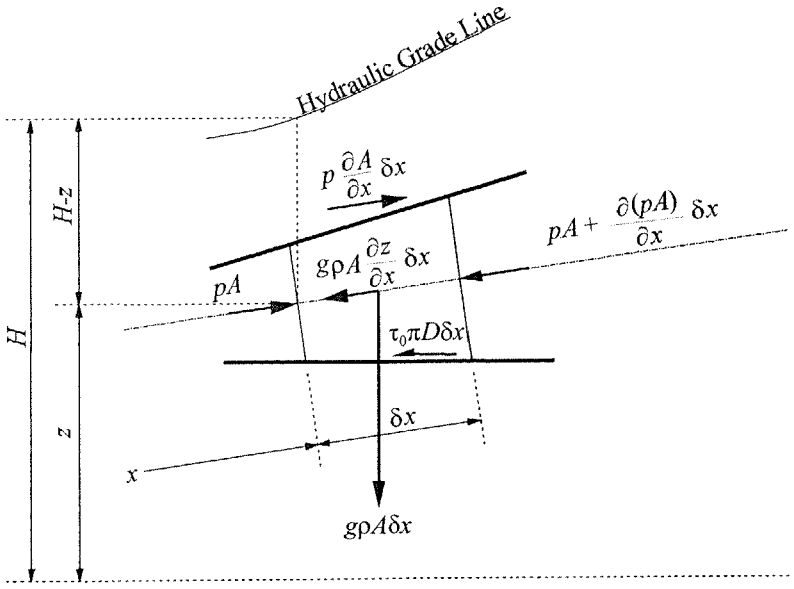

Figure 3.2 Free-Body Diagram of Forces Acting on a Control Volume for Equation of Motion

After examination of Figure 3.2, the sum of forces (pressure, gravity and shear) acting on the control volume in the x direction (along the centreline of the pipe) is described by

$$\sum F_x = pA - \left[pA + \frac{\partial(pA)}{\partial x}\delta x\right] + p\frac{\partial A}{\partial x}\delta x - g\rho A\frac{\partial z}{\partial x}\delta x - \tau_0\pi D\delta x \quad \text{.....(3.2.19)}$$

Finally, Eqs. 3.2.18 and 3.2.19 can be combined and divided by δx to form the one-dimensional equation of motion (Eq. 3.2.20). Eq. 3.2.20 is sometimes referred to as the equation of momentum and is in the so-called *conservative* form.

$$\frac{\partial(\rho AV)}{\partial t}+\frac{\partial(\rho AV^2)}{\partial x}+A\frac{\partial p}{\partial x}+g\rho A\frac{\partial z}{\partial x}+\tau_0\pi D=0 \quad \text{.....(3.2.20)}$$

An additional cancellation can be performed if the first two terms in Eq. 3.2.20 are partially expanded,

$$V\left[\frac{\partial(\rho A)}{\partial t}+\frac{\partial(\rho AV)}{\partial x}\right]+\rho A\frac{\partial V}{\partial t}+\rho AV\frac{\partial V}{\partial x}+A\frac{\partial p}{\partial x}+g\rho A\frac{\partial z}{\partial x}+\tau_0\pi D=0 \quad \text{.....(3.2.21)}$$

The square bracketed term is zero from the equation of continuity, Eq. 3.2.6. The equation of motion, now in the *non-conservative* form, is

$$\rho A\frac{\partial V}{\partial t}+\rho AV\frac{\partial V}{\partial x}+A\frac{\partial p}{\partial x}+g\rho A\frac{\partial z}{\partial x}+\tau_0\pi D=0 \quad \text{.....(3.2.22)}$$

The distinction between the two forms of the equation, Eqs. 2.3.20 and 3.2.22, becomes important when applying numerical methods. The shear stress on the pipe wall for turbulent steady flow may be related to the velocity and the Darcy-Weisbach friction factor (Eq. 3.2.23). The steady state friction assumption, although not accurate for unsteady flows, is commonly made and is discussed at length in Chapters 8 and 9 (under unsteady friction).

$$\tau_0=\frac{\rho fV^2}{8} \quad \text{.....(3.2.23)}$$

Substituting the steady state friction relationship (Eq. 3.2.23) into Eq. 3.2.22 and dividing through by $g\rho A$ yields

$$\frac{1}{g}\left(\frac{\partial V}{\partial t}+V\frac{\partial V}{\partial x}\right)+\frac{1}{g\rho}\frac{\partial p}{\partial x}+\frac{\partial z}{\partial x}+\frac{fV|V|}{2gD}=0 \quad \text{.....(3.2.24)}$$

in which the absolute value sign is introduced so that the friction shear acts in the direction opposite to the direction of flow. Eq. 3.2.24 is a simplified form of the one-dimensional equation of motion.

3.2.3 Simplification of Governing Equations

In engineering practice hydraulic head and flow are commonly used, however, Eqs. 3.2.17 and 3.2.24 describe unsteady state fluid flow in conduits in terms of pressure and velocity. Pressure and elevation can be replaced with the hydraulic head, H, using the definition

$$H = \frac{p}{g\rho} + z \quad \text{.....(3.2.25)}$$

where z equals the elevation of the centreline of the pipe at point x. Differentiation of the hydraulic head (Eq. 3.2.25) with respect to distance along the pipe and time is given in Eqs. 3.2.26 and 3.2.27 respectively.

$$\frac{\partial H}{\partial x} = \frac{1}{g\rho}\frac{\partial p}{\partial x} + \frac{\partial z}{\partial x} \quad \text{.....(3.2.26)}$$

$$\frac{\partial H}{\partial t} = \frac{1}{g\rho}\frac{\partial p}{\partial t} \quad \text{.....(3.2.27)}$$

Substituting Eq. 3.2.27 into Eq. 3.2.17 and Eq. 3.2.26 into Eq. 3.2.24 modifies the equations of continuity and motion to

$$\frac{\partial H}{\partial t} + V\frac{\partial H}{\partial x} + \frac{a^2}{g}\frac{\partial V}{\partial x} = 0 \quad \text{.....(3.2.28)}$$

$$\frac{1}{g}\frac{\partial V}{\partial t} + \frac{V}{g}\frac{\partial V}{\partial x} + \frac{\partial H}{\partial x} + \frac{fV|V|}{2gD} = 0 \quad \text{.....(3.2.29)}$$

The introduction of the volumetric flow rate, $Q = VA$, changes Eqs. 3.2.28 and 3.2.29 to the simplified form of the governing equations for unsteady flow in pipelines.

$$\frac{\partial H}{\partial t} + V\frac{\partial H}{\partial x} + \frac{a^2}{gA}\frac{\partial Q}{\partial x} = 0 \quad \text{.....(3.2.30)}$$

$$\frac{1}{gA}\frac{\partial Q}{\partial t} + \frac{V}{gA}\frac{\partial Q}{\partial x} + \frac{\partial H}{\partial x} + \frac{fQ|Q|}{2gDA^2} = 0 \quad \text{.....(3.2.31)}$$

A number of assumptions were made in the derivation of the governing unsteady equations. The assumptions are briefly summarised below:

- Liquid flow is one-dimensional and homogenous. Total head does not change in the axial direction. Density is constant in the axial direction. Although velocity varies in the axial direction in a real pipe, it is assumed uniform and the average value is used.
- The pipe is full at all times, i.e. no column separation or boiling where pressure is lower than vapour pressure.
- Both the pipe and fluid are assumed to deform according to linear elasticity.
- Friction is evaluated according to the Darcy-Weisbach equation, and unsteady friction loss is assumed to be the same as steady flow friction loss.

3.2.4 *Properties, Boundary Conditions and Initial Conditions*

Hyperbolic partial differential equations, such as the unsteady flow equations, describe the propagation of disturbances through media. The speed of disturbance propagation, the wave speed a, was defined previously in Section 3.2.1. The propagation path of a disturbance, defined as a line in Figure 3.3, is called a *characteristic*. The slope of the characteristic line for a disturbance propagating in the positive x direction is $V+a$ and is called the positive characteristic (C^+). Conversely, propagation in the negative x direction (of slope $V-a$) is called the negative characteristic (C^-).

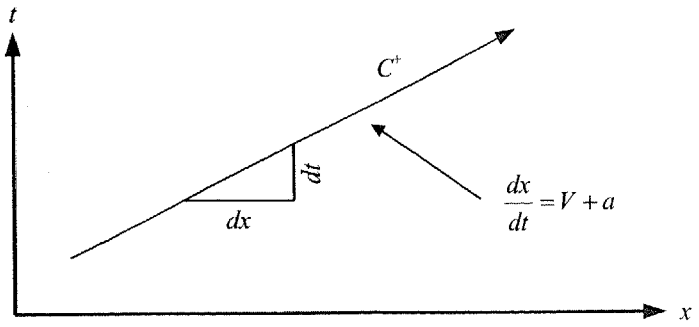

Figure 3.3 A Positive Characteristic

The wave nature of the hyperbolic partial differential equations promotes solution along characteristic lines. Solution methods, such as the method of characteristics (Section 3.3.2), transform the partial derivatives into directional derivatives that are valid along characteristic lines.

The pattern of the characteristics describes the dependence and influence of a point in the x-t plane. Considering the point P in Figure 3.4, its *range of influence* extends forward in time bounded by positive and negative characteristic lines that originate from P. A point that lies outside of the range of influence of point P is ignorant of any disturbance at point P.

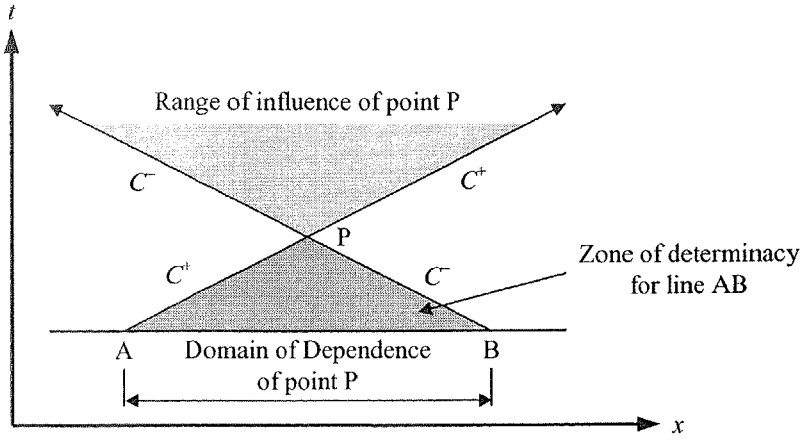

Figure 3.4 Domain of Dependence and Range of Influence

A complete solution will exist at point P if data along the initial line AB are specified. The line AB is called the *domain of dependence* of point P. In fact, data along the initial line AB will determine a complete solution within the *zone of determinacy* of AB. On the other hand, point P is dependent on conditions defined by the extension of characteristic lines backward in time from point P. A disturbance originating from outside the domain of dependence of point P has no effect on point P.

Initial and boundary conditions are necessary for the solution of partial differential equations. For unsteady flow equations these conditions define the edges of the solution region in the x-t plane (Figure 3.5). The initial conditions consist of specified dependent variables along an "initial boundary," usually the line $t = 0$. Boundary conditions, which may change with time, are specified along characteristic boundaries, usually lines where $x =$ constant. A point from which two characteristic lines stem when moving forward in time is called an "initial point." If one characteristic line stems from a point moving forward in time and one characteristic line stems from a point moving backward in time, that point is a "boundary point."

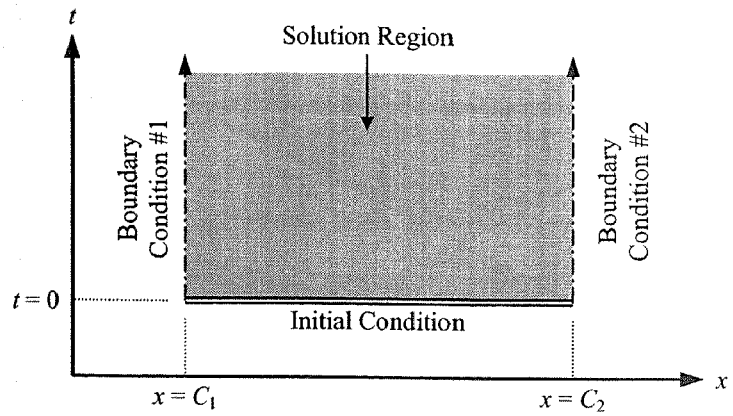

Figure 3.5 Initial and Boundary Conditions

3.3 Solution of the Governing Equations

Currently the most popular technique used to solve the governing unsteady state equations is the method of characteristics. Other methods used in the past, with varying accuracy and difficulty, are rigid water column theory (Fox, 1977), the graphical method (Fox, 1977) and the finite difference method (Sánchez-Bribiesca, 1981; Arfaie and Anderson, 1991). Little work has been performed using a finite element method but, for completeness, it yields solutions close to those of the finite difference method (Watt *et al.*, 1980). The graphical method was historically the most commonly used but, with the advent of high-speed computers, has fallen into disuse. A reason for the shift from the graphical method is that the method of characteristics is faster, better suited for network applications and easier to program into a computer.

3.3.1 Numerical Methods

Numerical methods must be used to solve the governing equations. There are two main types of numerical methods for the solution of hyperbolic partial differential equations: the method of characteristics, which is based on the characteristic form of the equations, and finite difference methods, which are based on the equations as is. Both methods may be solved on a fixed grid in the *x-t* plane (Figure 3.6). The details of the method of characteristics are discussed in Section 3.3.2.

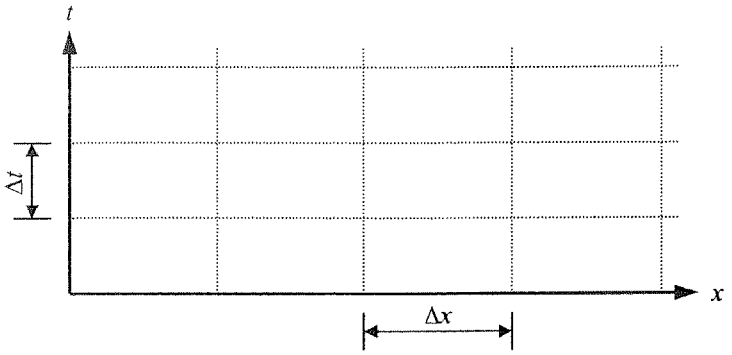

Figure 3.6 Fixed Grid in the *x-t* Plane

For a finite difference method, the partial derivatives are approximated by finite differences on the fixed grid. There are two types of finite difference scheme: an explicit scheme where the equations are arranged to solve one point at a time, and an implicit scheme where a group of advanced points are solved using simultaneous equations including the unknowns at all points in the group. Errors are introduced through the approximation of partial derivatives by finite differences. A difference scheme is stable if errors do not grow with time and unstable if the errors grow as time progresses. Different stability criteria exist for the two schemes (Liggett, 1975), however the main stability criterion is the Courant-Friedrich-Lewy (CFL) stability criterion. The CFL stability criterion does not apply as much to a numerical method as to the fixed grid. The Courant number, C_r, is defined as

$$C_r = \frac{a\Delta t}{\Delta x} \qquad \text{.....(3.3.1)}$$

where Δx and Δt are the grid spacing in the space and time directions respectively. The CFL stability criterion states that if $C_r \leq 1$ then errors due to the approximation of the partial derivatives will not grow with time. Although the CFL stability criteria does not apply to the method of characteristics (because the characteristics are followed), the definition of the Courant number is useful when describing interpolations between computational units in Section 3.7.

3.3.2 *The Method of Characteristics*

The method of characteristics (MOC) is one of the simplest and most computationally efficient techniques used to solve the unsteady state pipe flow equations. The basis for this method is the ability to transform the partial differential equations (for which no closed-form solution is available) into ordinary differential equations that apply along specific lines called characteristics. The MOC, being an extremely flexible solution scheme, can easily implement networks, boundary conditions, non-pipe elements, and friction. In addition, the MOC is good at handling discontinuities such as those caused by very fast valve closure. To begin, the two simplified governing unsteady state pipe flow equations are rewritten as

$$L_1 = \frac{\partial H}{\partial t} + V\frac{\partial H}{\partial x} + \frac{a^2}{gA}\frac{\partial Q}{\partial x} = 0 \quad \text{.....(3.3.2)}$$

$$L_2 = \frac{1}{gA}\frac{\partial Q}{\partial t} + \frac{V}{gA}\frac{\partial Q}{\partial x} + \frac{\partial H}{\partial x} + \frac{fQ|Q|}{2gDA^2} = 0 \quad \text{.....(3.3.3)}$$

A linear combination of Eqs. 3.3.2 and 3.3.3 is made using the multiplier λ as

$$\lambda L_1 + L_2 = \frac{1}{gA}\left[\frac{\partial Q}{\partial t} + \left(V + \lambda a^2\right)\frac{\partial Q}{\partial x}\right] + \lambda\left[\frac{\partial H}{\partial t} + \left(V + \frac{1}{\lambda}\right)\frac{\partial H}{\partial x}\right] + \frac{fQ|Q|}{2gDA^2} = 0 \quad \text{.....(3.3.4)}$$

The bracketed terms are reduced to form the directional derivatives of Q, $\frac{dQ}{dt} = \frac{\partial Q}{\partial t} + \frac{dx}{dt}\frac{\partial Q}{\partial x}$ and H, $\frac{dH}{dt} = \frac{\partial H}{\partial t} + \frac{dx}{dt}\frac{\partial H}{\partial x}$ in which dx/dt is defined to be

$$\frac{dx}{dt} = V + \lambda a^2 = V + \frac{1}{\lambda} \quad \text{.....(3.3.5)}$$

Solving for the multiplier λ in Eq. 3.3.5 gives

$$\lambda = \pm\frac{1}{a} \quad \text{.....(3.3.6)}$$

Therefore, the derivative of the displacement with respect to time becomes

$$\frac{dx}{dt} = V \pm a \quad \text{.....(3.3.7)}$$

Eq. 3.3.7 represents the propagation velocity of a disturbance in a pipe. The wave speed, a, is constant to a high degree of approximation according to Eq. 3.2.15 but the presence of the velocity (V) in Eq. 3.3.7 causes the characteristic lines to be curved. A further assumption can be made if the wave speed is large compared to the velocity

($V << a$). In water pipelines the wave speed is typically three orders of magnitude larger than the velocity. Making this approximation results in

$$\frac{dx}{dt} = \pm a \quad \text{.....(3.3.8)}$$

Eq. 3.3.8 defines two lines along which the variables are differentiated, one with the positive sign and one with the negative sign. These lines are called characteristics. The C^+ characteristic is defined as $dx/dt = a$ and the C^- characteristic is defined as $dx/dt = -a$. The equations become

$$C^+: \quad \frac{a}{gA}\frac{dQ}{dt} + \frac{dH}{dt} + \frac{fQ|Q|a}{2gDA^2} = 0 \quad \text{along} \quad \frac{dx}{dt} = +a \quad \text{.....(3.3.9)}$$

and

$$C^-: \quad \frac{a}{gA}\frac{dQ}{dt} - \frac{dH}{dt} + \frac{fQ|Q|a}{2gDA^2} = 0 \quad \text{along} \quad \frac{dx}{dt} = -a \quad \text{.....(3.3.10)}$$

Eqs. 3.3.9 and 3.3.10, referred to as *compatibility equations* (similar to the Riemann invariants in open channel flow), can be used to solve for points in the x-t plane as shown in Figure 3.7.

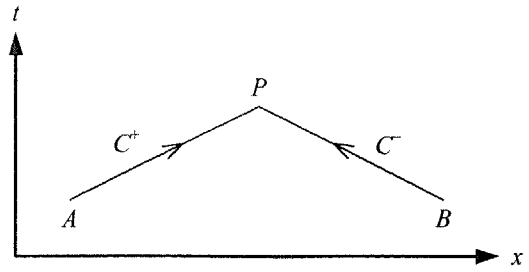

Figure 3.7 Characteristic Lines for a Solution on the *x-t* Plane

The solution of the compatibility equations is achieved by integrating Eqs. 3.3.9 and 3.3.10 along their respective characteristic lines.

$$C^+: \quad \frac{a}{gA}\int_A^P dQ + \int_A^P dH + \frac{fa}{2gDA^2}\int_A^P Q|Q|dt = 0 \quad \text{.....(3.3.11)}$$

$$C^-: \quad \frac{a}{gA}\int_B^P dQ - \int_B^P dH + \frac{fa}{2gDA^2}\int_B^P Q|Q|dt = 0 \quad \text{.....(3.3.12)}$$

The equations are integrated using a finite difference approximation for the friction term (the last term), which restricts results to a small increment in time and space

C^+: $$\frac{a}{gA}(Q_P - Q_A) + (H_P - H_A) + \frac{fQ_{AP}|Q_{AP}|a\Delta t}{2gDA^2} = 0 \quad \text{.....(3.3.13)}$$

C^-: $$\frac{a}{gA}(Q_P - Q_B) - (H_P - H_B) + \frac{fQ_{BP}|Q_{BP}|a\Delta t}{2gDA^2} = 0 \quad \text{.....(3.3.14)}$$

where Q_{AP} and Q_{BP} are flow rates in the friction terms, representing symbolic flows that indicate an "average" flow along the characteristic during period Δt. Finally, the friction terms in Eqs. 3.3.13 and 3.3.14 are written by defining the grid spacing so that $\Delta x = a\Delta t$, producing

C^+: $$\frac{a}{gA}(Q_P - Q_A) + (H_P - H_A) + \frac{fQ_{AP}|Q_{AP}|\Delta x}{2gDA^2} = 0 \quad \text{.....(3.3.15)}$$

C^-: $$\frac{a}{gA}(Q_P - Q_B) - (H_P - H_B) + \frac{fQ_{BP}|Q_{BP}|\Delta x}{2gDA^2} = 0 \quad \text{.....(3.3.16)}$$

Integration of the friction term between two points in the characteristic grid requires an approximation of the behaviour of the flow between those points. Historically, the friction has been approximated using the flow from the previous time step (Fox, 1977; Jaeger, 1977), such as for the friction term in Eq. 3.3.15,

$$\frac{fQ_{AP}|Q_{AP}|\Delta x}{2gDA^2} \approx \frac{fQ_A|Q_A|\Delta x}{2gDA^2} \quad \text{.....(3.3.17)}$$

Arfaie *et al.* (1993) found that the best representation of the flow (for low to moderate velocity cases) in the pipe friction term was given by a linear approximation (Eq. 3.3.18), which was first suggested by Wylie (1983) and Ivanov and Bournaski (1983), that uses the flow at one end of the interval in one of the Q-terms and the flow at the other end in the other Q-term. This relationship can be derived using integration by parts.

$$\frac{fQ_{AP}|Q_{AP}|\Delta x}{2gDA^2} \approx \frac{fQ_P|Q_A|\Delta x}{2gDA^2} \quad \text{.....(3.3.18)}$$

For high velocity cases, Arfaie *et al.* (1993) suggested a non-linear approximation by Propson (1972) (a variant of the Streeter (1972) centred implicit method). Eq. 3.3.19 effectively averages flows at either end of the characteristic line and is solvable only using iteration.

$$\frac{fQ_{AP}|Q_{AP}|\Delta x}{2gDA^2} \approx \frac{f}{2gDA^2}\frac{(Q_A + Q_P)}{2}\frac{|Q_A + Q_P|\Delta x}{2} \quad \text{.....(3.3.19)}$$

Streeter and Lai (1962), amongst others, showed that steady state friction approximations do not generate a sufficient level of damping when compared to experimental results (the lack of damping is not caused by the approximation of the steady friction term but something more fundamental). Chapter 8 addresses these problems and discusses the use unsteady friction to account for the extra damping.

A simultaneous solution can be found to the two compatibility equations for conditions at an unknown point *P*, given that conditions at a previous time step are known. A grid can be formed of the small units (representing a solution of the compatibility equations) depicted in Figure 3.8. This grid is named the *characteristic grid.*

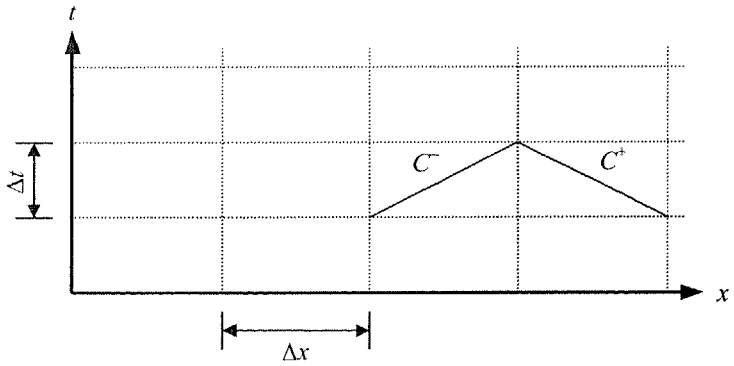

Figure 3.8 *x-t* Plane with Characteristics Grid

The characteristic grid can take two forms; either the rectangular grid or the diamond grid (Figure 3.9). Historically, the rectangular grid was in use first. It is, in fact, two separate interlaced diamond grids. For fast valve closing procedures, an error is apparent because each diamond grid (of the rectangular grid) is subjected to slightly different transient conditions. This phenomenon is called *grid separation.* The rectangular grid is, however, useful for network applications, especially when the network is to be solved using matrix techniques.

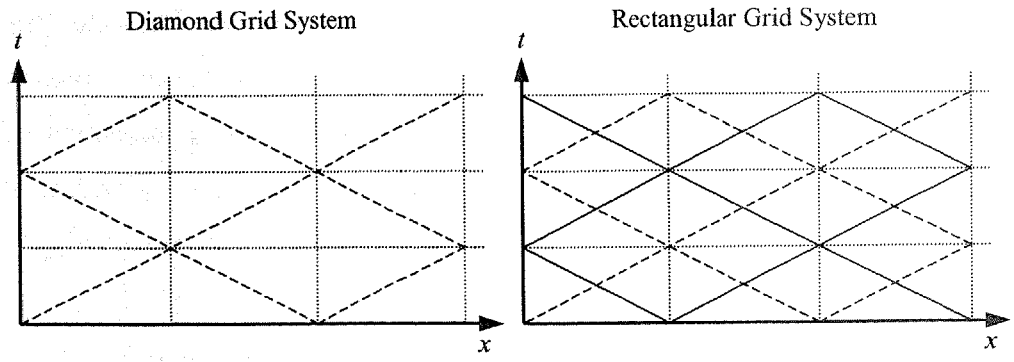

Figure 3.9 Diamond and Rectangular Grid Systems

Traditionally, the explicit MOC solution technique was the first method used to solve the characteristic equations. The term "explicit" implies that the compatibility equations can be solved explicitly and one at a time for unknowns at a single point at the advanced time line, as opposed to appearing in equations that must be solved simultaneously for a group of unknowns. The compatibility equations are rearranged to form simplified expressions Eqs. 3.3.15 and 3.3.16 (including an appropriate friction term such as Eq. 3.3.17) for the unknown conditions at P.

C^+: $$H_P = C_P - BQ_P \quad \text{.....(3.3.20)}$$

C^-: $$H_P = C_M + BQ_P \quad \text{.....(3.3.21)}$$

where C_P and C_M are constants that depend on the known conditions at the previous time step and are defined as

C^+: $$C_P = H_A + Q_A(B - R|Q_A|) \quad \text{.....(3.3.22)}$$

C^-: $$C_M = H_B - Q_B(B - R|Q_B|) \quad \text{.....(3.3.23)}$$

Two more constants, named the characteristic impedance and the characteristic resistance (denoted B and R respectively), are introduced

$$B = \frac{a}{gA} \quad \text{and} \quad R = \frac{f\Delta x}{2gDA^2} \quad \text{.....(3.3.24)}$$

For an internal node, the compatibility equations can be solved explicitly for H_P

$$H_P = \tfrac{1}{2}(C_P + C_M) \quad \text{.....(3.3.25)}$$

Q_P can be calculated using either Eqs. 3.3.20 or 3.3.21 since now H_P is known. For a boundary node, the value of one of the dependent variables is known. In the case of a constant head reservoir at the end of a C^+ characteristic, H_P is equal to the reservoir head (and therefore known) and the flow Q_P can be calculated using Eq. 3.3.22. Boundary conditions, other than a constant head reservoir, may include hydraulic devices such as valves and pumps. Considerable research has been done on boundary

conditions. Solution methods have been refined and comprehensive systems created to deal with an assortment of boundary conditions (Karney, 1984; McInnis, 1992; Wylie and Streeter, 1993).

3.3.3 The Implicit MOC Solution

In an implicit method the unknowns at a group of points, usually but not necessarily along the entire length of a pipe, are solved together using simultaneous equations, as opposed to solving for the unknowns one point at a time. For example consider Figure 3.10, an explicit MOC scheme solves for conditions at points A, B, C and D separately, whereas an implicit MOC scheme solves for conditions at points A, B, C and D simultaneously.

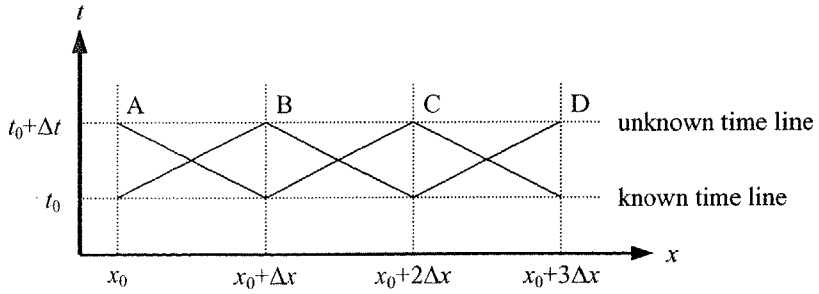

Figure 3.10 Implicit MOC Solution on *x-t* Plane

The previous section demonstrated an explicit MOC solution scheme. The implicit MOC solution scheme is formed from the compatibility equations and boundary conditions relating head and flow at a known timeline to head and flow an unknown timeline. The set of equations forms a *simultaneous system* for the calculation of the transient conditions at an advanced time line from a known time line. The general simultaneous system, expressed in matrix form, is

$$[M]\{v^*\} = \{R\} \quad \text{.....(3.3.26)}$$

where matrix $[M]$ (an sometimes called a coefficient matrix) contains the coefficients that are multiplied by the unknowns. The vector $\{v^*\}$ contains the unknown conditions (both head and flow) or the variables to be solved for at a particular time step. The final vector, $\{R\}$, contains all constants including relationships formed from known conditions. The formation of the simultaneous system is better explained using an

example. Figure 3.11 shows an example pipeline between two tanks. The pipeline is discretised into three sections. The head and flow at all nodes are known at a time $t = t_0$. The objective is to form a simultaneous system relating the head and flow at the current known time line ($t = t_0$) to an advanced unknown time line ($t = t_0 + \Delta t$).

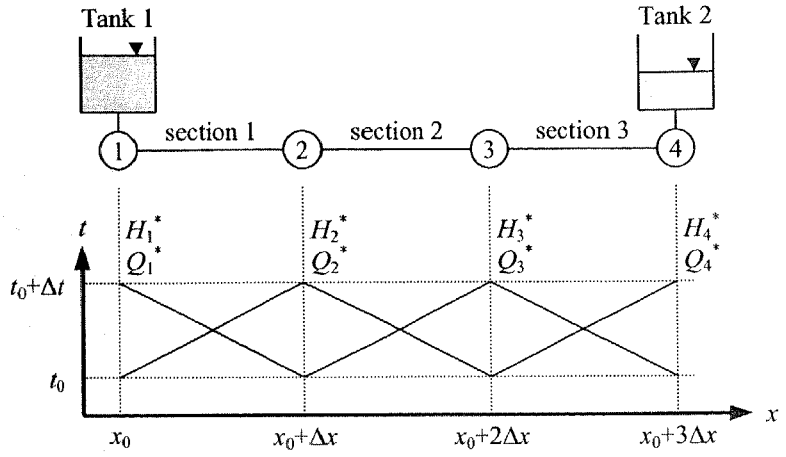

Figure 3.11 Example of Implicit MOC Solution

The unknown variables are H_1^*, Q_1^*, H_2^*, Q_2^*, H_3^*, Q_3^*, H_4^* and Q_4^*, they are superscripted with a * to signify they are at a time of $t = t_0 + \Delta t$, whereas no superscript signifies a known variable at a time of $t = t_0$. The positive and negative compatibility equations are considered for the first pipe section. The compatibility equations, including the friction term shown in Eq. 3.3.17, are

C^+:
$$\frac{a}{gA}\left(Q_2^* - Q_1\right) + \left(H_2^* - H_1\right) + \frac{fQ_1|Q_1|\Delta x}{2gDA^2} = 0 \quad \text{.....(3.3.27)}$$

C^-:
$$\frac{a}{gA}\left(Q_1^* - Q_2\right) - \left(H_1^* - H_2\right) + \frac{fQ_2|Q_2|\Delta x}{2gDA^2} = 0 \quad \text{.....(3.3.28)}$$

Moving all known terms to the right hand side of Eqs. 3.3.27 and 3.3.28 and retaining the unknown terms on the left hand side produces

C^+:
$$\left[\frac{a}{gA}\right]Q_2^* + H_2^* = \left[\frac{a}{gA}Q_1 + H_1 - \frac{fQ_1|Q_1|\Delta x}{2gDA^2}\right] \quad \text{.....(3.3.29)}$$

C^-:
$$\left[\frac{a}{gA}\right]Q_1^* + [-1]H_1^* = \left[\frac{a}{gA}Q_2 - H_2 - \frac{fQ_2|Q_2|\Delta x}{2gDA^2}\right] \quad \text{.....(3.3.30)}$$

The introduction of coefficients A, B and R simplifies Eqs. 3.3.29 and 3.3.30 to

C^+:
$$A_1^+ Q_2^* + B_1^+ H_2^* = R_1^+ \quad \text{.....(3.3.31)}$$

C^-: $$A_1^- Q_1^* + B_1^- H_1^* = R_1^- \quad \text{.....(3.3.32)}$$

where the subscripts on the coefficients A, B, and R signify the pipe section number and the superscripts the characteristic type. The boundary conditions are the tanks at both ends of the pipeline. They specify the head at each end of the pipe,

$$H_1^* = H_{T1} \quad \& \quad H_4^* = H_{T2} \quad \text{.....(3.3.33)}$$

where H_{T1} = the hydraulic head at tank 1 and H_{T2} = the hydraulic head at tank 2. The positive and negative compatibility equations for the three pipe sections and the two boundary conditions form a simultaneous system of equations representing the calculation of conditions at an advanced time line from a current (known) time line. There are eight unknowns and eight equations so a solution may be determined. The simultaneous system of equations ($[M]\{v^*\} = \{R\}$) for the example pipeline is

$$\begin{bmatrix} 1 & 0 & 0 & 0 & 0 & 0 & 0 & 0 \\ 0 & 0 & A_1^+ & B_1^+ & 0 & 0 & 0 & 0 \\ A_1^- & B_1^- & 0 & 0 & 0 & 0 & 0 & 0 \\ 0 & 0 & 0 & 0 & A_2^+ & B_2^+ & 0 & 0 \\ 0 & 0 & A_2^- & B_2^- & 0 & 0 & 0 & 0 \\ 0 & 0 & 0 & 0 & 0 & 0 & A_3^+ & B_3^+ \\ 0 & 0 & 0 & 0 & A_3^- & B_3^- & 0 & 0 \\ 0 & 0 & 0 & 0 & 0 & 0 & 1 & 0 \end{bmatrix} \begin{Bmatrix} H_1^* \\ Q_1^* \\ H_2^* \\ Q_2^* \\ H_3^* \\ Q_3^* \\ H_4^* \\ Q_4^* \end{Bmatrix} = \begin{Bmatrix} H_{T1} \\ R_1^+ \\ R_1^- \\ R_2^+ \\ R_2^- \\ R_3^+ \\ R_4^- \\ H_{T2} \end{Bmatrix} \quad \text{.....(3.3.34)}$$

The coefficient matrix in Eq. 3.3.34 is sparse, even more so for larger problems, and may be more efficiently stored in computer memory and solved using sparse matrix techniques. The solution of Eq. 3.3.34 determines all conditions at the time $t = t_0 + \Delta t$. However, if the friction term in Eq. 3.3.19 is used the simultaneous system of equations becomes nonlinear. In this case, the simultaneous system of equations is linearised, solved and the nonlinear terms updated forming an iterative procedure that proceeds until there is little change in the solution. Chen (1995) used three iterations for convergence. Numerical testing using a simple pipe network showed good convergence in three iterations. However, it is possible that some problems may require more than three iterations and, in any case, the convergence should always be checked. Although it may seem that calculations are performed more efficiently one point at a time (i.e. the explicit MOC scheme), the implicit MOC scheme reduces the complexity of equations, especially for large systems of equations such as those you would find describing a large pipe network.

3.4 Joukowsky Pressure Rise

Joukowsky (1900) found a special solution of the governing unsteady pipe flow equations, corresponding to the pressure rise after an instantaneous valve closure. He formulated an expression (and experimentally verified it) by ignoring convective terms and frictional resistance, and by assuming that the pipe is horizontal. This expression, named the Joukowsky pressure rise formula, relates the change in velocity to the resulting change in pressure (Eq. 3.4.1). The change in velocity at a location must take effect in a time that is less than the time for a reflected characteristic to return to that location. For the closure of a valve at one end of a pipeline, ΔV must occur in less than $2L/a$ seconds, where L is the length of the pipeline. The Joukowsky rise in head is

$$\Delta H = -\frac{a}{g}\Delta V \qquad \text{.....(3.4.1)}$$

For a valve closing instantaneously and completely, the resulting pressure rise is given as a function of the flow velocity just previous to closure, V_0 (Eq. 3.4.2),

$$\Delta H = \frac{a}{g}V_0 \qquad \text{.....(3.4.2)}$$

Experimentally calibrated values of flow, pressure and valve coefficients are checked using Eqs. 3.4.2 and 3.4.2 in Chapter 10.

3.5 Wave Speed in a Conduit

In the derivation of the equation of continuity (Section 3.2.1) the wave speed or celerity, a, was introduced. The wave speed is the speed at which a pressure disturbance propagates through the fluid in a pipeline relative to the velocity. The expression derived for the wave speed in Sections 3.2.1 (Eq. 3.2.15) is for a simple case. A generalised formula (Wylie and Streeter, 1993) for the wave speed in a thin walled elastic conduit (where $D/e > 25$) is

$$a = \sqrt{\frac{K/\rho}{1+\frac{K}{E}\frac{D}{e}\phi}} \qquad \text{.....(3.5.1)}$$

where K = bulk modulus of elasticity of the fluid, E = Young's elasticity of the pipe material, D = pipe diameter, e = thickness of the pipe wall and ρ is the density of the fluid. The parameter ϕ is dependent on the pipe anchoring. Table 3.1 lists a few common pipe anchorage conditions and their corresponding values of ϕ, where μ is the Poisson's ratio of the pipe material. Other expressions for wave speed exist (e.g. Karney, 1984), but Eq. 3.5.1 is most commonly used.

Table 3.1 ϕ Values for Pipe Anchorage Condition

Pipe Anchorage Condition	Parameter, ϕ
Anchored against longitudinal movement throughout its length	$1 - \mu^2$
Anchored against longitudinal movement at the upstream end and free at the downstream end	$1 - \frac{1}{2}\mu$
Expansion joints along its length	1

3.6 Networked Piping Systems

The method of characteristics is well suited to the computation of transients in pipe networks. The elements around the node, which may be pipes or sections of pipes, contain one characteristic length and are called *computational units*. Computational units are defined in the x-direction, not in the t-direction. A pipeline may be thought of as a network of computational units connected in series.

There are three different ways variables (heads and flows) may be allocated to computational units, all of which are shown in Figure 3.12. The type of transient problem determines which variable allocation type is applicable. The different variable allocation types may be thought of as the minimum allocation of variables needed to describe the transient problem at hand. The variable allocation type I is applicable for a pipeline with no leaks (used in Section 3.3.3). Each node in the in the pipeline requires one value of head and one value of flow. The variable allocation type II is applicable to pipe networks with leaks or junctions that have no losses (used in Section 3.6.1). Each node in the network requires one flow variable for each computational unit connected to the node but only one head variable (since the head is common at the node for each connecting pipe). Finally, the variable allocation type III is applicable for networks

with losses at junctions or valves specified as nodes. In this case, a head and a flow variable must be allocated for each connecting computational unit around a node.

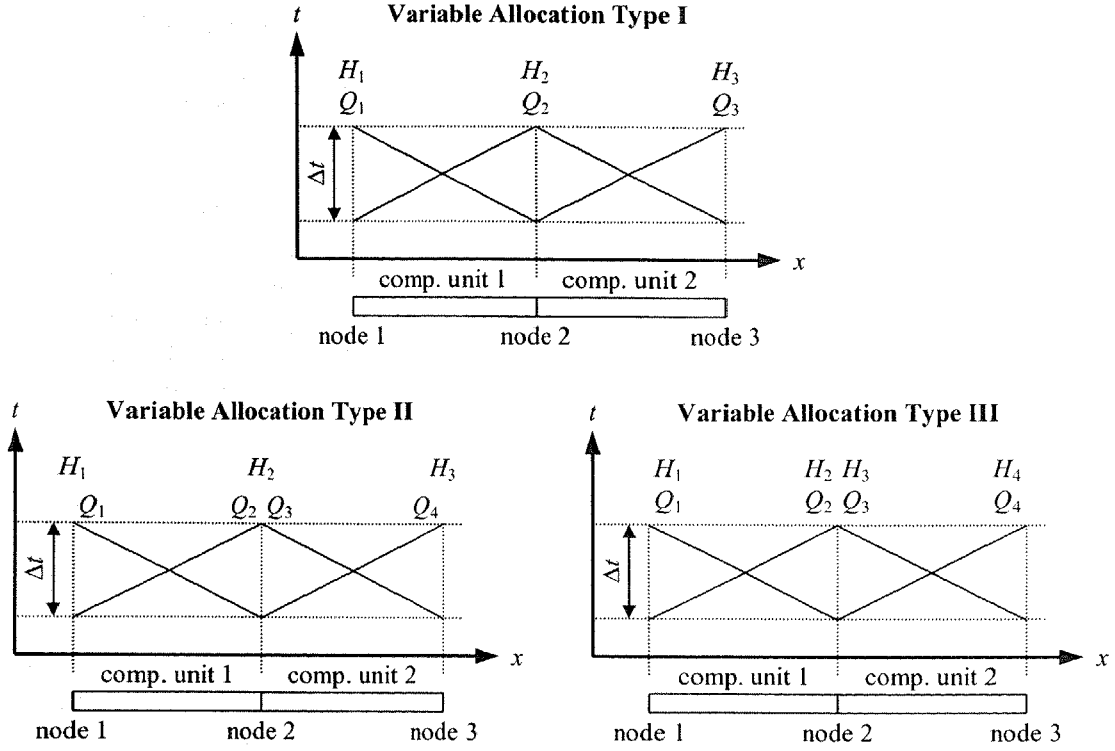

Figure 3.12 Computational Units - Variable Allocation Types

The explicit MOC solution at a junction is demonstrated using an example network junction (Figure 3.13) consisting of three pipes (or computational units). The positive x-direction in pipes 1 and 2 is defined into the junction and the positive x-direction in pipe 3 is defined out of the junction.

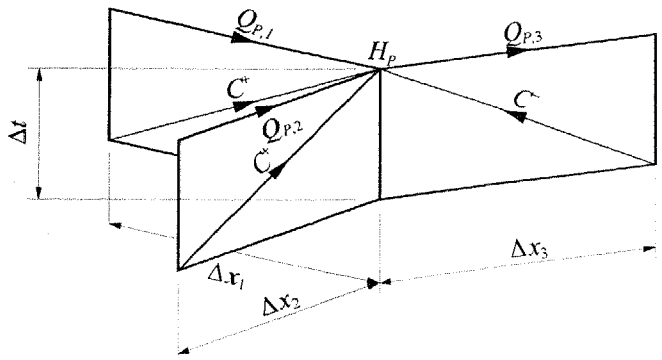

Figure 3.13 Characteristic Lines at an Example Junction

The characteristic equations are used to solve for the head at the junction and for the flow in each of the pipes (four unknowns). The two relationships used, which apply to steady state conditions as well, are the continuity of flows at the node and the common hydraulic head at the node. Eqs. 3.6.1 and 3.6.2 are the compatibility equations (defined in Section 3.3.2) for flow in pipes entering (C^+) and exiting (C^-) the node.

C^+: $$Q_{P,1} = \frac{C_{P,1} - H_P}{B_1} \quad \& \quad Q_{P,2} = \frac{C_{P,2} - H_P}{B_2} \qquad (3.6.1)$$

C^-: $$Q_{P,3} = \frac{H_P - C_{M,3}}{B_3} \qquad (3.6.2)$$

where H_P = the common head at the junction in Figure 3.13, $Q_{P,i}$ = the flow for the i^{th} pipe, B_i = the characteristic impedance in the i^{th} pipe and $C_{P,i}$ and $C_{M,i}$ are terms based on conditions at the previous time step (defined in Section 3.3.2) for the positive and negative compatibility equations for the i^{th} pipe. The continuity of flows (the flows entering a node must equal the flows exiting that node) at the node is

$$\sum_{i=1}^{4} Q_{P,i} = Q_{P,1} + Q_{P,2} - Q_{P,3} = 0 \qquad (3.6.3)$$

where flows entering a node are defined positive and flows exiting a node are defined negative. Substituting the compatibility relationships (Eqs. 3.6.1 and 3.6.2.) into the continuity equation produces

$$0 = -H_P\left(\frac{1}{B_1} + \frac{1}{B_2} + \frac{1}{B_3}\right) + \left(\frac{C_{P,1}}{B_1} + \frac{C_{P,2}}{B_2} + \frac{C_{M,3}}{B_3}\right) \qquad (3.6.4)$$

Rearranging Eq. 3.6.4 for the common hydraulic head gives

$$H_P = \frac{\frac{C_{P,1}}{B_1} + \frac{C_{P,2}}{B_2} + \frac{C_{M,3}}{B_3}}{\frac{1}{B_1} + \frac{1}{B_2} + \frac{1}{B_3}} \qquad (3.6.5)$$

Eqs. 3.6.1 and 3.6.2 can then be solved explicitly for the flows using H_P.

3.6.1 The Implicit MOC Scheme in Networks

Alternatively, an implicit MOC scheme may be used for the transient analysis of pipe networks. The implicit MOC scheme, as previously demonstrated in Section 3.3.3, solves for all heads and flows at an advanced time step simultaneously. Again, the

implicit MOC scheme for a pipe network is better demonstrated using an example. Figure 3.14 shows an example pipe network consisting of three pipes and four nodes. The system is fed by three tanks. For simplicity each pipe is considered as one computational unit. The pipe lengths, diameters and wave speeds are equal for all pipes therefore the Courant number for each computational unit is unity. No losses are assumed at the junction therefore only one variable for the head (at the junction) is required, i.e. variable allocation type I (see Figure 3.12) is used.

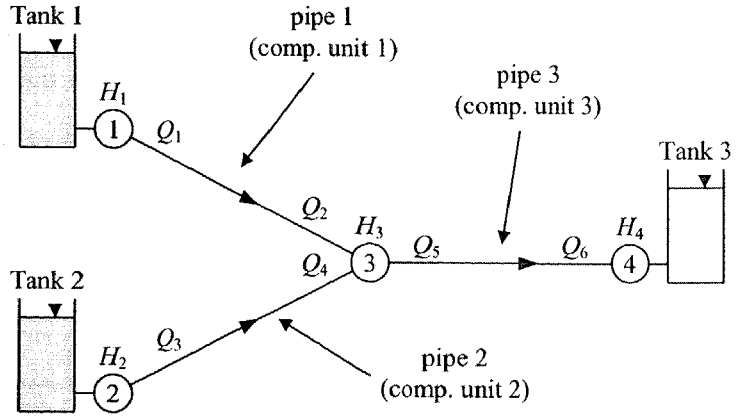

Figure 3.14 Example Pipe Network

The variables to be determined at each time step are the nodal heads H_1, H_2, H_3 and H_4 and the flows at ends of each pipe (or computational unit) Q_1, Q_2, Q_3, Q_4, Q_5 and Q_6. A superscript * denotes the variables are at an advanced time step and are unknown, no superscript means the variables are at the current time step and are known (a similar notation is used in Section 3.3.3 and Appendix A). The boundary conditions for the example pipe network are the specified heads in tanks 1, 2 and 3, given as

$$H_1^* = H_{T1}, \quad H_2^* = H_{T2} \quad \& \quad H_4^* = H_{T3} \qquad (3.6.6)$$

where the head at tanks 1, 2 and 3 is H_{T1}, H_{T2} and H_{T3} respectively. The conservation of mass applies at the junction (node 3). For the example pipe network, the flow entering node 3 must equal the flow exiting node 3 which, given in equation form, is

$$Q_2^* + Q_4^* - Q_5^* = 0 \qquad (3.6.7)$$

The final set of equations is the positive and negative compatibility equations for each computational unit. Section 3.3.3 showed how each compatibility equation may be written for a computational unit using coefficients A, B, and R. For computational unit 1 the compatibility equations are

C^+:
$$A_1^+ Q_2^* + B_1^+ H_2^* = R_1^+ \qquad (3.6.8)$$

C^-: $$A_1^- Q_1^* + B_1^- H_1^* = R_1^- \quad \text{.....(3.6.9)}$$

where the superscripts on the constants A, B and R represent the characteristic type and the subscripts denote the pipe (or computational unit) number. The compatibility equations for pipes 2 and 3 may be similarly written. The three boundary condition equations, conservation of mass at the junction equation and the compatibility equations for each of the three pipes form a set of simultaneous equations relating the head and flow at a current time step to the head and flow to an advanced time step for the example pipe network. The simultaneous system written in matrix form is

$$\begin{bmatrix} 1 & 0 & 0 & 0 & 0 & 0 & 0 & 0 & 0 & 0 \\ 0 & 0 & 0 & 1 & 0 & 0 & 0 & 0 & 0 & 0 \\ 0 & 0 & 1 & 0 & 0 & 1 & 0 & -1 & 0 & 0 \\ 0 & 0 & 0 & 0 & 0 & 0 & 0 & 0 & 0 & 1 \\ 0 & 0 & A_1^+ & B_1^+ & 0 & 0 & 0 & 0 & 0 & 0 \\ B_1^- & A_1^- & 0 & 0 & 0 & 0 & 0 & 0 & 0 & 0 \\ 0 & 0 & 0 & B_2^+ & 0 & A_2^+ & 0 & 0 & 0 & 0 \\ 0 & 0 & 0 & 0 & A_2^- & 0 & B_2^- & 0 & 0 & 0 \\ 0 & 0 & 0 & 0 & 0 & 0 & 0 & 0 & A_3^+ & B_3^+ \\ 0 & 0 & 0 & B_3^- & 0 & 0 & 0 & A_3^- & 0 & 0 \end{bmatrix} \begin{Bmatrix} H_1^* \\ Q_1^* \\ Q_2^* \\ H_2^* \\ Q_3^* \\ Q_4^* \\ H_3^* \\ Q_5^* \\ Q_6^* \\ H_4^* \end{Bmatrix} = \begin{Bmatrix} H_{T1} \\ H_{T2} \\ 0 \\ H_{T3} \\ R_1^+ \\ R_1^- \\ R_2^+ \\ R_2^- \\ R_3^+ \\ R_3^- \end{Bmatrix} \quad \text{.....(3.6.10)}$$

A more compact representation of Eq. 3.6.10 is

$$[M]\{v^*\} = \{R\} \quad \text{.....(3.6.11)}$$

where $[M]$ = a matrix of the coefficients of the unknown variables, $\{v^*\}$ = a vector of the unknown heads and flows at an advanced time step and $\{R\}$ = a vector containing other relationships not dependent on the unknown variables. Eq. 3.6.10 is sparse and is best solved using sparse matrix techniques. The implicit MOC method is flexible for describing pipe networks and complicated boundary conditions such as valves, pumps and leaks. However valves, pumps and leaks (and some friction formulations) contain nonlinear relationships, and therefore if a network contains any of these hydraulic elements then Eq. 3.6.11 represents a system of nonlinear simultaneous equations. For a nonlinear set of simultaneous equations, a successive substitution method is used. The nonlinear terms are linearised to form a set of simultaneous linear equations. After the set of simultaneous linear equations is solved, the linearised nonlinear terms are updated using the solution variables and re-solved. This iterative process is repeated until there is little change in the solution variables. A detailed example of the implicit MOC method containing a nonlinear hydraulic element (a leak) is shown in Appendix A.1.

3.7 Interpolations

Numerical methods for the simulation of transient events in a pipe network require a common time step. In real pipe networks, the wave travel time for different computational units (defined by their characteristics) are rarely the same or exact multiples of one another. Different pipe lengths and wave speeds in adjacent computational units typically cause different wave travel times. Figure 3.15 shows characteristic lines for two adjacent computation units with even and uneven wave travel times.

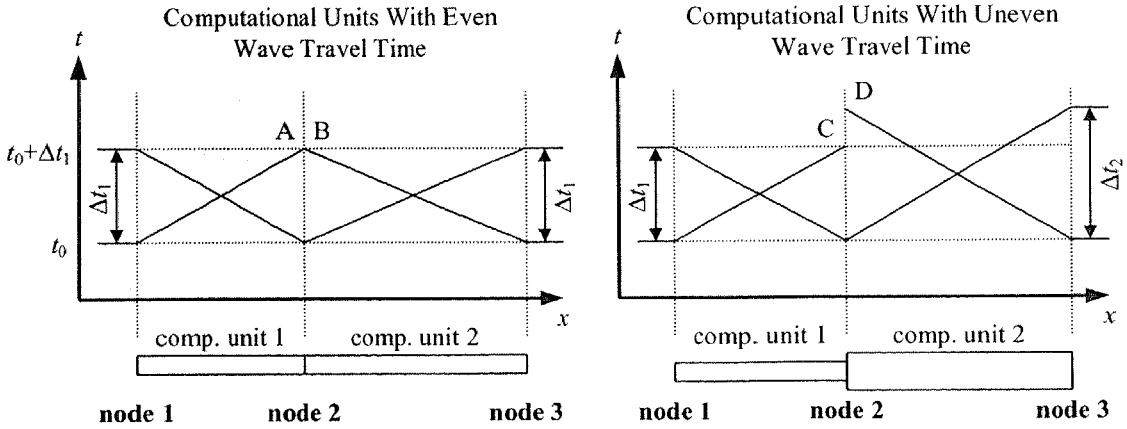

Figure 3.15 Characteristic Lines for Adjacent Computational Units With Even and Uneven Wave Travel Times

Consider the calculation of conditions at node 2 for an advanced time step $t = t_0 + \Delta t_1$. The solution is determined at the intersection of the two characteristics lines using the compatibility equations for each characteristic. For the even wave travel time case, the ends of the two characteristic lines (point A for the positive characteristic in computational unit 1 and point B for the negative characteristic in computational unit 2) meet at a common time. However for the uneven wave travel time case, the ends of the two characteristic lines (point C for the positive characteristic in computational unit 1 and point D for the negative characteristic in computational unit 2) do not meet at a common time. In order for a solution, for the uneven wave travel time case, some interpolation between points C and D must be involved. For a pipe network with

uneven wave travel times between computational units the time step Δt is chosen as the shortest wave travel time in all of the computational units. The Courant number of the i^{th} computational unit is defined as

$$(C_r)_i = \frac{a_i \Delta t}{\Delta x_i} \quad \text{.....(3.7.1)}$$

where a_i = wave speed of the i^{th} computational unit, Δx_i = length of the i^{th} computational unit and Δt = time step that is common to all computational units. For the shortest computational unit $C_r = 1$. When the Courant number of a computational unit is less than 1 interpolation is required. The minimum Courant number for a pipe network can be improved by the careful discretisation of pipes and a smaller common time step selection, however, there is a trade-off between the accuracy and computational time from these improvements. Interpolation attempts to deliver additional accuracy without having to use a smaller common time step. In following sections (Sections 3.7.1, 3.7.2 and 3.7.3), various interpolation schemes are presented.

3.7.1 Spaceline Interpolations

The spaceline interpolation method extends the characteristic line back from a point at which conditions are unknown (point *P* in Figure 3.16) to the space line of the previous time step (point *A*). An interpolation method is applied along the space line between two known points to obtain values of flow and pressure at the point *A*. Then, the MOC can be applied between points *A* and *P*. Through the use of energy relationships, Ghidaoui *et al.* (1998) showed that a linear spaceline scheme produces smaller numerical errors compared to linear timeline and wave speed adjustment schemes. Higher order interpolation schemes improve approximations of the movement of wave fronts (Sibetheros *et al.*, 1991) and thus improve results. Cubic interpolation schemes (Sibetheros *et al.*, 1991) are related to Hermite schemes and have been shown by Holly and Preissmann (1977) to be of the same accuracy (as the Hermite scheme) and unconditionally stable. A main drawback, when implementing a higher order interpolation scheme, is the need for extra data points along the spaceline for the construction of the interpolation polynomial. If spaceline interpolation is required near a boundary or a pipe junction, extra points may not be available. Furthermore, utilisation of extra points that exist outside of the domain of dependence of the variable

begin solved for degrades its solution. Higher order spaceline interpolation schemes are not well suited to pipe network analysis so a compact form of the higher order interpolation for transient analysis may be used (Verwey and Yu, 1993). Compact interpolations use spatial derivatives of pressure and flow to construct higher order interpolation schemes, thus eliminating the need for data points outside of the computational unit. A disadvantage of the compact scheme is that the spatial derivatives must also be calculated.

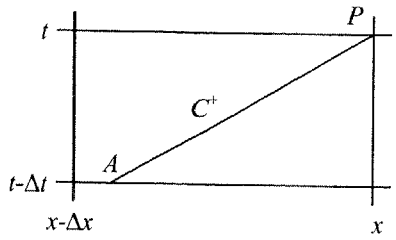

Figure 3.16 Spaceline Interpolation, *x-t* plane

3.7.2 Timeline Interpolations

The timeline interpolation scheme extends the characteristic line back from point P (at which conditions are unknown) to a point on the time line between the previous two steps (point B in Figure 3.17). Conditions at B are found by interpolation between known points on either side of B along the time line. Then, the MOC is applied from point B along the characteristic line to point P. Like spaceline interpolation, timeline interpolation has been advanced to include higher order interpolation polynomials and compact schemes (Yang and Hsu, 1990). All timeline interpolation schemes are suited to pipe networks because they do not use data from adjacent computational units. Timeline interpolation schemes need not be compact, like their equivalent spaceline schemes (because they do not use data from adjacent computational units), and therefore do not require the calculation of derivatives of the hydraulic head and flow. Cubic timeline interpolations are acknowledged as the best method for pipe networks (Chen, 1995).

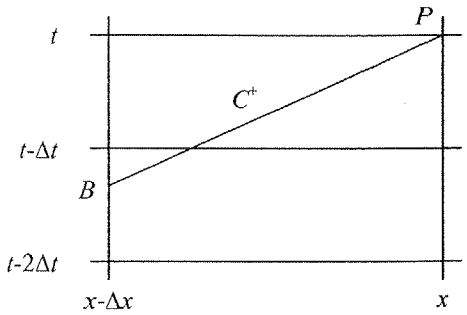

Figure 3.17 Timeline Interpolation at Known Level, *x-t* plane

3.7.3 Wave Speed Adjustment

The wave speed adjustment interpolation scheme is the easiest to implement. By adjusting the wave speed in a computational unit, equality is ensured between adjacent computational unit's numerical wave travel times, although the real wave travel times may be different. Effectively, the slope of the assumed characteristic line changes as shown in Figure 3.18 and departs from the actual characteristic line. Ghidaoui *et al.* (1998) showed, using energy relations, that linear spaceline and timeline interpolation schemes remove energy from a system whereas the wave speed interpolation scheme preserves the total energy. The performance of the wave speed interpolation was superior in this respect. The main drawback with the wave speed adjustment scheme is its effect on the timing of wave front propagation, which introduces error in the calculation. If the waves are steep, the error can be large. Chen (1995) showed that higher order spaceline and timeline interpolations out performed the wave speed adjustment scheme.

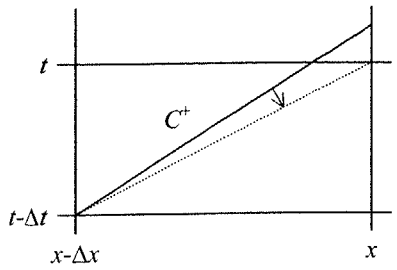

Figure 3.18 Wave Speed Adjustment, *x-t* plane

For the simulation of a transient event, the use of wave speed adjustment is satisfactory for finding the general shape of the pressure curve but leads to alteration of the timing. The timing is important for inverse transient analysis, therefore, wave speed adjustment is not an acceptable interpolation method.

Different interpolation schemes have different computational loads. For example, the wave speed adjustment method is intrinsically faster than the linear interpolation techniques, which are in turn faster than the higher order interpolation techniques, with the slowest being the compact high order interpolation schemes. Similar to the trade-off described at the beginning of this section between the accuracy of the interpolation scheme and the minimum Courant number, there is another trade-off between different interpolation schemes whereby a computationally faster scheme could be used with a smaller common time step than a slower more accurate scheme with a larger common time step. Ultimately the basis for comparison should be the accuracy versus the total computation time. This thesis does not discuss the finer points of interpolation efficiency but attempts to use the most accurate interpolation scheme wherever possible, however, for techniques that use repeated transient analyses (such as the inverse transient method in Chapter 4) the most computationally efficient scheme should be used.

3.8 Variable Position Valve Simulation

One of the most common hydraulic devices in a pipe network is a valve. The procedure for simulation is different for explicit and implicit MOC schemes. For convenience, valves are modelled as a node for explicit schemes and as a link for implicit schemes (McInnis *et al.*, 1997). The equation that describes the headloss across a valve (ΔH_V) to the flow (Q) through the valve is

$$Q = C_d A_V \sqrt{2g\Delta H_V} \quad \text{.....(3.8.1)}$$

where C_d = coefficient of discharge, A_V = cross-sectional valve area and H_V = head at the valve. Eq. 3.8.1 is written at some reference condition (subscripted with 0). Typically, the reference condition is when the valve is fully open. The valve equation, applied at the reference condition, is

$$Q_0 = (C_d A_V)_0 \sqrt{2g(\Delta H_V)_0} \quad \text{.....(3.8.2)}$$

The valve equation (Eq. 3.8.1) is divided by the valve equation at the reference condition (Eq. 3.8.2). The result is the non-dimensional relationship

$$\frac{Q}{Q_0} = \frac{C_d A_V}{(C_d A_V)_0} \sqrt{\frac{\Delta H_V}{(\Delta H_V)_0}} \quad \text{.....(3.8.3)}$$

Eq. 3.8.3 is rearranged to form

$$Q = \frac{C_d A_V}{(C_d A_V)_0} \frac{Q_0}{\sqrt{(\Delta H_V)_0}} \sqrt{\Delta H_V} \quad \text{.....(3.8.4)}$$

Eq. 3.8.4 is written in a simplified form introducing a dimensionless valve opening parameter τ and a coefficient C_V at the reference conditions. Eq. 3.8.5 is used in following valve formulations.

$$Q = \tau C_V \sqrt{\Delta H_V} \quad \text{.....(3.8.5)}$$

where the parameters τ and C_V are defined as

$$\tau = \frac{C_d A_V}{(C_d A_V)_0} \quad \text{and} \quad C_V = \frac{Q_0}{\sqrt{(\Delta H_V)_0}} \quad \text{.....(3.8.6)}$$

The dimensionless valve-opening coefficient, τ, varies between 1 and 0 for a fully open and fully closed valve respectively. Figure 3.19 depicts a valve modelled as a link between two nodes, i.e. a computational unit, where $\Delta H_V = H_1 - H_2$.

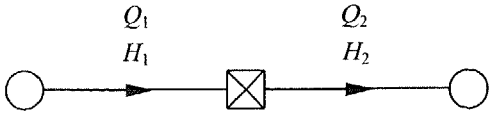

Figure 3.19 Valve Element Diagram

The valve equation (Eq. 3.8.5) is written for the valve element in Figure 3.19 as

$$Q|Q| = (\tau C_V)^2 (H_1 - H_2) \quad \text{.....(3.8.7)}$$

The valve equation can be solved explicitly with the compatibility equations, resulting in a quadratic solution. Care must be taken to ensure that the result is consistent with the direction of flow (because the modulus term cannot be included in the quadratic solution).

On the other hand, implicit implementation makes use of the modulus term and therefore the direction of flow does not need to be checked (as in the explicit implementation). The valve equations are written as linearised combinations of flow and hydraulic head (for use in matrices). First, a linear continuity equation is written stating that the flow is unchanged on either side of the valve,

$$Q_1 - Q_2 = 0 \quad \text{.....(3.8.8)}$$

Then, the valve equation is linearised. The nonlinear component (the Q^2 term) is estimated using a flow from the previous nonlinear iteration, Q'_1, as shown in Eq. 3.8.9. Provided that Q'_1 is an adequate estimation of Q_1, Eq. 3.8.9 is convergent. Unfortunately, Eqs. 3.8.8 and 3.8.9 are indeterminate, when solving the forward transient problem using a linear solver, if the valve is closed. This problem is overcome by setting Q_1 equal to zero when $\tau = 0$. The valve behaviour is described by Eqs. 3.8.9 and 3.8.10 for the open and closed cases respectively.

if $\tau > 0$: $$Q_1|Q'_1| - (\tau C_V)^2 H_1 + (\tau C_V)^2 H_2 = 0 \quad \text{.....(3.8.9)}$$

if $\tau = 0$: $$Q_1 = 0 \quad \text{.....(3.8.10)}$$

3.9 Nodal Leakage Simulation

Leakage is simulated most easily at nodal points in the characteristic grid. The leaking node is solved using two compatibility equations (from adjacent pipes) and an orifice equation (Eq. 3.9.1) that describes the leak. Of course, Eq. 3.9.1 is valid only if the pressure at the node is above zero (atmospheric), otherwise the equation is undefined.

$$Q_L = C_d A_L \sqrt{2gH_L} \quad \text{.....(3.9.1)}$$

where Q_L = leaking flow, A_L = area of the leak hole, C_d = coefficient of discharge and H_L = hydraulic head at the leak. A diagram of a leak at a node is shown in Figure 3.20.

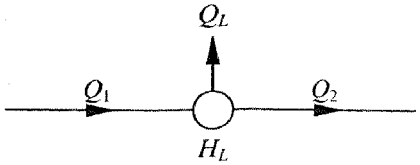

Figure 3.20 Leak at a Node

When solving for variables at the leaking node, continuity of mass must be applied. Eq. 3.9.2 represents the sum of the flows entering (positive) and exiting (negative) from the node, which is equal to zero. The elevation of the leak is assumed to be zero in Eq. 3.9.1. The leak equation is generalised later in Eq. 3.9.8.

$$Q_1 - Q_2 - Q_L = 0 \quad \text{.....(3.9.2)}$$

Substituting the orifice equation into the continuity equation at a node, the hydraulic head can be determined using the quadratic formula. When introducing leakage in an implicit MOC scheme, the leak equation is formulated differently. Eq. 3.9.3 shows the continuity of the flows around a node including a leak. The nonlinear leak equation is linearised by introducing the variable H'. H' is the hydraulic head at the leaking node from a previous iteration and is updated when a new value of H is solved for, the process is repeated until there is little difference between H and H'.

$$Q_1 - Q_2 - \left(C_d A_L \sqrt{\frac{2g}{H'}} \right) H = 0 \quad \text{.....(3.9.3)}$$

There are different formulations of Eqs. 3.9.2 and 3.9.3 that account for different leaking element types. An example is given by Wiggert (1968) that accounts for distributed leakage along a pipeline.

Numerical algorithms, used in the inverse transient method for leak detection, may trial sets of lumped leak coefficients that cause a negative pressure at a leak. A negative pressure at a leak causes an undefined solution for the forward problem due to the computation of the square root of a negative number (and hence a large problem for the numerical algorithm). A solution is to restrict the numerical algorithm to trial parameter sets that do not produce negative pressures at leaks, but this approach is often detrimental to the performance of the numerical algorithm. Another approach is to allow leaks to occur at negative pressures. A leak at a negative pressure is an injection. An expression that allows leaks at negative pressures is

$$Q_L = C_d A_L \phi_{H_L} \sqrt{2g|H_L|} \quad \text{.....(3.9.4)}$$

where ϕ_{H_L} = a sign operator dependent on the hydraulic head at the leak. The operator is defined as

$$\phi_{H_L} = \begin{cases} +1 & \text{if} \quad H_L \geq 0 \\ -1 & \text{if} \quad H_L < 0 \end{cases} \quad \text{.....(3.9.5)}$$

Eq. 3.9.4 can be written equivalently as

$$Q_L|Q_L| = (C_d A_L)^2 2gH_L \quad \text{.....(3.9.6)}$$

Eq. 3.9.6 can be solved using the quadratic formula if care is taken with the sign operator. Implementation in an MOC scheme of the form $[M]\{v\} = \{R\}$ is relatively straightforward. The linearised leak equation is (compared with leak term in Eq. 3.9.3)

$$Q_L = C_d A_L \sqrt{\frac{2g}{|H_L'|}} H_L \quad \text{.....(3.9.7)}$$

More precisely, the leak equation as given by Eq. 3.9.1, if in terms of the head at the leak, should include an elevation term (z_L). The use of the hydraulic head will cause errors when the leaks are at different elevations. The leak equation, including the elevation of the leak, is

$$Q_L = C_d A_L \sqrt{2g(H_L - z_L)} \quad \text{.....(3.9.8)}$$

Another source of error is if the lumped leak coefficient ($C_d A_L$) is assumed to have no dependence on the Reynolds number of the flow through the leak. In reality, the coefficient of discharge (C_d) does have a dependence on the Reynolds number of the leak flow (Rouse, 1978). The dependence is seen in Figure 3.21.

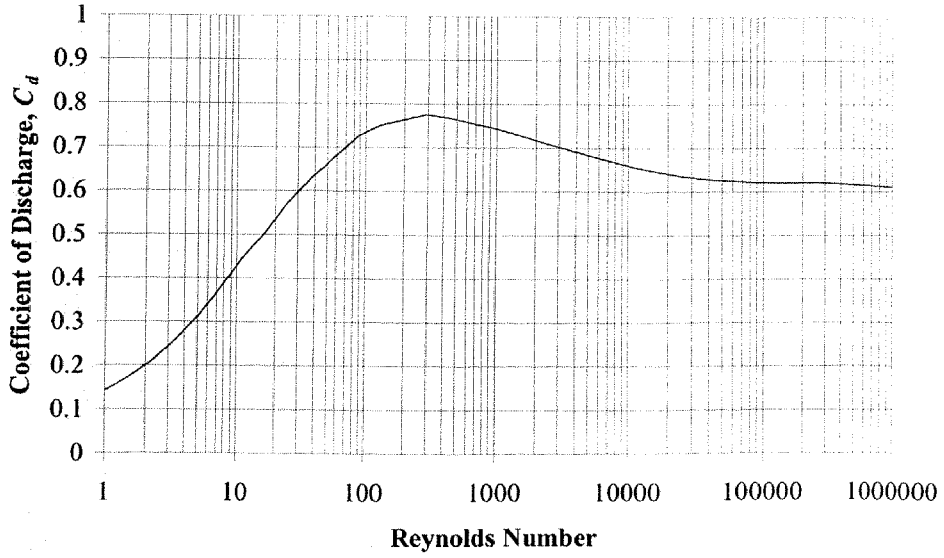

Figure 3.21 Coefficient of Discharge Versus Reynolds Number (from Rouse, 1978)

An observation is that, after a Reynolds number of about 10,000, the coefficient of discharge becomes almost constant. The dependence of C_d on the leak flow is not

expected to be a major problem, since most leaks will have high Reynolds numbers (due to high pressures) and thus be in the constant C_d region. Cases where the Reynolds number of the leak flow is small (perhaps for leaks with small diameters) also are not expected to cause problems because their effect is negligible due to the small amount of fluid being lost through the leak.

It is quite possible that, if a leak has been occurring underground for a while, the leak is discharging into a liquid that is at a higher pressure than the atmospheric pressure. This situation causes a change in the leakage equation, whereby the leakage is dependent on the difference in pressure between the inside and outside (usually ignored) of the pipe. A relationship for a leak discharging into a pressurised fluid is

$$Q_L = C_d A_L \phi_{(H_L - H_{OUT} - z_L)} \sqrt{2g|H_L - H_{OUT} - z_L|} \quad \text{.....(3.9.9)}$$

where H_{OUT} = the pressure of the fluid outside of the pipe and $\phi_{(H_L - H_{OUT} - z_L)}$ = a sign operator dependent on pressures inside and outside of the pipe and the elevation of the leak. The sign operator is defined as

$$\phi_{(H_L - H_{OUT} - z_L)} = \begin{cases} +1 & \text{if} \quad (H_L - H_{OUT} - z_L) \geq 0 \\ -1 & \text{if} \quad (H_L - H_{OUT} - z_L) < 0 \end{cases} \quad \text{.....(3.9.10)}$$

Eq. 3.9.9 may be expressed by the equivalent expression Eq. 3.9.11 (for solution using the quadratic formula).

$$Q_L|Q_L| = (C_d A_L)^2 2g(H_L - H_{OUT} - z_L) \quad \text{.....(3.9.11)}$$

The representation of leaks using the classical orifice equation may not, in reality, be correct. Real leaks may have a relation that depends on pressure in a more complex way (Germanopoulos, 1985). In some cases the orifice opening itself can deform and change the effective leak area and orifice shape when the pipe is stressed. In this thesis the classical orifice relation is used, however, future studies might use a more general power law expression.

3.10 Non-Nodal Leakage Simulation

Nodal leakage was described in the previous section and is easily implemented using the method of characteristics. Unfortunately, most leakage does not occur at nodal positions in a pipe network. The traditional method is to discretise the pipe network into smaller sections and thus increase the number of nodal positions available for a leak to exist. Although satisfactory in transient simulation, it is not satisfactory when using the inverse transient method. The inverse transient method can determine parameters, such as leak areas, friction factors and wave speeds, from measured pressure head data from a transient event. The inverse transient method (also called inverse transient analysis) is described in detail in Chapter 4. The use of finer discretisation in a pipe network increases the computation time needed to analyse the network (for the same amount of real time). Thus, an increase in the simulation time can cause a large increase in the computation time of the inverse transient method. In addition, a finer discretisation creates more nodal positions as candidates for possible leak locations, which creates more unknowns to be solved for. There is a two-fold effect on the inverse transient method. The first effect is an increase in the number of transient simulations required for the minimisation method due to the increased number of parameters. The second effect is more subtle, when the number of leak parameters is increased, the search space is increased and thus solutions may be harder to find.

The following sections show that non-nodal leakage can be approximately solved for at intermediate positions in a computation unit. The proposed method is called the non-nodal leak formulation. The leak relationship is

$$Q_L = C_d A_L \sqrt{2gH_L} \quad \text{.....(3.10.1)}$$

Eq. 3.10.1 is regarded as the most popular leakage relationship (assuming the elevation of the leak is zero and the pressure outside the leak is zero) and is used for the remainder of this thesis.

3.10.1 Previous Non-Nodal Transient Leakage Studies

A problem of the inverse transient method for leak detection (Liggett and Chen, 1994) is that frequently leaks do not occur at nodal points in a pipeline. Leaks can occur at any point along a pipeline and with different hole geometries. Koelle *et al.* (1996) performed inverse transient analysis for leaks at non-nodal positions. The non-nodal leak was modelled as a constant demand, assuming that the leak flow was known. Pressure dependent leakage, as shown in Eq. 3.10.1, causes damping in transient models, however constant demands do not cause any damping in transient models and, therefore, questions the validity of Koelle *et al.*'s formulation. Koelle *et al.* (1996), however, did not describe adequately how they incorporated the leakage. Wiggert (1968) derived a relationship for distributed leakage along a pipe under unsteady state conditions. The distributed leak is modelled by a continuous leak orifice defined by

$$q_L = C_d b\sqrt{2gH} \quad \text{.....(3.10.2)}$$

where q_L = leak flow per unit length, C_d = a discharge coefficient and b = leakage width. The governing unsteady state equations including the distributed leakage become Eqs. 3.10.3 and 3.10.4 for the equations of motion and continuity respectively.

$$\frac{\partial H}{\partial x} + \frac{1}{g}\frac{dV}{dt} + \frac{fV|V|}{2gD} + \frac{(C_\beta - 1)Vq_L}{gA} = 0 \quad \text{.....(3.10.3)}$$

$$\frac{a^2}{g}\frac{\partial V}{\partial x} + \frac{dH}{dt} + \frac{a^2 q_L}{gA} = 0 \quad \text{.....(3.10.4)}$$

where C_β is a momentum coefficient which relates the mean velocity in the control volume, V, to the velocity of the fluid leaking from the distributed leak, v. The relationship between V and v is

$$v = C_\beta V \quad \text{.....(3.10.5)}$$

C_β depends on the velocity distribution in the conduit because the leakage is drawn off the fluid in the boundary layer. Under unsteady state conditions Wiggert (1968) suggested that $C_\beta = 1$ for orifice outflow, and for outflow that leaves through lateral branches normal to the pipe, $C_\beta = 0$. His model was checked numerically through comparison to a pipeline with many small leakage points at equal spacing (a continuous manifold) along the pipe with good results. Experimental tests also provided good matches with the numerical model.

3.10.2 Non-Nodal Leak Formulation

An explicit formulation is developed in this section for incorporating a non-nodal leak into the method of characteristic equations. The formulation is performed using an intermediate method of characteristics step. Figure 3.22 depicts a leak on the C^+ characteristic of a computational unit positioned at a distance x_L from the point A.

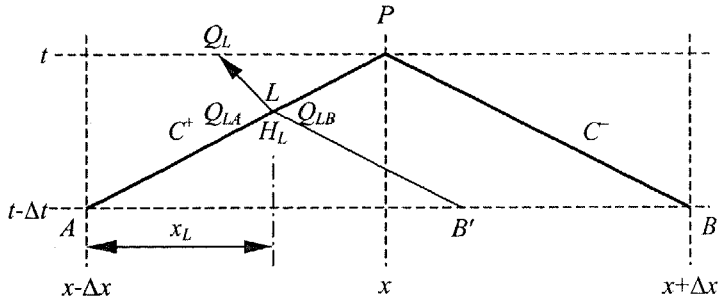

Figure 3.22 Leakage at a Non-Nodal Position in the C^+ Characteristic

The first step, required to incorporate a non-nodal leak into the method of characteristics, is to create a construction point, B'. The values of variables at B' are determined using interpolation between points A and B. A linear interpolation is produces Eqs. 3.10.6 and 3.10.7. Higher order interpolation schemes may improve results for point B′.

$$H_{B'} = H_A + \frac{x_L}{2\Delta x}(H_B - H_A) \quad \text{.....(3.10.6)}$$

$$Q_{B'} = Q_A + \frac{x_L}{2\Delta x}(Q_B - Q_A) \quad \text{.....(3.10.7)}$$

Then, the interpolated values of H and Q at B' are used in conjunction with conditions at point A and, using the MOC and the leak equation, conditions at the leak (point L) are determined. The equations describing the non-nodal leak, shown in Eqs. 3.10.8 to 3.10.11, determine the leak flow (Q_L) and flows either side of the leak (Q_{LA} and Q_{LB}).

$$(H_L - H_A) + \frac{a}{gA}(Q_{LA} - Q_A) + \frac{fQ_A|Q_A|x_L}{2gDA^2} = 0 \quad \text{.....(3.10.8)}$$

$$(H_L - H_{B'}) - \frac{a}{gA}(Q_{LB} - Q_{B'}) - \frac{fQ_{B'}|Q_{B'}|x_L}{2gDA^2} = 0 \quad \text{.....(3.10.9)}$$

$$Q_{LA} - Q_{LB} - Q_L = 0 \quad \text{.....(3.10.10)}$$

$$Q_L = C_d A_L \sqrt{2gH_L} \quad \text{.....(3.10.11)}$$

Reformulating the characteristic equations between points A and P, a relationship including leakage is developed. First, the integral C^+ compatibility equation is examined.

$$\int_A^P dH + \frac{a}{gA}\int_A^P dQ + \frac{f}{2gdA^2}\int_A^P Q|Q|dx = 0 \quad \text{.....(3.10.12)}$$

The integral is split into two separate integrals, the first between points A and L, and the second between points L and P. Each component of Eq. 3.10.12 is addressed separately. First the heads are considered. Given that the heads either side of the leak are assumed to be equal, the head at the leak is not needed. The relationship reduces to

$$\int_A^P dH = \int_A^L dH + \int_L^P dH = (H_L - H_A) + (H_P - H_L) = H_P - H_A \quad \text{.....(3.10.13)}$$

Considering the integral of the flow term, the flows on either side of the leak are known (from the intermediate method of characteristics step) so the integral can be split in much the same way as for the heads

$$\int_A^P dQ = \int_A^L dQ + \int_L^P dQ = (Q_{LA} - Q_A) + (Q_P - Q_{LB}) \quad \text{.....(3.10.14)}$$

The difference in the flow on either side of the leak is the leak flow, Q_L.

$$Q_{LA} - Q_{LB} = Q_L \quad \text{.....(3.10.15)}$$

Substituting Eq. 3.10.15 into Eq. 3.10.14 simplifies the integral to

$$\int_A^P dQ = Q_P + Q_L - Q_A \quad \text{.....(3.10.16)}$$

The friction formulation uses the flow at the foot of the characteristic line. The integral containing the Q^2 term is evaluated using two separate integrals

$$\int_A^P Q|Q|dx = \int_A^L Q|Q|dx + \int_L^P Q|Q|dx \quad \text{.....(3.10.17)}$$

A 1st order approximation of the integral produces Eq. 3.10.18, where each integration is based on known values of flow.

$$\int_A^P Q|Q|dx = Q_A|Q_A|x_L + Q_{LB}|Q_{LB}|(\Delta x - x_L) \quad \text{.....(3.10.18)}$$

All of the integral terms (Eqs. 3.10.3, 3.10.16, and 3.10.18) are substituted into Eq. 3.10.12 to form the C^+ compatibility equation incorporating non-nodal leakage

$$(H_P - H_A) + \frac{a}{gA}(Q_P + Q_L - Q_A) + \frac{f\left[Q_A|Q_A|x_L + Q_{LB}|Q_{LB}|(\Delta x - x_L)\right]}{2gDA^2} = 0 \quad \text{..(3.10.19)}$$

A similar procedure is performed for the C^- characteristic, where the intermediate method of characteristics step uses interpolated values of flow and head at a point A' (Figure 3.23).

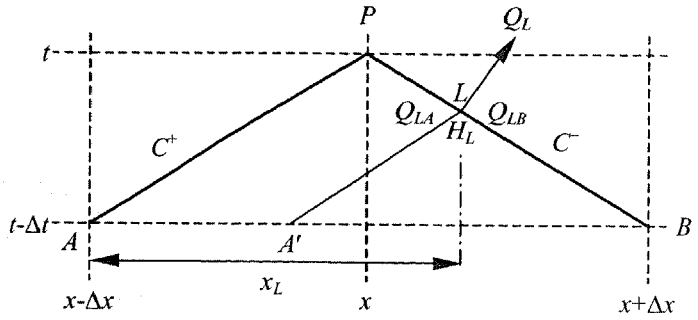

Figure 3.23 Leakage at a Non-Nodal Position in the C^- Characteristic

The distance to the leak is measured from the left hand side of the computational unit to maintain consistency. The relationship for the C^- compatibility equation is

$$(H_P - H_B) - \frac{a}{gA}(Q_P - Q_L - Q_B) - \frac{f\left[Q_B|Q_B|(2\Delta x - x_L) - Q_{LA}|Q_{LA}|(x_L - \Delta x)\right]}{2gDA^2} = 0 \quad \text{.....(3.10.20)}$$

The application of the non-nodal leak formulation near a boundary condition is different compared to an internal node. Spaceline interpolation cannot be used due to the proximity of the boundary condition. An example of a non-nodal leak occurring near a boundary condition is shown in Figure 3.24. Here, the non-nodal leak occurs at a distance of x_L from the boundary condition. Again, the flows around the leak at location L are needed for the correct integration of the C^- compatibility equation from point B to point P.

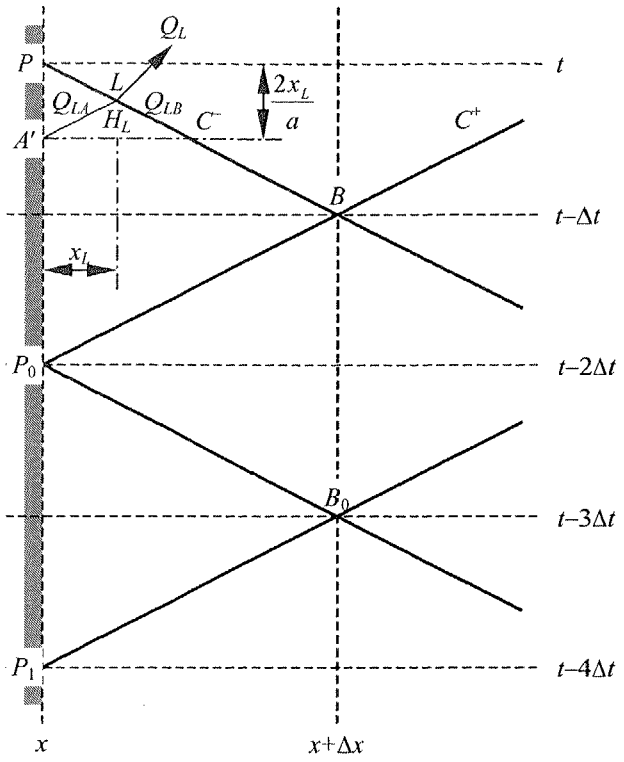

Figure 3.24 Non-Nodal Leak Near Boundary

An intermediate method of characteristics calculation is required to determine conditions at the leak location L. In contrast to the previous formulation for a non-nodal leak in an internal node, the method of characteristics calculation is performed with different length characteristic lines. In Figure 3.24, the C^+ characteristic line is x_L in length whereas the C^- characteristic line is $(\Delta x - x_L)$ in length (where length is measured in the spatial direction). Conditions at a point A', at the base the C^+ characteristic line, are required. A linear timeline interpolation between points P_0 and P_1 is used along the boundary condition to determine A'. Eqs. 3.10.21 and 3.10.22 show a linear interpolation for the hydraulic head and flow at A'. Higher order interpolations may improve $H_{A'}$ and $Q_{A'}$.

$$H_{A'} = \left(2 - \frac{x_L}{\Delta x}\right)\left(H_{P_0} - H_{P_1}\right) + H_{P_1} \quad \text{.....(3.10.21)}$$

$$Q_{A'} = \left(2 - \frac{x_L}{\Delta x}\right)\left(Q_{P_0} - Q_{P_1}\right) + Q_{P_1} \quad \text{.....(3.10.22)}$$

The equations for the calculation of flow conditions at A' are shown in Eqs. 3.10.23 to 3.10.26. The different length characteristic lines only affect the friction terms in each compatibility equation.

$$(H_L - H_{A'}) + \frac{a}{gA}(Q_{LA} - Q_{A'}) + \frac{fQ_{A'}|Q_{A'}|x_L}{2gDA^2} = 0 \quad \text{.....(3.10.23)}$$

$$(H_L - H_B) - \frac{a}{gA}(Q_{LB} - Q_B) - \frac{fQ_B|Q_B|(\Delta x - x_L)}{2gDA^2} = 0 \quad \text{.....(3.10.24)}$$

$$Q_{LA} - Q_{LB} - Q_L = 0 \quad \text{.....(3.10.25)}$$

$$Q_L = C_d A_L \sqrt{2gH_L} \quad \text{.....(3.10.26)}$$

Once the flow conditions at A' are known, the C^- compatibility equation from point B to point P is formed,

$$(H_P - H_B) - \frac{a}{gA}(Q_P - Q_L - Q_B) - \frac{f\left[Q_B|Q_B|(\Delta x - x_L) + Q_{LA}|Q_{LA}|x_L\right]}{2gDA^2} = 0 \quad \text{.....(3.10.27)}$$

Eq. 3.10.27 is similar to Eq. 3.10.20.

3.10.3 Performance of the Non-Nodal Leak Formulation

The non-nodal leak formulation is tested using an example pipeline bounded by two tanks at constant pressure. The example pipeline is shown in Figure 3.25. The diameter of the pipeline is 22.1 mm, length is 37.2 m, and all leaks are modelled using a lumped leakage coefficient of $C_dA_L = 1.0\times10^{-6}$ m^2. A sharp transient is used to show the time delays between the original and the reflected pressure waves from the leak. The sharp transient event is expected to show the difference between leaks at two similar positions more clearly than a slow transient event. An instantaneous valve closure generates the transient event. An initial velocity of 0.14 m/s is sufficiently low so that negative pressures, in the pipeline or at the leak, do not occur due to the instantaneous valve closure.

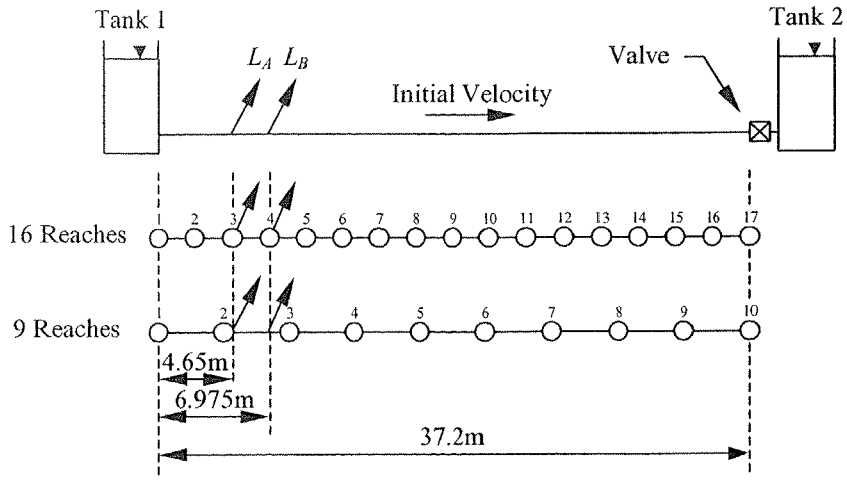

Figure 3.25 Example Pipeline, Separate Leakage

The example pipeline in Figure 3.25 is discretised using two different numbers of computational reaches. Results for nodal leaks use a discretisation of 16 reaches and for non-nodal leaks, a discretisation of 9 reaches. Two leaks are positioned in the pipeline at locations L_A and L_B. The locations of these leaks are at 4.65 m and 6.975 m from Tank 1 respectively. The locations of the two leaks correspond exactly to nodes 3 and 4 for the 16 reach nodal leak case (Figure 3.25). The location of the leaks, however, does not correspond to any nodal positions in the non-nodal case. For the 9 reach non-nodal leak case, the leaks are found in the computational unit between nodes 2 ($x = 4.133$ m) and 3 ($x = 8.267$ m) shown in Figure 3.25.

The pressure response at the valve for separately occurring leaks located at L_A and L_B is calculated using the nodal leak formulation. Figure 3.26 shows the difference in the shape of the peaks and troughs due to the different leak positions. The spatial difference between the leaks (equal to 2.325 m) is represented by a difference in timing of the features in the peaks and troughs of the pressure response.

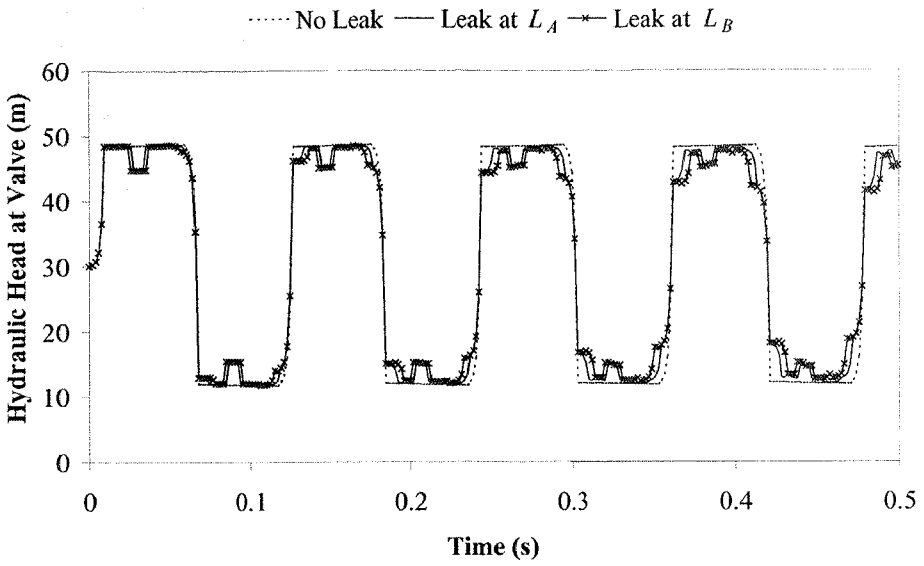

Figure 3.26 A Comparison of 1) No Leaks, 2) a Leak at L_A and 3) a Leak at L_B Using a 16 Reach Nodal Leak Formulation

Now, the separately occurring leaks at locations L_A and L_B are analysed using the 9 reach non-nodal leak formulation. The pressure responses at the valve are shown in Figure 3.27. The results are similar to those of the nodal leak formulation. One difference, however, is that the timing of the features in the peaks and troughs of the pressure response relating to the interaction of the leak is not so well produced by the non-nodal formulation. An explanation is that the propagation of information from each leak (at L_A and L_B) is a function of the discretisation of the pipeline. Although the leaks fall within a computational unit in the 9 reach non-nodal case, the transmission of information still depends on the nodes. Therefore, information propagates based on the grid spacing of the nodes (rather than the actual location of the leaks).

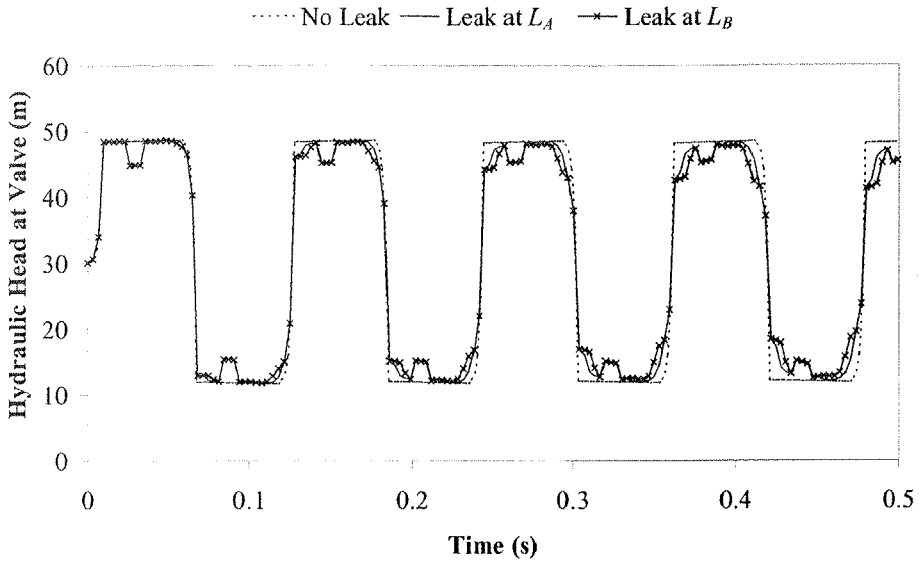

Figure 3.27 A Comparison of 1) No Leaks, 2) a Leak at L_A and 3) a Leak at L_B Using a 9 Reach Non-Nodal Leak Formulation

A comparison of results for a single leak occurring at L_B in the pipeline for both formulations is shown in Figure 3.28. The two formulations show a good match, suggesting that the non-nodal leak formulation produces adequate results (compared to the exact nodal formulation results).

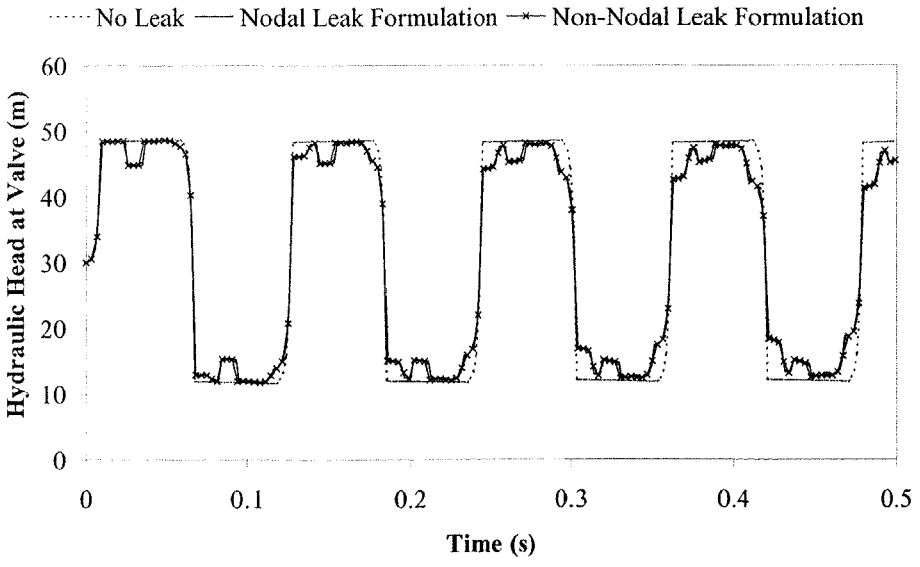

Figure 3.28 Leak at L_B Using Nodal and Non-Nodal Leak Formulations

A final test of the non-nodal leak formulation is performed using two simultaneous leaks at positions L_C and L_D, as shown in Figure 3.29. The leaks are located at distances of 4.65 m and 18.6 m from Tank 1, corresponding to leaks at nodes 3 and 9 in the 16 reach pipeline used by the nodal leak formulation. For the non-nodal formulation (9 reaches), the leaks occur in the computational sections between nodes 2 and 3 and between nodes 5 and 6. The pipeline characteristics and transient event are the same as used previously for the separate leaks.

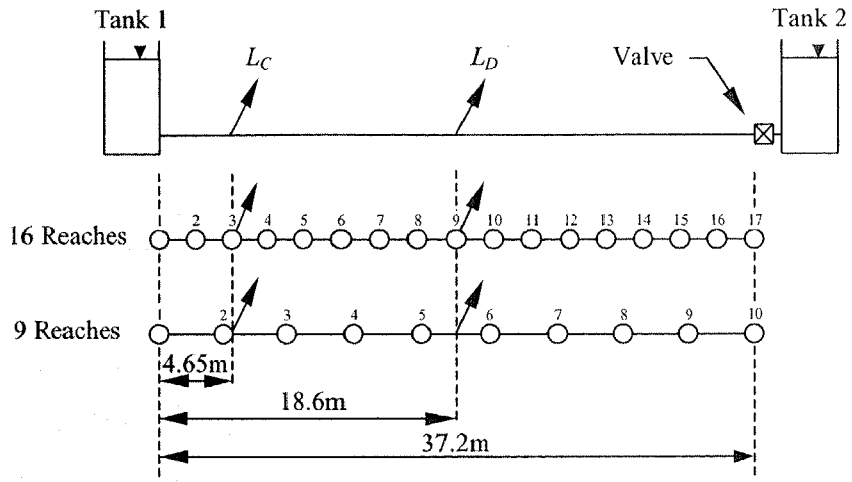

Figure 3.29 Example Pipeline, Multiple Leakage

Results using the nodal and non-nodal leak formulation for the two simultaneous leaks at L_C and L_D are shown in Figure 3.30. The nodal and non-nodal leak formulations match well. The small timing error from the non-nodal leak formulation persists.

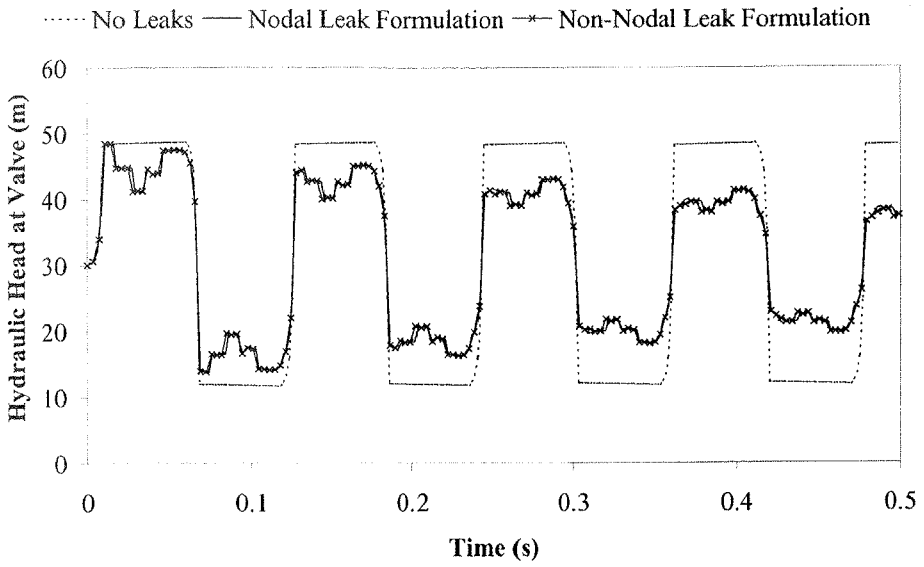

Figure 3.30 Multiple Leakage Using Nodal and Non-Nodal Leak Formulations

Simulation of leaks at non-nodal positions is useful for the inverse transient method (Chapter 4) because leaks do not occur typically at nodal positions in a pipe network. Rather than using ever finer discretisation to find a non-nodal leak using the nodal formulation, the non-nodal leakage formulation could be used with a coarser discretisation, thus saving on computation time. Computation time is of great concern to the inverse transient method, which may require many transient simulations.

3.11 Summary

The investigation of water hammer in pipe networks is important. Karney and McInnis (1990) showed that some transient folklore is incorrect. The assumption that looped networks alleviate high water hammer pressures was shown to be incorrect. Their study showed that, under the right conditions, the pressure peak generated in a network can be larger than that in an equivalent pipeline. In another paper, McInnis and Karney (1995) tested the validity of the simulation of a water distribution network against experimental results. The network considered was in the City of Calgary, Canada. Although the first surges were predicted adequately, the long term decay was poorly represented, thus suggesting that pipe network modelling of transients still needs improvement.

This chapter has presented methods for the simulation of unsteady pipe flow in networks including leakage. The method of characteristics was the principal tool for solving the governing unsteady pipe flow equations of motion and continuity. Two different method of characteristic implementations were investigated, an explicit and an implicit MOC scheme. The implicit scheme was presented in a matrix form, making it useful for implementation on a computer and handling the topology of pipe networks. New research was presented for the modelling of variable position valves and both nodal and non-nodal leaks. There is debate as to whether an implicit or explicit MOC formulation should be used for algorithms that use repeated transient analyses (for such methods as the inverse transient method). Arguments are usually posed based on computation time. The answer depends upon the nonlinearity of the system of equations. For example, if the integration of friction term is evaluated using a first-order-accurate scheme (such as Eq. 3.3.17) and other relationships, such as leaks and valves, are quadratic, then the explicit MOC formulation will be computationally more efficient than the implicit MOC formulation. This results from the problem being linear. The nonlinear parts can be directly solved using the quadratic formula. However, if the friction is nonlinear (such as Eq. 3.3.19) and the valve and leak relationships are not quadratic in nature, then a nonlinear solver must be used at each computational node. In this case the implicit MOC formulation is more efficient than the explicit MOC formulation.

Other modelling concerns presented were the initial and boundary conditions, wave speed calculation and interpolation schemes. A basis for unsteady flow simulation was presented in this chapter that is used in further chapters.

Chapter 4

Inverse Transient Analysis

4.1 Introduction

This chapter presents background and new work on inverse transient analysis. The background begins by defining the minimisation problem, giving rise to the least squares objective function. Achieving the least squares minimisation requires a numerical optimisation algorithm (such as the Levenberg-Marquardt algorithm). The Levenberg-Marquardt algorithm requires the calculation of the Hessian and gradient of the objective function, both of which can be formed from the Jacobian. Typically, the Jacobian is calculated using a divided difference method, which is slow and inefficient. Alternative methods for calculation of the Jacobian are presented in this chapter. A new formulation of the adjoint method is presented and shown to be equivalent to an analytic method. A new fast analytic method is proposed, showing superior performance over other methods. The fast analytic method shows potential for large decreases in the inverse transient method's computation time. New relationships are presented that convert partial derivatives with respect to friction factors into partial derivatives with respect to pipe roughnesses, thus promoting a more physically based parameter rather than assuming a constant Darcy-Weisbach friction factor. Also, the fast analytic method is extended to include the calculation of temporal and spatial derivatives. Analysis of data requirements for the inverse transient method shows advantages over inverse steady state methods. Convergence of the minimisation method is discussed.

The variances in the solved parameters are inferred from the variances in the measured data using a Taylor series expansion and, along with goodness-of-fit criteria and sensitivity analysis, can indicate the confidence one has in the determined parameters (and also the transient model used). A study of theoretical inverse transient analysis is contained in this chapter.

4.2 The Inverse Problem

By definition an inverse problem is one where measurements of an event are known but the parameters defining the physical condition or status of the event, and perhaps even the governing equations, are unknown. A transient event in a pipeline system may be generated using valve opening or closures, pipe rupture, pump failure or changes of water level in a reservoir to which the pipe is connected. In inverse transient analysis, the measured data are the observed pressures at various locations in a pipe or pipe network. Inverse transient analysis involves the measurement of variables (pressure or flow) at given times during a transient event, then back-calculates the system parameters from these measurements. Typically, the measured variable is pressure due its ease of measurement (compared to flow). Possible system parameters might include the leak areas, pipe roughness coefficients and wave speeds. These parameters are required for the calibration of a network, design of additional infrastructure or maintenance of networks. Leak detection is important for indicating anomalies in a network and unauthorised use of water. Also, leaks are a precursor to pipe failure.

There are two methods to obtain an inverse solution, a direct and an indirect method. Each method has advantages and disadvantages (Neuman, 1973). The direct method treats the model parameters as the dependent variables in a formal inverse boundary value problem from which a direct solution of the parameters is made. The direct method requires that the data (and derivatives of the data) are exact and complete. Errors in the data may cause the problem to become improperly posed and solutions might only exist for certain restricted conditions. The indirect method minimises the difference between measured and calculated data. Essentially, the indirect method uses a trial and error process. An advantage of the indirect method is that data (and

derivatives of the data) need not be known at all points and times in the network. In pipe networks, the data are measured at particular locations and certainly not over the entire domain of the dependent variables (required by the direct method). Henceforth, the indirect method is used in this research.

4.3 Formulation of the Minimisation Problem

The inverse transient problem fits measured pressure data to a transient model that is dependent on a set of parameters, which may contain leak areas (also called lumped leak coefficients), friction factors and wave speeds. The least squares fit is the most common method used to fit parameters of a model to data. The origin of the least squares fit is the subject of *maximum likelihood estimators*. It is meaningless to ask what is the probability that a particular set of fitted parameters is correct because there is no statistical universe of models from which the parameters are drawn, rather just one model. It is far better to ask, given a particular set of parameters, what is the probability that this data set could have occurred? Press *et al.* (1992) present a thorough derivation of the least squares approach to minimisation.

Consider the fitting of M measured pressure head data points H_i^m, $i = 1, ..., M$, to a model that is dependent on N unknown parameters a_j, $j = 1, ..., N$. If each measured pressure head has a random measurement error that is normally distributed (with a standard deviation = σ_i) around the true model ($\mathbf{H}(\bar{\mathbf{a}})$), then the probability of the data set occurring is the product of the probabilities of each of the i^{th} data points (H_i) occurring within $H_i \pm \Delta H$ (the i^{th} data point to have the maximum value of $H_i + \Delta H$ and the minimum value of $H_i - \Delta H$ with index i spanning space and time). A bold variable represents a vector and an overscore represents an average. The total probability P is

$$P \propto \prod_{i=1}^{M} \left\{ \exp\left[-\frac{1}{2} \left(\frac{H_i^m - H_i(\mathbf{a})}{\sigma_i} \right)^2 \right] \Delta H \right\} \qquad (4.3.1)$$

Maximising P finds the best fit parameters to the model for the given set of measurement data. Maximising the total probability is equivalent to maximising its logarithm, or minimising the negative of its logarithm (Eq. 4.3.2).

$$-\log(P) \propto \left[\sum_{i=1}^{M} \frac{\left(H_i^m - H_i(\mathbf{a})\right)^2}{2\sigma_i^2} \right] - M\log(\Delta H) \quad \text{.....(4.3.2)}$$

Dropping the constant factor of 2 and the constant logarithmic term in Eq. 4.3.2, produces the *chi-square statistic* for the fitted parameters (once minimised). The chi-square statistic is

$$\chi^2 = E = \sum_{i=1}^{M} \frac{\left(H_i^m - H_i\right)^2}{\sigma_i^2} \quad \text{.....(4.3.3)}$$

The chi-square statistic becomes important when estimating the error in the solution parameters (Section 4.8). The variance of the error in the measured data is assumed constant (and most often unknown) and commonly dropped yielding the basic least squares expression

$$LS = E = \sum_{i=1}^{M} \left(H_i^m - H_i\right)^2 \quad \text{.....(4.3.4)}$$

Many different fields of research use Eqs. 4.3.3 and 4.3.4 when model parameters are calculated from measured data. Both Eqs. 4.3.3 and 4.3.4 are referred to as the objective function (or sometimes the merit function) and denoted E. The following sections discuss the minimisation of the least squares function.

4.3.1 The Newton-Raphson Method

The Newton-Raphson method is used widely to find roots to a set of nonlinear equations. The purpose of its inclusion in this thesis, although not used to minimise the objective function, is to define the Jacobian. The Jacobian is an important quantity for other minimisation methods and its calculation is the focus of new research presented in this chapter. Rather than solve the least squares function (Eq. 4.3.4), the set of normalised differences between measured and modelled pressure heads are considered. A set of M equations, E_i, are formed that equal zero when the model pressure heads match the measured pressure heads

$$E_i(\mathbf{a}) = \frac{H_i^m - H_i(\mathbf{a})}{H_i^m} = 0 \qquad i = 1, 2, ..., M \quad \text{.....(4.3.5)}$$

Using a Taylor series expansion in the neighbourhood of **a**, the set of equations, E_i, become

$$E_i(\mathbf{a}+\delta\mathbf{a}) = E_i(\mathbf{a}) + \sum_{j=1}^{M} \frac{\partial E_i}{\partial a_j}\delta a_j + O(\delta\mathbf{a}^2) \quad \text{.....(4.3.6)}$$

where $O(\delta\mathbf{a}^2)$ are higher order terms from the expansion. The matrix of the partial derivatives in Eq. 4.3.6 is the negative of the Jacobian matrix, **J**, and is defined as

$$J_{ij} = -\frac{\partial E_i}{\partial a_j} = \frac{\partial H_i}{\partial a_j} \quad \text{.....(4.3.7)}$$

Eq. 4.3.6 is expressed in matrix form (using the Jacobian matrix) as

$$\mathbf{E}(\mathbf{a} + \delta\mathbf{a}) = \mathbf{E}(\mathbf{a}) - \mathbf{J}\cdot\delta\mathbf{a} + O(\delta\mathbf{a}^2) \quad \text{.....(4.3.8)}$$

By neglecting the terms of order $\delta\mathbf{a}^2$ or higher and setting $\mathbf{E}(\mathbf{a} + \delta\mathbf{a}) = 0$, a set of linear equations are obtained for corrections that move each function closer to a zero value for a trial set of parameters, **a**.

$$\mathbf{J}\cdot\delta\mathbf{a} = \mathbf{E}(\mathbf{a}) \quad \text{.....(4.3.9)}$$

Once Eq. 4.3.9 is solved, the correction to the parameters, $\delta\mathbf{a}$, are used to update the old parameters, **a**, to find a new set of parameters, **a′**

$$\mathbf{a}' = \mathbf{a} + \delta\mathbf{a} \quad \text{.....(4.3.10)}$$

The parameters are updated until some convergence criteria are satisfied. There are problems associated with the Newton-Raphson method. One problem is that the technique may become trapped in local minima or even become undefined. This problem is wholly dependent on the topology of the search space and often can be remedied by choosing different initial parameters.

4.3.2 The Levenberg-Marquardt Method

A more robust minimisation method is the Levenberg-Marquardt method. The Levenberg-Marquardt method is, in fact, the melding of two separate solution methods. The two methods contained within the Levenberg-Marquardt method are the *steepest descent* and *inverse Hessian* solution methods. The Levenberg-Marquardt method uses the best qualities of each method to form a superior minimisation algorithm. It is useful to derive these relationships from the objective function following Press *et al.* (1992). To begin, a truncated Taylor series expansion of the objective function is performed about a point $\mathbf{a}_0$, which is sufficiently close to some minimum point **a**

$$E(\mathbf{a}) \approx E(\mathbf{a}_0) + \sum_i \frac{\partial E}{\partial a_i}\delta a_i + \frac{1}{2}\sum_{i,j}\frac{\partial^2 E}{\partial a_i \partial a_j}\delta a_i \delta a_j \quad \text{.....(4.3.11)}$$

Substituting $(\mathbf{a} - \mathbf{a}_0)$ for $\delta\mathbf{a}$ simplifies Eq. 4.3.11. The derivatives in the second and third terms of Eq. 4.3.11 are called, respectively, the *gradient* and *Hessian* of the objective function. The gradient and Hessian are evaluated at $\mathbf{a}_0$ and, therefore, are constants giving

$$E(\mathbf{a}) = E(\mathbf{a}_0) + \nabla E\big|_{\mathbf{a}_0}(\mathbf{a} - \mathbf{a}_0) + \tfrac{1}{2}(\mathbf{a} - \mathbf{a}_0)\mathbf{H}\big|_{\mathbf{a}_0}(\mathbf{a} - \mathbf{a}_0) \quad \text{.....(4.3.12)}$$

where $\nabla E\big|_{a_0}$ = the gradient and $\mathbf{H}\big|_{a_0}$ = the Hessian both evaluated at $\mathbf{a}_0$. The differentiation of Eq. 4.3.12 with respect to the parameter set $(\mathbf{a})$ produces

$$\nabla E = \nabla E\big|_{\mathbf{a}_0} + (\mathbf{a} - \mathbf{a}_0)\mathbf{H}\big|_{\mathbf{a}_0} \quad \text{.....(4.3.13)}$$

The gradient (∇E on the left side of Eq. 4.3.13) is set to zero (i.e. at the minimum of the objective function, the gradient equals zero). Rearranging Eq. 4.3.13 yields an expression relating a point near the minimum to the minimum point. The inverse Hessian method for function minimisation is

$$\mathbf{a} = \mathbf{a}_0 - \nabla E\big|_{\mathbf{a}_0} \cdot \mathbf{H}^{-1}\big|_{\mathbf{a}_0} \quad \text{.....(4.3.14)}$$

To simplify the above expression, two extra variables are defined as

$$\alpha_{jk} = \frac{1}{2}\frac{\partial^2 E}{\partial a_j \partial a_k} \quad , \quad \beta_j = -\frac{1}{2}\frac{\partial E}{\partial a_j} \quad \text{.....(4.3.15)}$$

The matrix $[\alpha]$ is called the *curvature matrix* and is one-half of the Hessian and is the curvature of the objective function. The vector $\{\beta\}$ is minus one-half of the gradient of the objective function. In a simpler form, the inverse Hessian expression (Eq. 4.3.14) becomes

$$\sum_{k=1}^{N} \alpha_{jk}\delta a_k = \beta_j \quad \text{.....(4.3.16)}$$

If the trial point is a long way from the minimum point and the problem is nonlinear, the Taylor series expansion (used in the derivation of the inverse Hessian method) is not necessarily a good local approximation. In addition, the Hessian matrix is not guaranteed to be positive definite, which is necessary to ensure a decrease in the objective function. In the case where the inverse Hessian method does not lead to an improved solution, the Levenberg-Marquardt method switches to the steepest descent method defined by

$$\delta a_k = \text{constant} \times \beta_k \quad (4.3.17)$$

Actually the Levenberg-Marquardt method is a hybrid that uses a mixture of the inverse Hessian and the steepest descent methods to address the shortcomings of each minimisation method. The inverse Hessian method exhibits quadratic convergence near the minimum while it sometimes performs poorly at a point far from the minimum (in fact convergence is not guaranteed). On the other hand, the steepest descent method ensures travel in a downhill direction towards the minimum from a point far from the minimum, but converges slowly near the minimum. The Levenberg-Marquardt method uses the best qualities of each method to progress towards a minimum by using each in a weighted formula. Eq. 4.3.16 is modified to

$$\sum_{k=1}^{N} \alpha'_{jk} \delta a_k = \beta_j \quad (4.3.18)$$

where α' is defined as

$$\alpha'_{jj} = \alpha_{jj}(1 + \lambda) \quad \text{and} \quad \alpha'_{jk} = \alpha_{jk} \quad (4.3.19)$$

and where λ is a weighting factor. For small values of λ the solution of Eq. 4.3.18 approaches the inverse Hessian method, while for large values, Eq. 4.3.18 approaches the steepest descent method. The Levenberg-Marquardt method is initiated using a moderate value of λ (e.g. $\lambda = 0.001$). If the objective function is improved by the solution to Eq. 4.3.18, that solution is kept and the multiplier is reduced by a factor of 10 (or some other substantial value). If the solution makes to error greater, that solution is discarded and λ is decreased by a factor of 10. As the solution approaches the optimum, the inverse Hessian method becomes dominant, leading to quadratic convergence. The process is repeated until the convergence criteria are satisfied. The Levenberg-Marquardt method is computationally intensive (with respect to the calculation of the gradient and Hessian) and, as will be shown in Section 4.3.3, uses the same Jacobian information as the Newton-Raphson method. The Levenberg-Marquardt method is commonly the method of choice for nonlinear least squares problems due to its efficiency and robustness.

4.3.3 Calculation of the Jacobian, Gradient and Hessian

The Newton-Raphson and Levenberg-Marquardt nonlinear solution methods rely on the calculation of the gradient, Jacobian and Hessian. For unsteady state pipe flow

problems, these matrices are difficult to find analytically (see Section 4.4) and, typically, are found numerically. The formulation of a numerical method to calculate these matrices begins with the definition of the objective function (Eq. 4.3.3). The least squares minimisation function, E, is defined as the sum of the difference between the measured (H_i^m) and calculated pressure heads (H_i,) squared for all M measured data points,

$$E = \sum_{i=1}^{M} \frac{\left(H_i^m - H_i\right)^2}{\sigma_i^2} \quad \text{.....(4.3.20)}$$

The pressure head is calculated using some function (a transient simulation model) of a set of parameters, **a**, which may include lumped leakage coefficients, friction factors and wave speeds,

$$H_i = H_i\left(a_1, a_2, \ldots, a_N\right) = H_i(\mathbf{a}) \quad \text{.....(4.3.21)}$$

It is assumed that the partial derivatives of the pressure head can be determined numerically or analytically with respect to each parameter (methods for achieving this are presented in Section 4.4). The Jacobian, **J**, is defined as the matrix containing the partial derivatives of the pressure heads with respect to each of the parameters. The Jacobian is

$$\mathbf{J} = \left[\frac{\partial H_i}{\partial a_j}\right] \quad \text{.....(4.3.22)}$$

The Levenberg-Marquardt method uses the gradient vector and the Hessian matrix. The first derivative of the objective function is the gradient and is

$$\frac{\partial E}{\partial a_j} = -2\sum_{i=1}^{M}\left[\frac{\left(H_i^m - H_i\right)}{\sigma_i^2}\frac{\partial H_i}{\partial a_j}\right] \quad \text{.....(4.3.23)}$$

The Hessian is the second derivative of the objective function. The derivative of Eq. 4.3.23 is

$$\frac{\partial^2 E}{\partial a_j \partial a_k} = -2\sum_{i=1}^{M}\frac{1}{\sigma_i^2}\left[H_i^m \frac{\partial^2 H_i}{\partial a_j \partial a_k} - \left(\frac{\partial H_i}{\partial a_j}\frac{\partial H_i}{\partial a_k} + H_i \frac{\partial^2 H_i}{\partial a_j \partial a_k}\right)\right] \quad \text{.....(4.3.24)}$$

Collecting like terms reduces Eq. 4.3.24 to

$$\frac{\partial^2 E}{\partial a_j \partial a_k} = -2\sum_{i=1}^{M}\frac{1}{\sigma_i^2}\left[\left(H_i^m - H_i\right)\frac{\partial^2 H_i}{\partial a_j \partial a_k} - \frac{\partial H_i}{\partial a_j}\frac{\partial H_i}{\partial a_k}\right] \quad \text{.....(4.3.25)}$$

The first term in brackets contains $\left(H_i^m - H_i\right)$, which is small when close to the solution (assuming a good fit). $\left(H_i^m - H_i\right)$ is the random error and, therefore, may be positive or negative and tends to sum to zero even far from solution. Therefore, the first term in the parenthesis in Eq. 4.3.25 is neglected and is set to zero,

$$\left(H_i^m - H_i\right)\frac{\partial^2 H_i}{\partial a_j \partial a_k} \approx 0 \quad \text{.....(4.3.26)}$$

Neglecting that term will not change the final solution but will alter the path to the final solution. Now, the second derivative of the objective function is dependent on the multiplication of two separate partial derivatives of the pressure head (Eq. 4.3.27). The two partial derivatives are elements of the Jacobian matrix,

$$\frac{\partial^2 E}{\partial a_j \partial a_k} = 2\sum_{i=1}^{M}\left(\frac{1}{\sigma_i^2}\frac{\partial H_i}{\partial a_j}\frac{\partial H_i}{\partial a_k}\right) \quad \text{.....(4.3.27)}$$

The Hessian matrix (**H**) consists of elements defined by Eq. 4.3.27 for all parameters and is

$$\mathbf{H} = \left[\frac{\partial^2 E}{\partial a_j \partial a_k}\right] \quad \text{.....(4.3.28)}$$

This section shows how the gradient and Hessian can be found using the Jacobian. But the calculation of the Jacobian is the most computationally expensive component of any gradient based minimisation method. Therefore, efficient calculation of the Jacobian can greatly decrease the time spent on minimisation. The following section investigates methods of calculation of the Jacobian.

4.4 Calculation of Parameter Derivatives

The Jacobian matrix may be used to find other useful properties such as the gradient and Hessian of the objective function (Section 4.3.3). Partial derivatives of the variables (flows and heads) with respect to the parameters (lumped leak coefficients and friction factors) compose the Jacobian. These partial derivatives are called *parameter derivatives*. Nash and Karney (1999) partially investigated the calculation of sensitivities (similar to parameter derivatives) but not in a general sense as shown by Liggett and Chen (1994). The following work considers the divided difference method,

the adjoint method (Liggett and Chen, 1994), an analytical method and a fast analytic method for calculating parameter derivatives, and hence, the Jacobian matrix. This section develops the analytic method. Then, the analytic method for the calculation of parameter derivatives is extended forming an efficient, and so called, fast analytic method. Also, the adjoint method of Liggett and Chen (1994) is revisited and the relative merits of each method are discussed.

4.4.1 The Divided Difference Method

The simplest, but most computationally intensive, method to generate parameter derivatives is the divided difference method. The divided difference method is

$$\frac{\partial \nu}{\partial a_i} \approx \frac{\nu(\mathbf{a}+\delta a_i)-\nu(\mathbf{a})}{\delta a_i} \quad \text{.....(4.4.1)}$$

where the partial derivative of ν is found with respect to a specific parameter a_i and where $\mathbf{a}$ = a vector containing all of the parameters (such as lumped leak coefficients and friction factors), $\{\nu\}$ = a vector containing the unknown heads and flows calculated using a transient solver and δa_i = the perturbation in the i^{th} parameter. The divided difference method is inefficient because it requires $N+1$ evaluations of the transient solver for N parameters. A decrease in the size of the perturbation δa_i increases accuracy until roundoff errors, due to approximations when storing a number in computer memory, become a problem, thus it is difficult to determine a proper size of δa_i so that the numerical derivatives are sufficiently accurate and roundoff errors are not a problem. The divided difference method is useful when analytic parameter derivatives cannot be found easily.

4.4.2 An Analytic Method for the Calculation of Parameter Derivatives

An analytic method for the calculation of the Jacobian is developed in this section. First, the simultaneous system of the forward transient solver is (see Section 3.3)

$$[M]\{\nu\}=\{R\} \quad \text{.....(4.4.2)}$$

where $[M]$ = coefficient matrix and $\{R\}$ = right hand side vector. The simultaneous system of equations (Eq. 4.4.2) relates the heads and flows in a pipe network from a

previous time step to a current time step. A detailed explanation of this notation is discussed in Chapter 3 and by the example in Appendix A. Differentiating Eq. 4.4.2 with respect to a parameter a_i forms

$$[M]\left\{\frac{\partial \nu}{\partial a_i}\right\}+\left[\frac{\partial M}{\partial a_i}\right]\{\nu\}=\left\{\frac{\partial R}{\partial a_i}\right\} \quad \text{.....(4.4.3)}$$

Rearranging Eq. 4.4.3 into the general form of a solvable set of linear equations, the Jacobian, $\{\partial \nu/\partial a_i\}$, may be determined as

$$[M]\left\{\frac{\partial \nu}{\partial a_i}\right\}=\left\{\frac{\partial R}{\partial a_i}\right\}-\left[\frac{\partial M}{\partial a_i}\right]\{\nu\} \quad \text{.....(4.4.4)}$$

The partial derivative term $\{\partial \nu/\partial a_i\}$ on the left hand side of Eq. 4.4.4 represents one column of the Jacobian matrix. The nonlinear terms in $[M]$ from the forward transient solution are now known. However, the $[\partial M/\partial a_i]$ and $\{\partial R/\partial a_i\}$ terms in Eq. 4.4.4 contain $\{\partial \nu/\partial a_i\}$. These terms are the partial derivatives of the nonlinear terms (such as friction, valves, and leaks) in $[M]$, thus requiring the Eq. 4.4.4 be iterated for solution. Iteration slows the analytic method to approximately the same speed as the divided difference method (if not slightly slower). The matrix $[M]$ does not change when iterating $[\partial M/\partial a_i]$ and $\{\partial R/\partial a_i\}$ since $[M]$ does contain any $\{\partial \nu/\partial a_i\}$ terms. If the inverse of $[M]$ is computed and stored, it would not have to be recalculated for each of the iterations. Storing $[M]^{-1}$ reduces the computation time because, apart from the first iteration, all other iterations (solutions of Eq. 4.4.4) only require back-substitution or matrix multiplication (rather than matrix inversion). Also, $[M]$ is sparse and therefore linear solvers that take advantage of its sparsity may be used. An example of the analytic method is located in Appendix A.3.2.

4.4.3 Further Development of the Adjoint Method

Chen (1995) first proposed an adjoint method for the calculation of the Jacobian. This section develops a similar, but different, adjoint method. The derivation of the adjoint method begins with the definition of the objective function, E. The objective function in vector notation is

$$E=\{\nu^m-\nu\}^{\mathrm{T}}\{\nu^m-\nu\} \quad \text{.....(4.4.5)}$$

where $\{\nu\}$ = the vector of all H and Q for the current time step and $\{\nu^m\}$ = the vector of observed or measured H (or Q, but typically flow is not used). The inverse solution is found when the objective function is minimised subject to constraints. The objective function is constrained by the unsteady state governing equations. The simultaneous system over the whole transient period (Eq. 4.4.6) represents the constraints of E,

$$[M]\{\nu\} = \{R\} \quad \text{.....(4.4.6)}$$

Using Lagrange multipliers, the constraints are combined with the objective function. Chen (1995) calls the Lagrange multipliers an adjoint vector, denoted as $\{\psi^*\}$. The constrained objective function is

$$E = \{\nu^m - \nu\}^T\{\nu^m - \nu\} - \{\psi^*\}^T([M]\{\nu\} - \{R\}) \quad \text{.....(4.4.7)}$$

Eq. 4.4.7 is differentiated with respect to a parameter a_i,

$$\frac{\partial E}{\partial a_i} = -2\left\{\nu^m - \nu\right\}^T\left\{\frac{\partial \nu}{\partial a_i}\right\} - \left\{\psi^*\right\}^T\left(\left[\frac{\partial M}{\partial a_i}\right]\{\nu\} + [M]\left\{\frac{\partial \nu}{\partial a_i}\right\} - \left\{\frac{\partial R}{\partial a_i}\right\}\right) \quad \text{.....(4.4.8)}$$

Recalling that the goal is to evaluate the Jacobian (or $\{\partial\nu/\partial a_i\}$ term) inexpensively, Eq. 4.4.8 is rearranged to collect the Jacobian terms,

$$\frac{\partial E}{\partial a_i} = \left(-2\left\{\nu^m - \nu\right\}^T - \left\{\psi^*\right\}^T[M]\right)\left\{\frac{\partial \nu}{\partial a_i}\right\} + \left\{\psi^*\right\}^T\left(\left\{\frac{\partial R}{\partial a_i}\right\} - \left[\frac{\partial M}{\partial a_i}\right]\{\nu\}\right) \quad \text{.....(4.4.9)}$$

Since the adjoint vector $\{\psi^*\}$ is arbitrary, it is defined such that the Jacobian term (which is not known) is removed from Eq. 4.4.9 by choosing the arbitrary vector such the bracketed term preceding the Jacobian term equals zero. Thus set

$$-2\{\nu^m - \nu\}^T - \{\psi^*\}^T[M] = 0 \quad \text{.....(4.4.10)}$$

Then, Eq. 4.4.10 is rearranged and the transpose taken forming a solvable linear system (Eq. 4.4.11). Solving Eq. 4.4.11 determines the adjoint vector, $\{\psi^*\}$. Note that $[M]$ and $\{\nu\}$ are already known from the solution of the forward transient problem so Eq. 4.4.11 is a linear system,

$$[M]^T\{\psi^*\} = -2\{\nu^m - \nu\} \quad \text{.....(4.4.11)}$$

The simplified form of Eq. 4.4.9 is

$$\frac{\partial E}{\partial a_i} = \left\{\psi^*\right\}^T\left(\left\{\frac{\partial R}{\partial a_i}\right\} - \left[\frac{\partial M}{\partial a_i}\right]\{\nu\}\right) \quad \text{.....(4.4.12)}$$

The $[\partial M/\partial a_i]$ and $\{\partial R/\partial a_i\}$ terms are determined by differentiating $[M]$ and $\{R\}$ with respect to a parameter a_i and contain terms that are unknown at the current time step (see Appendix A.3.2). Iteration for the calculation of $[\partial M/\partial a_i]$ and $\{\partial R/\partial a_i\}$ severely

degrades the performance of the adjoint method. An element of the gradient of the objective function (or the $\partial E/\partial a_i$ term) can be calculated using matrix arithmetic, assuming that $\{\psi^*\}$ was selected to satisfy Eq. 4.4.10.

The problem of finding the Jacobian still remains and was resolved by Chen (1995) using a decomposition of the objective function (and other vectors) into component elements (i.e. a particular head at a certain time). A [g] matrix, composed of zeros mostly and some ones, was defined. Nonzero elements of [g] turn on the analysis for specific elements of the Jacobian. The [g] matrix facilitates a back-substitution for separating out the gradient into Jacobian elements.

The Chen (1995) process, in which the gradient is decomposed into a column of the Jacobian, is complicated. A different method simplifies the Chen (1995) process by making a substitution for the adjoint vector $\{\psi^*\}$. The substitution involves a new quantity called the adjoint matrix, $[\varphi^*]$. The relationship between the adjoint vector and the adjoint matrix is

$$\{\psi^*\} = -2[\varphi^*]^T\{\nu^m - \nu\} \quad (4.4.13)$$

Substituting Eq. 4.4.13 into Eq. 4.4.12 produces

$$\frac{\partial E}{\partial a_i} = -2\{\nu^m - \nu\}^T\left[\varphi^*\right]\left(\left\{\frac{\partial R}{\partial a_i}\right\} - \left[\frac{\partial M}{\partial a_i}\right]\{\nu\}\right) \quad (4.4.14)$$

Differentiation of the objective function (Eq. 4.4.4) with respect to a parameter a_i produces a relationship between the gradient and the Jacobian,

$$\frac{\partial E}{\partial a_i} = -2\{\nu^m - \nu\}^T\left\{\frac{\partial \nu}{\partial a_i}\right\} \quad (4.4.15)$$

Substitution of the definition of the gradient (Eq. 4.4.15) into Eq. 4.4.14 results in

$$-2\{\nu^m - \nu\}^T\left\{\frac{\partial \nu}{\partial a_i}\right\} = -2\{\nu^m - \nu\}^T\left[\varphi^*\right]\left(\left\{\frac{\partial R}{\partial a_i}\right\} - \left[\frac{\partial M}{\partial a_i}\right]\{\nu\}\right) \quad (4.4.16)$$

The simplification of Eq. 4.4.16, by cancelling like terms, gives

$$\left\{\frac{\partial \nu}{\partial a_i}\right\} = \left[\varphi^*\right]\left(\left\{\frac{\partial R}{\partial a_i}\right\} - \left[\frac{\partial M}{\partial a_i}\right]\{\nu\}\right) \quad (4.4.17)$$

The adjoint matrix $[\varphi^*]$ is calculated by substituting Eq. 4.4.13 (for the adjoint vector) into Eq. 4.4.11 resulting in

$$-2([\varphi^*][M])^T\{v^m - v\} = -2\{v^m - v\} \quad (4.4.18)$$

Upon observation of Eq. 4.4.18, $[M][\varphi^*]$ must equal the identity matrix to maintain equality

$$[M][\varphi^*] = \mathbf{I} \quad (4.4.19)$$

where $\mathbf{I}$ = the identity matrix, which is similar to the $[g]$ matrix used in the Chen (1995) derivation. The adjoint matrix is the inverse of the coefficient matrix from the forward transient system of equations,

$$[\varphi^*] = [M]^{-1} \quad (4.4.20)$$

Examination of Eqs. 4.4.17 and 4.4.20 shows that the adjoint method is exactly the same as the analytic method. The calculation of the adjoint matrix is equivalent to storing of the $[M]^{-1}$ matrix in the analytic method. The adjoint method points more directly to this time saving technique. Interestingly, Chen (1995) did not recognise that iteration is required for resolving the nonlinear terms in the $\{\partial R/\partial a_i\}$ vector and the $[\partial M/\partial a_i]$ matrix, thus presenting a flaw in his derivation where $[\partial M/\partial a_i]$ and $\{\partial R/\partial a_i\}$ are approximations of their true values (or incorrect). Non-iteration could lead to poor estimates of the Jacobian, gradient and Hessian and, perhaps, resulting in nonconvergence of the Levenberg-Marquardt method.

4.4.4 A Fast Analytic Method for the Calculation of Parameter Derivatives

The analytic method has little or no advantage over both the divided difference and the adjoint method but improvements in the calculation of the parameter derivatives still remain. These improvements are the basis for a new fast analytic method that is developed as part of this thesis. The fast analytic method begins by differentiating the set of equations that describe the simultaneous system of the forward transient solution with respect to an independent parameter, referred to as *IP*. A independent parameter (in this sense) can be thought of as similar to time (t). This system of equations is called the base simultaneous system for finding derivatives with respect to an independent parameter and is denoted with the subscript *IP*. The base simultaneous system is written in matrix form as

$$[M_D]\left\{\frac{\partial v}{\partial a_i}\right\} = \{R_{IP}\} \quad (4.4.21)$$

where $\{\partial v/\partial a_i\}$ = the vector of unknown partial derivatives of H and Q with respect to an independent parameter, $[M_D]$ = a coefficient matrix and $\{R_{IP}\}$ = the known right hand side vector. A worked example using Eq. 4.4.21 can be found in Appendix A.3.3. Eq. 4.4.21 is analogous to the simultaneous system for the forward transient problem where all unknowns are moved to the left side of the equation and all knowns to the right. It is not particularly useful to find derivatives with respect to an independent parameter (they would equal zero anyway). It is more useful to find the parameter derivatives with respect to a dependent parameter (such as a friction factor or a leak area). The simultaneous system restated with respect to a dependent parameter a_i is

$$[M_D]\left\{\frac{\partial v}{\partial a_i}\right\} = \{R_{a_i}\} \quad \text{.....(4.4.22)}$$

where $\{R_{a_i}\}$ = right hand side vector for a dependent parameter a_i. The right hand side of Eq. 4.4.22 contains extra terms formed from the product rule of differentiation. The extra term from the product rule of differentiation is shown using an example of a leak at an internal node. The continuity at a leaking internal node in a pipeline (see Figure 3.10) is described by

$$Q_1 - Q_2 - C_d A_L \sqrt{2gH_L} = 0 \quad \text{.....(4.4.23)}$$

where Q_1 = flow upstream of the leak, Q_2 = flow downstream of the leak, H_L = hydraulic head at the leak, C_dA_L = leak area times the discharge coefficient (the "lumped leak coefficient") and g = gravitational acceleration. Eq. 4.4.23 could represent one row of the simultaneous system for the forward transient problem ($[M]\{v\} = \{R\}$). The differentiation of Eq. 4.4.23 with respect to an independent parameter, such as a friction factor f, results in

$$\frac{\partial Q_1}{\partial f} - \frac{Q_2}{\partial f} - C_d A_L \sqrt{\frac{g}{2H_L}} \frac{\partial H_L}{\partial f} = 0 \quad \text{.....(4.4.24)}$$

The differentiation of Eq. 4.4.23 with respect to a dependent parameter, such as the lumped leak coefficient of the leak, results in

$$\frac{\partial Q_1}{\partial (C_d A_L)} - \frac{Q_2}{\partial (C_d A_L)} - C_d A_L \sqrt{\frac{g}{2H_L}} \frac{\partial H_L}{\partial (C_d A_L)} - \sqrt{2gH_L} = 0 \quad \text{.....(4.4.25)}$$

Comparison of Eqs. 4.4.24 and 4.4.25 shows an extra term in Eq. 4.4.25 from the product rule of differentiation. A generalised simultaneous system of equations for the partial derivatives with respect to a dependent parameter a_i is

$$[M_D]\left\{\frac{\partial v}{\partial a_i}\right\} = \{R_{IP}\} + \{\text{extra product rule terms for dependent parameter } a_i\} \quad \text{.....(4.4.26)}$$

The extra product rule terms for all equations (with respect to all parameters) are collected and formed into a dependent parameter vector $\{R_{DP}\}$. The rows of $\{R_{DP}\}$, a column vector, correspond to each equation in the simultaneous system. A new matrix $[g_a]$ is defined as a matrix full of zeros except at positions that coincide with partial derivatives with respect to that corresponding dependent parameter (which equals one). An example of $[g_a]$ is shown in Appendix A.3.3. The $[g_a]$ matrix is used to decode the dependent parameter vector $\{R_{DP}\}$ (using Eq. 4.4.27) for each parameter a_i forming the dependent parameter matrix $[R_{DP}]$. Eq. 4.4.27 works on single elements of the $\{R_{DP}\}$ vector and the $[g_a]$ matrix where column i corresponds to each parameter and row j corresponds to an equation in the simultaneous system.

$$[R_{DP}]_{i,j} = [g_a]_{i,j}\{R_{DP}\}_j \quad \text{.....(4.4.27)}$$

The independent parameter vector $\{R_{IP}\}$ and the dependent parameter matrix $[R_{DP}]$ combine to form a total right hand side matrix $[R_D]$.

$$[R_D] = [\{R_{IP}\} \; \vdots \; \cdots \; \vdots \; \{R_{IP}\}] + [R_{DP}] \quad \text{.....(4.4.28)}$$

The total right hand side matrix is used to define a simultaneous system of equations for the derivatives of flow and pressure with respect to all parameters, as

$$[M_D]\left[\left\{\frac{\partial v}{\partial a_1}\right\} \; \vdots \; \cdots \; \vdots \; \left\{\frac{\partial v}{\partial a_N}\right\}\right] = [R_D] \quad \text{.....(4.4.29)}$$

The column vectors containing the partial derivatives now become one matrix. The matrix of the partial derivatives of the pressure and flow with respect to all of the parameters in Eq. 4.4.29 is the Jacobian. Thus, Eq. 4.4.29 is written simply as

$$[M_D][J] = [R_D] \quad \text{.....(4.4.30)}$$

where $[J]$ is the Jacobian matrix. The matrix $[M_D]$ is common with respect to all parameters (see example in Appendix A.3.3). Thus, calculation of the Jacobian requires only one matrix inversion. Since full matrix inversion is computationally expensive one LU decomposition of $[M_D]$ and a back-substitution for each parameter is more efficient than one matrix inversion and one matrix multiplication (Press *et al.*, 1992). Eq. 4.4.30 is a linear system (in the parameter derivatives) and therefore requires no iteration for nonlinear terms, as was needed in both the adjoint and analytic methods. Thus, the fast analytic method is faster than these other methods (see next section and Appendix A.3.4). Much like the solution of the forward problem, initial and boundary conditions

must be defined. The boundary conditions for the $[\partial v/\partial a]$ matrix are equal to zero (parameters such as lumped leak coefficients and friction factors having no effect) and the initial conditions known, often found from a steady state solver (the initial steady state conditions are dependent on the parameters). Appendix A.3.3 shows an example of the fast analytic method.

4.4.5 Discussion of Parameter Derivative Methods

Ultimately, the fastest method will be chosen to calculate the Jacobian. Based on the number of evaluations of a linear solver, the relative speed of each method can be assessed. The divided difference method uses $N_P + 1$ calls to the forward transient solver to define the Jacobian matrix for N_P parameters (one call for a base set of parameters and N_P calls with a perturbation in each parameter). The forward transient solver is nonlinear and uses N_I calls to a linear solver to resolve the nonlinearities (Chen, 1995, uses $N_I = 3$). Thus, the total number of linear equation solutions used by the divided difference method is equal to $(N_P + 1) \times N_I$. The total number of linear solver calls required to find the Jacobian using the analytic method (without storing the matrix $[M]^{-1}$) is $N_I + (N_I \times N_P)$, equalling the divided difference and analytic methods. The equality exists because $[\partial M/\partial a_i]$ and $\{\partial R/\partial a_i\}$, needed for the analytic method, are iterated N_I times to resolve nonlinearities. For practical purposes, the value of N_I may be 1 or 2 for the calculation of the parameter derivatives since the nonlinearities need not be resolved exactly. Error only changes the path to the solution, not the solution, whereas it is more important to resolve the nonlinearities in the forward problem sufficiently (hence $N_I = 3$). The analytic method has a higher overhead, due to equation complexity, than the divided difference method and, therefore, may be slower.

The adjoint method and the analytic method (with storing of $[M]^{-1}$) are the same and therefore use the same number of linear solver calls. The quantities needed for the adjoint method are $[M]$, $\{v\}$ and $\{v^m\}$ to calculate the adjoint vector $\{\psi^*\}$, and then $[\partial M/\partial a_i]$ and $\{\partial R/\partial a_i\}$ are also needed to find the Jacobian. New quantities, such as the $[g]$ matrix of Chen (1995), are required by the adjoint method to extract the Jacobian from what is best suited for the calculation of the gradient. The quantities needed for

the analytical method are $[M]$, $\{v\}$, $[\partial M/\partial a_i]$ and $\{\partial R/\partial a_i\}$, two less quantities than required by the analytic method. Also, the adjoint method includes an extra matrix operation (to find the adjoint vector), which is avoided by the analytic process. Based on these reasons, the analytic method should be slightly faster than the adjoint method. In addition, the adjoint method of Chen (1995) is unduly complicated.

The fast analytic method shows promise for finding the Jacobian in an efficient and quick manner. The fast analytic method requires $N_I + N_P$ linear solver calls for N_P parameters. The number of linear solver calls compares well to the other methods. The actual performance can be improved if LU decomposition is used to decompose the $[M_D]$ matrix and then N_P back-substitutions performed for each parameter. LU decomposition is faster than performing linear solver calls, because $[M_D]$ is constant for any parameter.

Table 4.1 Breakdown of Derivative Method Performance

Method Type	Linear Solver Calls	Complexity of Equations
Forward Problem Only	N_I	low
Divided Difference Method	$N_I + N_I \times N_P$	low
Analytic Method (without storing $[M]^{-1}$)	$N_I + N_I \times N_P$	high
Adjoint Method / Analytic Method (storing $[M]^{-1}$)	$N_I + N_I \times N_P$*	high
Analytic Method (LU decomposition of $[M]$)	$N_I + N_I \times N_P$**	high
Fast Analytic Method	$N_I + N_P$**	low

where N_I = number of nonlinear iterations and N_P = number of parameters.
* less than this because $[M]^{-1}$ is only computed once and stored.
** less than this using LU decomposition and back substitution.

Recall that the adjoint and analytic methods for finding the Jacobian are identical, but the iteration of $[\partial M/\partial a_i]$ and $\{\partial R/\partial a_i\}$ slow these methods. The fast analytical method is the extension of the forward transient solution method. The linear nature of the simultaneous system of equations (for the parameter derivatives) is fully exploited. The full Jacobian matrix is found rather than single columns of the Jacobian like the other methods. Also, the fast analytic method can be used in the usual time-marching manner. A numerical example, using all of the aforementioned methods, for finding the parameter derivatives is in Appendix A where the performance of each method is judged with respect to accuracy and computation time.

4.5 Conversion of Friction Factor Derivatives to Roughness Derivatives

Previous application of inverse transient analysis performed calibration of pipe networks by determining a constant Darcy-Weisbach friction factor for each pipe (Liggett and Chen, 1994). However, the friction factor is function of the Reynolds number and the pipe roughness and thus can change with changing flow conditions. It is more meaningful, in a physical sense, to describe the friction in terms of the roughness of the pipe wall (for turbulent flows) than the friction factor. Therefore, a better parameter is the pipe roughness (ε) or the relative roughness (ε_D) rather than the friction factor. Thus, for gradient based minimisation methods, the parameter derivatives need to be with respect to the pipe roughness. The relative roughness is equal to the roughness height divided by the pipe diameter,

$$\varepsilon_D = \frac{\varepsilon}{D} \qquad (4.5.1)$$

The parameter derivatives, where those parameters have no dependence on any other variables, are determined in Section 4.4. If the inverse transient method is used to determine pipe roughness rather than friction factors, relationships are required for parameter derivatives with respect to the pipe roughness. In general, parameter derivatives with respect to the friction factor are more easily calculated than parameter derivatives with respect to the pipe roughness. Work presented in this section develops relationships that transform parameter derivatives with respect to the friction factor into parameter derivatives with respect to the relative roughness. The chain rule of differentiation is applied to the derivative of a variable with respect to the relative roughness $\partial v/\partial \varepsilon_D$,

$$\frac{\partial v}{\partial \varepsilon_D} = \frac{\partial v}{\partial f}\frac{\partial f}{\partial \varepsilon_D} \qquad (4.5.2)$$

The previously determined partial derivative $\partial v/\partial f$ is transformed into $\partial v/\partial \varepsilon_D$ using Eq. 4.5.2. Fortunately, $\partial f/\partial \varepsilon_D$ can be found by differentiating a function relating the Reynolds number of the flow and the relative roughness to the friction factor. The Colebrook-White equation (Colebrook and White, 1937) relates the relative roughness to the friction factor,

$$\frac{1}{\sqrt{f}} = -0.86\ln\left(\frac{\varepsilon_D}{3.7} + \frac{2.51}{\mathbf{R}\sqrt{f}}\right) \quad \text{.....(4.5.3)}$$

Eq. 4.5.3 is an implicit function in f requiring a nonlinear solver for solution. Differentiating with respect to the relative roughness produces

$$-\frac{0.5}{f^{3/2}}\frac{\partial f}{\partial \varepsilon_D} = -0.86\left(\frac{\varepsilon_D}{3.7} + \frac{2.51}{\mathbf{R}\sqrt{f}}\right)^{-1}\left(\frac{1}{3.7} - \frac{1.255}{\mathbf{R}f^{3/2}}\frac{\partial f}{\partial \varepsilon_D}\right) \quad \text{.....(4.5.4)}$$

Moving all known terms to the right hand side results in a rather complex expression for $\partial f/\partial \varepsilon_D$,

$$\frac{\partial f}{\partial \varepsilon_D} = \frac{1.72 f^{3/2}}{3.7}\left(\frac{\varepsilon_D}{3.7} + \frac{2.51}{\mathbf{R}\sqrt{f}}\right)^{-1}\left[1 + \frac{2.51}{\mathbf{R}}\left(\frac{\varepsilon_D}{3.7} + \frac{2.51}{\mathbf{R}\sqrt{f}}\right)^{-1}\right]^{-1} \quad \text{.....(4.5.5)}$$

Eq. 4.5.5 is explicit in nature since both f and $\mathbf{R}$ are already known from the forward transient solution. An alternative to the Colebrook-White equation is the simpler, explicit Swamee-Jain equation (Swamee and Jain, 1976) for relating the Reynolds number of the flow and the relative roughness to the friction factor

$$f = 1.325\left[\ln\left(\frac{\varepsilon_D}{3.7} + \frac{5.74}{\mathbf{R}^{0.9}}\right)\right]^{-2} \quad \text{.....(4.5.6)}$$

Differentiating Eq. 4.5.6 with respect to the relative roughness produces

$$\frac{\partial f}{\partial \varepsilon_D} = -\frac{2.65}{3.7}\left[\ln\left(\frac{\varepsilon_D}{3.7} + \frac{5.74}{\mathbf{R}^{0.9}}\right)\right]^{-3}\left(\frac{\varepsilon_D}{3.7} + \frac{5.74}{\mathbf{R}^{0.9}}\right)^{-1} \quad \text{.....(4.5.7)}$$

Eq. 4.5.7 seems less complex than Eq. 4.5.5 and can be further simplified if the friction factor is stored during the forward transient solution. Substitution of the Swamee-Jain expression (Eq. 4.5.6) for the terms containing the relative roughness and the Reynolds number in Eq. 4.5.7 produces

$$\frac{\partial f}{\partial \varepsilon_D} = -\frac{2.65}{3.7}\left(\frac{f}{1.325}\right)^{3/2} e^{-\sqrt{\frac{1.325}{f}}} = -0.4696 f^{3/2} e^{-\left(\frac{1.151}{\sqrt{f}}\right)} \quad \text{.....(4.5.8)}$$

Eq. 4.5.8 is only dependent on the friction factor and not as complex as the other expressions. Note that the negative sign was selected in the exponential term in Eq. 4.5.8.

In summary, once the partial derivatives with respect to the friction factor are known (and the friction factors stored during forward transient analysis), Eq. 4.5.8 can be used

to transform the partial derivatives with respect to the friction factor into partial derivatives with respect to the pipe roughness.

4.6 Calculation of Temporal and Spatial Derivatives

The Brunone *et al.* (1991) unsteady friction model requires estimates of the temporal and spatial derivatives at various times and locations in the characteristic grid. The divided difference method produces adequate results for the temporal derivatives but estimates of the spatial derivatives can be inaccurate. Also, accurate derivatives are useful for interpolation schemes (in networks with minimum Courant numbers lower than 1.0) that are compact and of high order. In the following sections these temporal and spatial derivatives are accurately calculated using analytic methods.

4.6.1 Divided Difference Method for Temporal and Spatial Derivatives

The divided difference method is the simplest way to calculate temporal and spatial derivatives. This method has been used extensively in the past in the calculation of unsteady friction. The temporal and spatial derivatives are calculated using points on the characteristic grid,

$$\frac{\partial Q}{\partial t} = \frac{Q_{x,(t+\Delta t)} - Q_{x,t}}{\Delta t} \quad \text{.....(4.6.1)}$$

$$\frac{\partial Q}{\partial x} = \frac{Q_{(x+\Delta x),t} - Q_{x,t}}{\Delta x} \quad \text{.....(4.6.2)}$$

The spacing of the characteristic grid limits the accuracy of this method (also because the derivatives are one sided). Typically, the accuracy of the divided difference method is sufficient for the temporal derivatives but not for the spatial derivatives where the spatial distance Δx is large compared to the time step Δt.

4.6.2 Analytic Method for Temporal Derivatives

An analytic method for the calculation of temporal derivatives is formed in the same manner as for the parameter derivatives. The set of boundary conditions, junction equations and characteristic equations, which describe the transient solution of a pipe network, are differentiated with respect to time. The temporal head boundary condition can be either specified or calculated using a divided difference approximation of the boundary head data H_{BC}

$$\frac{\partial H_{BC}}{\partial t} \approx \frac{H_{BC,(t+\Delta t)} - H_{BC,t}}{\Delta t} \quad \text{.....(4.6.3)}$$

An example junction is shown in Figure 4.1 for the junction of three pipes (two flows entering and one exiting).

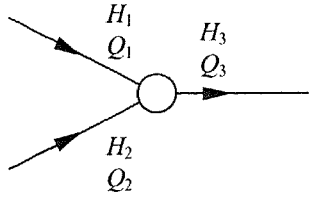

Figure 4.1 An Example Junction

The relationships describing this junction are the equality of heads and the continuity of flows around the node

$$H_1 = H_2 = H_3 \quad \text{.....(4.6.4)}$$

$$Q_1 + Q_2 = Q_3 \quad \text{.....(4.6.5)}$$

Differentiating Eqs. 4.6.4 and 4.6.5 with respect to time forms equations for the equality of temporal head derivatives and the continuity of temporal flow derivatives around the node,

$$\frac{\partial H_1}{\partial t} = \frac{\partial H_2}{\partial t} = \frac{\partial H_3}{\partial t} \quad \text{.....(4.6.6)}$$

$$\frac{\partial Q_1}{\partial t} + \frac{\partial Q_2}{\partial t} = \frac{\partial Q_3}{\partial t} \quad \text{.....(4.6.7)}$$

The final set of equations that describe a transient pipe network system are the characteristic equations (Eqs. 3.2.31 and 3.2.32). The characteristic equations are differentiated with respect to time forming

$$\frac{\partial}{\partial t}\left(\frac{\partial H}{\partial t}\right)+\frac{a^2}{gA}\frac{\partial}{\partial x}\left(\frac{\partial Q}{\partial t}\right)=0 \quad \text{.....(4.6.8)}$$

$$\frac{1}{gA}\frac{\partial}{\partial t}\left(\frac{\partial Q}{\partial t}\right)+\frac{\partial}{\partial x}\left(\frac{\partial H}{\partial t}\right)+\frac{f|Q|}{gDA^2}\left(\frac{\partial Q}{\partial t}\right)=0 \quad \text{.....(4.6.9)}$$

The solution of Eqs. 4.6.8 and 4.6.9 using the method of characteristics (Section 3.3.1) forms two compatibility equations that are valid along characteristic lines. The boundary condition, junction equation and characteristic equations, which were differentiated with respect to time, form a linear system of equations,

$$[M_T]\left\{\frac{\partial v}{\partial t}\right\}=\{R_T\} \quad \text{.....(4.6.10)}$$

The solution of Eq. 4.6.10 determines the partial derivatives of the flow and pressure with respect to time. The analytic method (described here) produces temporal derivatives of greater accuracy than the divided difference method.

4.6.3 Analytic Method for Spatial Derivatives

The analytic method for the calculation of spatial derivatives is somewhat more complicated than the analytic method for the temporal derivatives. It involves the conversion of the system of simultaneous equations, which includes the boundary condition, junction and characteristic equations, describing the temporal derivatives to their spatial equivalents. Substitution of the governing unsteady equations into the temporal derivative relationships achieves this conversion. The governing unsteady equations (see Section 3.2) of continuity and motion respectively are

$$\frac{\partial H}{\partial t}=-\frac{a^2}{gA}\frac{\partial Q}{\partial x} \quad \text{.....(4.6.11)}$$

$$\frac{\partial Q}{\partial t}=-gA\frac{\partial H}{\partial x}-\frac{f|Q|Q}{2DA} \quad \text{.....(4.6.12)}$$

Substituting Eq. 4.6.11 into the temporal derivative head boundary condition (Eq. 4.6.3) forms a spatial derivative flow boundary condition. Conversion of temporal derivatives into spatial derivatives changes the variable type, e.g. head changes to flow as

$$\frac{\partial Q_{BC}}{\partial x}=-\frac{gA}{a^2}\frac{\partial H_{BC}}{\partial t} \quad \text{.....(4.6.13)}$$

A similar conversion is performed on the temporal derivative junction equations (Eqs. 4.6.6 and 4.6.7). Now, the substitution uses both governing unsteady equations (Eqs. 4.6.11 and 4.6.12). The equality of temporal head derivatives at a junction becomes a weighted equality of spatial flow derivatives at the junction and the continuity of temporal flow derivatives becomes an expression containing spatial head derivatives and known flows,

$$\frac{a_1^2}{A_1}\frac{\partial Q_1}{\partial x} = \frac{a_2^2}{A_2}\frac{\partial Q_2}{\partial x} = \frac{a_3^2}{A_3}\frac{\partial Q_3}{\partial x} \quad \text{.....(4.6.14)}$$

$$gA_1\frac{\partial H_1}{\partial x} + \frac{f_1 Q_1|Q_1|}{2D_1A_1} + gA_2\frac{\partial H_2}{\partial x} + \frac{f_2 Q_2|Q_2|}{2D_2A_2} = gA_3\frac{\partial H_3}{\partial x} + \frac{f_3 Q_3|Q_3|}{2D_3A_3} \quad \text{.....(4.6.15)}$$

The governing unsteady equations are differentiated simply with respect to distance x,

$$\frac{\partial}{\partial t}\left(\frac{\partial H}{\partial x}\right) + \frac{a^2}{gA}\frac{\partial}{\partial x}\left(\frac{\partial Q}{\partial x}\right) = 0 \quad \text{.....(4.6.16)}$$

$$\frac{1}{gA}\frac{\partial}{\partial t}\left(\frac{\partial Q}{\partial x}\right) + \frac{\partial}{\partial x}\left(\frac{\partial H}{\partial x}\right) + \frac{f|Q|}{gDA^2}\frac{\partial Q}{\partial x} = 0 \quad \text{.....(4.6.17)}$$

Transforming Eqs. 4.6.16 and 4.6.17 into directional derivatives along characteristics forms two compatibility equations that are valid along characteristic lines. The spatial derivative boundary conditions, junction equations and compatibility equations form a linear system of equations,

$$[M_X]\left\{\frac{\partial v}{\partial x}\right\} = \{R_X\} \quad \text{.....(4.6.18)}$$

The solution of Eq. 4.6.18 produces all of the spatial derivatives of the flow and pressure in a pipe network under transient conditions. The analytic method for spatial derivatives is more complex than the analytic method for temporal derivatives, due to the spatial derivative boundary condition and junction expressions, which are not quite intuitive. An example of the analytic method for the calculation of spatial derivatives is shown in Appendix A.

4.6.4 Temporal Conversion Method for Spatial Derivatives

The temporal conversion method for the calculation of spatial derivatives is simpler than the analytic method. The temporal conversion method relies on first using the analytic method to determine the temporal derivatives of the heads and flows (Section

4.6.2). Then, the governing unsteady equations are rearranged in terms of the already known temporal derivatives and heads and flows. The governing unsteady equations of continuity and motion are

$$\frac{\partial Q}{\partial x} = -\frac{gA}{a^2}\frac{\partial H}{\partial t} \quad \text{.....(4.6.19)}$$

$$\frac{\partial H}{\partial x} = -\frac{1}{gA}\frac{\partial Q}{\partial t} - \frac{f|Q|Q}{2gDA^2} \quad \text{.....(4.6.20)}$$

The governing equations transform the temporal derivatives of the heads and flows into spatial derivatives. The temporal conversion method is similar in accuracy to the analytic method. Appendix A shows an example of the temporal conversion method for spatial derivatives.

4.6.5 Chen's (1995) Method for Spatial Derivatives

Chen (1995) tested different interpolation methods. One of these methods, a compact cubic spaceline interpolation, requires the spatial derivatives of head and flow. Chen (1995) determined the spatial derivatives in a manner similar to the analytic method for temporal derivatives. The governing unsteady equations (Eqs. 4.6.16 and 4.6.17) were differentiated with respect to the distance x and the method of characteristics applied, just as in the analytic method for spatial derivatives (Section 4.6.3). However, the Chen (1995) method differs from the analytic spatial method for the boundary and junction equations. Considering the head boundary condition and junction example (again) best shows the difference. Chen (1995) proposed that the spatial derivative head boundary condition be found by dividing the temporal derivative boundary condition by the wave speed,

$$\frac{\partial H_{BC}}{\partial x} = \frac{1}{a}\frac{\partial H_{BC}}{\partial t} \quad \text{.....(4.6.21)}$$

Eq. 4.6.21 produces incorrect spatial boundary condition derivatives. In addition, the junction example helps explain the difference between the Chen (1995) method and the analytic method for spatial derivatives. Chen (1995) introduces an average spatial derivative of head at a node and assumes continuity of spatial flow derivatives

$$\frac{\partial H_{node}}{\partial x} = \frac{1}{3}\left(\frac{\partial H_1}{\partial x} + \frac{\partial H_2}{\partial x} + \frac{\partial H_3}{\partial x}\right) \quad \text{.....(4.6.22)}$$

$$\frac{\partial Q_1}{\partial x} + \frac{\partial Q_2}{\partial x} = \frac{\partial Q_3}{\partial x} \quad \text{.....(4.6.23)}$$

The spatial derivative boundary conditions, junction and compatibility equations form a linear system of equations for a transient pipe network.

4.6.6 Summary on the Calculation of Temporal and Spatial Derivatives

Analytic derivatives potentially provide higher accuracy and more efficient calculation of temporal and spatial derivatives for unsteady friction models and interpolation schemes than numerical differentiation would. Divided difference methods, typically used to calculate temporal and spatial derivatives, produce inaccurate results, which can have large errors and effects on subsidiary algorithms that use them. All of the schemes are linear, unlike the simultaneous system for the forward solution. The temporal conversion method for spatial derivatives is preferred over the analytic method because it is simpler and should produce results of similar accuracy in a similar computation time. The Chen (1995) method for finding spatial derivatives produces incorrect results. Appendix A shows these schemes applied to an example pipeline.

4.7 Data Requirements

The solvability of parameters in a water distribution network is hampered by two deficiencies. The two deficiencies are classed as mixed-determinant systems and time-lagged systems, and are required to be addressed when solving the forward transient problem and when using data in the inverse transient method. A mixed-determinant system may result in a partial solution of a pipe network or no solution at all. A time-lagged system suffers from a lack of data needed to determine the parameters using the inverse transient method. Liggett and Chen (1994) identified similar deficiencies for the solution of the forward transient problem, however in this section, the deficiencies apply to the inverse transient problem only.

4.7.1 Underdetermined and Overdetermined Systems

In a mixed-determined system, the parameters in one or more sections of a network cannot be solved because there is insufficient measurement information. It occurs due to the positioning of data measurement sites and the general topology of the network. For example, consider the calibration of the friction factors in Figure 4.2 using inverse steady state analysis. Pressure head measurements are made at node 3. The friction factors in pipes 1 and 2 can be determined using two demand cases (extended period simulations); however, the friction factor in pipe 3 cannot be determined, no matter how many extra demand cases are used. Figure 4.2 demonstrates a mixed-determined system because it shows both determinate and indeterminate properties (when using inverse steady state analysis). Note that the inverse transient method can determine the friction factor in pipe 3, whereas inverse steady state analysis cannot.

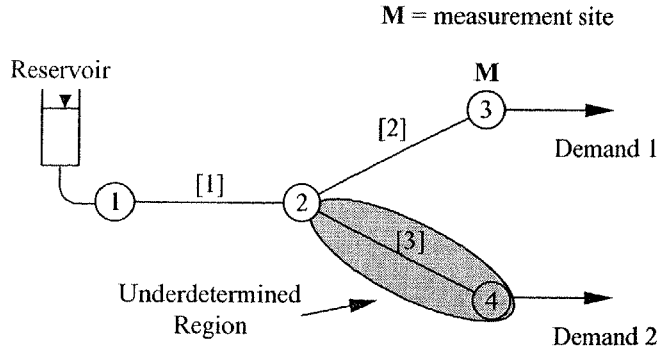

Figure 4.2 Mixed-Determined System

Liggett and Chen (1994) suggested a solution to the detection of potential indeterminate regions in pipe networks and data arrangements for transient analysis. The use of singular value decomposition (SVD, Press *et al.*, 1992) identified areas of indeterminacy. Combined with SVD, other methods may be used to solve for the determined portions of the network while ignoring the underdetermined parts. A cause of underdetermined regions in a pipe network in inverse transient analysis is the damping of pressure waves before they arrive at a measurement site. Damping is a potential problem in long pipelines where steady and unsteady frictional effects on the pressure wave are large, and therefore information, useful for leak detection or calibration, is lost (hence causing indeterminable parameters). Identification and solution of mixed-determined problems is an area for further research.

4.7.2 Time Levels in Parameters

A time-lagged problem in transient analysis exists due to the time required for a pressure wave to propagate to different regions in a network (Liggett and Chen, 1994). The time-lag defines time levels in parameters (or at nodes) that are observable on the characteristic gird (sometimes called a "lattice diagram" by electrical engineers). An example demonstrates the time levels for different regions in a pipe network. Consider the example branched pipeline system shown in Figure 4.3.

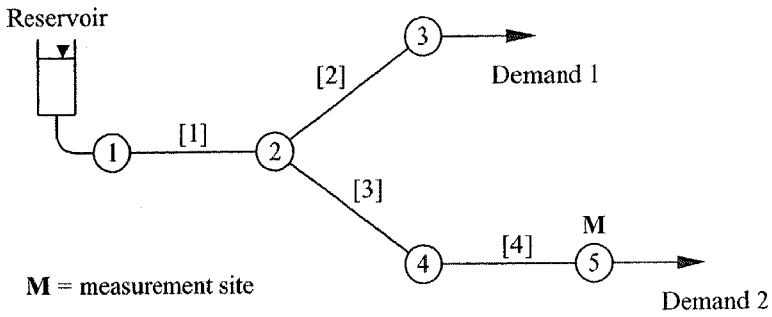

Figure 4.3 Example Branched System

In Figure 4.3, pipe numbers are in square brackets and node numbers are in circles. The boundary conditions for the example branched network are a known head at node 1 and known demands at nodes 3 and 5. Steady conditions exist in the example branched system before time $t = 0$. While at steady state, the friction factor in pipe 2 is underdetermined while the friction factors in pipes 1, 3 and 4 are determined, hence the system is mixed-determined (for inverse friction factor calibration). Consider a transient event in the example branched system initiated at node 5 at time $t = 0$. The propagation of information (due to the transient event) throughout the example network is shown in Figure 4.4 on the characteristic grid (pipe by pipe).

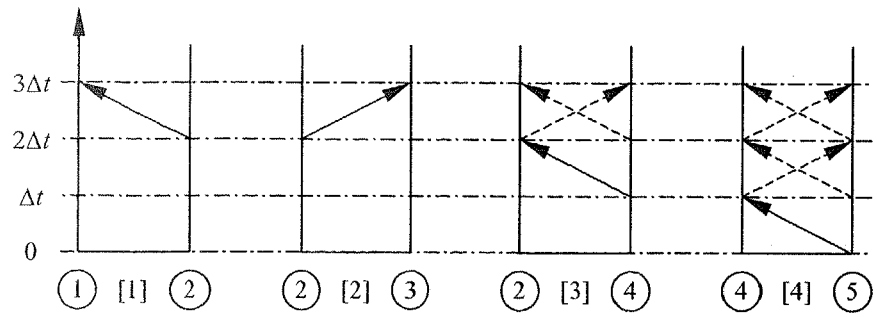

Figure 4.4 Time Levels in the Example Branched System

The continuous arrows in Figure 4.4 show the primary propagation of transient information from the event originating from node 5. The dashed arrows show the propagation of secondary information caused by reflections from the propagation of the primary event past junctions or changes in the boundary conditions at node 5 for times after $t = 0$. As shown, the transient information from node 5 reaches node 4 at time $t = \Delta t$, then reaches node 2 at time $t = 2\Delta t$, and then arrives at nodes 1 and 3 at time $t = 3\Delta t$. A summary of the time levels for the example branched system is shown in Table 4.2.

Table 4.2 Time Level of Nodes (Measurement at Node 5)

Node	Time Level
1	$3\Delta t$
2	$2\Delta t$
3	$3\Delta t$
4	Δt
5	0

The time level is useful to predict when underdetermined regions of a pipe network become determined for inverse transient analysis. In the example branched system, when the system is at steady state (before time $t = 0$), the friction factor in pipe 2 is underdetermined. However, at time $t = 3\Delta t$ no underdetermined regions exist in the system. The propagation of information in the system has increased the determinedness of the system.

Although the example branched system might seem trivial, time levels are important in a large network. Minimum times of simulation are required for signals to reach all parts of the network and provide sufficient information for leak detection and calibration. Liggett and Chen (1994) suggested that the time levels be found for every node in the

pipe system with respect to every measurement node. Therefore, a node may have a number different time levels associated with different measurement sites. Then, the smallest time level is selected, thus defining the time level for that node. Because of the time level effect, solutions for parameters may exist at different locations in the system (in both time and space) depending upon where the unknown parameters and measurement sites are located.

4.8 Error Estimation in Fitted Parameters

Parameters determined using the inverse transient method are more useful if the likely error in their calculation is known. Quoting a value of a parameter to a certain precision is inappropriate if the error in that parameter is larger than the quoted precision. Chen (1995) provided an approach for estimating the errors in the parameters (calculated through the inverse transient method) from the errors in the measured data. Consider the inverse problem defined as $a_j = f\left(H_1^m, H_2^m, \ldots, H_M^m\right)$, where the parameter a_j is a function of the measured data, $\mathbf{H^m}$. Now assume that the inverse problem has been solved an infinite number of times so that the most probable value for a_j is $\bar{a}_j = f\left(\bar{H}_1^m, \bar{H}_2^m, \ldots, \bar{H}_M^m\right)$, where an overscore on a variable represents the expected value of that variable. Performing a Taylor series expansion of a_j about $\bar{a}_j$ yields

$$a_j = \bar{a}_j + \left(H_1^m - \bar{H}_1^m\right)\frac{\partial a_j}{\partial H_1^m} + \left(H_2^m - \bar{H}_2^m\right)\frac{\partial a_j}{\partial H_2^m} + \ldots \quad \text{.....(4.8.1)}$$

The variance of a_j, assuming a good fit and normally distributed measurement errors, is

$$\sigma_{a_j}^2 = \lim_{K\to\infty}\left[\frac{1}{K}\sum_{k=1}^{K}\left(a_{j,k} - \bar{a}_{j,k}\right)^2\right] \quad \text{.....(4.8.2)}$$

where K = the total number of repeated inverse transient analyses and $a_{j,k} = a_j$ from the k^{th} repeated inverse transient analysis. Moving $\bar{a}_j$ to the left hand side of Eq. 4.8.1 and neglecting terms of second or higher order and combining with Eq. 4.8.2 yields

$$\sigma_{a_j}^2 = \lim_{K\to\infty}\sum_{k=1}^{K}\frac{1}{K}\left[\left(H_1^m - \bar{H}_1^m\right)\frac{\partial a_{j,k}}{\partial H_1^m} + \left(H_2^m - \bar{H}_2^m\right)\frac{\partial a_{j,k}}{\partial H_2^m} + \ldots\right]^2 \quad \text{.....(4.8.3)}$$

The squared expression inside of the sum is expanded forming

$$\sigma_{a_j}^2 = \lim_{K\to\infty}\sum_{k=1}^{K}\frac{1}{K}\left[\left(H_1^m - \overline{H}_1^m\right)^2\left(\frac{\partial a_{j,k}}{\partial H_1^m}\right)^2 + \left(H_2^m - \overline{H}_2^m\right)^2\left(\frac{\partial a_{j,k}}{\partial H_2^m}\right)^2 + 2\left(H_1^m - \overline{H}_1^m\right)\left(H_2^m - \overline{H}_2^m\right)\left(\frac{\partial a_{j,k}}{\partial H_1^m}\right)\left(\frac{\partial a_{j,k}}{\partial H_2^m}\right) + \ldots\right] \quad \text{.....(4.8.4)}$$

Including the variances and covariances of the measurement data, where $\sigma_{H_i^m H_j^m}$ represents the covariance for H_i^m and H_j^m, Eq. 4.8.4 becomes

$$\sigma_{a_j}^2 = \sigma_{H_1^m}^2\left(\frac{\partial a_j}{\partial H_1^m}\right)^2 + \sigma_{H_2^m}^2\left(\frac{\partial a_j}{\partial H_2^m}\right)^2 + \ldots + 2\sigma_{H_1^m H_2^m}\left(\frac{\partial a_j}{\partial H_1^m}\right)\left(\frac{\partial a_j}{\partial H_2^m}\right) + \ldots \quad \text{.....(4.8.5)}$$

Eq. 4.8.5 is called the *error propagation equation*. If the errors in any two of the measured heads are uncorrelated, the last term of Eq. 4.8.5 can be neglected, thus producing the approximate expression

$$\sigma_{a_j}^2 \approx \sigma_{H_1^m}^2\left(\frac{\partial a_j}{\partial H_1^m}\right)^2 + \sigma_{H_2^m}^2\left(\frac{\partial a_j}{\partial H_2^m}\right)^2 + \ldots \quad \text{.....(4.8.6)}$$

Eq. 4.8.6 explicitly gives the size of the uncertainty for the fitted parameter a_j with contribution from each of the measured data. However, a problem arises that, much like the calculation of the Jacobian and Hessian in Section 4.3.3, the parameters are not an explicit function of the measurements. The derivatives in Eq. 4.8.6 may be approximated using the divided difference method. The derivative of a_j with respect to H_i^m is approximately

$$\frac{\partial a_j}{\partial H_i^m} \approx \frac{a_j\left(\mathbf{H^m} + \delta H_i^m\right) - a_j\left(\mathbf{H^m}\right)}{\delta H_i^m} \quad \text{.....(4.8.7)}$$

where $\mathbf{H^m}$ is a vector of measurement data and δH_i^m is a small perturbation in measurement i. Unfortunately, the calculation of the derivatives of the parameters using Eq. 4.8.7 is extremely inefficient. It would take $M + 1$ inverse calculations if each piece of data were to be used. However, if the errors in the data are randomly distributed with small standard deviations, the perturbation δH_i^m may be replaced with the standard deviation $\sigma_{H_i^m}$. The difference in the parameters due to the perturbation, $a_j\left(\mathbf{H^m} + \delta H_i^m\right) - a_j\left(\mathbf{H^m}\right)$, is replaced by $\delta a_j\left(H_i^m\right)$. Implementing these changes to Eq. 4.8.7 results in

$$\frac{\partial a_j}{\partial H_i^m} = \frac{\delta a_j\left(H_i^m\right)}{\sigma_{H_i^m}} \quad \text{.....(4.8.8)}$$

The substitution of Eq. 4.8.8 into Eq. 4.8.6 results in an expression for the variance of parameter a_j in terms of the sum of the perturbations in a_j generated from perturbations in each measured head,

$$\sigma_{a_j}^2 = \sum_{i=1}^{M}\left[\delta a_j\left(H_i^m\right)\right]^2 \quad \text{.....(4.8.9)}$$

An expression for the perturbation in parameter a_j generated from the perturbation in a measured head can be determined by recalling the inverse Hessian solution described in Section 4.3.2. The inverse Hessian solution written in matrix form is

$$[\alpha]\{\delta a\} = \{\beta\} \quad \text{.....(4.8.10)}$$

where elements of the $[\alpha]$ matrix and the $\{\beta\}$ vector are respectively

$$\alpha_{jk} = \sum_{i=1}^{N} \frac{1}{\sigma_{H_i^m}^2} \frac{\partial H_i}{\partial a_j} \frac{\partial H_i}{\partial a_k} \quad \text{.....(4.8.11)}$$

$$\beta_j = \sum_{i=1}^{N} \frac{\left(H_i^m - H_i\right)}{\sigma_{H_i^m}^2} \frac{\partial H_i}{\partial a_j} \quad \text{.....(4.8.12)}$$

Pre-multiplying Eq. 4.8.10 by $[\alpha]^{-1}$ results in an expression for the vector $\{\delta a\}$,

$$\{\delta a\} = [\alpha]^{-1}\{\beta\} \quad \text{.....(4.8.13)}$$

The correction δa_j for a particular parameter a_j is found by multiplying the j^{th} row of $[\alpha]^{-1}$ by $\{\beta\}$ in which an element of the inverse of matrix $[\alpha]$ is represented by C_{jk}.

$$\delta a_j = \sum_{k=1}^{N} C_{jk}\beta_k \quad \text{.....(4.8.14)}$$

Eq. 4.8.14 relates the perturbation in a_j to the perturbations in all measured pressure heads (contained in $[\alpha]$ and $\{\beta\}$). But in the case of Eq. 4.8.9, the perturbation in a_j is generated from a perturbation in one measured pressure head only. Taking this into consideration, Eq. 4.8.14 may be written as

$$\delta a_j\left(H_i^m\right) = \sum_{k=1}^{N} C_{jk}\beta_k\left(H_i^m\right) \quad \text{.....(4.8.15)}$$

where each of the vector components β_k is defined for only one measured pressure head H_i^m. The expression for the vector element $\beta_k\left(H_i^m\right)$ is

$$\beta_k\left(H_i^m\right) = \frac{\left(H_i^m - H_i\right)}{\sigma_{H_i^m}^2} \frac{\partial H_i}{\partial a_k} \quad \text{.....(4.8.16)}$$

A further simplification is made by replacing the perturbation in the measured pressure head $\left(H_i^m - H_i\right)$ by the standard deviation in that measured pressure head $\sigma_{H_i^m}$. The resulting expression for $\{\beta\}$ is

$$\beta_k\left(H_i^m\right) = \frac{1}{\sigma_{H_i^m}} \frac{\partial H_i}{\partial a_k} \quad \text{.....(4.8.17)}$$

Substitution of Eq. 4.8.17 into 4.8.15 produces an expression for the perturbation in parameter a_j generated by a perturbation in measured pressure head H_i^m

$$\delta a_j\left(H_i^m\right) = \sum_{k=1}^{N} C_{jk} \frac{1}{\sigma_{H_i^m}} \frac{\partial H_i}{\partial a_j} \quad \text{.....(4.8.18)}$$

Substitution of Eq. 4.8.18 into Eq. 4.8.9 creates a relationship for the estimated variance of parameter a_j

$$\sigma_{a_j}^2 = \sum_{i=1}^{M} \left[\sum_{k=1}^{N} C_{jk} \frac{1}{\sigma_{H_i^m}} \frac{\partial H_i}{\partial a_k} \right]^2 \quad \text{.....(4.8.19)}$$

Expanding the squared term in Eq. 4.8.19 as the product of two summations gives

$$\sigma_{a_j}^2 = \sum_{i=1}^{M} \left[\left(\sum_{k=1}^{N} C_{jk} \frac{1}{\sigma_{H_i^m}} \frac{\partial H_i}{\partial a_k} \right) \left(\sum_{l=1}^{N} C_{jl} \frac{1}{\sigma_{H_i^m}} \frac{\partial H_i}{\partial a_l} \right) \right] \quad \text{.....(4.8.20)}$$

The product of two summations may be expressed as a double summation,

$$\sigma_{a_j}^2 = \sum_{i=1}^{M} \left[\sum_{k=1}^{N} \left(\sum_{l=1}^{N} C_{jk} C_{jl} \frac{1}{\sigma_{H_i^m}^2} \frac{\partial H_i}{\partial a_k} \frac{\partial H_i}{\partial a_l} \right) \right] \quad \text{.....(4.8.21)}$$

Then, rearranging Eq. 4.8.21 forms

$$\sigma_{a_j}^2 = \sum_{k=1}^{N} \left[C_{jk} \sum_{l=1}^{N} \left(C_{jl} \sum_{i=1}^{M} \frac{1}{\sigma_{H_i^m}^2} \frac{\partial H_i}{\partial a_k} \frac{\partial H_i}{\partial a_l} \right) \right] \quad \text{.....(4.8.22)}$$

The term in the inner parentheses of Eq. 4.8.22 is simply an element of the [α] matrix (shown in Eq. 4.8.11). Substitution of the matrix element α_{kl} into Eq. 4.8.22 results in

$$\sigma_{a_j}^2 = \sum_{k=1}^{N} \left[C_{jk} \sum_{l=1}^{N} \left(C_{jl} \alpha_{kl} \right) \right] \quad \text{.....(4.8.23)}$$

Matrix [C] was previously defined as the inverse of the [α] matrix. Therefore, the inner summation term of Eq. 4.8.23 results in an element of the identity matrix [I] and

$$\sigma_{a_j}^2 = \sum_{k=1}^{N} C_{jk} I_{jk} \quad \text{.....(4.8.24)}$$

in which I_{jk} is the element of the identity matrix in the j^{th} row and k^{th} column. Hence, Eq. 4.8.24 simplifies to

$$\sigma_{a_j}^2 = C_{jj} \quad \text{.....(4.8.25)}$$

Analogously, the covariance between parameters a_j and a_k is

$$\sigma_{a_j a_k} = C_{jk} \quad \text{.....(4.8.26)}$$

The matrix $[C]$ (or $[\alpha]^{-1}$) is called the *covariance matrix* (Press *et al.*, 1992). Thus, without any additional calculation at the end of the minimisation process, the standard error estimate for all parameters is determined assuming the uncertainties in the measured data are known. Nash and Walker-Smith (1987) state that, through Monte Carlo simulation testing, parameter error estimates found using Eqs. 4.8.25 and 4.8.26 are superior to other techniques, particularly when numerical approximations to derivatives were used. Concepts from this section are used in Chapter 7 to find the optimal number and location of measurement sites.

4.9 Test of Goodness-of-Fit

For data fitting, it is important to know whether a model is appropriate to describe the processes being modelled. Thus the question becomes, even though a set of best-fit parameters have been found, how well does the model match the measured data? The goodness-of-fit criterion is a standard statistic that is useful in describing the agreement between measured data and model, using the best-fit parameters. The goodness-of-fit criterion is defined in terms of the reduced chi-square statistic, defined as

$$\chi_\nu^2 = \frac{\chi^2}{\nu} = \frac{s^2}{\sigma^2} \quad \text{.....(4.9.1)}$$

where the chi-square statistic χ^2 has ν degrees of freedom. For the inverse transient problem, ν equals $M-N$ or the number of measured data (M) minus the number of parameters to be fitted (N). The variance of the fit, s^2, is

$$s^2 = \frac{1}{\nu}\sum_{i=1}^{M}\left[H_i^m - H_i(\mathbf{a})\right]^2 \quad \text{.....(4.9.2)}$$

The chi-square test for the goodness-of-fit states that if the fitting function is a good approximation of the parent function, then the reduced chi-square is approximately

equal to one. That is to say that the estimated variance, s^2, should be similar to the parent variance, σ^2. If the fitting model is not appropriate for describing the data, then the deviations between the model and data will be large and the estimated variance in the data will be small, yielding a reduced chi-square value greater than one. Conversely, a small chi-square value of significantly less than one may indicate a poor fit. It could indicate unknown uncertainties in the fitting process such as overestimation of the variances of data. The general rule for the examination the goodness-of-fit is to compare the final value of the chi-square function with the numbers of degrees of freedom. Similar values indicate a good fit.

The check for goodness-of-fit is meaningless unless the uncertainties in the data are known. The uncertainties are rarely known in common practice, but if a good fit assumed, the variance of the data can be approximated as

$$\sigma^2 = \frac{1}{\nu}\sum_{i=1}^{M}\left[H_i^m - H_i(\mathbf{a})\right]^2 \quad \text{.....(4.9.3)}$$

The goodness-of-fit criterion is useful in the analysis of experimental data (see Chapters 11 and 12), and is useful for a complete understanding of minimisation problems using the chi-square statistic (sum of the squares of the differences between measured and computed pressures).

4.10 Convergence of the Inverse Transient Method

It is important to know if the parameters have converged when using the inverse transient technique. There are many types of convergence criteria but the most commonly used in an iterative solution process is to assume convergence when the derivatives (or changes) in the objective function become smaller than machine accuracy. This criterion can be a pointless goal, especially when the computational effort is high between iterations of a minimisation scheme. The extra computational effort required to find the parameters to a higher accuracy can outweigh whether the extra accuracy is significant enough to warrant the effort. Press *et al.* (1992) suggest that a tolerance for convergence should be such that the changes in the parameters are smaller than the square root of the machine precision. Also, two other statistically

relevant criteria for convergence are described by Press *et al.* (1992). The first criterion states that a change in the objective function per degree of freedom of less than 1% from one trial set of parameters to another is probably not significant and the minimisation should stop. The second criterion states that, since extra iterations are computationally wasteful, a change in parameters that changes chi-square by an amount much less than one is never statistically relevant.

Of course if local minima exist, there is a chance that the minimisation procedure used in the inverse transient technique could become trapped. This situation is characterised by the minimised vector of parameters cycling around a few specific vectors while the objective function fluctuates outside the convergence criterion. The easiest way to remedy this problem is to start from a different set of trial parameters in the hope that the minimisation method will travel down a different path to the solution. Another method is to use a different objective function, which is certain to proceed down a different path to the solution. An example of a different objective function (compared to Eq. 4.3.3) is

$$E = \sum_{i=1}^{M} \left| \frac{H_i^m - H_i}{\sigma_i} \right| \qquad (4.10.1)$$

Another common method to change the path to a solution is to introduce set ranges within which the parameters are constrained.

4.11 Sensitivity Analysis

Parameter sensitivities are useful in determining the sensitivity of both the minimisation method and model to changes in the parameters. The sensitivities show the effects of parameters on the objective function (Stoner, 1970; Chen, 1995). The calculation of the sensitivities should be simple and rely only on the calculation of the forward transient problem (for fast computation).

One of the most important sensitivities is the convergence sensitivity. The convergence sensitivity is a vector containing the partial derivatives of the objective function with respect to each of the parameters,

$$\left\{\frac{\partial E}{\partial a_i}\right\} \quad \text{.....(4.11.1)}$$

The convergence sensitivity indicates how sensitive the objective function is to a small change in parameter a_i and therefore can be thought of as how successful the minimisation scheme is likely to converge with regard to a_i. For example, a large absolute value of the convergence sensitivity corresponding to parameter a_i means that a small change in that parameter is likely to have large effects on the objective function, indicating that the parameter can be calculated accurately. Conversely, a small absolute value of the convergence sensitivity will mean that parameter a_i does not have a large effect on the objective function and raises the possibility that a large range of values for the parameter will satisfy the minimisation criteria, and that the parameter is not expected to be well determined.

Another important sensitivity measure is the model sensitivity. The model sensitivity forms a matrix representing how certain parameters influence the dependent pressure heads and flows in a pipe network. It is formed by calculating the partial derivatives of the pressure heads with respect to a parameter a_i,

$$\left[\frac{\partial H_j}{\partial a_i}\right] \quad \text{.....(4.11.2)}$$

The model sensitivity may be calculated with respect to the flow as well but, since the pressure is usually the observed property and used in the objective function, is not usually calculated. The model sensitivity is related closely to the calculation of the Jacobian and, is therefore, rather important to the minimisation method. Like the convergence sensitivity, the larger the absolute model sensitivity, the more influence a parameter has on a particular nodal pressure head at a certain time step, thus providing information as to which parts of the network are insensitive to certain parameters. The convergence and model sensitivities provide a basis for the determination of optimum measurement site configurations in Chapter 7.

4.12 Conclusions

This chapter describes the general methods used to determine parameters using the inverse transient technique, given measurement data. The minimisation problem was defined, showing that the least squares objective function originates from maximum likelihood estimators. Two common solutions methods were described, the Newton-Raphson and Levenberg-Marquardt methods, for the minimisation of the objective function. Both of these methods use the Jacobian.

Original research presented in this chapter derives different methods for determining the Jacobian (or the parameter derivatives). Two new methods are proposed, called the analytic and fast analytic methods. The analytic method was found to be the same as the adjoint method (first applied to inverse transient analysis by Liggett and Chen, 1994). The fast analytic method is superior in computational speed and simplicity (compared to the analytic and adjoint methods). A worked numerical example in Appendix A confirms these findings. The partial derivatives with respect to the friction factors were transformed into more physically meaningful partial derivatives with respect to the pipe roughnesses using the Colebrook-White and Swamee-Jain formulas.

The calculation of temporal and spatial derivatives, used in the Brunone *et al.* (1991) model and in interpolation schemes, was investigated. Analytic schemes were derived for both the temporal and spatial derivatives. An additional scheme was produced called the temporal conversion method for spatial derivatives, due to the complexity of the analytic method for spatial derivatives. Again, previous methods for the calculation of derivative were discussed.

The calculation of the parameter derivatives using the fast analytic method provides additional impetus for the use of the implicit MOC method. When using the explicit MOC formulation, the parameter derivatives must be solved for each parameter separately, whereas when using the implicit MOC formulation, the parameter derivatives are solved more efficiently using decomposition and back-substitution for all parameters at once. Thus the use of the implicit MOC formulation points towards higher efficiencies in the inverse transient method where a derivative-based algorithm is used for the minimisation.

Other important issues discussed, specific to transient analysis, were data requirements. Inverse steady state analysis could be of a mixed-determinate nature, while inverse transient analysis was likely to be determinate, mainly due to the propagation of transient information. Regions of a pipe network were shown to have an associated time level due to the time taken for a transient wave to reach them from a measurement site. Time levels are important for applications of the inverse transient method in large pipe networks.

Finally, a complete picture of inverse analysis is painted by exploring methods for estimating the error in solved parameters. Also, goodness-of-fit criteria, convergence criteria and sensitivity analysis for inverse methods are discussed. Thus, a complete methodology for inverse methods is presented. Elements of this chapter are used throughout later chapters of this thesis.

Chapter 5

The Effect of Initial Conditions on Inverse Transient Analysis

5.1 Introduction

The effect of initial conditions on the inverse transient method is investigated in this chapter. Previous research by Chen (1995) did not focus on initial conditions (IC), but rather on the transient response after initialisation of the event. New research presented in this chapter shows that the initial conditions are important with respect to the implementation of the inverse transient method. Two case studies, one using a single pipeline and the other using a small pipe network, show the importance of initial conditions.

Incorrect initial conditions may have a detrimental effect on the accuracy of the inverse transient method. The initial conditions need to be compatible with the governing unsteady pipe flow equations and the initial boundary conditions. An approximate steady state commonly exists in pipe networks, however, in the experimental pipeline (see Chapter 10) a true steady state exists before each transient event. Steady state conditions can be determined from a steady state solver (e.g., EPANET) or by running a transient solver for a long simulation period with no change in the boundary conditions.

The initial conditions used by Chen (1995) were set as the steady state conditions for the solution parameters. These initial conditions did not change throughout the progress of the minimisation algorithm, during which better estimates of the parameters were calculated. The result is a bias towards the solution parameters and a false sense of good and efficient leak detection and calibration results (Liggett and Chen, 1994). A question that may be asked is: when are the initial conditions important and do they have an effect on inverse transient analysis? The answer to these questions is demonstrated using two case studies. The first case study uses a simple pipeline, the analysis of which provides a clear understanding of the importance of initial conditions. The second case study is a repeat of results from Liggett and Chen (1994) and Chen (1995) using a small example pipe network.

5.2 The Effect of Initial Conditions: Case Study #1

A simple pipeline highlights the effect of incorrect initial conditions on the inverse transient method. The pipeline is based on the apparatus used in experimental verification of the inverse transient method (Figure 5.1) as presented in Chapters 10, 11 and 12. It consists of a 37.2 m, 22.1 mm internal diameter copper pipe connected between two pressurised tanks. A single leak is located at node 5 of size $(C_d A_L)_5 = 6.5\times10^{-7}$ m^2. In the example pipeline, the pressure difference between the tanks is 10 metres. The same pipeline is used for experimental measurements later in Chapter 10.

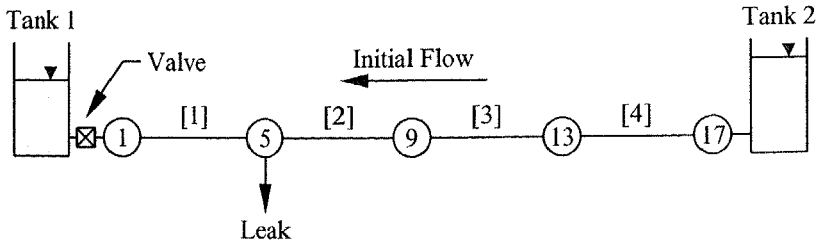

Figure 5.1 Simple Pipeline Example

A transient event is initiated by a partial valve closure (adjacent to Tank 1 in Figure 5.1) and opening over time period of 0.1 s. The valve is partially closed and opened such that the head variation at the valve changes linearly with respect to time during opening and again during closing. The pipeline is discretised into 16 computational reaches where nodes 5 and 13 are at the quarter points and node 9 is at the centre of the pipeline. The steady state initial conditions for the non-leaking and leaking cases are shown in Table 5.1.

Table 5.1 Steady State Conditions for the Simple Pipeline Example

	No Leak	Leak at Node 5
Head at Leak (m)	22.5	22.445
Flow U/S of Leak (m^3/s)	9.258×10^{-4}	9.156×10^{-4}
Flow D/S of Leak (m^3/s)	9.258×10^{-4}	9.292×10^{-4}
Leak Flow (m^3/s)	0.0	1.36×10^{-5}

Figure 5.2 shows the calculated head at the middle, quarter points and ends of the pipeline for the valve closure with no leaks.

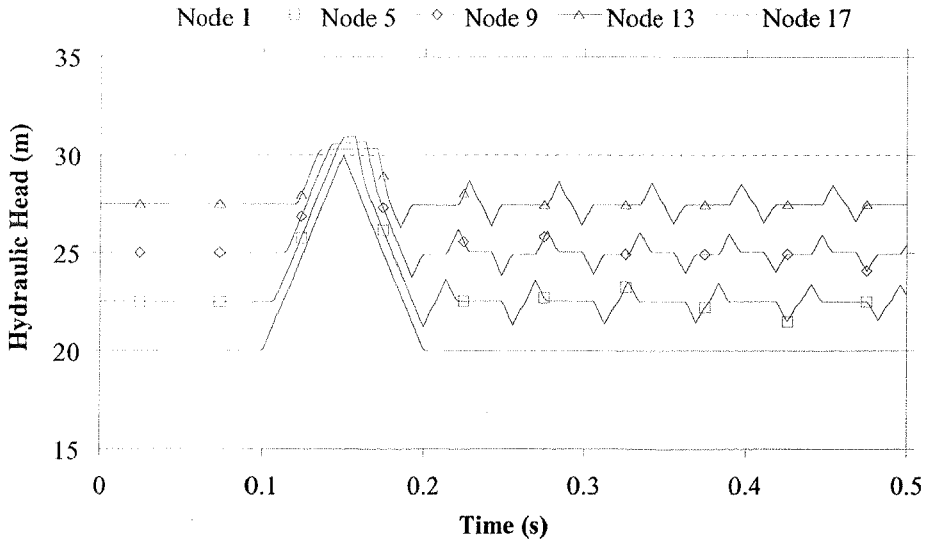

Figure 5.2 Transient Response, No Leaks. Correct Initial Conditions

Figure 5.3 shows the head in the pipeline for the same valve movement with a leak of magnitude $(C_d A_L)_5 = 6.5\times10^{-7}$ m^2 positioned at the first quarter point (node 5). The correct initial steady state conditions are used for this analysis (see Table 5.1). In the initial period of analysis (t = 0 to 0.2 s) there is little difference between Figures 5.2 and

5.3. The main difference is in the decay of the oscillations after there is no further change in the position of the valve (after a time of 0.2 s). The amplitude of these oscillations decays much faster when there is a leak present in the system. Figures 5.2 and 5.3 provide an example of the extra dissipation caused by a leak in a transient event.

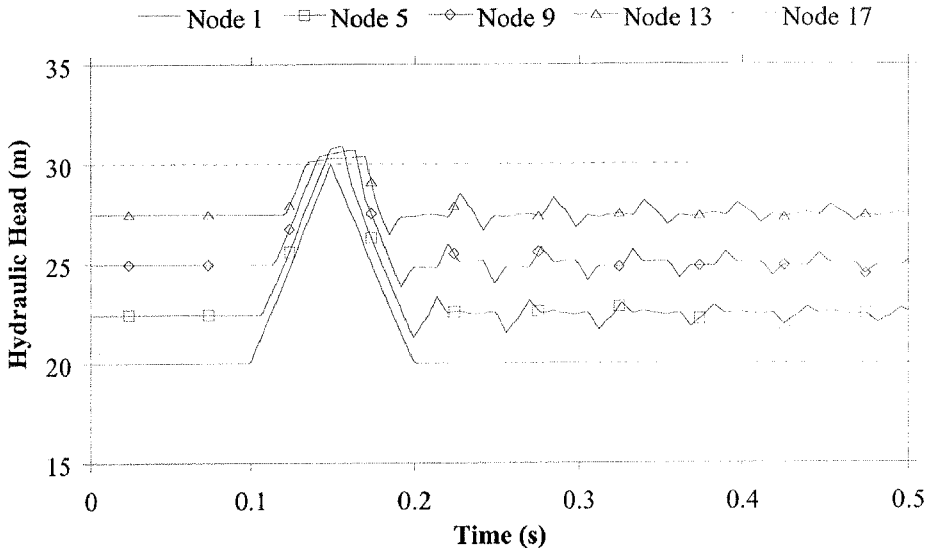

Figure 5.3 Transient Response, Leak at Node 5. Correct Initial Conditions

Figure 5.4 depicts what can happen if initial conditions are incorrect. In this case, the initial steady state conditions used for Figure 5.2, when there is no leak, are used when there is a leak (see Table 5.1). The result is an incorrect initial flow in the pipeline. Even before the transient event has been initiated, the mismatch in flow (and to a smaller extent in the head) is seen as an immediate pressure fall at node 5. The pressure fall can be calculated using the Joukowsky pressure change formula and the mismatch in initial flows (between the correct and incorrect steady state conditions). The mismatch in flows causes a superimposed transient event on top of the true event (Figure 5.3) called the *transient correction* for incorrect initial conditions.

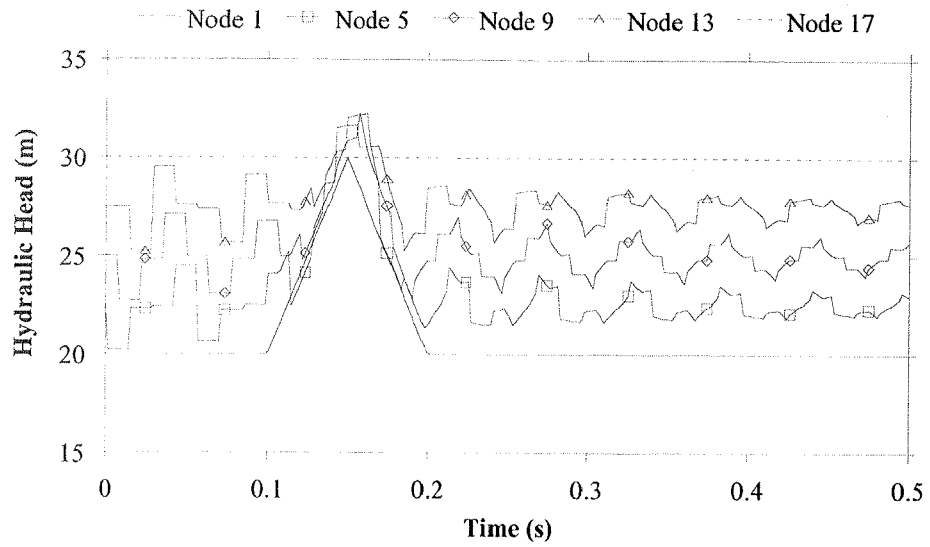

Figure 5.4 Transient Response, Leak at Node 5. Incorrect Initial Conditions

A comparison of the pressure trace at node 5 from Figures 5.2, 5.3 and 5.4 provides a clearer view of what is happening, as shown in Figure 5.5. The initial conditions are important for accurately modelling a transient event given a set of boundary conditions.

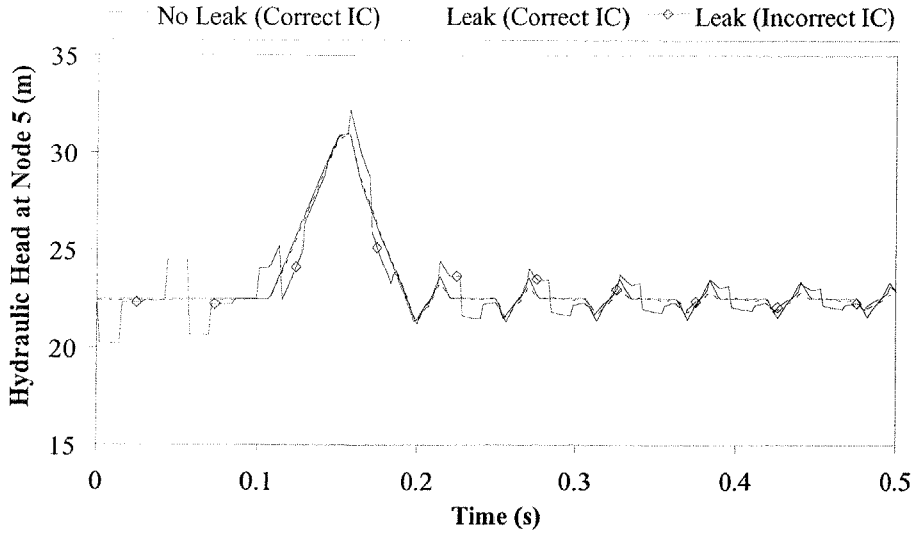

Figure 5.5 Transient Response at Node 5. Comparison Between No Leak and Leaking Cases Using Correct and Incorrect Initial Conditions

The transient correction has some interesting effects, especially with regards to the inverse transient method. Liggett and Chen (1994) used a constant set of initial

conditions throughout their minimisation algorithm (as shown in Section 5.3). The initial conditions used by Liggett and Chen (1994) corresponded to the correct leak configuration. In reality, it is impossible to know the true initial conditions throughout a network if the position and size of the leaks are initially unknown and/or if the friction parameters are unknown. The use of constant correct initial conditions, as used by Chen (1995), leads to fast convergence of the inverse transient method. Figure 5.6 shows, for the inverse transient method of leak detection, the convergence of the lumped leak coefficient at node 5 in the pipeline shown in Figure 5.1 and the assumed measured pressure trace in Figure 5.3 when using constant correct initial conditions (corresponding to steady state conditions with a leak occurring at node 5) for each iteration. The measured pressure head data are presented in tabulated form in Appendix D.2.1.

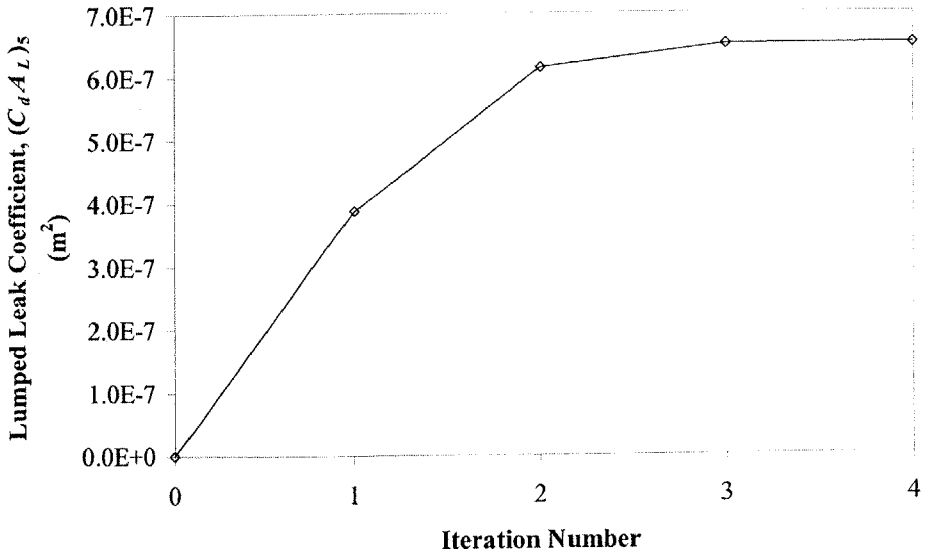

Figure 5.6 Convergence of $(C_d A_L)_5$. Constant Correct Initial Conditions

Although convergence is fast, the problem being solved is biased towards the assumed initial conditions for the predicted transient trace (which were determined for the correct solution). An explanation why convergence is strongly biased may be argued using the transient correction idea. The inverse transient method, rather than trying to fit the transient response, will try to minimise the effect of the transient correction. The minimum occurs when the pipeline parameters are almost correct for both the initial conditions and for the measured pressure data. Thus, the inverse transient method

solution is governed or influenced by the assumed initial conditions. In reality, a good guess of the initial conditions might be the "no leak" situation (incorrect initial conditions). Figure 5.7 shows the convergence (or lack thereof) of the inverse transient method when the initial conditions for the predicted transient trace are set to the "no leak" steady state conditions (see Table 5.1).

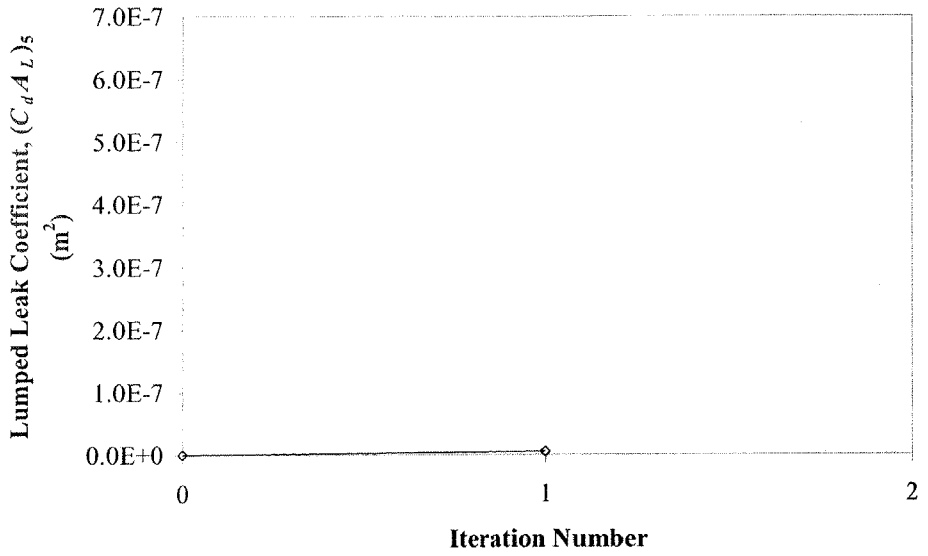

Figure 5.7 Lack of Convergence of $(C_d A_L)_5$. Constant Incorrect Initial Conditions

To find the leak correctly, rather than use constant initial conditions, initial conditions must be continuously updated for any set of test parameters. Basically, for every new network configuration that is assumed (or computed in the minimisation process), new initial conditions are needed. For example, every iteration of the Levenberg-Marquardt algorithm requires the calculation of partial derivatives with respect to the current lumped leak coefficient (for $[\alpha]$ and $\{\beta\}$, see Section 4.3.2). In this chapter, the partial derivatives are calculated using the divided difference method (see Section 4.4.1). For the divided difference method, the initial conditions must be calculated twice for the partial derivative (with respect to the lumped leak coefficient at node 5). Once for a trial lumped leak coefficient and again for a perturbed trial lumped leak coefficient (used in the divided difference method). The steady state solution for the initial conditions was calculated using a pipeline steady state solver. The results of an inverse transient method run with updating initial conditions are shown in Figure 5.8.

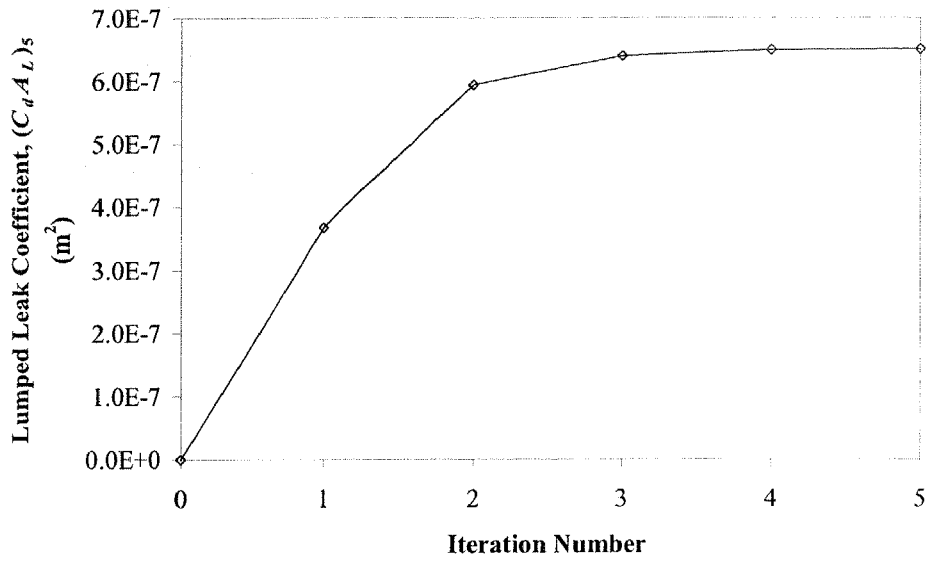

Figure 5.8 Convergence of $(C_dA_L)_5$. Updated Initial Conditions

Figure 5.8 shows that the convergence rate is similar to the convergence rate with constant initial conditions, which were already at the solution.

5.2.1 The Effect of Initial Conditions: Case Study #1 – Sensitivities

The previous section's results use perfect measured pressure data (see Figure 5.3). In reality the measurement data will contain errors. The errors might reduce the effectiveness of the inverse transient method. The sensitivity of the heads with respect to the lumped leak coefficient at node 5 (for this case study) is an indicator of the likely performance of the inverse transient method in the presence of measurement errors. Therefore, to investigate the effect of incorrect and correct initial conditions on the performance of the inverse transient method with measurement error, it is necessary to look at these sensitivities. Figure 5.9 shows the partial derivative of the pressure head at node 5 (the measurement data site) with respect to the leak at node 5 ($\partial H_5/\partial(C_dA_L)_5$).

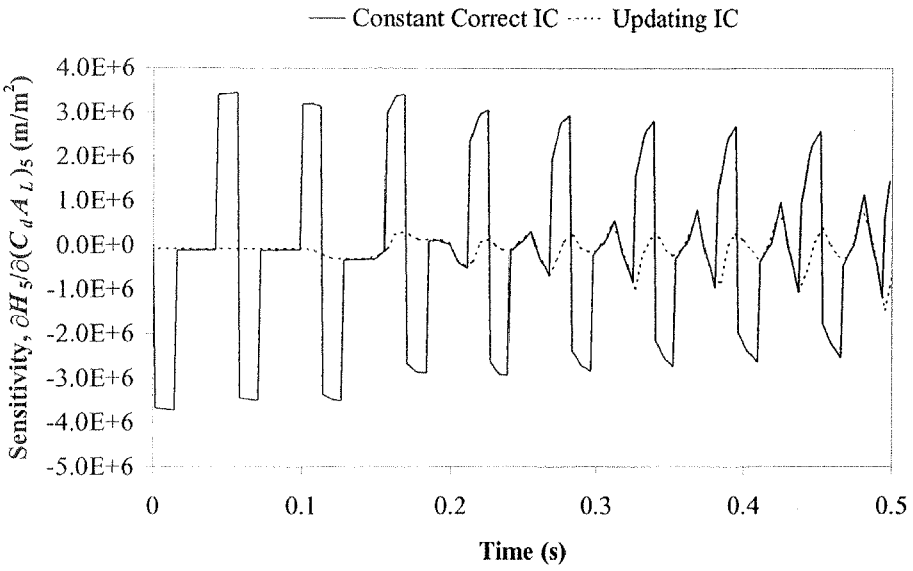

Figure 5.9 Sensitivity, $\partial H_5/\partial(C_dA_L)_5$. Comparison Between Constant and Updated Initial Conditions

A parameter (such as the lumped leak coefficient at node 5, $(C_dA_L)_5$) will be solved for faster and with a greater degree of confidence if it has a high associated sensitivity. As a general rule, sensitivity is equal to the absolute values of the partial derivatives (see Section 4.11) of, in this case, the pressure heads with respect to the lumped leak coefficients ($|\partial H_5/\partial(C_dA_L)_5|$). As observed, the sensitivities associated with the constant correct initial conditions in Figure 5.9 are much higher than those with the updated initial conditions. An interesting observation about Figure 5.9 is that the sensitivity for the constant initial conditions case actually decreases with time, leading to the observation that the usefulness of a data point (in the inverse transient method) decreases as time increases. The sensitivity for the case of updated initial conditions increases with time, leading to the more intuitive result where the greater the amount of data used in analysis, the better the solution. Similar observations (constant correct initial conditions resulting in higher sensitivities than updated initial conditions) are made when considering calibration of the pipe friction factors. A plot of the partial derivatives of pressure with respect to the friction factor in pipe 1 ($\partial H_5/\partial f_1$) is shown in Figure 5.10.

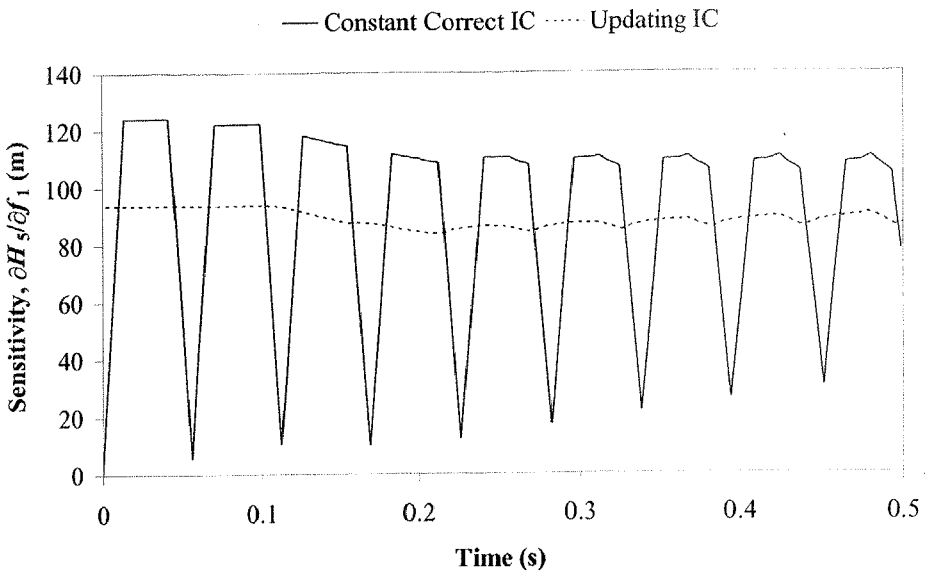

Figure 5.10 Sensitivity, $\partial H_5/\partial f_1$. Comparison Between Constant Correct and Updated Initial Conditions

Perhaps a better way to compare sensitivities is using the overall sensitivity. The overall sensitivity is calculated by summing up the absolute of the individual sensitivities over all time steps (see Section 4.11). Figure 5.11 shows the overall sensitivity with respect to the lumped leak coefficient ($\sum|\partial H_5/\partial(C_dA_L)_5|$).

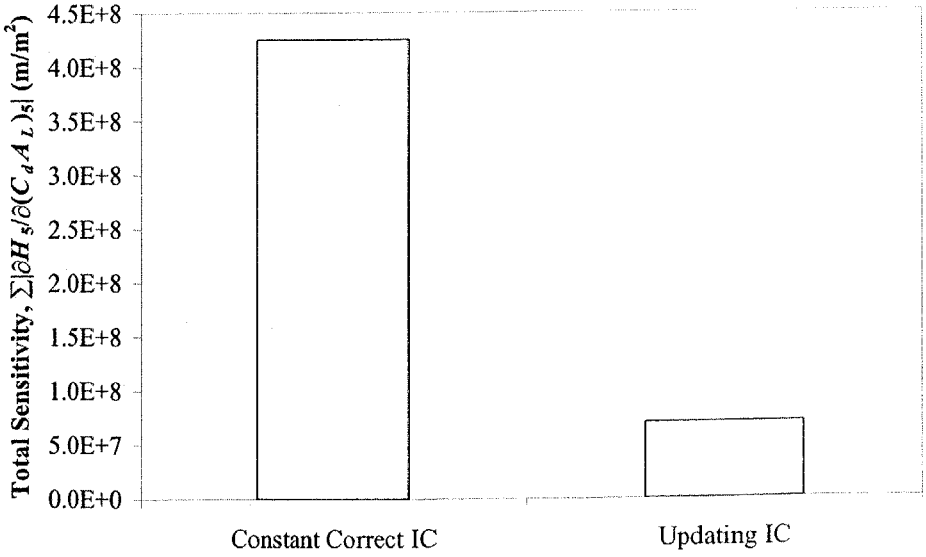

Figure 5.11 Total Sensitivity, $\sum|\partial H_5/\partial(C_dA_L)_5|$. Comparison Between Constant Correct and Updated Initial Conditions

As expected, the constant correct initial condition results assumed for the predicted data show a far greater sensitivity than the updated initial condition results. The same analysis of the overall sensitivity is performed for the friction factor in pipe 1 ($\sum|\partial H_5/\partial f_1|$), as shown in Figure 5.12. These results show the overall sensitivity is similar between the use of constant correct and updated initial conditions, although the constant correct initial condition value is slightly higher.

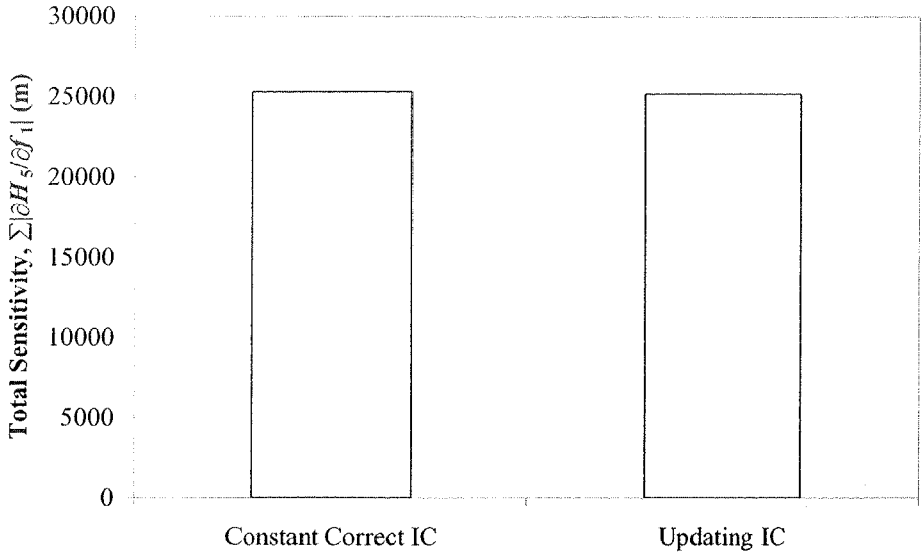

Figure 5.12 Total Sensitivity $\sum|\partial H_5/\partial f_1|$. Comparison Between Constant Correct and Updated Initial Conditions

Another way to visualise the comparison between constant and updated initial conditions is to look at the objective function with respect to the lumped leak coefficient at node 5. The objective function E is the sum of the squares of the differences between the calculated (or predicted) and observed pressures. The objective functions for constant and updated initial conditions are shown together in Figure 5.13.

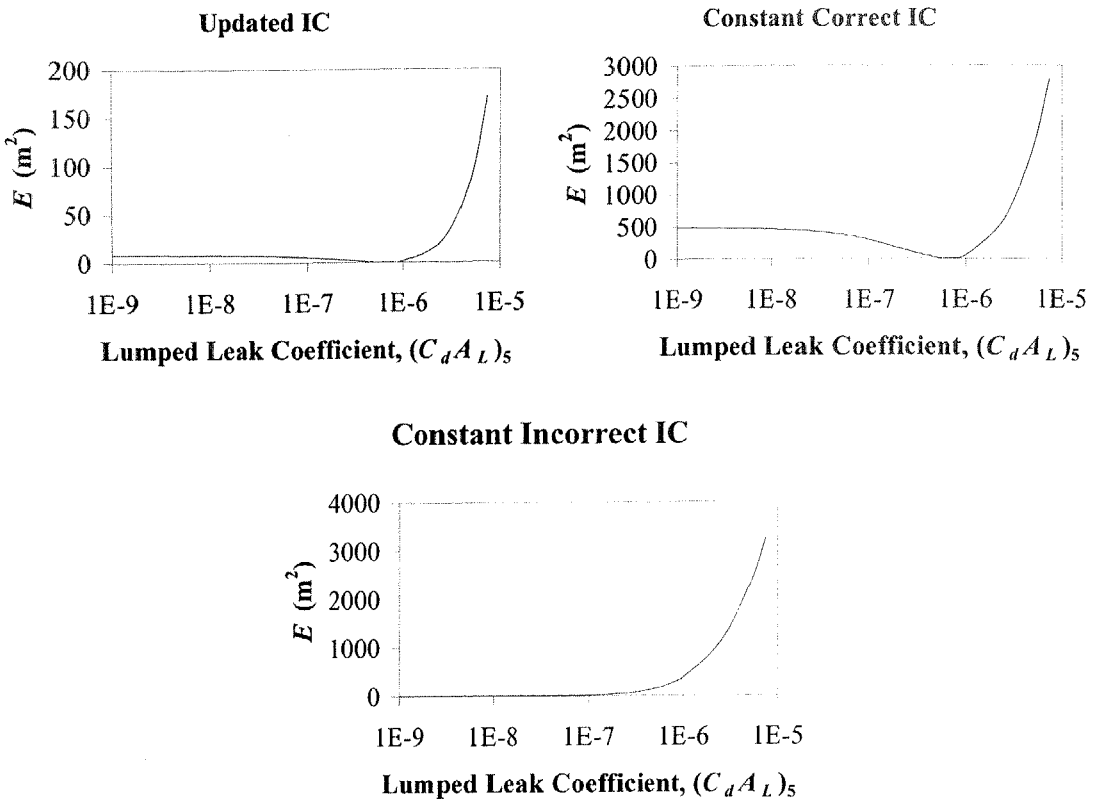

Figure 5.13 Objective Function, *E*. Comparison Between Constant Correct, Updated and Constant Incorrect Initial Conditions (Separate Plots)

The plots in Figure 5.13 are useful for explaining why the use of constant incorrect initial conditions failed to converge while the others did converge. The minimum of the objective function (E) is located at the correct value of the lumped leak coefficient at node 5 ($(C_dA_L)_5 = 6.5\times10^{-6}$ m^2) for constant correct and updated initial conditions. The inverse transient results for the leak at node 5 using constant correct and updated initial conditions converged to the correct value. However, the plot of the objective function for constant incorrect initial conditions shows that there is no minimum over the lumped leak coefficient range considered and, therefore, the inverse transient method failed to converge. Plotting them all on the same axis, as shown in Figure 5.14, creates another view of the objective function for constant and updated initial conditions. When updated initial conditions are used the objective function becomes markedly flatter.

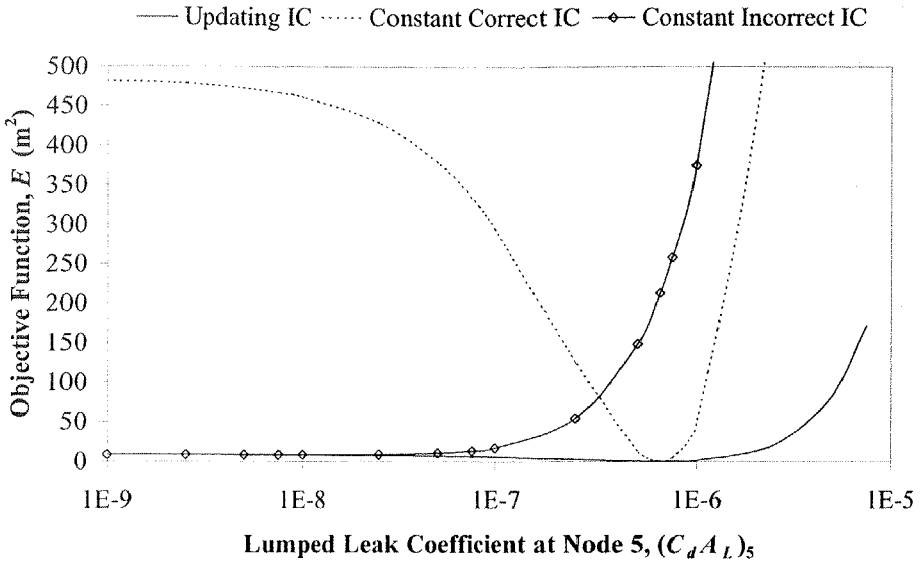

Figure 5.14 Objective Function, *E*. Comparison Between Constant Correct, Updated and Constant Incorrect Initial Conditions

Figure 5.14 shows that the updated initial condition's objective function is much smaller in magnitude than the others. An interesting observation is made by imagining an inverse transient application using an initial guess for the lumped leak coefficient of zero (a sensible guess). The slope of the objective function at both the beginning of a search and end of a search (at the minimum) are particularly flat (see Figure 5.13). A flat slope may cause gradient based minimisation techniques to convergence slowly or not at all. If an initial guess of $(C_dA_L)_5 = 0.0$ m^2 was used, the gradient of the objective function $(\partial E/\partial(C_dA_L)_5)$ at the initial guess is close to zero. If the next iteration of $(C_dA_L)_5$ is based on the gradient of the objective function, the next iteration would over-shoot beyond the capacity of the pipeline (where the leak is too large for a valid steady state solution or physically unrealistic to be considered) or not converge at all.

5.3 The Effect of Initial Conditions: Case Study #2

Work performed by Chen (1995) used initial conditions that correspond to the correct inverse transient solution and were held constant during the inverse transient solution process. This information would not be known when applying the inverse transient method to a real problem. The focus of this section is to reproduce results found in

Chen (1995) and then to redo them with updated initial conditions based on current parameter guesses. Chen used the example network as shown in Figure 5.15.

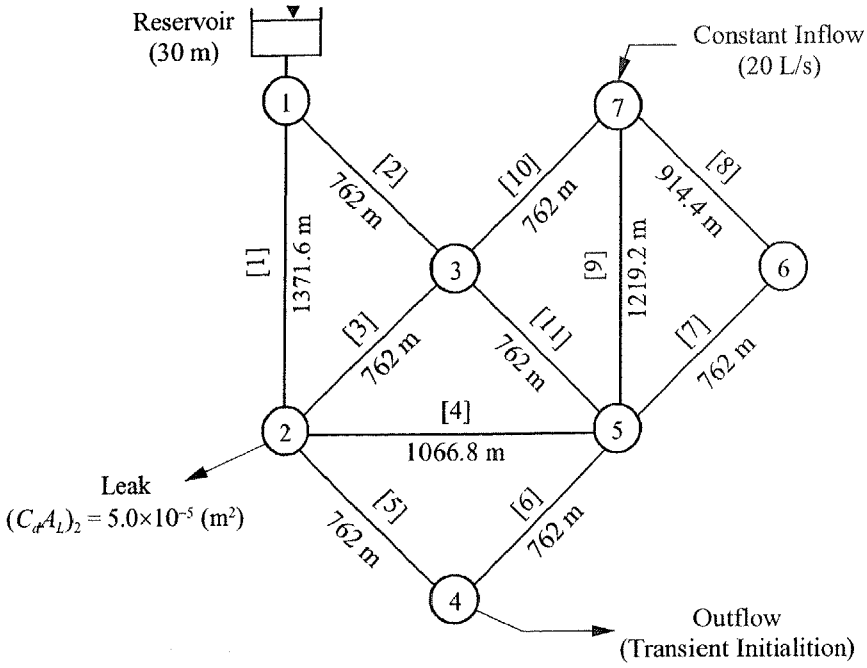

Figure 5.15 Example Network (from Chen, 1995)

The pipe lengths are shown underneath each pipe in Figure 5.15. All of the pipes had a common diameter of 254 mm, a pipe wall thickness of 10 mm and a Young's modulus of elasticity of the pipe wall of 207 GPa. The elevation of all nodes in the network is equal to zero and the elevation of the water surface of the reservoir at node 1 is 30 m. The pipes in this network are divided into integer numbers of reaches (of length 152.4 m) such that the wave travel time for all pipes in the network is equal. The Darcy-Weisbach friction factor in all pipes has a "real" value of 0.020 but for the purpose of calibration the friction factor is initially guessed at 0.030 for all pipes. The pipes were placed into 4 pipe groups with each group sharing a common friction factor, thus reducing the number of unknown friction factors from 11 to 4. The pipe groups were pipes 1, 2 and 3; pipes 4, 5, and 6; pipes 7, 8 and 9; and pipes 10 and 11. A leak was situated at node 2 with a lumped leak coefficient of 5×10^{-5} m^2. In Chen (1995), node 2 is the only node suspected of a leak with an initial guess of the lumped leak coefficient of 0.0 m^2. The transient event was initiated by restricting the demand at node 4 followed by an increase back to its original level. A plot of the transient initialisation at node 4 is shown in Figure 5.16.

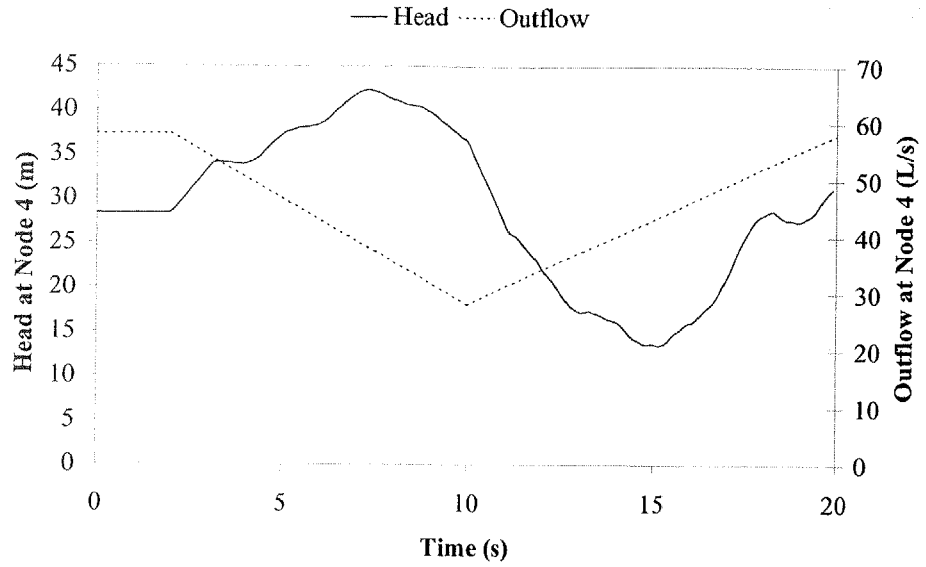

Figure 5.16 Initiation of Transient Event at Node 4

For the inverse transient method, 20 seconds of measured pressure data were considered at nodes 3, 5 and 6 corresponding to about 160 time steps in the numerical algorithm. A plot containing the measured data at each of the measurement nodes is shown in Figure 5.17. The measured pressure head data are shown in tabulated form in Appendix D.2.2.

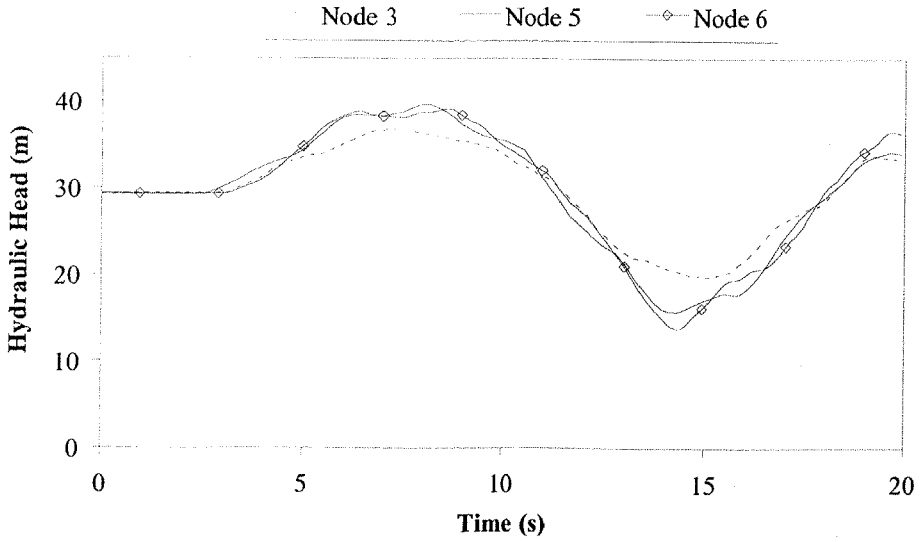

Figure 5.17 Measurement Data Used in Inverse Transient Analysis

Figure 5.18 shows the convergence of the parameters to their correct values in a couple of iterations using the inverse transient method with constant correct initial conditions.

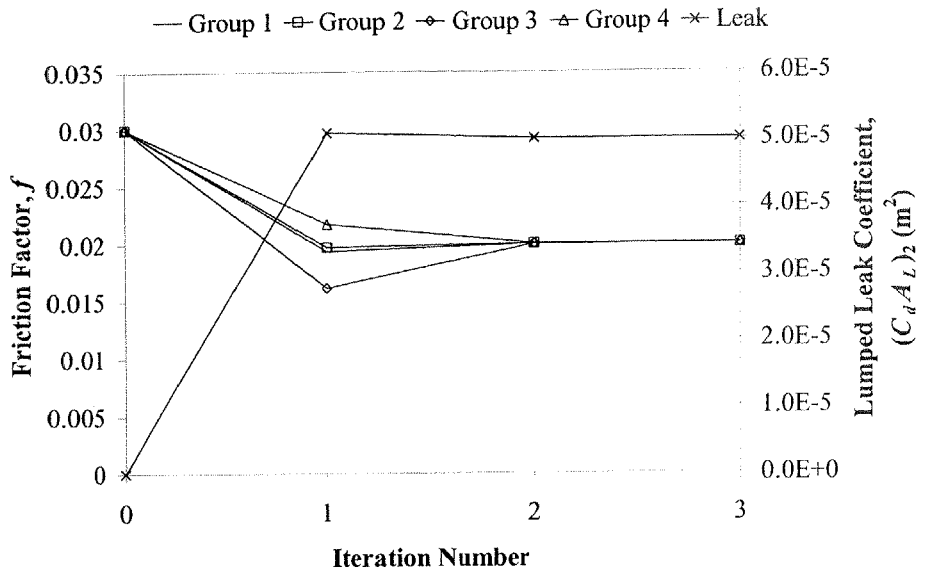

Figure 5.18 Convergence of Parameters. Constant Correct Initial Conditions

The convergence is hardly surprising because the Chen (1995) initial conditions are already at the solution.

Now, the effect of using constant incorrect initial conditions is considered. The inverse transient method is applied with constant initial conditions that coincide with initial guesses of the parameters (that is all friction factors equal to 0.03 and the lumped leak coefficient at node 5 equal to zero). The inverse transient result is shown in Figure 5.19 and compared to results using constant correct initial conditions (Figure 5.18). Figure 5.19 shows a lack of convergence after the first iteration. The non-convergence is due to the initial conditions not satisfying the steady state solution (causing a transient correction). In effect, the inverse transient method is trying to reduce the transient correction caused by the unsatisfactory initial conditions, and drives the inverse transient solution towards the initial guesses of the parameters, which in this case, causes divergence.

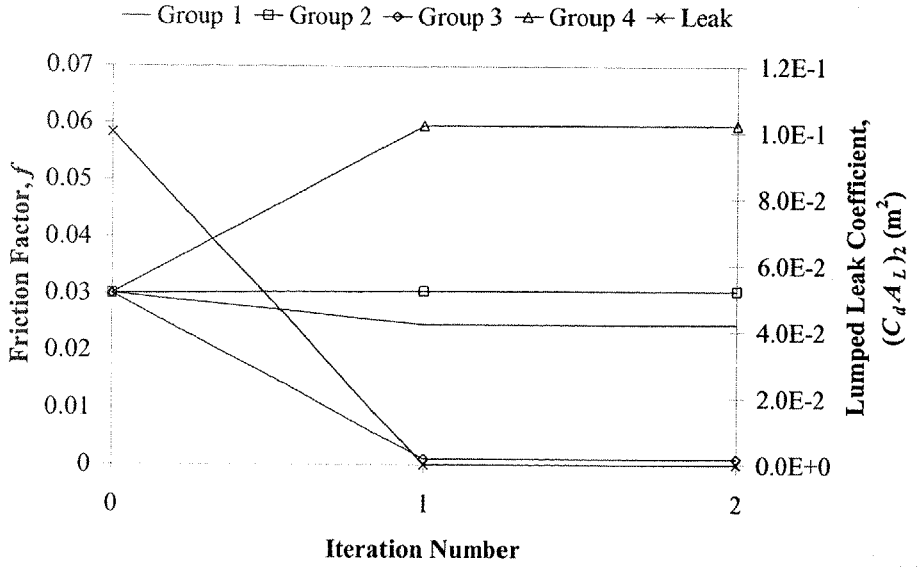

Figure 5.19 Lack of Convergence of Parameters. Constant Incorrect Initial Conditions

The transient correction is observed as the difference between the curves in Figure 5.20 (which was shown for the previous case study in Figure 5.5). The transient correction is smaller in magnitude for the example network than in the previous case study, but still causes the inverse transient method to fail.

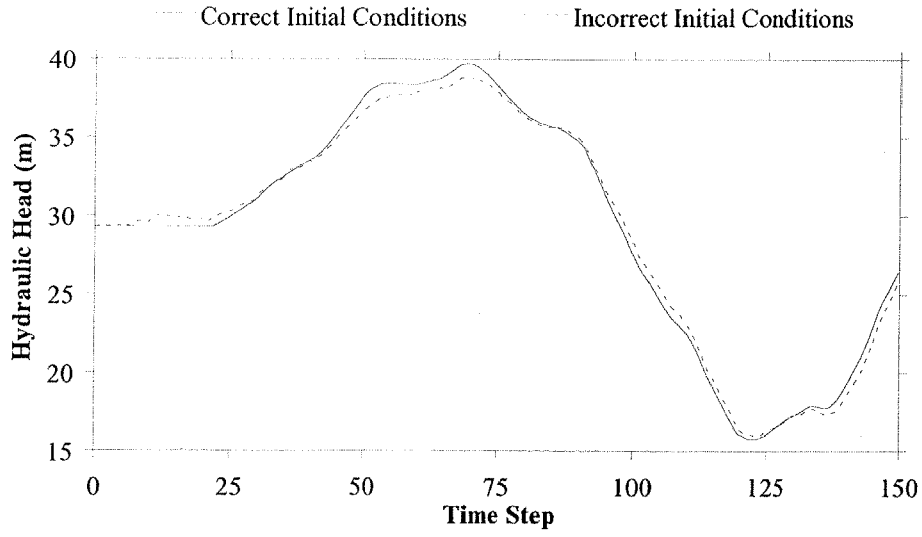

Figure 5.20 Hydraulic Head at Node 5. Correct and Incorrect Initial Conditions

It is clear that Chen (1995) was solving an incorrect or biased problem. Not considering the variable nature of the steady state initial conditions as the solution scheme progresses has a serious effect on whether the inverse transient method will work. Although the inclusion of updated steady state conditions has only a small effect on the sensitivities (some of which are used in the solution scheme, see Section 5.3.1), they have a large effect on the outcome of the minimisation process. Generally, there are only small differences in the head when a leak (of an average size) is present compared to when there is none. The main difference that the change in flow due to the leak causes a transient correction that, because small changes in flow cause large associated changes in the head (see Joukowsky pressure rise in Section 3.4), vastly changes the topology of the search space. If the steady state initial conditions are not known and those of the initial guess are used, it was shown that the Chen (1995) results, using constant initial conditions, failed to find a solution or even converge. Figure 5.21 shows that convergence of the parameters occurs when using updated initial conditions, as proposed in this thesis.

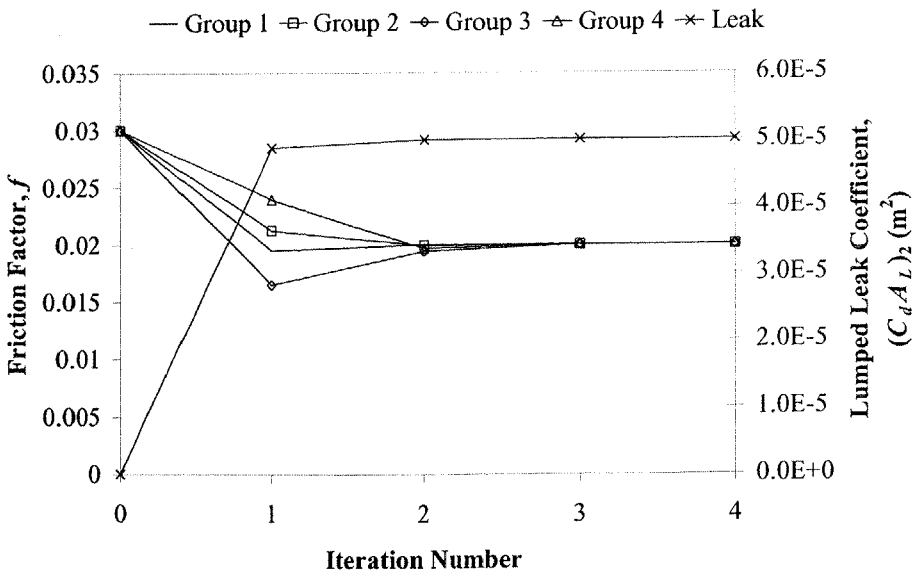

Figure 5.21 Convergence of Parameters. Updated Initial Conditions

The convergence is similar to that shown by Chen (1995) in Figure 5.18, suggesting that there is little change in the rate of convergence when using updated or constant correct initial conditions. In a realistic implementation of the inverse transient method, the correct initial conditions are not likely to be known. This section showed that

convergence is possible if the initial conditions are updated for each iteration, but impossible if constant incorrect initial conditions are used.

5.3.1 The Effect of Initial Conditions: Case Study #2 – Sensitivities

Chen (1995) produces many different graphs showing various sensitivity properties that are used in the Levenberg-Marquardt algorithm (used to calculate [α] and {β}, see Section 4.3.2). Graphs of the various sensitivities are reproduced in the following set of figures. The first of these are the partial derivatives of the head with respect to each of the friction factors ($\partial H/\partial f$). The partial derivatives are calculated using the divided difference method (see Section 4.4.1). Plots in Figure 5.22 show the sensitivities at nodes 3, 5, and 6 respectively.

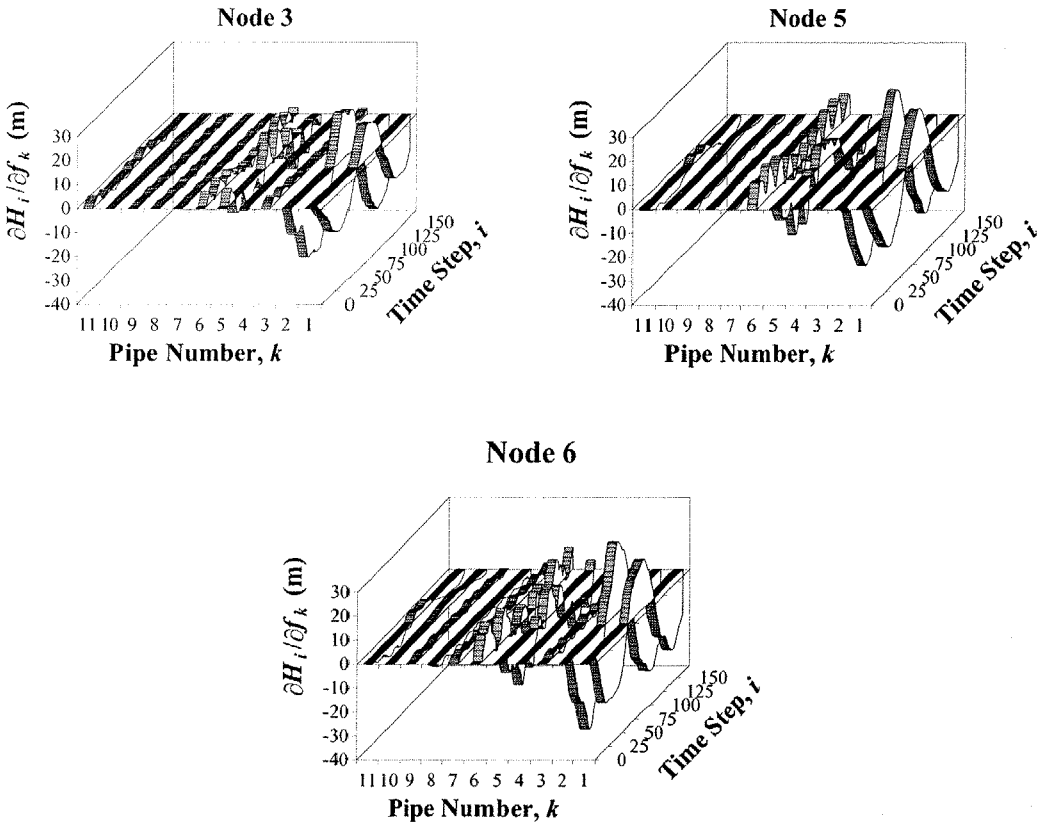

Figure 5.22 $\partial H/\partial f$ at Nodes 3, 5 and 6. Constant Correct Initial Conditions

Each plot in Figure 5.22 shares similar characteristics, where the sensitivities with respect to pipes 1 and 2 are far greater than those of any other pipe. The high sensitivities in pipes 1 and 2 suggest that these parameters will be more likely to be solved with a higher degree of confidence (since they have a greater effect on the computed heads than other friction factors). Similar partial derivatives are calculated with respect to the lumped leak coefficient ($\partial H/\partial(C_dA_L)_2$). The plots for the sensitivity of the hydraulic head with respect to the leak at the three measurement nodes are shown in Figure 5.23.

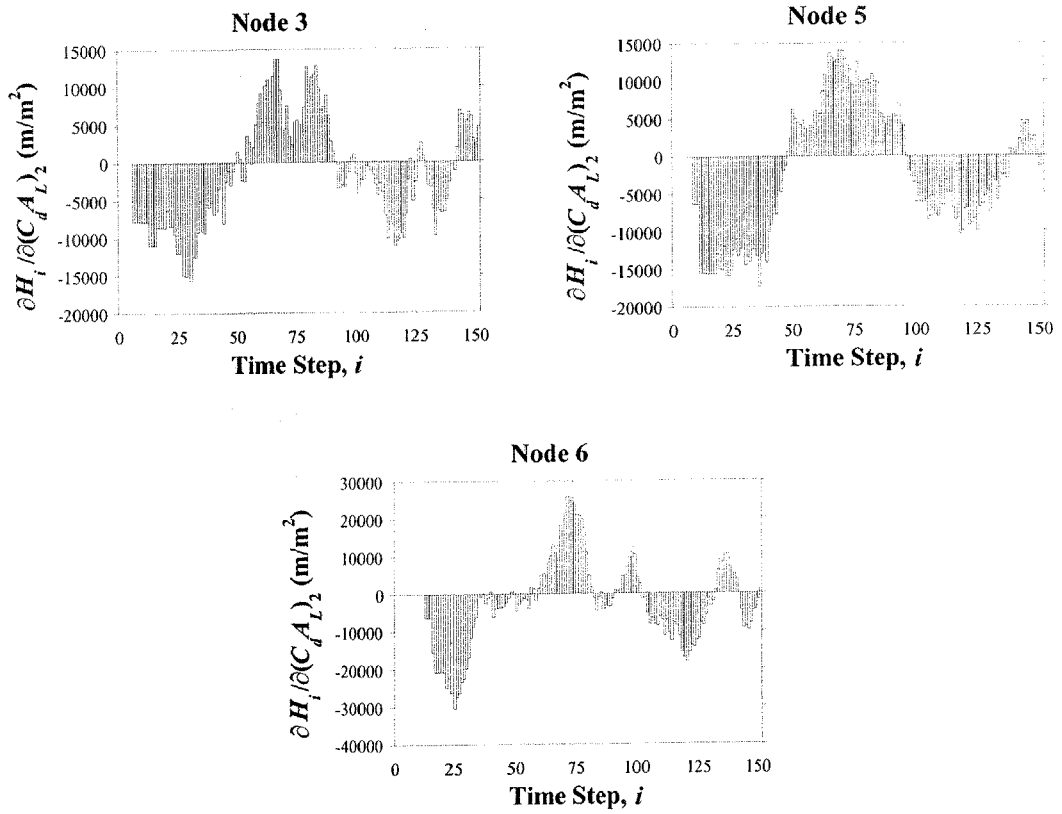

Figure 5.23 $\partial H/\partial(C_dA_L)_2$ at Nodes 3, 5 and 6. Constant Correct Initial Conditions

The sensitivities with respect to the lumped leak coefficient are approximately three orders of magnitude larger than those with respect to the friction factors, thus suggesting that the lumped leak coefficients would be more likely to be found than the friction factors. In Chen (1995), the parameters that were solved for in Figure 5.18 were on a pipe group basis rather than at the individual pipe level, hence sensitivity plots that have more relevance to Figure 5.18 are shown in Figure 5.24. The plots in Figure 5.24

show the sensitivity of the pressure at nodes 3, 5 and 6 with respect to the four pipe groups ($\partial H/\partial f$ by pipe group).

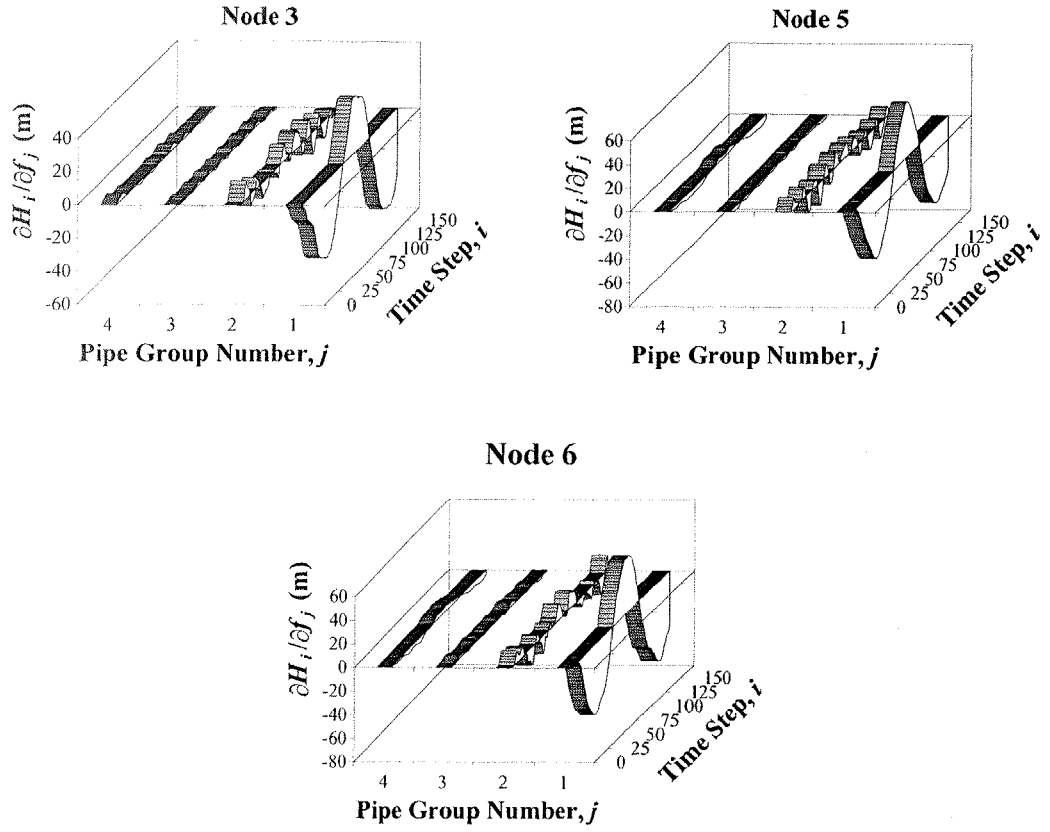

Figure 5.24 $\partial H/\partial f$ at Nodes 3, 5 and 6 (by pipe group). Constant Correct Initial Conditions

The plots in Figure 5.24 echo much of what was seen in Figure 5.22. The first pipe group, containing pipes 1 and 2, exhibits the greatest sensitivity followed by group 2. Groups 3 and 4 have low sensitivities. Observation of the sensitivity of the objective function eliminates the need to produce a separate graph for each measurement node over multiple time steps, and may be thought of as an aggregate sensitivity. Figures 5.25 and 5.26 show the partial derivative of the objective function with respect to the friction factor ($\partial E/\partial f$) for individual pipes and then for pipe groups.

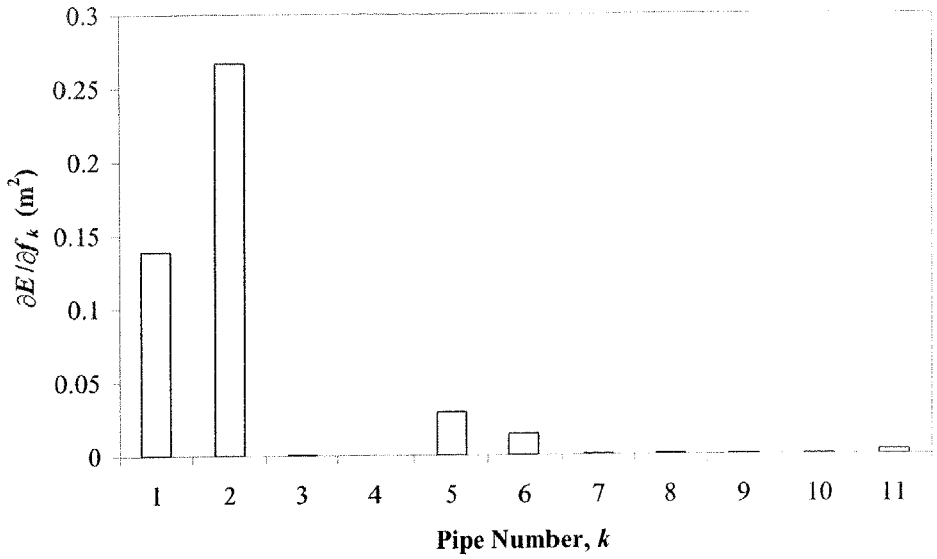

Figure 5.25 $\partial E/\partial f$ by Individual Pipes. Constant Correct Initial Conditions

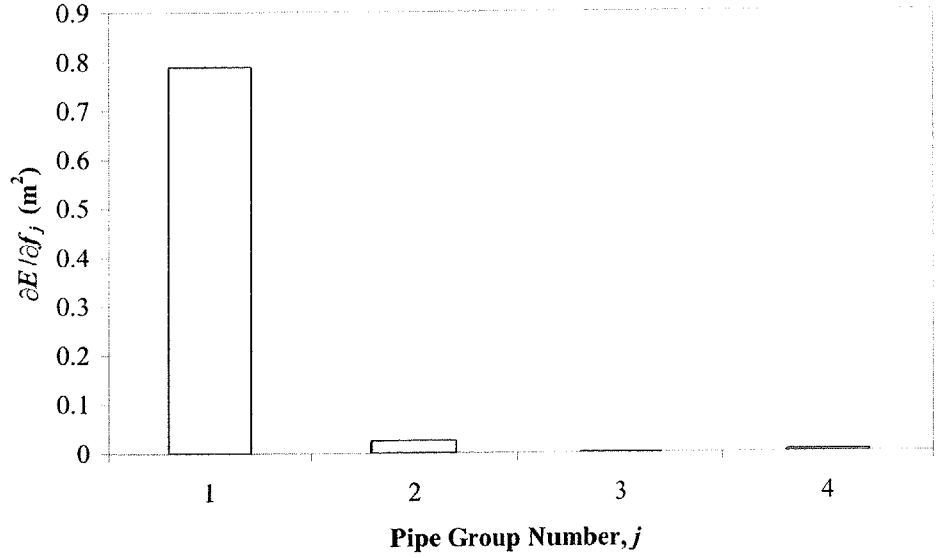

Figure 5.26 $\partial E/\partial f$ by Pipe Group. Constant Correct Initial Conditions

Figures 5.25 and 5.26 reinforce what other plots have shown where friction factors associated with pipes 1 and 2 or pipe group 1 have a higher sensitivity than others and hence are more likely to be solved with a higher degree of confidence.

The same analysis (that was performed using constant correct initial conditions) is performed using updated initial conditions. In this analysis, the initial conditions are updated every time the transient solver is called. The plots in Figure 5.27 are equivalent

to plots in Figure 5.22 except with updated initial conditions. There is little difference between the magnitude of these sensitivities between the plots other than when updated initial conditions are included, the magnitudes are slightly lower. The main observable difference is the high and constant initial sensitivities (for the first 25 time steps) exhibited when updated initial conditions are used. These high initial sensitivities are indicative of the initial steady state conditions and are constant until the transient event is initiated. The high initial sensitivities link the inverse steady state method to the inverse transient method (if the steady period of the transient event is used).

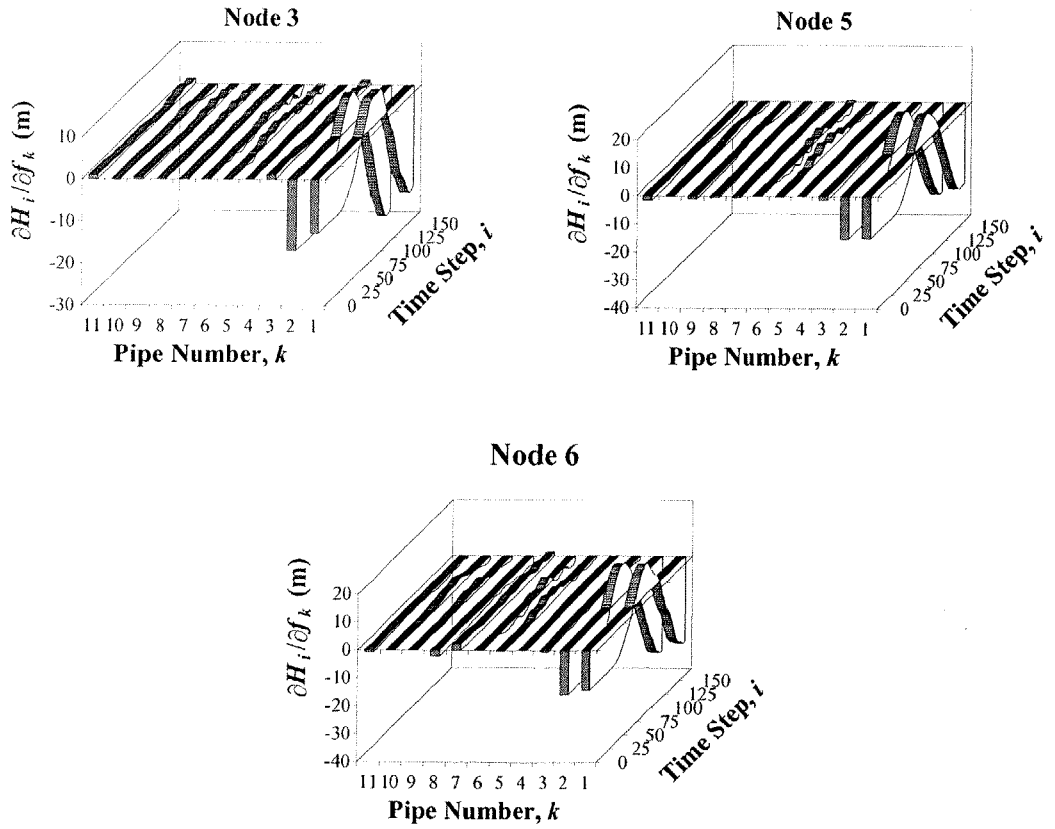

Figure 5.27 $\partial H/\partial f$ at Nodes 3, 5 and 6. Updated Initial Conditions

Similar comparisons may be drawn between the plots in Figure 5.23 (using constant correct initial conditions) and the plots in Figure 5.28 (using updated initial conditions) for $\partial H/\partial(C_d A_L)_2$ at nodes 3, 5 and 6. The latter plots are smoother than those that use constant initial conditions, due to the sudden nature of the network response to the incorrect initial conditions at the first time step (none occurs when using updated initial

conditions). Again, there is a small constant sensitivity for the first time steps that is caused by the inclusion of the steady state solver.

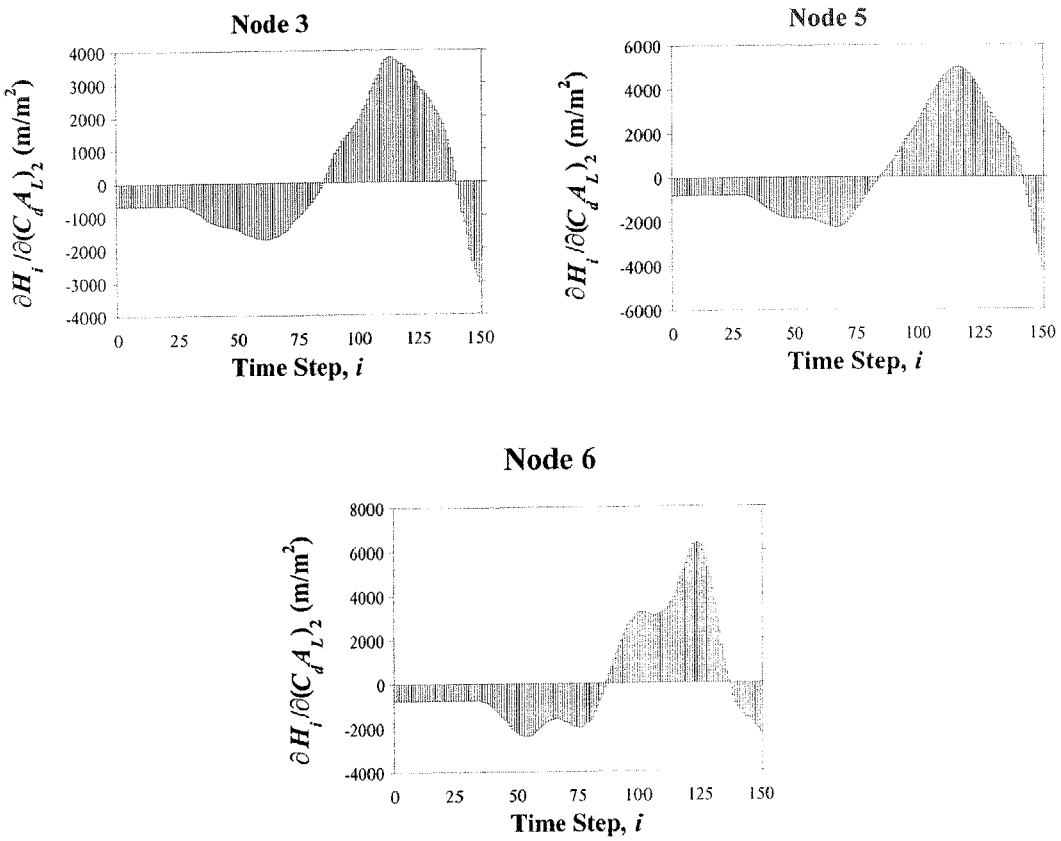

Figure 5.28 $\partial H/\partial(C_dA_L)_2$ at Nodes 3, 5 and 6. Updated Initial Conditions

Again, similar comparisons are made when looking at the sensitivities with respect to the friction factor ($\partial H/\partial f$) for the pipe groups. Plots in Figure 5.29 (using updated initial conditions) are compared with the previous plots in Figure 5.24 (using constant correct initial conditions). The same comments about the previous differences between the two groups of figures are valid (lower values, a smoother curve and a constant initial sensitivity when using updated initial conditions). The only extra difference is that the relative magnitude between pipe group 1 and the other pipe groups across the three plots is greater.

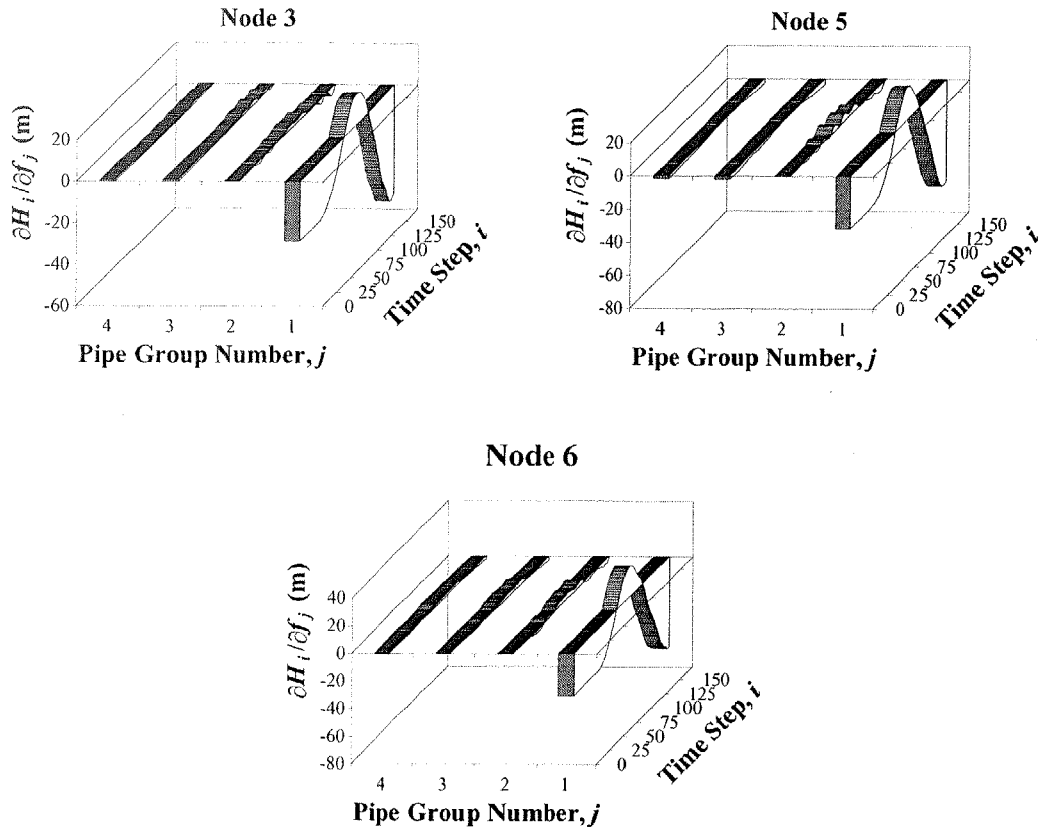

Figure 5.29 $\partial H/\partial f$ at Nodes 3, 5 and 6 (by pipe group). Updated Initial Conditions

Overall, the magnitude of the sensitivities when using updated initial conditions is smaller then when using constant correct initial conditions. Therefore, the parameters to be solved by the inverse transient method using constant correct initial conditions are more likely to be found and with a greater confidence than when using updated initial conditions (although using constant correct initial conditions creates a biased, unrealistic problem since initial conditions are generally not known).

The sensitivity of the objective function with respect to each pipe's friction factor ($\partial E/\partial f$) highlights the overall behaviour of the previous sensitivities ($\partial H/\partial f$) over all time steps and all measurement nodes. Comparison of Figures 5.25 (constant correct initial conditions) and 5.30 (updated initial conditions) show that the magnitudes of the sensitivities when initial conditions are updated are of half the size of those when constant initial conditions are used. Again, much like previous results, the relative difference in sensitivities between pipe groups has increased for the updated initial condition case.

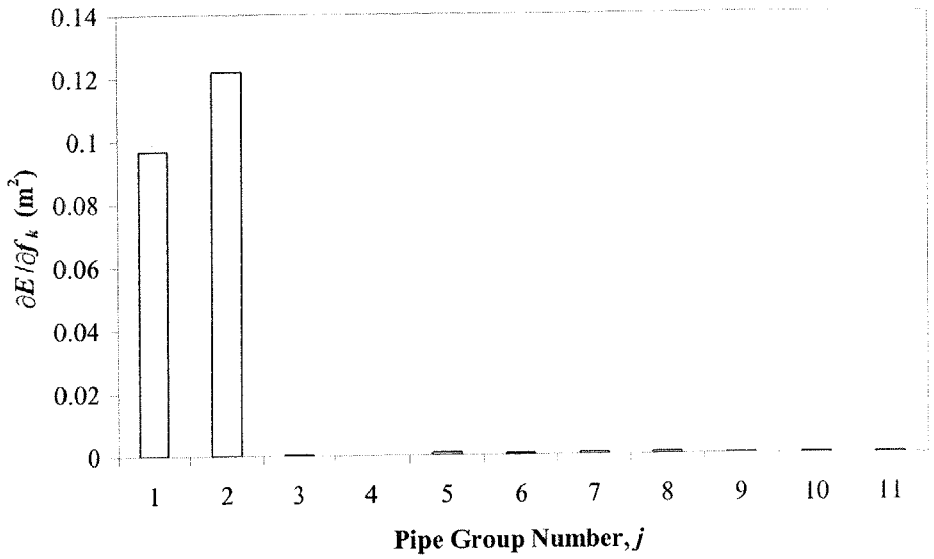

Figure 5.30 $\partial E/\partial f$ by Individual Pipes. Updated Initial Conditions

The sensitivities of the objective function with respect to the friction factor ($\partial E/\partial f$) for each pipe group using updated initial conditions are shown in Figure 5.31, and are comparable with Figure 5.26 when using constant correct initial conditions. The sensitivities are smaller for the updated initial condition case, reinforcing observations made in previous comparisons.

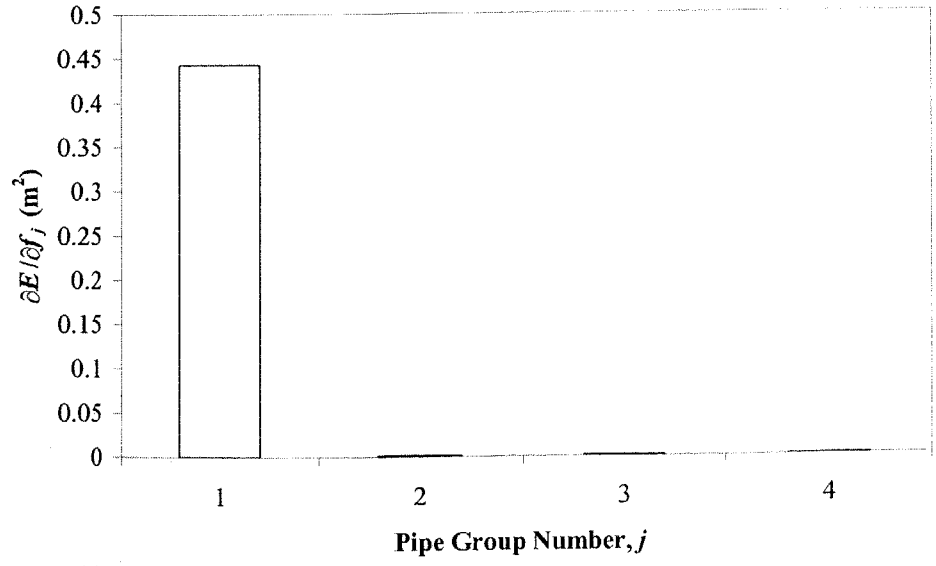

Figure 5.31 $\partial E/\partial f$ By Pipe Groups. Updated Initial Conditions

5.4 Time Influence of Initial Conditions

In a pipe network the heads and flows are approximately steady but always in a state of flux. In this case, the initial conditions are not known and cannot be determined using a steady state solver. Any incompatible initial conditions will result in a transient correction, which is detrimental to the inverse transient method. A solution is to use approximate initial conditions, such as the steady state solution (Section 5.5), and then simulate the network for an amount of time until the network "forgets" the initial conditions. Figure 5.32 shows the application of a continuous inverse transient method, in which the time taken for the forward solver to "forget" the initial conditions is T_{IIC} and the simulation time used in the inverse transient method is T_{ITA}.

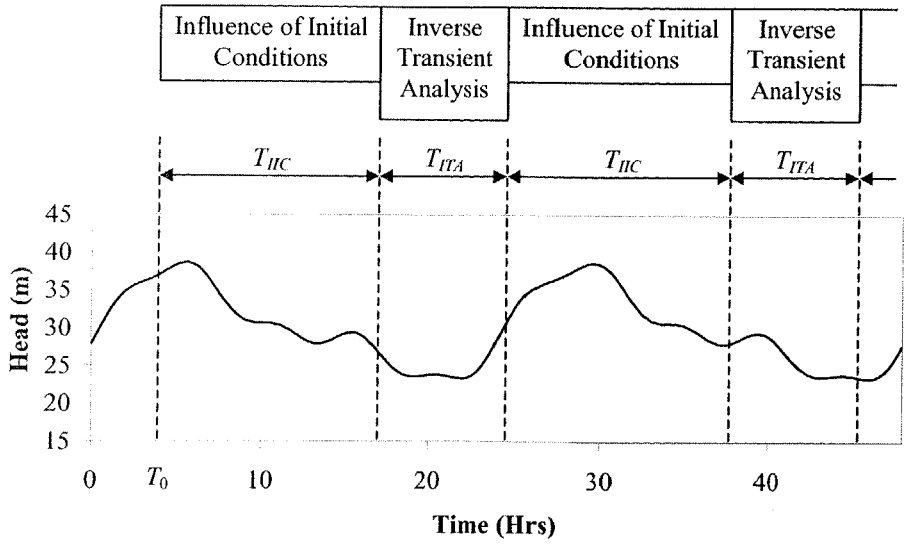

Figure 5.32 Inverse Transient Analysis With Approximate Initial Conditions

The continuous inverse transient procedure begins at a time T_0, where approximate initial conditions and parameter guesses are defined and the transient solver run for an amount of time that is sufficient for the network to "forget" the approximate initial conditions (T_{IIC}). Then the inverse transient problem is solved using a certain amount of simulation time (T_{ITA}). The parameters, such as the leak areas and the friction factors, are updated with the solution parameters from the inverse transient analysis. Repetition of these steps forms an iterative process whereby estimates of the parameters are

successively made. The time required for n iterations is $n(T_{IIC} + T_{ITA})$. The continuous inverse transient procedure continuously calibrates pipe networks, however, the process may be halted if a leak is identified.

Another option is to reuse the measured data from the first repetition (from $t = T_0$ to $t = T_0 + T_{IIC} + T_{ITA}$) rather than moving to the next time period. The initial conditions remain the same, but estimates of the parameters are successively determined until the parameters do not change. Then the next time period of measured data is considered (from $t = T_0 + T_{IIC} + T_{ITA}$ to $t = T_0 + 2(T_{IIC} + T_{ITA})$).

An estimation of the time influence of the initial conditions (the "forgetting" time) may be considered by the calculation of steady state conditions using transient analysis. Steady state conditions in a pipe network can be viewed as a sub-problem of the solution to the general unsteady state set of equations. A detailed derivation of the governing unsteady pipe flow equations is shown in Section 3.2. The unsteady pipe flow equations of continuity and motion are restated as

$$\frac{dH}{dt} + \frac{a^2}{g}\frac{\partial V}{\partial x} = 0 \quad \text{.....(5.4.1)}$$

$$\frac{\partial H}{\partial x} + \frac{1}{g}\frac{dV}{dt} + J = 0 \quad \text{.....(5.4.2)}$$

where H = head, a = wave speed, g = gravitational acceleration, V = velocity, x = distance, t = time and J = the total head loss per unit distance due to frictional effects. The steady state equations are obtained by setting all partial derivatives of variables (such as flow, Q, and head, H) with respect to time equal to zero,

$$\frac{\partial Q}{\partial t} = 0 \quad \text{and} \quad \frac{\partial H}{\partial t} = 0 \quad \text{.....(5.4.3)}$$

In fact, just satisfying one of these conditions automatically satisfies the other, as used by Shimada (1988) with good results. Shimada treated each pipe in a network as one reach. Each pipe's wave speed was adjusted so that the wave travel time through all of the pipes was equal. Fast convergence was achieved by reducing the spectral radius of a coefficient matrix, which was composed of the governing unsteady state equations and boundary conditions (linearised about the steady state condition). A similar approach by Wylie (2000) also found quick convergence using the pipeline impedance modification.

Steady state conditions are calculated by running the transient solver for a long simulation period with constant boundary conditions. The damping of pressure oscillations (the transient correction) by steady state friction is used to determine the steady state conditions. The steady friction relationship, as shown in terms of the unit head loss term (J) that appears in the governing unsteady equation of motion, is

$$J = \frac{fV|V|}{2gD} \quad \text{.....(5.4.4)}$$

The final steady state is independent of the initial conditions used, however, the time taken to converge to the steady state is dependent on the initial conditions. The time taken to converge to the steady state is analogous with the time required to "forget" the initial conditions. The investigation of steady state calculation is performed on the same example network as was shown in Section 5.3, which is repeated in Figure 5.33 for clarity.

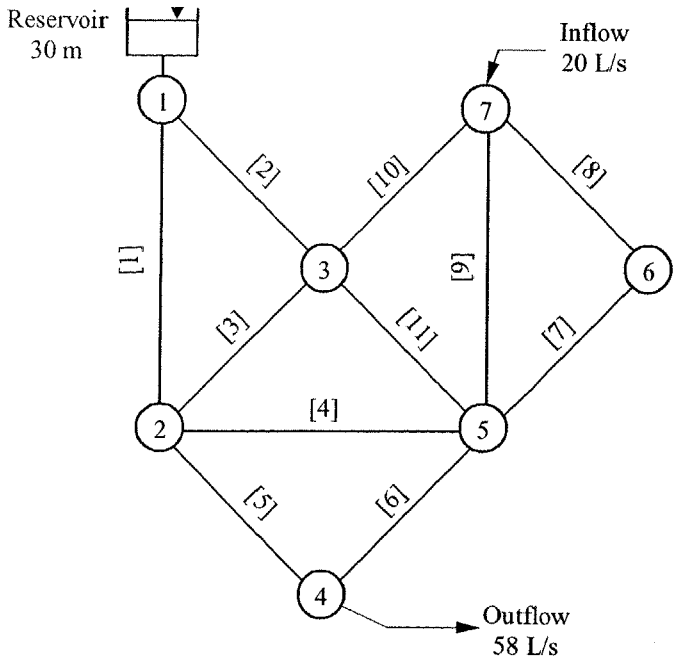

Figure 5.33 Example Network

All pipes in the network are 762mm in length with a common wave speed, hence, the wave travel time in all pipes in the network is equal. Each pipe is 254 mm in diameter, has a wall thickness of 1.6 mm and a friction factor of 0.020. The elevation of the reservoir is 30 m. For the following steady state calculations initial flows and heads in

the example network are specified for the transient solver. The initial conditions (initial heads and flows) are randomly generated with all flows and heads being within ±10% of the correct steady state values. The calculation of the steady state conditions using steady state friction, typified by the head at node 2, is shown in Figure 5.34.

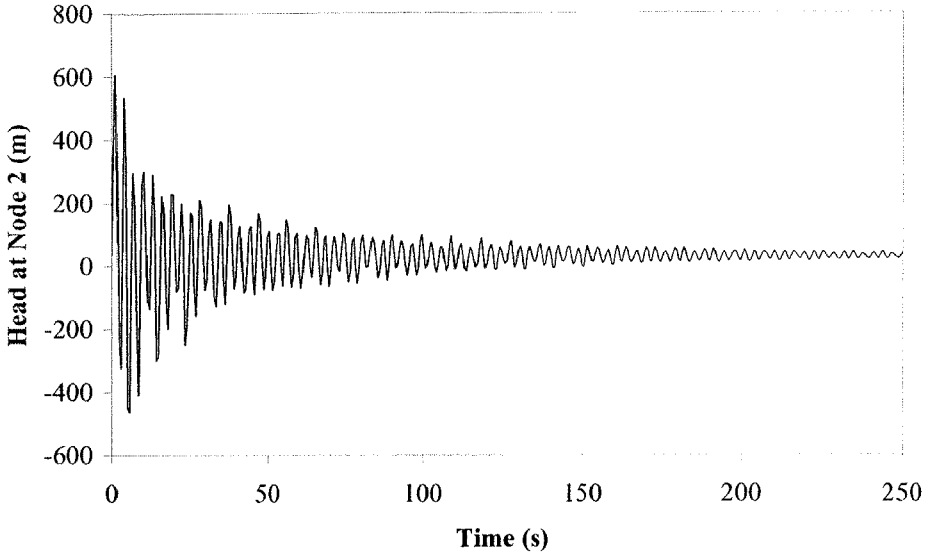

Figure 5.34 Steady Friction Damping, Head at Node 2

Figure 5.34 shows a slow convergence to steady conditions. The oscillations in the pressure are created by water hammer waves caused by the initial conditions not coinciding with the steady state solution. This non-coincidence does not dissipate quickly. A better way to visualise the convergence to steady state conditions is to calculate an average absolute error in the pressure head compared to the final steady state pressure head. Averaging is used to smooth the oscillations in the pressure response to see the underlying trend. The type of averaging used was a moving average with a window (averaging width) size of 15 time steps ($\Delta t = 0.58$ s). The averaged absolute error in the pressure at node 2 is shown in Figure 5.35 using a log scale.

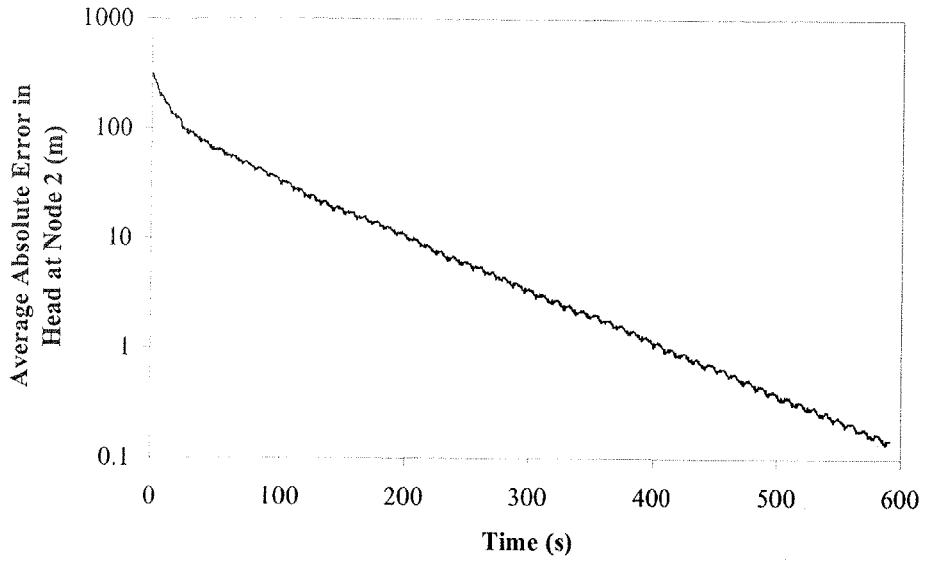

Figure 5.35 Steady Friction Damping, Average Absolute Error at Node 2

A constant convergence slope is observed for the calculation of steady state conditions using steady friction. The linear relationship observed in Figure 5.35 suggests that the damping due to steady friction is approximately exponential in form.

This section showed that the influence of incorrect initial conditions exists for a considerable period of time. Thus, it is important to determine good estimates of the initial conditions. In many cases steady state conditions are a good estimate of the initial conditions. The next section shows how steady state conditions may be calculated efficiently.

5.5 The Calculation of Steady State Initial Conditions

A traditional method to determine the steady state conditions in a network is by solving the set of nonlinear equations describing the steady solution. The nonlinear steady state equations are defined by two relationships. The first is the continuity of flow at a node, as written for a node with a demand, is

$$\sum_{i=1}^{N} Q_i + Q_D = 0 \qquad (5.5.1)$$

where N = number of pipes joining a node, Q_D = nodal demand and the flow in the i^{th} pipe is Q_i. The second relationship relates the head loss between two nodes in the pipe network,

$$H_j - H_k = \frac{f_i L_i Q_i |Q_i|}{2gD_i A_i^2} \quad \text{.....(5.5.2)}$$

where H_j = head at upstream node, H_k = head at downstream node, f_i = Darcy-Weisbach friction factor in pipe i, L_i = the length of pipe i, D_i = the diameter of pipe i and A_i = the cross-sectional area of pipe i. Pipe i is the pipe connecting the two nodal heads H_j and H_k. Eqs. 5.5.1 and 5.5.2, for all pipes and nodes in a pipe network, form a system of nonlinear equations describing the steady state, the solution of which is the steady state. The Newton-Raphson method (see Section 4.3.1) is used for the calculation of steady state conditions of the example network (Figure 5.33), the results of which (the head at node 2) are shown in Figure 5.36.

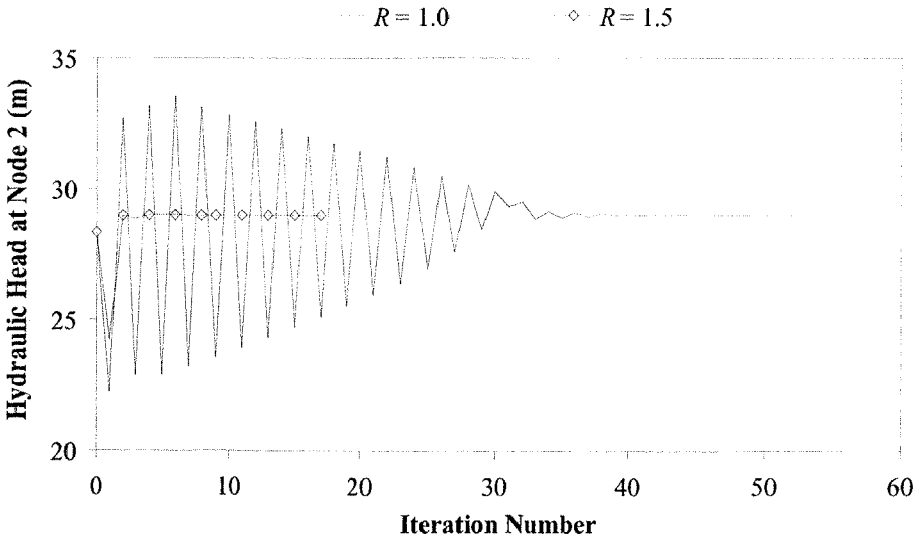

Figure 5.36 Newton-Raphson Method (Hydraulic Head at Node 2)

Results of the implementation of the Newton-Raphson method (R = 1.0) in Figure 5.36 show oscillation in the pressure response due to over-shoot from the Newton-Raphson solver. The over-shoot is remedied by the use of a relaxation coefficient,

$$v_{i+1} = v_i + \tfrac{1}{R}\Delta v \quad \text{.....(5.5.3)}$$

where the heads and flows are represented by the vector v and R is the relaxation coefficient. A relaxation coefficient of 1.5 produces good results, as also shown in

Figure 5.36. A plot of the average absolute error in the head at node 2 is shown in Figure 5.37.

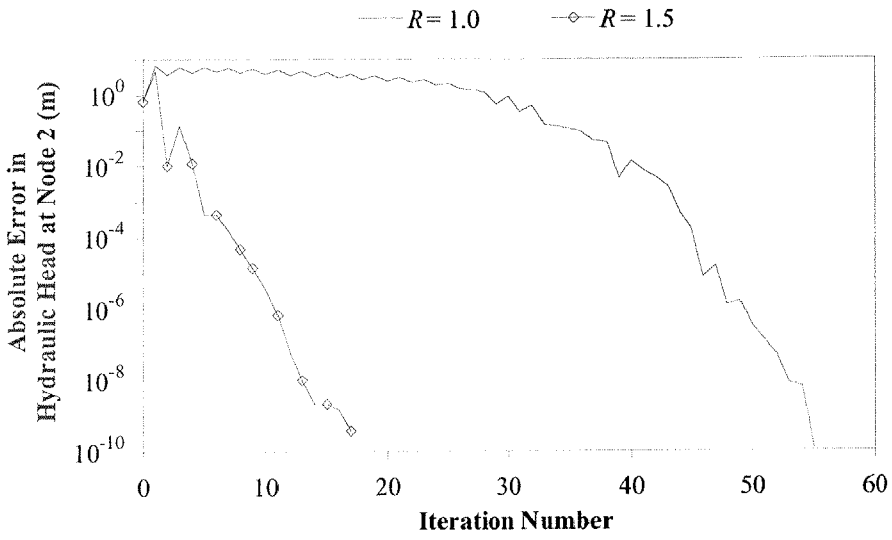

Figure 5.37 Newton-Raphson Method (Absolute Error at Node 2)

The use of relaxation in the Newton-Raphson technique shows a dramatic improvement in the convergence rate. A remaining difficulty, with the Newton-Raphson method, is the selection of an optimal relaxation coefficient that maximises the convergence rate to the steady state solution for all network cases.

5.6 Summary

This chapter has analysed the effects of the correct and incorrect use of initial conditions in the inverse transient method. Previous implementation of the inverse transient method by Chen (1995) did not account for the initial conditions properly. In reality, the initial conditions are never known. Research presented in this chapter using two case studies showed that initial conditions are important. The selection of initial conditions for the transient solver must satisfy the steady state solution (of the configuration of the pipe network being tested); otherwise, a transient correction is created. Unsatisfactory initial conditions are detrimental to the inverse transient method, causing non-convergence. The inclusion a steady state solver allows the

calculation of initial conditions that do satisfy the steady state solution. Including updating of the initial conditions during the inverse transient method appears to have little effect on the effectiveness of the inverse transient method, not taking significantly more iterations for solution. The decrease in sensitivity when using updating initial conditions, however, does point towards a greater effect of measurement error on inverse transient analysis results.

The time influence of the initial conditions was tested showing that it took a long time for an example network to "forget" the initial conditions. This suggests that good estimates of the initial conditions are necessary for successful inverse transient analysis. A steady state solver can provide these estimates. A traditional approach that solved the steady state equations using the Newton-Raphson method was considered. Relaxation between Newton-Raphson iterations improved the convergence rate. The steady state solver used in future chapters of this thesis (for calculation of initial conditions in the inverse transient method) is the solution of the steady state equations by the Newton-Raphson method.

Chapter 6

Inverse Transient Analysis Using Genetic Algorithms

6.1 Introduction

A genetic algorithm is a powerful optimisation technique that borrows ideas from population genetics to search for a near optimal solution by evaluating only a tiny proportion of the total search space. The genetic algorithm technique begins by randomly generating a population of solutions that may or may not satisfy all of the constraints that define the problem at hand. Each of these solutions is represented by a string that acts much like a chromosome does in nature. The strings consist of bits that define the characteristics of a particular solution. Using the cost of implementation of a solution and penalty costs (derived from constraint violation), the fitness of a string can be calculated. The fitness describes how well strings perform in their environment or problem. Through the implementation of genetic operators (used to manipulate strings), successive generations of solutions are produced that converge to near optimal solutions. The real power of the genetic algorithm technique is the ability to deal with highly non-linear problems with non-continuous parameters and complex optimisation objectives. Genetic algorithms are simple in principle and able to implemented for any type of optimisation problem.

This chapter presents the application of genetic algorithm optimisation to the inverse transient method (rather than the Levenberg-Marquardt algorithm as discussed in Chapter 4). A general description of genetic algorithms is presented separately from the application of genetic algorithms to the inverse transient method, mainly because genetic algorithms are applied to a different problem in Chapter 7. A new genetic algorithm scheme is proposed using a continuous representation of the bits in a chromosome. New genetic operators are formulated for this continuous scheme. Numerical results are presented for both pipe friction calibration and leak detection. Numerical comparisons between discrete and continuous schemes are presented together with the effects of varying the number of measurement sites and length of transient record. Conclusions are drawn from these studies.

6.2 Genetic Algorithm Review

Results using genetic algorithm optimisation have been well documented for distribution network optimisation (in design) by Goldberg and Kuo (1987), Simpson *et al.* (1993), Murphy *et al.* (1993, 1994) and Simpson and Goldberg (1994). Experience suggests that reduction in distribution network costs as a result of using genetic algorithm optimisation can be in the order of 4% to 15%. Other fields that have benefited from genetic algorithms are: gas network design (Boyd and Radcliffe, 1994), water distribution network optimisation (Simpson *et al.*, 1993), water distribution network rehabilitation (Engelhardt, 1999), optimisation of water quality in water distribution networks (Hewitson, 2000), artificial wetland design (Tye, 2000), water network calibration (Savic and Walters, 1995), rainfall-runoff model calibration (Wu, 1994) and structural Design (Sved *et al.*, 1991). Software (or source code) for genetic algorithm implementation has been offered by many sources, these include: SGA (Goldberg, 1989), SUGAL (Hunter, 1996) and GENALG (Anderson and Simpson, 1996).

6.3 Genetic Algorithm Implementation

There are nine basic steps that describe the implementation of a genetic algorithm to an engineering problem (Simpson and Goldberg, 1994). Each step is vital to the successful implementation of a genetic algorithm. These steps are:

1. Encoding of a string.
2. Generation of an initial population.
3. Computation of a string cost.
4. Analysis of each string.
5. Assigning a penalty cost to a string if constraints are violated.
6. Computation of the total cost of a string.
7. Computation of the fitness of a string.
8. Generation of a new population using genetic operators.
9. Production of successive generations.

The encoding of a string or chromosome defines the characteristics of particular solutions. Each bit or groups of bits in a string correspond directly to one parameter in the problem definition. There are many different encoding schemes, some of the types are: binary coding (under which Gray coding is a type), integer coding and real coding. For a binary coding scheme the string is composed of zeros and ones.

Typically, the generation of a population is accomplished by applying a uniform random number generator to create a set of initial strings. An estimate of the optimal population size can be obtained using a trial and error process where the best population size is one from which any increase to a larger size will not yield, on average, better solutions. An adequately sized population should ensure that the average signal-to-noise ratios are favourable to the discrimination of the best building blocks (Goldberg *et al.*, 1992). Simpson and Goldberg (1994) conservatively calculated a theoretical population size.

The cost of a particular solution is calculated by decoding the string using a look-up table then, using the decoded parameters and their associated costs, a material cost for a string is calculated (although this is not needed for leak detection and calibration). For

each string or possible solution, the violation of constraints is tested. Each string is decoded into its associated decision variable values, then these values are passed to an analysis unit. The analysis unit returns various results to the genetic algorithm to ascertain the performance of the particular string or solution and whether the constraints are violated or not.

There are three different ways to penalise strings that do not satisfy the problem's constraints (Grant, 1995). The three different methods are elimination, high penalty, and moderate penalty. Each penalty method has its own advantages and disadvantages. Ideally the penalty cost should be such that it lies on the boundary between the feasible and infeasible solution space (Richardson *et al.*, 1989). A common method to determine the penalty cost is by trial and error where some bounds for the penalty are found that maximise diversity, while still producing an increased number of feasible solutions. The total cost for a particular string in the population is the sum of the material and the penalty costs (for inverse transient analysis the material cost is zero and the penalty cost is equal to an objective function). Weights may be applied to the penalty costs if a multiobjective function is being used.

A numerical comparison between different strings in the population is achieved using each string's corresponding fitness (typically calculated as the reciprocal of the cost). If a string has a higher fitness, it is a better solution than others with a lower fitness. Therefore, the objective of a genetic algorithm is to find strings that maximise the fitness.

Once the fitness of each string in the population is determined, genetic operators are used to generate a new population. There are three main genetic operators each having an important role for maximising the flow of genetic material towards an optimal solution. The operators are:

- Selection or Reproduction (Section 6.4.1).
- Crossover (Section 6.4.2).
- Mutation (Section 6.4.3).

Steps 3 to 8 of the nine basic steps listed at the beginning of this section demonstrate the production of successive generations in a genetic algorithm run. These steps are repeated many times to ensure that low cost or fit solutions evolve. Typically, the number of generations ranges from 100 to 1000 (Simpson *et al.*, 1994) depending upon how fast the solution is converging. After each generation, a list of the top ten (or another number) solutions is updated, and their strings and costs are stored in case an outstanding solution is lost during mutation or crossover operations. A method to test if the algorithm has converged is to check whether the average cost in the stored list changes significantly from the previous generation. If the list has not changed over a number of generations, the solution has converged. Usually the problem size, complexity, and number of decision variables determines the total number of generations needed.

6.4 Genetic Operators

Genetic operators are performed on the population and have a direct analogy to population genetics. The following sections discuss three of the most common genetic operators.

6.4.1 Reproduction or Selection Operators

A mating pool facilitates the generation of a new population from an old population. A selection scheme is used to form the mating pool. There are four main kinds of selection schemes: proportionate selection, tournament selection, linear ranking, and Genitor (steady-state) selection.

The proportionate scheme, described by Goldberg (1989), works like a biased roulette wheel where solutions are selected randomly in proportion to their fitness relative to the fitnesses of all other solutions in the current generation. One drawback with the proportionate scheme is that after many generations, the fitnesses of different solutions are similar. Similar fitnesses cause the proportionate scheme to revert to a uniform,

unbiased regime where good solutions might be lost due to a lack of selection pressure (Simpson and Goldberg, 1994).

The tournament selection scheme randomly pairs all of the strings, then the string with the highest fitness in a pair progresses to the mating pool for the next generation. This process is called a binary or a two-member tournament and corresponds to a selection pressure of 2. Because only half of the strings progress, another tournament is held with another set of random pairs and the winners make up the other half of the mating pool for the next generation. Two copies of the best string will progress to the mating pool and no copies of the worst string will be replicated. All other strings will have either zero, one or two copies depending upon with whom they compete with in the tournament. To increase the selection pressure, an s-member tournament may be used where strings are randomly collected into groups of size s. To decrease the selection pressure to less than 2, the tournament size remains at two and the winner is chosen with a probability, P_S (in the range 0.5 to 1.0). Then, the selection pressure is $s = 2P_S$ (Simpson and Goldberg, 1994).

The linear ranking method begins by sorting the population from best to worst fitness. Each string is assigned a number of copies that it should receive according to a non-increasing assignment function. Then, proportionate selection is applied using each string's assignment. The term linear refers to the assignment function expression.

The Genitor selection scheme operator works on an individual-by-individual basis rather than on a population scale. An offspring is chosen according to linear ranking, and the worst individual is always replaced with that offspring. The individual-by-individual nature of the Genitor scheme makes direct comparison with other population scale schemes difficult.

Goldberg and Deb (1991) compared the four selection methods. Proportionate selection had the slowest time for finding a minimum cost solution, while the binary tournament selection was on par with the Genitor selection. Simpson *et al.* (1993) found that an exponential scaling of the fitness function in proportionate selection increases selection pressure. Binary tournament selection produces the best results consistently when

compared to the Genitor or linear ranking selections, and can produce even better results if the tournament size is increased (Simpson and Goldberg, 1994).

6.4.2 Crossover Operators

A crossover operator facilitates the partial exchange of bits between two parent strings. The crossover operator randomly pairs up strings from the population, and tests if the exchange will take place based on the probability of crossover. The probability of crossover (P_C) is typically in the range of 0.5 to 0.7. There are many types of crossover operators, such as one-point crossover, two-point crossover, uniform crossover, and average crossover.

When using one-point crossover, a position is chosen at random in the chromosome then the bits past this position from both parent strings are swapped. In Figure 6.1, the crossover position is at the beginning of bit six. A disadvantage of one-point crossover is that it excludes certain combinations of the features encoded on the chromosomes (Davis, 1991).

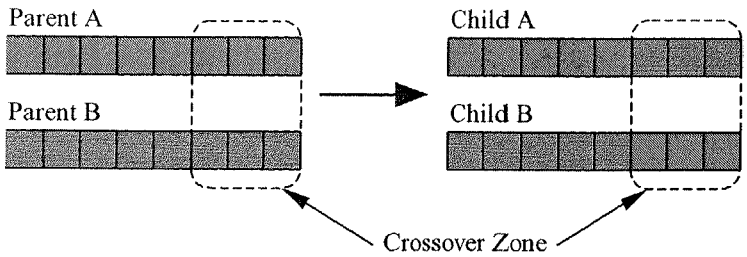

Figure 6.1 One-Point Crossover

The two-point crossover operator randomly chooses two positions in the chromosome then swaps the bits between these two positions in the parent strings, as shown in Figure 6.2. Similar to one-point crossover, two-point crossover may exclude certain combinations of bits, but the probability of this occurring is much smaller (Simpson and Goldberg, 1994).

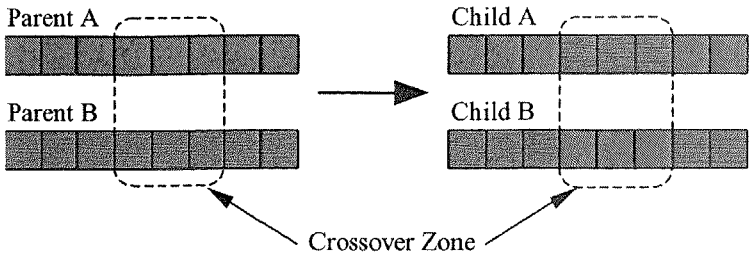

Figure 6.2 Two-Point Crossover

In uniform crossover, each bit in the child string is chosen from either one of the parents' bits at the same corresponding position on a probability basis. The probability that bits are swapped is 0.5, thus creating offspring strings that are unbiased towards either of the parents.

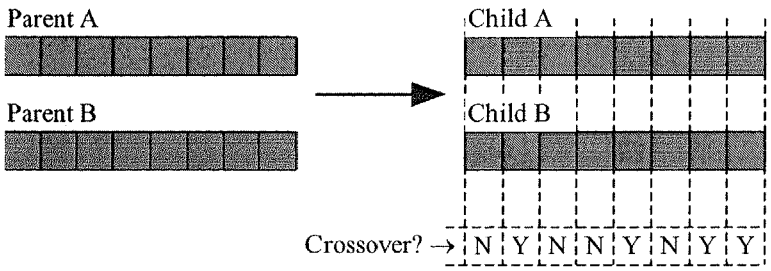

Figure 6.3 Uniform Crossover

The average crossover operator is specifically used for strings that consist of real numbers (Savic and Walters, 1995). This operator takes two parent strings and produces only one child string. The resulting offspring is comprised of bits that are the average of parent's corresponding bits,

$$z_j = \frac{x_j + y_j}{2} \qquad \text{.....(6.4.1)}$$

where x_j , $y_j = j^{\text{th}}$ bit of parents x and y's string and $z_j = j^{\text{th}}$ bit of child's string.

Simpson and Goldberg (1994) showed that the choice of crossover operator is not vital, but the two-point crossover operator produced better solutions on average, while the uniform crossover operator produced a greater number of superior solutions and less inferior ones. The two-point crossover scheme can be expanded to an N-point crossover scheme, but it is generally acknowledged that an N-point crossover scheme ($3 \leq N \leq 5$) is less effective than a uniform crossover scheme. Thierens and Goldberg (1993) and

Goldberg *et al.* (1993) found that various combinations of crossover probability, P_C, and selection pressure, s, can give good results if the population is adequately sized. By increasing the selection pressure, the solutions will converge faster to an optimal solution, but may converge prematurely.

6.4.3 Mutation Operators

The mutation operator ensures that no important genetic material is overlooked during the genetic algorithm run. Each string in the population is tested on a probabilistic basis to determine whether or not it will be mutated. The probability of mutation is denoted as P_M. There are three distinct groups of mutation operators: genome creation, random mutation, and adjacency mutation.

The genome creation operator randomly chooses a string for mutation then recreates it by choosing values for each bit in the chromosome from an allowable set of alleles (possible gene values) based on a uniform probability distribution (Boyd *et al.*, 1994). The genome creation operator works in a similar way to the creation of the initial population.

Alternatively, random mutation (also called bit-wise mutation) considers each string bit by bit. A uniform random number is generated and if it is smaller than P_M, the bit is reversed (i.e. change 1 to a 0 or vice-versa) for binary encoding, or randomly chosen for other schemes. Typical values of the probability for random mutation range between 0.01 and 0.025 (Boyd *et al.*, 1994) per string. It is not entirely clear how important the use of mutation is if the population is adequately sized (Simpson and Goldberg, 1994).

Adjacency mutation is used in problems where the parameters are discrete in nature. A bit is chosen randomly from a randomly chosen string (as in random mutation), by the use of a small probability, P_A. Then, the bit has an opportunity to change up to the next larger adjacent value, or down to the next lower adjacent value. In adjacency mutation, P_D denotes the probability of moving to a smaller parameter value and typically is equal to 0.5 (Simpson and Goldberg, 1994; Murphy *et al.*, 1993). Typically, discrete

parameter values are usually bounded; therefore if the bit is initially set at the lowest bound the probability of moving to the next larger adjacent value is 1.

Simpson and Goldberg (1994) compared genetic algorithm runs with and without mutation, however genome creation was not used. The runs that included mutation produced better results, on average, than the runs that did not include mutation. Other studies with long chromosome lengths do not, however, support these results. Typically, the mutation probability, P_M, is selected in the range

$$\frac{1}{n} < P_M < \frac{1}{l} \quad \text{.....(6.4.2)}$$

where n = population size and l = chromosome length (assuming $n > l$).

6.5 Genetic Algorithm Code

Anderson and Simpson (1996) developed the program GENALG (GENetic-ALGorithm) in the Department of Civil and Environmental Engineering at Adelaide University. The source code is freely available for research use. The code is flexible, allowing the simple incorporation of different applications into the genetic algorithm. GENALG, programmed in FORTRAN 77 (in which much existing engineering code is written), is based on the Goldberg (1989) genetic algorithm with many extra features. GENALG includes the seeding of random numbers, which allows consistency over initial populations and random decisions. The chromosomes are coded with floating point numbers, thus allowing the choice of binary, integer and real coding schemes. A multiple member tournament section is used, thus alleviating problems (mainly with regards to proportional selection) when the population is near convergence and similar string fitnesses are common. In GENALG, crossover is allowed between any number of strings at multiple points in the chromosome. The population size may be fixed or adaptively altered depending on the level of diversity in the population. Automatic replacement of a string may be performed if it is noticed that that string is invalid given its chromosome (and cannot be simulated). The population can be refreshed (sometimes referred to as immigration) to increase the diversity of the population. To reduce the amount of simulations needed in a generation (especially useful for machine

intensive simulations) the population is scanned for duplicate strings. A running list of the best chromosomes is kept in case a good solution is mutated or lost between successive generations. Above all, GENALG has been created for flexibly with regards to different applications. The evaluation of the fitness function and the mutation (and inversion) method can be user defined to suit different applications.

6.6 Inverse Transient Analysis Using Genetic Algorithms

The inverse transient method of Liggett and Chen (1994) involves fitting a numerically modelled pressure or head trace to a measured head trace by minimising the differences between calculated and measured values. This section presents a new approach to the inverse transient method based on genetic algorithm optimisation. New chromosome representation, chromosome coding and genetic operators are presented. Genetic algorithms maximise the fitness of a string. For the inverse transient method, the fitness is the negative of the sum of absolute differences between the measured and modelled head (compare with Eq. 4.10.1),

$$fitness = -\sum_{i=1}^{M} \left| H_i^m - H_i \right| \quad \text{.....(6.6.1)}$$

where M = the total number of data points, H_i^m = the measured hydraulic head and H_i = modelled hydraulic head.

6.6.1 Chromosome representation

The inverse transient method (Liggett and Chen, 1994) performs both leak detection and friction factor calibration simultaneously using a Levenberg-Marquardt algorithm. An alternative minimisation method is the genetic algorithm, details of which are developed in this thesis (Vítkovský *et al.*, 2000). The genetic algorithm chromosome represents both the friction factor (f) in each pipe (or pipe group) and the lumped leak coefficient ($C_d A_L$) at each suspected leak location, as shown in Figure 6.4.

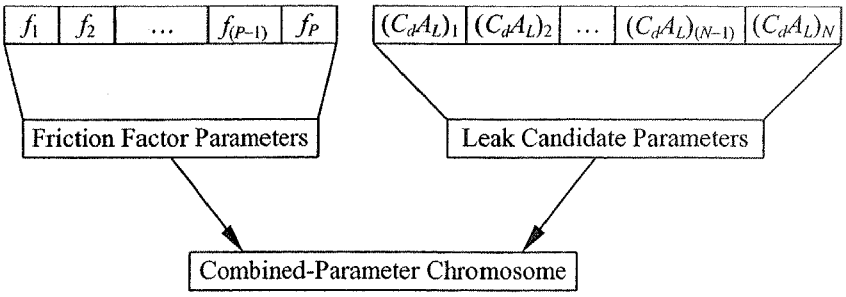

Figure 6.4 Chromosome Representation for Friction Factors and Leaks

Where there are P pipes (or pipe groups) and N suspected leak locations. The chromosome, which contains both friction factors and leak coefficients, is called a combined-parameter chromosome. In further sections of this chapter, the inverse transient method using genetic algorithms uses a combined-parameter chromosome representation.

6.6.2 Discrete and Continuous Coding Schemes

A coding scheme describes how the bits (relating to the decision variables) in the chromosome are defined. Chromosome bits may be defined as either discrete or continuous. Traditionally, genetic algorithm optimisation uses a discrete coding scheme, however, Savic and Walters (1995) use a continuous coded scheme. The decision variable range, requiring a lower and an upper bound, define both of these coding schemes. Representation of decision variables within a genetic algorithm string is usually by discrete values within a continuous range. For a discrete coding scheme, a lookup table relating a code (either binary or integer) with a corresponding discrete value (for example, $f = 0.015$, 0.016, etc.) is necessary. To suit the continuous nature of the friction factor and lumped leak coefficient values, a continuous coding scheme is developed for implementation of the genetic algorithm in this thesis. Generation of an initial population of strings, which contain unknown friction factors and leaks in the genetic algorithm process, uses randomly selected values from the continuous range between lower and upper bounds using a uniform probability distribution. The ranges for the friction factors and the lumped leak coefficients are different depending on the relative magnitudes of each parameter.

6.6.3 Continuous Scheme Genetic Algorithm Operators

A new crossover operator, called two-child staggered average crossover (TCSAX), is developed to exploit the continuous nature of the variables being represented by the string (Vítkovský and Simpson, 1997; Vítkovský *et al.*, 2000). The TCSAX operator is based on a crossover operator first used by Savic and Walters (1995) named "one child average crossover." A schematic of the TCSAX operator with three crossover points is shown in Figure 6.5. The TCSAX operator averages the corresponding bit values from segments of a pair of parent strings and places the result in one child, while keeping the original bits from one parent in the other child. The TCSAX operator differs from the Savic and Walters (1995) operator in that it maintains some of the original genetic information from each parent string.

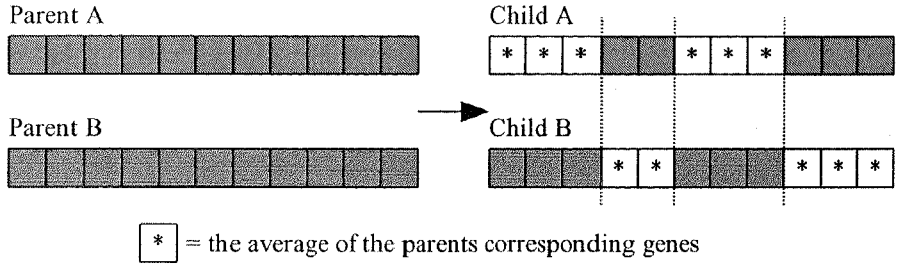

Figure 6.5 Two-Child Staggered Average Crossover Example

A new mutation operator is developed also for continuous variables (Vítkovský *et al.*, 2000). The mutation operator alters the gene (friction factor or lumped leak coefficient) to a new value within a range of *Step_Size* below or above the current value. Figure 6.6 illustrates the mutation operator. The mutated gene value is given by

$$gene_{NEW} = gene_{OLD} + Step\_Size(2 \times RND - 1) \quad \text{.....(6.6.2)}$$

where *RND* is a uniformly distributed random number between 0.0 and 1.0, and *Step_Size* is the maximum increment allowed in a gene. The *Step_Size* values are different for different types of parameters. For example, the *Step_Size* for a friction factor is about three orders of magnitude larger than that for a lumped leak coefficient. Due to the small size of the lumped leak coefficient and its sensitivity, it is necessary to search for leaks in logarithmic space, which allows strings to move efficiently between differing magnitudes of leaks and avoids negative lumped leak coefficients.

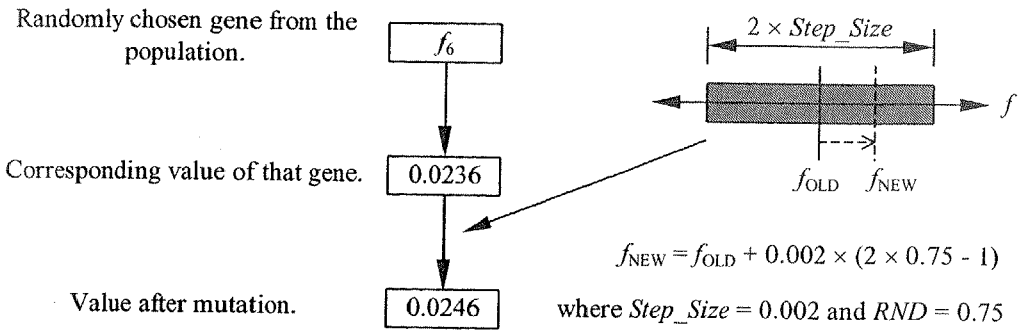

Figure 6.6 Continuous Adjacency Mutation Example

6.7 Numerical Testing Using an Example Network

Evaluation of the inverse transient method using genetic algorithms uses an example pipe network. The following section defines the example pipe network. Comparisons between the discrete and continuous coding schemes, the effects of varying the number of measurement sites and the length of measurement data at each node are made.

6.7.1 Definition of the Example Network

Figure 6.7 shows the example water distribution pipe network considered in this section. The example network consists of 11 pipes and 7 nodes (see also Section 5.2). A reservoir at node 1 and a constant inflow (20 L/s) at node 7 supply the example network. The Darcy-Weisbach friction factors and the pipe lengths for the network are shown in Figure 6.7 below each pipe. All pipes are 254 mm in diameter with a wall thickness of 1.6 mm. The network is based on a network examined by Pudar and Liggett (1992).

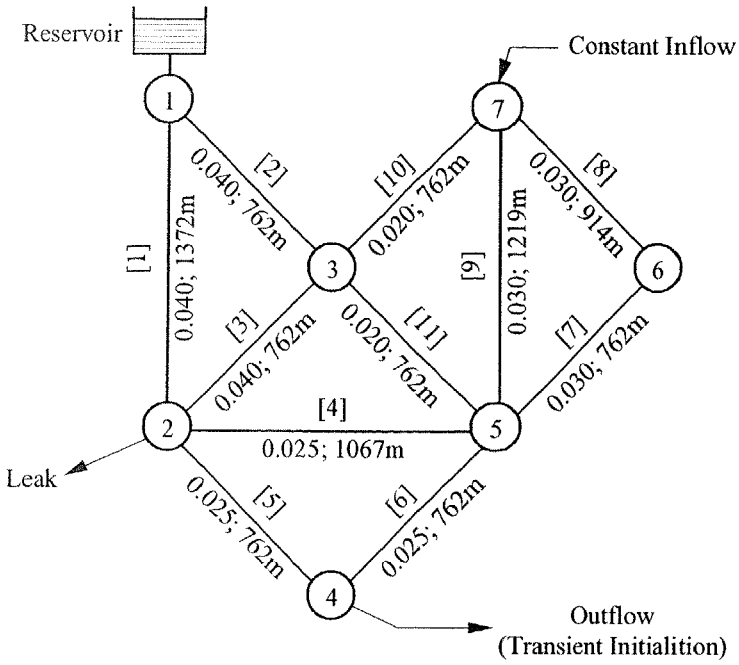

Figure 6.7 Layout of Example Network

Varying the discharge at node 4 initiates the transient event, as shown in Figure 6.8. The measurement data for the example network are the heads at up to six nodes over a 40-second interval (corresponding to 72 data points per node). A simulated leak exists at node 2. The simulated leak at node 2 has a lumped leak coefficient of $C_d A_L = 1.0 \times 10^{-4}$ m^2, corresponding to an approximate leak hole diameter of 13 mm (the pipe being 254 mm in diameter). Both the friction factors and the lumped leak coefficients are determined simultaneously using the genetic algorithm search technique.

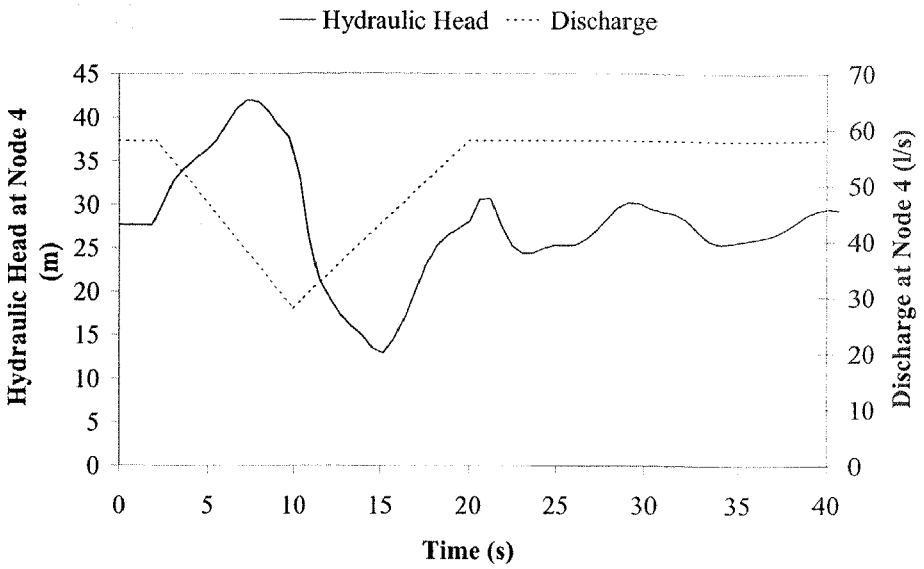

Figure 6.8 Initiation of Transient Event at Node 4

Figure 6.9 shows an example of the measurement data used for the inverse transient method using genetic algorithms (the variation in hydraulic head at nodes 2, 3 and 6). Appendices D.3.1 and D.3.2 present the measured pressure-head data in tabular form for the "no leak" case (used in Sections 6.7.3, 6.7.4 and 6.7.5) and the "with leak" case (used in Section 6.7.2) respectively.

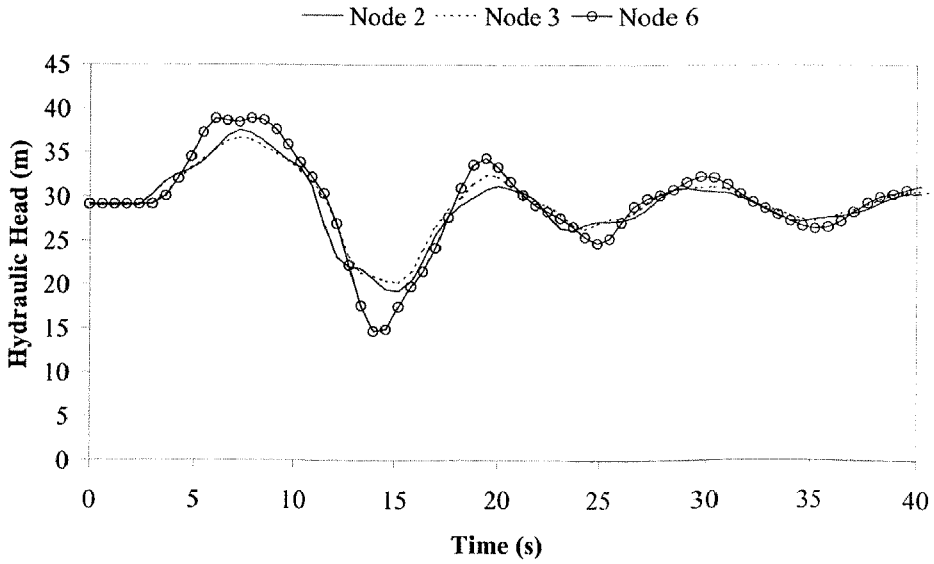

Figure 6.9 Measured Hydraulic Head for Nodes 2, 3 and 6 in Example Network

The inverse transient method attempts to match the modelled pressure data to the measured pressure data. Figure 6.10 shows the beginning of this process for the measured data at node 3. This figure shows the pressure trace using a randomly generated set of parameters of pipe friction and lumped leak coefficients. This randomly generated set of parameter values is characteristic of the strings in the initial population.

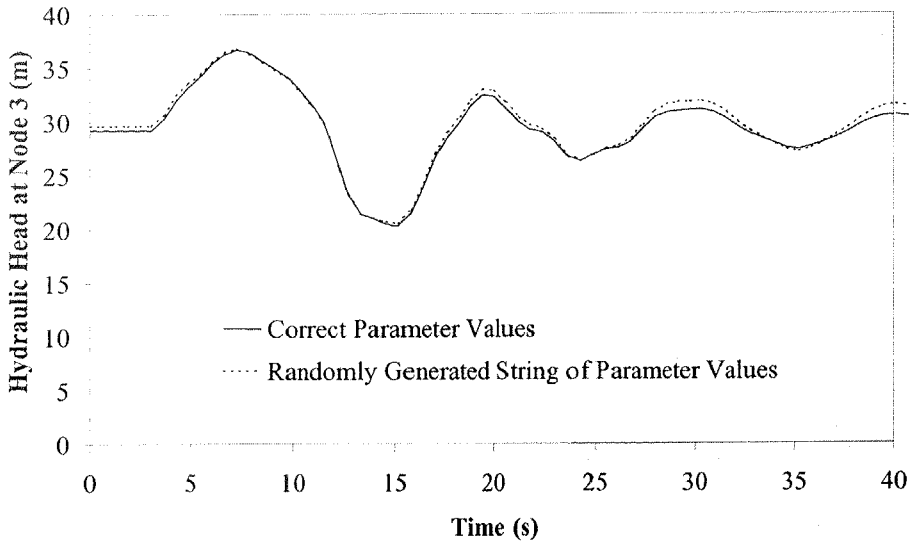

Figure 6.10 Hydraulic Head at Node 3 Using Correct and Incorrect Parameters

The following sections present numerical results for leak detection and calibration of the example network.

6.7.2 Numerical Results for Calibration and Leak Detection

A typical result from an application of the genetic algorithm calibration and leak detection is shown in Tables 6.1 and 6.2 that corresponds to friction factors and leaks respectively. The average error in the friction factors is 3.43% and the error for the leak at node 2 is 0.50%. The sizes of the calibrated leaks at the nodes where there were no real leaks were approximately three orders of magnitude smaller than that of the real leak. Their effect on the transient model is negligible and corresponds to a hole in the pipe of diameter ≈ 0.5 mm. They may be discounted as being too small to be of any consequence.

Table 6.1 Genetic Algorithm Friction Factor Calibration Results

Pipe No.	Darcy-Weisbach Friction Factor, f		
	Correct Results	Typical GA Run	Percentage Error
1	0.040	0.0410	2.50%
2	0.040	0.0393	-1.84%
3	0.040	0.0388	-2.89%
4	0.025	0.0253	1.20%
5	0.025	0.0259	3.60%
6	0.025	0.0247	1.34%
7	0.030	0.0283	-5.52%
8	0.030	0.0268	-10.6%
9	0.030	0.0300	0.00%
10	0.020	0.0215	7.61%
11	0.020	0.0199	0.67%
Overall Average Absolute Error			3.43%

Table 6.2 Genetic Algorithm Leak Detection Results

Leak Candidate	Lumped Leak Coefficient, $C_d A_L$ (m^2)		
	Correct Results	Typical GA Run	Percent Error
Node 2	1.0×10^{-4}	9.95×10^{-5}	-0.50%
Node 3	0.0	1.19×10^{-7}	/
Node 4	0.0	1.33×10^{-7}	/
Node 5	0.0	1.89×10^{-7}	/
Node 6	0.0	1.83×10^{-7}	/

In comparison to the detection of the leak, there is a relatively large variation in the friction factors determined by the genetic algorithm calibration. This large variation may be explained using the sensitivity of the fitness function with respect to each of the parameters types. The total sensitivity with respect to each parameter is calculated by the addition of the absolute partial derivatives of the fitness with respect to that parameter. The total sensitivity shows the relative ease with which a parameter can be determined as compared to another parameter. A large sensitivity in a parameter corresponds to a greater confidence in a solution for that parameter. Figures 6.11 and 6.12 show the sensitivities with respect to the friction factors and the lumped leak coefficients respectively. The friction factors exhibit a low sensitivity compared to the sensitivities of the lumped leak coefficients, thus suggesting that leaks will be determined more easily than the friction factors. The sensitivity of the lumped leak parameters is approximately 3 orders of magnitude larger than the friction factor sensitivities. The sensitivities reflect the observation that the calculated lumped leak coefficients have less error than the calculated friction factors (Tables 6.1 and 6.2).

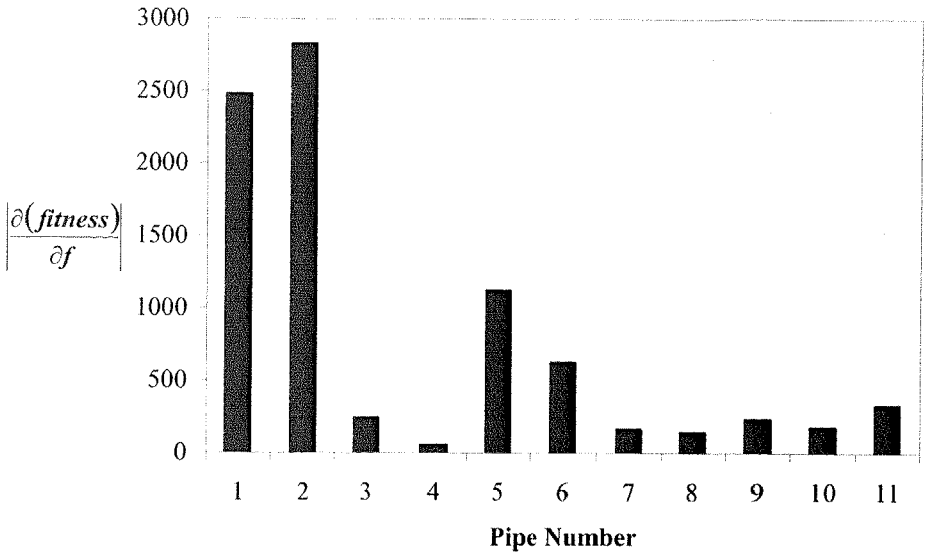

Figure 6.11 Sensitivity of Fitness with Respect to Friction Factors

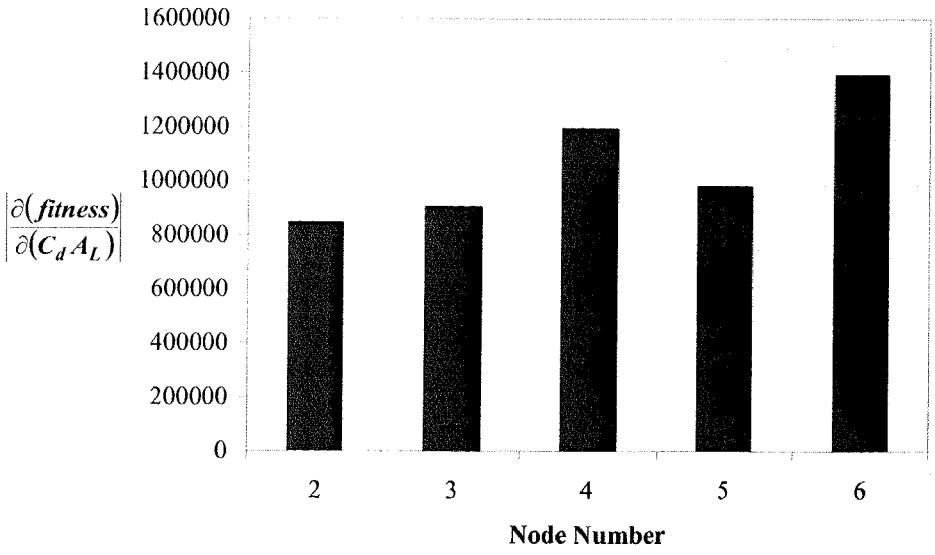

Figure 6.12 Sensitivity of Fitness with Respect to Lumped Leak Coefficients

Figure 6.13 shows a plot of the convergence of the fitness for this GA run. The convergence is fast at the beginning of the genetic algorithm run but slower towards the end of the run. A reason for the slow convergence at the end of the GA run is the low sensitivity of friction factors for pipes 4, 7, 8 and 10, which are the last to be determined. Any changes in these parameters do not tend to have a great affect on the fitness of a string, and therefore many strings may have similar fitnesses while having differing friction factors (for the low sensitivity pipes). The difference in sensitivities

for different parameter types means that some parameters are less important when modelling and should have a lower associated confidence.

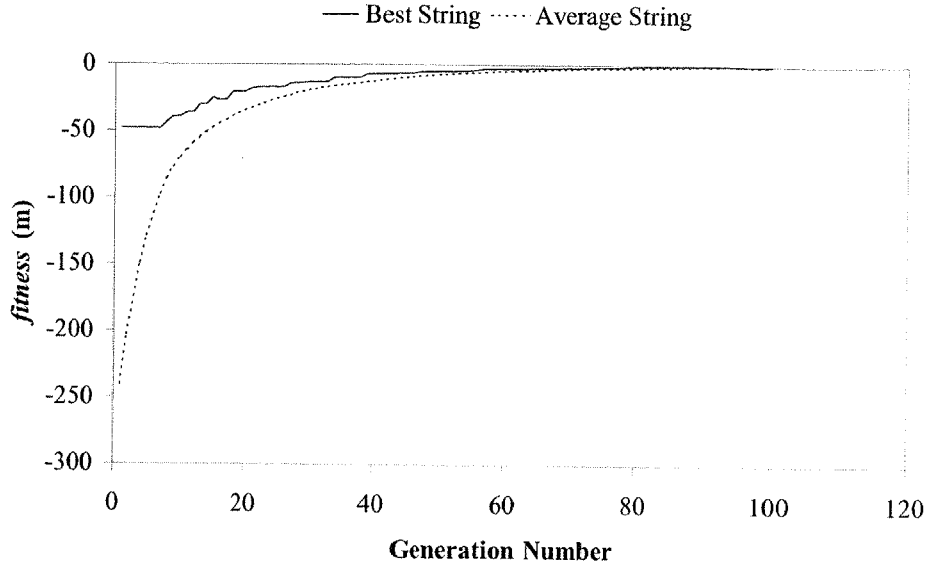

Figure 6.13 Convergence of Genetic Algorithm

6.7.3 Comparison of Discrete and Continuous Coding Schemes

A comparison between the discrete and continuous coded genetic algorithm is made based on the friction factor calibration (only) of the example network using the inverse transient method. The comparison uses measured data generated by a forward transient as described in the Section 6.7.1. Tournament selection is used with a tournament size, $s = 2$. Also, the following genetic algorithm parameters are used: population, $n = 1000$; probability of crossover, $P_C = 0.4$; and probability of mutation, $P_M = 0.0$. A mutation rate of zero is selected as Simpson and Goldberg (1994) suggest that mutation has little impact on the effectiveness of the genetic algorithm search. An advantage of a mutation rate of zero is that the population of solutions will eventually contain identical solutions for all strings, thus concluding the genetic algorithm search. Each genetic algorithm result uses an average of 10 runs with each run using a different starting random number seed.

There are two possible genetic algorithm runs available for the comparison of the two coding schemes. These two possibilities are:

1. Genetic algorithm runs with unknown friction factors that exist within the search space of the discrete coding scheme. For example, the friction factors in column (2) of Table 6.3. These friction factors would be expected to favour the discrete coded scheme given the choice table shown in Table 6.4.
2. Genetic algorithm runs with unknown friction factors that do not exist within the search space of the discrete coding scheme. For example, the friction factors in column (3) of Table 6.3. These friction factors should favour the continuous coded scheme as they can only be approximated by the values in the discrete choice table of Table 6.4.

In this case study, the discrete coding scheme that is used to represent the Darcy-Weisbach friction factors has a range for friction factors of between 0.010 and 0.051 with an interval of 0.001, as shown in the choices in Table 6.3, thus creating 42 possible values for each pipe. The genetic algorithm constrains the parameters within the specified range easily, whereas constraining parameters in other derivative-based minimisation techniques can, in some cases, inhibit convergence. The search space of possible friction factor combinations for the example pipe problem in Figure 6.7 is 7.17×10^{17} (for the discrete coded scheme). For the continuous coding scheme, the bits representing friction factors range between 0.010 and 0.051 (taking any continuous number in between); therefore, the size of the search space cannot be quantified due to the infinite number of possibilities for each bit in a chromosome.

Table 6.3 Pipe Properties for Example Network

Pipe Number (1)	*f* in Discrete Search Space (2)	*f* NOT in Discrete Search Space (3)
1	0.040	0.02839
2	0.040	0.02839
3	0.040	0.02839
4	0.025	0.03979
5	0.025	0.03979
6	0.025	0.03979
7	0.030	0.01860
8	0.030	0.01860
9	0.030	0.01860
10	0.020	0.02241
11	0.020	0.02241

Table 6.4 Genetic Algorithm Choice Table for the Discrete Coding Scheme

Integer Code	Friction factor	Integer Code	Friction factor	Integer Code	Friction factor
1	0.010	15	0.024	29	0.038
2	0.011	16	0.025	30	0.039
3	0.012	17	0.026	31	0.040
4	0.013	18	0.027	32	0.041
5	0.014	19	0.028	33	0.042
6	0.015	20	0.029	34	0.043
7	0.016	21	0.030	35	0.044
8	0.017	22	0.031	36	0.045
9	0.018	23	0.032	37	0.046
10	0.019	24	0.033	38	0.047
11	0.020	25	0.034	39	0.048
12	0.021	26	0.035	40	0.049
13	0.022	27	0.036	41	0.050
14	0.023	28	0.037	42	0.051

The measured pressure data used in this section are taken at six measurement sites with eighteen time steps of pressure transient information at each site. Table 6.5 gives GA results for both of the above friction factor groups. Errors are given at the bottom of the table. The error E_A is the average of the absolute differences in friction factors (those found by genetic algorithm compared with the correct values). The error E_B is the average head difference at all nodes in the network while the error E_C is the average head difference when only the measurement sites are considered. The results indicate that individual runs using the discrete coded genetic algorithm produce the best results (columns (3) and (6)) and found the correct solution for friction factors in all 11 pipes in five out of ten genetic algorithm runs.

Table 6.5 Results for Discrete and Continuous Friction Factor Sets

Pipe Number (1)	f in Discrete Search Space			f NOT in Discrete Search Space		
	Correct f (2)	Discrete Coding (3)	Continuous Coding (4)	Correct f (5)	Discrete Coding (6)	Continuous Coding (7)
1	**0.040**	0.0396	0.0400	**0.02839**	0.0282	0.02880
2	**0.040**	0.0402	0.0399	**0.02839**	0.0286	0.02812
3	**0.040**	0.0395	0.0373	**0.02839**	0.0291	0.02540
4	**0.025**	0.0216	0.0222	**0.03979**	0.0388	0.02939
5	**0.025**	0.0245	0.0238	**0.03979**	0.0397	0.03940
6	**0.025**	0.0260	0.0271	**0.03979**	0.0398	0.04040
7	**0.030**	0.0294	0.0281	**0.01860**	0.0192	0.01971
8	**0.030**	0.0297	0.0282	**0.01860**	0.0187	0.02004
9	**0.030**	0.0300	0.0306	**0.01860**	0.0185	0.01829
10	**0.020**	0.0207	0.0246	**0.02241**	0.0196	0.02374
11	**0.020**	0.0211	0.0222	**0.02241**	0.0222	0.02320
E_A	-	3.12 %	7.27 %	-	2.22 %	6.04 %
E_B (mm)	-	5.1	6.2	-	3.7	3.8
E_C (mm)	-	4.7	8.3	-	10.4	6.3

Table 6.5 shows that the discrete coded scheme has a lower error in the friction factors (E_A) compared to the continuous coding scheme. The average discrete coded genetic algorithm results display approximately the same average head difference (E_B) as the continuous coded scheme but only one-third of the error in friction factors (E_A). Also, Table 6.5 shows no significant difference in the average absolute friction factor difference (E_A) when searching for friction factors that are not in the discrete coded genetic algorithm's search space, thus suggesting that for data containing no errors, the discrete coded scheme is a more efficient search method than the continuous scheme. Another reason for the discrete scheme's performance could be that the search space for the discrete coded genetic algorithm is far smaller than the continuous coded genetic algorithm's search space, which appears to allow the discrete coded scheme to search more successfully. The following studies will be for friction factors in the group 1 search space only.

6.7.4 Comparison of Varying Number of Measurement Sites

In a large pipe network it is not effective to measure pressure at all nodes. Tests to investigate the performance of each coding scheme when different numbers of measurement sites are specified use calibration of friction factors only. Table 6.6 shows

average results for ten genetic algorithm runs using all six measurement sites, three measurement sites (nodes 2, 3 and 6), and one measurement site (node 5).

Table 6.6 Results for Varying Numbers of Measurement Sites

(1)	(2)	(3)	(4)	(5)	(6)	(7)	(8)
Pipe Number	Correct f	Discrete Coded Scheme			Continuous Coded Scheme		
		No. of Measurement Sites			No. of Measurement Sites		
		1	3	6	1	3	6
1	**0.040**	0.0400	0.0399	0.0401	0.0402	0.0400	0.0404
2	**0.040**	0.0398	0.0401	0.0399	0.0393	0.0400	0.0397
3	**0.040**	0.0313	0.0373	0.0384	0.0333	0.0364	0.0362
4	**0.025**	0.0266	0.0212	0.0231	0.0254	0.0247	0.0253
5	**0.025**	0.0238	0.0238	0.0248	0.0234	0.0234	0.0238
6	**0.025**	0.0264	0.0261	0.0253	0.0266	0.0271	0.0272
7	**0.030**	0.0292	0.0304	0.0306	0.0281	0.0287	0.0286
8	**0.030**	0.0227	0.0293	0.0305	0.0281	0.0267	0.0276
9	**0.030**	0.0334	0.0305	0.0299	0.0304	0.0304	0.0307
10	**0.020**	0.0254	0.0181	0.0219	0.0267	0.0251	0.0239
11	**0.020**	0.0223	0.0221	0.0207	0.0247	0.0221	0.0217
E_A	-	10.5 %	5.18 %	2.83 %	9.48 %	7.08 %	6.31 %
E_B (mm)	-	18.9	6.0	2.7	22.4	8.6	8.3
E_C (mm)	-	4.8	7.7	9.4	2.7	7.9	7.8

Table 6.6 shows that the error in the friction factors decreases as the number of measurement sites increases for both the discrete and continuous coding schemes, as expected. For the largest number of measurement sites (6 sites) the discrete coded scheme yielded a lower average error in the friction factors (E_A)—column (5)—than the continuous coded scheme—column (8). The opposite behaviour was seen for the lowest number of measurement sites (1 site)—columns (3) and (6). Here, the continuous coded scheme produces a slightly lower average error in the friction factors (E_A). It appears that the discrete scheme performs better than the continuous scheme especially for the range of 3 to 6 measurement sites. There is a significant decrease of error when the three and six measurement sites are used rather than one site.

6.7.5 Comparison of Different Transient Record Lengths

Differing lengths of transient record (the measurement data) were investigated for the calibration of friction factors only using inverse transient analysis and genetic algorithms. Three different record lengths are used; 18, 36 and 72 time steps that correspond to 10, 20 and 40 seconds of transient pressure data. Measurement data at

three nodes (nodes 2,3 and 6) were used. Table 6.7 shows the results from these tests for the different coding schemes.

Table 6.7 Results for Varying Lengths of Transient Record

Pipe Number	Correct f	Discrete Coded Scheme			Continuous Coded Scheme		
		Number of Time Steps			Number of Time Steps		
		18	36	72	18	36	72
1	**0.040**	0.0399	0.0401	0.0399	0.0400	0.0401	0.0401
2	**0.040**	0.0401	0.0399	0.0401	0.0400	0.0399	0.0399
3	**0.040**	0.0373	0.0356	0.0373	0.0364	0.0353	0.0353
4	**0.025**	0.0212	0.0185	0.0255	0.0247	0.0252	0.0251
5	**0.025**	0.0238	0.0236	0.0234	0.0234	0.0232	0.0234
6	**0.025**	0.0261	0.0265	0.0252	0.0271	0.0269	0.0272
7	**0.030**	0.0304	0.0304	0.0306	0.0287	0.0295	0.0288
8	**0.030**	0.0293	0.0284	0.0288	0.0267	0.0267	0.0255
9	**0.030**	0.0305	0.0303	0.0304	0.0304	0.0311	0.0305
10	**0.020**	0.0181	0.0241	0.0227	0.0251	0.0255	0.0249
11	**0.020**	0.0221	0.0226	0.0216	0.0221	0.0225	0.0226
E_A	-	5.18 %	8.18 %	4.12 %	7.08 %	7.23 %	7.80 %
E_B (mm)	-	6.0	7.2	8.6	8.6	9.0	8.9
E_C (mm)	-	7.7	9.3	7.3	7.9	6.5	5.1

Results for differing lengths of record are not conclusive when the average absolute differences (E_A) are considered but they do indicate that the discrete coded scheme performs slightly better on average than the continuous coded scheme. These results do not show any conclusions about the length of data used and the accuracy of calibrated friction factors found.

6.8 Summary

The inverse transient method is a powerful technique for leak detection and calibration of friction factors in water distribution systems. Transient techniques have a distinct advantage over traditional steady state calibration techniques in that they provide much more data. The previous implementation of the inverse transient method by Liggett and Chen (1994) used derivative-based methods of optimisation. Such methods may fail to converge or converge to a local minimum, rather than the global minimum, for complex objective function spaces. An alternative to derivative methods is a genetic algorithm search method. This chapter implements the inverse transient method using a genetic algorithm search method. There is a trade-off between the fast speed of a derivative-

based method of optimisation and the slower (compare with inverse transient results for the same problem using the Levenberg-Marquardt algorithm in Section 5.3), but potentially more robust and comprehensive, genetic algorithm search. The genetic algorithm has the ability to bound its search in the parameter space, which is a distinct advantage over gradient-based methods where bounding may cause the optimisation method to fail.

Leak detection and friction factor calibration using the inverse transient method and genetic algorithms were performed using an example network. A continuous variable representation for use in the genetic algorithm was proposed in this chapter along with new continuous crossover and mutation operators.

Two chromosome representation schemes for the genetic algorithm were compared—a discrete scheme and a continuous scheme—using two different sets of friction factors. For friction factor calibration, the discrete coding scheme performed better than the continuous scheme, which was independent of whether the solution friction factors were contained in the discrete coding scheme's search space or not.

Also, the influence of the number of measurement sites and the length of record was investigated. The investigation of the performance of the genetic algorithm with different numbers of measurement sites showed that the greater the number of sites, the better the estimates of friction factors—as would be expected. The results for varying the length of the measurement data record showed little difference or no discernible trend. Overall, the discrete coded scheme appears to perform better than the continuous scheme.

Chapter 7

Improving Inverse Transient Analysis

Performance

7.1 Introduction

Different aspects that can be used to further improve the inverse transient method's performance are investigated in this chapter. The different areas can be summarised in the form of questions including:

- How many measurement sites are necessary in a network for adequate results?
- Where should these measurement sites be placed in a network to produce the best results?
- What length of data is needed to produce accurate results?
- What degree of confidence is associated with the results?

Methods are proposed and implemented in this chapter to address each of these questions. Performance indicators are defined as an aid in answering these questions. Two case studies are considered. One is a small example network (11 Pipes) on which much of the verification of the performance indicators is performed. The other case

study is performed in a larger network (51 Pipes), which is used to solve problems with application to large numbers of parameters.

An objective of this chapter is to identify performance indicators that provide a good indication of how well a particular configuration of measurement sites will perform when using the inverse transient method. It is desirable that the calculation of these performance indicators be efficient so that a search for optimal measurement site configurations will not be hindered by a slow calculation scheme. Testing of each of the proposed indicators is performed in the following section using an example network that can be fully enumerated (all possible measurement site configurations evaluated).

7.2 A Measure of Performance in Inverse Transient Analysis

To answer the questions posed in the introduction, criteria must be formed to differentiate between the performance of various measurement site configurations. A measure of performance is, given that random error will inevitability exist in measured data, the level of error that will be propagated through the inverse transient method to the solution parameters. Superior measurement site locations and numbers are those that inhibit the transmission of measurement error to the parameters in the inverse transient method. Other measures of performance are possible but are not investigated in this thesis. A technique that can be used to evaluate this transmission is the Monte Carlo simulation method (see next section). A distributed error can be inserted into the measured data and the result of that error can be observed in the parameters that are calculated by the inverse transient method. Unfortunately, the Monte Carlo simulation method is computationally intensive, requiring many solutions of the inverse transient problem. Other methods (or indicators) provide a computationally cheaper way to determine the error transmission of the measured error to the parameters. These computationally cheaper indicators of the performance of various measurement site configurations on the inverse transient method are tested against results found using the Monte Carlo simulation method. Useful performance indicators are determined and then used to answer the questions posed in the introduction. A definition of the Monte Carlo simulation method is presented in the next section.

7.2.1 Monte Carlo Simulation Method

The Monte Carlo simulation (MCS) method was originally used for the evaluation of complicated integrals (Weisstein, 2000). This method has also been successfully used for finding the probability distributions in complicated problems (Nash and Walker-Smith, 1987). It is in this second application that the Monte Carlo simulation technique is used to find the distribution of parameter error calculated by the inverse transient method using an introduced error in the measured data.

A Monte Carlo simulation scheme is defined as any method that solves a problem by generating suitable random numbers and observing that fraction of the numbers obeying some property or properties. The method is useful for obtaining numerical solutions to problems that are too complicated to solve analytically (Weisstein, 2000).

The Monte Carlo scheme evaluates the complicated function in question a number of times using randomly distributed error in the independent variables. After a sufficient number of repetitions, the average set of solved dependent variables from each repetition will converge to the true distribution of these dependent variables.

In the inverse transient method, the error used in the pressure data is assumed to be normally (Gaussian) distributed with a set variance and the mean equal to zero, which is close to actual conditions if other error modes, such as systematic errors (e.g. the use of a biased pressure gauge), are not present. Each Monte Carlo run uses different randomly generated errors added to the uncontaminated pressure data. The parameters found after an application of the inverse transient method are saved for each run. After a sufficient number of runs have been performed, the saved parameter set can then be analysed to determine the probability distribution of the parameters.

Two quantities can be found (from the parameters) to describe the confidence in each parameter for a particular measurement site configuration. The first is the standard deviation of the parameter set found from the Monte Carlo simulations,

$$\sigma_j = \sqrt{\frac{1}{(N_{MR}-1)}\sum_{i=1}^{N_{MR}}\left(a_j^m - (a_j)_i\right)^2} \quad \text{.....(7.2.1)}$$

where σ_j = standard deviation of the error in the j^{th} parameter, N_{MR} = number of Monte Carlo simulation repetitions, $(a_j)_i$ = value of the j^{th} parameter from i^{th} Monte Carlo simulation repetition and a_j^m = mean or true value of the j^{th} parameter. The other is the average sum of the absolute differences in each parameter from the known value for that parameter,

$$AAE_j = \frac{1}{N_{MR}}\sum_{i=1}^{N_{MR}}\left|a_j^m - (a_j)_i\right| \quad \text{.....(7.2.2)}$$

in which AAE_j = average absolute error in the j^{th} parameter. These two quantities are useful, one being the square root of the variance in each parameter, and the other, the average absolute error in each parameter.

The relationship between these quantities is almost linear and therefore either can be used. The remainder of this chapter uses the average absolute error in parameters to gauge performance. The MCS error for each parameter in vector form is

$$\mathbf{MCS} = \left\{\frac{1}{N_{MR}}\sum_{i=1}^{N_{MR}}\left|a_1^m - (a_1)_i\right|, \ldots, \frac{1}{N_{MR}}\sum_{i=1}^{N_{MR}}\left|a_N^m - (a_N)_i\right|\right\} \quad \text{.....(7.2.3)}$$

where N = number of parameters.

7.3 Definition of Performance Indicators

The definition of a performance indicator in this thesis is any property that measures the accuracy of the inverse transient method. The performance indicator predicts the accuracy (or relative accuracy) of the parameters that result from inverse transient calculations for a given set of measurement data. These indicators are based on processes within the inverse transient method and the transient solver. The processes include the calculation of the gradient, Jacobian, and Hessian. Given that these relationships are used in the inverse transient method, they should indicate how much confidence is expected in a set of solved parameters given a particular measurement site configuration.

The indicators must be efficient in their calculation because a search of possible measurement site configurations will require many evaluations of indicators (especially for large pipe networks). Therefore, computationally efficient indicators are of most interest. Additionally, performance indicators are chosen so that the higher the performance indicator value, the worse the accuracy of an application of the inverse transient method (or the higher the expected error). The next sections outline possible candidates for the prediction of the performance of the inverse transient method for parameter estimation.

7.3.1 Performance Indicator SE

The **SE** performance indicator is related to the convergence of the objective function, E. It is derived from the gradient of the objective function. Recalling the objective function for minimisation (Section 4.3), the chi-square statistic is

$$E = \sum_{i=1}^{M} \left[\frac{\left(H_i^m - H_i\right)^2}{\sigma_i^2} \right] \quad \text{.....(7.3.1)}$$

where H_i = pressure head at i, H_i^m = measured pressure head at i, σ_i = standard deviation of measured pressure head at i and M = the number of measured data points. Taking the derivative of the objective function with respect to parameters (for example, lumped leak coefficients or friction factors) yields the gradient vector. An element of the gradient vector is

$$\frac{\partial E}{\partial a_j} = -2 \sum_{i=1}^{M} \left[\frac{\left(H_i^m - H_i\right)}{\sigma_i^2} \frac{\partial H_i}{\partial a_j} \right] \quad \text{.....(7.3.2)}$$

where a_j = the j^{th} parameter (such as a lumped leak coefficient or friction factor). These elements represent the sensitivity of the objective function with respect to a parameter and therefore could be used to indicate which parameters will be found with a high confidence (parameters with a high associated sensitivity). The constant terms (2 and σ_i) from Eq. 7.3.2 are dropped since it is unlikely that the variance of the error, σ^2, in the measured data will be known and σ^2 will be similar for each data point if similar data acquisition methods are used for each measurement site. The magnitudes of the elements $\partial E/\partial a_j$ are important (the sign is of little importance) so the modulus of each

element is taken. These elements (each for a certain parameter) can be formed into a vector. This performance indicator vector is denoted **SE**,

$$\mathbf{SE} = \left\{ \left| \sum_{i=1}^{M} \left(\left(H_i^m - H_i \right) \frac{\partial H_i}{\partial a_1} \right) \right|^{-1}, \ldots, \left| \sum_{i=1}^{M} \left(\left(H_i^m - H_i \right) \frac{\partial H_i}{\partial a_N} \right) \right|^{-1} \right\} \quad \text{.....(7.3.3)}$$

The **SE** indicator, much like the indicators to follow, is a vector of the length of the number of parameters, *N*. Because it is parameter based, it can show the relative convergence between parameters; therefore, it shows which parameters will be easiest found (those having the smallest absolute values of $\mathbf{SE}_j$ for the associated parameter *j*).

7.3.2 Performance Indicator SH

The performance indicator **SH** is related to the sensitivity of the pressure heads calculated by the transient model with respect to the parameters. It illustrates how sensitive each of the simulated pressures are with respect to each parameter where a high sensitivity indicates that the effect of that parameter on the transient model is large and that parameter can be found with a high confidence. The Jacobian is defined as the matrix of partial derivatives for each simulated pressure head with respect to each of the parameters,

$$\left[\frac{\partial H}{\partial a} \right] \quad \text{.....(7.3.4)}$$

This matrix is of little use, mainly because it has three-dimensions (number of parameters, number of measurement nodes and number of time steps). To reduce it to a two-dimensional matrix, it is summed for each node along each time step using the absolute value of each element. The number of time steps, N_{TS}, is equal to the total number of measurements divided by the number of measurement nodes.

$$\left[\sum_{i=1}^{N_{TS}} \left| \frac{\partial H_{i,l}}{\partial a_j} \right| \right] \quad \text{.....(7.3.5)}$$

where $i = i^{\text{th}}$ time step, $j = j^{\text{th}}$ parameter and $l = l^{\text{th}}$ measurement node. To reduce the matrix even further, nodes that are not measurement positions are discarded. The matrix elements (shown in Eq. 7.3.5) are then summed up for each measurement node. Elements are raised to the power –1 so that high performance indicator values should produce poor inverse solutions and vice-versa. The performance indicator vector **SH** is

$$\mathbf{SH} = \left\{ \left(\sum_{i=1}^{N_{MN}} \sum_{l=1}^{N_{TS}} \left| \frac{\partial H_{i,l}}{\partial a_1} \right| \right)^{-1}, \ldots, \left(\sum_{i=1}^{N_{MN}} \sum_{l=1}^{N_{TS}} \left| \frac{\partial H_{i,l}}{\partial a_N} \right| \right)^{-1} \right\} \quad \text{.....(7.3.6)}$$

where N_{MN} = number of measurement nodes.

7.3.3 Performance Indicator SV

The variance indicator **SV** is formed from the covariance matrix (previously defined in Section 4.8). **SV** relates the variance in the measured pressure head data to the variance in the solution parameters values. The covariance matrix is formed from the calculation of the Hessian and is related to the inverse Hessian minimisation method (Section 4.3). The [α] matrix, or the curvature matrix, is the starting point for the formulation of the covariance matrix. The [α] matrix is defined as the second derivative of the objective function. An approximation, defined in Section 4.3.3, is

$$\alpha_{j,k} = \sum_{i=1}^{M} \left(\frac{1}{\sigma_i^2} \frac{\partial H_i}{\partial a_j} \frac{\partial H_i}{\partial a_k} \right) \quad \text{.....(7.3.7)}$$

The variance in the measured heads is dropped since it is unlikely that the variance of the error in the measured data σ^2 will be known and, if similar data acquisition is used, σ^2 will be almost constant over the measurement points. The result is a matrix that only depends on the partial derivatives of the pressure head with respect to parameters,

$$\alpha'_{j,k} = \sum_{i=1}^{M} \left(\frac{\partial H_i}{\partial a_j} \frac{\partial H_i}{\partial a_k} \right) \quad \text{.....(7.3.8)}$$

The covariance matrix is then formed by finding the inverse of the [α] matrix. The diagonal elements of $[\alpha]^{-1}$ are equivalent to the estimated variances in each parameter, which can be inferred from the variance in the measured heads. The diagonal elements of the $[\alpha']^{-1}$ matrix form the **SV** indicator,

$$\mathbf{SV} = \left\{ \sqrt{\left([\alpha']^{-1} \right)_{1,1}}, \ldots, \sqrt{\left([\alpha']^{-1} \right)_{N,N}} \right\} \quad \text{.....(7.3.9)}$$

7.3.4 Performance Indicator SAH

The sensitivity of the parameters with respect to the measured pressure heads (**SAH**) is one of the best indicators of inverse transient performance because it uses a number of runs of the inverse problem. Unfortunately, the inverse problem is quite computationally intensive and multiple runs of the inverse problem can take a considerable amount of time to complete. Nevertheless, there are ways to reduce the number of inverse runs that need to be performed. The **SAH** indicator is defined as the partial derivative of the parameters with respect to the measured pressure heads,

$$\left[\frac{\partial \mathbf{a}}{\partial H^m}\right] \quad \text{.....(7.3.10)}$$

The derivative gives rise to three slightly different ways to achieve the **SAH** sensitivity type. The most computationally intensive way to find the **SAH** indicator is to evaluate the partial derivatives of the parameters with respect to the measurement pressure heads separately for each node and each time step. The individual sensitivities are then summed (the absolute sum) for each measurement site and for each time step. This indicator is named the $\mathbf{SAH_1}$ vector,

$$\mathbf{SAH}_1 = \left\{ \sum_{i=1}^{N_{MS}} \sum_{l=1}^{N_{TS}} \left| \frac{\partial a_1}{\partial H_{i,l}^m} \right|, \ldots, \sum_{i=1}^{N_{MS}} \sum_{l=1}^{N_{TS}} \left| \frac{\partial a_N}{\partial H_{i,l}^m} \right| \right\} \quad \text{.....(7.3.11)}$$

A less computationally intensive approach is to calculate the partial derivatives with respect to the measurement nodes only. When calculating the partial derivatives by the divided difference method, an identical small perturbation is added, one measurement node at a time, to each of the measured pressure heads over all of the time steps. The results are then summed over all of the measurement nodes forming the second indicator called the $\mathbf{SAH_2}$ vector,

$$\mathbf{SAH}_2 = \left\{ \sum_{i=1}^{N_{MS}} \left| \frac{\partial a_1}{\partial H_i^m} \right|, \ldots, \sum_{i=1}^{N_{MS}} \left| \frac{\partial a_N}{\partial H_i^m} \right| \right\} \quad \text{.....(7.3.12)}$$

The final variant of the **SAH** indicator is even less computationally intensive. The divided difference method is again used to calculate the partial derivatives. The perturbation is applied to all measurement nodes over all time steps forming the $\mathbf{SAH_3}$ vector,

$$\mathbf{SAH}_3 = \left\{ \left| \frac{\partial a_1}{\partial H^m} \right|, \ldots, \left| \frac{\partial a_N}{\partial H^m} \right| \right\} \quad \text{.....(7.3.13)}$$

Although these indicators provide accurate estimates of the performance of the inverse method (given that they use inverse transient analysis and are related to the error propagation equation, see Section 4.8), all three indicators are far too expensive to compute. The **SE**, **SH** and **SV** indicators are preferred because they only use forward transient analysis. For completeness, the variants $\mathbf{SAH_1}$, $\mathbf{SAH_2}$ and $\mathbf{SAH_3}$ will be examined.

7.3.5 Discussion of Performance Indicators

The performance indicators can be categorised in two different ways. The first divides the different performance methods into two groups depending upon what solution method is used in their calculation (Table 7.1). The two types of solution methods are forward transient solution based and inverse transient solution based as indicated in Table 7.1.

Table 7.1 Performance Indicator Categorisation Based on Analysis Method

Forward Solution Based	Inverse Solution Based
SE	$\mathbf{SAH_1}$
SH	$\mathbf{SAH_2}$
SV	$\mathbf{SAH_3}$
	MCS

Where **SE** = performance indictor based on the sensitivity of the objective function, **SH** = performance indicator based on the sensitivity of the pressure heads in the transient model, **SV** = performance indicator based on the covariance matrix, $\mathbf{SAH_1}$, $\mathbf{SAH_2}$, $\mathbf{SAH_3}$ = performance indicators based on the sensitivity of the parameters and **MCS** = performance indicator based on the Monte Carlo simulation method. The performance indicators that are forward transient solution based require much less computation because they only rely on $N+1$ calls to the forward transient solver, in contrast to the inverse solution based methods, which use many full applications of the inverse transient method. Since the inverse transient method makes many times the number of forward solution calls than the forward solution based performance indicators, the inverse solution based performance indicators more inefficient. They become less desirable when a search is performed to find an optimum set of measurement site

configurations where many evaluations of a performance indicator must be performed for different measurement site configurations.

The second categorisation, shown in Table 7.2, is to separate the performance indicators into groups depending upon their common basic component. A common basic component is the simplest unit that is used in the calculation of a performance indicator. In most cases the basic component will be a partial derivative of some kind.

Table 7.2 Performance Indicator Categorisation Based on Basic Component

Performance Indicator	Basic Component	Total Number of Function Calls
SE and **SH**	$\partial H/\partial a$	$N+1^{*}$
SV	$\partial H/\partial a$	$N+1^{**}$
$\mathbf{SAH_1}$	$\partial a/\partial H^m$	$N_{MSC}\times(M+1)^{***}$
$\mathbf{SAH_2}$	$\partial a/\partial H^m$	$N_{MSC}\times(N_{MS}+1)^{***}$
$\mathbf{SAH_3}$	$\partial a/\partial H^m$	$N_{MSC}\times 2^{***}$
MCS	Inverse Solution	$N_{MCS}\times N_{MR}^{***}$

* Forward solution calls, ** Forward solution calls plus a matrix inversion, *** Inverse solution calls

Where N = number of parameters, M = number of data points, N_{MS} = number of measurement sites, N_{MSC} = number of measurement site combinations and N_{MR} = number Monte Carlo simulation repetitions. Table 7.2 shows the basic components for each of the performance indicators and the total number of calls to either the forward or inverse solution functions used in their evaluation for all measurement site configurations (for a fixed number of measurement sites). The most useful feature in Table 7.2 is that performance indicators **SE**, **SH** and **SV**, once found for one measurement site combination, can be found for any other combination of measurement sites with no further calls to the forward transient solver. After $N+1$ calls to the forward transient solver, all partial derivatives have been calculated at all nodes and time steps. If these partial derivatives are stored, then the performance indicators **SE**, **SH** and **SV** can be formed from the stored partial derivatives for any measurement site configuration, whereas the others must be fully recalculated.

7.4 Numerical Study of Performance Parameters Using a Small Example Network

A study of each of the performance indicators is implemented in this section using a small pipe network. A number of different comparisons can be made using results from this network. These results can be viewed at three different levels. The first level is for a single measurement site configuration. Results for a single measurement site indicate how successful a performance indicator is at predicting how well each parameter is found. The second level is for a common number (greater than one) of measurement sites. Results for a common number of measurement sites can be used to gauge how well a performance indicator is at discerning between different measurement site configurations. These results can be used to answer to the question of the best locations for measurement sites. The third level is for all numbers and configurations of measurement sites. Performance indicators that succeed for different numbers of measurement sites and different configurations can be used to answer the question of how many measurement sites are adequate for good inverse transient analysis results.

7.4.1 Definition of Example Network for Numerical Study

The Small Example Network (Figure 7.1) has been utilised in other chapters in this thesis. This network is based on one first utilised by Pudar and Liggett (1992) and then by Liggett and Chen (1994). The Small Example Network is a partly gravity fed system with a constant inflow of 20 L/s at node 7. The network consists of eleven pipes and seven nodes. All of the pipes share a common diameter of 254 mm and a common length of 762 m. The transient event used to generate measurement data was initiated by partially closing the outflow valve at node 4, such that it restricts the outflow from 58 to 28 L/s in a linear fashion in 10 s then restores the flow to 58 L/s in another 10 s (as previously shown in Figure 6.8).

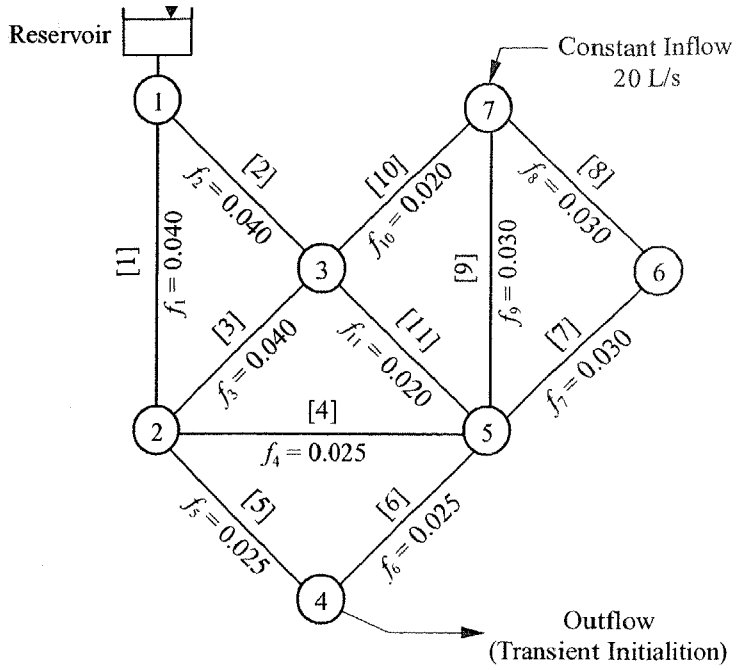

Figure 7.1 Layout of the Small Example Network

A Courant number of one is achieved in all pipes (with computational nodes coincident with pipe junctions). Since no interpolation is necessary, the numerical error is minimal. The "measured" pressure heads (obtained by separate forward runs) in nodes 2, 3, 4, 5, 6 and 7 are shown in Figure 7.2 (node 1 is the constant head reservoir). The measured pressure data are tabulated in Appendix D.4.1.

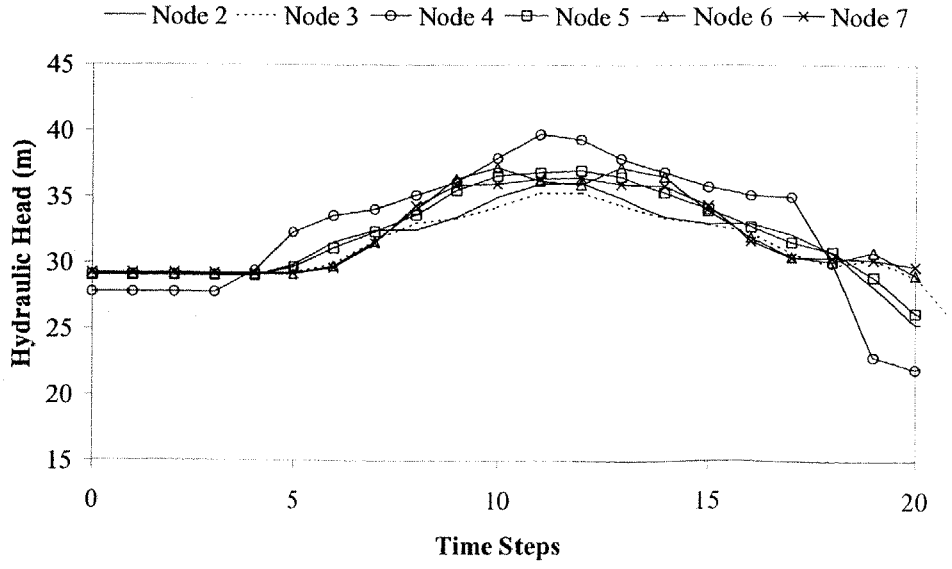

Figure 7.2 Measured Pressure Head Data from the Small Example Network

Each performance indicator relies on parameters, such as the perturbation size, for the calculation of the partial derivatives obtained by the divided difference method. The selection of suitably sized performance indicator parameters is presented in Appendix D.1.

7.4.2 Numerical Results for a Single Measurement Site Configuration

Each performance indicator is checked for usefulness in describing the confidence in each parameter for a certain measurement site configuration. In this case, the Small Example Network has been used with 20 time steps of pressure record at nodes 4 and 6 (see Figure 7.2). The measured pressure heads are determined using the forward transient solver with the friction factors shown in Figure 7.1. No random error was introduced for the calculation of the indicators **SE**, $\mathbf{SAH_1}$, $\mathbf{SAH_2}$ or $\mathbf{SAH_3}$. The Monte Carlo simulation method is used to evaluate each performance indicator. The size of the transmission of error from the measured pressure data (standard deviation = σ) to the parameters (**MCS**) is given by the normalised variable **MCS**/σ. Normalised variables are used in subsequent sections of this chapter. The objective of this section is to determine any observable trends between the indicators **SE**, **SH**, **SV**, $\mathbf{SAH_1}$, $\mathbf{SAH_2}$, $\mathbf{SAH_3}$ and the performance of parameters gained through the inverse transient method (given by MCS). Plots are presented for each performance indicator showing the performance indicator components (corresponding to each friction factor) versus results from the MCS method.

The first performance indicator is **SE** (section 7.3.1, Eq. 7.3.3), which represents the sensitivity of the objective function with respect to the parameters (the friction factors in this case). Sensitivity analysis suggests that those parameters that have the lowest associated **SE** should provide high confidence parameters. Figure 7.3 shows values of the performance indicator **SE** (for each friction factor represented by a diamond) against the expected error returned from the Monte Carlo simulation. A trend line has been inserted (dashed line, polynomial of order two) to clearly show the behaviour of the **SE** indicator.

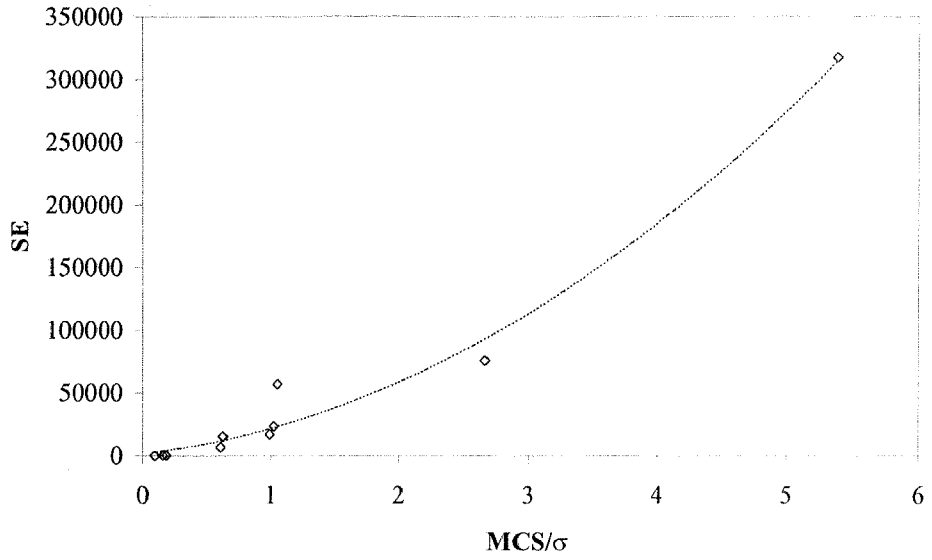

Figure 7.3 SE Versus MCS/σ (Single Measurement Site Configuration)

The relationship between **SE** and the expected parameter error from MCS is apparent and seems to be one of a squared relationship. Chen (1995) made the same observation where a trend was noticed between the sensitivity of the objective function with respect to the parameters, and the speed at which a parameter was converging (the higher the sensitivity, the better that parameter would be found). Chen (1995) also observed a similar relationship for the partial derivative of pressure with respect to the parameters (lumped leak coefficients and friction factors). In this case, the performance indicator **SH** is equivalent to that observation by Chen (1995). **SH** represents the sensitivity of the modelled pressure heads with respect to the parameters (see Section 7.3.2, Eq. 7.3.6). A plot of **SH** versus MCS results is displayed in Figure 7.4 where the diamonds correspond to values of the indicator **SH** for each friction factor. The dashed line is a trend line found through linear regression.

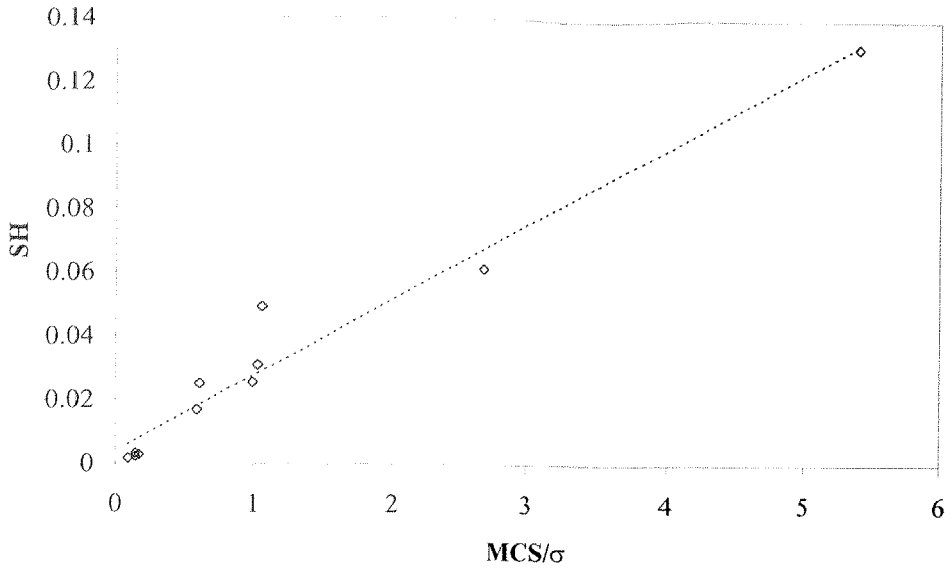

Figure 7.4 SH Versus MCS/σ (Single Measurement Site Configuration)

Rather than a squared trend exhibited by the **SE** indicator, Figure 7.4 exhibits a linear trend for the **SH** indicator. Chen (1995) commented that the larger the sensitivity (similar to $\mathbf{SH}^{-1}$), the better the confidence in that parameter.

The **SV** indicator is based on a method that estimates the error in each parameter from the error in the measured pressure data (Section 4.8). **SV** was previously defined in Section 7.3.3 (see Eq. 7.3.9) and can be considered as a general amplification factor relating the measured pressure-head data error to the estimation of the error in each parameter (in this case the friction factors). Figure 7.5 shows the relationship between **SV** and the normalised average absolute error in parameters calculated from the MCS method (**MCS/σ**). Each diamond in Figure 7.5 represents a friction factor and the dashed line is a trend line produced using linear regression.

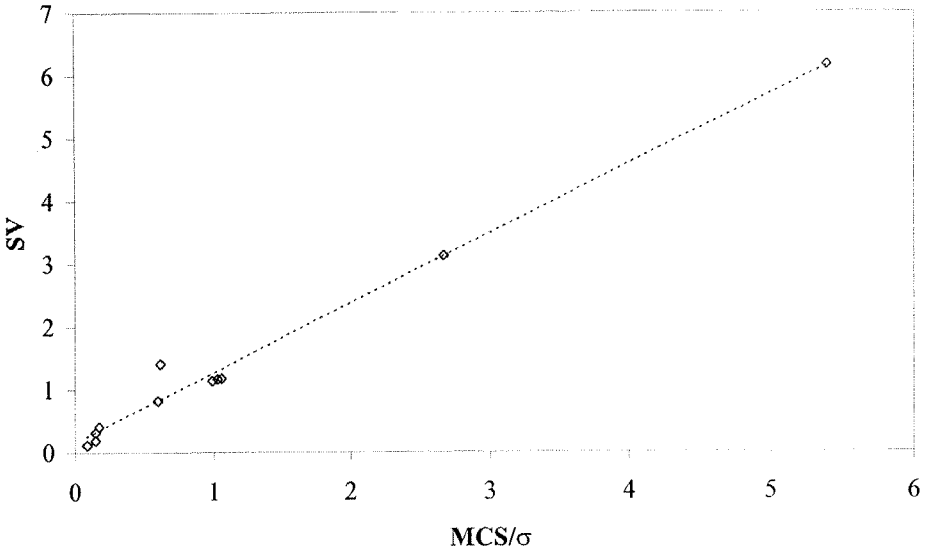

Figure 7.5 SV Versus MCS/σ (Single Measurement Site Configuration)

Figure 7.5 shows a linear trend between **SV** for each friction factor and the normalised MCS results (**MCS/σ**). There is minimal scatter from the regression line, which is to be expected because the **SV** indictor is based on a method for the estimation of parameter error (see Section 4.8). For low levels of error in the pressure data, the relationship between the estimated variance in the parameters and the variance in the data is linear. However, this relationship may not be true for large errors in the measured pressure head data. The **SE**, **SH** and **SV** performance indicators all show a similar trend when compared to the MCS results, which is not surprising since they are all based on the partial derivative $\partial H/\partial a$ in one way or another.

Figures 7.6, 7.7 and 7.8 show the behaviour of performance indicators $\mathbf{SAH_1}$, $\mathbf{SAH_2}$ and $\mathbf{SAH_3}$, respectively, against the normalised average absolute error in parameters from the MCS method (**MCS/σ**). These indicator are defined in Section 7.3.4 (see Eqs. 7.3.11, 7.3.12 and 7.3.13 for $\mathbf{SAH_1}$, $\mathbf{SAH_2}$ and $\mathbf{SAH_3}$ respectively). $\mathbf{SAH_1}$, $\mathbf{SAH_2}$ and $\mathbf{SAH_3}$ should produce a linear relationship with **MCS/σ** (especially $\mathbf{SAH_1}$) since they are related to the error propagation equation (all of which are formed from $\partial a/\partial H^m$, see Section 4.8). The diamonds in the figures correspond to individual friction factors and dashed lines are lines of trend (created by regression) that are plotted where applicable. The first indicator $\mathbf{SAH_1}$, the most computationally intensive, generates the best results.

The lack of scatter in the results is mainly due to the large amount of inverse solution calculations used by this indicator, which leads to long computation times.

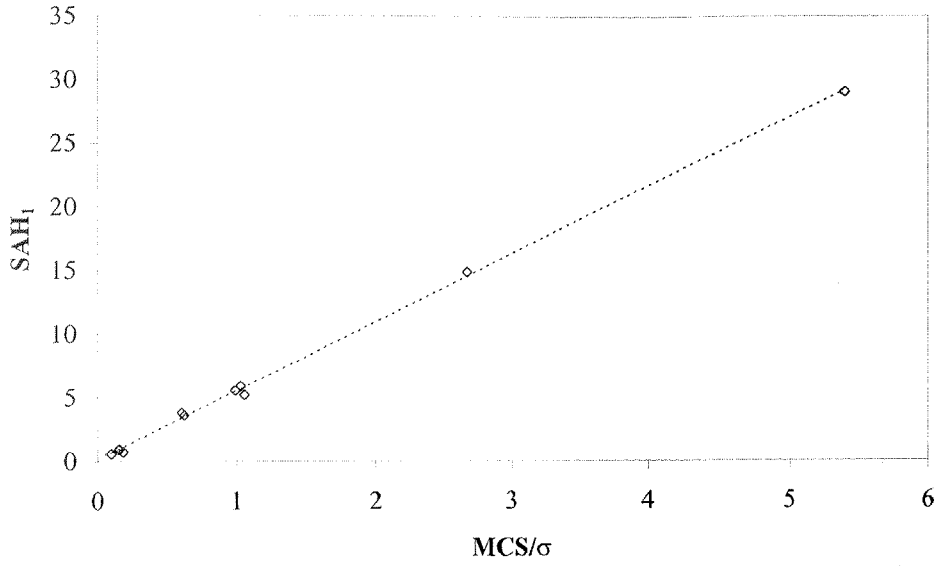

Figure 7.6 SAH_1 Versus MCS/σ (Single Measurement Site Configuration)

The performance indicator $\mathbf{SAH_2}$ produces a similar linear relationship to **MCS/σ** as shown previously by $\mathbf{SAH_1}$ but with more scatter in the results. The calculation of $\mathbf{SAH_1}$ requires the determination of $\partial a/\partial H^m$ for every measured data point whereas the calculation of $\mathbf{SAH_2}$ requires the determination of $\partial a/\partial H^m$ for each measurement site. Because there are fewer sites than measured data points, the calculation of $\mathbf{SAH_2}$ is much faster, but the resulting decrease in resolution has an adverse affect on results (extra scatter from the regression line).

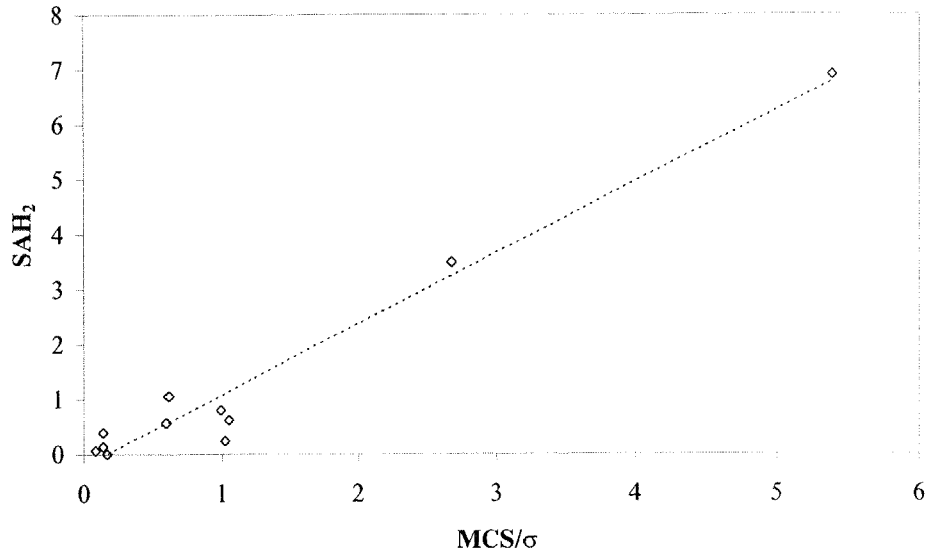

Figure 7.7 SAH_2 Versus MCS/σ (Single Measurement Site Configuration)

The final indicator considered is SAH_3. Similar to SAH_1 and SAH_2, SAH_3 is based on the partial derivative of the parameters with respect to the measured pressure-head data ($\partial a/\partial H^m$). The difference is that the perturbation (used in the calculation of the partial derivatives by the divided difference method) in the measured pressure head is applied over all measurement data at one time (rather than each measured data point like SAH_1 or for each measurement site like SAH_2). The result of the comparison between SAH_3 and the normalised average absolute error in friction factors from the MCS (**MCS/σ**) is shown in Figure 7.8. The plot shows no general trends.

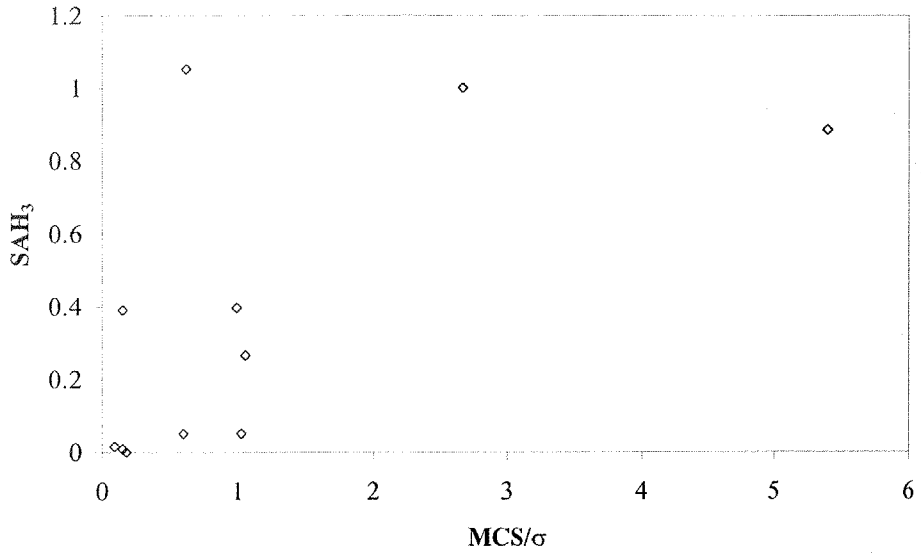

Figure 7.8 SAH_3 Versus MCS/σ (Single Measurement Site Configuration)

The results for all performance indicators are presented in Table 7.3. The relative performance of each indicator is ranked according to the trend between the indicator and the normalised MCS results for a single measurement site configuration. A rank of 1 corresponds to the indicator that exhibits the strongest trend and 6 the weakest (or lack of trend). The r^2 regression parameter indicates the goodness of fit assuming a linear trend, a value of 1 indicates a good fit while a value of 0 indicates no fit. The indicators that exhibited the strongest trend were **SAH_1** and **SV** while a complete lack of trend was shown by **SAH_3**. The best indicator (of the forward transient analysis based indicators) is **SV**. If the indicators give equivalent inverse transient performance information, the forward transient analysis based indicators (**SE, SH** and **SV**) are preferred over inverse transient analysis based indicators (**SAH_1, SAH_2, SAH_3** and **MCS**) because they are less computationally intensive.

Table 7.3 Performance of Indicators (Single Measurement Site Configuration)

Rank	Performance Indicator	r^2 from Regression
1	**SAH_1**	0.999
2	**SV**	0.987
3	**SAH_2**	0.963
4	**SH**	0.960
5	**SE**	0.935
6	**SAH_3**	0.383

7.4.3 Numerical Results for a Common Number of Measurement Sites

A primary application for performance indicators is to predict which configuration of measurement sites will yield high confidence solutions of the parameters (lumped leak coefficients and friction factors). Optimal location of measurement sites minimise the expected error in parameters. The number of measurement sites is kept constant during an optimisation run. It is then a matter of checking each performance indicator for desirable trends that might be useful for optimisation. A desirable trend corresponds to an observable relationship between two variables, for example a linear relationship. All combinations of measurement site configurations are enumerated using the MCS method and using each performance indicator. There are six possible numbers of measurement sites for the Small Example Network (given that no pressure head measurement was allowed at the reservoir at node 1). For each such number of sites there are several combinations of measurement site configurations. All of the different measurement site configurations are shown in Table 7.4 for each number of measurement sites.

Table 7.4 Measurement Site Combinations for the Small Example Network

Number of Measurement Sites	Number of Measurement Site Combinations*	Different Combinations of Measurement Site Configurations*
1	6	{2}, {3}, {4}, {5}, {6}, {7}
2	15	{2,3}, {2,4}, {2,5}, {2,6}, {2,7}, {3,4}, {3,5}, {3,6}, {3,7}, {4,5}, {4,6}, {4,7}, {5,6}, {5,7}, {6,7}
3	20	{2,3,4}, {2,3,5}, {2,3,6}, {2,3,7}, {2,4,5}, {2,4,6}, {2,4,7}, {2,5,6}, {2,5,7}, {2,6,7}, {3,4,5}, {3,4,6}, {3,4,7}, {3,5,6}, {3,5,7}, {3,6,7}, {4,5,6}, {4,5,7}, {4,6,7}, {5,6,7}
4	15	{2,3,4,5}, {2,3,4,6}, {2,3,4,7}, {2,3,5,6}, {2,3,5,7}, {2,3,6,7}, {2,4,5,6}, {2,4,5,7}, {2,4,6,7}, {2,5,6,7}, {3,4,5,6}, {3,4,5,7}, {3,4,6,7}, {3,5,6,7}, {4,5,6,7}
5	6	{2,3,4,5,6}, {2,4,5,6,7}, {2,3,5,6,7}, {2,3,4,6,7}, {2,3,4,5,7}, {3,4,5,6,7}
6	1	{2,3,4,5,6,7}

* Pressure head measurement was not allowed at the reservoir (node 1)

The first performance indicator investigated is **SE**, shown Figure 7.9. The **SE** indicator is based on the sensitivity of the objective function with respect to the friction factors (see Section 7.3.1 and Eq. 7.3.3). The figure shows 5 plots, each corresponding to measurement site numbers of 1, 2, 3, 4, 5 and 6. The diamonds on each of the plots

represent a particular measurement site configuration given that number of measurement sites. Average values of each performance indicator and the normalised results from the MCS method are used in each plot. An example of the average of the performance indicator **SE** and the average normalised results from MCS are

$$\text{Average}\,\mathbf{SE} = \frac{1}{N}\sum_{j=1}^{N}\mathbf{SE}_j \qquad \text{.....(7.4.1)}$$

$$\text{Average}\,\mathbf{MCS}/\sigma = \frac{1}{N}\sum_{j=1}^{N}\left(\frac{\mathbf{MCS}}{\sigma}\right)_j \qquad \text{.....(7.4.2)}$$

The averaging is necessary to achieve a single value (for a performance indicator) that describes a particular measurement site configuration.

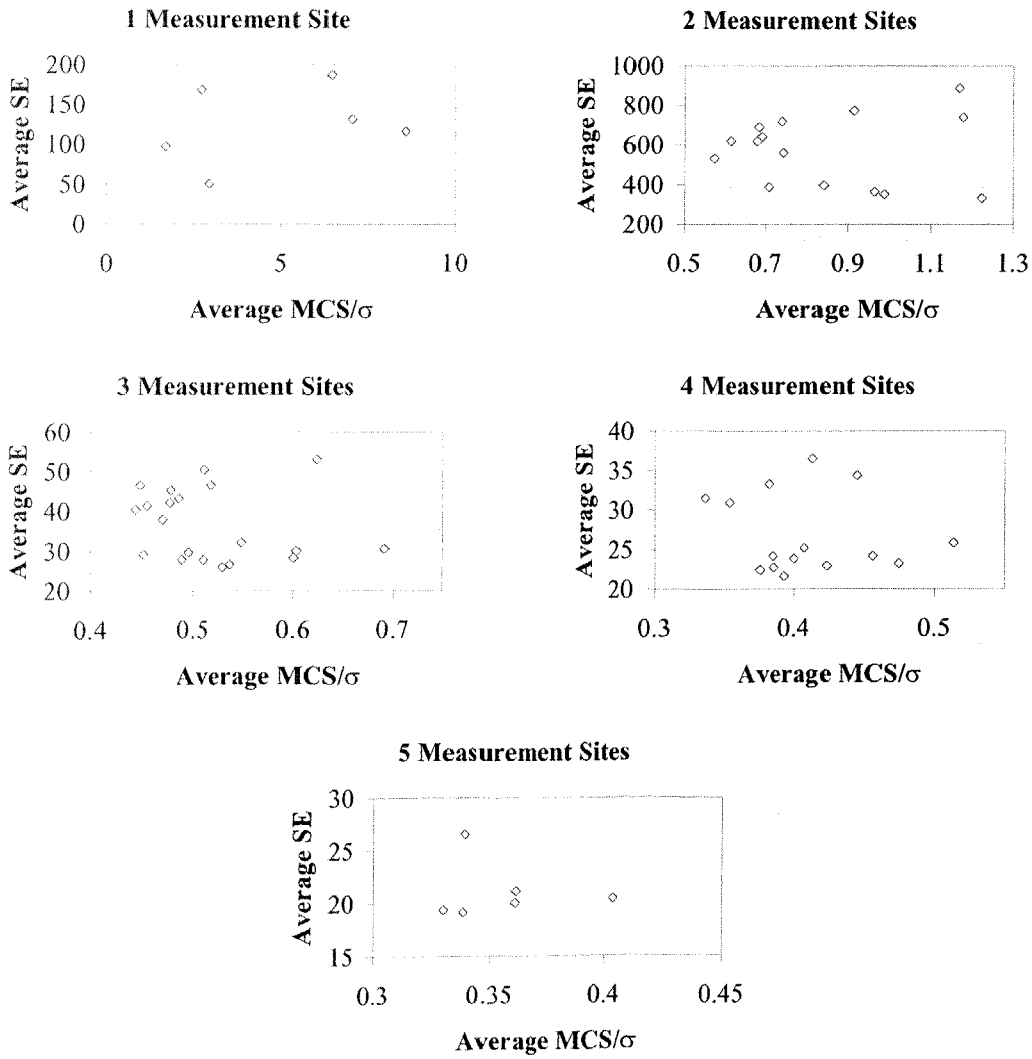

Figure 7.9 Average SE Versus Average MCS/σ (Common Number of Measurement Sites)

No trends are observable in Figure 7.9 for the indicator **SE** (against the average normalised MCS results) for any number of measurement sites. This result is different from the testing for a single measurement site configuration (see Section 7.4.2, Figure 7.3) where a trend was observed. It suggests that the **SE** indicator is not useful for the comparison of different measurement site configurations with common numbers of measurement sites.

The **SH** indicator is based on the sensitivity of the model pressure heads with respect to the friction factors (see Section 7.3.2 and Eq. 7.3.6). The average **SH** value (calculated in a similar fashion to average **SE**, see Eq. 7.4.3) is compared to the average MCS results for the different measurement site configurations for each number of measurement sites, separately.

$$\text{Average}\,\mathbf{SH} = \frac{1}{N}\sum_{j=1}^{N}\mathbf{SH}_j \qquad \text{.....(7.4.3)}$$

Plots for each number of measurement sites are shown in Figure 7.10 where the diamonds indicate different measurement site combinations.

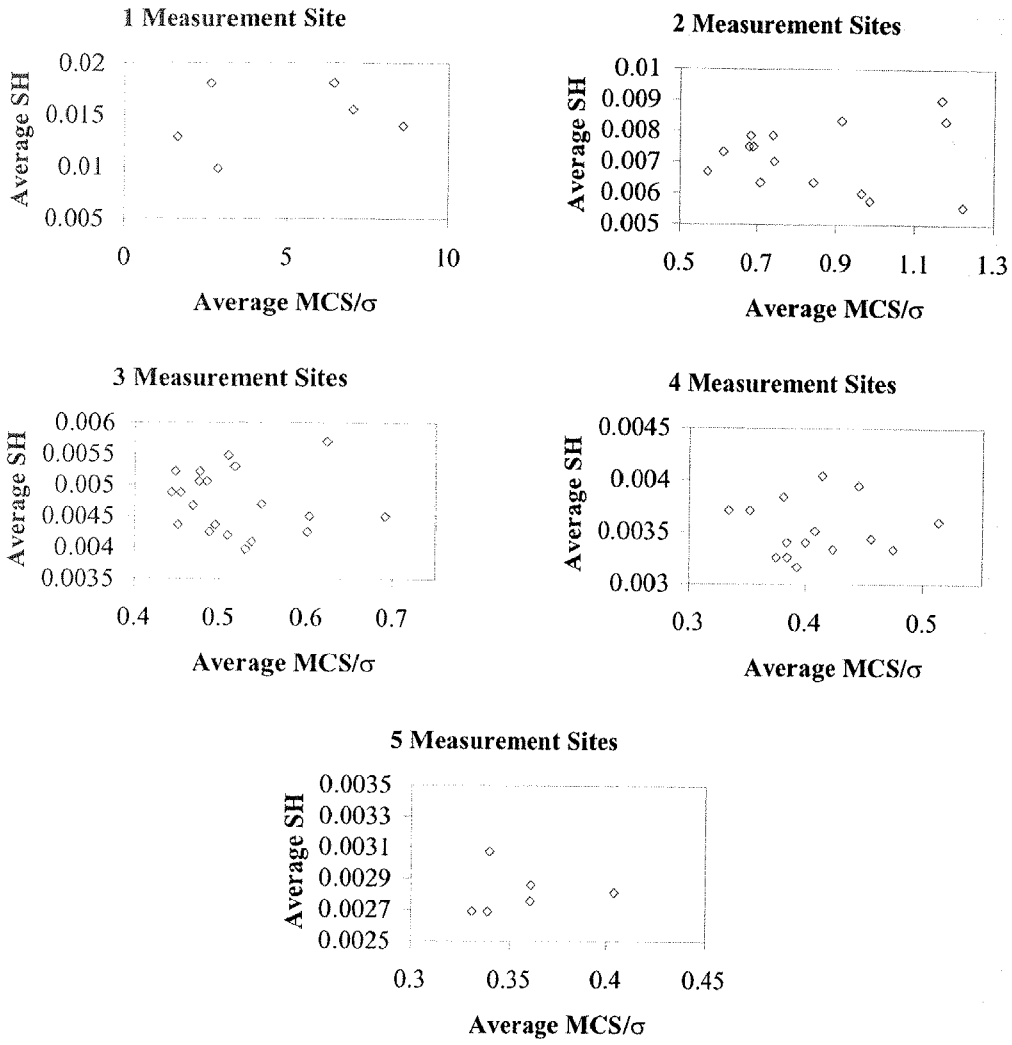

Figure 7.10 Average SH Versus Average MCS/σ (Common Number of Measurement Sites)

There is no observable trend between the average **SH** and the average normalised MCS results (**MCS/σ**) for the different measurement site configurations, which is in contrast to the results observed for a single measurement site configuration (see Section 7.4.2, Figure 7.4) where a trend was present. The results for average **SE** and average **SH** are similar (e.g. a noticeable trend for a single measurement site but no noticeable trend for different measurement site configurations) due to their similar definitions (see Eqs. 7.3.3 and 7.3.6, respectively).

The behaviour of the average **SV** indicator compared to the average normalised MCS results (**MCS/σ**) is shown in Figure 7.11. The **SV** indicator is based on the transmission of the error in the measured pressure heads to the solution parameters (see Section 7.3.3,

Eq. 7.3.9). The average **SV** indicator for a particular measurement site configuration is formed in a similar fashion to the average **SE** indicator (see Eq. 7.4.4) by taking an average of each component SV_j over all parameters.

$$\text{Average } \mathbf{SV} = \frac{1}{N}\sum_{j=1}^{N} SV_j \quad \text{.....(7.4.4)}$$

The diamonds in each plot correspond to measurement site configurations and the dashed lines are trend lines created using linear regression.

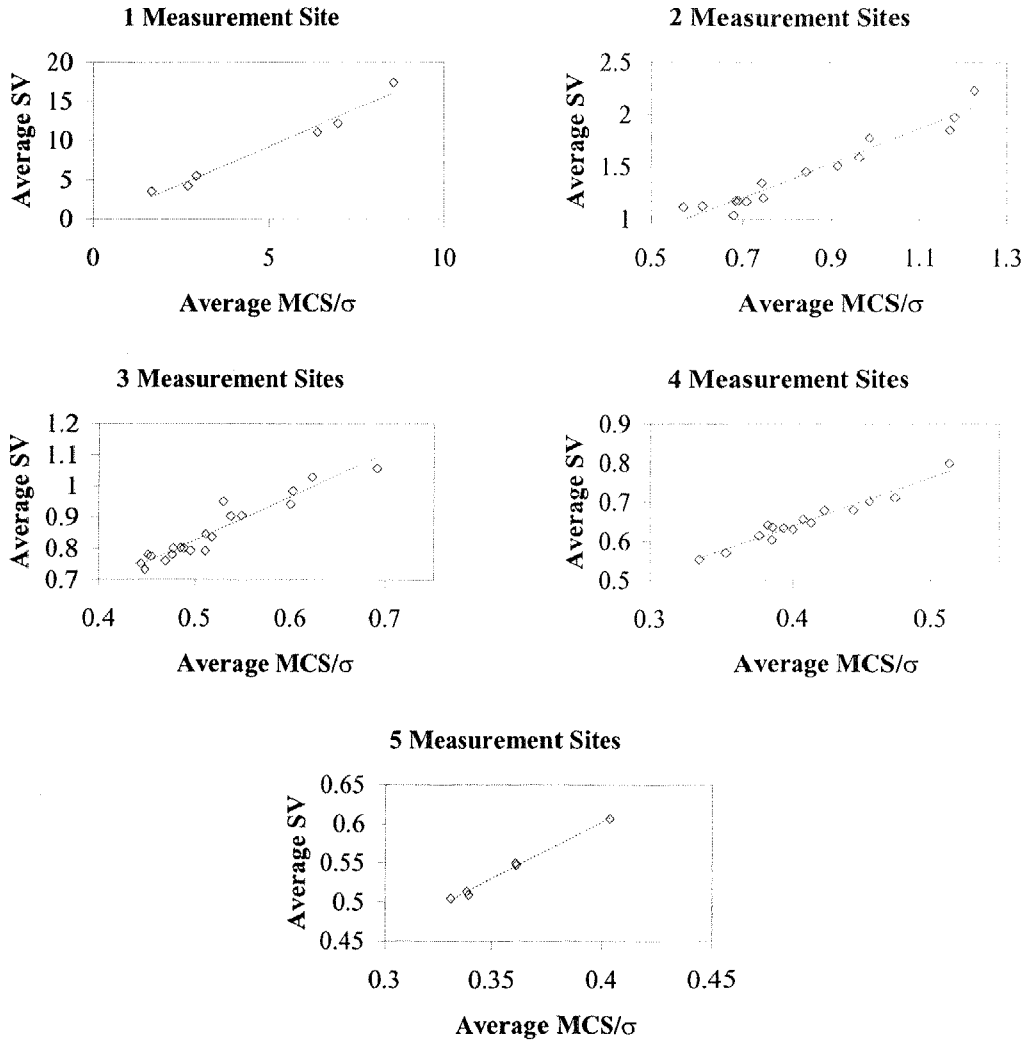

Figure 7.11 Average SV Versus Average MCS/σ (Common Number of Measurement Sites)

Similar to results for the SV indicator for a single measurement site configuration (see Section 7.4.2, Figure 7.5), a linear trend is observed for all measurement site numbers considered. These trends suggest that, as well as being a good indicator of the

performance of the inverse transient method for a single measurement site configuration, the **SV** indicator is a good indicator of inverse transient performance for different measurement site configurations with a common number of measurement sites.

The indicators that are based on the partial derivative of the parameters with respect to the measured pressure head ($\partial a/\partial H^m$), $\mathbf{SAH_1}$, $\mathbf{SAH_2}$, and $\mathbf{SAH_3}$, are now considered. These indicators are defined in Section 7.3.4 (see Eqs. 7.3.11, 7.3.12 and 7.3.13 for indicators $\mathbf{SAH_1}$, $\mathbf{SAH_2}$ and $\mathbf{SAH_3}$ respectively). An average value of each indicator is assigned for each measurement site configuration. The definition of the average of indicators $\mathbf{SAH_1}$, $\mathbf{SAH_2}$ and $\mathbf{SAH_3}$ are

$$\text{Average}\,\mathbf{SAH_1} = \frac{1}{N}\sum_{j=1}^{N}(\mathbf{SAH_1})_j \quad \text{.....(7.4.5)}$$

$$\text{Average}\,\mathbf{SAH_2} = \frac{1}{N}\sum_{j=1}^{N}(\mathbf{SAH_2})_j \quad \text{.....(7.4.6)}$$

$$\text{Average}\,\mathbf{SAH_3} = \frac{1}{N}\sum_{j=1}^{N}(\mathbf{SAH_3})_j \quad \text{.....(7.4.7)}$$

Figure 7.12 shows the comparison of the average $\mathbf{SAH_1}$ with the average normalised MCS results. The diamonds correspond to individual measurement site configurations and the dashed lines are trend lines formed through linear regression. These results show a favourable trend for all numbers of measurement sites considered (similar to the results for a single measurement site configuration in Section 7.4.2, Figure 7.6). The $\mathbf{SAH_1}$ indicator could be used to select measurement site configurations (from a set of configurations with a common number of measurement sites) that have a low transmission of error from the measured pressure head data to the parameters.

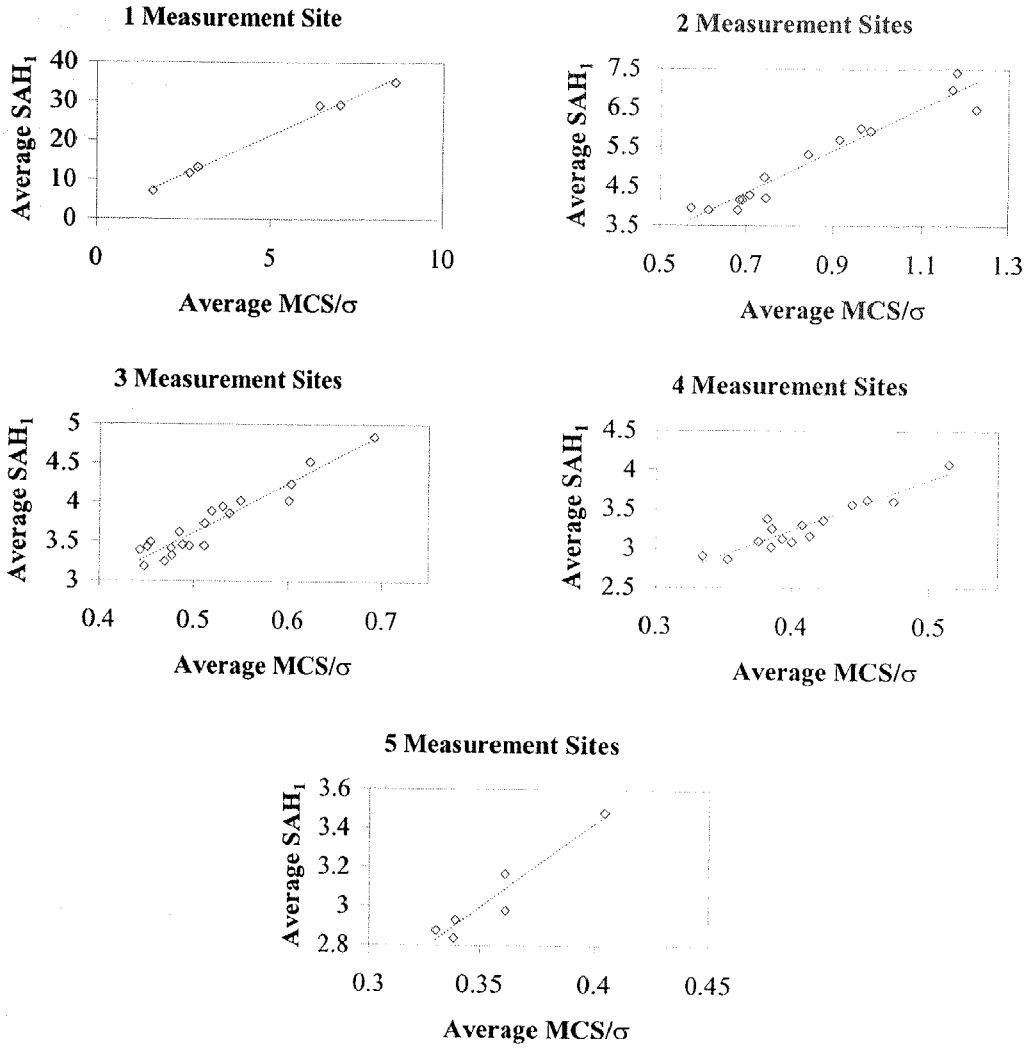

Figure 7.12 Average SAH_1 Versus Average MCS/σ (Common Number of Measurement Sites)

Results for the SAH_2 indicator are shown in Figure 7.13. These results show a greater scatter than those for the previous indicator, SAH_1 (see Figure 7.12). The increased scatter about linear trend line in each plot (corresponding to a different number of measurement sites) degrades the usefulness of this indicator for the prediction of the performance of the inverse transient method.

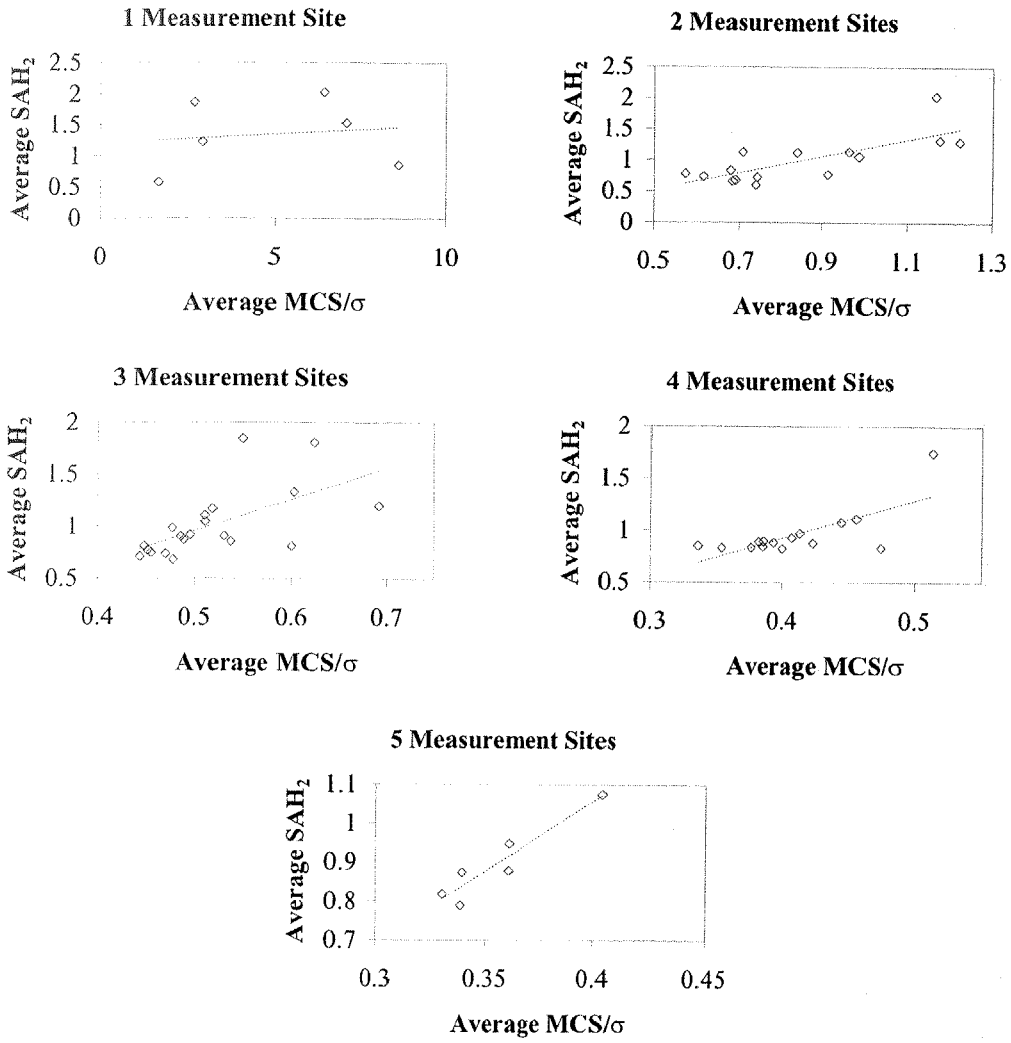

Figure 7.13 Average SAH_2 Versus Average MCS/σ (Common Number of Measurement Sites)

Results for the **SAH_3** indicator are shown in Figure 7.14. These results show an even greater scatter than those for the previous indicators, **SAH_1** and **SAH_2** (see Figures 7.12 and 7.13)

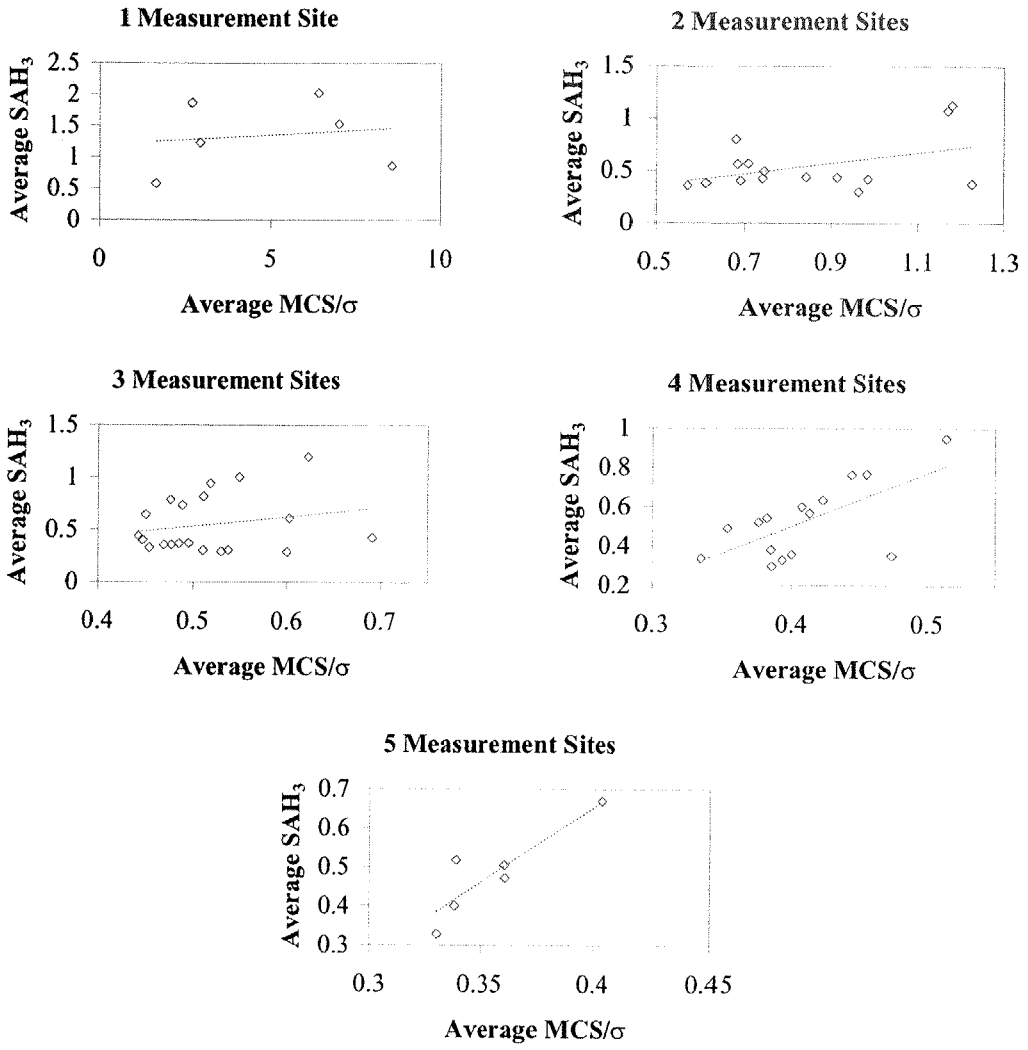

Figure 7.14 Average SAH_3 Versus Average MCS/σ (Common Number of Measurement Sites)

The results for all performance indicators are presented in Table 7.5. The relative performance of each indicator is ranked according to the trend between the indicator and the normalised average MCS results for a common number of measurement sites. A rank of 1 corresponds to the indicator that exhibits the strongest trend and 6 the weakest (or lack of) trend. The r^2 regression parameter (averaged over all numbers of measurement sites) indicates the goodness-of-fit assuming a linear trend; a value of 1 indicates a good fit while a value of 0 indicates no fit. The indicators that exhibited the strongest trend were **SV** and $\mathbf{SAH_1}$ while a complete lack of trend was shown by **SE** and **SH**. The best of the forward transient analysis based indicators is **SV**.

Table 7.5 Performance of Indicators (Common Number of Measurement Sites)

Rank	Performance Indicator	Average r^2 from Regression
1	**SV**	0.953
2	**SAH_1**	0.924
3	**SAH_2**	0.483
4	**SAH_3**	0.294
5	**SE**	0.037
6	**SH**	0.018

7.4.4 Numerical Results for All Measurement Site Configurations

The previous sections (7.4.2 and 7.4.3) presented results for the comparison of performance indicators to the Monte Carlo simulation (MCS) results for a single measurement site configuration and measurement site configurations with a common number of measurement sites. The single measurement site configuration tests are useful for identifying which parameters will be prone (or not prone) to the influence of measurement data error. The common number of measurement site tests are useful for the identification of measurement site configurations that are prone (or not prone), on average, to the influence of the transmission of measured data error to the parameters. A similar comparison (of the performance indicators against the average normalised results from the MCS) can be performed for all measurement site configurations over all numbers of measurement sites. These results are useful to identify what number of measurement sites is adequate for a successful application of the inverse transient method. The purpose of this section is to investigate how each indicator performs in the prediction of the inverse transient analysis performance (given by the MCS method) for all measurement site configurations over all numbers of measurement sites.

The **SE** indicator is first tested. It represents the sensitivity of the objective function with respect to the parameters (which are the friction factors in this case). The **SE** indicator is defined in Section 7.3.1 (see Eq. 7.3.3). The average of **SE** (see Eq. 7.4.1) over the parameters is used to assign a single value to a certain measurement site configuration. The average **SE** is tested against the average normalised MCS results (average **MCS**/σ) for the existence of any desirable trends. A plot of average **SE** versus average **MCS**/σ for all of the possible measurement site configurations is presented in Figure 7.15. The diamonds in the plot represent single measurement site configurations.

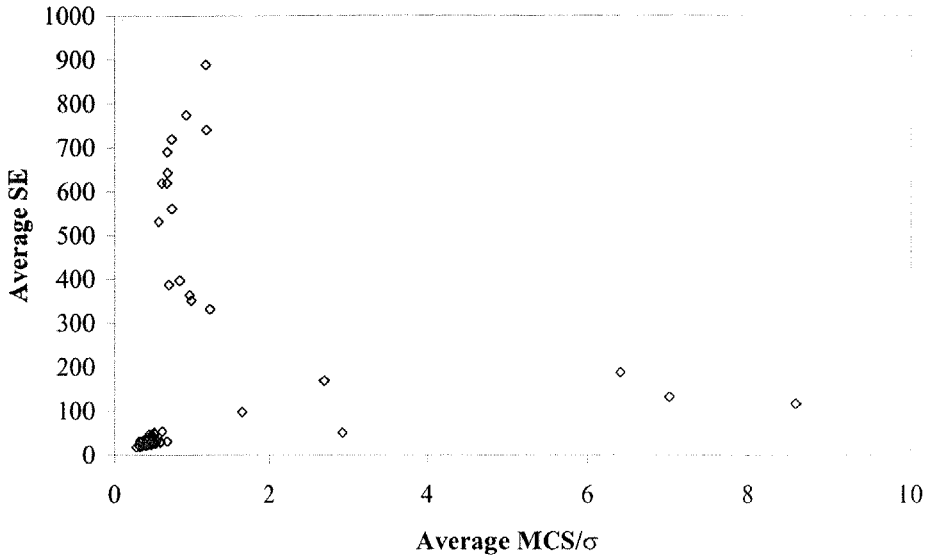

Figure 7.15 Average SE Versus Average MCS/σ (All Measurement Site Configurations)

There is no observable trend between the average **SE** indicator and the MCS results, suggesting that **SE** is not an effective indicator for determining the optimum number of measurement sites. This lack of trend is consistent with the results for a common number of measurement sites for the indicator **SE** (Section 7.4.3, Figure 7.9).

Figure 7.16 shows the comparison of the average **SH** indicator against the average normalised MCS results (**MCS/σ**). The **SH** indictor is based on the sensitivity of the model pressure heads with respect to the friction factors (see Section 7.3.2 and Eq. 7.3.6). An average value for **SH** was used (Eq. 7.4.3) to produce a single **SH** value for a particular measurement site configuration. A diamond in Figure 7.16 represents an individual measurement configuration. The trend line, formed through logarithmic regression, is shown in the figure.

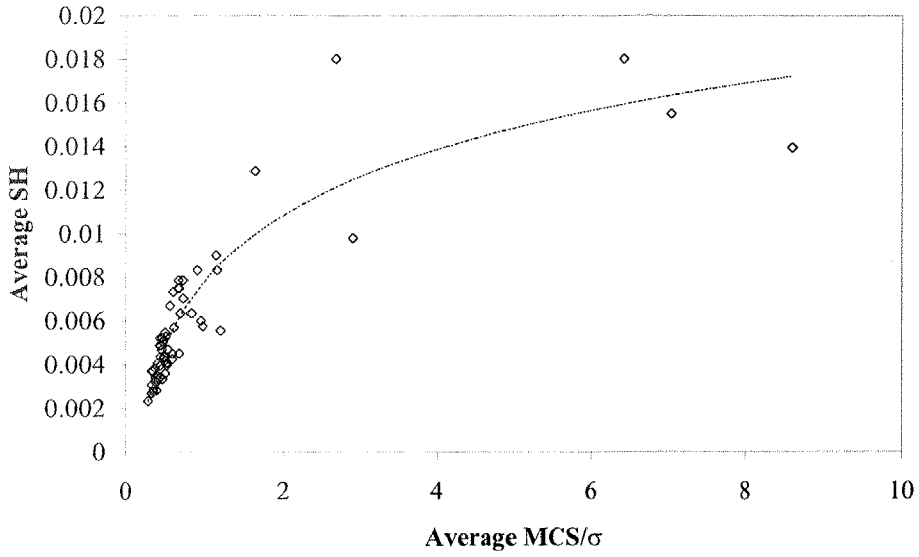

Figure 7.16 Average SH Versus Average MCS/σ (All Measurement Site Configurations)

The scatter in these results suggests that measurement site configurations with large average errors in parameters produce the most scatter. Many points form a cluster that is associated with configurations of low average error in parameters, which is an indication of the **SH** indicator's inability to differentiate between different measurement site configurations.

The **SV** performance indicator is the best of the forward-analysis-based indicators for the past two sections (see Section 7.4.2, Figure 7.5 and Section 7.4.3, Figure 7.11). The average **SV** indicator for a particular measurement site configuration is found by taking an average of each component $\mathbf{SV}_j$ over all parameters (see Eq. 7.4.4). Figure 7.17 shows the behaviour of the average **SV** indicator against the average normalised MCS results for all measurement site configurations. The diamonds correspond to individual measurement site configurations and the dashed line is a trend line formed through linear regression.

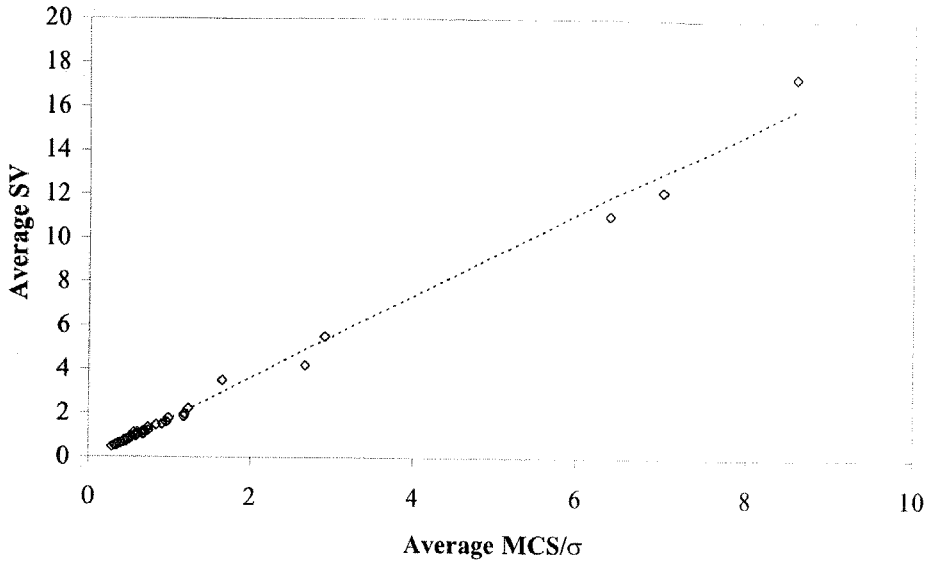

Figure 7.17 Average SV Versus Average MCS/σ (All Measurement Site Configurations)

The performance indicator **SV** shows little scatter from the linear trend line. This indicator, being based upon the estimated transmission of measurement data error to the error in parameters, works well in the present case but remains untested in systems that have a larger error in the data. The observed trend suggests that the **SV** indicator could be used to find the optimal number of measurement sites.

The indicators based on inverse transient analysis ($\mathbf{SAH_1}$, $\mathbf{SAH_2}$ and $\mathbf{SAH_3}$) are now considered for all measurement site configurations. $\mathbf{SAH_1}$, $\mathbf{SAH_2}$ and $\mathbf{SAH_3}$ use the partial derivative of each parameter with respect to the measured data ($\partial a/\partial H^m$) as their basic component. These indicators were previously defined in Section 7.3.4 (see Eqs. 7.3.11, 7.3.12 and 7.3.13 for $\mathbf{SAH_1}$, $\mathbf{SAH_2}$ and $\mathbf{SAH_3}$ respectively). An average value of each indicator is assigned to each measurement site configuration. The definitions of the average of the indicators $\mathbf{SAH_1}$, $\mathbf{SAH_2}$ and $\mathbf{SAH_3}$ are shown in Eqs. 7.4.5, 7.4.6 and 7.4.7 respectively. Figure 7.18 shows a plot of the average $\mathbf{SAH_1}$ indicator versus the average normalised MCS results (**MCS/σ**). The diamonds correspond to an individual measurement site configuration and the dashed line is a trend line formed through a linear regression. The average $\mathbf{SAH_1}$ indicator produces little scatter. This linear behaviour is to be expected because the $\mathbf{SAH_1}$ indicator closely resembles the error propagation equation (see Section 4.8), which linearly relates the partial derivatives

$\partial a/\partial H^m$ to the error in the parameters. Therefore, the $\mathbf{SAH_1}$ indicator would be useful for finding the optimal number of measurement sites.

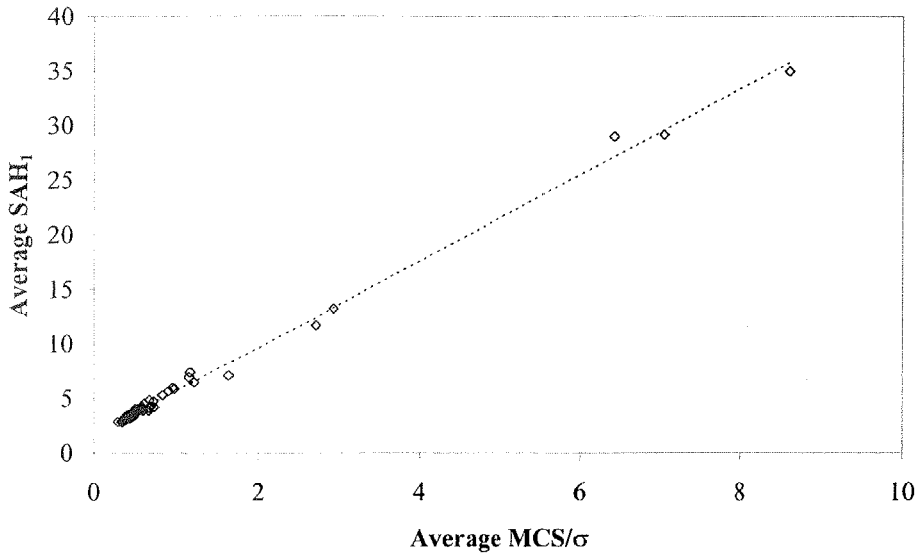

Figure 7.18 Average $\mathbf{SAH_1}$ Versus Average MCS/σ (All Measurement Site Configurations)

There is a different result when the indicator $\mathbf{SAH_2}$ is considered. Figure 7.19 shows no noticeable trends against the normalised average error in parameters for all measurement sites, in contrast to tests performed with measurement site configurations with common numbers of sites (Figure 7.13) and on a single measurement site configuration (Figure 7.7). $\mathbf{SAH_2}$ has a limit to its usefulness when comparing different numbers of measurement sites.

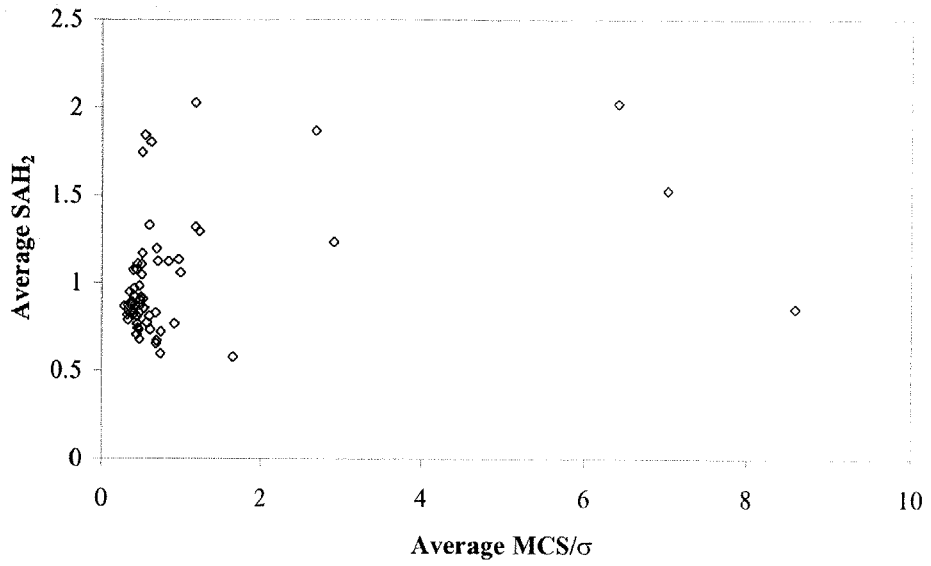

Figure 7.19 Average SAH_2 Versus Average MCS/σ (All Measurement Site Configurations)

The final indicator considered is SAH_3. A plot of the average SAH_3 indicator versus the average normalised MCS results is shown in Figure 7.20. There is a lack of trend in the SAH_3 results, suggesting that SAH_3 would not be useful for finding the optimal number of measurement sites. In all of the previous analyses performed using the SAH_3 indicator (see Figure 7.8 for a single measurement site configuration and Figure 7.14 for a common number of measurement sites), SAH_3 has not shown any trends at all.

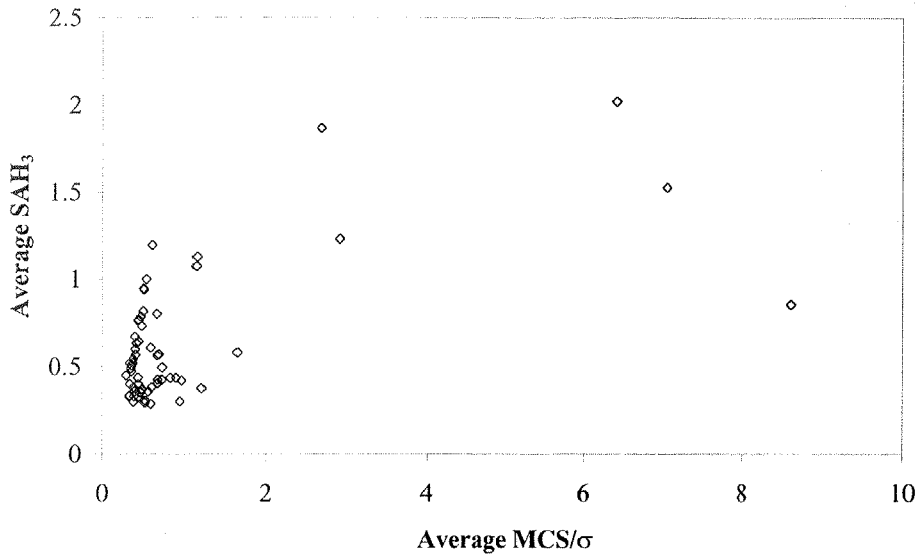

Figure 7.20 Average SAH_3 Versus Average MCS/σ (All Measurement Site Configurations)

The results for all performance indicators are presented in Table 7.6. The relative performance of each indicator is ranked according to the trend between the indicator and the normalised average MCS results for all numbers of measurement sites. A rank of 1 corresponds to the indicator that exhibits the strongest trend and 6 the weakest (or lack of trend). The r^2 regression parameter indicates the goodness of fit assuming a linear trend where a value of 1 indicates a good fit while a value of 0 indicates no fit. The indicators that exhibited the strongest trend are **SAH_1** and **SV** while a complete lack of trend is shown by **SAH_2**, **SAH_3** and **SE**. Again, the best forward transient analysis based indicator is **SV**.

Table 7.6 Performance of Indicators (All Measurement Site Configurations)

Rank	Performance Indicator	r^2 from Regression
1	**SAH_1**	0.996
2	**SV**	0.991
3	**SH**	0.637
4	**SAH_3**	0.371
5	**SAH_2**	0.122
6	**SE**	0.004

7.4.5 Discussion of Numerical Results

The combined performance of each of the indicators for a single measurement site, configurations with common numbers of measurement sites and over all measurement sites is shown in Table 7.7. A rank of 1 is associated with the indicator that performed best and a rank of 6 for the worst.

Table 7.7 Overall Performance of Indicators

Rank	Single Measurement Site Configuration	Common Number of Measurement Sites	All Measurement Site Configurations
1	**SAH_1**	**SV**	**SAH_1**
2	**SV**	**SAH_1**	**SV**
3	**SAH_2**	**SAH_2**	**SH**
4	**SH**	**SAH_3**	**SAH_3**
5	**SE**	**SE**	**SAH_2**
6	**SAH_3**	**SH**	**SE**

These results show that the **SAH_1** and **SV** indicators are the best at predicting the success of the inverse transient method (based on the Monte Carlo simulation method and error transmission from the measured data to the parameters) for a single measurement site configuration, a common number of measurement sites and for all measurement site configurations. These indicators can now be used to search for optimal measurement site configurations and the optimal number of measurement sites. Of these two indicators, the **SV** indicator is preferred because it only requires forward transient analyses rather than inverse transient analyses. For a searching routine, the speed of calculation of an indicator is important.

7.5 Optimal Measurement Site Configurations for a Small Example Network

Using the Monte Carlo simulation (MCS) data, optimal measurement site configurations for the Small Example Network are found for the determination of friction factors in each of the pipes by the inverse transient method. The same principles could be applied for lumped leak coefficients as well. The layout of the Small Example Network is repeated in Figure 7.21; a full description is found in Section 7.4.1.

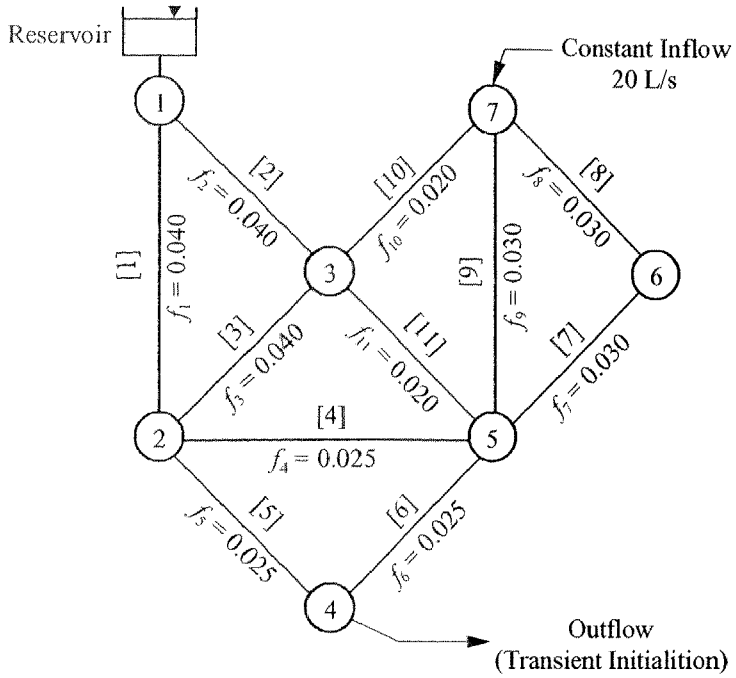

Figure 7.21 Layout of the Small Example Network

The MCS data represents the influence that the measurement error has on the solution parameters (friction factors) calculated through the inverse transient method. An optimal measurement site configuration is a configuration that minimises the influence of the measurement error on the solution parameters from the inverse transient method. The average of the MCS data for a particular measurement site configuration (for a more details see Section 7.2.1) is

$$\text{Average } \mathbf{MCS}/\sigma = \frac{1}{N}\sum_{j=1}^{N}\left(\frac{\mathbf{MCS}}{\sigma}\right)_j \quad \text{.....(7.5.1)}$$

where **MCS**/σ = the ratio of the error in the solution parameters to the error in the measurement data calculated using the Monte Carlo simulation method and N = number of parameters. An average **MCS**/σ value can be calculated for all measurement site configurations for the Small Example Network (see Table 7.4 for all configurations). The average **MCS**/σ value for each measurement site configuration (corresponding to a cross) is plotted against the number of measurement sites in Figure 7.22.

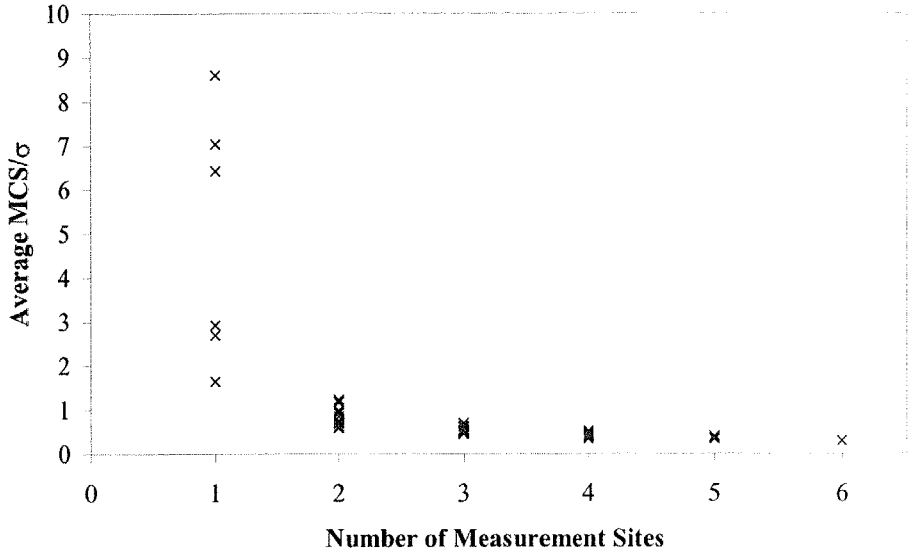

Figure 7.22 Average MCS/σ Versus Number of Measurement Sites

For higher numbers of measurement site configurations the average **MCS/σ** is almost constant suggesting that the effect of measurement error on the solution parameters from the inverse transient method decreases for larger numbers of measurement sites. Figure 7.22 also demonstrates the existence of superior measurement site configurations and numbers of measurement site configurations that minimise the transmission of measured data error to the solution parameters from the inverse transient method. The optimal location of measurement sites and the optimal number of measurement sites are presented for the Small Example network in Sections 7.5.2 and 7.5.3 respectively.

7.5.1 The Optimisation Objective

The search for the optimal location of measurement sites requires an objective function to discern between different configurations. Two methods are considered to find superior measurement site configurations. The first method is to find the average error in the parameters and then find configurations with the minimum average error in the parameters,

$$\text{Optimisation Objective} = \min\left(\frac{1}{N}\sum_{j=1}^{N}\varepsilon_j\right) \quad \text{.....(7.5.1)}$$

where N = number of parameters and ε_j = ratio between the error in parameter j (from the inverse transient method) and the measurement error in the data. ε_j can be predicted using performance indicators.

The other method is to find the parameter that exhibits the maximum error compared to all other parameters for a measurement site configuration. The minimum of this maximum error parameter then becomes the objective of the optimisation algorithm,

$$\text{Optimisation Objective} = \min\left(\max\left(\varepsilon_j\right)\right) \quad (7.5.2)$$

Both of these methods can be used to find superior measurement site configurations that maximise confidence in the resulting parameters. Methods that can predict the performance of each parameter for a measurement site configuration must be first studied. That is the subject of the rest of this chapter.

7.5.2 Optimal Location of Measurement Sites

Using the average **MCS/σ** results for particular measurement site configurations, the Small Example Network (Figure 7.21) was completely enumerated for all numbers and configurations of measurement sites (a total of 63 possible combinations of measurement sites for all numbers of measurement sites). The optimal measurement site configuration, for each number of measurement sites, is characterised by the lowest associated value of average **MCS/σ**. The process consists of taking the lower limit of the points in Figure 7.22, thus forming a Pareto optimal front as shown in Figure 7.23.

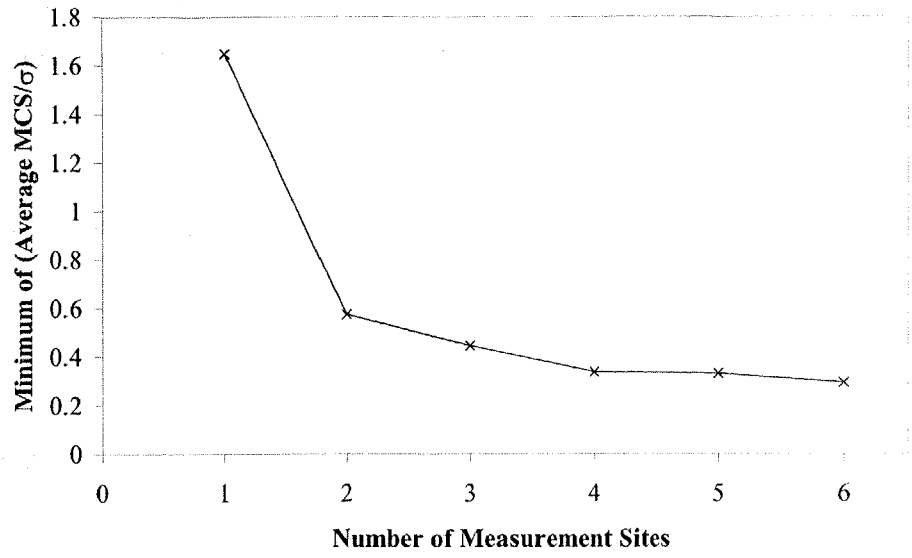

Figure 7.23 Optimal Measurement Site Location Curve (Small Example Network)

The Pareto optimal front allows the selection of optimal measurement site configurations given a certain number of measurement sites. The optimal measurement site configurations for the Pareto optimal front are shown in Table 7.8.

Table 7.8 Measurement Site Configurations for Pareto Optimal Front

Number of Measurement Sites	Optimal Measurement Site Configuration
1	6
2	6, 7
3	3, 6, 7
4	2, 5, 6, 7
5	2, 3, 4, 5, 6
6	2, 3, 4, 5, 6, 7

7.5.3 Optimal Number of Measurement Sites

The optimal number of measurement sites can be gauged by taking the average of the average **MCS/σ** (for a single measurement site configuration) for all combinations of measurement site configurations for a particular number of measurement sites. In equation form

$$\text{Average of } (\text{Average MCS/s})_k \text{ for } j \text{ measurement sites} = \frac{1}{(N_{MSC})_j} \sum_{k=1}^{(N_{MSC})_j} (\text{Average MCS} / \sigma)_{jk} \quad \text{.....(7.5.1)}$$

where $(N_{MSC})_j$ = number of measurement site combinations for j measurement sites and (Average MCS/σ)$_{jk}$ = ratio of the parameter error to the measurement error averaged over the parameters for the k^{th} measurement site configuration using j measurement sites. The application of Eq. 7.5.1 to the Small Example Network is shown in Figure 7.24.

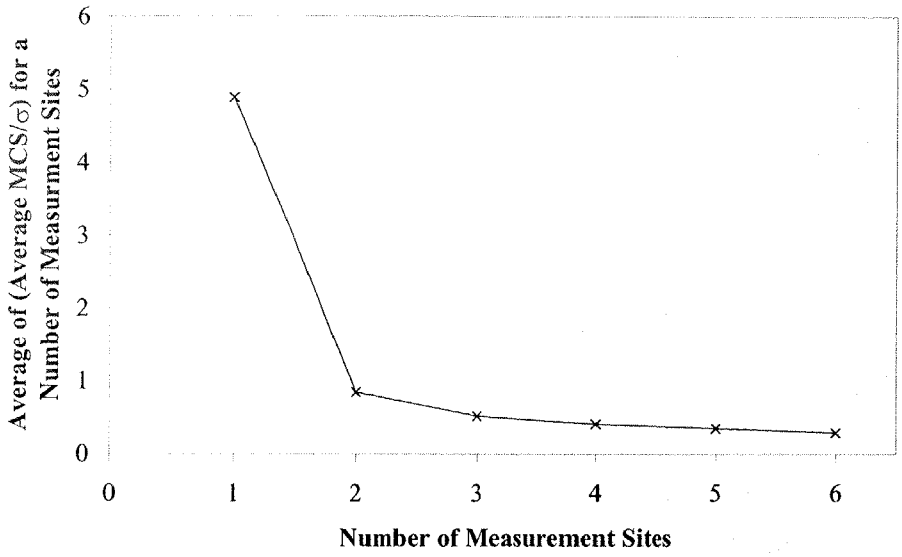

Figure 7.24 Trade-Off Curve for Optimal Number of Measurement Sites (Small Example Network)

Figure 7.24 shows that there is negligible improvement in the performance of the inverse transient method for numbers of measurement sites above three.

7.5.4 Discussion of the Small Example Network Results

The optimal measurement site locations for the Small Example Network were found in Section 7.5.2 through the full enumeration of measurement site combinations. The optimal number of measurement sites was identified (Section 7.5.3). The Pareto optimum curve (Figure 7.23) is a trade-off curve because there is a trade-off between the expected performance of the inverse transient method and the number of measurement sites. Using results from this section, a strategy for the selection of optimal measurement site configurations can be formed as follows:

1. Define the pipe network for a transient model.
2. Identify the parameters to be found using the inverse transient method.
3. Identify the possible measurement site locations.
4. Use an appropriate indicator (perhaps **SV**) to predict the expected error in the parameters.
5. Form a trade-off curve to identify a sufficient number of measurement sites (see Section 7.5.3).
6. Perform a search to find the best measurement site locations for a fixed number of sites (see Section 7.5.2).
7. Use the best measurement site configuration in the inverse transient method.

This method to find the optimal measurement site configuration could also incorporate leak detection as well as the friction factor calibration illustrated in this section. The same principles could be applied to find optimal measurement site numbers and select locations to calculate lumped leakage coefficients. There still exists a compatibility problem with respect to the units and magnitudes of the two different parameters (friction factors and lumped leak coefficients). As has been noted, the sensitivity of leak areas is much larger than the sensitivity of friction factors (Liggett and Chen, 1994). This difference in sensitivities would be manifested in the performance indicators since they are all dependent on sensitivities of some form (i.e. partial derivatives like $\partial E/\partial a$, $\partial H/\partial a$ and $\partial a/\partial H^m$). A suitable normalisation of each performance indicator would alleviate this problem (and they would become comparable with each other) and could be based on the sensitivities of the objective function to each type of parameter.

In a real pipe network with a large number of pipes, the trade-off curve could be made by randomly generating a set of measurement site configurations then computing their respective expected inverse transient performance (maybe using the **SV** indicator) and creating a trade-off curve. This trade-off curve could be used as an approximation of the true curve because the analysis of large networks requires large simulation times, making a complete enumeration for every possible combination of measurement sites impractical. A solution to this problem is to use a genetic algorithm to perform a combinatorial search. This type of search cuts down the amount of evaluations needed

to find near optimal solutions. The application to larger pipe networks is the focus of the next section of this chapter.

7.6 Optimal Measurement Site Configurations for a Large Example Network

Finding the optimal number of measurement sites and the optimal locations of these sites is a more difficult problem in a large pipe network compared to a small pipe network (as described in the previous section). In a large pipe network, full enumeration of the possible measurement site configurations is impossible due to the required computation time. Different solutions to the problem are presented in this section.

7.6.1 The Optimisation Method

The problem of finding the optimum number of measurement sites and their locations is multi-objective in nature. One objective is to use the least number of measurement sites, and the second objective is to find what combination of these sites gives the best or most confident solution?

Due to the combinatorial nature of this multi-objective problem, many configurations with low numbers of measurement sites can be fully enumerated to find the optimum configuration. Higher numbers of measurement sites produce massive numbers of combinations making the problem too computationally intensive to completely enumerate every combination. Genetic algorithms have been used to search reduced search spaces with good results. They are good at finding optimum solutions in complex and highly non-linear solution spaces.

7.6.2 New Genetic Algorithm Operators

Within a genetic algorithm formulation, selection and mutation can be applied in a standard manner (see Section 6.3) for the combinatorial search problem. Binary tournament selection and random mutation (excluding the creation of illegal chromosomes) have been used here. However, standard *N*-point crossover and partially mapped crossover (PMX), described in Goldberg (1989), do not work for this problem for a variety of reasons. In the case of *N*-point crossover there is no ability by which the genetic algorithm operator can deal with the non-repeatability of bits in a chromosome. PMX can ensure that bits are not repeated in the chromosome, but when applying it to a chromosome where ordering is not important and there are a greater number of bit values than the chromosome length (number of bits values equal the chromosome length in PMX), illegal chromosomes can be formed. To provide a crossover operator that does not create illegal chromosomes and is flexible requires the introduction of a new crossover operator named non-ordered, extended set, combinatorial crossover (NOESCX). The process for NOESCX is seen in Figure 7.25. Essentially each bit that is located in the crossover zone of one chromosome is checked to see if there is a matching bit in the other chromosome, if there is no match, then the bit is copied to the corresponding position in the other chromosome. The NOESCX operator produces no repeated bit values in the chromosomes (if both chromosomes are legal) and order is not important.

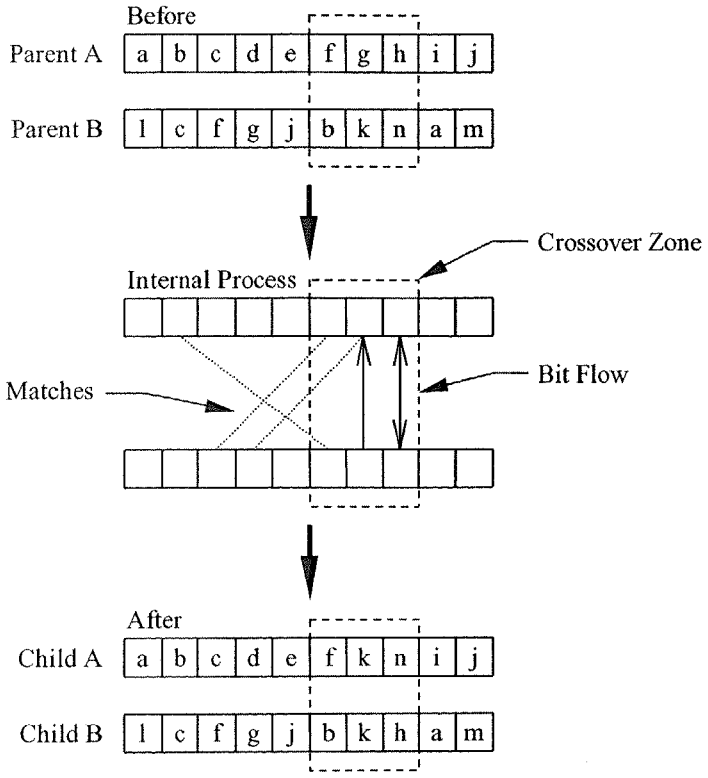

Figure 7.25 Non-Ordered, Extended Set, Combinatorial Crossover (NOESCX)

This genetic operator (together with selection and mutation) can be used to create a new population. The production of successive generations (see Section 6.3) is repeated until convergence or the number of generations exceeds some maximum number of generations. Anderson and Simpson (1996) developed the base source code used for this new genetic algorithm. For low numbers of measurement site configurations, the number of possible combinations can be lower than the expected number function evaluations used by the genetic algorithm. For these low numbers of combinations, full enumeration is used, creating an optimisation scheme combining enumeration and genetic algorithm (EGA) searching.

7.6.3 Application to a Large Network

After initial results were confirmed on a small test network, the optimisation method was put to use on a larger gravity-fed (by three reservoirs) system of 51 pipes and 35 nodes (based on a network first created by Jeppson, 1976). The pipes in the network were discretised such that each computational unit had a Courant number of one, increasing the size of the network to 75 pipes and 59 nodes. Figure 7.26 shows a

schematic of the network. The transient event for the following examples was generated by instantaneously closing a valve at node 7.

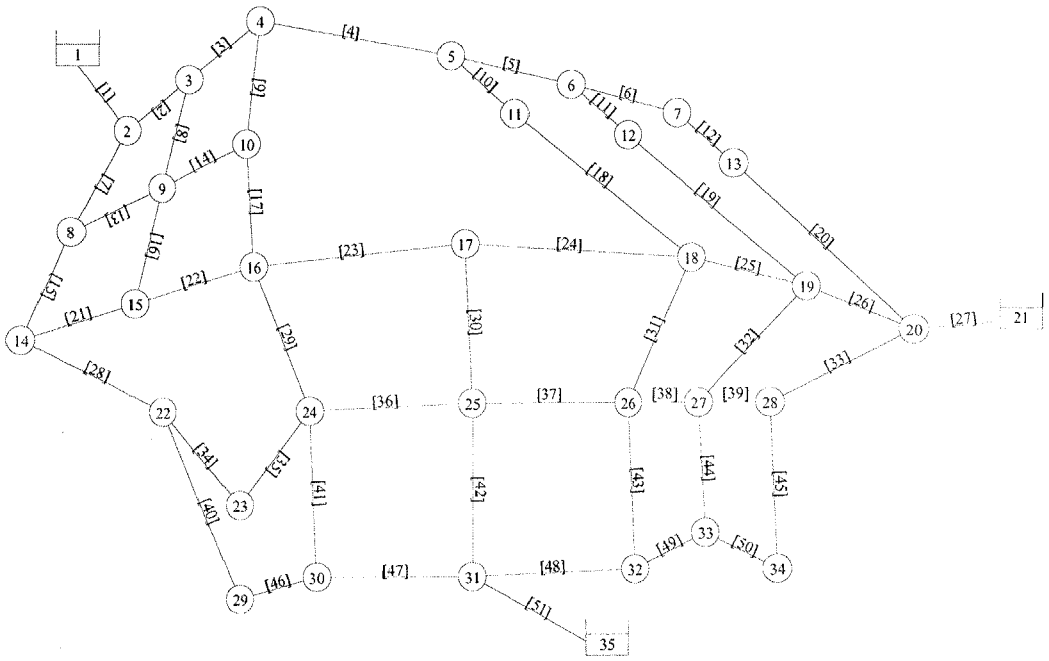

Figure 7.26 Layout of the 51 Pipe Network

A complete description of the network and water properties is given in Appendix D.4.2. For the Small Example Network, the number of possible measurement sites can be determined manually (see Table 7.4). For larger networks, the number of possible measurement site combinations can be calculated from

$$\text{Number of Combinations} = \binom{n}{k} = \frac{n!}{k!(n-k)!} \quad \text{.....(7.6.1)}$$

where n = total number of measurement site locations and k = number of measurement sites selected. The number of possible measurement sites in the 51 pipe network is 32. No measurement sites were allowed at the three reservoirs. The number of possible measurement site configurations given a certain number of measurement sites selected is shown in Table 7.9. Numbers of measurement sites greater than ten are not considered because it is likely that, in reality, there will be considerably less measurement sites than nodes in a pipe network.

Table 7.9 Number of Measurement Site Combinations for the 51 Pipe Network

Number of Measurement Sites	Number of Possible Measurement Site Configurations
1	32
2	496
3	4960
4	35960
5	201376
6	906192
7	3365856
8	10518300
9	28048800
10	64512240

7.6.4 Sampled Results

Due to the large number of measurement site combinations for the 51 pipe network, the calculation of the performance indicator **SV** for every measurement site combination is too computationally intensive. A convenient method to reduce the amount of computation needed to gain an approximation of the optimal measurement site front and the trade-off curve for the optimal number of measurement sites is to take a number of sample measurement site configurations. The sample results are representative of the true (or population) results for both curves. The **SV** indicator has been shown to produce results that predict the performance of a measurement site configuration (given that performance was defined as the ratio of the measured data error to the solved parameter error). The average **SV** value for a measurement site configuration is defined as

$$\text{Average}\,\mathbf{SV} = \frac{1}{N}\sum_{j=1}^{N}\mathbf{SV}_j \qquad (7.6.2)$$

where N = number of parameters and $\mathbf{SV}_j$ = value of **SV** for parameter j previously defined in Section 7.3.3. The sample results are used to generate an approximate optimal curve for the optimal measurement site locations by finding the measurement site configuration (out of the 20 sampled) with the minimum (Average **SV**). This approximate (sampled) optimal measurement site curve is shown in Figure 7.27.

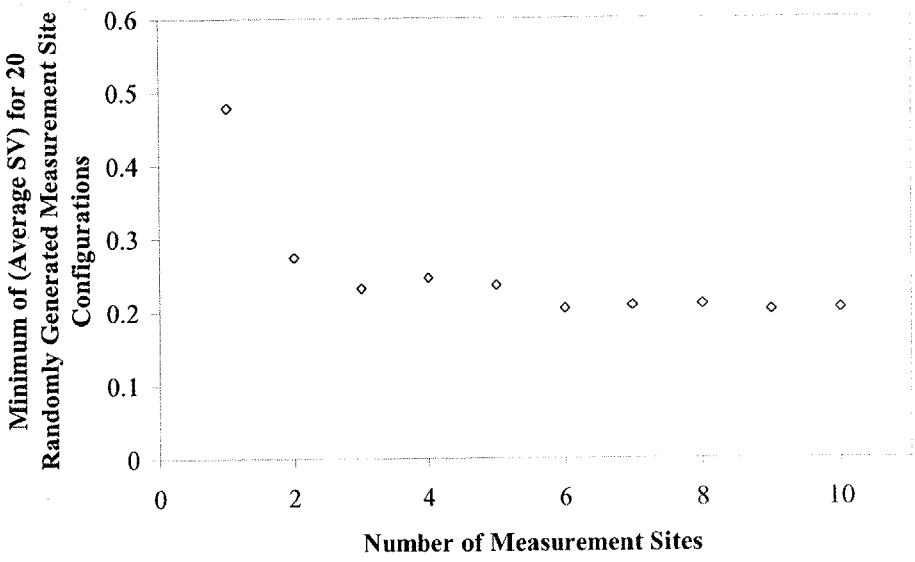

Figure 7.27 Optimal Measurement Site Configurations for the 51 Pipe Network (20 Randomly Generated Measurement Site Configurations)

The diamonds in Figure 7.27 represent the optimal measurement site configurations from the 20 sampled measurement site configurations (for each number of measurement sites selected). The optimal sampled measurement site configurations for each number of sites selected are shown in Table 7.10 together with their corresponding average **SV** value.

Table 7.10 Results for Best Sampled Sites (51 Pipe Network)

Number of Measurement Sites	Best of 20 Randomly Generated Measurement Site Configurations	Average SV
1	7	0.479
2	12, 14	0.274
3	3, 12, 34	0.233
4	7, 10, 22, 33	0.246
5	5, 8, 16, 17, 29	0.235
6	2, 5, 9, 13, 14, 23	0.204
7	2, 3, 5, 8, 17, 27, 29	0.208
8	3, 5, 8, 10, 11, 12, 17, 23	0.209
9	8, 9, 10, 12, 14, 20, 24, 31, 34	0.202
10	5, 11, 13, 16, 17, 19, 23, 24, 31, 33	0.203

These sampled results are useful for the assessment of an adequate number of measurement sites for the inverse transient method. They are also useful as a check for the EGA optimisation to find the best location of measurement sites (presented in the following section). The optimal number of measurement sites is found for the sampled

results in a similar fashion to the method of Section 7.5.3 for the Small Example Network. The average of the average **SV**'s for each measurement site configuration is

$$\text{Average of } (\text{Average SV})_k \text{ for } j \text{ measurement sites} = \frac{1}{(N_{SAM})_j} \sum_{k=1}^{(N_{SAM})_j} (\text{Average SV})_{jk} \quad \text{.....(7.6.1)}$$

where N_{SAM} = number of randomly generated measurement site configurations (samples). Figure 7.28 shows a sample optimal measurement site curve using 20 random measurement site configurations for each number of measurement sites selected (one to ten measurement sites).

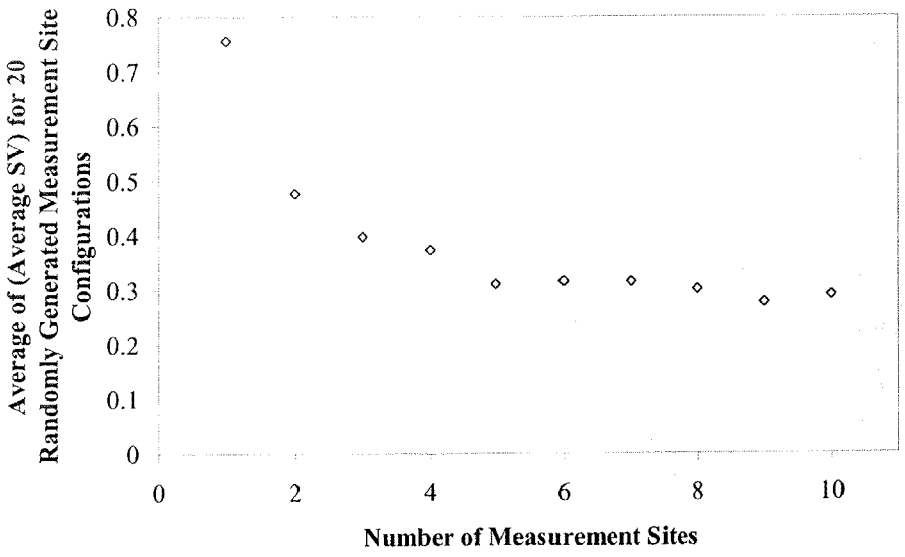

Figure 7.28 Sample Trade-Off Curve for Optimal Number of Measurement Sites (51 Pipe Network)

There is little decrease in the average **SV** for the 20 randomly generated measurement site configurations for numbers of measurement sites greater than five, suggesting that more than five measurement sites does not materially improve results. That is, five sites may or may not produce good results, but more than five site would not improve the situation. The following section applies the EGA technique (Section 7.6.2) to produce better optimal measurement site configurations than by taking random samples.

7.6.5 Optimisation Results

The search space sizes for the different numbers of measurement site combinations dictates what type of strategy should be used in the EGA optimisation. The population size for this problem was set at 1000 members and the maximum number of generations allowed was 200. Genetic algorithm optimisation was not needed if the number of possible combinations was lower than 200,000 meaning that full enumeration should be used for numbers of measurement sites equal to 1, 2, 3, and 4, and the genetic algorithm for higher numbers of measurement sites. In other words, if the total number of combinations is smaller than the number genetic algorithm evaluations, then it is more effective to use full enumeration (e.g., the total number of genetic algorithm evaluations is 200,000 and, for four measurement sites, the number of possible combinations is 35,960. In this case it is more effective to use full enumeration). The maximum number of measurement sites considered was limited to ten. The results from the EGA optimisation are shown in Figure 7.29. The minimum (average **SV**) measurement site configurations from the 20 randomly sampled measurement site configurations are represented by a cross. The minimum (average **SV**) configurations found through the use of the EGA method correspond to the diamonds.

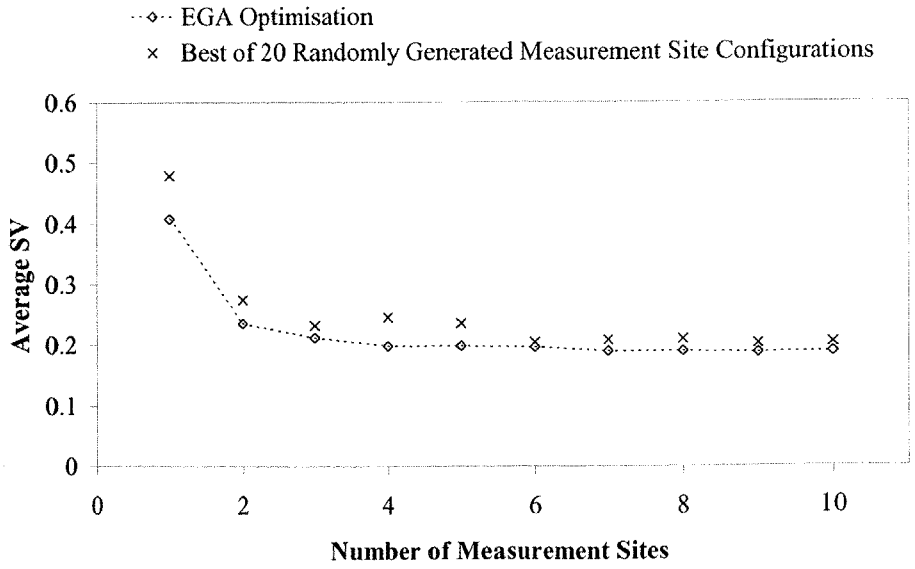

Figure 7.29 Optimal Measurement Site Front (51 Pipe Network)

Figure 7.29 shows the optimal front for the placement of measurement sites where each point on the Pareto curve front represents a configuration of measurement sites that provides the lowest (average **SV**) values for the 51 Pipe network. The sampled results (from 20 randomly generated measurement site configurations) are within the optimal front showing that the optimisation is working. Table 7.11 shows the search space size, search method, optimal sites and the average expected error for each number of measurement sites considered.

Table 7.11 Tabulated Results for Sensitivity Runs (51 Pipe Network)

Number of Measurement Sites	Search Method	Search Space Size	Optimal Measurement Site Configurations	Average **SV**
1	*E*	32	11	0.408
2	*E*	496	11, 12	0.235
3	*E*	4960	11, 23, 34	0.212
4	*E*	35960	11, 12, 23, 34	0.198
5	*GA*	201376	7, 11, 12, 23, 34	0.198
6	*GA*	906192	4, 11, 12, 23, 27, 34	0.196
7	*GA*	3365856	4, 11, 12, 19, 23, 27, 34	0.189
8	*GA*	10518300	4, 6, 11, 12, 19, 23, 27, 34	0.189
9	*GA*	28048800	6, 7, 11, 12, 16, 19, 23, 27, 34	0.187
10	*GA*	64512240	5, 6, 11, 12, 16, 19, 23, 27, 33, 34	0.188

In Table 7.11 *GA* indicates that genetic algorithms were used for optimisation and *E* indicates full enumeration was used. Some sites are consistently found in the optimal set. Sites such as nodes 11, 12, 23 and 34 feature in all runs and can be considered to be sites that will produce good convergence of the minimisation algorithm due to their high sensitivities. Convergence of the genetic algorithm part of the multiple objective process can be seen in Figure 7.30 where there are ten measurement site locations to find.

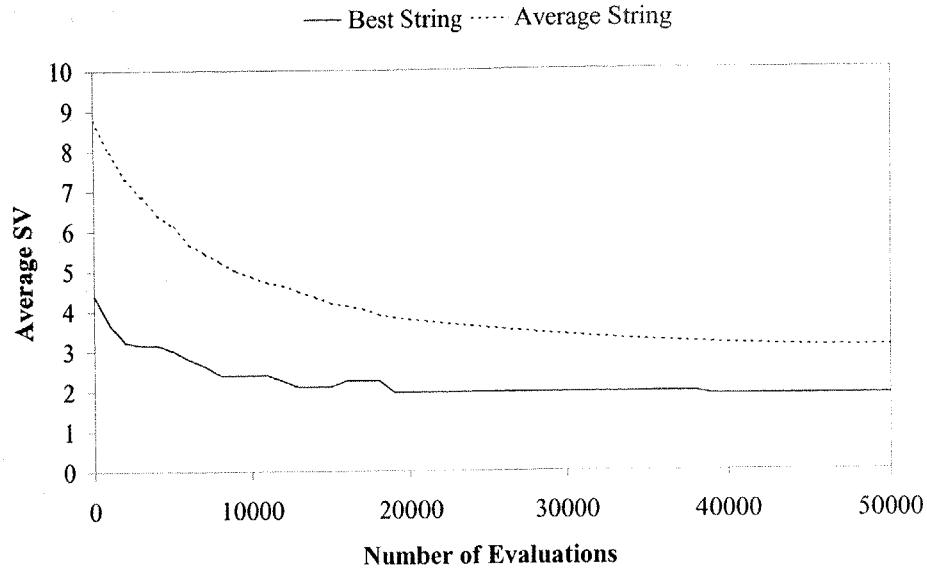

Figure 7.30 Convergence of Population for Selection of 10 Measurement Sites

7.6.6 Discussion of the Large Example Network Results

Calculation of a Pareto optimum front for the placement of measurement sites increases the success of any inverse transient solution. This method need not only be applied to the inverse solution to transient water distribution systems, other applications and other analysis methods could be improved by smarter measuring site placement. Another use for the performance indicator **SV** is to verify the expected error predicted by derivations in Section 4.8 and what length of transient record is sufficient. Discussion of these questions is presented in Sections 7.7 and 7.8.

7.7 Verification of Expected Variance

The expected variance of the parameters for a particular solution from the inverse transient method is a useful quantity. It can be used to predict how much confidence to associate with each solved parameter and, ultimately, how successful the inverse transient method has been. In previous sections of this chapter, the **SV** performance indicator is shown to predict the overall performance from the inverse transient method given a particular configuration of measurement sites. The **SV** indicator is based on the

expected variance relationships derived in Section 4.8. The verification of these relationships is achieved through the use of Monte Carlo simulations using the inverse transient method. Using the Small Example Network (Figure 7.1) a small normally distributed error ($\mu = 0.0$ m, $\sigma = 0.01$ m) is introduced into the measured pressure data. The length of the measured data is 40 s (72 time steps) with sites located at nodes 4 and 6. A plot of the pressure head is shown in Figure 7.31. The pressure head is tabulated in Appendix D.4.1.

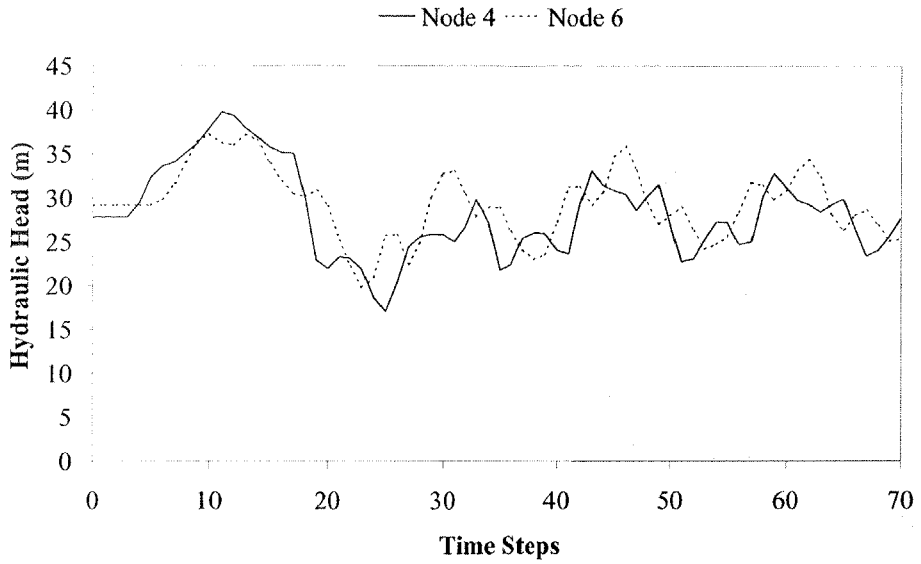

Figure 7.31 Pressure Head Data for Monte Carlo Simulation Testing

The number of Monte Carlo simulations (MCS) is 10,000. The error distribution for each friction factor is calculated from these 10,000 simulations. The mean of the calculated friction factors for each of the 11 pipes from the MCS is compared to the predicted friction factors (which are already known and were used to generate the measured data). The results are shown in Figure 7.32.

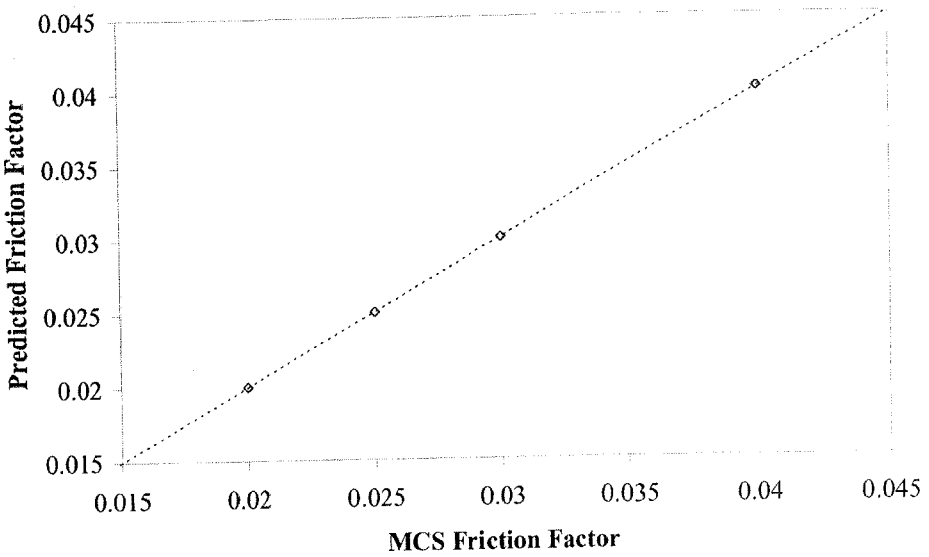

Figure 7.32 Predicted Friction Factor Versus MCS Friction Factor

Along the dashed the predicted friction factors are equal to the friction factors calculated by the MCS. The results show that the mean friction factors plot nearly exactly on that line. The same analysis, performed for the standard deviation predicted by the expected variance relationships and the MCS, is shown in Figure 7.33 (with the dashed line indicating equality between the two quantities).

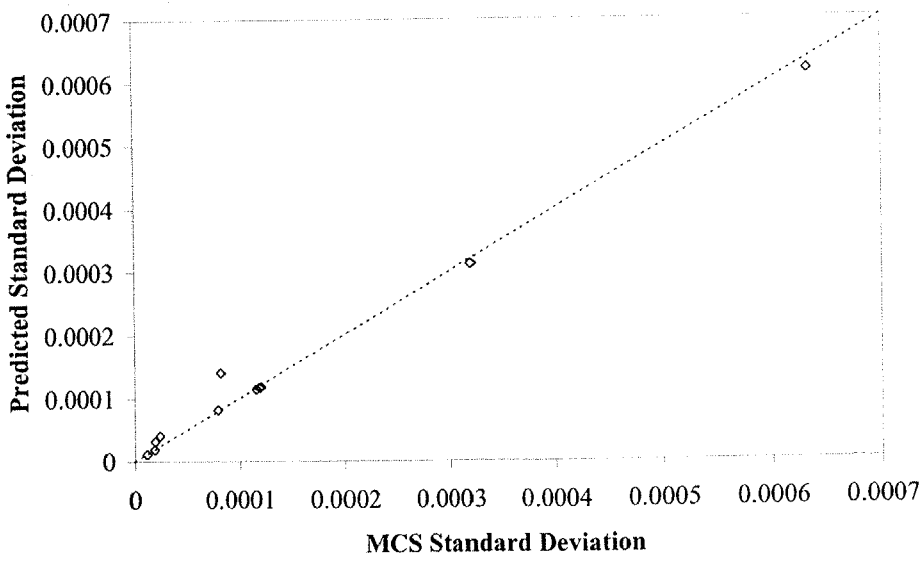

Figure 7.33 Predicted Standard Deviation Versus MCS Standard Deviation

An adequate match is observed between the predicted standard deviation and the MCS standard deviation. The only point that does not fall on the dashed line is the one corresponding to the friction factor in pipe 3. It is expected that this problem would not exist with the use of a greater number of MCS. Table 7.12 shows the mean and standard deviations for each friction factor calculated using MCS and **SV**.

Table 7.12 Actual and Predicted Results for Friction Factors

Pipe Number	MCS Results		Predicted Results		
	μ	σ	μ	σ	**SV**
1	0.03999	2.39×10^{-5}	0.040	4.08×10^{-5}	0.166
2	0.03999	1.91×10^{-5}	0.040	3.19×10^{-5}	0.102
3	0.03995	8.22×10^{-5}	0.040	1.40×10^{-4}	1.97
4	0.025	6.34×10^{-4}	0.025	6.15×10^{-4}	37.9
5	0.025	1.14×10^{-5}	0.025	1.16×10^{-5}	0.0135
6	0.025	1.85×10^{-5}	0.025	1.88×10^{-5}	0.0354
7	0.030	1.17×10^{-4}	0.030	1.14×10^{-4}	1.31
8	0.030	1.20×10^{-4}	0.030	1.17×10^{-4}	1.36
9	0.030	1.21×10^{-4}	0.030	1.18×10^{-4}	1.39
10	0.020	3.21×10^{-4}	0.020	3.12×10^{-4}	9.73
11	0.020	7.95×10^{-5}	0.020	8.16×10^{-5}	0.667

The calculation of the standard deviation assumes that the final distribution of the friction factors from the MCS is normal in nature. The shape of this distribution can be found from the MCS data. The distribution shape is calculated for two possibilities of friction factors, namely for high and low sensitivity friction factors. The friction factor in pipe 5 has a high associated sensitivity (low value of **SV** in Table 7.12). Solutions using the inverse transient method for this friction factor are of high confidence. The predicted probability distribution (Yevjevich, 1972) is

$$f(x)=\frac{1}{\sigma_x\sqrt{2\pi}}e^{-(x-\mu_x)^2/2\sigma_x^2} \qquad \text{.....(7.7.1)}$$

where $f(x)$ = probability density function of a parameter x, μ_x = mean of parameter x and σ_x = standard deviation of parameter x. The predicted probability density of the friction factor in pipe 5 is compared to the Monte Carlo simulation method results and is shown in Figure 7.34.

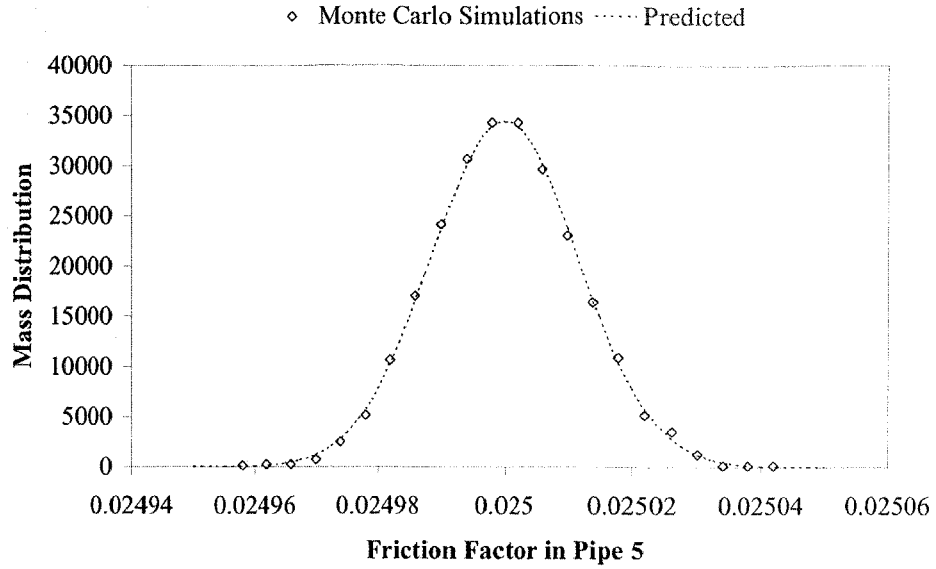

Figure 7.34 Predicted Versus MCS Distribution in Friction Factor in Pipe 5

The MCS distribution matches the predicted distribution of the value of the friction factor in pipe 5 well. The same cannot, however, be said for a low sensitivity friction factor. The friction factor in pipe 10 has a low associated sensitivity (high value of **SV** in Table 7.12). The results for a predicted and MCS distribution of the friction factor in pipe 10 are shown in Figure 7.35.

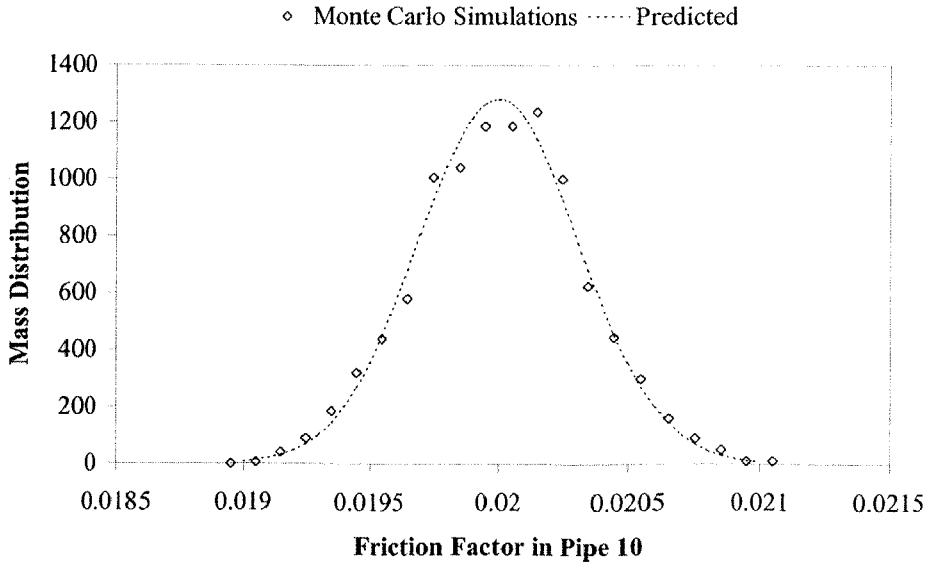

Figure 7.35 Predicted Versus MCS Distribution of Friction Factor in Pipe 10

These results show that that MCS distribution is similar to the predicted distribution. A greater number of simulations (for MCS) are needed to generate a better shaped distribution of the friction factor in pipe 10. The problem of low sensitivities with MCS is common and requires a large number of simulations to generate an adequate distribution of parameters. An example of the different associated confidences between the friction factors in pipes 5 and 10 can be observed by plotting both of their distributions on the same curve as shown in Figure 7.36.

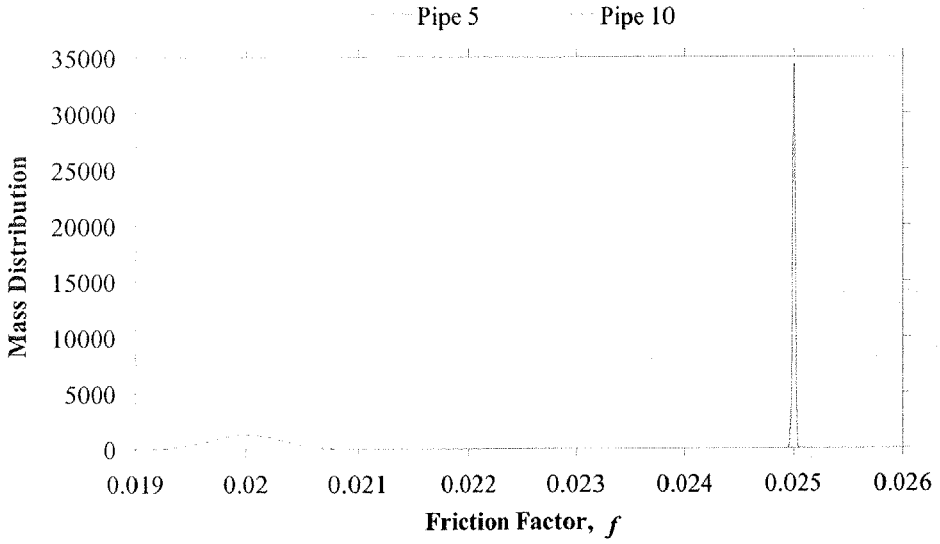

Figure 7.36 Predicted Friction Factor Distributions in Pipes 5 and 10

The distribution for the low confidence friction factor in pipe 10 is much wider and smaller than that for the friction factor in pipe 5. Given that the area beneath each curve is equal to 1.0, the standard deviation (an indication of the width the distribution) is a good indicator of the relative associated confidence for the friction factor in each pipe.

A further step can be taken by considering the expected covariance (also found when calculating the expected variance, see Section 4.8). The covariance can be used to check if there is any correlation between friction factors. The correlation coefficient (ρ) can be calculated between any two friction factors (Yevjevich, 1972). A value of ± 1.0 represents pure correlation and a value of zero, no correlation. The correlation coefficient is defined as

$$\rho = \frac{\sigma_{xy}}{\sigma_x \sigma_y} \quad \text{.....(7.7.2)}$$

where σ_x standard deviation in parameter x, σ_y = standard deviation in parameter y and σ_{xy} = covariance between parameters x and y. Similarly to Eq. 7.7.1, a bivariate probability density function, $f(x,y)$, written for two normally distributed parameters x and y, is

$$f(x,y) = \frac{e^{-Q(1-\rho^2)/2}}{2\pi\sigma_x\sigma_y\sqrt{1-\rho^2}} \quad \text{.....(7.7.3)}$$

where the variable Q is equal to

$$Q = \frac{(x-\mu_x)^2}{\sigma_x^2} + \frac{(x-\mu_y)^2}{\sigma_y^2} - 2\rho\frac{(x-\mu_x)(x-\mu_y)}{\sigma_x\sigma_y} \quad \text{.....(7.7.4)}$$

The bivariate probability density function has been calculated for two pairs of friction factors exhibiting high and low correlation respectively. The first pair is the friction factors in pipes 5 and 10, which exhibit a low correlation equal to –0.004. Two types of plots of the probability density function are useful, a 3-dimensional plot and a contour plot (Figure 7.37). The scales on these plots are normalised with respect to the standard deviation of each parameter.

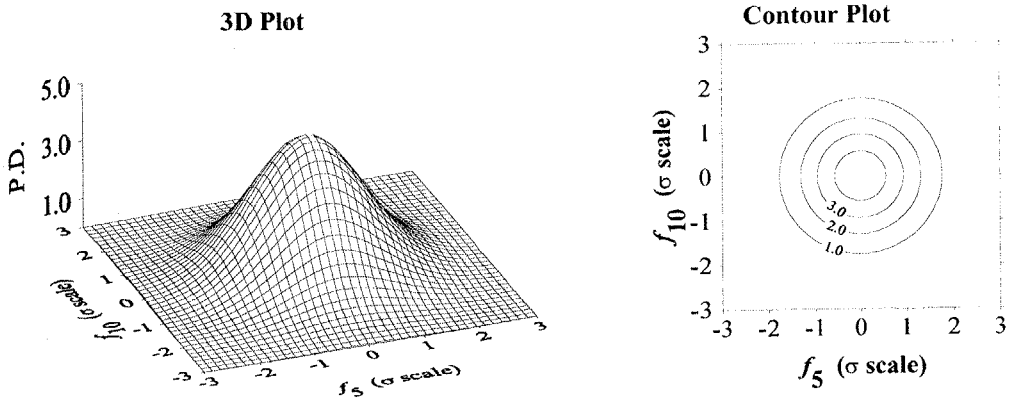

Figure 7.37 Bivariate Probability Density ($\times 10^6$) Between f_5 and f_{10}

Figure 7.37 indicates little correlation between the friction factors in pipes 5 and 10 as indicated by the perfectly circular concentric rings on the bivariate probability density contour plot. A different bivariate distribution is observed between the friction factors in pipes 7 and 9 where the correlation coefficient is equal to –0.722. The bivariate probability density for this case appears in Figure 7.38.

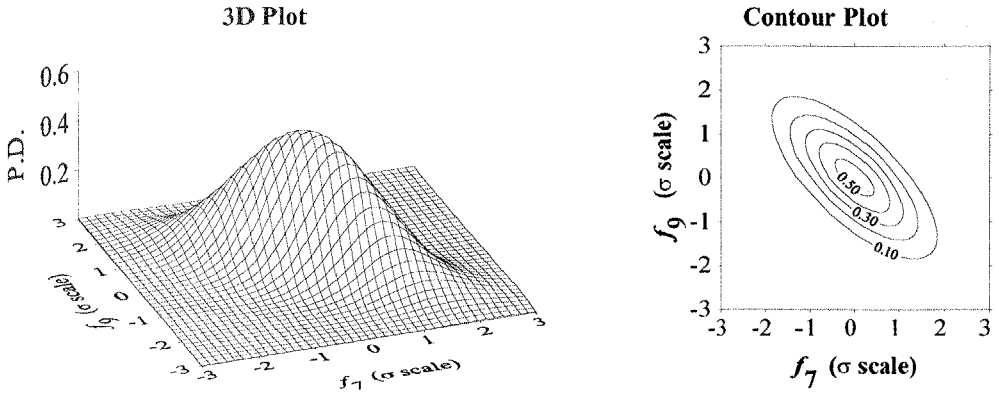

Figure 7.38 Bivariate Probability Density ($\times 10^6$) Between f_7 and f_9

The correlation between the friction factors in pipes 7 and 9 is indicated by the elliptic shape of the contours with the major axis of the ellipse along the diagonal $\sigma_y = -\sigma_x$. Since there is a relationship between the friction factors in pipes 7 and 9, perhaps, only one of these friction factors need be found when using the inverse transient method.

This section has verified the expected variance relationships derived in Section 4.8 by using Monte Carlo simulations and a Small Example Network. This section also suggests that a better statistical treatment of the inverse transient method could benefit results and the interpretation of results (such as the determination of correlation between parameters).

7.8 Optimal Length of Data

Much like the optimal number of measurement sites, the optimal length of data for the inverse transient method is a trade-off between the error in the solved parameters and the expense of data collection. The length of data trade-off curve is a useful tool for making the decision of what length of data is sufficient. The **SV** indicator relates the error in the measurements to the error in the solution parameters from the inverse transient method (see Section 4.8),

$$\sigma_j = \mathbf{SV}_j \times \sigma_m \quad (7.8.1)$$

where σ_j = standard deviation in parameter j, SV_j = element of the SV vector corresponding to parameter j and σ_m standard deviation in the measured data (assuming an equal level of error in all measurements). The trade-off curve is calculated for the small example network (Figure 7.1). In previous sections of this chapter (Sections 7.4 and 7.5), only 20 time steps of transient pressure data are used. The amount of pressure data in this section is from 1 time step (corresponding to the initial steady state conditions) to 70 time steps. The pressure head for the inverse transient method is measured at nodes 2, 3 and 6. The pressure heads are shown in Figure 7.39 in table form in Appendix D.4.1.

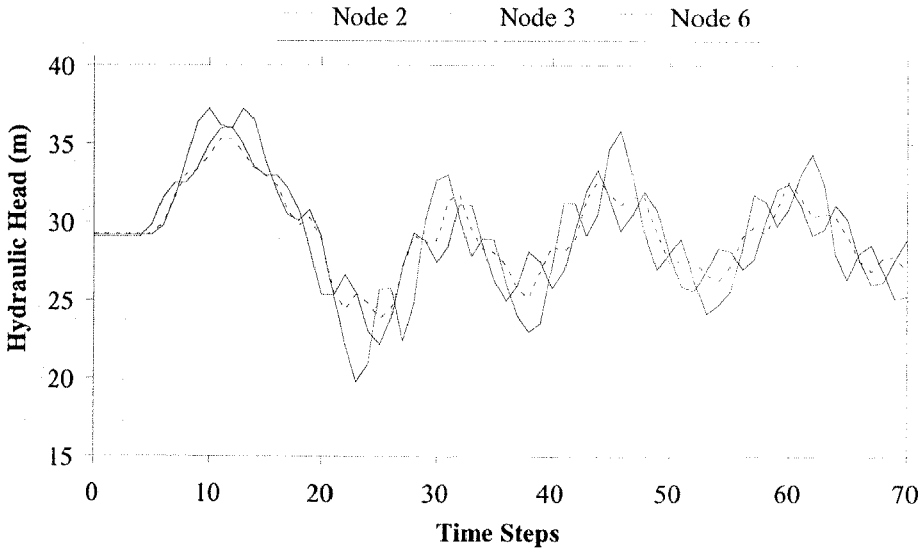

Figure 7.39 Transient Data

Steady state conditions are maintained for the first 5 time steps. The SV indicator can be calculated using different lengths of measured data from 1 to 70 time steps producing a vector of values for the friction factors in each pipe. The trade-off curve is created by taking the average of the values in the SV vector, leading to a single number that is representative of the average expected error in the friction factors for a particular length of data. The trade-off curve for the small example network is shown in Figure 7.40.

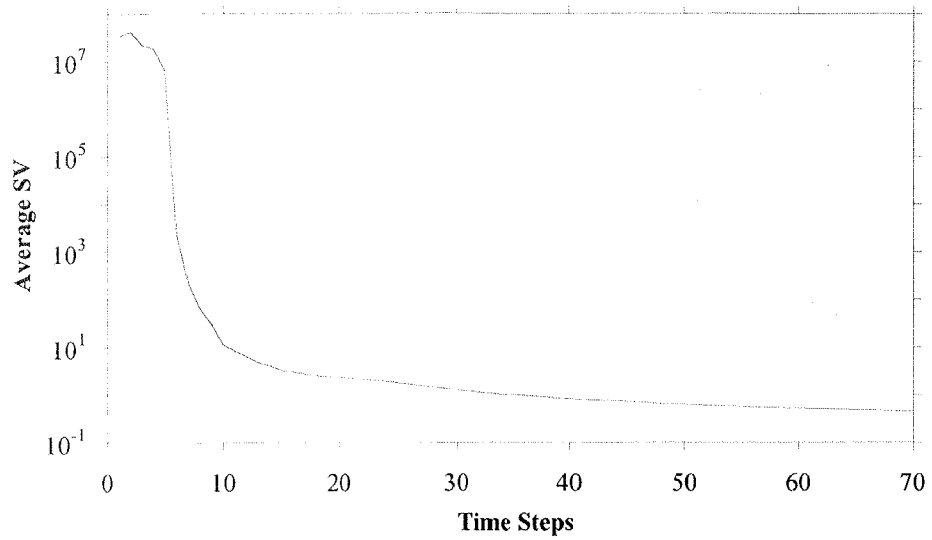

Figure 7.40 Effect of Data Length on Average SV

A high, flat region, corresponding to steady state conditions at the beginning of the transient event, exists for the first 5 time steps. Once the transient event has been initiated, the average expected error in the parameters decreases by 6 orders of magnitude, thus showing the advantages that inverse transient analysis has over inverse steady analysis. A sufficient amount of data can now be estimated based on the desired level of error required (using Eq. 7.7.1). For this example it could be argued that measurement data lengths greater than 50 time steps do not reduce the expected error level significantly (at least compared to the initial drop in expected error). The use of additional transient data decreases the average expected error; however, the effect on individual parameters can vary. Figure 7.41 shows values of the expected error vector for each pipe when both 1 and 70 time steps are used in the inverse method.

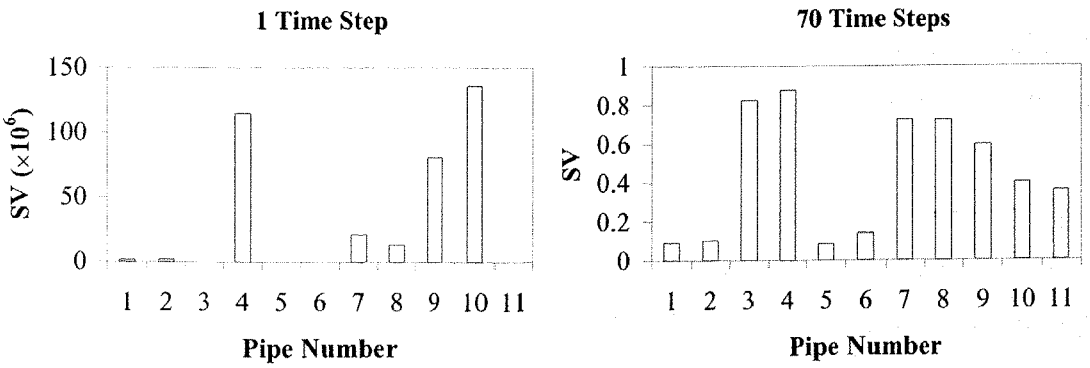

Figure 7.41 Effect of Data Length on SV

Although the average level of **SV** has fallen, the relative magnitudes of SV for different friction factors change as well. For a measured data length of 1, the parameters that would be most successfully found by the inverse transient method are friction factors in pipes 1, 2, 5, 6 and 11. For a measured data length of 70, the parameters that would be most successfully found are the same, although all friction factors, including those in pipes 3, 4, 7, 8, 9, and 10 become more defined.

7.9 Summary

This chapter presents original research related to the successful application of the inverse transient method. Many principles discussed in this chapter can be applied to problems other than the inverse transient problem. Methods are presented that answer such questions as: How many measurement sites are adequate? What length of data is adequate? and Where are the best locations to place the measurement sites? These problems are solved through the use of performance indicators. The performance indicators predict how successful an application of the inverse transient method might be for a particular configuration of measurement sites. Possible indicators were based on various sensitivity measures and other principles. Each was tested using results from Monte Carlo Simulations. The **SV** performance indicator, based on the expected variance derived in Section 4.8, was found to be the most successful and efficient. A small example pipe network was used for numerical testing. **SV** was then used to create trade-off curves for the number of measurement sites versus expected error and length of measured data versus expected error. The best configuration of measurement sites was found through full enumeration of measurement site combinations. A different approach, however, was needed for large networks. A large example network is used in conjunction with genetic algorithms to search for optimal measurement site configurations. A combined enumeration / genetic algorithm search was developed including a new crossover operator. Although the work presented in this chapter is only applied to friction factors in pipes, it is expected that it could be expanded to include lumped leak coefficients as well.

Chapter 8

Review of Unsteady Friction

8.1 Introduction

The traditional approach to incorporate frictional effects into the governing unsteady equations for pipe flow has been to approximate them with steady state friction relationships. Many experimental studies have tested the validity of this approximation. These previous results focussed on the first couple of pressure rises after a transient event given that they typically result in the largest pressures and are most detrimental to piping systems. However, in only focussing on the initial pressure rises, not much attention was given to the behaviour at longer times after the initiation of the transient event. The first pressure rise after an event is nearly independent of frictional considerations in a pipeline, and thus a good match (with the first rises) is typically found. As early as the 1950's researchers (Daily *et al.*, 1956; Carstens and Roller, 1959) have shown that steady state approximations are only partially correct and that the fluid acceleration plays an important role in damping. The extra frictional dissipation caused by the fluid acceleration is termed "unsteady friction."

Inverse transient analysis uses a history of transient pressure head data following an initiating event in a pipeline system. The incorporation of unsteady state friction allows a model to predict conditions for long periods of time and is essential for use in inverse transient analysis to detect leaks.

Unsteady friction models are included in the unsteady pipe flow equation of motion as

$$\frac{\partial H}{\partial x}+\frac{1}{g}\frac{\partial V}{\partial t}+\frac{V}{g}\frac{\partial V}{\partial x}+J=0 \quad \text{.....(8.1.1)}$$

where H = hydraulic head, V = velocity, g = gravitational acceleration, t = time, x = distance and J = the total head loss per unit length due to friction, which is composed of a steady component (J_S) and an unsteady component (J_U),

$$J=J_S+J_U \quad \text{.....(8.1.2)}$$

where the steady component is

$$J_S=\frac{fV|V|}{2gD} \quad \text{.....(8.1.3)}$$

and where f = Darcy-Weisbach friction factor and D = pipe diameter. The variables J, J_S and J_U are used throughout this chapter when describing unsteady friction models.

8.2 Previous Unsteady Friction Formulations

There are numerous models that make corrections to account for unsteady state friction, and all previous experimental testing has used smooth pipes. The first of these models was developed by Daily *et al.* (1956) who suggested that the instantaneous acceleration may be a factor that affects the shear stress along the pipe wall. Daily *et al.* (1956) used an analysis of the momentum equation to derive

$$J=J_S+\frac{C}{g}\frac{\partial V}{\partial t} \quad \text{.....(8.2.1)}$$

where C = an unsteady friction coefficient and $\partial V/\partial t$ = temporal acceleration. Daily *et al.* (1956) examined experimental turbulent flows through a smooth conduit and discovered that the unsteady quantity J is greater than the steady quantity J_S for accelerating flow and J is less than J_S for decelerating flows. Fitting coefficients to the experimental data produced two distinct values for C, 0.01 for accelerating flows and 0.62 for decelerating flows. Shuy (1996) also found these dual values (for acceleration and deceleration) in his experimental study.

Much like Daily *et al.* (1956), Carstens and Roller (1959) used linear momentum analysis to derive

$$J = J_S + \frac{k_1}{2g}\frac{\partial V}{\partial t} \quad \text{.....(8.2.2)}$$

which is similar in form to Eq. 8.2.1. The difference between Eq. 8.2.1 and 8.2.2 is the way that the coefficient, k_1 or C, is applied. Whereas Daily *et al.* (1956) had a different friction coefficient for decelerating and accelerating flows, the coefficient of Carstens and Roller (1959) depends on the Reynolds number. The coefficient k_1 was shown to be a function of n in Schlichting's (1955) universal power law for the velocity distribution in turbulent pipe flow where the velocity distribution is dependent on the Reynolds Number and is determined experimentally.

Results from the Carstens and Roller (1959) study showed considerable scatter and, compared to those of Daily *et al.* (1956), suggested that unsteady friction coefficients are not the same for deceleration and acceleration, but are of different magnitudes (with acceleration being the larger). Experimental tests performed by Shuy (1985) demonstrated that the Carstens and Roller formulation is not applicable to rapidly varying flows such as water hammer events.

The Zielke (1968) model for laminar flow utilises past weighted velocity changes at a computational section. It was formed from the analytical solution of the axi-symmetric unsteady laminar pipe flow equations. The expressions that describe laminar unsteady friction (Eqs. 8.2.3, 8.2.4, 8.2.5 and 8.2.6) have been formulated for the MOC using a diamond grid. The calculation of the total headloss due to steady and unsteady friction is

$$J_{i,k} = (J_S)_{i,k} + \frac{16\nu}{gD^2}\sum_{j=1}^{k-1}(V_{i,j+1} - V_{i,j-1})W(\tau) \quad \text{.....(8.2.3)}$$

where $J_{i,k}$ = total headloss due to steady and unsteady friction at space step i and time step k, $(J_S)_{i,k}$ = headloss due to steady friction at space step i and time step k, ν = kinematic viscosity, τ = dimensionless time and $W(\tau)$ = weighting function at dimensionless time τ. The dimensionless time is

$$\tau = \frac{4\nu}{D^2}(k - j)\Delta t \quad \text{.....(8.2.4)}$$

where j and k = multiples of the time step Δt. The weighting function $W(\tau)$ is approximated by two functions defined for different ranges of the dimensionless time τ. For $\tau > 0.02$,

$$W(\tau) = \sum_{i=1}^{5} e^{-n_i \tau} \quad \text{.....(8.2.5)}$$

and for $\tau \leq 0.02$,

$$W(\tau) = \sum_{i=1}^{6} m_i \tau^{(i-2)/2} \quad \text{.....(8.2.6)}$$

where m and n are coefficients of the weighting function. The coefficients for the weight function (Eqs. 8.2.5 and 8.2.6) are $\{n_i;\ i = 1,\ldots,5\}$ = {–26.3744, –70.8493, –135.0198, –218.9216, –322.5544} and $\{m_i;\ i = 1,\ldots,6\}$ = {0.282095, –1.25, 1.057855, 0.937500, 0.396696, –0.351563}.

The Zielke (1968) model has been modified by many researchers to either increase its computational efficiency or to model under different initial flow conditions. Trikha (1975) approximated the weighting function to improve computational efficiency. Kagawa *et al.* (1983) and Suzuki *et al.* (1991) developed a more efficient solution method (both of which are mathematically equivalent to Zielke's original method) based on fewer weighted past velocity changes. Trikha (1975) suggested that the Zielke (1968) unsteady friction model could be extended to low Reynolds number turbulent flows. However, Arlt (1983) found that there was not enough damping produced by the Zielke (1968) model in unsteady low Reynolds number turbulent flows. Bergant and Simpson (1994) also determined experimentally that the Zielke (1968) model did not produce sufficient damping for low Reynolds number turbulent flows.

Other researchers have found different weighting values (or functions) that make the Zielke (1968) model apply to turbulent flows. Some of these have been Brown (1984) who produced weighting factors that were negative for monotonic flows (pure acceleration), Vardy *et al.* (1993) who produced weights for low Reynolds number turbulent flows and Vardy (1992) for higher Reynolds number turbulent flows. Recently Vardy and Brown (1996) developed another analytical technique using the response of velocity profiles to imposed accelerations (based on a assumed eddy viscosity distribution in an axi-symmetric unsteady flow model) to find weights for the

Zielke (1968) model. The outcome of the later study was the generation of different weights for different Reynolds number flows plus a solution for the Brunone *et al.* (1991) unsteady friction coefficient (k_3).

Considerable research has been carried out for oscillating flow (zero mean displacement) in tubes. Hino *et al.* (1977) were the first to analyse this form of transient flow and found semi-empirically

$$J = \frac{0.1474V|V|}{2gD}\left(V\sqrt{\frac{L}{a\nu\pi}}\right)^{-0.351} \qquad \text{.....(8.2.7)}$$

where L = the pipe length and a = the wave speed. Although gaining good results for the particular transient situation at hand, studies such as those by Bergant and Simpson (1994) found that there was still not enough damping produced by Eq. 8.2.7 (compared to results from an experimental pipeline).

Another approach to modelling has been to move towards a two-dimensional model rather than the classical one-dimensional model by including the velocity distribution across a section of a pipe. A disadvantage is that the complexity of model formulation is increased and simulations take significantly longer to run. In addition boundary conditions are harder to model. Vardy and Hwang (1991) formulated a "shell" model where the water column is separated into thin shells sliding over each other. It was used to show that Zielke's model is accurate under laminar conditions. Similarly Brunone *et al.* (1995) developed a quasi-two-dimensional model, which they used to show that the velocity profile is closely linked to the damping of the pressure peaks. The convective terms ($V\partial H/\partial x$ and $V\partial V/\partial x$) were found to be negligible compared to other terms in the equations of continuity and motion. This model was used to confirm the behaviour produced by the Brunone *et al.* (1991) unsteady friction model.

Other models, such as the fluid structure interaction model of Elansary *et al.* (1994), have produced good results. Wood and Funk (1970) created a simple boundary layer model for use in general transient situations. Later Funk and Wood (1974) reported good matches in sinusoidal velocity fluctuations in transient flow.

Golia (1990) created a simple instantaneous acceleration model based upon the model previously developed in the Daily *et al.* (1956) study. The Golia (1990) model is

$$J = J_S + \delta \frac{k_2}{g} \frac{\partial V}{\partial t} \quad \text{.....(8.2.8)}$$

where k_2 = Golia's unsteady friction coefficient and δ = the Heaviside operator. Essentially this formulation assumes that when the fluid is accelerating there is an additional correction involving k_2 to the steady state friction term, while in decelerating flow the correction term is zero. The Heaviside operator is

$$\delta = \begin{cases} 1 & \text{if} \quad V\dfrac{\partial V}{\partial t} \geq 0 \\ 0 & \text{if} \quad V\dfrac{\partial V}{\partial t} < 0 \end{cases} \quad \text{.....(8.2.9)}$$

Results using this formulation are good (Golia, 1990), especially for flows that are monotonic in nature (i.e. not pulsed or periodic)

Brunone *et al.* (1991) opined that a step function relationship does not exist in real-world fluid flows. In an attempt to find a continuous function that approximated the Golia (1990) unsteady friction correction, Brunone *et al.* (1991) suggested that the correction term might also depend on the convective acceleration and proposed

$$J = J_S + \frac{k_3}{g}\left(\frac{\partial V}{\partial t} - a\frac{\partial V}{\partial x}\right) \quad \text{.....(8.2.10)}$$

where k_3 = the Brunone *et al.* (1991) unsteady friction coefficient and $\partial V/\partial x$ = the spatial (or convective) acceleration. The results using Eq. 8.2.10 produce similar results to those using Golia (1990). The match between results from the Golia (1990) and the Brunone *et al.* (1991) models may be explained by first examining the partial derivative terms (in each model). The subtraction of the local convective acceleration (multiplied by a) from the temporal acceleration (in Brunone *et al.*, 1991, model) acts much like the step function in the Golia (1990) formulation where under acceleration the two terms are additive and under deceleration they cancel. The summation or cancellation of the partial derivatives can only occur if the relative magnitudes of the partial derivatives are approximately

$$\left|\frac{\partial V}{\partial t}\right| \approx a\left|\frac{\partial V}{\partial x}\right| \quad \text{.....(8.2.11)}$$

Eq. 8.2.11 arises from the characteristic method (Section 3.3.2) during the re-composition of a directional derivative of velocity from temporal and convective partial derivatives of the velocity. Eq. 8.2.11 can be used produce an approximate relationship between the Brunone *et al.* (1991) unsteady state friction coefficient (k_3) and the Golia (1990) unsteady state friction coefficient (k_2). The approximate relationship is derived by equating the unsteady frictional effects produced by the Golia (1990) model and the Brunone *et al.* (1991) model giving

$$J_S + \delta \frac{k_2}{g} \frac{\partial V}{\partial t} = J_S + \frac{k_3}{g}\left(\frac{\partial V}{\partial t} - a\frac{\partial V}{\partial x}\right) \quad \text{.....(8.2.12)}$$

The steady friction components are cancelled along with the gravitational acceleration g. A monotonically accelerating flow is then assumed. For this type of flow the Heaviside operator in the Golia (1990) model is equal to one and the temporal and convective accelerations in the Brunone *et al.* (1991) model add. Given Eq. 8.2.11, the convective acceleration in the Brunone *et al.* (1991) model is replaced with the temporal acceleration. Eq. 8.2.12 becomes

$$k_2 \frac{\partial V}{\partial t} \approx k_3\left(\frac{\partial V}{\partial t} + \frac{\partial V}{\partial t}\right) \quad \text{.....(8.2.13)}$$

Thus an approximate relationship between the k_2 and k_3 unsteady friction coefficients is

$$k_3 \approx \tfrac{1}{2}k_2 \quad \text{.....(8.2.14)}$$

The Golia (1990) and Brunone *et al.* (1991) unsteady friction models are formulated such that the unsteady friction is significantly larger than the steady state friction for accelerating flows and negligible for decelerating flows. In 1996 Shuy performed experiments that showed that in some cases the unsteady friction for deceleration was, in fact, larger than the steady friction for acceleration, which is contradictory to other studies. Shuy explains that his result may be due to relaminarisation of the fluid. Shuy and Apelt (1983) tested five different friction models under a range of conditions. The five models were the constant f (based on initial conditions) steady state friction, the quasi-steady friction, Carstens and Roller (1959), Trikha (1975) and Hino *et al.* (1977) models. Their results showed that significant discrepancies occurred between models where there should have been agreement suggesting that research is still needed to find a comprehensive model that works under general conditions. Shuy and Apelt (1983) also give some guidelines for the use of unsteady state friction for oscillating flows. Three regions were proposed: quasi-steady, intermediate, and inertial dominant. For

laminar flow, the boundaries between these regions are defined using the square root of the dimensionless frequency,

$$\sqrt{\omega'} \quad \text{.....(8.2.15)}$$

where the dimensionless frequency (ω') is defined as

$$\omega' = \frac{R^2\omega}{\nu} \quad \text{.....(8.2.16)}$$

and R = the pipe radius and ν = kinematic viscosity and ω = circular frequency. In oscillatory flow, the circular frequency is defined as

$$\omega = 2\pi f \quad \text{.....(8.2.17)}$$

where f = frequency of oscillation. The different regions in oscillating laminar flow are shown in Table 8.1.

Table 8.1 Frequency Dependent Laminar Flow Regions

$\sqrt{\omega'}$	Flow Type
< 1.32	Quasi-Steady
1.32 – 28.0	Intermediate
> 28.0	Inertial Dominant

The same three regions were found for turbulent flow. The boundaries of these regions for turbulent flows were found to depend upon

$$\sqrt{\frac{\omega'}{f_S \mathbf{R}_{ta}}} \quad \text{.....(8.2.18)}$$

where $\mathbf{R}_{ta}$ = time-averaged Reynolds number and f_S = the steady state Darcy-Weisbach friction factor. The boundaries between the different regions for turbulent flows are shown in Table 8.2.

Table 8.2 Frequency Dependent Turbulent Flow Regions

$\sqrt{\frac{\omega'}{f_S \mathbf{R}_{ta}}}$	Flow Type
< 0.145	Quasi-Steady
0.145 – 1.50	Intermediate
> 1.50	Inertial Dominant

The demarcation between the flow regions (where different types of transient model are applicable) are used for the experimental tests in Chapter 11. Although the experimental tests are not true oscillatory flows—they show decay towards zero flow—

the flows are approximately oscillatory over small periods of time. The time averaged Reynolds number and the friction factor for the turbulent flow calculations can be approximated by the initial flow. The frequency of the oscillations is equal to the natural frequency of the pipeline.

A typical experimental test presented in Chapter 11 is a fast valve closure with an initial fluid velocity of 0.3 m/s. The initial Reynolds number of the flow is 6584 and the steady state friction factor f_S = 0.034. The natural frequency of the pipeline, calculated from the wave speed (a = 1319 m/s) and the pipeline length (L = 37.2 m), is found to be $f = a/4L$ = 8.86 Hz. The circular frequency (ω) is equal to 55.7 rad/s and the dimensionless frequency (ω') is equal to 6,753. Therefore, the turbulent flow region factor (Eq. 8.2.18) is equal to 5.42, showing that the quasi-steady friction approximation is not suitable for the modelling of the typical transient events presented in Chapter 11 (see values in Table 8.2). Thus, an unsteady friction model must be used.

8.3 Classification of Unsteady Friction Models

Unsteady friction models may be categorised into broad groups. Bergant and Simpson (1994) have proposed a previous categorisation. There are two basic classifications available. The first classification system considers the following:

1. *Instantaneous velocity based models*: Originally an approximation of the headloss due to friction was assumed to be dependent on the instantaneous velocity. The friction was approximated by steady state friction (Streeter and Wylie (1983); Propson, 1972; Arfaie *et al.*, 1993). This model is often used in conjunction with other unsteady friction models to provide the correct steady state solution. Hino *et al.* (1977) developed a relationship for unsteady friction that was dependent on the velocity (different from the steady state headloss relationship) for oscillatory flow.
2. *Simple temporal acceleration based models*: The temporal acceleration, $\partial V/\partial t$, is used directly to evaluate the extra dissipation due to unsteady friction during a transient event (Daily *et al.*, 1956; Carstens and Roller, 1959; Safwat and Polder,

1973; Kurokawa and Morikawa, 1986). Shuy and Apelt (1987) (and later Shuy, 1996) have proposed regions of flow where this type of model is useful.

3. *Complex temporal acceleration based models*: These models use the temporal acceleration quantity, $\partial V/\partial t$, with other fluid properties to form models that can simulate more complex behaviour. Zielke (1968) used a history of weighted accelerations for laminar flow that allowed frequency dependent friction to be modelled. Later the Zielke model was improved by Trikha (1975), Kagawa *et al.* (1983) and Suzuki *et al.*(1991). The Zielke model was extended to model turbulent flows with the use of different weighting functions (Vardy *et al.*, 1993; Vardy and Brown, 1996). Golia (1990) used the acceleration parameter $V(\partial V/\partial t)$ and the Heaviside operator, and Brunone *et al.* (1991) introduced the convective acceleration parameter $\partial V/\partial x$.
4. *Derivative of acceleration based models*: These models suggest that the extra dissipation due to unsteady friction during a transient event is proportional to $\partial^2 V/\partial x^2$. Svingen (1996) and Vennatrø (1996) have used this assumption. Denisov (1970) proposed the use of both $\partial V/\partial t$ and $\partial^2 V/\partial t^2$ to model turbulent transient events.
5. *Boundary layer based models*: These models determine an approximate boundary layer thickness and divide the pipe cross-section into a turbulent core and laminar sub-layer (Wood and Funk, 1970; Funk and Wood, 1974).
6. *Velocity profile "shell" models.* These models use the axi-symmetric governing equations and define a velocity profile at all locations along the pipe and in all times. The velocity profile can then be used to find the instantaneous boundary shear stress (Vardy and Hwang, 1991).
7. *Turbulence based models*: A turbulence formulation uses computational fluid dynamics to model the fluid in the pipeline. It is the most versatile model but can be slow and is not well suited to larger systems, which require many elements to model sufficiently. Models such and the k-ε and k-ω models have been used (Ohmi *et al.*, 1985; Bratland, 1986; Eichinger and Lein, 1992; Raabe and Olbrich, 1992); however, these models have exhibited problems with adverse pressure gradients and flows with shocks. A simple turbulence model was proposed by Pezzinga (1999) using mixing length concepts.

An alternative classification for unsteady friction models is to observe their range of applicability. Many models have been experimentally verified under specific tests and are therefore only applicable to the conditions of verification. The following list shows the basic groups of flow types that have been used for testing unsteady friction models:

1. *Steady flows*: Steady flows are a special case of unsteady flows. All models should be able to predict steady behaviour (Wylie and Streeter, 1993).
2. *Purely accelerating or decelerating flows*: These were some of the most common test types, essentially consisting of flows with monotonically increasing or decreasing flow velocities. Such experiments were used to investigate high Reynolds number flows (Daily *et al.*, 1956; Carstens and Roller, 1959; Shuy and Apelt, 1987; Kurokawa and Morikawa, 1986; Fuamba *et al.*, 1996; Shuy, 1996).
3. *Oscillating flows*: Tests for these types of flows are often performed in U-tubes. A predefined forcing flow function (usually sinusoidal) is used excite the flow. Research by Uchida (1956), Safwat and Polder (1973), Funk and Wood (1974), Letelier and Leutheusser (1976), Hino *et al.* (1977) and Ohmi *et al.* (1985) have been performed in this area.
4. *Water hammer flows*: In a transient (water hammer) event many different flow types can be observed. The pulsed and oscillating flows are sub-sets of water hammer flows. Water hammer flows can be split into laminar and turbulent flows. The laminar water hammer flows have been analytically solved by Zielke (1968) and good experimental matches have been found (Suo and Wylie, 1989; Elansary *et al.*, 1994). Turbulent water hammer flows show different behaviour than laminar ones. Recently, good matches with experimental tests were found by Golia (1990), Brunone *et al.* (1991) and Bergant and Simpson (1994) for turbulent flows.
5. *Transitional flows*: The transition from laminar to turbulent and the from turbulent to laminar have caused some problems for researchers where uncharacteristic behaviour is generated from experiments (Shuy, 1996). Research by Lefebvre and White (1989) has found critical parameters that describe where this transition occurs based on the convective acceleration.
6. *Generalised flows*: All of the previous flow types are included in this group. As yet there are no models that successfully work under all different flow types. Perhaps computational fluid dynamics, in particular the direct numerical solution (DNS)

with the Navier-Stokes equation, is the only way to find a model that spans all flow types.

7. *Other flow types*: These include cavitating flows (Streeter, 1969; Wylie, 1984; Bergant and Simpson, 1994) and where fluid structure interaction is important (Tijsseling and Lavooij, 1990; Elansary *et al.*, 1994; Svingen, 1996).

Generally, experimental tests have shown that laminar water hammer flows are well simulated by the Zielke model (and its derivative models). The turbulent water hammer flows are simulated well by the temporal acceleration models, in particular the Brunone *et al.* (1991) unsteady friction model, but not for all possible transient cases. The focus of Chapter 9 is the presentation of a development of temporal acceleration-based unsteady friction models for turbulent water hammer events for experimental verification in Chapter 11.

8.4 Previous Unsteady Friction Implementation

The implementation of the Brunone *et al.* (1991) unsteady friction model in the method of characteristics can be achieved in two ways. The first is to use the derivatives (in the unsteady friction model) to alter the wave speed and the characteristic grid—i.e., include the unsteady friction in the directional derivatives and the variation of the variables along the lines of the directional derivatives. The alternative is to use unsteady friction as an addition to the Darcy-Weisbach friction as though it did not contain derivatives. In this thesis, these two methods as are referred to as [the unsteady friction model] "included in the directional derivatives" and "treated as an addition to steady friction." This section (together with Appendix B.1) outlines the different methods to apply the Brunone *et al.* (1991) unsteady friction model.

The implementation of the Brunone *et al.* (1991) model treated as an addition to steady friction was first performed by Brunone *et al.* (1991) and then by Bergant and Simpson (1994). If the unsteady friction model is treated as an addition to the steady friction, then approximations of the partial derivatives (in the unsteady friction model) must be made. Different formulations are presented in Appendix B.1 to evaluate these partial

derivatives. Results for the different formulations show similar behaviour suggesting that conceptually easier and simpler to implement schemes could be used over the more complicated and more accurate schemes. The use of diamond and rectangular grid types is also investigated. Results show that errors occur when using a rectangular grid but can be avoided by not linking the two grids. The consistency of the Brunone *et al.* (1991) model was tested in Appendix B.1.4 using different numbers of computational reaches in a pipeline. The degree of coarseness of the grid was shown to effect the shape of the transient response (with coarse grids) but not the amplitude of the response.

Bughazem and Anderson (1996) first performed implementation of the Brunone *et al.* (1991) unsteady friction model included in the directional derivatives. This approach was reinforced by Wylie (1997) and then again by Bughazem and Anderson (2000). An incorrect but similar solution was performed by Axworthy *et al.* (2000). For comparison with future work presented in Chapter 9, the Bughazem and Anderson (1996) implementation is shown below.

The equation of motion of unsteady pipe flow including the Brunone *et al.* (1991) unsteady friction model is

$$L_1 = \frac{\partial H}{\partial x} + \frac{1}{g}\frac{\partial V}{\partial t} + \frac{fV|V|}{2gD} + \frac{k_3}{g}\left(\frac{\partial V}{\partial t} - a\frac{\partial V}{\partial x}\right) = 0 \quad \text{.....(8.4.1)}$$

and the equation of continuity is

$$L_2 = \frac{\partial H}{\partial t} + \frac{a^2}{g}\frac{\partial V}{\partial x} = 0 \quad \text{.....(8.4.2)}$$

A linear combination of these two equations is made using a multiplier λ. This linear combination can be described by $L_1 + \lambda L_2$ and results in

$$\frac{\partial H}{\partial x} + \frac{1}{g}\frac{\partial V}{\partial t} + \frac{fV|V|}{2gD} + \frac{k_3}{g}\left(\frac{\partial V}{\partial t} - a\frac{\partial V}{\partial x}\right) + \lambda\left(\frac{\partial H}{\partial t} + \frac{a^2}{g}\frac{\partial V}{\partial x}\right) = 0 \quad \text{.....(8.4.3)}$$

Rearranging Eq. 8.4.3 and grouping together the partial derivatives of the pressure head and of the velocity produces

$$\lambda\left[\frac{\partial H}{\partial t} + \frac{1}{\lambda}\frac{\partial H}{\partial x}\right] + \frac{(1+k_3)}{g}\left[\frac{\partial V}{\partial t} + \frac{a(\lambda a - k_3)}{(1+k_3)}\frac{\partial V}{\partial x}\right] + \frac{fV|V|}{2gD} = 0 \quad \text{.....(8.4.4)}$$

The partial derivatives in Eq. 8.4.4 are transformed into directional derivatives along the characteristic line of slope

$$\frac{dx}{dt} = \frac{1}{\lambda} = \frac{a(\lambda a - k_3)}{(1+k_3)} \quad \text{.....(8.4.5)}$$

The solution of Eq. 8.4.5 for the multiplier λ can be found using the quadratic formula, producing the solutions

$$\lambda = -\frac{1}{a} \quad \text{and} \quad \frac{(1+k_3)}{a} \quad \text{.....(8.4.6)}$$

The velocity of a disturbance in the pipe (dx/dt) and the slope of the characteristic lines are

$$\frac{dx}{dt} = -a \quad \text{and} \quad \frac{a}{(1+k_3)} \quad \text{.....(8.4.7)}$$

The characteristic grid is asymmetrical in the Brunone *et al.* (1991) model, which is further discussed in Section 9.4. Eq. 8.4.4 is now expressed in terms of total (directional) derivatives as

$$\lambda \frac{dH}{dt} + \frac{(1+k_3)}{g}\frac{dV}{dt} + \frac{fV|V|}{2gD} = 0 \quad \text{.....(8.4.8)}$$

The solutions for the multiplier λ are substituted into Eq. 8.4.8 forming two compatibility equations. The C^+ and C^- compatibility equations are

$$C^+: \quad \frac{(1+k_3)}{a}\frac{dH}{dt} + \frac{(1+k_3)}{g}\frac{dV}{dt} + \frac{fV|V|}{2gD} = 0 \quad \text{along} \quad \frac{dx}{dt} = \frac{a}{(1+k_3)} \quad \text{.....(8.4.9)}$$

$$C^-: \quad -a\frac{dH}{dt} + \frac{(1+k_3)}{g}\frac{dV}{dt} + \frac{fV|V|}{2gD} = 0 \quad \text{along} \quad \frac{dx}{dt} = -a \quad \text{.....(8.4.10)}$$

Finally, these two compatibility equations are further simplified using their corresponding characteristic slopes forming

$$C^+: \quad dH + \frac{a}{g}dV + \frac{fV|V|}{2gD}dx = 0 \quad \text{along} \quad \frac{dx}{dt} = \frac{a}{(1+k_3)} \quad \text{.....(8.4.11)}$$

$$C^-: \quad dH - \frac{a(1+k_3)}{g}dV - \frac{fV|V|}{2gD}dx = 0 \quad \text{along} \quad \frac{dx}{dt} = -a \quad \text{.....(8.4.12)}$$

A graphical representation of the calculation of conditions at x and at a time of t on the characteristics grid when using the Brunone *et al.* (1991) unsteady friction model is shown in Figure 8.1.

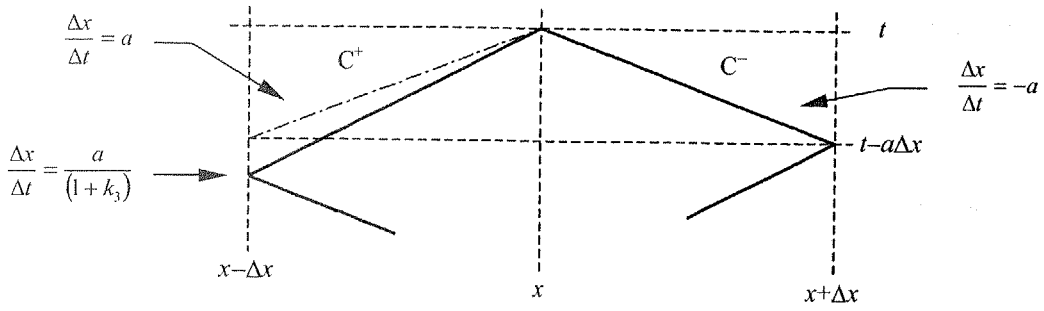

Figure 8.1 Characteristic Grid for Brunone *et al.* (1991) Unsteady Friction Model

Figure 8.1 and Eqs. 8.4.11 and 8.4.12 show the intrinsic asymmetry of the Brunone *et al.* (1991) unsteady friction model. Unlike the solution of the standard governing unsteady pipe flow equations (see Section 3.3.1) in which there are two equal but opposite disturbance propagation velocities (when the fluid velocity is neglected), when the Brunone *et al.* (1991) model is included there are two different disturbance propagation velocities. Correct implementation then requires interpolation when using a fixed grid. Wylie (1997) suggested that no interpolations are needed if the unsteady friction coefficient is neglected from Eq. 8.4.7; however, is neglecting the unsteady friction coefficient a worse approximation than neglecting the velocity? The approximation of dx/dt is investigated using $V \approx 1.0$ m/s, $a \approx 1000$ m/s and $k_3 \approx 0.03$, which are typical for water hammer. In neglecting the velocity, $dx/dt = V \pm a$ is approximated as $dx/dt = \pm a$ corresponding to $\approx 0.1\%$ error. In neglecting k_3, $dx/dt = a/(1 + k_3)$ is approximated as $dx/dt = a$ corresponding to $\approx 3.0\%$ error. The latter approximation overestimates the disturbance propagation velocity by an order of magnitude than the other, the effect of which is evident when modelling fast valve closure events. Treatment of unsteady friction included in the directional derivatives produces more accurate solutions than treatment of unsteady friction as an addition to steady friction. Differences between the two implementation methods are greatest for sharp transient events; however, for slower events, there is little difference between them. One useful property of treating unsteady friction as an addition to steady friction is that implementation is easier.

8.5 Extension of Unsteady Friction Models for Low Reynolds Number Turbulent Flows

The performance of unsteady friction models for turbulent flows has not been as satisfactory as that for laminar flows. Most of the experimental tests on turbulent flow were at large Reynolds number flows and use pure accelerations or decelerations (Shuy and Apelt, 1983), which are not typical of water hammer, because the study of water hammer events at these Reynolds numbers has a great risk of high pressures and column separation. At these high Reynolds number turbulent flows, the initial velocity profile is fairly uniform across the cross-section. On the other hand, for low Reynolds number turbulent flows, the velocity profile will be more pronounced as in laminar flows. Non-uniform velocity distributions require the use of a momentum correction factor β and an energy correction factor α. These factors account for the non-uniform velocity distribution by taking an integral of energy and momentum across the cross-section of the pipe. For unsteady flow at a low Reynolds number in turbulent flows, α and β effects become important. The following paragraph provides an explanation for these effects.

The simplified governing transient equations for pipe flow are well defined for 1D transient flows (Wylie and Streeter, 1993). An assumption made in the 1D unsteady pipe flow equations is that the velocity distribution is uniform. In real flows the velocity distribution is not uniform and only approaches the uniform distribution at high Reynolds numbers, making the calculation of energy and momentum inaccurate if the uniform-velocity assumption is used. There are two correction coefficients that can be applied to the 1D analysis to take account of non-uniform velocity distributions. The first is the kinetic energy correction coefficient α (also called the Coriolis coefficient) that corrects the velocity head $\alpha V^2/2g$,

$$\alpha = \frac{\int_A v^3 dA}{V^3 A} \qquad \text{.....(8.5.1)}$$

The second correction is the momentum correction coefficient β (also called the Boussinesq coefficient) that corrects the momentum flux $\beta \rho Q V$,

$$\beta = \frac{\int_A v^2 dA}{V^2 A} \qquad \text{.....(8.5.2)}$$

For a uniform velocity distribution as assumed in the one-dimensional flow these coefficients are equal to unity ($\alpha = \beta = 1$) and for steady laminar flow where the velocity profile is parabolic $\alpha = 2$ and $\beta = 4/3$. For strong transient flows β can attain higher values than the laminar maximum value (Betâmio de Almeida and Koelle, 1992), due to the more complex shaped velocity distributions experienced during an unsteady event (especially velocity reversal).

By examining the 1D unsteady momentum and energy equations with the corrective terms included, the effect of non-uniform velocity profiles can be seen (Betâmio de Almeida, 1981). The momentum correction factor (β) is included in the equation of motion,

$$\frac{1}{g}\frac{\partial V}{\partial t} + \frac{\beta V}{g}\frac{\partial V}{\partial x} + \frac{V^2}{g}\frac{\partial \beta}{\partial x} + \frac{\partial H}{\partial x} + J_S + J_U = 0 \quad \text{.....(8.5.3)}$$

Betâmio de Almeida (1981) derived Eq. 8.5.3 by studying the conservation of linear-momentum for a control volume and considering the steady state velocity distribution. An alternative derivation of this relationship is found in Appendix B.3. The friction is expressed using the total head loss per unit length term, *J*.

Energy relations for unsteady flows have been investigated by McInnis and Karney (1990), Karney (1990) and Silva-Araya and Chaudhry (1997) without correction factors. However, if the kinetic energy correction factor (α) and the momentum correction factor (β) are included, a different equation of motion derived from energy relationships is formed,

$$\frac{\beta}{g}\frac{\partial V}{\partial t} + \frac{\alpha V}{g}\frac{\partial V}{\partial x} + \frac{V}{2g}\frac{\partial \beta}{\partial t} + \frac{V^2}{2g}\frac{\partial \alpha}{\partial x} + \frac{\partial H}{\partial x} + J_S + J_U = 0 \quad \text{.....(8.5.4)}$$

Again, Betâmio de Almeida (1981) derived Eq. 8.5.4 by investigating the conservation of energy for a control volume and the steady state velocity distribution. A derivation of Eq. 8.5.4 is found in Appendix B.4. Betâmio de Almeida (1981) then equates Eqs. 8.5.3 and 8.5.4 using the convective derivative of the head, which is common to both expressions. The subtraction of Eq. 8.5.3 from Eq. 8.5.4 eliminates the convective derivative of the head. Solving for the total unsteady frictional head loss per unit length, *J*, produces an expression relating the total head loss per unit length to the steady and unsteady friction terms and the momentum and kinetic energy correction terms,

$$J = J_S + J_U + \frac{(\beta-1)}{g}\frac{\partial V}{\partial t} + \frac{V}{2g}\frac{\partial \beta}{\partial t} + \frac{(\alpha-\beta)V}{g}\frac{\partial V}{\partial x} + \frac{V^2}{2g}\frac{\partial \alpha}{\partial x} - \frac{V^2}{g}\frac{\partial \beta}{\partial x} \quad \text{.....(8.5.5)}$$

The remaining terms are lumped into the total head loss per unit length term, J, which is now comprised of three components. Two of these components are considered known (the steady, J_S, and unsteady friction, J_U).

$$J = J_S + J_U + J_M \quad \text{.....(8.5.6)}$$

where the last term contains the remaining terms created from the inclusion of the momentum and kinetic energy correction factors (denoted J_M) and is defined as

$$J_M = \frac{(\beta-1)}{g}\frac{\partial V}{\partial t} + \frac{V}{2g}\frac{\partial \beta}{\partial t} + \frac{(\alpha-\beta)V}{g}\frac{\partial V}{\partial x} + \frac{V^2}{2g}\frac{\partial \alpha}{\partial x} - \frac{V^2}{g}\frac{\partial \beta}{\partial x} \quad \text{.....(8.5.7)}$$

The convective terms (partial derivatives with respect to distance) are typically small compared to the other terms and can be ignored. For flows with small changes in acceleration the $\partial\beta/\partial t$ term is small, and when multiplied by the velocity, is even smaller compared to the first local acceleration term. Since there is a lack of experimental data to quantify the change in β with respect to time, it is neglected. Therefore, the momentum correction component J_M is approximated as

$$J_M = \frac{(\beta-1)}{g}\frac{\partial V}{\partial t} \quad \text{.....(8.5.8)}$$

J_M provides an inertial damping rather than a boundary shear damping in an unsteady event. It is the opinion of the author that mixing of the governing unsteady equations of motion derived using conservation of linear-momentum and energy is not a desirable thing to do. It is better to keep these concepts separate, in which case Eq. 8.5.8 can be thought of being derived from the conservation of energy only.

8.6 Previous Determination of Unsteady Friction Coefficients

Since the proposal of an unsteady friction model that depends on a coefficient multiplied by the local acceleration (Daily *et al.*, 1956; Carstens and Roller, 1959), there have been only a few analytic methods (other than experimental testing) proposed to deduce the unsteady friction coefficient k_3. The following sections review those previous analytic formulations for finding the unsteady friction coefficient for turbulent unsteady flows.

In order to revisit previous researchers' values of unsteady friction coefficients, it is important to see how previous coefficients relate to each other. The unsteady friction coefficients for Carstens and Roller (1959), Golia (1990) and Brunone *et al.* (1991) can all be approximately related to each other (models defined in Section 8.2). The Golia (1990) coefficient k_2 is related to Carstens and Roller's (1959) coefficient k_1 by

$$k_2 \approx \tfrac{1}{2}k_1 \quad \text{.....(8.6.1)}$$

The Brunone *et al.* (1991) coefficient k_3 has twice the effect of Golia's (1990) coefficient and the relationship is shown by

$$k_3 \approx \tfrac{1}{2}k_2 \quad \text{.....(8.6.2)}$$

Therefore k_3 is approximately one quarter of k_1.

Carstens and Roller (1959) were the first to offer an analytical method for the calculation of their unsteady friction coefficient k_1. Their analysis was based on an equality between a two-dimensional equation of motion and a one-dimensional equation of motion. Their coefficient k_1 is a function of n in universal power law for the velocity distribution,

$$\frac{v}{V} = \frac{(2n+1)(n+1)}{2n^2}\left(1-\frac{r}{r_0}\right)^{\frac{1}{n}} \quad \text{.....(8.6.3)}$$

where v = axial velocity at radial location r, V = average velocity, r = distance from the centre of the pipe and r_0 = radius of the pipe. Table 8.3 shows common values of k_1 for a given n.

Table 8.3 Carstens and Roller's k_1 Unsteady Friction Coefficient

n	7	8	9	10
k_1	0.449	0.391	0.346	0.310

The term n is dependent on the Reynolds Number of the average flow and has been determined experimentally (shown in Table 8.4; Schlichting, 1955).

Table 8.4 Dependence of n on Reynolds Number

R	4×10^3	2.3×10^4	1.1×10^5	1.1×10^6	2.0×10^6	3.2×10^6
n	6	6.6	7	8.8	10	10

By the use of interpolation techniques, Shuy and Apelt (1983) developed an expression for k_1 with respect to the Reynolds number. Their interpolation was based on Carstens and Roller's (1959) k_1 values. Their expression is

$$k_1 = 1.555 - 0.8522\mathbf{R}^{0.079} + 0.2043\mathbf{R}^{0.158} - 0.0183\mathbf{R}^{0.2367} \quad \text{.....(8.6.4)}$$

Brunone *et al.* (1995) detailed a method for determining a value for their unsteady friction coefficient k_3 experimentally using the magnitude of successive peaks in the measured pressure response from a transient event,

$$H_i - H_{i-1} = \frac{1}{1+k_3^2} \quad \text{.....(8.6.5)}$$

where H_i = head at peak i, H_{i-1} = head at a successive peak i–1. Eq. 8.6.5 was analytically established by Carravetta *et al.* (1992) and neglects steady state friction and thus the coefficient k_3 lumps together both unsteady and steady state friction. Eq. 8.6.5 indicates that the damping of the pressure peaks is arithmetic. Research, presented in Section 9.11 of this thesis shows, however, that the damping of pressure peaks is geometric and, therefore, casts doubt on the validity of Eq. 8.6.5. Recently Vardy and Brown (1996) derived an expression to analytically calculate k_3. Their approach was based on a simple idealisation of turbulent viscosity in a 2D axi-symmetric fluid flow model. Using the response of velocity profiles predicted by their model to the special case of uniformly accelerating flows, k_3 was determined as

$$k_3 = \tfrac{1}{2}\sqrt{C^*} \quad \text{.....(8.6.6)}$$

where C^* = the Vardy and Brown (1996) shear decay coefficient and k_3 = the Brunone *et al.* (1991) unsteady friction coefficient. The shear decay coefficient is $C^* = 0.00476$ for laminar flow and for turbulent flow and is a function of the Reynolds number,

$$C^* = \frac{7.41}{\mathbf{R}^{\kappa}} \quad \text{.....(8.6.7)}$$

where

$$\kappa = \log_{10}\left(\frac{14.3}{\mathbf{R}^{0.05}}\right) \quad \text{and} \quad \mathbf{R} = \frac{VD}{\nu} \quad \text{.....(8.6.8)}$$

For low Reynolds numbers, when flow is laminar, the coefficient C^* (and hence k_3) is high and for turbulent flow at higher Reynolds numbers it is much lower. Using this same analytical method applied to "ramp-like" velocity changes from one steady state to another, Vardy and Brown (1996) showed limits to the Brunone *et al.* (1991) formulation. Vardy and Brown (1996) predicted that the Brunone *et al.* (1991) unsteady friction model is capable of simulating high frequency events at high Reynolds numbers

rather than at lower frequency ones, thus suggesting that the Brunone *et al.* (1991) unsteady friction model may produce inaccurate results for slower events (with lower frequency oscillations). Eqs. 8.6.6 to 8.6.8 have been compared to experimental tests and, although there are only two such studies, a tentative match has been found. The experimental studies performed by Greco (1990) were taken from a best fit over a wide range of Reynolds numbers (4,000 to 60,000). The unsteady state friction coefficient (converted to the Brunone *et al.* (1991) k_3) was found to be 0.0852, which compares to Vardy and Brown's range of 0.0954 to 0.0352 (for Reynolds numbers of 4,000 to 60,000 respectively). Bergant and Simpson (1994) undertook another study in which water hammer experiments were performed at a Reynolds number of 5,600. The experimentally calibrated value for the unsteady state friction coefficient was determined as 0.085. Vardy and Brown's analytic formulae (Eqs. 8.6.6 to 8.6.8) were applied with a result of 0.0853 showing an almost exact match.

In the same paper by Vardy and Brown (1996) they state that the assumption of a constant C^* should be sufficiently accurate for practical applications. A constant C^* is found much in the same way as a constant friction factor. It is based upon the steady state conditions immediately preceding a transient event. The constant C^* was confirmed by Shuy (1985) using experimental data and resulting in the quote "...the solution does not tend to change if friction dissipation is based on the beginning of the time steps or based on average dissipation over the time steps..." thus confirming the use of constant friction coefficients based on conditions before a transient event.

A comparison of the Carstens and Roller (1959), Shuy and Apelt (1983) and Vardy and Brown (1996) methods for the calculation of the unsteady friction coefficient k_3 are shown in the Section 9.8.

8.7 Summary

This chapter provides an introduction to unsteady friction models. Various unsteady friction models are discussed and categorised to better understand the differences between them. Research presented in this thesis focuses on the Brunone *et al.* (1991)

unsteady friction model, which has produced good results for turbulent unsteady flow and for water hammer events. Also the Brunone *et al.* (1991) unsteady friction model is suited to large network analysis due to its simplicity and speed. The next chapter deals with the definition of new models based on the Brunone *et al.* (1991) unsteady friction model. Also the coefficients needed for their implementation are considered.

Chapter 9

New Unsteady Friction Models and Coefficients

9.1 Introduction

The previous chapter demonstrated some of the different methods used to model unsteady flow events for both laminar and turbulent flow regimes. This chapter presents extensions to unsteady friction models for unsteady events that occur for low Reynolds number turbulent flows. This study is based on the modified Brunone *et al.* (1991) unsteady friction model. The new models use energy and momentum concepts from derivations that include the velocity distribution to infer extra terms needed to describe unsteady friction in the familiar one dimensional water hammer model. A method is presented to include the new unsteady friction models in the method of characteristics in a way that reduces numerical error. This chapter also investigates methods for the quantification of unsteady friction coefficients, which is important for engineering design where experimental verification of an unsteady friction coefficient is not possible. A comparison of the equations of motion for one-dimensional (1D) and two-dimensional (2D) cases gives rise to a simple formula for unsteady friction coefficients in smooth pipes. That formula is then extended for unsteady friction coefficients in rough pipes as well. Comments are made on the effectiveness of the different unsteady friction models and coefficients for turbulent unsteady flows. Unsteady friction models and unsteady friction coefficient formulae produced in this chapter are verified experimentally in Chapter 11.

9.2 Investigation of the Brunone *et al.* (1991) Unsteady Friction Model

The Brunone *et al.* (1991) unsteady friction model has been shown to work well under certain types of experimental tests. These tests have consisted of a downstream valve closure. The testing of unsteady friction models using purely accelerating and decelerating flows produced models that were only applicable to those type of tests, and by extension the testing used for the validation of the Brunone *et al.* (1991) unsteady friction model may have produced a model applicable only to the downstream valve closure test. In this section a complete range of possible flow cases is discussed. The Brunone *et al.* (1991) unsteady friction model is then applied to each of these conditions. The Brunone *et al.* (1991) model fails in some of these flow cases and a generalisation is proposed to correct it. Finally, a complete view of the performance of the Brunone *et al.* (1991) model is shown with the use of theoretical flow events.

9.2.1 Introduction of 8 Transient Flow Conditions

The head loss for a steady flow is proportional to the square of the velocity,

$$h_f = \frac{fLV^2}{2gD} \qquad (9.2.1)$$

If the velocity, V, is not always positive,

$$h_f = \frac{fLV|V|}{2gD} \qquad (9.2.2)$$

produces the correct sign for the head loss.

Whereas there are two conditions, flow in the positive and negative directions, for the steady state flow, eight conditions exist for unsteady state flow. The eight unsteady conditions are flow in the positive and negative directions, acceleration and deceleration and propagation of the pressure wave in the positive and negative x directions. These eight unsteady conditions can be depicted on a theoretical method of characteristics grid (Figure 9.1). The calculation of an internal node (at distance x and time t) is shown on

each flow condition. The calculation of the partial derivatives $\partial V/\partial t$ and $\partial V/\partial x$ are needed for the Brunone *et al.* (1991) unsteady friction model and are circled. Theoretical velocities are shown above the nodes.

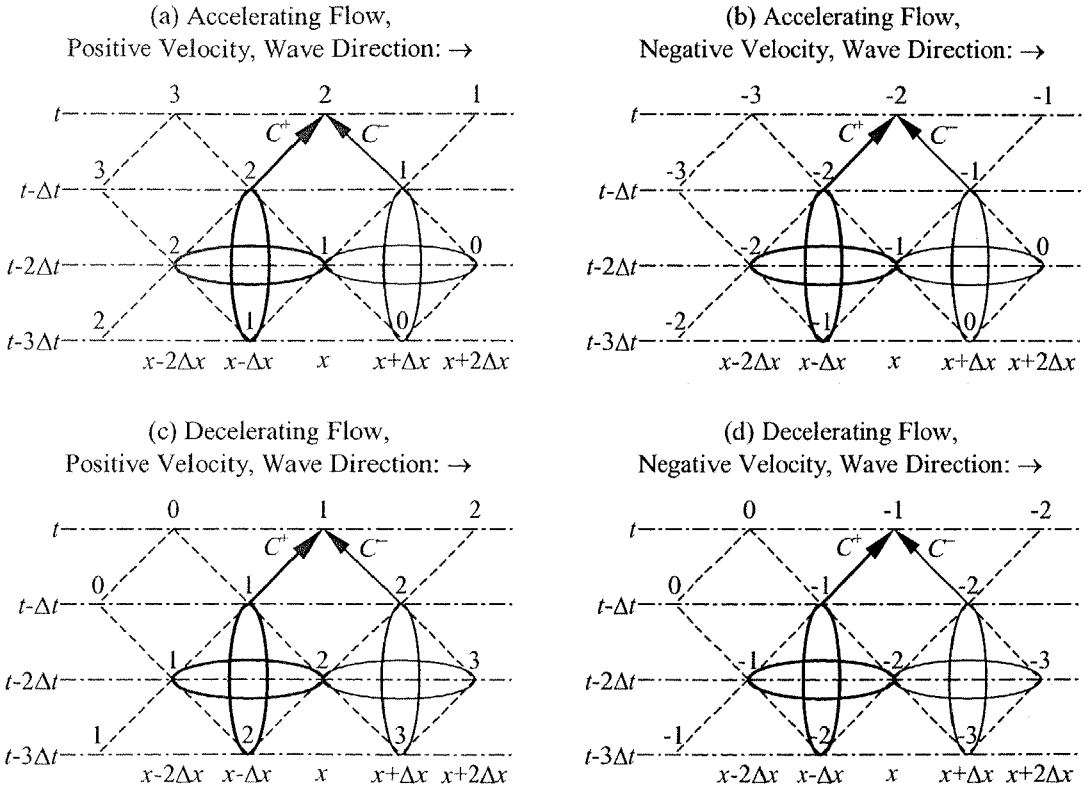

Figure 9.1 The 8 Unsteady Flow Conditions

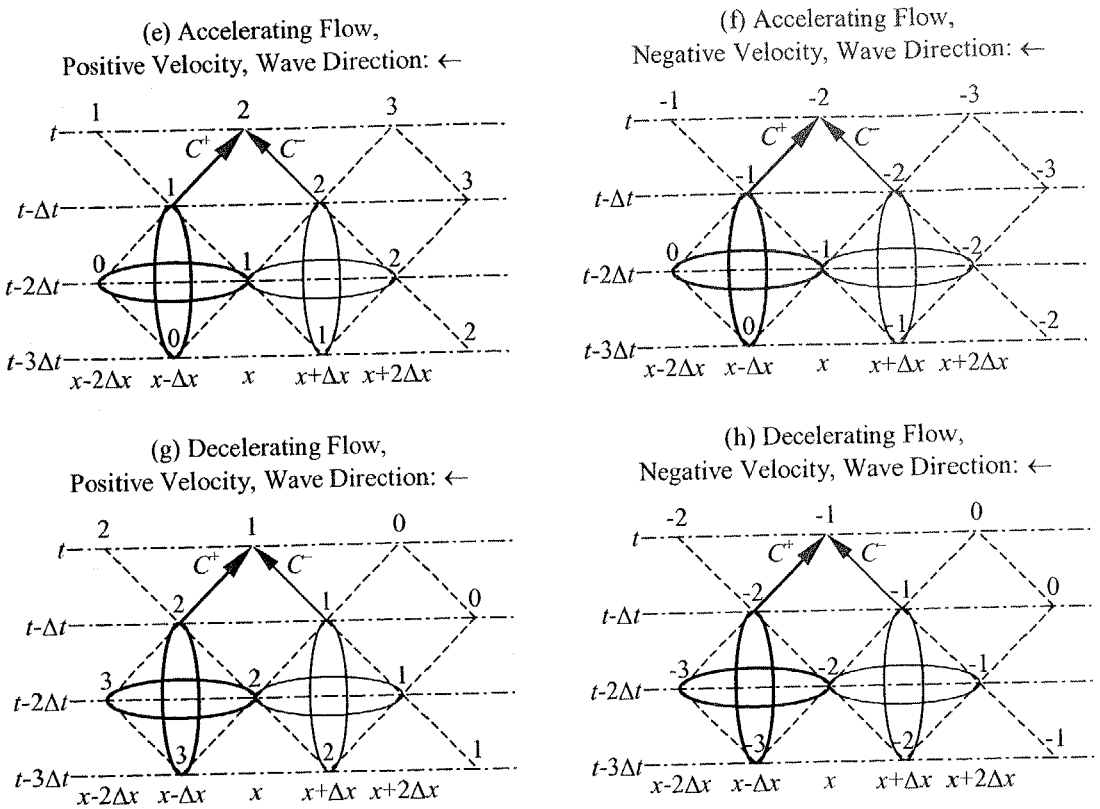

Figure 9.1 The 8 Unsteady Flow Conditions (continued)

If $V(\partial V/\partial t) > 0$ then the fluid is accelerating, if $V(\partial V/\partial t) < 0$ then decelerating. If $(\partial V/\partial t)(\partial V/\partial x) > 0$ then the wave is propagating in the negative x direction, if $(\partial V/\partial t)(\partial V/\partial x) < 0$ in the positive x direction. The meaning of each diagram in Figure 9.1 is summarised in Table 9.1. These unsteady flow conditions can be used in the next section to describe the behaviour of various unsteady friction models.

Table 9.1 Identification of Unsteady Flow Conditions

	Positive Velocity	Negative Velocity
Acceleration, Positive Wave Direction	(a)	(b)
Deceleration, Positive Wave Direction	(c)	(d)
Acceleration, Negative Wave Direction	(e)	(f)
Deceleration, Negative Wave Direction	(g)	(h)

The unsteady flow conditions are used in the following section to test the applicability of the Brunone *et al.* (1991) unsteady friction model over a greater number possible transient scenarios.

9.2.2 *Generalisation of the Brunone et al. (1991) Unsteady Friction Model*

In the original Brunone *et al.* (1991) formulation the unsteady friction correction produces incorrect results when flow is negative with respect to the positive x direction while producing correct results when flow is in the positive x direction. To understand why this occurs, it is necessary to examine the Brunone *et al.* (1991) formulation under all of the different scenarios concerned with acceleration and deceleration of a fluid. The eight different cases are: acceleration, deceleration with flow positive and negative with respect to the positive x direction, and finally the pressure wave travelling in the positive and negative direction with respect to the positive x direction. Each of these cases are shown in Figure 9.1 (positive direction flow on left, negative direction flow on right). These figures depict a single calculation along C^+ and C^- characteristic lines on the characteristic grid. The velocity is shown above each point on the grid. The values used for the calculation of the spatial and temporal partial derivatives are ringed and are only considered for the C^+ characteristic to illustrate their behaviour.

The different acceleration-based unsteady friction models as defined in Section 8.2 were used to calculate the total unsteady headloss per unit length, J. The term can be thought of as consisting of two parts, J_S the steady friction component and J_U the unsteady friction component and is restated as

$$J = J_S + J_U \qquad (9.2.3)$$

Before the Brunone *et al.* (1991) unsteady friction model is analysed, it is useful to investigate the Golia (1990) model. Implementation of this model has shown similar results to the Brunone *et al.* (1991) model with the exception that the Golia (1990) model does not incorrectly predict conditions for flow with negative velocities. The Golia (1990) model is restated as

$$J_U = \delta \frac{k_2}{g} \frac{\partial V}{\partial t} \qquad (9.2.4)$$

where the Heaviside operator (δ) is defined as

$$\delta = \begin{cases} 1 & \text{if} \quad V \dfrac{\partial V}{\partial t} \geq 0 \\ 0 & \text{if} \quad V \dfrac{\partial V}{\partial t} < 0 \end{cases} \qquad (9.2.5)$$

A sign table may be created by observing the sign of the unsteady proportion of the frictional dissipation, J. To begin with a sign table is made for the Golia (1990) unsteady friction model (Table 9.2).

Table 9.2 Sign Table for Golia (1990) Model

		Positive Velocity	Negative Velocity
Unsteady Friction Component		$\delta\frac{\partial V}{\partial t}$	$\delta\frac{\partial V}{\partial t}$
Positive Wave Direction	Acceleration	Positive	Negative
	Deceleration	Zero	Zero
Negative Wave Direction	Acceleration	Positive	Negative
	Deceleration	Zero	Zero

The original Brunone *et al.* (1991) unsteady friction model was created to remove the need for the Heaviside used by Golia (1990) while still producing the same results. The original Brunone *et al.* (1991) unsteady friction model is restated as

$$J_U = \frac{k_3}{g}\left(\frac{\partial V}{\partial t} - a\frac{\partial V}{\partial x}\right) \quad \text{.....(9.2.6)}$$

Application of the Brunone *et al.* (1991) formulation to each of the cases results in a table of signs (Table 9.3). In half of the cases the formulation returns the correct signs of the convective acceleration (acceleration, wave direction positive and deceleration, wave direction negative). The cases that show incorrect signs (acceleration, wave direction negative and deceleration, wave direction positive) have either no cancellation where there should some or vice-versa.

Table 9.3 Sign Table for Original Brunone *et al.* (1991) Model

		Positive Velocity		Negative Velocity	
Unsteady Friction Model Component		$\frac{\partial V}{\partial t}$	$-a\frac{\partial V}{\partial x}$	$\frac{\partial V}{\partial t}$	$-a\frac{\partial V}{\partial x}$
Positive Wave Direction	Acceleration	Positive	Positive	Negative	Negative
	Deceleration	Negative	Negative	Positive	Positive
Negative Wave Direction	Acceleration	Positive	Negative	Negative	Positive
	Deceleration	Negative	Positive	Positive	Negative

To address the problem with regards to the sign of the convective term in the Brunone *et al.* (1991) formulation, a modification was made. The modification ensures that the unsteady friction magnitude is negligible during deceleration and substantial during acceleration. Also when the fluid is accelerating, the sign of the unsteady friction term

is such that the shear stress acts in the opposite direction to the flow (thus damping occurs). These modifications lead to

$$J_U = \frac{k_3}{g}\left(\frac{\partial V}{\partial t} + a\phi_V\left|\frac{\partial V}{\partial x}\right|\right) \quad \text{.....(9.2.7)}$$

where the absolute of the convective acceleration term has been multiplied by an operator ϕ_V that depends on the sign of the velocity with respect to the positive x direction. The velocity sign operator is defined as

$$\phi_V = \begin{cases} +1 & \text{if} \quad V \geq 0 \\ -1 & \text{if} \quad V < 0 \end{cases} \quad \text{.....(9.2.8)}$$

This modified formulation produces the correct sign in all eight possible conditions (Table 9.4).

Table 9.4 Sign table for Modified Brunone *et al.* (1991) model

Unsteady Friction Model Component		Positive Velocity		Negative Velocity	
		$\frac{\partial V}{\partial t}$	$a\phi_V\left\|\frac{\partial V}{\partial x}\right\|$	$\frac{\partial V}{\partial t}$	$a\phi_V\left\|\frac{\partial V}{\partial x}\right\|$
Positive Wave Direction	Acceleration	Positive	Positive	Negative	Negative
	Deceleration	Negative	Positive	Positive	Negative
Negative Wave Direction	Acceleration	Positive	Positive	Negative	Negative
	Deceleration	Negative	Positive	Positive	Negative

9.2.3 Introduction of 8 Simple Transient Flow Events

The eight unsteady flow conditions only apply to monotonically accelerating or decelerating flows. Real water hammer events contain combinations of the unsteady flow conditions. The monotonic nature of the eight unsteady flow conditions can mask problems with potential unsteady friction formulations. It becomes more useful, in a practical sense, to define some basic set of unsteady events by examining a simple system comprised of a single pipeline between two reservoirs. A valve, located next to each reservoir, initialises the transient event. Eight different types of unsteady events are visualised in Figure 9.2, in which V_0 is the initial velocity (before a transient event) and V_f is the final velocity (after a transient event). The initial hydraulic grade lines are shown between each tank.

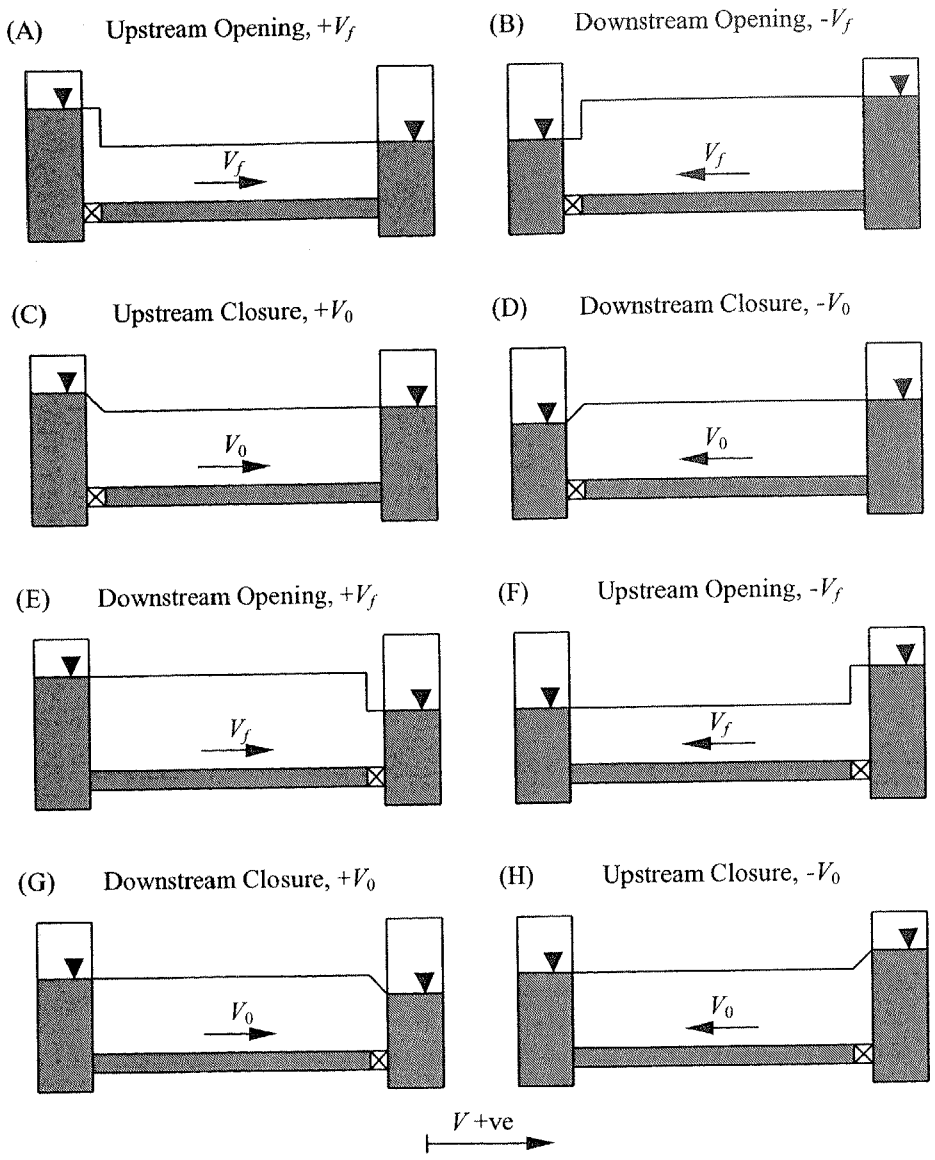

Figure 9.2 The 8 Simple Unsteady Flow Events

These events can be related to the eight unsteady flow conditions by imagining the first pressure rise or fall after the valve is either closed or opened. The upper case letters (A) to (G) in Figure 9.2 correspond to lower case letters (a) to (g) in Figure 9.1 and Table 9.1. Events (A) & (F), (B) & (E), (C) & (H) and (D) & (G) are mirror images of each other with respect to the direction of flow, thus reducing to four the number of distinct cases. These eight unsteady flow events are used in the next section to check the performance of the Brunone *et al.* (1991) unsteady friction model.

Figures depicting each transient event type are show in Appendix B.2. These show the pressure and flow changes during each event for periods of L/a. For each of these

periods a different unsteady flow condition dominates. Table 9.5 shows the unsteady flow conditions during each period of L/a for each unsteady flow event.

Table 9.5 Characterisation of Unsteady Flow Event Periods

	Unsteady Flow Event							
	U/S Opening $+V_f$	D/S Opening $-V_f$	U/S Closure $+V_0$	D/S Closure $-V_0$	D/S Opening $+V_f$	U/S Opening $-V_f$	D/S Closure $+V_0$	U/S Closure $-V_0$
Period	(A)	(B)	(C)	(D)	(E)	(F)	(G)	(H)
(i)	*ss*	*ss*	*ss*	*ss*	*ss*	*ss*	*ss*	*ss*
(ii)	(a)	(b)	(c)	(d)	(e)	(f)	(g)	(h)
(iii)	(e)	(f)	(f)	(e)	(a)	(b)	(b)	(a)
(iv)	(a)	(b)	(d)	(c)	(e)	(f)	(h)	(g)
(v)	(e)	(f)	(e)	(f)	(a)	(b)	(a)	(b)
(vi)	(a)	(b)	(c)	(d)	(e)	(f)	(g)	(h)

ss = initial steady state conditions

Each event has a sequence of unsteady flow conditions that does not change. The events can also be paired up with other events that use the same sequence but start at different positions in the sequence. The pairs of events are (A) & (E), (B) & (F), (C) & (D) and (G) & (H).

A result from observing the different unsteady flow conditions during the different unsteady flow events is that the resonant period (also called the natural period) of the pipeline is dependent on the boundary conditions. For those cases where the boundary conditions are a closed valve and a reservoir (events (C), (D), (G) and (H)) the resonant period is $4L/a$. For the other events where both boundary conditions are reservoirs (events (A), (B), (E) and (F)) the resonant period is $2L/a$.

Unsteady events using the Brunone *et al.* (1991) model that contain the unsteady flow conditions (c), (d), (e) and (f) produce incorrect results. Events (C) and (D) produce amplification rather than damping because they contain the unsteady flow conditions (c), (d), (e) and (f) (see Table 9.5) of which (c) and (d) produce amplification when using the Brunone *et al.* (1991) unsteady friction model (see Table 9.3, $(\partial V/\partial t - a\partial V/\partial x)$ has incorrect sign). Unsteady flow events (A), (B), (E) and (F) experience no damping or amplification effect from the Brunone *et al.* (1991) unsteady friction model because there is no contribution from the $a\partial V/\partial x$ term that cancels with itself when alternating between unsteady flow conditions (a) and (e) for unsteady flow events (A) and (E) and unsteady flow conditions (b) and (f) for unsteady flow events (B) and (F). The

remaining $\partial V/\partial t$ term left after the cancellation of $a\partial V/\partial x$ produces a change in phase of the pressure oscillations with no amplitude damping (see Sections 9.3.5 and 9.4 for the effect of the $\partial V/\partial t$ term by itself).

9.2.4 *Performance of Brunone et al. (1991) Unsteady Friction Model Under Simple Unsteady Events*

The original Brunone *et al.* (1991) unsteady friction model has been historically tested only on the downstream valve closure case, which is the case most useful for water hammer analysis. That case corresponds to one of the 8 simple unsteady flow events (event (G) in Figure 9.2) and no work has been performed to check results for the other seven unsteady flow events. Section 9.2.2 suggests that the original Brunone *et al.* (1991) model may have problems with some unsteady flow conditions and Section 9.2.3 suggests it may fail some of the simple unsteady events. Numerical results for the original Brunone *et al.* (1991) model are shown in Figure 9.3 using a simple pipeline. Comparisons are made against numerical results using quasi-steady friction only.

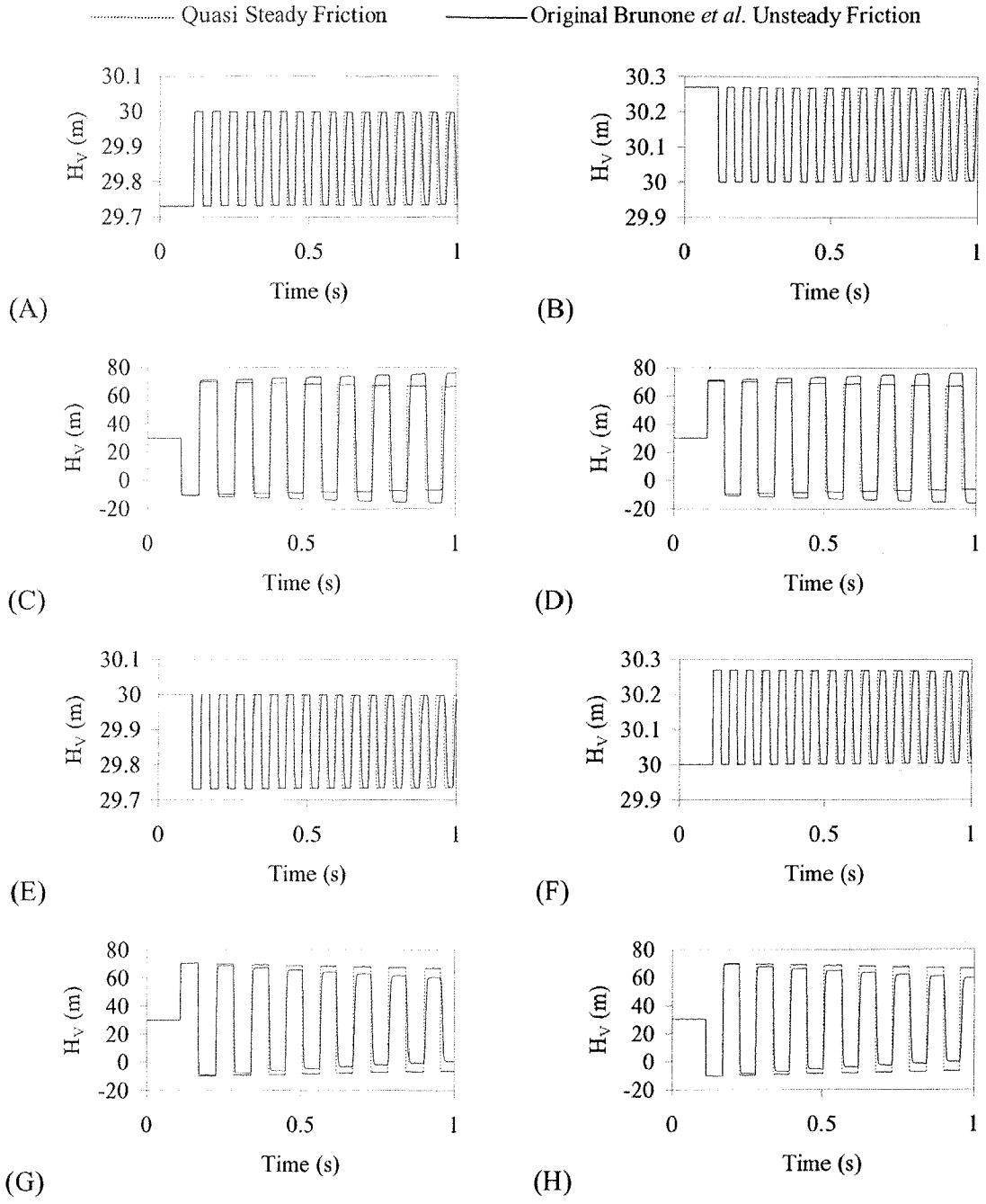

Figure 9.3 Numerical Testing of Original Brunone *et al.* (1991) Formulation

The results show plausible behaviour for cases (G) and (H). In cases (C) and (D), however, the pressure oscillations are amplified with time, implying that the unsteady friction model contains the wrong sign (as predicted, see previous section). Events (A), (B), (E) and (F) show a shift in the phase only (with a little rounding of the shape of the peaks, also predicted, see previous section). Results for these tests need to be verified experimentally. Figure 9.4 shows the performance of the modified Brunone *et al.* (1991) unsteady friction formulation, as performed in Section 9.2.2.

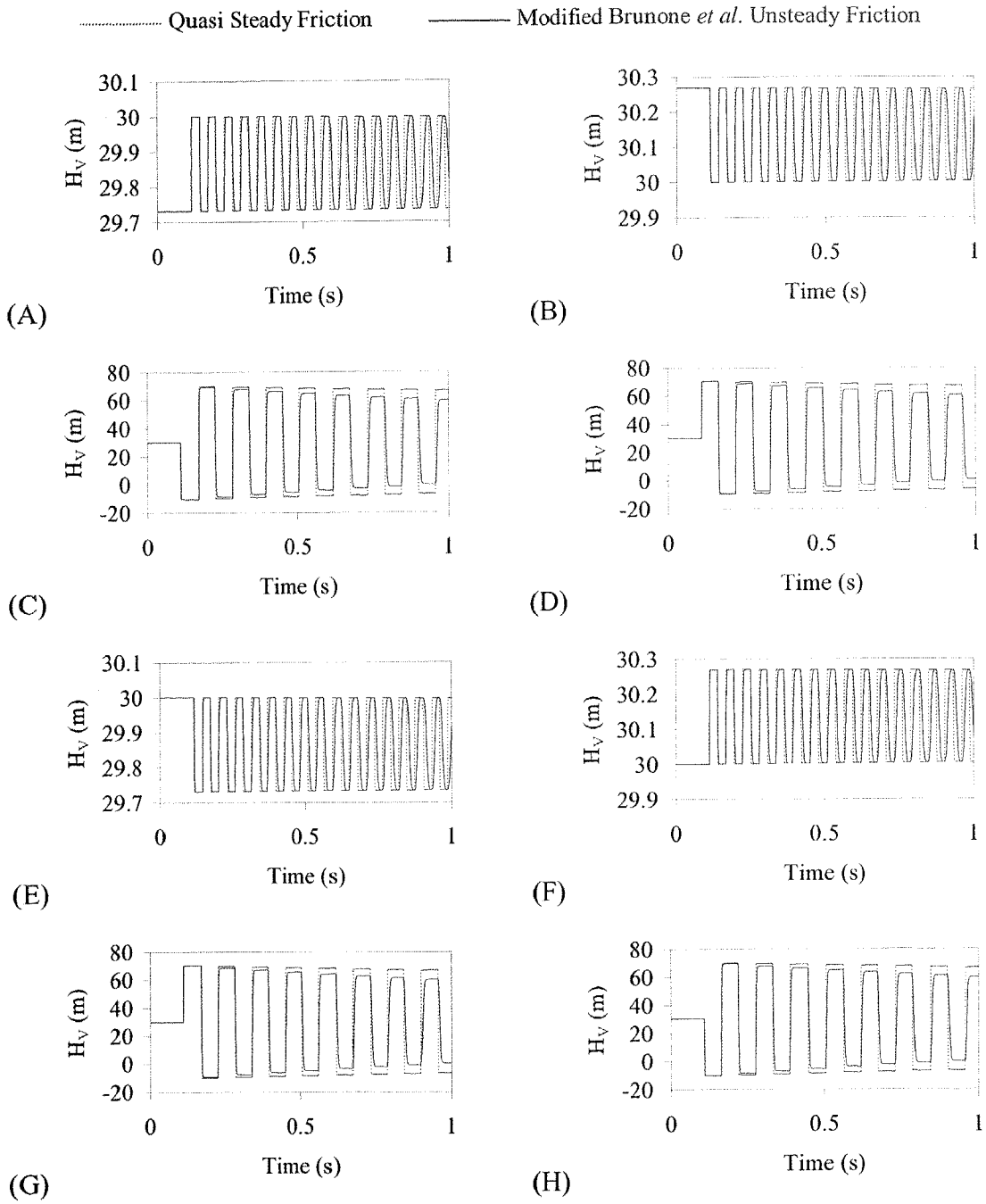

Figure 9.4 Numerical Testing of Modified Brunone *et al.* (1991) Formulation

In contrast to the original Brunone *et al.* (1991) model performance, the modified Brunone *et al.* (1991) model shows damping (rather than amplification) for unsteady events (C) and (D). The performance for unsteady events (A), (B), (E) and (F) remains unchanged for the modified Brunone *et al.* model (as expected).

9.2.5 Summary of Transient Investigation

This section has investigated the Brunone *et al.* (1991) unsteady friction model and found some problems. Tools that have been introduced to achieve this are the 8 unsteady flow conditions and the 8 unsteady flow events. These define cases that any unsteady model must produce adequate results for. A modification has been applied to the Brunone *et al.* (1991) model to fix some problems. Both models were tested numerically with the modified Brunone *et al.* (1991) model producing better results for unsteady events where the original model produces bad results. Ultimately these numerical results for each model must be tested against experimental data.

9.3 New Unsteady Friction Models for Turbulent Flow

Extensions to current turbulent unsteady friction models incorporated in the water hammer equations are described subsequently. The modified Brunone *et al.* (1991) unsteady friction model agrees with experimental data for high Reynolds number transient events. It is used as a basis for extensions developed in this thesis, which include momentum correction factor effects and the introduction of a variable unsteady friction factor that is dependent on instantaneous conditions. Five new unsteady friction models are discussed: a modified Brunone *et al.* (1991) model, a new turbulent k_3 & k_M model, a new variable k_3 model, a new variable k_3 & k_M model and a new turbulent k_A & k_P model.

9.3.1 A Modified Brunone et al. (1991) Model

The basic model utilised for simulating turbulent flows is the Brunone *et al.* (1991) unsteady friction model. However, the modified version is used as a basis for the following proposed models. Carstens and Roller (1959) suggested that turbulent flow (unlike laminar flow) does not depend on a time history of the flow conditions due to the strong lateral diffusion of the turbulent eddies, thus eliminating the dependence of the velocity profile on the flow history. This hypothesis allows instantaneous properties

to be used for the calculation of unsteady friction. The modified Brunone *et al.* (1991) model (from Section 9.2.2) is restated as

$$J = J_S + \frac{k_3}{g}\left(\frac{\partial V}{\partial t} + a\phi_V\left|\frac{\partial V}{\partial x}\right|\right) \quad \text{.....(9.3.1)}$$

The sign operator, ϕ_V, is equal to +1 for $V \geq 0$ and −1 for $V < 0$. The pre-modified version of this model has been shown to work well for high Reynolds number flows (Greco, 1990) but not as well for low Reynolds number turbulent flows (Bergant *et al.*, 1999).

9.3.2 A Turbulent k_3 & k_M Model

The extension of the Brunone *et al.* (1991) model includes an inertial term to compensate for the non-uniform velocity distribution experienced at low Reynolds number turbulent flows. Section 8.5 details reasons why the momentum correction factor plays a part in unsteady flows. The new model is

$$J = J_S + \frac{k_3}{g}\left(\frac{\partial V}{\partial t} + a\phi_V\left|\frac{\partial V}{\partial x}\right|\right) + \frac{k_M}{g}\frac{\partial V}{\partial t} \quad \text{.....(9.3.2)}$$

where the momentum correction coefficient, k_M, is

$$k_M = \beta - 1 \quad \text{.....(9.3.3)}$$

in which β is the standard momentum correction factor (Eq. 8.5.8). The value of k_M is the value at the initial steady state flow. This new model is referred to as the k_3 & k_M model. It maintains constant coefficients k_3 and k_M although there is no reason why they should be constant during a transient event. The next sections propose variations to the Modified Brunone *et al.* (1991) and the k_3 and k_M unsteady friction models where values of k_3 and k_M are dependent on the instantaneous Reynolds number.

9.3.3 A Variable k_3 Model

Situations that begin from stationary flows do not provide useful values of the unsteady friction coefficients (being based on initial conditions). A variable k model defines the unsteady friction coefficient in terms of the Reynolds number of the instantaneous flow. Vardy and Brown (1996) proposed a relationship between the unsteady friction factor

and the Reynolds number. Substituting $k_3 = k_3(\mathbf{R})$ into the modified Brunone *et al.* (1991) (shown in Eq. 9.3.1) model gives

$$J = J_S + \frac{k_3(\mathbf{R})}{g}\left(\frac{\partial V}{\partial t} + a\phi_V\left|\frac{\partial V}{\partial x}\right|\right) \quad \text{.....(9.3.4)}$$

9.3.4 A Variable k_3 & k_M Model

Eq. 9.3.2 can also be modified to use variable coefficients,

$$J = J_S + \frac{k_3(\mathbf{R})}{g}\left(\frac{\partial V}{\partial t} + a\phi_V\left|\frac{\partial V}{\partial x}\right|\right) + \frac{k_M(\mathbf{R})}{g}\frac{\partial V}{\partial t} \quad \text{.....(9.3.5)}$$

where $k_3(\mathbf{R})$ and $k_M(\mathbf{R})$ = unsteady friction coefficients k_3 and k_M as a function of the Reynolds number of the instantaneous flow.

9.3.5 A Turbulent k_A & k_P Model

The k_3 & k_M unsteady friction model can be separated into two independent components (Eq. 9.3.2). The first component controls the damping of the amplitude of the pressure oscillations. The amplitude damping factor is denoted k_A. The second component controls the phase of the pressure oscillations by means of k_P,

$$J = J_S + \phi_V\frac{k_A}{g}\left|\frac{dV}{dt}\right| + \frac{k_P}{g}\frac{dV}{dt} \quad \text{.....(9.3.6)}$$

The two coefficients are related to the coefficients in the Brunone *et al.* (1991) model with a momentum correction coefficient,

$$k_A = k_3 \quad \text{.....(9.3.7)}$$

$$k_P = k_3 + k_M \quad \text{.....(9.3.8)}$$

If the two coefficients are equal (i.e. $k_A = k_P$) then the k_A & k_P model becomes equivalent to the modified Brunone *et al.* (1991) model. It can handle inadequacies proposed by Vardy and Brown (1996) where the Brunone *et al.* (1991) model produced good results for fast valve closure events and poor results (out of phase) for slow valve closure events. Brunone and Greco (1990) have also observed out-of-phase results for the

Golia (1990) model. The k_A & k_P model specifies Eq. 9.3.8 for fast events and $k_P = 0.0$ for slow events.

9.4 A Solution for the k_A & k_P Unsteady Friction Model

As described in Section 8.4, there are two methods to implement an unsteady friction model; these are (1) treated as an addition to steady friction and (2) included in the directional derivatives (in the method of characteristics). Implementation of unsteady friction included in the directional derivative is not usually performed. Similar to the steady friction, the unsteady friction is treated as additional Darcy-Weisbach friction (Brunone *et al.*, 1991; Bergant and Simpson, 1994). Bughazem and Anderson (1996) first performed implementation of the Brunone *et al.* (1991) model included in the directional derivative. The result was greater accuracy, but it did not correctly model the transient events shown in Section 9.2.

For the implementation of the k_A & k_P model, consider the governing equations of motion and continuity,

$$\frac{\partial H}{\partial x}+\frac{1}{g}\frac{dV}{dt}+\frac{fV|V|}{2gD}+\frac{k_P}{g}\frac{dV}{dt}+\phi_V\frac{k_A}{g}\left|\frac{dV}{dt}\right|=0 \qquad (9.4.1)$$

$$\frac{dH}{dt}+\frac{a^2}{g}\frac{\partial V}{\partial x}=0 \qquad (9.4.2)$$

where ϕ_V is a sign operator dependent on the instantaneous velocity,

$$\phi_V=\begin{cases}+1 & \text{if} \quad V\geq 0\\ -1 & \text{if} \quad V<0\end{cases} \qquad (9.4.3)$$

Three different implementations of the k_A & k_P unsteady friction model are presented. They are the implementation of the k_A & k_P model (1) treated as an addition to the steady friction, (2) the k_P term included in the direction derivatives only and (3) totally included in the directional derivatives, as shown in Sections B.5, B.6 and B.7 in Appendix B.

The compatibility equations produced when treating the k_A & k_P model as an addition to steady friction are

$$(H_P - H_B) + \frac{a}{g}(V_P - V_A) + \frac{f\Delta x}{2gD}\frac{(V_A + V_P)}{2}\frac{|V_A + V_P|}{2} + \frac{k_P}{2g}\left(\frac{dV_A}{dt} + \frac{dV_P}{dt}\right)\Delta x + \phi_V^+ \frac{k_A}{2g}\left|\frac{dV_A}{dt} + \frac{dV_P}{dt}\right|\Delta x = 0 \quad \text{....(9.4.4)}$$

$$(H_P - H_B) - \frac{a}{g}(V_P - V_B) - \frac{f\Delta x}{2gD}\frac{(V_B + V_P)}{2}\frac{|V_B + V_P|}{2} - \frac{k_P}{2g}\left(\frac{dV_B}{dt} + \frac{dV_P}{dt}\right)\Delta x - \phi_V^- \frac{k_A}{2g}\left|\frac{dV_B}{dt} + \frac{dV_P}{dt}\right|\Delta x = 0 \quad \text{.....(9.4.5)}$$

where the velocity sign operator (ϕ_V) for each compatibility equation is

$$\phi_V^+ = \begin{cases} +1 & \text{if} \quad V_A + V_P \geq 0 \\ -1 & \text{if} \quad V_A + V_P < 0 \end{cases} \quad \& \quad \phi_V^- = \begin{cases} +1 & \text{if} \quad V_B + V_P \geq 0 \\ -1 & \text{if} \quad V_B + V_P < 0 \end{cases} \quad \text{.....(9.4.6)}$$

Eqs. 9.4.4 and 9.4.5 are valid along the characteristic lines of slope $\Delta x/\Delta t = +a$ and $\Delta x/\Delta t = -a$ respectively (Figure 9.5).

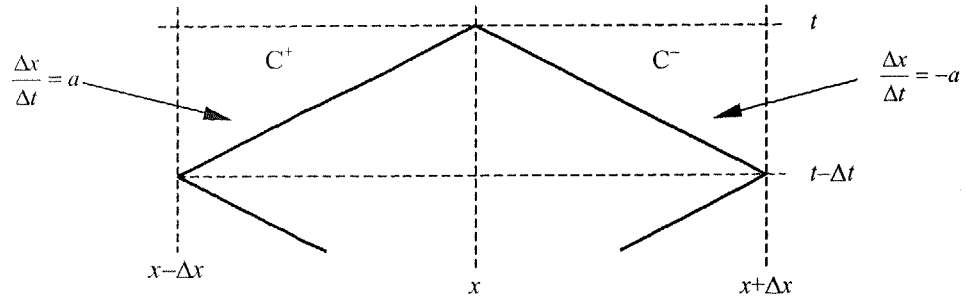

Figure 9.5 Characteristic Lines for the Analytic Solution of k_A & k_P Model (Treated as an Addition to Steady Friction)

The compatibility equations produced when including the k_P term in the directional derivatives only are

$$(H_P - H_A) + \frac{a\sqrt{1+k_P}}{g}(V_P - V_A) + \frac{f\Delta x}{2gD}\frac{(V_A + V_P)}{2}\frac{|V_A + V_P|}{2} + \phi_V^+ \frac{k_A}{2g}\left|\frac{dV_A}{dt} + \frac{dV_P}{dt}\right|\Delta x = 0 \quad \text{.....(9.4.7)}$$

$$(H_P - H_B) - \frac{a\sqrt{1+k_P}}{g}(V_P - V_B) - \frac{f\Delta x}{2gD}\frac{(V_B + V_P)}{2}\frac{|V_B + V_P|}{2} - \phi_V^- \frac{k_A}{2g}\left|\frac{dV_B}{dt} + \frac{dV_P}{dt}\right|\Delta x = 0 \quad \text{.....(9.4.8)}$$

where the velocity sign operator in the compatibility equation is given by Eq. 9.4.6. Eqs. 9.4.7 and 9.4.8 are valid along characteristic lines of slope $\Delta x/\Delta t = +a/\sqrt{1+k_P}$ and

$\Delta x/\Delta t = -a/\sqrt{1+k_P}$ respectively (Figure 9.6). The phase term (containing k_P) affects the characteristic line slope (the amplitude term, containing k_A, does not).

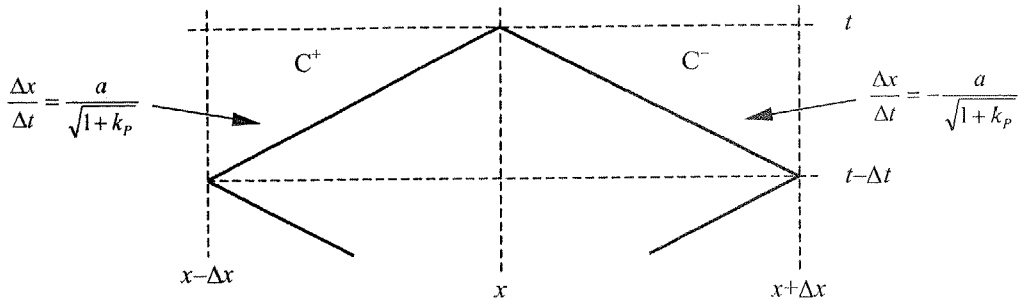

Figure 9.6 Characteristic Lines for the Analytic Solution of k_A & k_P Model (The k_P Term Included in the Directional Derivatives Only)

The compatibility equations produced when including the k_A & k_P model in the directional derivatives are

$$(H_P - H_A) + \frac{a\sqrt{1+k_P+\phi_A^+ k_A}}{g}(V_P - V_A) + \frac{f\Delta x}{2gD}\frac{(V_A+V_P)}{2}\frac{|V_A+V_P|}{2} = 0 \quad \text{.....(9.4.9)}$$

$$(H_P - H_B) - \frac{a\sqrt{1+k_P+\phi_A^- k_A}}{g}(V_P - V_B) - \frac{f\Delta x}{2gD}\frac{(V_B+V_P)}{2}\frac{|V_B+V_P|}{2} = 0 \quad \text{.....(9.4.10)}$$

where the acceleration sign operator (ϕ_A) for each compatibility equation is

$$\phi_A^+ = \begin{cases} +1 & \text{if } |V_P| \geq |V_A| \\ -1 & \text{if } |V_P| < |V_A| \end{cases} \quad \& \quad \phi_A^- = \begin{cases} +1 & \text{if } |V_P| \geq |V_B| \\ -1 & \text{if } |V_P| < |V_B| \end{cases} \quad \text{.....(9.4.11)}$$

Eqs. 9.4.9 and 9.4.10 are valid along the characteristic lines of slope $\Delta x/\Delta t = +a/\sqrt{1+k_P+\phi_A k_A}$ and $\Delta x/\Delta t = -a/\sqrt{1+k_P+\phi_A k_A}$ respectively. The slope of the characteristic lines when totally introducing the k_A & k_P model in the directional derivatives changes depending on whether the fluid is accelerating or decelerating along the characteristic line. The slope of the characteristic line for accelerating flows is $\Delta x/\Delta t = \pm a/\sqrt{1+k_P+k_A}$ and for decelerating flows is $\Delta x/\Delta t = \pm a/\sqrt{1+k_P-k_A}$. Figure 9.7 illustrates the different characteristic line slopes.

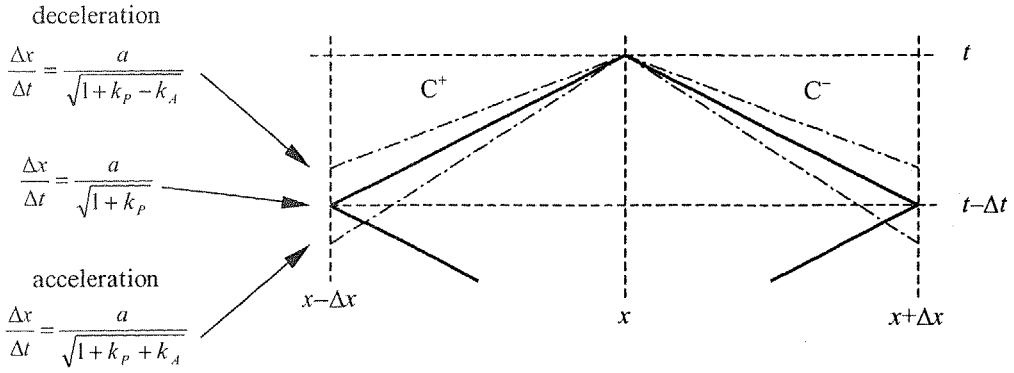

Figure 9.7 Characteristic Lines for the Analytic Solution of k_A & k_P Model (Included in the Directional Derivatives)

The different characteristic line slopes dictate that interpolations must be used when using a fixed grid. The solution using Eqs. 9.4.9, 9.4.10 and 9.4.11 must be found in an iterative manner because the current velocity (V_P) is need to decide if the fluid is accelerating or decelerating, thus changing the compatibility equations.

Wylie (1997) suggested for the Brunone *et al.* (1991) unsteady friction model that, since the unsteady friction coefficient is typically small, its effect on the characteristic slope is negligible and may be discarded. For the k_A & k_P unsteady friction model, the characteristic slope can be approximated as $\Delta x/\Delta t = \pm a/\sqrt{1+k_P}$ (no interpolations are required); however, no research has been performed to assess the effects of the approximation.

Numerical analysis using these three different implementations were performed on a pipeline similar to the experimental pipeline (Chapter 10). A downstream valve closure was used. The initial velocity of the flow was 0.3 m/s, corresponding to a Reynolds number of 6,584. The unsteady friction coefficients were assumed to be $k_A = 0.031$ and $k_P = 0.040$. The quasi-steady friction approximation was used for the steady state component of the friction. The pipeline was discretised into 16 reaches. Results when treating the k_A & k_P as an addition to the steady friction are shown in Figure 9.8. These results show the phase change, amplitude damping and smoothing of the pressure oscillations compared to results using the quasi-steady friction only.

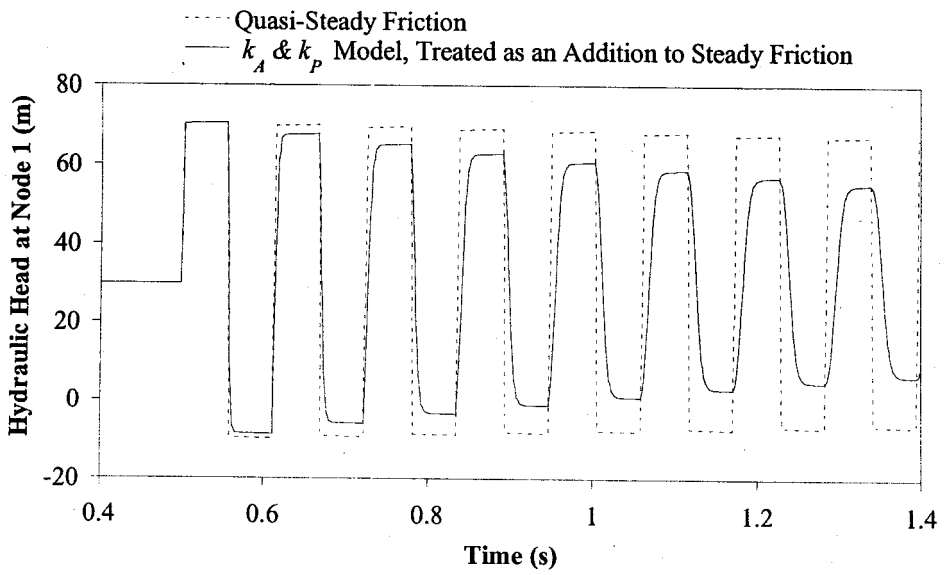

Figure 9.8 Results for the k_A & k_P Model (Treated as an Addition to Steady Friction)

Results for the k_A & k_P model including the k_P term in the direction derivatives only are shown in Figure 9.9. Unlike the previous results, the degree of smoothing of this implementation is minor. The phase change and the amplitude damping remain the same. An error is observed atop of the first pressure rise that becomes smaller with time. It is due to the approximation used to integrate the amplitude term along the characteristic line, in that the integration lags behind the calculation in time. The time lag corresponds to the frequency of the error oscillations.

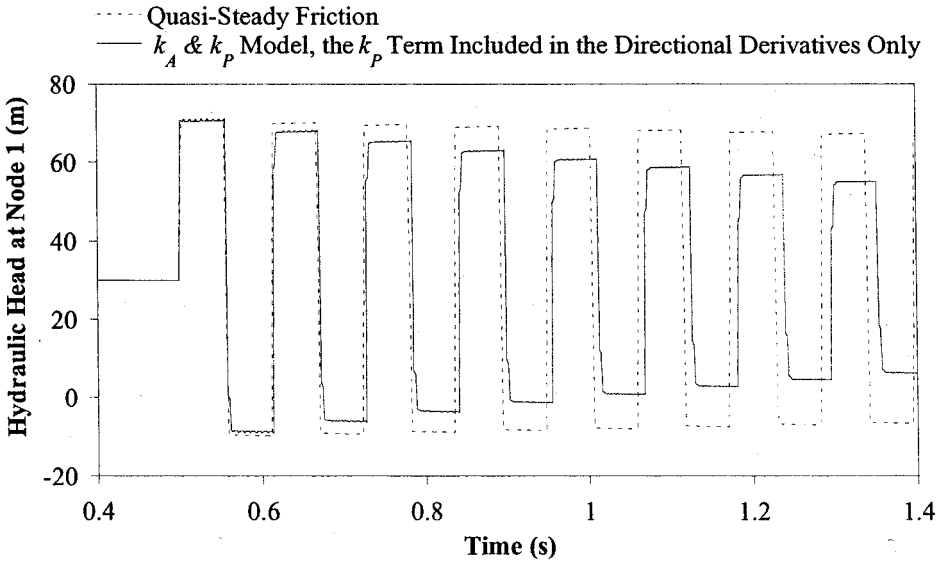

Figure 9.9 Results for the k_A & k_P Model (the k_P Term Included in the Directional Derivatives Only)

The results for the implementation of the k_A & k_P included in the directional derivatives are shown in Figure 9.10. They show a clean pressure response with no instabilities. The phase change and the amplitude damping are similar to the previous two implementations. The results from this implementation are assumed to be the most accurate, mainly due to the low number of approximations used. There is no smoothing of the pressure response, suggesting that the smoothing when the unsteady friction model was treated as an addition to the steady friction is numerical in nature (numerical diffusion). Experimental verification results performed by Brunone *et al.* (1991) and Bergant and Simpson (1994), both of whom used this formulation, indicates smoothing and produces better experimental matches. On this basis one can argue that numerical diffusion is advantageous in the absence of better unsteady friction models; however, if a numerical scheme in some unintended way mimics a natural diffusive process, then this suggests that some natural diffusive component is missing from the basic governing unsteady equations. Ultimately, one should aim to eliminate all sources of error, especially those that are numerical in nature. The identification of a missing diffusive term in the governing unsteady equations, although not addressed in this thesis, is certainly grounds for further investigation.

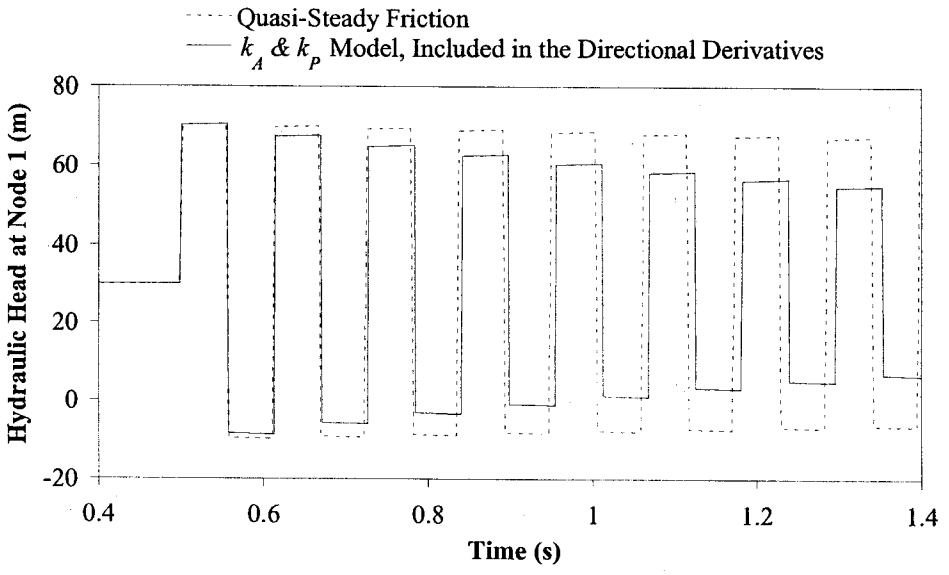

Figure 9.10 Results for the k_A & k_P Model (Totally Included in the Direction Derivatives)

The inclusion of the k_A & k_P unsteady friction model in the directional derivatives has implications for the measurement of the wave speed from experimental data. The wave speed can be calculated from the period or frequency of a pressure response (or timing the pressure wave propagation). Traditionally, the natural period for a valve closure event in a pipeline is $4L/a$. However, inclusion of the unsteady friction model causes a phase change in the pressure oscillations, which is dependent on the wave speed and the unsteady friction coefficient k_P. The period including the unsteady friction in the directional derivatives (in the method of characteristics) for a valve closure is now $\sqrt{1+k_P}\ 4L/a$. Not taking this into account will cause errors in the calculation of wave speed for fast transient events. If steady state friction is neglected, a variant of the Joukowsky pressure rise expression is

$$\Delta H = -\frac{a\sqrt{1+k_P+\phi_A k_A}}{g}\Delta V \qquad \text{.....(9.4.12)}$$

If $k_A = k_P$ and the fluid is decelerating, Eq. 9.4.12 reduces to the traditional Joukowsky pressure rise expression. The k_A & k_P model only produces damping if the sign of the velocity changes. For example, if the fluid accelerates from zero to steady state conditions, the velocity sign would not change and the k_A & k_P model would only produce a phase change rather than damping. This behaviour suggests limitations for

the k_A & k_P model for some transient event types (such as valve opening and establishment of flow events).

9.5 Determination of Unsteady Friction Coefficient k_3

Since the proposal of an unsteady friction model that depends on a coefficient multiplied by the local acceleration (Daily *et al.*, 1956; Carstens and Roller, 1959), there have been only a few analytical methods proposed (other than experimental testing) to determine the unsteady friction coefficient. In this section, the Carstens and Roller (1959) formulation is revisited and the unsteady friction coefficient is defined in terms of a function of the steady state velocity distribution. Carstens and Roller (1959) define a relationship between their unsteady friction coefficient k_1 and the Reynolds number. Their analysis applies to the case of small (unsteady) changes from a steady velocity distribution. To begin, three equations are needed. The first is the one-dimensional equation of motion for unsteady pipe flow,

$$\frac{\partial p}{\partial x}+\rho\frac{\partial V}{\partial t}+\frac{2}{r_0}\tau_{0U}=0 \qquad (9.5.1)$$

where ρ = density, r_0 = pipe radius and τ_{0U} = unsteady shear stress at the pipe wall. Eq. 9.5.1 uses average values across the velocity profile and is exactly the same as was shown in Chapter 3 except that the friction is in terms of the unsteady boundary shear stress, τ_{0U}. The dependent variables are pressure p and velocity V. The second equation is the two-dimensional equation of motion,

$$\frac{\partial p}{\partial x}+\rho\frac{\partial v}{\partial t}+\frac{1}{r}\frac{\partial(r\tau_U)}{\partial r}=0 \qquad (9.5.2)$$

where v = radial velocity, τ_U = radial unsteady shear stress and r = the radial distance from the centre of the pipe. The third and last equation describes the radial velocity distribution. It is expressed as a ratio of the radial velocity v and the average velocity V. The ratio is a function of the radial distance and is denoted as g_v,

$$g_v=\frac{v}{V} \qquad (9.5.3)$$

The function g_v can be quantified using boundary layer theory as described in Appendix B.9. Equating the two equations of motion (Eqs. 9.5.1 and 9.5.2) and multiplying the result by r gives

$$\frac{\partial(r\tau_U)}{\partial r} = \tau_{0U}\frac{2r}{r_0} + r\rho\frac{\partial V}{\partial t} - r\rho\frac{\partial v}{\partial t} \quad \text{.....(9.5.4)}$$

Substitution of the velocity distribution relationship (Eq. 9.5.3) into Eq. 9.5.4 replaces the radial velocities with the average velocity,

$$\frac{\partial(r\tau_U)}{\partial r} = \tau_{0U}\frac{2r}{r_0} + r\rho\frac{\partial V}{\partial t} - r\rho g_v\frac{\partial V}{\partial t} \quad \text{.....(9.5.5)}$$

Integration of Eq. 9.5.5 across the velocity profile eliminates the partial derivative with respect to r, resulting in

$$r\tau_U = \tau_{0U}\frac{r^2}{r_0} + \frac{\rho r^2}{2}\frac{\partial V}{\partial t} - \rho\frac{\partial V}{\partial t}\int_0^r rg_v dr \quad \text{.....(9.5.6)}$$

Dividing Eq. 9.5.6 by r and introducing a function F_1 (to gather all terms that are multiplied by the temporal acceleration) gives the shear stress,

$$\tau_U = \tau_{0U}\frac{r}{r_0} + F_1\rho r_0\frac{\partial V}{\partial t} \quad \text{.....(9.5.7)}$$

where the function F_1 is

$$F_1 = \frac{r}{2r_0} - \frac{1}{r_0 r}\int_0^r rg_v dr \quad \text{.....(9.5.8)}$$

Differentiation of Eq. 9.5.7 with respect to the radial distance r results in the shear stress gradient,

$$\frac{\partial\tau_U}{\partial r} = \frac{\tau_{0U}}{r_0} + F_2\rho\frac{\partial V}{\partial t} \quad \text{.....(9.5.9)}$$

where the function F_2 is

$$F_2 = \frac{1}{2} - g_v + \frac{1}{r^2}\int_0^r rg_v dr \quad \text{.....(9.5.10)}$$

The unsteady state shear stress equations (Eqs. 9.5.7 and 9.5.9) would be more useful if they were related to established shear stress equations in steady flow. The shear stress at the centre line of the pipe is equal to the derivative of the shear stress at the centre of the pipe (both equal to zero). Assuming all fluid particles were accelerated equally, the internal shear stresses would not be influenced by acceleration. Therefore, the change in the shear stress distribution must be attributed to the relative acceleration of adjacent particles in the cross section. Because the velocity distribution is symmetric about and

continuous through the centreline of the pipe, the relative acceleration between a particle on the centreline of the pipe and an adjacent particle will be minuscule (i.e. both particles accelerate together). As a result of the identical velocity distributions for unsteady and steady flow (an assumption), the shear stress gradients at the centreline of the pipe are equal (Carstens and Roller, 1959).

$$\left.\frac{d\tau_S}{dr}\right|_{r=0} = \left.\frac{\partial\tau_U}{\partial r}\right|_{r=0} \quad \text{.....(9.5.11)}$$

Also, the steady shear stress and the unsteady shear stress are equal to zero at the centre of the pipe (neglecting secondary current effects).

$$\tau_S|_{r=0} = \tau_U|_{r=0} = 0 \quad \text{.....(9.5.12)}$$

In steady flow, the shear stress distribution over a cross-section is linear and at its largest value (at the boundary) equal to τ_{S0} (Schlichting, 1955).

$$\frac{d\tau_S}{dr} = \frac{\tau_{0S}}{r_0} \quad \text{.....(9.5.13)}$$

These three concepts (Eqs. 9.5.11, 9.5.12 and 9.5.13) are substituted into Eq. 9.5.9. First, Eq. 9.5.9 is evaluated at the centre of the pipe and rearranged giving

$$\frac{\tau_{0U}}{r_0} = \left.\frac{\partial\tau_U}{\partial r}\right|_{r=0} - F_2|_{r=0}\rho\frac{\partial V}{\partial t} \quad \text{.....(9.5.14)}$$

Substitution of Eq. 9.5.11 into Eq. 9.5.14 forms

$$\frac{\tau_{0U}}{r_0} = \left.\frac{d\tau_S}{dr}\right|_{r=0} - F_2|_{r=0}\rho\frac{\partial V}{\partial t} \quad \text{.....(9.5.15)}$$

Substitution of Eq. 9.5.13 into Eq. 9.5.15 and multiplication by the radius yields

$$\tau_{0U} = \tau_{0S} - F_2|_{r=0} r_0\rho\frac{\partial V}{\partial t} \quad \text{.....(9.5.16)}$$

Eq. 9.5.16 relates the unsteady boundary shear stress to the steady boundary shear stress. Similarly, if the same concepts are introduced into Eq. 9.5.15 the radial distribution of the unsteady shear stress can be calculated. Substitution of Eq. 9.5.16 into Eq. 9.5.15 produces

$$\tau_U = \tau_{0S}\frac{r}{r_0} + F_3 r_0\rho\frac{\partial V}{\partial t} \quad \text{.....(9.5.17)}$$

Another function, F_3, is introduced to simplify the resulting expression by grouping all terms multiplied the temporal acceleration, where the function F_3 is

$$F_3 = F_1 - \frac{r}{r_0} F_2\Big|_{r=0} \quad \text{.....(9.5.18)}$$

Of course, the most important quantity is the unsteady shear stress at the boundary. Evaluating Eq. 9.5.17 at the pipe wall and the introducing the relationship between the Darcy-Weisbach friction factor and the boundary shear stress ($\tau = \rho f V^2/8$) produces the more familiar expression

$$f_U = f_S + F_3\Big|_{r=r_0} \frac{4D}{V^2} \frac{\partial V}{\partial t} \quad \text{.....(9.5.19)}$$

Rearranging Eq. 9.5.19 into a more useful form,

$$J = J_S + \frac{k_1}{2g} \frac{\partial V}{\partial t} \quad \text{.....(9.5.20)}$$

where J = the total resistive contribution in the equation of motion, J_S = the resistive contribution from steady friction and k_1 = the Carstens and Roller unsteady friction coefficient. k_1 is defined as

$$k_1 = 4F_3\Big|_{r=r_0} \quad \text{.....(9.5.21)}$$

Further simplification of Eq. 9.5.21 (shown in Appendix B.8) results in

$$k_1 = 2\left(g_v\Big|_{r=0} - 1\right) \quad \text{.....(9.5.22)}$$

where k_1 is found to depend only upon the value of g_v at the centre of the pipe, which is in turn dependent on the Reynolds number of the flow. This formulation is limited to small accelerations and decelerations and does not consider the time history of the flow (such as the Zielke, 1968, unsteady friction model).

The unsteady friction coefficients, derived by Carstens and Roller (1959), Shuy and Apelt (1987), Vardy and Brown (1996) and derivations presented in this thesis, are overestimated by a factor four when using the Brunone *et al.* (1991) and associated models (Shuy, 1985; Bergant *et al.*, 1999). Bergant *et al.* (1999) suggested that the coefficients, derived by Vardy and Brown (1996), should be one quarter of their derived size because Vardy and Brown (1996) used British definitions of the Darcy-Weisbach friction factor (e.g., $f_{\text{BRITISH}} = \frac{1}{4}f$). The correct reason for the overestimation is more easily explained using the k_A & k_P unsteady friction model (equivalent to the corrected Brunone *et al.*, 1991, model). The unsteady friction coefficients were derived for a small change in the flow rate with no flow reversal. Typically, the k_A & k_P unsteady friction model is applied to a transient event caused by a downstream valve closure,

both historically and in this thesis. A downstream valve closure results in full flow reversals and both accelerating and decelerating flows. The k_A & k_P unsteady friction model damps for accelerating and decelerating flow; however, experimental studies suggest that unsteady damping effectively increases the steady friction damping for accelerating flows and decreases the steady friction for decelerating flows. In terms of boundary layer theory, when a fluid accelerates from the steady state the boundary layer is stretched and becomes thinner, thus increasing the boundary shear stress on the pipe above that of the steady state. For a fluid decelerating from the steady state, the boundary layer thickens, thus decreasing the boundary shear stress on the pipe below that of the steady state. Given this behaviour, the unsteady coefficient used by the k_A & k_P model (k_{MODEL}), and hence the Brunone *et al.* (1991) model, is one quarter of the derived unsteady coefficient ($k_{DERIVED}$),

$$k_{MODEL} = \tfrac{1}{4}\, k_{DERIVED} \quad \text{.....(9.5.23)}$$

It is the method of implementation of unsteady friction rather than the unsteady friction model itself that causes the friction overestimation. From this point onwards in this thesis, the model unsteady friction coefficient is used.

9.6 Unsteady Friction Coefficients

Unsteady friction coefficients were derived in terms of the velocity distribution in Section 9.5 and the velocity distribution is defined in Appendix B.9. The combination of the velocity distribution formulae and the unsteady friction coefficient derivations provide relationships for the unsteady friction coefficients based on the Reynolds number of the flow for smooth and rough pipes.

9.6.1 Unsteady Friction Coefficients in Smooth Pipes

Inserting the smooth pipe logarithmic law with the transition function into Eq. 9.5.22 forms an analytic expression for the unsteady friction coefficient k_3. A full derivation is shown in Appendix B.10, the result being

$$k_3 = \sqrt{\frac{f}{512}}\left[A\ln\left(\mathbf{R}\sqrt{\frac{f}{32}} + 0.2093 - B\right) + B\right] - \frac{1}{8} \quad \text{.....(9.6.1)}$$

The calculation of the unsteady friction coefficient k_3 can be simplified by assuming that only the logarithmic velocity distribution law applies, which is justified by examining boundary layer theory (Streeter and Wylie, 1983) where the calculation of shear stress on a flat plate is dependent on the free stream velocity, which for pipe flow, is the velocity at the centre of the pipe. There is little influence from the viscous sub-layer at this position. Thus upon substituting the smooth pipe logarithmic law (Eq. B.9.5) into Eq 9.5.22 the unsteady friction coefficient, k_3, can easily be found and is a function of the Darcy-Weisbach friction factor and the Reynolds number (Eq. 9.6.1). A full derivation can be found in Appendix B.11. Upon numerical testing, little difference between values of k_3 calculated using the transition and logarithmic laws and only the logarithmic law was found for low Reynolds numbers and practically no difference for high Reynolds numbers.

$$k_3 = \sqrt{\frac{f}{512}}\left[A\ln\left(\mathbf{R}\sqrt{\frac{f}{32}}\right) + B\right] - \frac{1}{8} \quad \text{.....(9.6.2)}$$

Eq. 9.6.2 may be further reduced using the Colebrook–White equation (Eq. B.9.11) for smooth pipes ($k_S/r_0 = 0$), resulting in

$$k_3 = 2.201\times10^{-3} + 0.1539\sqrt{f} \quad \text{.....(9.6.3)}$$

The unsteady friction coefficient k_3 can also be found using the power law of velocity distribution (derivation in Appendix B.15). The relationship between the power exponent n and k_3 is

$$k_3 = \frac{(3n+1)}{16n^2} \quad \text{.....(9.6.4)}$$

The power exponent n is determined using either Eqs. B.9.20 or B.9.21. The unsteady friction coefficient k_3 can be plotted against the Reynolds number of the initial steady state flow. Figure 9.11 includes the value of k_3 calculated by Vardy and Brown (1996) for laminar flow conditions ($k_3 = 0.035$).

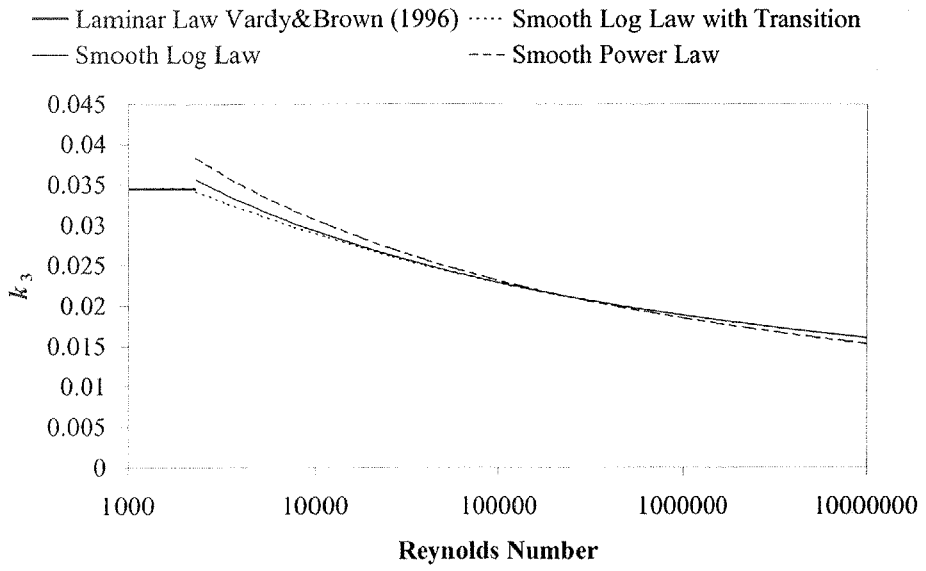

Figure 9.11 Unsteady Friction Coefficient k_3 Using Different Velocity Profiles

Figure 9.11 shows rather similar behaviour between the three methods used to define the velocity distribution. The logarithmic law k_3 agrees well with the logarithmic law including the transition formula k_3 for high Reynolds numbers. For low Reynolds numbers there is a slight difference due to the logarithmic law's inability to model correctly the laminar-turbulent transition. The power law also produces similar results to the other log law formulations. An interesting observation is made when observing the Vardy and Brown (1996) theoretical unsteady friction coefficient for laminar flow. The logarithmic law including the transition formula produces nearly the same value at the laminar boundary ($\mathbf{R} = 2{,}320$) as Vardy and Brown's theoretical laminar k_3. The most technically correct is the logarithmic law including the transition formula (due to the inclusion of the viscous sub-layer).

The momentum correction coefficient k_M can be found using the logarithmic law,

$$k_M = \frac{5f}{128\kappa^2} \qquad \text{.....(9.6.5)}$$

Eq. 9.6.5 shows the dependence of k_M on the friction factor f and was found directly from the Chen (1992) expression for the momentum correction factor. The momentum correction coefficient can also be found using the power law,

$$k_M = \frac{(5n+1)}{16n^2(n+2)} \qquad \text{.....(9.6.6)}$$

The derivations for Eqs. 9.6.5 and 9.6.6 can be found in Appendix B.16. The result of the use of different velocity distributions to find the momentum correction coefficient is shown in Figure 9.12. The curve for k_M using the logarithmic law including the viscous sub-layer was calculated by finding β by numerical integration.

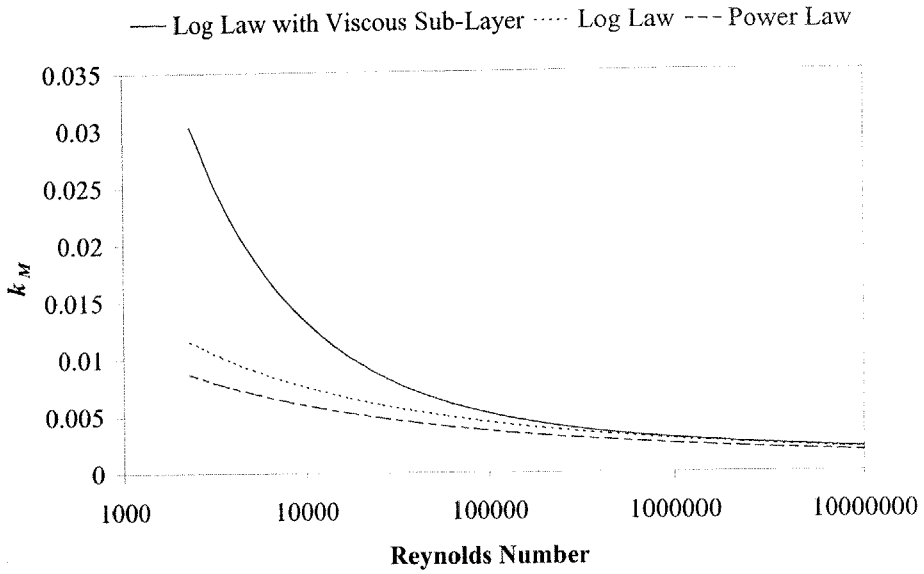

Figure 9.12 Unsteady Friction Coefficient k_M Using Different Velocity Profiles

Again, the most technically correct of the curves is the logarithmic law combined with both the transition formula and the viscous sub-layer law (due to modelling all velocity distribution regions). This curve produces far greater values of the k_M (and β as well) for low Reynolds numbers due to the inclusion of the viscous sub-layer, which has a more parabolic-like shape (and grows thick at low Reynolds numbers). At high Reynolds numbers all of the three curves converge.

9.6.2 Unsteady Friction Coefficients in Rough Pipes

The relationships for the unsteady friction coefficients k_3 and k_M for smooth pipes can be extended to rough pipes. The coefficient k_3 if found by inserting the rough pipe logarithmic law including the transition formulae (Eq. B.9.16) into Eq. 9.5.22,

$$k_3 = \sqrt{\frac{f}{512}}\left[A\ln\left(\mathbf{R}\sqrt{\frac{f}{32}} + 0.2093 - B_R\right) + B_R\right] - \frac{1}{8} \quad \text{.....(9.6.7)}$$

The derivation of Eq. 9.6.7 can be found in Appendix B.13. A simplification can be made if the transition formulae are not used, resulting in

$$k_3 = \sqrt{\frac{f}{512}}\left[A\ln\left(\mathbf{R}\sqrt{\frac{f}{32}}\right) + B_R\right] - \frac{1}{8} \quad \text{.....(9.6.8)}$$

Eq. 9.6.8 is simplified by expanding the velocity distribution parameter B_R using Eqs. B.9.12 and B.9.13 (full derivation in Appendix B.14) forming

$$k_3 = 3.75\sqrt{\frac{f}{512}} \quad \text{.....(9.6.9)}$$

The rough pipe expression for k_3 using the power law is does not change from the smooth pipe one (Eq. 9.6.4). The rough pipe logarithmic laws should be able to be applied to smooth pipes as well because the Colebrook-White equation was used to define the transition between smooth and completely rough regimes. A plot of the smooth pipe unsteady friction coefficients using logarithmic laws and the simple rough pipe relationship for k_3 applied to smooth pipes is shown in Figure 9.13.

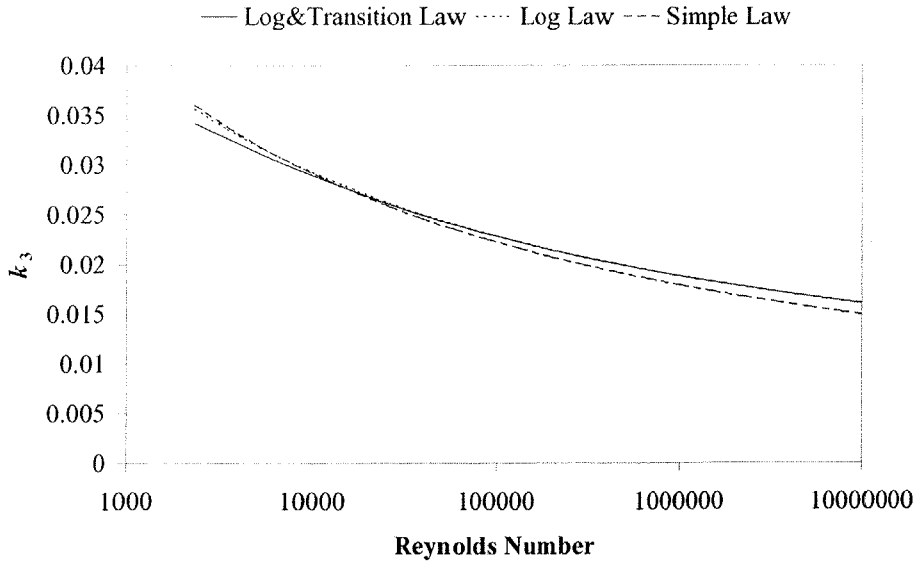

Figure 9.13 Comparison Between Log Law Formulas for k_3

As shown, the simple rough pipe expression is also applicable to smooth pipes and produces only minimal difference to the smooth pipe equation (Eq. 9.8.3). This small difference is due to slight differences in the coefficients in the Colebrook-White equation between different formulae. The use of the transition formula in the logarithmic law produces slightly lower values of k_3 for low Reynolds numbers.

Using the universal velocity distribution formulae, the analysis for the unsteady friction coefficient k_3 can be expanded to include pipes of different roughnesses. Figure 9.14 shows how k_3 varies with increasing relative roughnesses (the simple rough pipe law is used). As may be expected, the higher relative roughness cases have an associated higher unsteady friction coefficient.

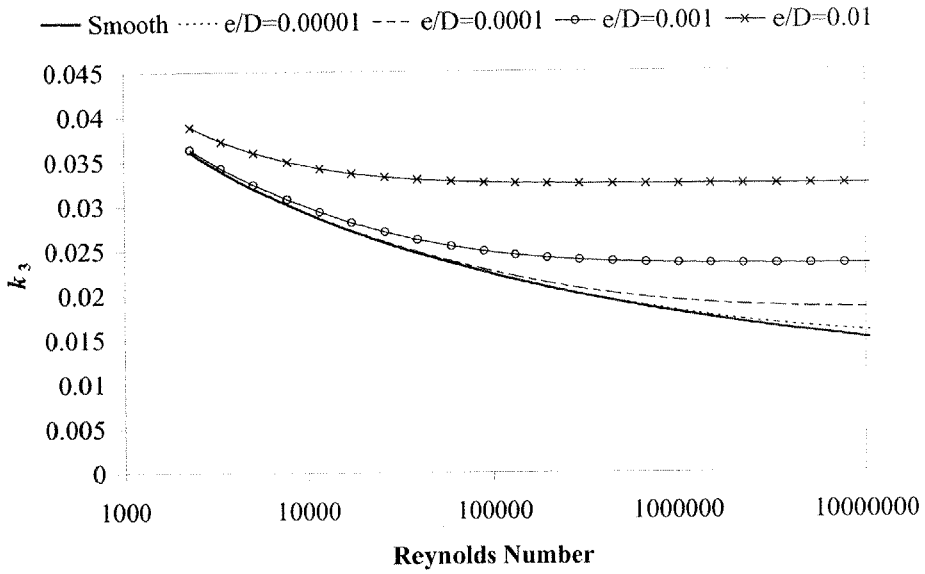

Figure 9.14 Rough Pipe k_3 Using the Log Law Approximation

Likewise, expressions for the momentum correction coefficient k_M for rough pipes are identical to the smooth pipe ones derived from both the logarithmic law (Eq. 9.8.4) and the power law (Eq. 9.8.5). The unsteady momentum correction coefficient k_M can also be expanded to cover cases of differing relative roughness. Figure 9.15 shows k_M for different relative roughnesses using the logarithmic law for calculation.

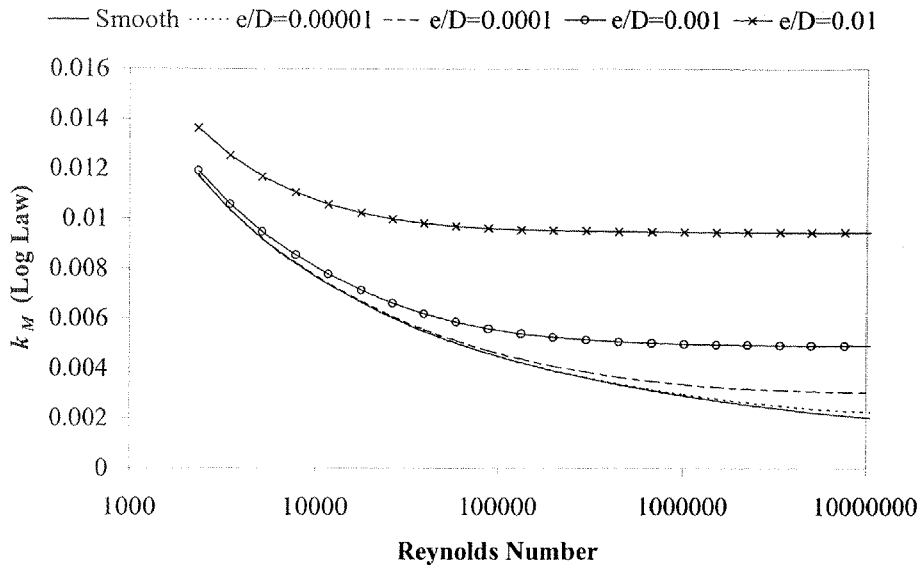

Figure 9.15 Rough Pipe k_M Using the Log Law Approximation

9.7 Numerical Investigation of Proposed Unsteady Models

This section compares the different turbulent unsteady friction models proposed in section 9.3. A numerical basis is used to highlight differences between models. The model that serves as a starting point for other proposed models is the modified Brunone *et al.* (1991) unsteady friction model. All of the numerical analyses are performed on a simple pipeline with a fast closing valve at the downstream end. The head shown in each plot is taken next to the valve. In each case the pipeline characteristics were length = 37.2 m; diameter = 0.02214 m; wave speed = 1,319 m/s; initial velocity = 0.3 m/s. Figure 9.16 shows results using the Brunone *et al.* (1991) model and the traditional quasi-steady friction model. The quasi-steady friction model shows under damping and negligible phase shift.

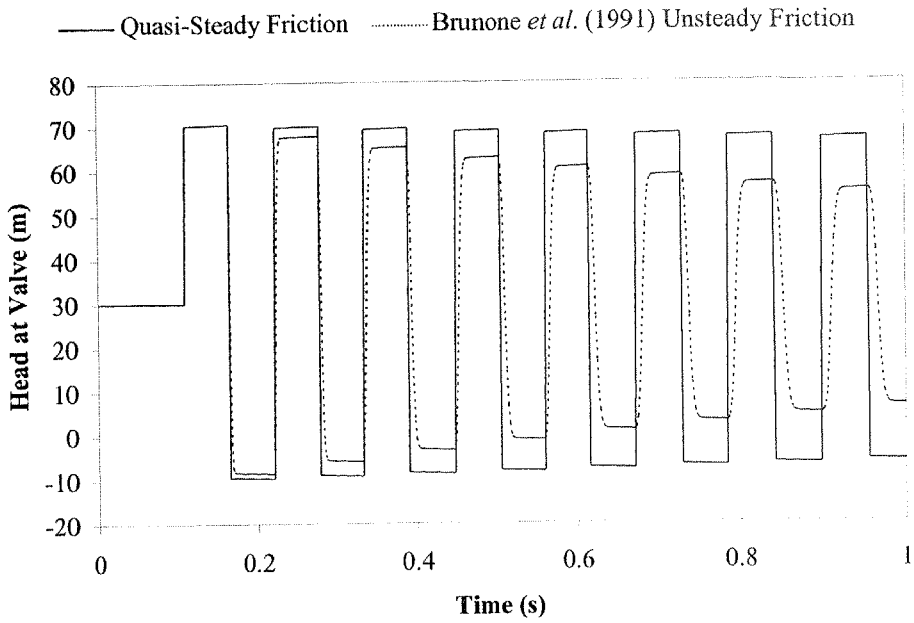

Figure 9.16 Comparison of Quasi-Steady Model and Modified Brunone *et al.* (1991) Model

Figure 9.17 shows results using the Brunone *et al.* (1991) model when using a k_3 derived from Vardy and Brown's formulae and from the proposed logarithmic law with transition formulae. The use of Vardy and Brown's k_3 produces less damping than the logarithmic law's k_3 does. The difference in damping between the formulae is expected to be more pronounced for higher Reynolds number flows.

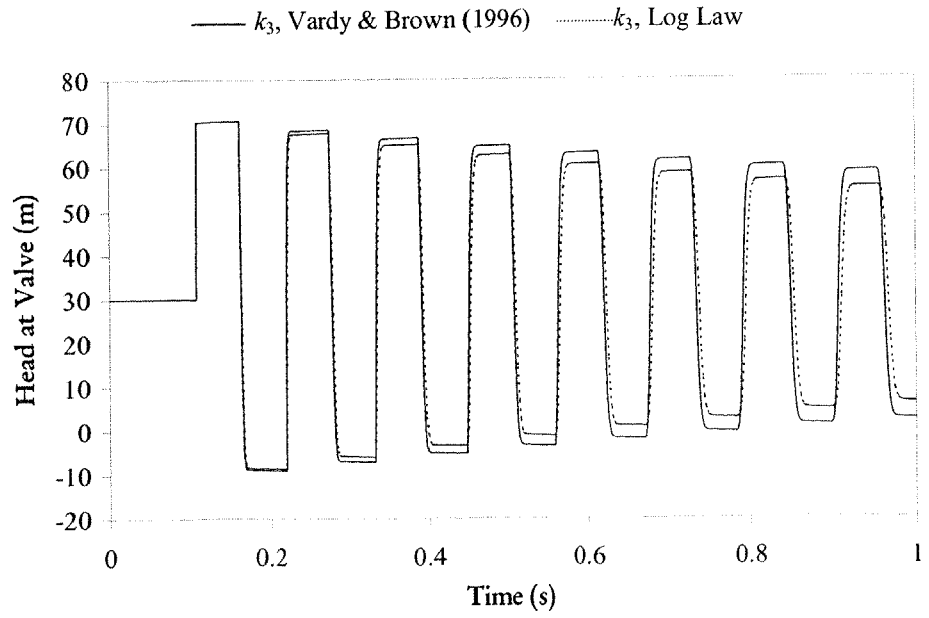

Figure 9.17 Comparison of Different k_3 Functions in Constant k_3 Model

The addition of the momentum correction coefficient k_M (Figure 9.18) produces a slight positive shift in the phase of the pressure oscillations.

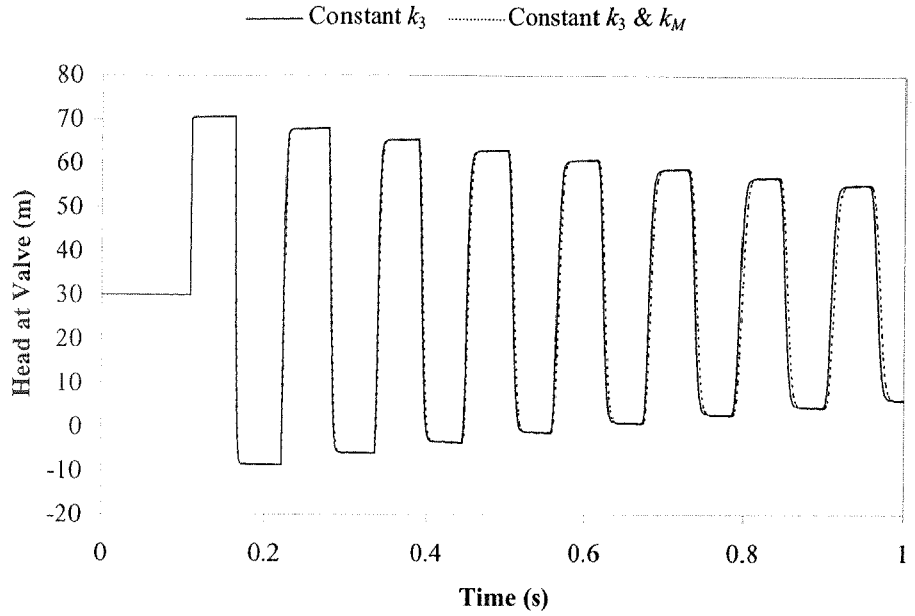

Figure 9.18 Comparison of Constant k_3 Model and Constant k_3 and k_M Model

An alternative to the use of the modified Brunone *et al.* (1991) unsteady friction model with a traditional constant k_3 is to use a variable k_3, which would solve problems where the initial velocity distribution is not known or changes dramatically during the transient event (such as rapidly accelerating flow that begins from rest). A constant value of k_3 cannot be found based on the initial velocity distribution (i.e., fluid at rest has no velocity distribution). The unsteady friction coefficient k_3 can be related to the Reynolds number (Sections 9.6.1 and 9.6.2) and these relationships used to define an instantaneous value for k_3. Figure 9.19 shows the difference between using a constant value of k_3 (Vardy and Brown based on initial conditions) and a variable value of k_3 (Vardy and Brown based on instantaneous conditions).

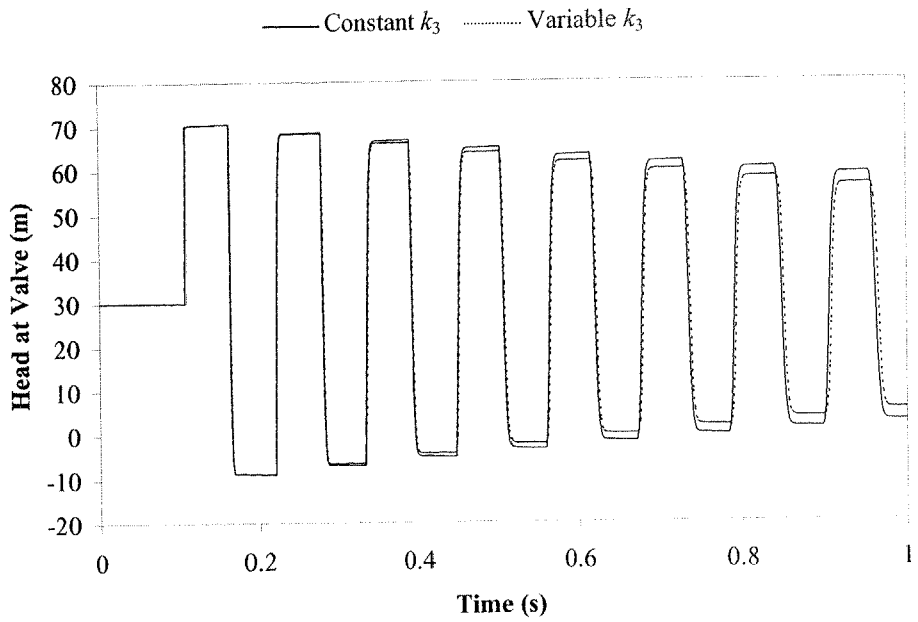

Figure 9.19 Comparison between Constant *k* Model and Variable *k* Model

Figure 9.19 shows that the variable k_3 implementation produces extra damping due to the velocity oscillations spending more time in the laminar range where k_3 is higher.

A comparison is made between different definitions of k_3 for the variable k models and the addition of a variable momentum correction coefficient k_M (Figure 9.20). All of the variable k models produce similar results for the example considered because they all spend about the same of time in low Reynolds number flow situations where the unsteady coefficient k_3 is similar between models. A difference between the Vardy and Brown (1996) model and the proposed logarithmic law definition of k_3 would be more pronounced for higher Reynolds number flows (due to the greater difference in values of k_3). The addition of a variable k_M component has little effect other than a slight positive change in the phase of the pressure oscillations.

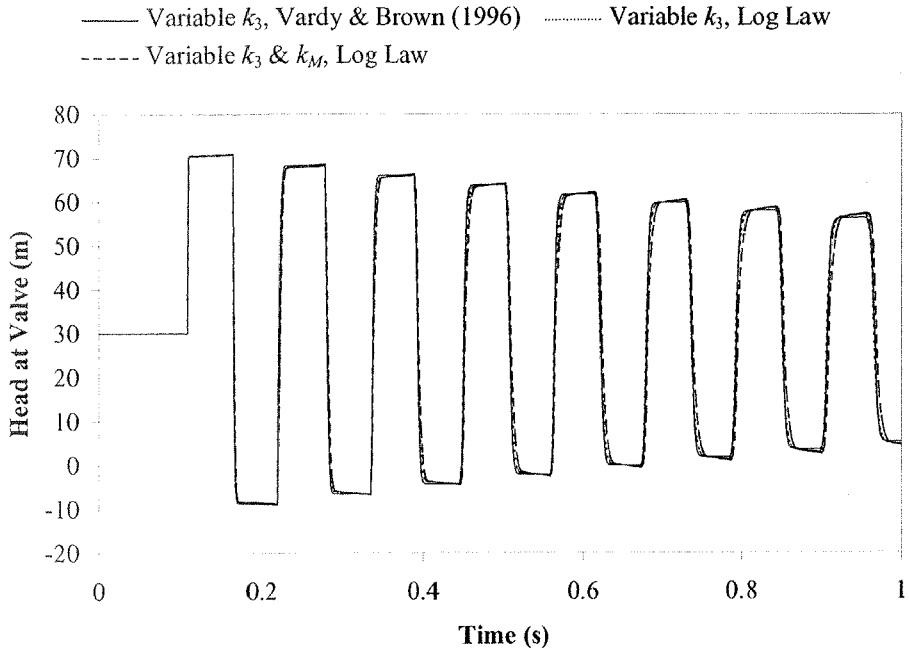

Figure 9.20 Comparison of Variable *k* Models

The k_3 & k_M model is equivalent to the k_A & k_P model, which splits the behaviour into pure amplitude and phase components. Figure 9.21 shows a near exact match between the two models given the selection of compatible coefficients. The k_3 & k_M model and the modified Brunone *et al.* (1991) model are subsets of the k_A & k_P model.

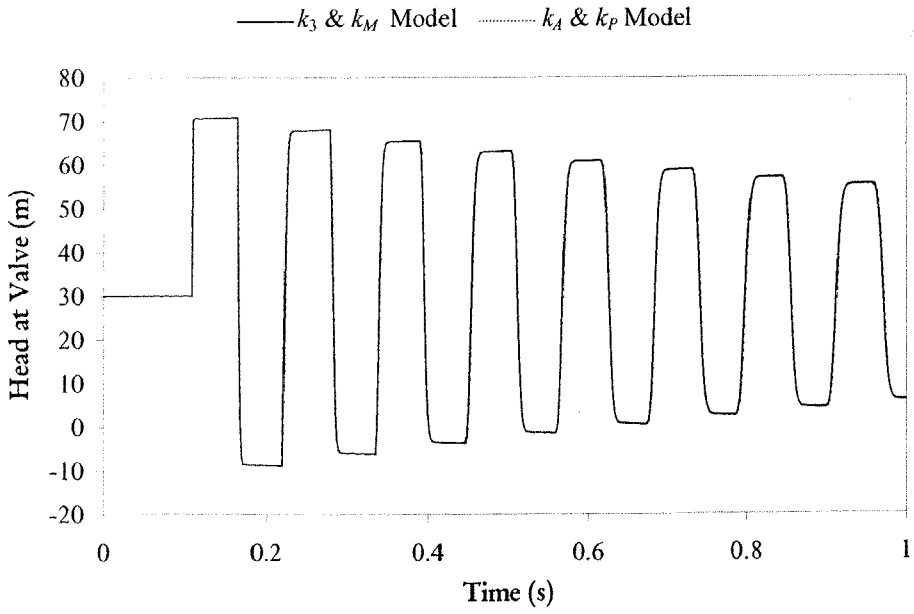

Figure 9.21 Comparison of k_A & k_P Model and k_3 & k_M Model

The behaviour of the k_A & k_P model can be further explored by a simple parametric study. Each coefficient is changed and the resulting behaviour is noted. The k_A coefficient is changed first. Figure 9.22 shows the results when k_A is halved. The amplitude of the pressure oscillations increases because of the lessening of the damping effect caused by k_A. The phase of the pressure oscillations remains unchanged.

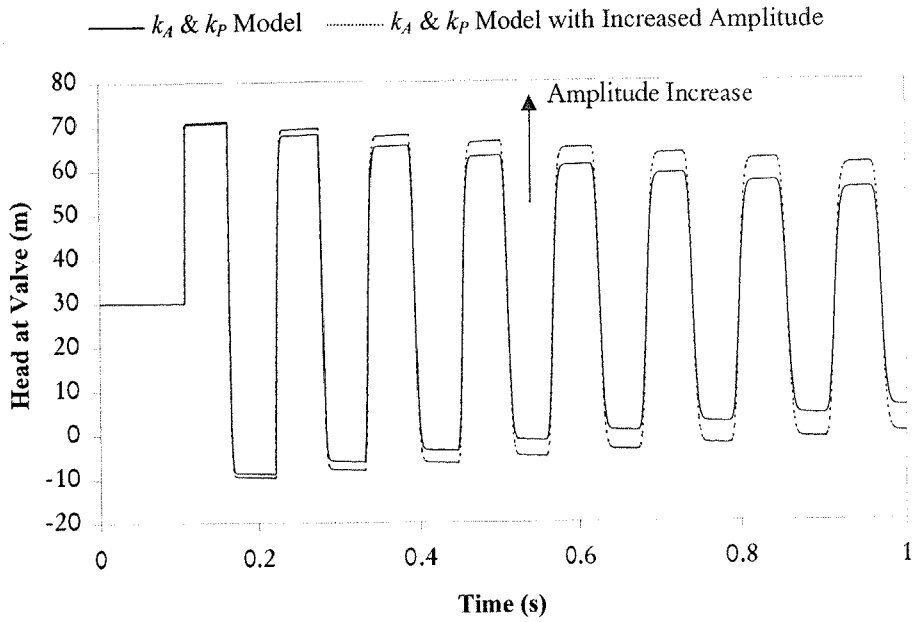

Figure 9.22 Demonstration of Amplitude Increase in k_A & k_P Model

The coefficient k_P is increased by 50% in Figure 9.23 producing a positive phase shift. There is a slight initial amplification due to the initial head rise being slightly higher because of the effect of the k_P parameter on the Joukowsky pressure rise (see Section 9.4) rather than in the subsequent pressure oscillations. The slight amplification also exists in the Zielke (1968) laminar unsteady friction model (and derivatives of it).

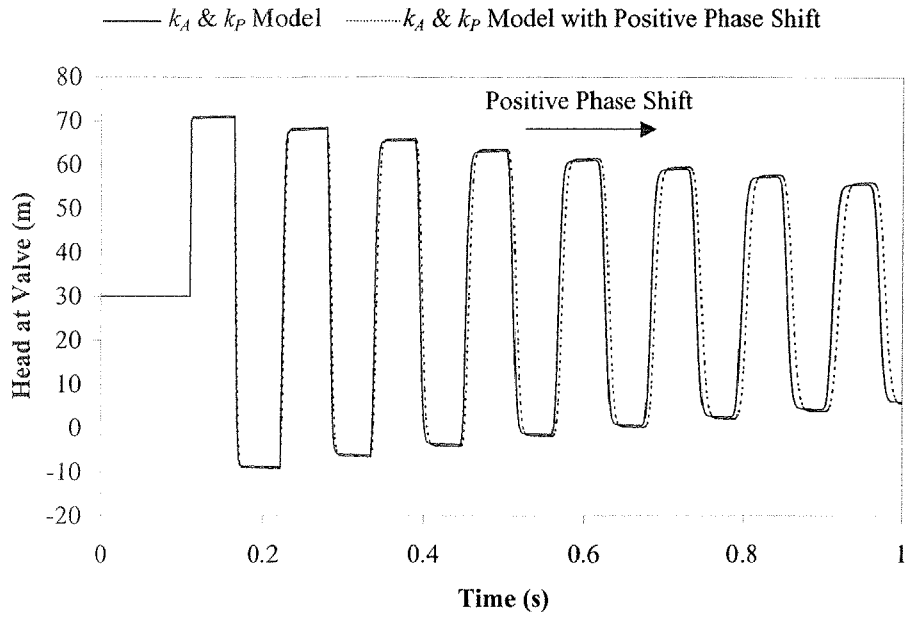

Figure 9.23 Demonstration of Phase Shift in k_A & k_P Model

9.8 Numerical Investigation of Unsteady Friction Coefficients

There are three previous formulae (Section 8.6) and one proposed formula (Eq. 9.6.1) for the analytic calculation of unsteady friction coefficient k_3 in a smooth pipe. This coefficient represents the extra boundary shear above that predicted by the steady state analogue. The different methods for the calculation of k_3 are shown in Figure 9.24. The Carstens and Roller (1959), Shuy and Apelt (1983) and the proposed relationship show approximate agreement with each other because they are all based on similar analysis (in fact, the Shuy and Apelt (1983) function is a fitted function of the Carstens and Roller (1959) function). The main observable difference is that the Vardy and Brown (1996) relationship produces unsteady friction coefficients that are much lower than the other methods for higher Reynolds numbers.

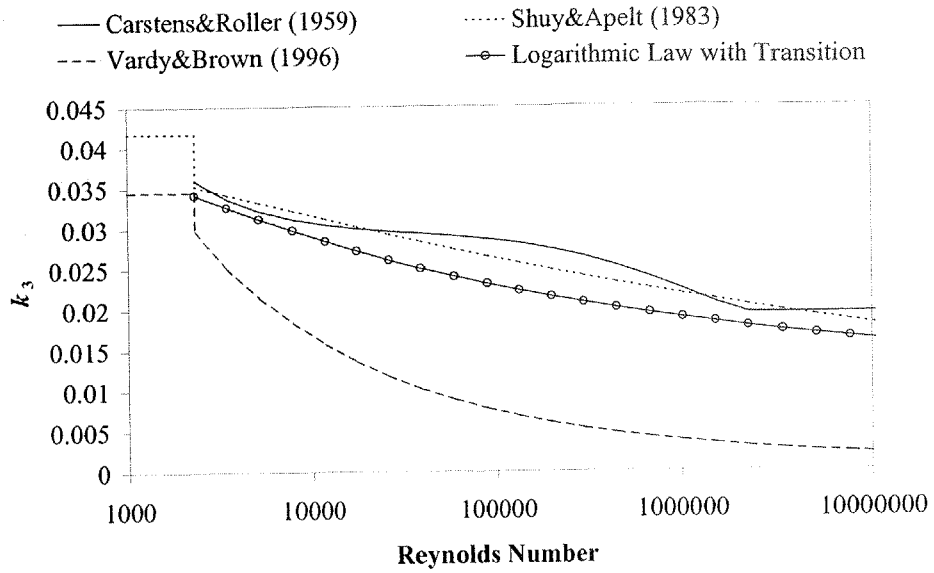

Figure 9.24 Comparison of Different k_3 Functions (Smooth Pipe)

No conclusions can be made on the different unsteady friction coefficient formulae without experimental testing. Experimental results are presented for the verification of unsteady friction coefficients in Chapter 11.

9.9 Analytic Damping Coefficient for Unsteady Friction

The magnitude of unsteady friction coefficients k_A and k_P affects the damping of pressure oscillations after a transient event. The damping of the magnitude of these oscillations is exponential in nature. The exponential damping coefficient is easily measurable from experimental data; however, the unsteady friction coefficients are not. A relationship between the exponential damping coefficient and unsteady friction coefficients would be useful to estimate the unsteady friction coefficients. If such a relationship existed, an estimate of the unsteady friction coefficient for an unsteady event could be found by first determining the exponential decay coefficient (of the pressure oscillations) and then deriving values of unsteady friction coefficients from that decay coefficient. This section develops such a relationship.

9.9.1 Analytic Relationship for Peak Magnitude for a Simple Pipeline

The effect of changing the number of reaches in a pipeline (or discretisation) when using unsteady friction is investigated in Appendix B.1.4, which shows that the number of reaches has no effect on the magnitude of the pressure oscillations. Therefore, for the study of the damping of the pressure oscillation magnitudes, the coarsest grid is satisfactory. The coarsest grid is achieved when the computational reach length is equal to the whole length of the pipeline, as shown in Figure 9.25.

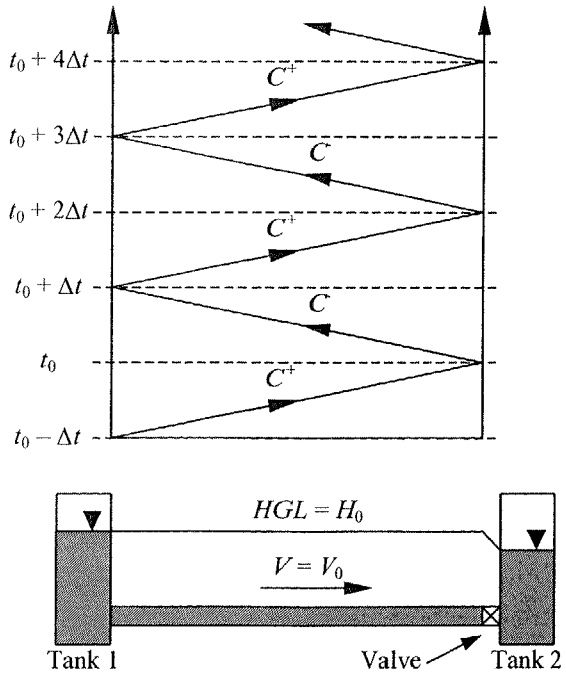

Figure 9.25 Simple Pipeline and Characteristic Grid

The unsteady friction model used in this derivation is the newly proposed k_A & k_P model. The k_A & k_P model may be written in terms of the unsteady headloss term J_U (in the governing equation of motion) as

$$J_U = \phi_V \frac{k_A}{g}\left|\frac{dV}{dt}\right| + \frac{k_P}{g}\frac{dV}{dt} \qquad \text{.....(9.9.1)}$$

where the velocity sign operator, ϕ_V, is

$$\phi_V = \begin{cases} +1 & \text{if} \quad V \geq 0 \\ -1 & \text{if} \quad V < 0 \end{cases} \qquad \text{.....(9.9.2)}$$

The steady state friction is set to zero so that all dissipation effects are solely due to the unsteady state friction. Therefore, the effect of unsteady friction can be isolated from

other forms of damping. The compatibility equations, written for both the C^+ and the C^- characteristics, are

$$C^+: \quad (H_P - H_A) + \frac{a\sqrt{1+k_P+\phi_A^+ k_A}}{g}(V_P - V_A) = 0 \quad \text{.....(9.9.3)}$$

$$C^-: \quad (H_P - H_B) - \frac{a\sqrt{1+k_P+\phi_A^- k_A}}{g}(V_P - V_B) = 0 \quad \text{.....(9.9.4)}$$

where the acceleration sign operator, ϕ_A, is defined for both compatibility equations as

$$\phi_A^+ = \begin{cases} +1 & \text{if} \quad |V_P| \geq |V_A| \\ -1 & \text{if} \quad |V_P| < |V_A| \end{cases} \quad \& \quad \phi_A^- = \begin{cases} +1 & \text{if} \quad |V_P| \geq |V_B| \\ -1 & \text{if} \quad |V_P| < |V_B| \end{cases} \quad \text{.....(9.9.5)}$$

The slopes of the characteristic lines are approximately equal to $\Delta x/\Delta t = \pm a/\sqrt{1+k_P}$ for alternatively accelerating and decelerating flows.

Now the compatibility equations are used to model the magnitude of the peaks and troughs resulting from a fast valve closure. To begin, the flow in the pipeline is steady with a velocity of V_0. The pipe is frictionless; therefore, the head along the pipe is constant and equal to H_0. The steady state conditions (preceding the transient event) are

$$H_{t_0-\Delta t} = H_0 \quad \& \quad V_{t_0-\Delta t} = V_0 \quad \text{.....(9.9.6)}$$

At time t_0 the valve shuts fully producing a fast valve closure ($t_c < 2L/a$). The positive compatibility equation is used to predict the first pressure peak. The acceleration sign operator is equal to -1 because the fluid is decelerating. The velocity boundary condition at the valve is $V = 0$ (since the valve is now closed). The conditions at the valve at time $t = t_0$ are

$$H_{t_0} = H_0 + \sqrt{1+k_P-k_A}\,\frac{aV_0}{g} \quad \& \quad V_{t_0} = 0 \quad \text{.....(9.9.7)}$$

Conditions at time $t_0 + \Delta t$ are determined using the negative compatibility equation. The acceleration sign operator is now equal to +1 because the fluid is accelerating. The head boundary condition at tank 1 is equal to H_0. The conditions at a time $t = t_0 + \Delta t$ are

$$H_{t_0+\Delta t} = H_0 \quad \& \quad V_{t_0+\Delta t} = -\frac{\sqrt{1+k_P-k_A}}{\sqrt{1+k_P+k_A}}V_0 \quad \text{.....(9.9.8)}$$

The preceding analysis is repeated for the first trough at time $t = t_0 + 2\Delta t$ and successive times. However, of more importance are the values of head at successive peaks. The head at the second peak at a time of $t = t_0 + 4\Delta t$ is

$$H_{t_0+4\Delta t} = H_0 + \frac{(1+k_P-k_A)^{1.5}}{(1+k_P+k_A)}\frac{aV_0}{g} \quad \text{.....(9.9.9)}$$

The head at the third peak (at time $t_0 + 8\Delta t$) is

$$H_{t_0+8\Delta t} = H_0 + \frac{(1+k_P-k_A)^{2.5}}{(1+k_P+k_A)^2}\frac{aV_0}{g} \quad \text{.....(9.9.10)}$$

The equations for the head at the first three peaks (Eqs. 9.9.7, 9.9.9 and 9.9.10) are functions of the initial Joukowsky pressure rise and the unsteady friction coefficients k_A and k_P. A general expression for the head at the N^{th} peak (at a time $t = t_0 + (N+1)4\Delta t$) is

$$H_{\text{Peak }N} = H_0 + \frac{(1+k_P-k_A)^{N-0.5}}{(1+k_P+k_A)^{N-1}}\frac{aV_0}{g} \quad \text{.....(9.9.11)}$$

9.9.2 Determination of Decay Coefficient α

The reduction in the amplitude of the pressure oscillations after a full valve closure can be defined by examining two successive pressure peaks. The loss in amplitude between these two peaks is represented by a decay coefficient denoted α,

$$\alpha = \frac{H_{\text{Peak }N} - H_0}{H_{\text{Peak }(N-1)} - H_0} \quad \text{.....(9.9.12)}$$

Expressions for the head at two consecutive peaks are determined using Eq. 9.9.11. The head at the $(N-1)^{th}$ and N^{th} peaks is

$$H_{\text{Peak }N} = H_0 + \frac{(1+k_P-k_A)^{N-0.5}}{(1+k_P+k_A)^{N-1}}\frac{aV_0}{g} \quad \text{.....(9.9.13)}$$

$$H_{\text{Peak }(N-1)} = H_0 + \frac{(1+k_P-k_A)^{N-1.5}}{(1+k_P+k_A)^{N-2}}\frac{aV_0}{g} \quad \text{.....(9.9.14)}$$

Substitution of Eqs. 9.9.13 and 9.9.14 into Eq. 9.9.12 results in an expression for the decay coefficient α,

$$\alpha = \frac{1+k_P-k_A}{1+k_P+k_A} \quad \text{.....(9.9.15)}$$

From Eq. 9.9.15 the decay of successive pressure peaks is dependent on both the k_A and k_P unsteady friction coefficients (rather than just the amplitude coefficient k_A). The decay coefficient, however, is much more sensitive to k_A rather than k_P (shown in

subsequent figures in Section 9.9.4). A useful relationship between the head at two successive peaks (a peak at time t and its previous peak at time $t - 4\Delta t$) is

$$H_t = H_0 + \alpha(H_{t-4\Delta t} - H_0) \quad \text{.....(9.9.16)}$$

Eq. 9.9.16 is used in the next section.

9.9.3 Determination of Exponential Decay Coefficient D_U

Typically, the decay of a property is defined in terms of an exponential decay function. An exponential decay function for the magnitude of the pressure oscillations after a full valve closure is defined as

$$H_t = H_0 + (H_B - H_0)e^{\left(-D_U\frac{(t-t_B)}{T}\right)} \quad \text{.....(9.9.17)}$$

where a base head (H_B) occurs at a time t_B. The subsequent peak pressure heads at time t are denoted H_t. The exponential decay coefficient is denoted D_U. The time terms (in the exponential) are normalised by dividing by the period for one complete transient pressure oscillation. The natural period of the pressure oscillations for a pipeline with a closed valve at one end and a reservoir at the other is

$$T = \frac{4L\sqrt{1+k_P}}{a} = 4\Delta t \quad \text{.....(9.9.18)}$$

A relationship between α and D_U is achieved by considering the exponential decay equation (Eq. 9.9.17) applied to two successive pressure peaks $H_{t-4\Delta t}$ and H_t. The time difference between the peaks is $4\Delta t$.

$$H_t = H_0 + (H_{t-4\Delta t} - H_0)e^{\left(-D_U\frac{4\Delta t}{T}\right)} \quad \text{.....(9.9.19)}$$

The relationship between the two successive peaks (in terms of α) is Eq. 9.9.16, substitution of which into Eq. 9.9.19 gives

$$H_0 + \alpha(H_{t-4\Delta t} - H_0) = H_0 + (H_{t-4\Delta t} - H_0)e^{-D_U} \quad \text{.....(9.9.20)}$$

The subtraction of H_0 from both sides and division by $(H_{t-4\Delta t} - H_0)$ leaves

$$\alpha = e^{-D_U} \quad \text{.....(9.9.21)}$$

Eq. 9.9.21 is an expression that only involves the decay coefficients α and D_U. Taking the logarithm of both sides and rearranging the resulting expression shows the dependence of the exponential decay coefficient D_U on the decay coefficient α,

$$D_U = -\ln(\alpha) \quad \text{.....(9.9.22)}$$

Finally, the substitution of Eq. 9.9.15 into Eq. 9.9.22 produces an expression relating the exponential decay coefficient D_U to the unsteady friction coefficients k_A and k_P,

$$D_U = \ln\left(\frac{1+k_P+k_A}{1+k_P-k_A}\right) \quad \text{.....(9.9.23)}$$

9.9.4 Numerical Verification of Decay Expressions

Numerical verification of the unsteady friction decay relationships is performed for the pipeline defined in Figure 9.25. The parameters used for this pipeline are: diameter = 22.1 mm, length = 37.2 m, wave speed = 1,319 m/s, unsteady friction coefficients k_A and k_P both equal 0.031, initial velocity = 0.3 m/s and tank head = 30.0 m. The valve is fully closed instantaneously at a time of 0.1 s. Figure 9.26 shows the pressure oscillations at node 1 (next to the valve) for a period of 1.0 second.

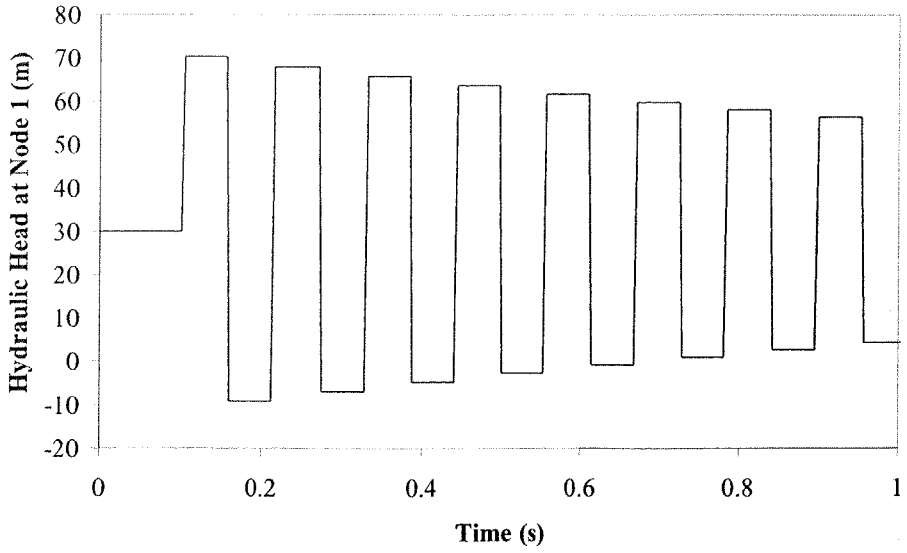

Figure 9.26 Head at Valve for Simple Pipeline ($k_A = k_P = 0.031$)

From the numerical data the decay coefficient α is calculated from successive peaks. Figure 9.27 shows the values of the decay coefficient, given at the time of the later peak used in the numerical calculation.

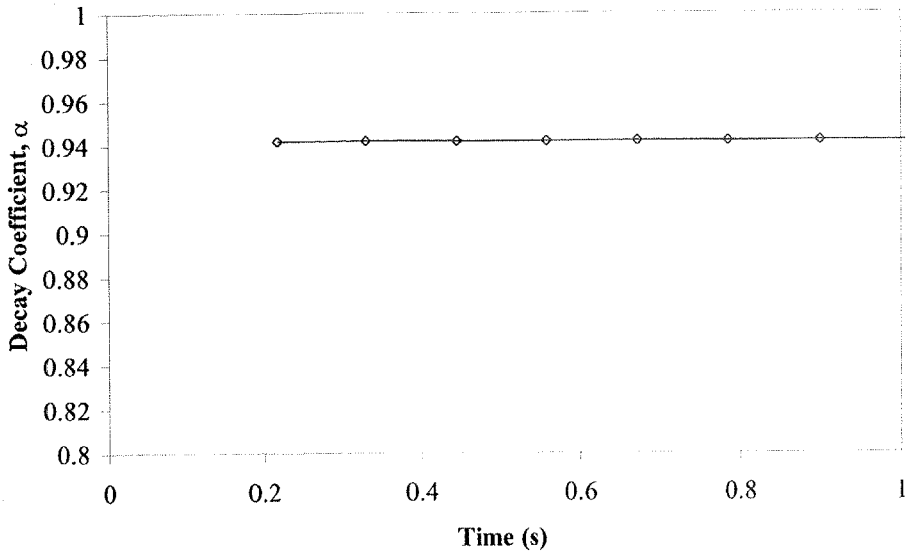

Figure 9.27 Numerical Decay Coefficient α ($k_A = k_P = 0.031$)

Figure 9.27 shows that the decay coefficient is constant at 0.942. A calculated value from the numerical data was determined as 0.941, showing a good agreement with the analytic relationship. Using Eq. 9.9.23, the exponential decay coefficient (D_U) is calculated as 0.0602. Figure 9.28 shows the exponential decay curve (Eq. 9.9.17) plotted against the numerical data. The analytically derived exponential decay curve shows a good match with the numerically modelled pressure peaks.

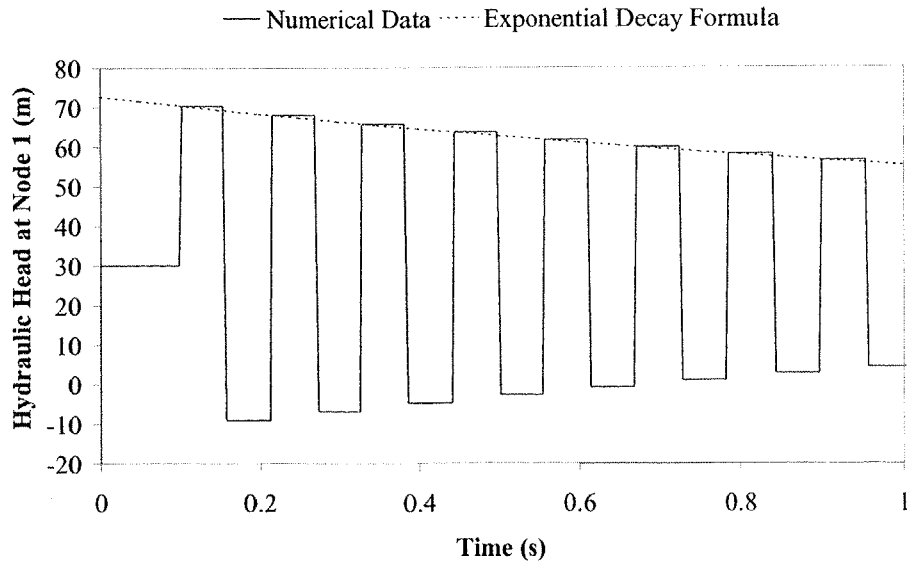

Figure 9.28 Performance of Exponential Decay Formula ($k_A = k_P = 0.031$)

Other relationships can be observed between the decay coefficients and the unsteady friction coefficients. The first of these is the relationship between the decay coefficient α and the unsteady friction coefficients k_A and k_P. The range of k_A is typically between 0 (no unsteady friction) and 0.05 (for a rough pipe in low Reynolds number turbulent flows). The variation of α over this range is plotted in Figure 9.29 and two cases were investigated. The first was when $k_P = 0$ (for slow transients) and the other was $k_A = k_P$ (for fast transients). An approximately linear relationship is observed for both cases with little difference between them.

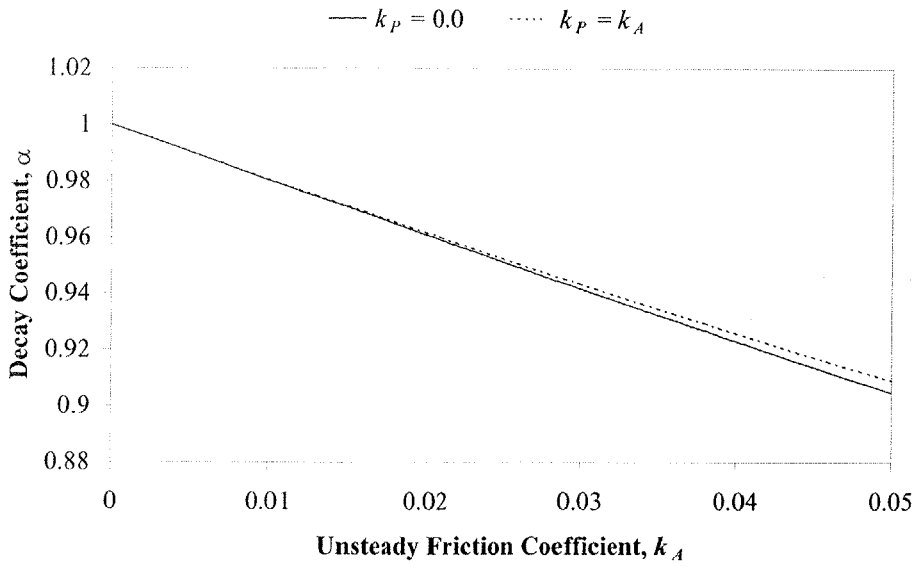

Figure 9.29 Decay Coefficient α Versus Unsteady Friction Coefficient k_A

The behaviour of the exponential damping coefficient (D_U) is also shown with respect to the unsteady friction coefficients where D_U is calculated using Eq. 9.9.23. Figure 9.30 shows results for D_U for both $k_P = 0$ (slow transient event) and $k_P = k_A$ (fast transient event).

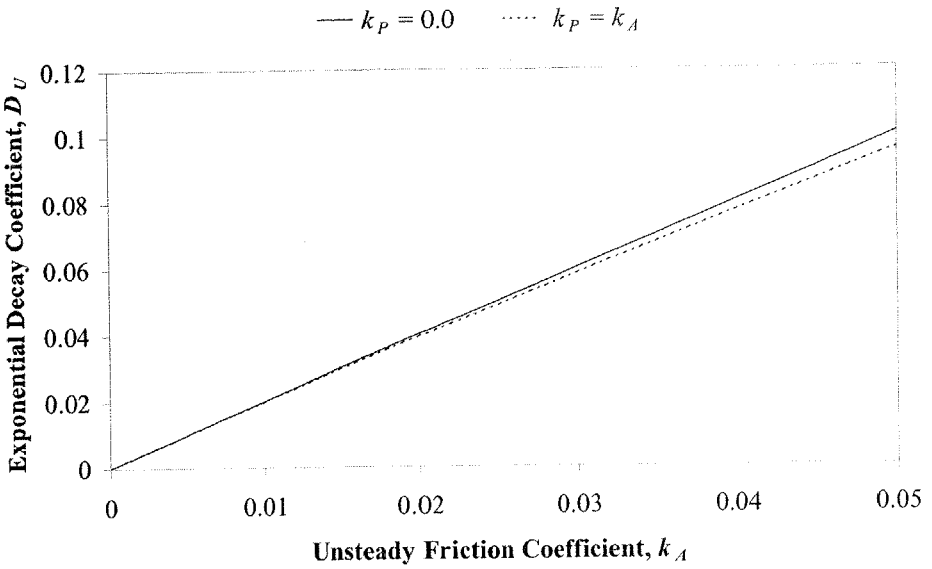

Figure 9.30 Decay Coefficient α Versus Unsteady Friction Coefficient k_A

Again the curves in Figure 9.30 are approximately linear in form and there is little difference between $k_P = 0$ and $k_P = k_A$. The behaviour of the exponential decay coefficient is further investigated by observing how it changes for different Reynolds numbers. A general relationship between the unsteady friction factor (k_A) and the steady friction factor (f) was derived in Section 9.6.2 and is repeated here as

$$k_A = 3.75\sqrt{\frac{f}{512}} \qquad \text{.....(9.9.24)}$$

The steady friction factor is related to the Reynolds number using the Colebrook-White equation. The Colebrook-White equation is restated as

$$\frac{1}{\sqrt{f}} = -0.86\ln\left(\frac{\varepsilon}{3.7D} + \frac{2.51}{\mathbf{R}\sqrt{f}}\right) \qquad \text{.....(9.9.25)}$$

Using the relationship derived in this section for the exponential decay coefficient D_U and k_A (Eq. 9.9.23) and Eqs. 9.9.24 and 9.9.25, the behaviour of D_U with the Reynolds number is indicated in Figure 9.31 for a smooth pipe ($\varepsilon/D = 0$).

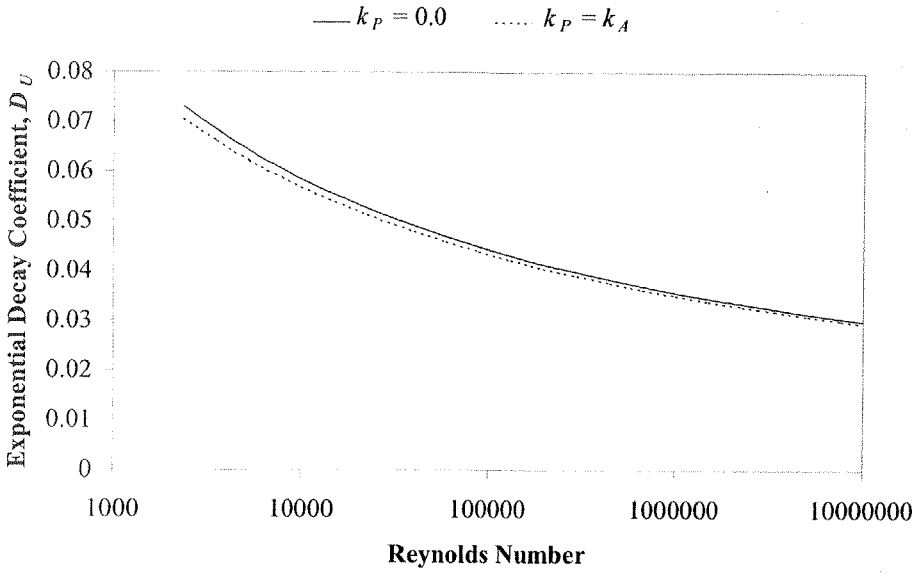

Figure 9.31 Decay Coefficient D_U Versus Reynolds Number

The formulations derived in this section are specifically for a pipeline with a closed valve at one end and a reservoir at the other end. For other configurations of transient events, the resulting formulae may be different.

9.10 Summary

In this chapter three main sections of work are presented that represent a guide for the modelling of turbulent transient events with unsteady friction.

9.10.1 New Unsteady Friction Models

A brief review was made regarding the evolution from early models to the present Brunone *et al.* (1991) model. The new concepts of unsteady flow states and unsteady flow events were created to explain the shortcomings of the original Brunone *et al.* (1991) model. A modified version of the Brunone *et al.* (1991) model was proposed and produced favourable results when numerically tested.

Improved variations to the modified Brunone *et al.* (1991) unsteady friction model have been proposed. These improvements included momentum correction factor effects that take account 2D effects that are not included in the 1D governing equations. These new models are applicable to turbulent unsteady flows and in particular to low Reynolds number turbulent flows. The k_A & k_P model shows how the modified Brunone *et al.* (1991) model and the k_3 & k_M model can be decomposed into pure amplitude and phase components. The most promising model is the k_3 & k_M model, which is made up of a boundary shear component (k_3) and a momentum correction component (k_M). These are separate effects and can be analytically derived by investigating the 2D governing equations and how they relate to the 1D water hammer equations. The solution of the governing equations, including the k_A & k_P unsteady friction model in the directional derivatives, reduces numerical error.

9.10.2 Analytic Unsteady Friction Coefficients

Traditionally the coefficients for the unsteady friction models considered would be experimentally derived. This chapter has analytically derived relationships for k_1, k_2, k_3, k_M, k_A, and k_P. Many of these unsteady friction coefficients are related to each other; however, the principal coefficients are k_3 and k_M. The universal velocity distribution laws were used in the derivations. The coefficients are based on steady state relationships and this limits their use.

9.10.3 Analytic Exponential Damping Coefficient

An analytic expression for the damping of the pressure oscillations after a transient event was found for the k_A & k_P unsteady friction model, which is particularly useful when analysing experimental results. A quick computation of the damping coefficient from an experimental test can be readily converted to an approximate unsteady friction coefficient. Alternatively, the damping coefficient could be useful to discern the magnitude of other forms of damping (such as steady state friction damping or damping due to valves and leaks) from the unsteady friction damping.

Relationships derived for the unsteady friction coefficients have given rise to models that use variable values for the coefficients depending on instantaneous conditions. The coefficients are dependent on the Reynolds number of the instantaneous flow. These proposed models and coefficients are tested against experimental results in Chapter 11.

Chapter 10

The Experimental Apparatus

10.1 Introduction

This chapter outlines the experimental apparatus and methods used to generate and collect data that are used in this thesis. Important features of the apparatus such as the pipeline, pressurised tanks, data acquisition system, valve and leakage units are described. The measurement of flow and pressure are described in detail. Calibration of the pressure transducers, steady state friction factors, wave speeds, leakage units and the valve are presented. These properties are needed to simulate a transient in the pipeline and, furthermore, to apply the inverse transient method. Filtering of the measured pressure and valve position data as input for the transient model is necessary. The performance of various filters is presented. The correct application of filtering is shown with different levels of filtering required for different types of transient event. Finally, it is shown that using the pressure head next to the valve as a boundary condition produces misleading results.

10.2 The Apparatus

The apparatus is a single pipeline in the Robin Hydraulics Laboratory in the Civil and Environmental Engineering Department at the Adelaide University. It was initially built by Bergant and Simpson (1995) using the funds from a large Australian Research Council (ARC) grant. Figure 10.1 shows a schematic of the pipeline.

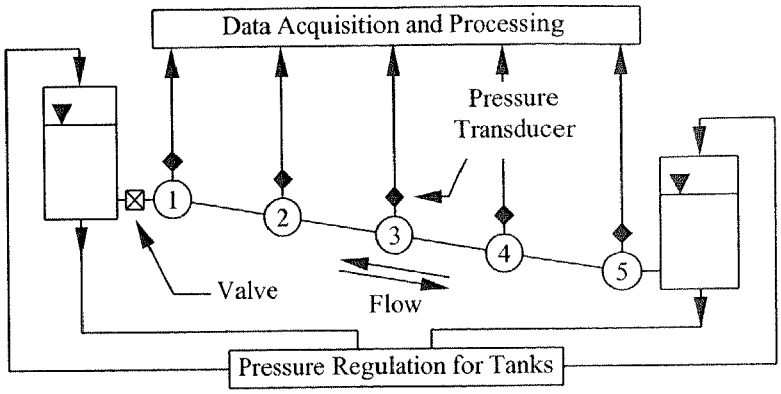

Figure 10.1 Experimental Pipeline Schematic

It is composed of a 37.2 m long copper pipe with an inside diameter of 22.1 mm and a wall thickness of 1.6 mm. A photograph of the pipeline is shown in Figure 10.2. To prolong its life the water used in the pipeline is demineralised (obtained from the Department of Chemical Engineering at the Adelaide University).

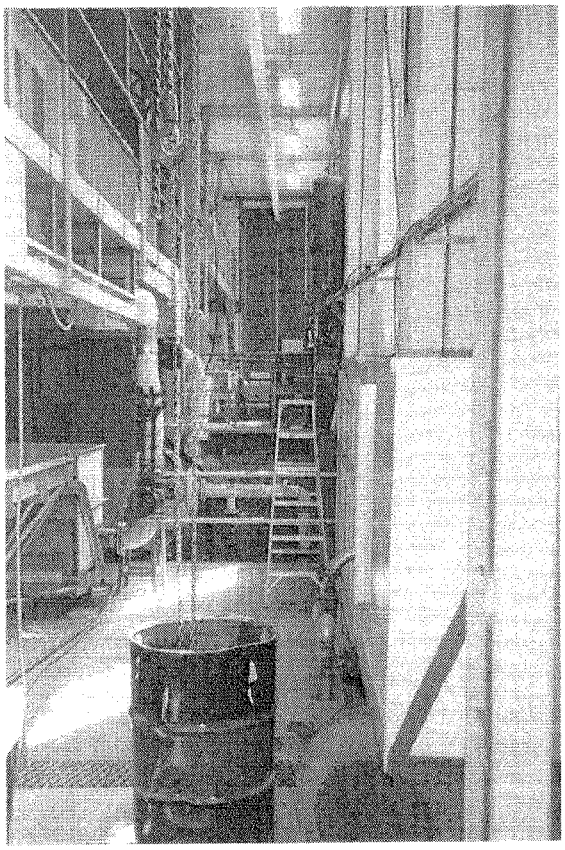

Figure 10.2 Overall Layout of Pipeline (from Bergant and Simpson, 1995)

10.2.1 Pressurised Boundary Tanks

Two pressurised tanks at each end control the initial pressure and flow in the pipeline. A computer controlled pressure regulation unit regulates the pressure in each tank. Each tank has a maximum allowable pressure of 70 m head, but the air compressor that supplies the two tanks is capable of a maximum pressure of only 45 m. Photographs of the two tanks are shown in Figure 10.3. Figure 10.3(a) shows the tank at node 1, with the pressure regulation unit shown below the tank. Figure 10.3(b) shows that tank at node 5 assuming the discretisation shown in Figure 10.1.

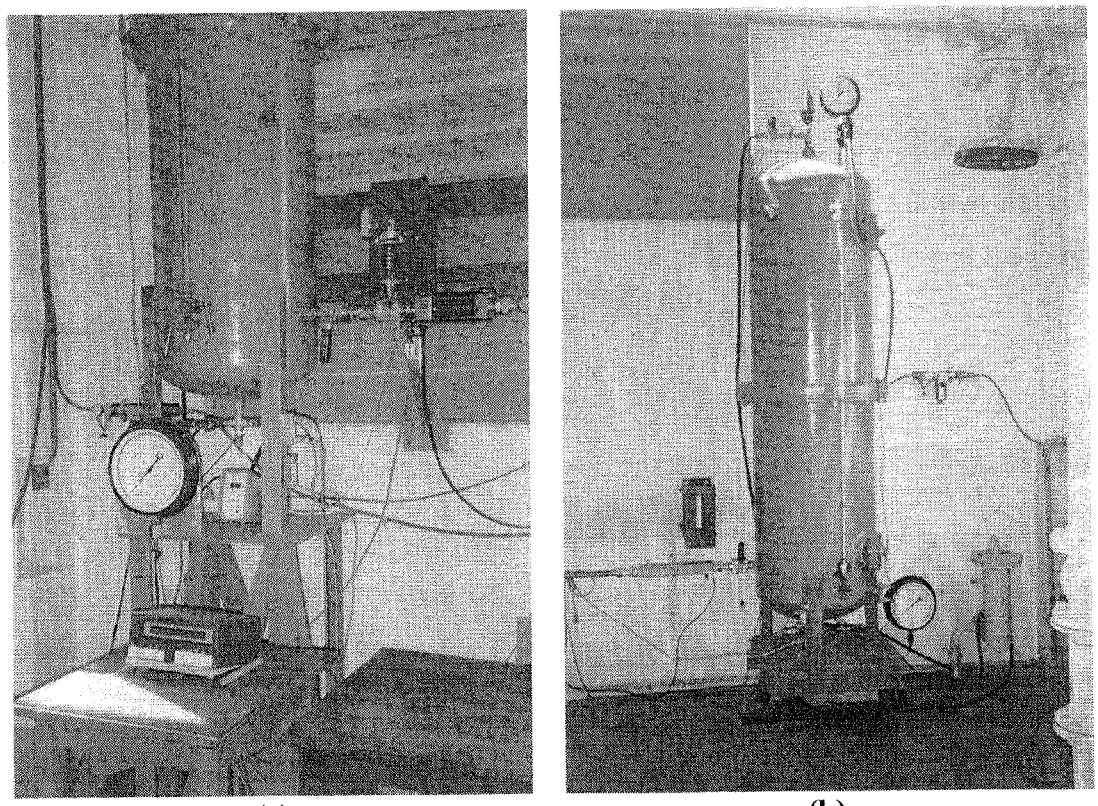

(a) (b)

Figure 10.3 Node 1 and Node 5 Boundary Tanks
(from Bergant and Simpson, 1995)

10.2.2 Valve at Node 1

The transient event in the experimental pipeline is initiated using a valve located next to the tank at node 1. The valve is of type Whitey 65TF16, inner diameter 22.2 mm. It has little friction loss making it ideal for initiating the transient event. The valve can be closed at two speeds, the first of which is a fast valve closure. A spring loaded valve actuator is capable of closing the valve in approximately 9 ms (Bergant and Simpson, 1995), which is considerably faster than the definition of a fast valve closure time (56 ms) based on the $2L/a$ period of the pipeline assuming a wave speed of 1,319 m/s. Figure 10.4 shows a photograph of the fast valve closure apparatus. Optical sensors are used to measure the valve position.

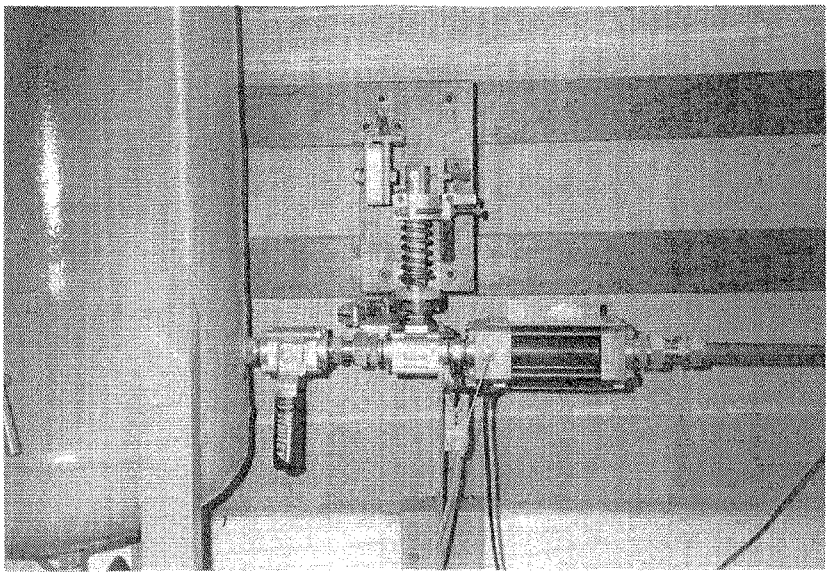

Figure 10.4 Fast Closing Valve (from Bergant and Simpson, 1995)

For slow valve closures the operation is performed manually. The actual position of the valve during the closure event is more important for slow valve closure than for fast valve closure. The position is measured using a potentiometer (POT) that is attached to the valve handle. The valve position is displayed above the valve using a LCD screen and also collected in the data acquisition process. Figure 10.5 shows a photograph of the slow valve closure apparatus.

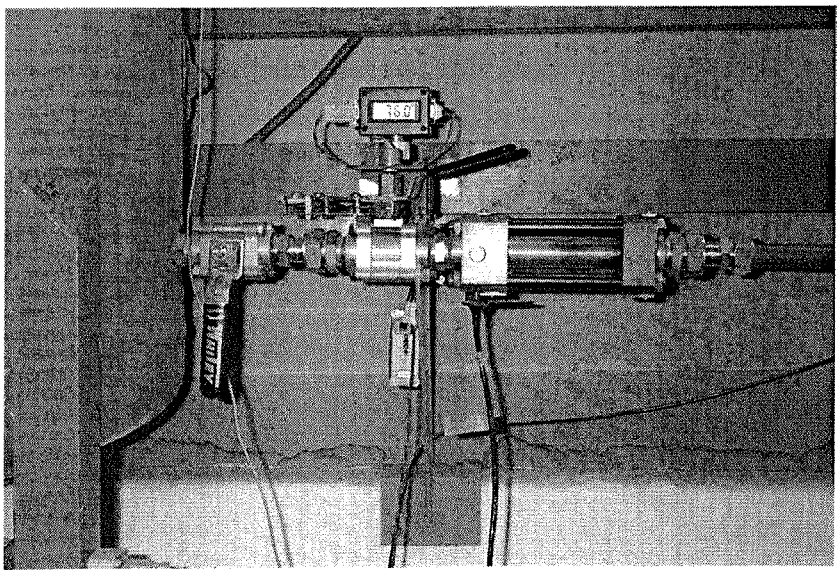

Figure 10.5 Slow Closing Valve

10.2.3 Leakage Blocks

One of the goals of the research presented in this thesis is to detect a leak using the inverse transient method. Therefore, leakage must be able to be simulated at different locations in the experimental pipeline. "Leakage units" are installed along the pipeline at the quarter points (nodes 2 and 4 in Figure 10.1). They are mounted in the pipeline using a brass block, a schematic of which is shown in Figure 10.6.

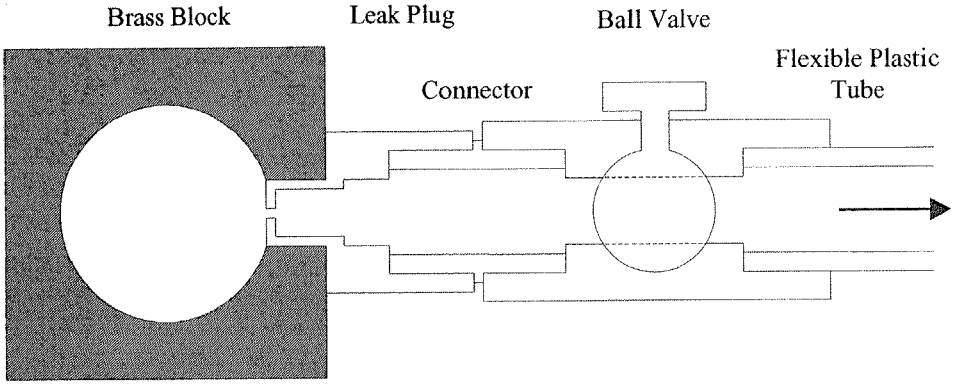

Figure 10.6 Leakage Unit Schematic

The brass block mounting allows different size leaks to be installed whenever needed. The leaks may be switched on or off using a small ball valve. One point of concern is that, due to the size of the inner chamber in the leakage unit, the leak may not behave as a true orifice. Therefore, it is likely that the calibrated behaviour will differ slightly from the orifice equation as the chamber may act like a small pipe section. Figure 10.7 shows a photograph of a 1.0 mm leak at node 2.

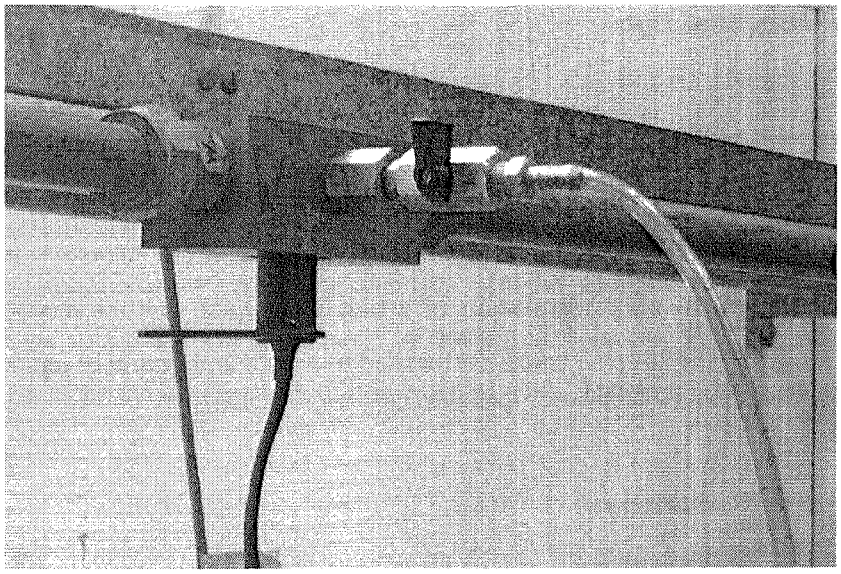

Figure 10.7 Photo of Leakage Unit

Four leakage units were manufactured. Their sizes (the diameter of the orifice) are 1.0 (two units), 1.5 and 2.0 mm.

10.2.4 Data Acquisition System

The data acquisition for the apparatus is performed on a 150 MHz Pentium computer using an Intelligent Instrumentation data acquisition card and Visual Designer software. The data acquisition card is of type PCI-20428W-1, which can accept 16 single-ended analogue input channels. The conversion of these analogue signals to digital signals is performed with 12-bit resolution. The possible voltage ranges accepted are ±5 V, ±10 V, 0-5 V and 0-10 V, of which the range 0-10 V was used. The card has a maximum sampling rate of 100,000 Hz for one channel; however, depending upon how many channels are being input, the maximum sampling rate may be lower. The Visual Designer software provides an easy-to-use graphical representation of the data acquisition process. Control over the number of input channels, sampling rates, processing of data and storage of the data in a file are all controlled via the software.

10.3 Measurement of Data

The measurement of pressure (at the tanks and along the pipeline), initial flow and valve position are most important. These measurements are used as inputs for initial conditions or boundary conditions for the transient model. Poor measurement of these quantities will result in poor simulation of a transient event. Other measurements of pressure are used by the inverse transient method to locate and quantify leaks.

10.3.1 Pressure Measurement

The pressure is measured at five positions along the pipeline (as indicated in Figure 10.1) using five Druck PDCR 810 flush fit pressure transducers. The flush fit is important so they do not interfere with the fluid flow or produce undesirable effects (such as the transducer ringing as illustrated in Simpson and Bergant, 1994). The rise time for these transducers is 5×10^{-6} s. The absolute pressure range is 0 to 600 kPa and the uncertainty is ±0.1% of full span. The transducers are mounted in brass blocks. Figure 10.8 shows a photograph of the transducer and transducer block. An amplifier is needed to amplify the electrical output signal from the pressure transducers (seen on the left side of Figure 10.8).

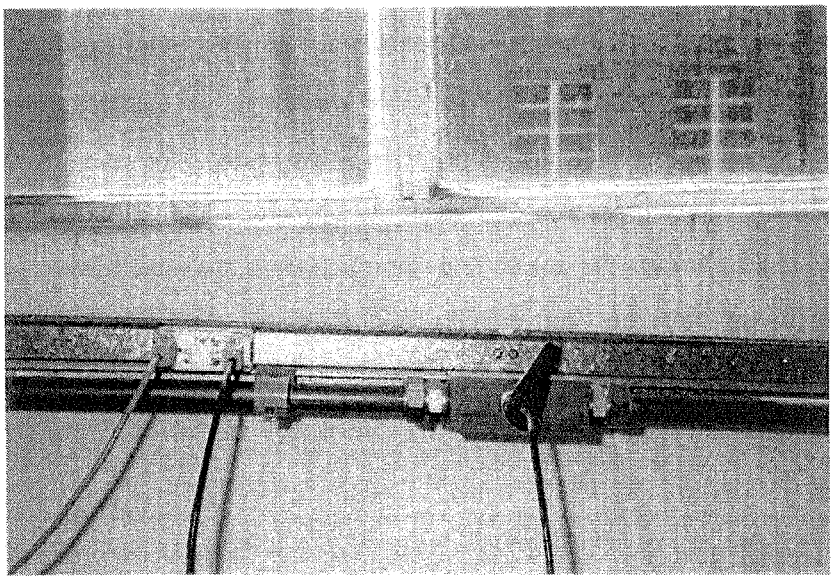

Figure 10.8 Pressure Transducer and Transducer Block (from Bergant and Simpson, 1995)

10.3.2 Initial Velocity Measurement

The initial steady state velocity of the flow in the pipeline is an important measurement that must be made for any experimental test. In the absence of a flow meter other means must be found for the calculation of the initial velocity, V_0. Three methods are used for a transient event: (i) a volumetric method, (ii) a fast transient method and (iii) a slow transient method.

(i) The initial velocity in the pipeline can be found by observing the changing water levels in the supply and delivery tanks, a volumetric method, where the tank level changes over time is related to a calibrated volumetric constant,

$$V_0 = \frac{\Delta z}{t_{\Delta z} c_v} \quad \text{.....(10.3.1)}$$

where Δz = change in water level, $t_{\Delta z}$ = time for water level change and c_v = calibrated volumetric constant. The volumetric constant was calibrated in Bergant and Simpson (1995). For Tank 1 it is 2.104×10^{-3}; for Tank 2, $c_v = 1.540\times10^{-3}$.

(ii) If the valve closure is fast (that is, a closure time $t_c < 2L/a$) the Joukowsky pressure rise formula can be used to calculate the initial velocity, which is called the fast transient method. The equation for the Joukowsky pressure head rise is Eq. 3.4.1 in Section 3.4. Rearranging the Joukowsky equation for the initial velocity gives

$$V_0 = \frac{g}{a}\Delta H \quad \text{.....(10.3.2)}$$

where V_0 = initial velocity, ΔH = change in pressure head, g = gravitational acceleration and a = wave speed.

Finally, (iii) if the valve closure is slow, a back calculation of the initial velocity can be performed, which is called the slow transient method. Requirements for this method are that the valve closure is slow ($t_c > 2L/a$) and the head at the valve and the valve position are known. The slow transient method is applied by first guessing a value of the initial velocity. A transient simulation is then performed using the measured head as a boundary condition. The valve position data are used to find the time at which the valve

is fully closed (a velocity of zero). The velocity is found, through the transient simulation, for that time. If the final velocity is not zero, the process is repeated with different initial velocities until an initial velocity is found that produces zero velocity when the valve is closed.

The slow transient method is best demonstrated through the use of an example. The pressure head at the valve and the valve position have been measured for a slow transient event ($t_c = 0.7$ s), as shown in Figure 10.9. The measured time of closure is 1.23 s.

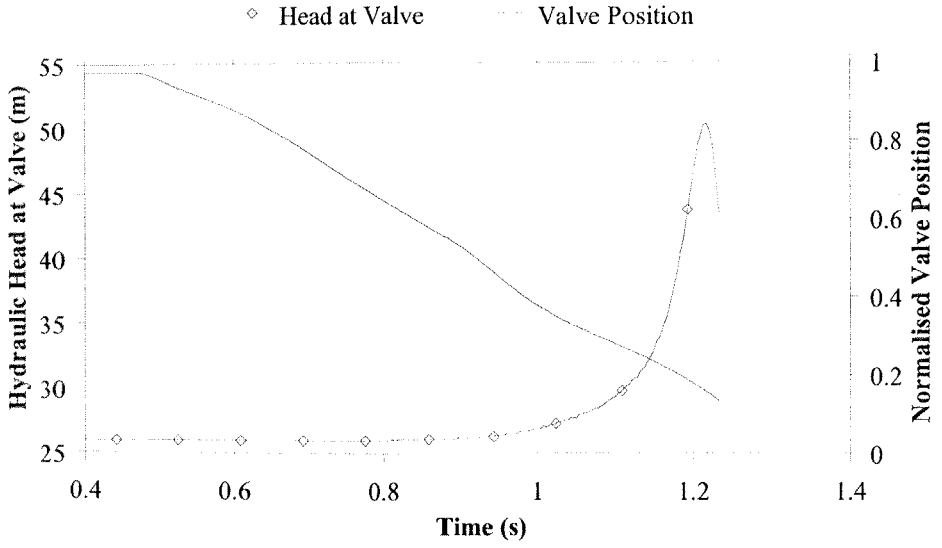

Figure 10.9 Measured Head at Valve and Valve Position

The initial velocity is guessed as 0.418 m/s. The flow at the valve is calculated using the pressure head data, as shown in Figure 10.10. If the guess is correct, the final flow at the valve would be zero when the valve is completely closed. For the guess, the final calculated flow is not equal to zero (-1×10^{-5} m^3/s). After a few iterations, the correct initial velocity is calculated as 0.438 m/s.

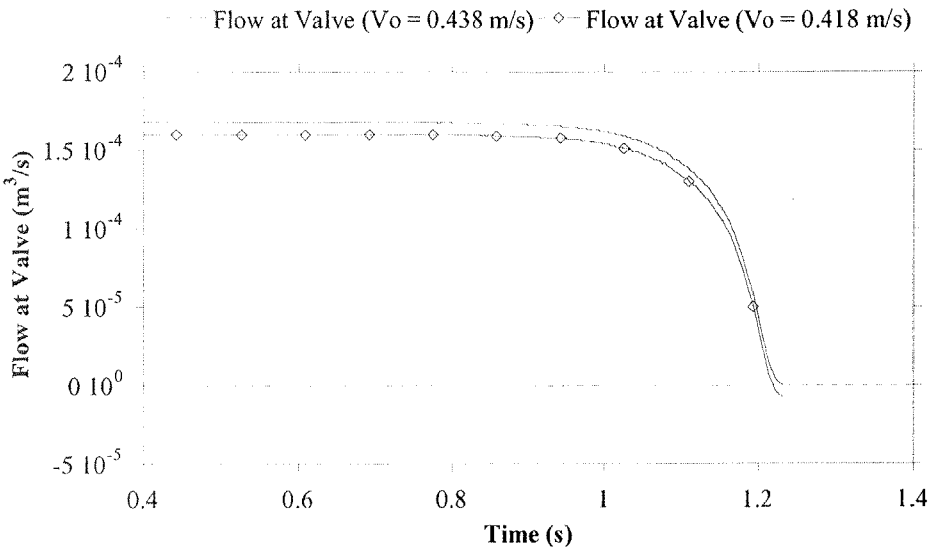

Figure 10.10 Calculated Flow at Valve

10.3.3 Valve Position Measurement

Measurement of the valve position is important because it is used as an input in the transient model. The measurement is performed differently for fast and slow valve closures. For fast valve closures, four optical sensors (of type RS 306-06, rise time 5×10^{-6} s), located at 0° (fully open), 30°, 60° and 90° (fully closed) positions, are used to track the position of the valve (Figure 10.4). A time is logged when the valve passes each of these optical sensors, and is used to verify the closure time. A detailed account of the valve position is needed for slow valve closures but not for fast valve closures. For slower speeds of valve closure, the valve position was measured using a potentiometer attached to the top of the valve (Figure 10.5), which provided a variable resistance that was used to produce an output voltage that was dependent on the valve position.

10.4 Calibration Results

Various properties of the experimental pipeline need to be known for accurate numerical modelling. This section presents calibration results for the pressure

transducers, wave speed, valve, leaks and the verification of the steady state friction factor.

10.4.1 Transducer Calibration

The pressure transducers were calibrated using a hand pressure tester. Calibration was performed for each of the five pressure transducers. The result of the calibration of the pressure transducer at node 1 is shown in Figure 10.11 in which a linear relationship between voltage and pressure is indicated. From a linear regression the R^2 term in each case is close to 1, indicating a good fit. Calibration curves for the other transducers are found in Appendix C.1.

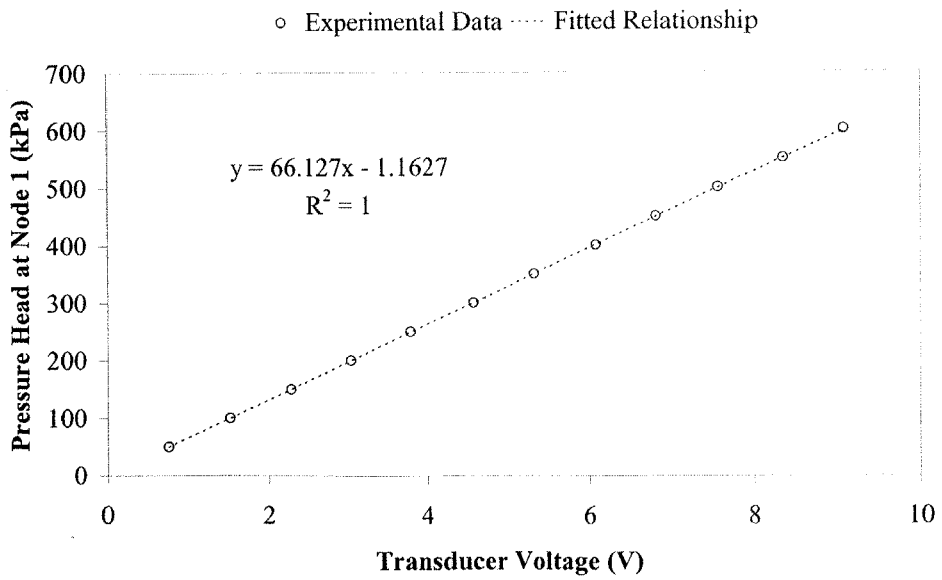

Figure 10.11 Calibration of Node 1 Pressure Transducer

An important property of the pressure measurement is the error associated with each transducer. The random error is caused by electromagnetic interference (EMI). Small random currents are induced into the cable from environmental electromagnetic radiation. The error is visualised by observing the scatter from the pressure produced from each transducer. Figure 10.12 shows the scatter for the pressure transducer at node 1. The resolution of the 12 bit data acquisition card produces the blocky appearance of the signal.

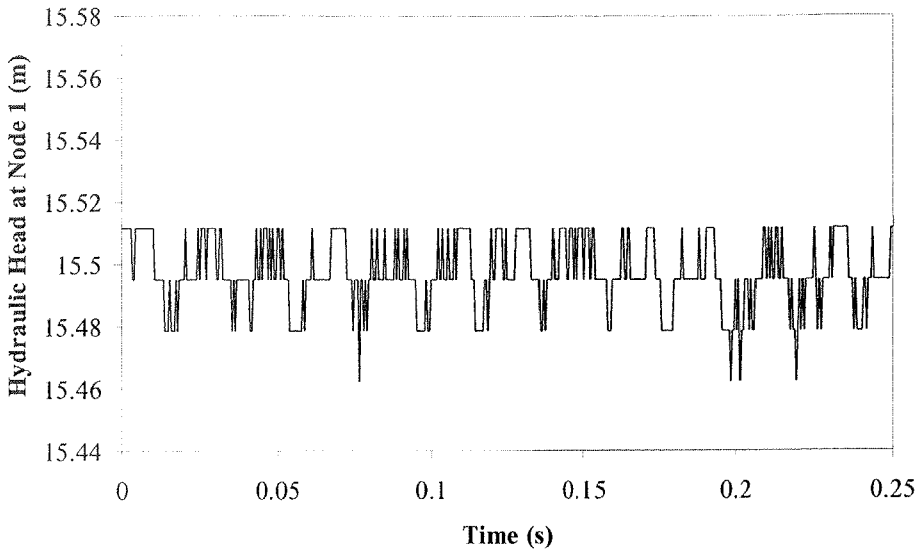

Figure 10.12 Pressure Transducer Noise at Node 1, No Flow

The expected accuracy of the measured pressure is indicated in Figure 10.12. The range of the transducer is 67 m of pressure head and the resolution of the data acquisition system is 12 bit (2^{12}). Thus, the resolution of measured pressure is 16.4 mm. Assuming that the error has a normal (Gaussian) distribution, the standard deviation of the error at node 1 is 13 mm. Figure 10.13 shows the error in the measured pressure at node 5, which is larger than the error at node 1. The reason for the larger error is that there is a longer length of cable between the data acquisition system and the transducer (even though shielded cable is used). The standard deviation for the transducer at node 5 was calculated as 31 mm.

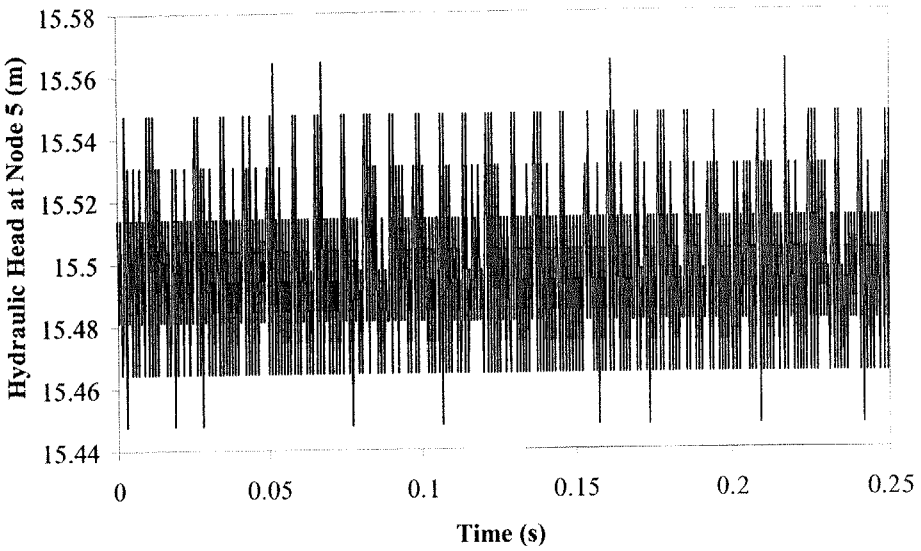

Figure 10.13 Pressure Transducer Noise at Node 5, No Flow

The previous errors were measured when there was no flow in the pipeline. The same analysis was repeated when there was flow in the pipeline (not shown in this thesis) with a Reynolds number of 10,450 and a fully open valve. The standard deviation of the errors at each of the nodes is compared to the zero flow case (Table 10.1). There is no significant difference between the standard deviations in the two instances, suggesting that the turbulence in the flowing water produces a smaller error in the measured pressure data than the error caused by EMI on the cable.

Table 10.1 Standard deviation at Pressure Transducers

Type of Test	Standard Deviation (m)				
	Node 1	Node 2	Node 3	Node 4	Node 5
No Flow	0.013	0.010	0.019	0.026	0.031
Flow, **R** = 10450	0.009	0.009	0.017	0.025	0.028
¼ Open Valve, **R** = 8579	0.072	0.107	0.107	0.110	0.036

The error in the measured pressure was also found for steady flow controlled by a quarter open valve. Figure 10.14 shows the pressure measurement at node 1 with a much greater error compared to the no flow case.

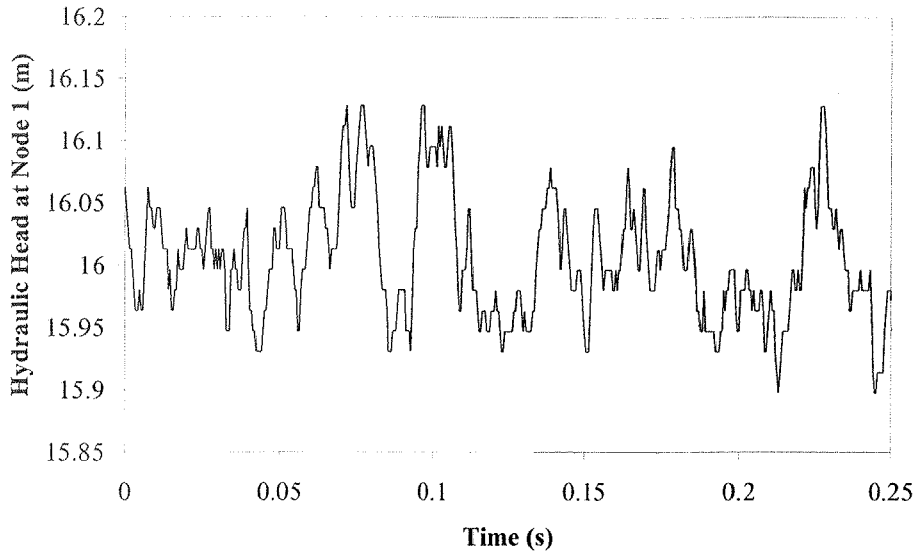

Figure 10.14 Pressure Transducer Noise at Node 1, ¼ Open Valve

The standard deviation of the error at node 1 is 72 mm, which is over five time the size of the error when the valve is fully open. The standard deviation of the errors in the measured pressures for each node is also shown in Table 10.1. The turbulence created by the quarter open valve is large and can affect the measurement of pressure. Therefore, the size of the error at each node is different and a function of the position of the valve. The standard deviation of the errors in the measured data can be used to estimate the standard deviation of the error in the solved lumped leak coefficients. A solution method is presented in Section 4.8 and is applied to experimental data in Section 12.2.4. The estimated error can then be used as a guide to quantify how confident one can be in a solution from the inverse transient method.

10.4.2 Wave Speed Calibration

The theoretical wave speed is calculated using a relationship defined in Section 3.5, the result of which is 1,321 m/s. Bergant and Simpson (1995) calculated the wave speed by timing of the wave front along the pipeline using a fast valve closure. The calibration produced a wave speed of 1,319 m/s, which is used in further analysis of the experimental pipeline.

An important note is that for a fast valve closure, the calculation of the wave speed can produce misleading results. Results from Section 11.3 show that for an initially turbulent fast valve closure, there is an associated change in phase of the pressure oscillations after the event. If Fourier techniques are used to estimate the wave speed from the frequency of the pressure oscillations (the natural frequency is theoretically equal to $a/4L$), misleading frequencies could be found because of the phase change. To avoid misleading frequencies slow valve closure events ($t_c > 2L/a$) are used for leak detection.

10.4.3 Steady State Friction Factor Calibration

The Colebrook-White or the Swamee-Jain relationships predict the Darcy-Weisbach friction factor, which is dependent on the Reynolds number of the flow and the roughness of the pipe wall for turbulent flow. The experimental pipeline is made from drawn copper tubing. The estimated roughness of the pipe is 0.0015 mm, giving a relative roughness (ε_D) value of 6.8×10^{-5}. For the range of velocities possible in the pipeline (a maximum Reynolds number of 100,000) the roughness can be assumed to be zero; therefore, the pipe can be called "smooth." The friction factor relationships at steady state conditions are verified using the pressure difference measured between node 2 and 4 and the measured flow, the result of which is shown in Figure 10.15. Experimental results for steady state conditions below a Reynolds number of 10,000 could not be plotted because the pressure difference was smaller the measurement resolution.

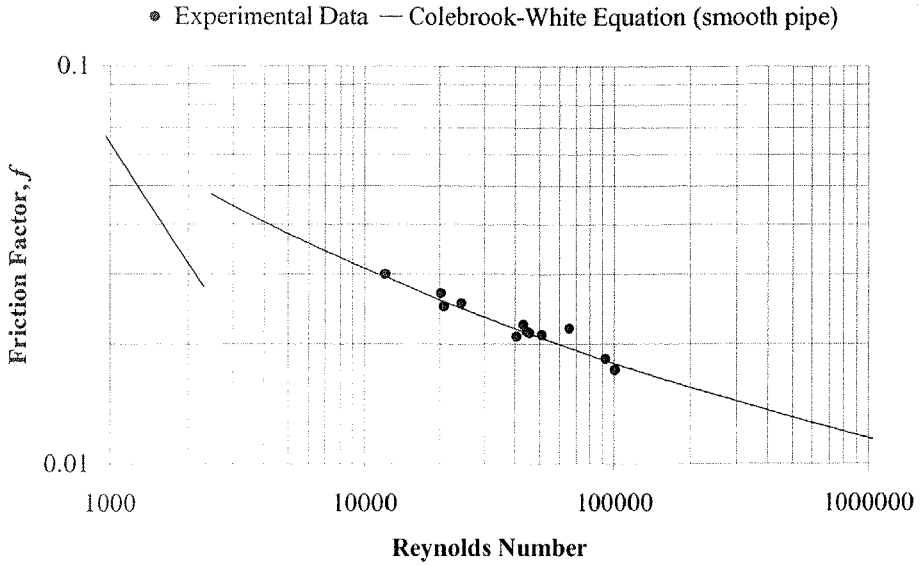

Figure 10.15 Calibration of Steady State Friction Factor

The experimental data fits the Colebrook-White relationship, which provides a useful verification of the behaviour of the steady state friction factor that is used by the quasi-steady friction model in the transient calculation. The quasi-steady friction model is used in conjunction with unsteady friction models in many chapters of this thesis.

10.4.4 Valve Calibration

The calibration of the valve in the experimental pipeline is pivotal for modelling transient events. The valve equation (Section 3.8) is restated as

$$Q_V = \tau C_V \sqrt{\Delta H_V} \quad \text{.....(10.4.1)}$$

where Q_V = flow through the valve, τ = dimensionless valve-opening coefficient, C_V = valve coefficient and ΔH_V = head loss across valve. The relationship between τ and the valve position must be known accurately to ensure a good match between the model and experimental data. The calibration of the valve was performed in situ using a transient method. The transient method (created in this thesis) uses pressure data to back-calculate τ versus valve position. The transient event used for valve calibration was a slow valve closure (t_c = 0.7 s). The initial velocity was 0.438 m/s, which corresponds to a Reynolds number of 9,612. Figure 10.16 shows the measured pressure head at the valve and the measured valve position. The valve position (based on the angle of the

valve lever) has been normalised such that a value of 1.0 corresponds to fully open and 0.0 to fully closed. Due to the geometry of the ball valve, the position of total closure corresponds to a normalised valve position of approximately 0.14. Further closure (from a normalised value position of 0.14 to 0.0) has no effect on the flow.

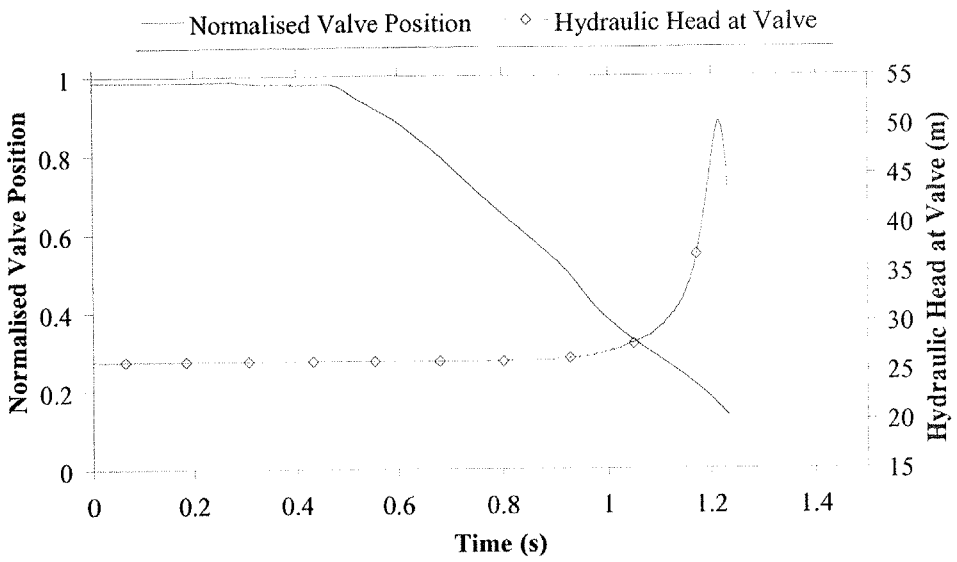

Figure 10.16 Measured Valve Position and Head at Valve Versus Time

The flow through the valve is calculated using a transient method with the boundary condition at the valve determined from pressure head data. The subsequent transient analysis provided the flow at the valve. Unsteady friction was used in the transient model using the k_A & k_P model with coefficient values of $k_A = 0.029$ and $k_P = 0.0$. The valve coefficient, C_V, is set as 0.0019 so that τ for a fully open valve approximately equals 1.0. Both the computed flow through the valve and τ are shown in Figure 10.17.

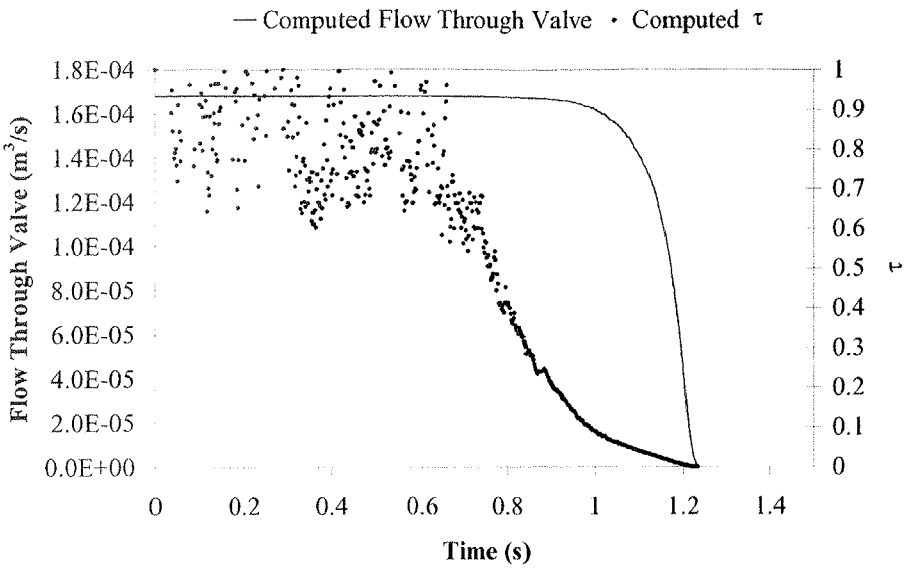

Figure 10.17 Computed Flow Through Valve and τ Versus Time

The ball valve is smooth and the head loss (when fully open) is smaller than the resolution of the measured pressure data, which causes scatter in the computed τ values when the valve is almost fully open. The scatter does not have a great effect because the head loss at the valve for an almost fully open ball valve (in this case anyway) is negligible. To model a valve correctly, the τ versus valve position curve, which is plotted in Figure 10.18, must be known.

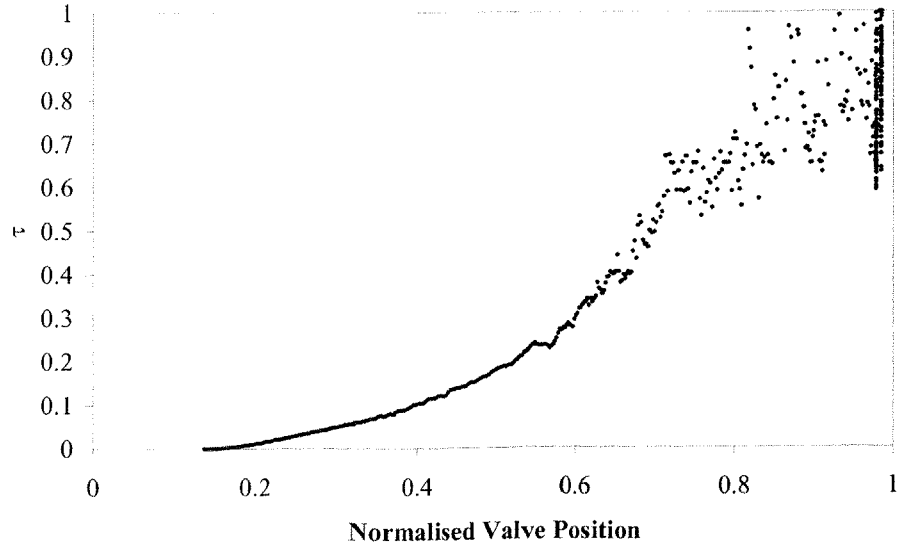

Figure 10.18 τ Versus Normalised Valve Position

The most critical section of the τ versus valve position curve is the region from approximately half closed to fully closed, which is not clear in Figure 10.18. A better way to show the curve is by a plot of the logarithm of τ against the logarithm of the valve position (Figure 10.19).

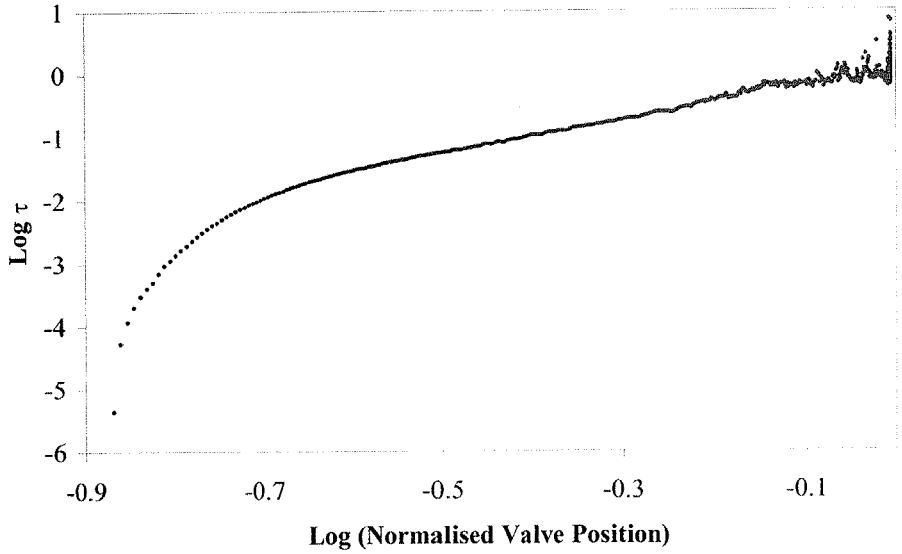

Figure 10.19 Log (τ) Versus Log (Normalised Valve Position)

Two polynomials were fitted to different regions of the curve. A fifth order polynomial was used for the range of logged normalised valve position values from –0.7 to 0.0. A ninth order polynomial was used for the remaining region, which included the steeper behaviour near closure. Care was taken so that the connection of these two fitted curves (at a logged normalised valve position of –0.7) was continuous in magnitude and slope. Figure 10.20 shows the fitted curve.

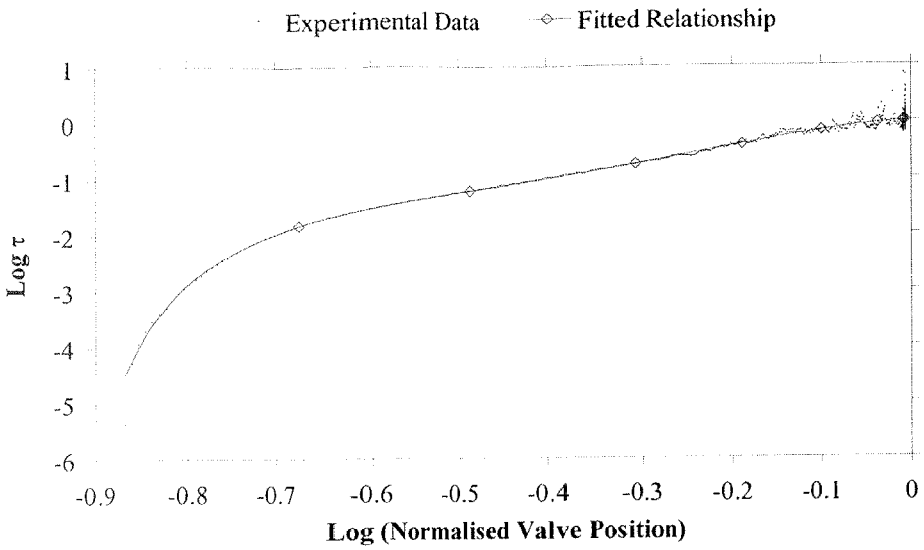

Figure 10.20 Experimental and Fitted Relationship τ Curves

10.4.5 Leak Calibration

Calibration of the four leak units is necessary for the verification of the inverse transient method. The behaviour of each leak is checked by subjecting the leak to different pressures and measuring the flow rate of the fluid exiting through the leak. The flow rate was found volumetrically. Several tests were made to compute an average flow rate. The results from the calibration for the four leak units are shown in Figure 10.21. The four leak units are of diameter 1.0 mm (two units), 1.5 mm and 2.0 mm.

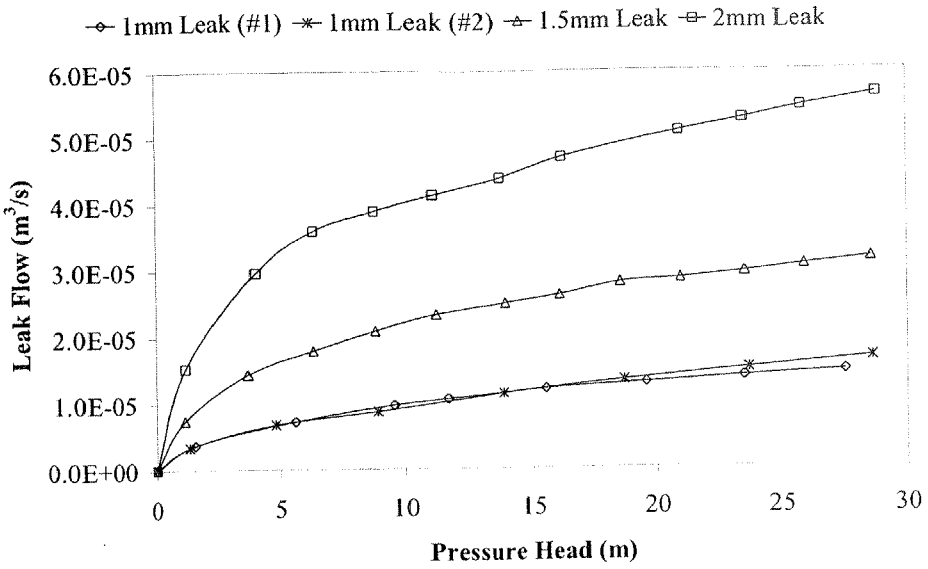

Figure 10.21 Leak Flow Versus Pressure Head

The results of fitting the leak equation for each leak unit are presented in Appendix C.2. The 1.5 mm and 2.0 mm leaks show a deviation from the leak equation, but this deviation is small compared with the range presented in the calibration results. The leak equation is restated as

$$Q_L = C_d A_L \sqrt{2g(H_L - z_L)} \quad \text{.....(10.4.2)}$$

where Q_L = flow through the leak, C_d = coefficient of discharge, A_L = diameter of leak, g = gravitational acceleration, H_L = pressure head at leak and z_L = elevation of leak. The deviations from the leak equation could be explained by the geometry of the leak unit. For large flows, the chamber in the unit before the valve would fill with water, becoming a small pipe section and changing the behaviour of the leak. Overall, these results show that the leak equation approximately represents the calibrated behaviour observed in Figure 10.21. The coefficient of discharge (C_d) is calculated from the pressure and flow data, the results of which are shown in Figure 10.22. The discharge coefficient through an orifice is dependent on the Reynolds number of the discharge. The relationship for a true orifice is shown in Section 3.9. Similar behaviour is observed in the experimental calibration data. These curves should fall onto a common curve but do not for the four leaks, which is due, in part, to small differences in the leak unit geometry and, especially for the larger diameter leak units, the filling of the pipe-section downstream of the leak orifice.

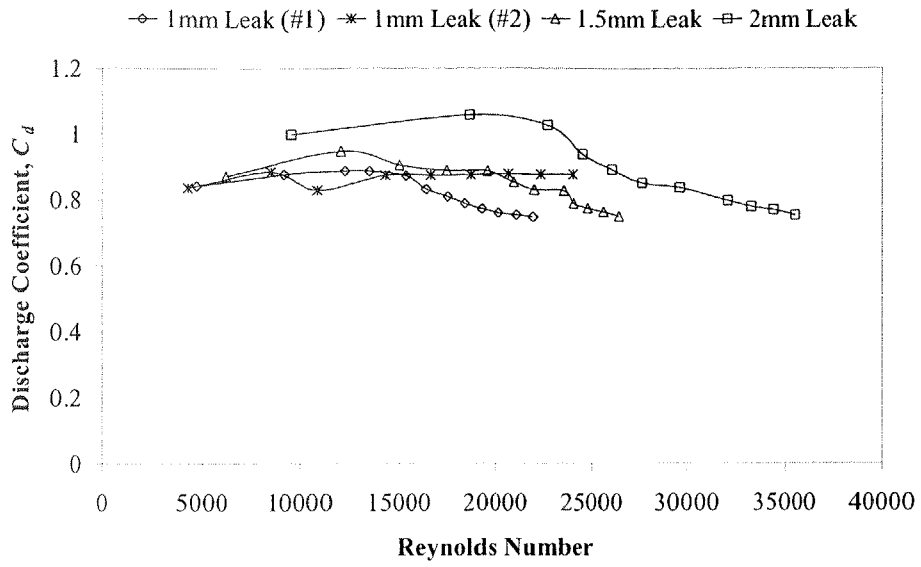

Figure 10.22 Discharge Coefficient Versus Reynolds Number

A more useful relationship is found from a plot of the lumped leak coefficient (C_dA_L) since this is the parameter to be found by the inverse transient method. The lumped leak coefficient versus the Reynolds number of the flow through the leak is shown in Figure 10.23.

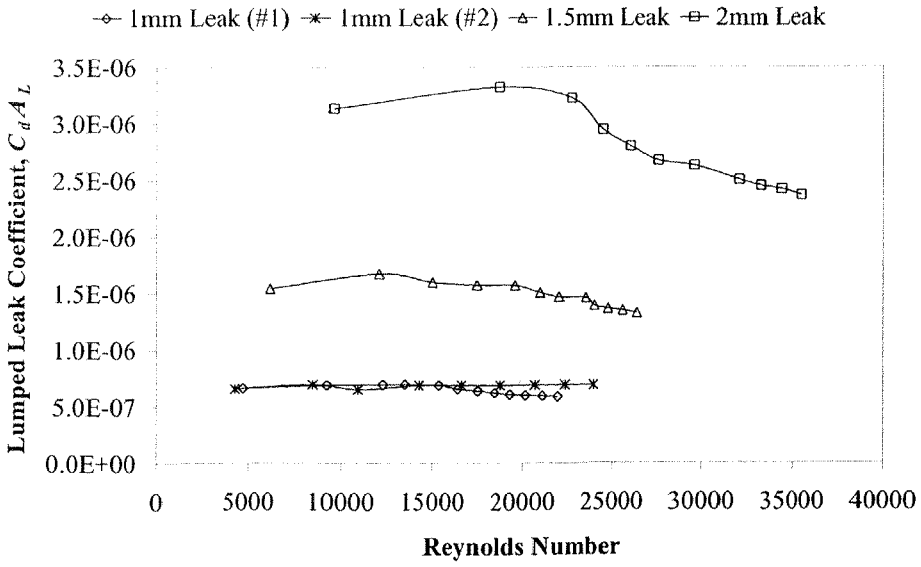

Figure 10.23 Lumped Leak Coefficient Versus Reynolds Number

Another useful plot of the lumped leak coefficient is a plot against the pressure at the leak (Figure 10.24).

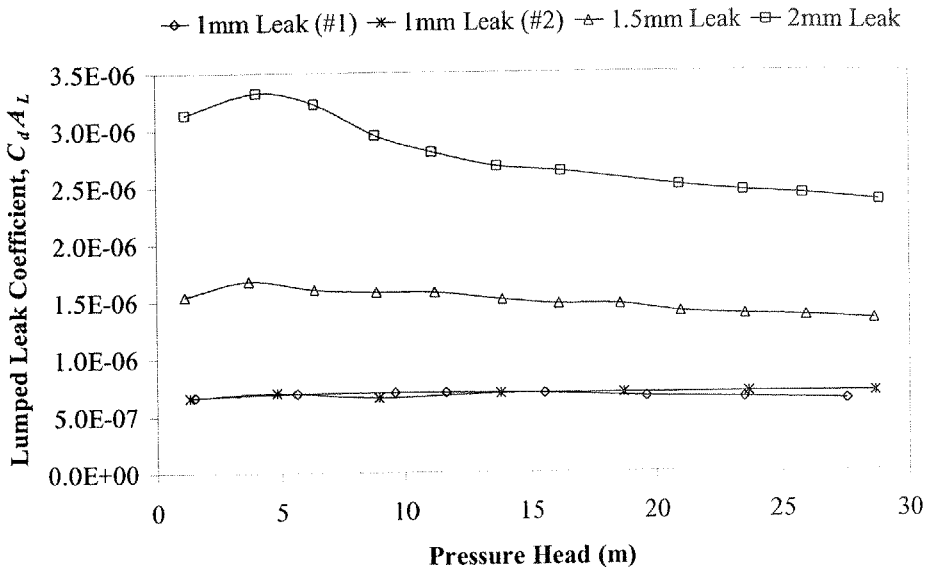

Figure 10.24 Lumped Leak Coefficient Versus Pressure Head

In Figure 10.24, the lumped leak coefficient varies with the flow through the leak and that flow varies with the pressure at the leak. In a transient event, the pressure at the leak varies suggesting that lumped leak coefficient will vary also. The variation in C_dA_L is needed when assessing results from the inverse transient method (see Section 12.2.1).

10.5 Data Filtering

Data filtering of both the measurement pressure and the valve position (for boundary conditions) is essential to model correctly a transient event. Raw data from the data acquisition system invariably contains random noise. In addition, the data acquisition system can only measure data at a certain resolution, giving data a "stepped" appearance. The need for filtering of the measured data is dictated by how they are to be used. No filtering is needed if the measured data are to be used for a data fitting algorithm (such as the Levenberg-Marquardt algorithm in the inverse transient method) because the algorithm will make a best fit with the measured data, effectively performing a regression. If, on the other hand, the measured data are used as input to the transient model, measurement errors can have a detrimental effect on the model performance. Measured data can be used in a transient model in two ways. The first is

as measured pressure head specified as a boundary condition and the other is as the valve position used as a boundary condition. The following sections outline how the boundary condition data can be filtered and then outline some problems due to over and under filtering.

Three types of filters are considered. These are infinite impulse response (IIR) filters, moving average smoothing filters and Savitzky-Golay smoothing filters (Press *et al.*, 1992). The performance of each of these filters is tested on measured pressure data collected from a transient event initiated by a partial valve closure and subsequent re-opening of the valve. The measured pressure data, sampled at a rate of 2,000 Hz, are shown in Figure 10.25.

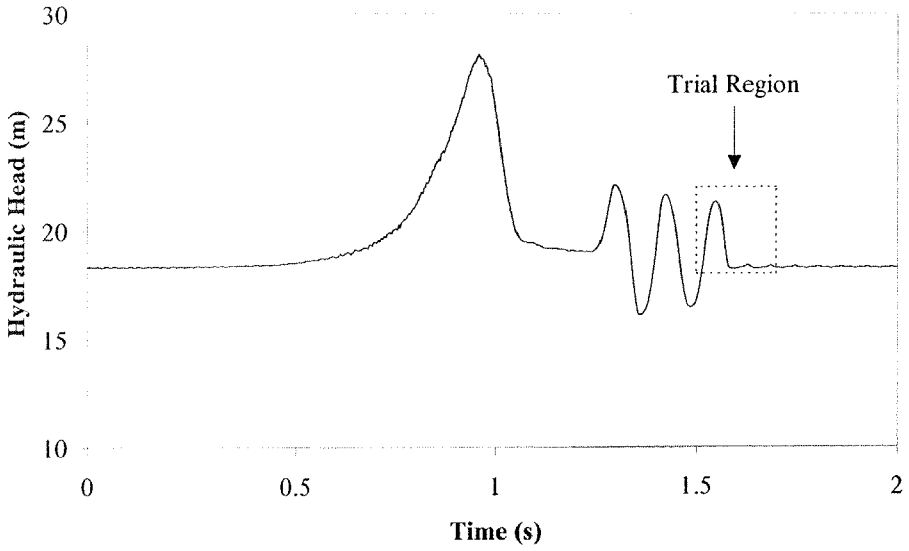

Figure 10.25 Filter Test Data (Before Filtering)

The performance of the filters is conducted for the trial region, shown in Figure 10.25, which was selected because it has large and abrupt changes in slope. Moving average filters are easy to apply by simply averaging a range, a window, of data points. Window sizes in this section are defined as the total range (or window width). The equation that describes a moving average filter is

$$y_i = \frac{1}{(2N+1)} \sum_{j=-N}^{N} x_{i+j} \quad \text{.....(10.5.1)}$$

where $y_i = i^{th}$ filtered data point, $x_i = i^{th}$ raw data point and N = number of preceding data points (equal to the number of proceeding data points, window size $N_p = 2N + 1$). A moving average filter with window sizes of 11, 21, 41 and 81 data points is applied to the measured data, the results of which are shown in Figure 10.26 for the trial region.

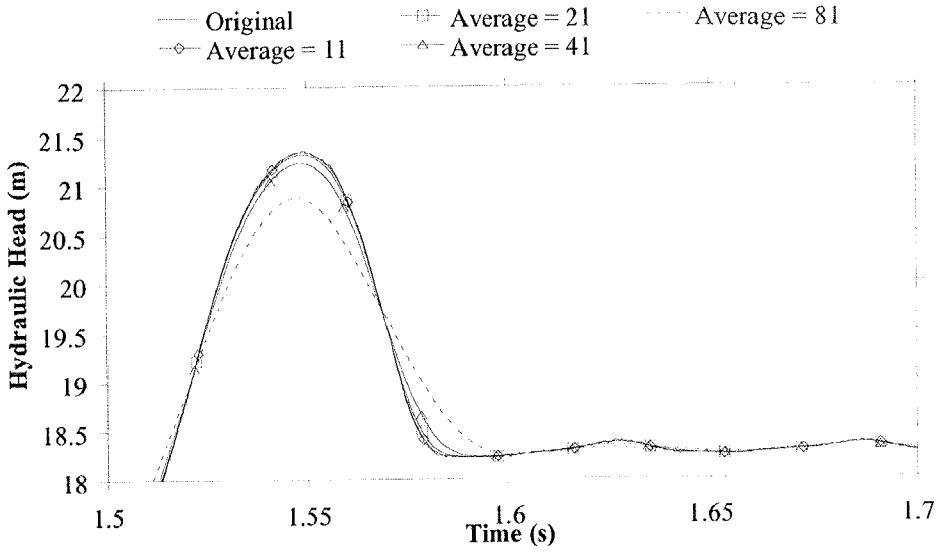

Figure 10.26 Moving Average Filtering Using Different Widths

The result is an attenuation of the pressure peaks for window sizes of 21, 41 and 81 data points, but not for a window size of 11, suggesting that small moving-average window sizes are necessary to avoid attenuation of peaks. Although the small window sizes avoid attenuation, little smoothing occurs. The lack of smoothing causes problems during transient analysis (see Appendix C.3).

A better way to achieve a good degree of smoothing is to use Savitzky-Golay smoothing filters. Rather than perform a local average around a point (like the moving average filter) the Savitzky-Golay method uses an M^{th} order polynomial. The moving average filter can be thought of as a 1^{st} order Savitzky-Golay smoothing filter. The use of higher order polynomials improves the filter's ability to match data with many peaks and troughs. Two parameters describe the Savitzky-Golay filter, a polynomial of order M and the size of the moving window over which the data are averaged (N_p). The equation describing a Savitzky-Golay filter is

$$y_i = \sum_{j=-N}^{N} c_j x_{i+j} \quad \text{.....(10.5.2)}$$

where c_j = Savitzky-Golay coefficient and the moving window width $N_p = 2N + 1$. The test data are used to show the performance of a 2nd order Savitzky-Golay smoothing filter with varying window widths (Figure 10.27). The different window widths are 11, 21, 41 and 81 data points.

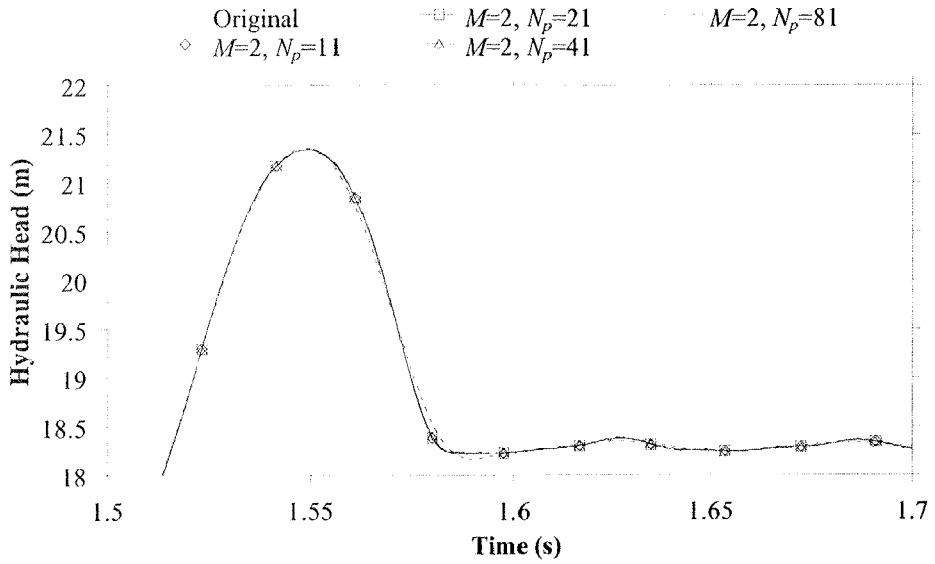

Figure 10.27 Savitzky-Golay Filtering Using Different Window Widths

The results show that for a 2nd order Savitzky-Golay smoothing filter, adequate results are found for all cases except for a window size of 81 data points. A significant improvement is realised over the moving average results for the same window widths, suggesting that increasing the order of the filter can improve results. Figure 10.28 shows results for varying the filter order while keeping the window width constant.

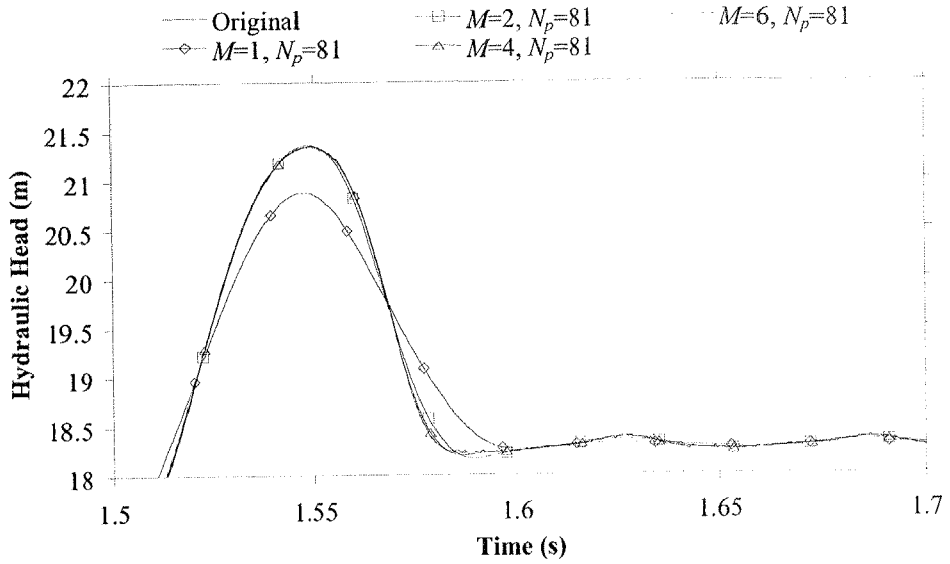

Figure 10.28 Savitzky-Golay Filtering Using Different Orders

Increasing the order of the filter improves results, but in practice, the order cannot be increased indefinitely. Problems occur if the filter order is similar to the window size (Press *et al.*, 1992).

The final type of filter tested is the IIR filter that works by filtering in the frequency domain. The data are transformed from the time domain into the frequency domain through the use of Fourier transformations. Once the data are in the frequency domain, all of the high frequency noise can be damped using filter functions (such as the Butterworth, Chebyshev, and elliptical functions—Rorabaugh, 1997). Then the frequency domain data are transformed back into the time domain. This type of IIR filter is called a low-pass filter because all of the low frequency components of the data are allowed to pass through the filter whereas the high frequency components are not. In this study an elliptical filter function is used. There are many different parameters that are needed to describe an elliptical filter function but the most important is the cut-off frequency, F_C, below which frequency components are allowed to pass through the filter. Results using different cut-off frequencies (applied to the test data) are shown in Figure 10.29.

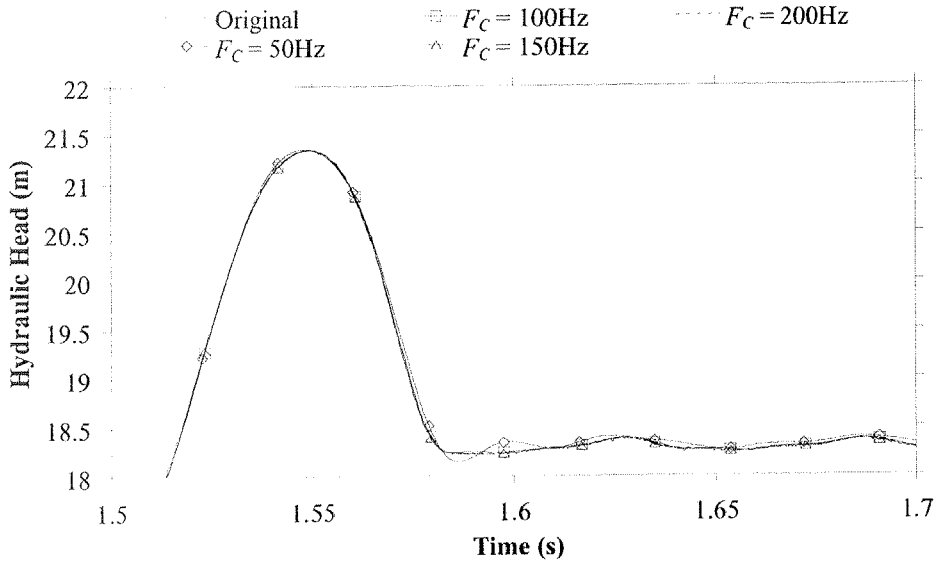

Figure 10.29 Filtering Using an IIR Filter

For low cut-off frequencies the IIR filter produces some overshoot after the peak (for example 50 Hz—the diamond points). Other cut-off frequencies show a good match with the original unfiltered data. The IIR filters are not well suited for data that are to be included as boundary conditions because, even though the high frequencies are eliminated (for example using $F_C = 50$ Hz), the frequencies that remain in the data are still higher than the natural frequency of the pipeline (in the example the natural frequency is 8.86 Hz). These remaining high frequencies cause shocks in the transient model that amplify over time (see under filtering in Appendix C.3). Based on these results, the best type of filter for the pressure and valve position data is the Savitzky-Golay filter. The filter used in the experimental verification chapters (Chapters 11 and 12) is a Savitzky-Golay filter of order 2 with a window width of 21 data points. Appendix C.3 demonstrates the effects of incorrect filtering.

10.6 Boundary Conditions for Simulations

The selection of the correct method of modelling a transient event can be important. Different boundary condition types may produce seemingly satisfactory results but, in fact, may be misleading, an example of which is presented in this section. A seemingly easy way to simulate the behaviour of a transient event is to measure the pressure head

at both ends of the pipeline, then use these measured heads as boundary conditions in the transient model. As an illustration the use of two measured head boundary conditions is performed for a slow valve closure (t_c = 1.2 s). The initial velocity of the flow is 0.510 m/s corresponding to a Reynolds number of 11,200. Experimentally gathered data used for the transient model are shown in Figure 10.30

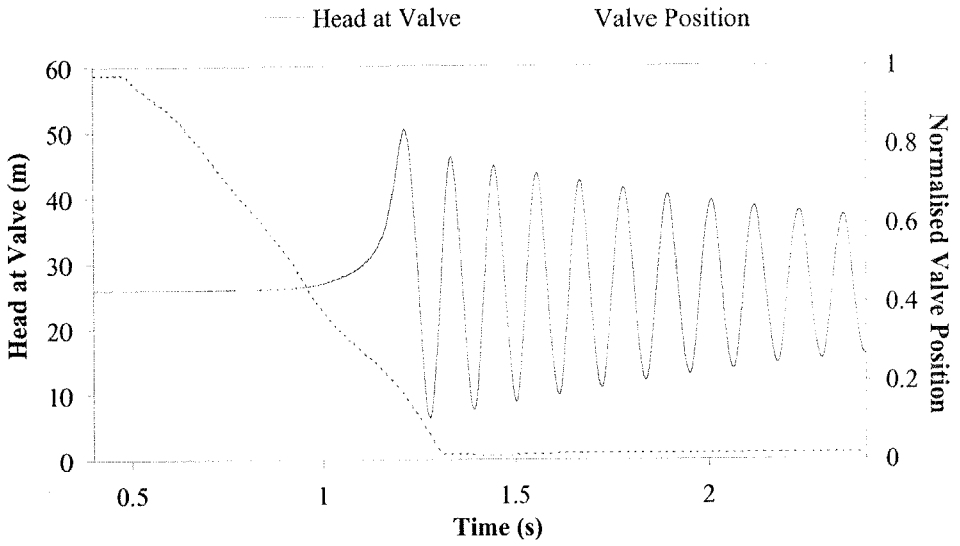

Figure 10.30 Experimental Boundary Condition Data

The pressure head data at node 1 were used as a boundary condition in the transient model. No unsteady friction was used in the transient model. Figure 10.31 shows the measured pressure head at node 2 with the calculated pressure head at node 2. As observed, the match between measured and calculated heads is good.

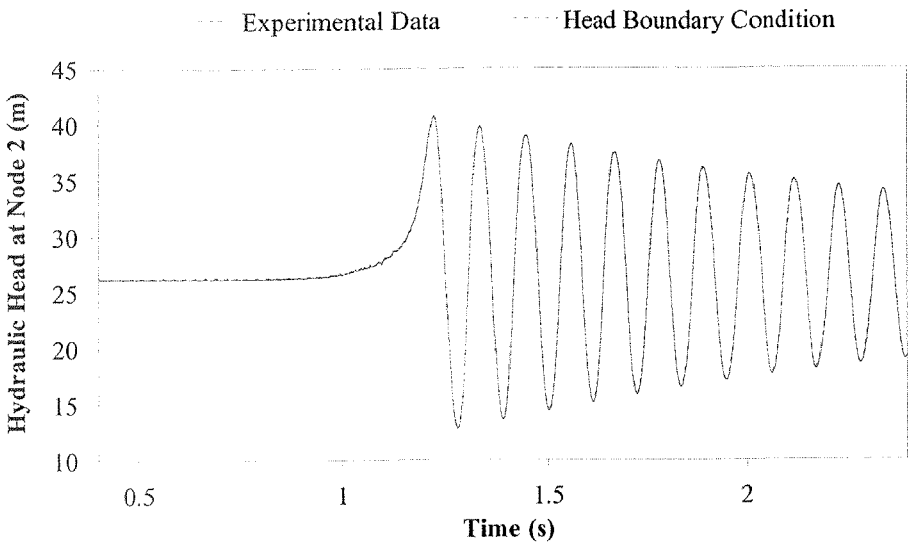

Figure 10.31 Simulation Using Measured Head Boundary Condition

However, the good agreement between measured and calculated pressure head at node 2 shown in Figure 10.31 is not all that it seems. The transient solver should produce under-damped results due to the exclusion of unsteady friction. A reason for the apparent good result is that, although the model does not include unsteady frictional effects, the measured data at node 1 do i.e., the use of the measured pressure head at node 1 as a boundary condition effectively includes all frictional dissipation in the model results. Essentially, the head boundary condition is not independent of the transient behaviour being modelled. Therefore, for correct modelling, a transient model must use an independent boundary condition. In this case, a more appropriate boundary condition would be valve position. Valve position is independent of the pressure head response, whereas the use of the measured pressure at node 1 is not independent of the pressure response at other positions in the pipeline. Figure 10.32 shows the results from the use of the valve position as a boundary condition.

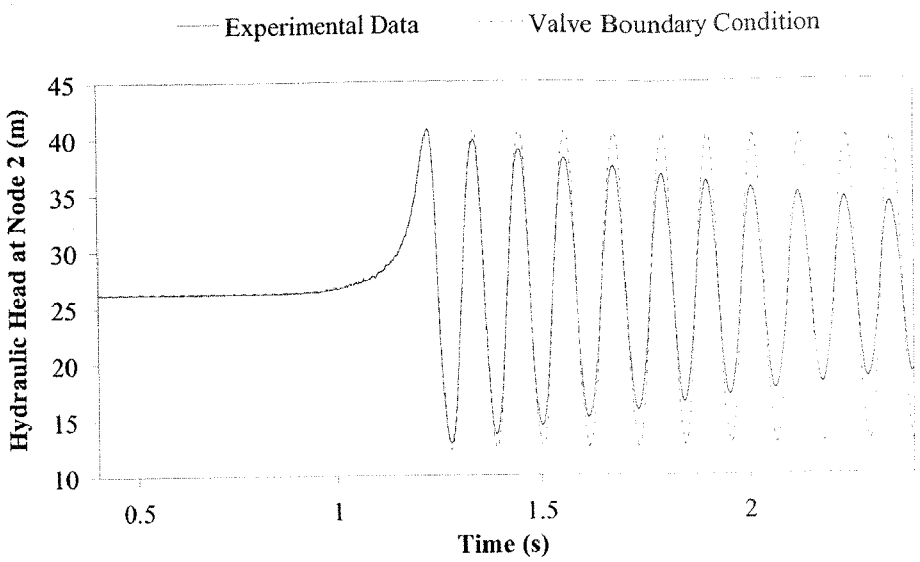

Figure 10.32 Simulation Using Valve Boundary Condition

The use of a valve position boundary condition produces different and more realistic results than the use of the measured head as a boundary condition. The effect of steady state friction alone does not produce a large amount of damping (compared to results using the head boundary condition). The same analysis has been repeated with and without a leak in the pipeline with similar results (not shown in this thesis). When using a head boundary condition, the effect on the pressure response with and without a leak was the same. When using a valve boundary condition, the effect on the pressure response with and without a leak was noticeable. Thus, if the effect on the pressure response with a leak is the same as without a leak (when using a head boundary condition), then leak detection is impossible. Measured pressure head boundary conditions are not used in transient modelling in the experimental verification Chapters 11 and 12.

10.7 Summary

This chapter presents information that is needed for verification of unsteady friction models in Chapter 11 and verification of the inverse transient method in Chapter 12. The experimental apparatus pipeline is described, its components calibrated and its measurement discussed, all of which are required to either simulate a transient event or

provide measured data for the inverse transient method. Filtering of the measured pressure and valve position data was discussed. The Savitzky-Golay smoothing filter was chosen as the best filter. The use of a measured pressure head boundary condition is shown to produce misleading simulation results.

Chapter 11

Experimental Verification of Unsteady Friction Models

11.1 Introduction

This chapter is concerned with the experimental verification of unsteady friction models discussed and proposed in Chapters 8 and 9. Work presented here has importance with regard to the successful application of the inverse transient method to experimental data. Before leaks can be modelled and detected, accurate modelling of the transient behaviour without leaks must first be verified. Experimental results show different behaviour depending upon the initial flow state of the transient event. Two types of behaviour are observed. These depend on whether the flow is initially laminar or initially turbulent. In addition, different behaviours are also observed depending on the speed of the valve closure for initially turbulent transient events. Experimental tests are presented that span the different unsteady flow event types described in Chapter 8. The scope of unsteady friction models is shown by comparison with experimental tests. Experimentally determined unsteady friction coefficients are found for low Reynolds number, initially turbulent events. These, together with high Reynolds number coefficients (Shuy and Apelt, 1987), are used to validate relationships for the unsteady friction coefficients derived in Chapter 9. Traditionally, these coefficients were

determined experimentally. The validation of relationships that determine unsteady friction coefficients eliminates the need for their experimental calibration.

The experimental pipeline apparatus is described in depth in Chapter 10. The layout of the pipeline is repeated in Figure 11.1 for clarity.

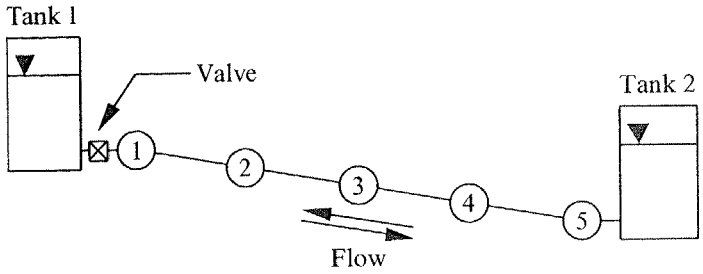

Figure 11.1 Experimental Pipeline Apparatus

11.2 Verification of Laminar Transient Model for Fast Valve Closure

A "fast valve closure" is defined as having a closure time (t_c) of less than $2L/a$, the time for the initial pressure wave to travel from the valve to Tank 2 and back again. This section presents experimental results for fast valve closures with initially laminar flow. In the experiments a spring actuator is used to close a downstream valve in a time of less than $2L/a$ ($t_c = 0.009$s). As indicated in Chapter 8, initially laminar flow events are modelled well by the analytic Zielke (1968) unsteady friction model, which is only applicable for laminar flows. It does not require coefficients that need to be determined experimentally. Experimental data, together with results from the model, are shown in Figure 11.2 (results at nodes 1, 2, 3 and 4 for graphs (a), (b), (c) and (d) respectively). The initial flow velocity in the pipeline before the valve closure was 0.1 m/s (Reynolds number = 2,195). The Zielke (1968) model performs well, accurately modelling the phase, magnitude and shape of the experimental data.

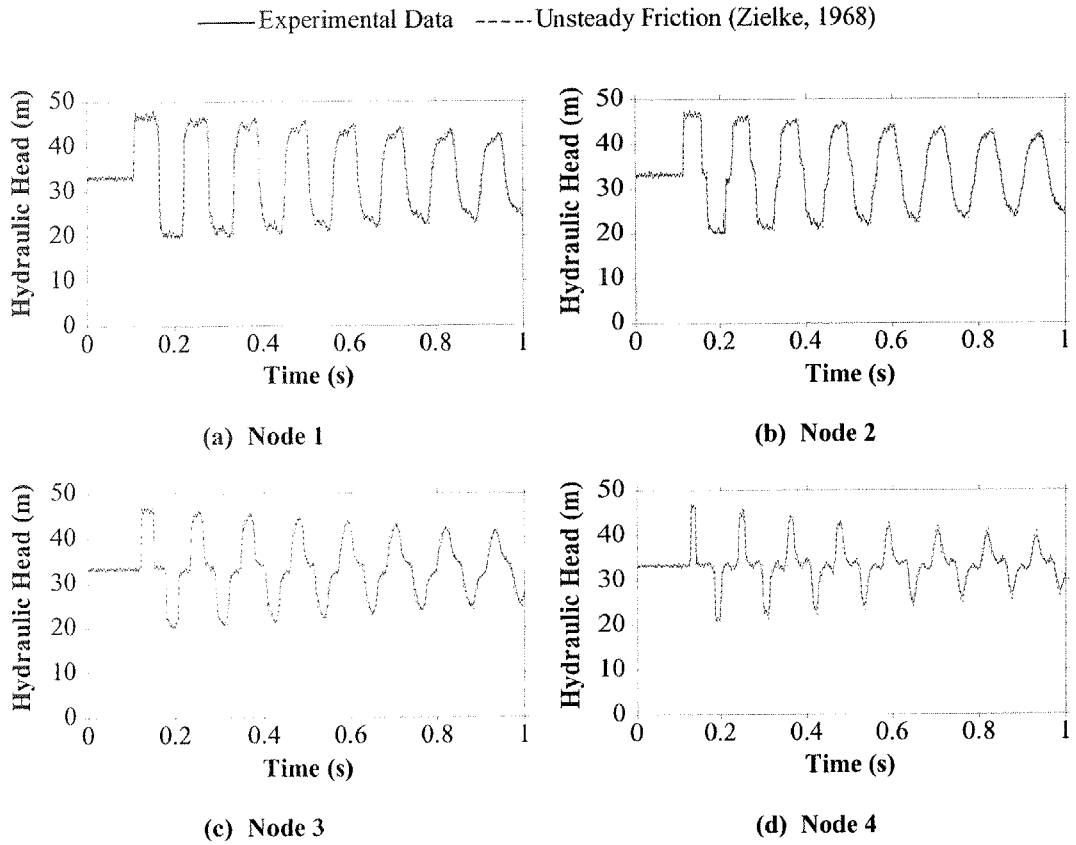

Figure 11.2 Downstream Valve Closure, Initially Laminar Flow

The good match confirms previous studies performed using the Zielke (1968) unsteady friction model. Similar to previous studies, it produces sharp peaks and troughs that are not present in the experimental data (see node 4 especially). The small mismatch grows slightly larger with time but is not detrimental to the overall fit.

11.3 Verification of Turbulent Transient Models for Fast Valve Closure

To test turbulent flows, an initial steady state velocity of 0.3 m/s (corresponding to a Reynolds number of 6,584) was set. A closure time of $t_c = 0.009$s was used. Experimental results are shown in Figure 11.3 for initially turbulent flow data together with unsteady friction results using the Zielke (1968) model.

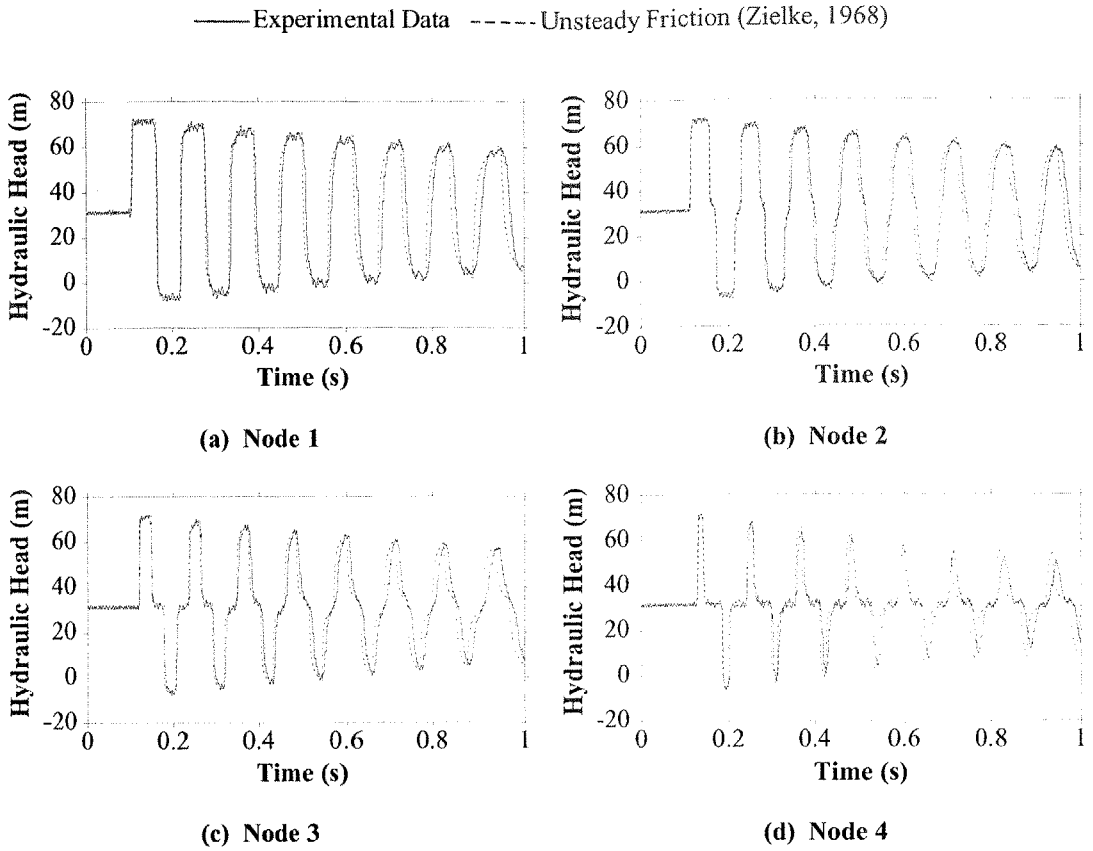

Figure 11.3 Downstream Valve Closure, Initially Turbulent Flow

The Zielke (1968) model produces damping of the pressure oscillations that is similar to the experimental data, but it fails to model the correct phase and shape of the experimental data. The failure, of course, could have been expected because the Zielke model was derived for laminar flow so is not applicable to turbulent flow. Chapter 9 presents theoretical turbulent flow models. These models originated from the Brunone *et al.* (1991) unsteady friction model (also called the k_3 model). Figure 11.4 shows the experimental application of the Brunone *et al.* (1991) unsteady friction model ($k_3 = 0.124$, found using Eq. 9.6.9). The unsteady friction is included in the directional derivatives (in the method of characteristics) (see Section 9.4). Results are presented only at node 1 in the pipeline (next to the valve). Results using the quasi-steady friction model are also plotted.

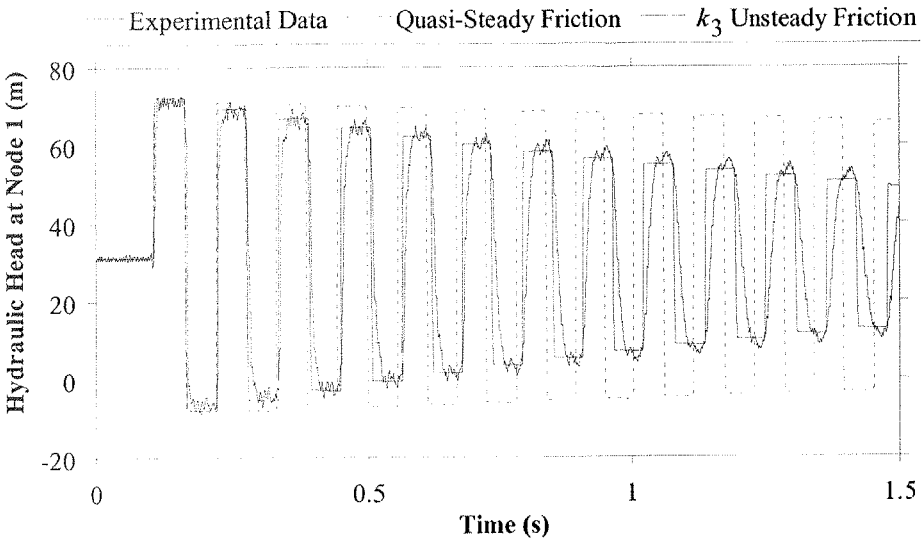

Figure 11.4 k_3 Unsteady Friction Model and Experimental Data

As observed, the Brunone *et al.* (1991) unsteady friction model produces a better match with the data than does the quasi-steady friction model, which does not produce enough dissipation and fails to predict the change in phase and shape of the experimental data. The Brunone *et al.* (1991) model matches the damping but not the shape of the data. The mismatch in the phase change is more prominent for the Zielke (1968) and quasi-steady models. For the rest of this section, the unsteady friction formulations are included as an addition to the steady friction (see Appendix B.1). Figure 11.5 repeats the analysis shown in Figure 11.4, the results of which indicate numerical smoothing (diffusion) of the pressure oscillations and better fit the experimental data than in Figure 11.4.

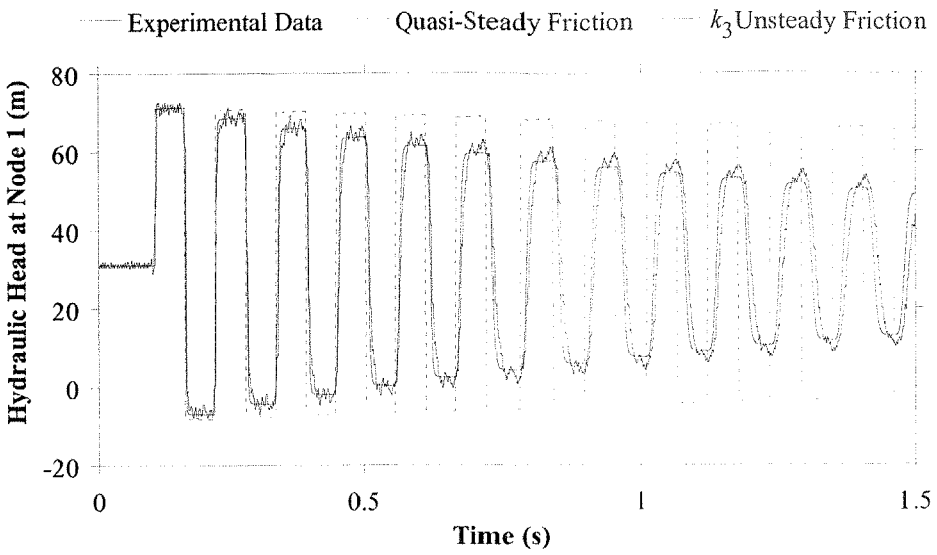

Figure 11.5 k_3 Unsteady Friction Model and Experimental Data

The small mismatch in the phase shown by the Brunone *et al.* (1991) model can be corrected by the use of the k_3 & k_M model (a sub-model of the k_A & k_P model, see Sections 9.3.2 and 9.3.5). The k_M parameter is specific to low Reynolds number turbulent flows and only affects the phase of the pressure oscillations. The value of $k_M = 0.034$ (calculated using Eq. 9.6.5) is based on a Reynolds number of 6,584. The results from modelling based on the Brunone *et al.* (1991) model and the k_3 & k_M unsteady friction model are shown in Figure 11.6. The k_3 & k_M model reproduces the correct phase change, damping and shape of the experimental data, suggesting that the low Reynolds number correction parameter k_M is needed for fast events of this nature.

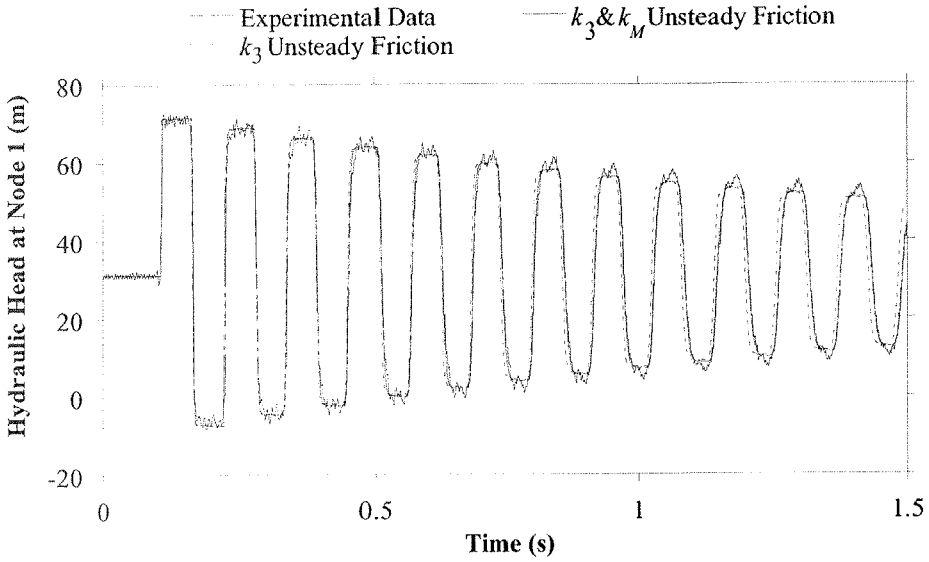

Figure 11.6 k_3 & k_M Unsteady Friction Model and Experimental Data

The parameters k_3 and k_M used in the modified Brunone *et al.* (1991) and the k_3 & k_M unsteady friction models are assumed to be constant. A disadvantage is that the initial conditions must be known and an unsteady friction parameter must be inferred from them. For a transient event where the initial flow is zero (such as for a valve opening), unsteady friction parameters cannot be estimated. A solution to this problem is to use unsteady friction factors that are dependent on the instantaneous Reynolds number. The analytic relationships derived in Chapter 9 are used to update the unsteady friction parameters. Both the k_3 and k_3 & k_M models are treated in this way and are named the variable k_3 and variable k_3 & k_M unsteady friction models. Figure 11.7 shows the variable k_3 and the constant k_3 models compared to experimental data. The results from both models are similar to those of the variable k_3 model showing slightly greater damping and greater positive phase shift.

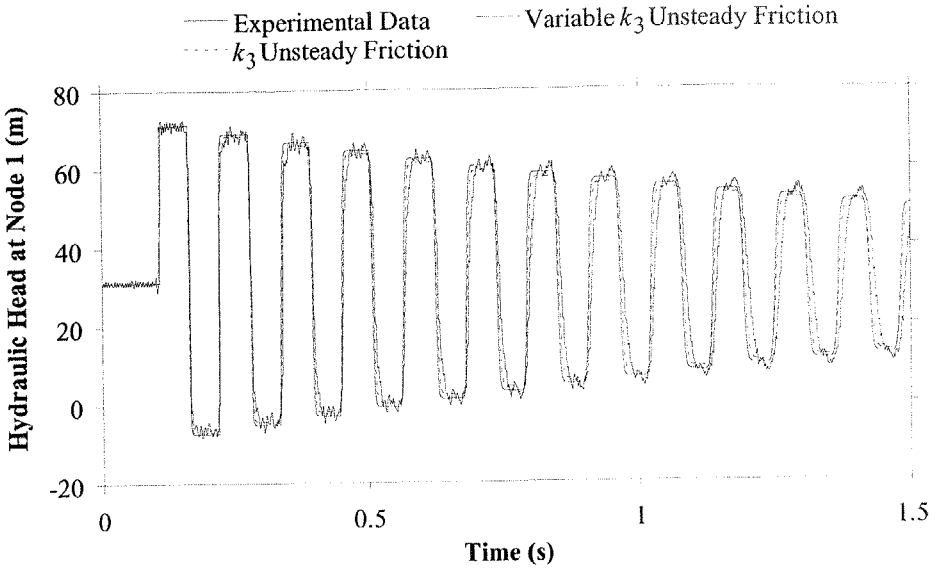

Figure 11.7 Variable k_3 Unsteady Friction Model and Experimental Data

A variable k_3 & k_M model is created in a similar manner. Analytic relationships derived in Chapter 9 are used to update the parameters k_3 and k_M depending on the instantaneous Reynolds number. The performance of the constant k_3 & k_M model and the variable k_3 & k_M model against experimental data appears in Figure 11.8.

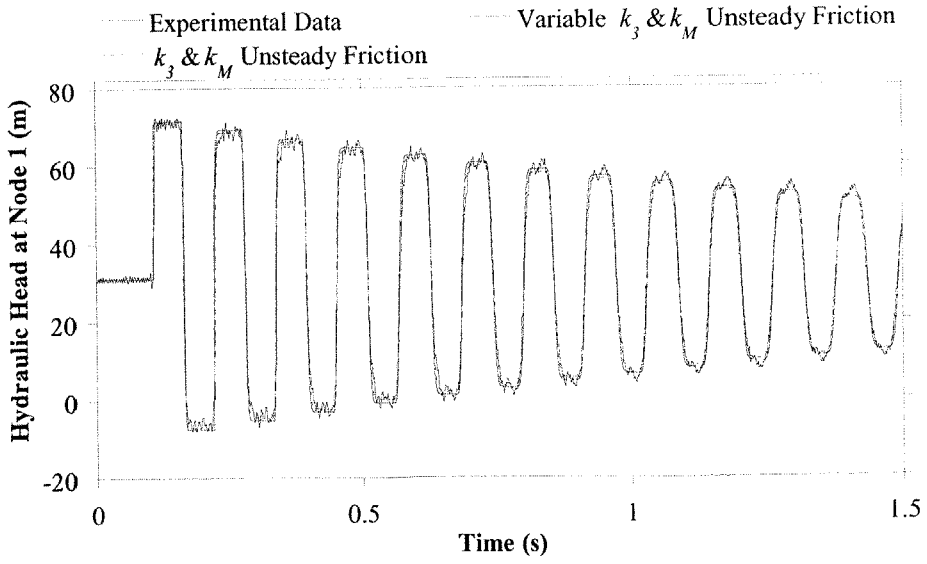

Figure 11.8 Variable k_3 & k_M Unsteady Friction Model and Experimental Data

There is no observable difference between the two calculations, suggesting that both the variable and constant k_3 & k_M models produce similar behaviour and sufficiently model

the experimental behaviour. The variable k_3 & k_M model does not require any parameter values to be input; therefore, it can be used without the need for calibration in cases where calibration is difficult. The results presented in this section have been confirmed across a number of tests for initial velocities of 0.1, 0.2 and 0.3 m/s for both fast upstream and downstream valve closures (not presented in this thesis).

11.4 Verification of Turbulent Transient Models for Slow Valve Closure

The previous section presented experimental results for fast valve closure, turbulent transient events ($t_c = 0.009$ s). This section focuses on events using closure times greater than $2L/a$, namely 0.07, 0.70 and 1.4 s. These correspond, in terms of L/a for the 37.2 m long experimental apparatus, to closure times of $2.5L/a$, $25L/a$ and $50L/a$ respectively. Experimental data of head near the valve (node 1) and results using the quasi-steady friction model are shown in Figure 11.9 for a slow event. The initial velocity was 0.493 m/s (**R** = 10,817) and the valve closure time was 0.7 s ($25L/a$).

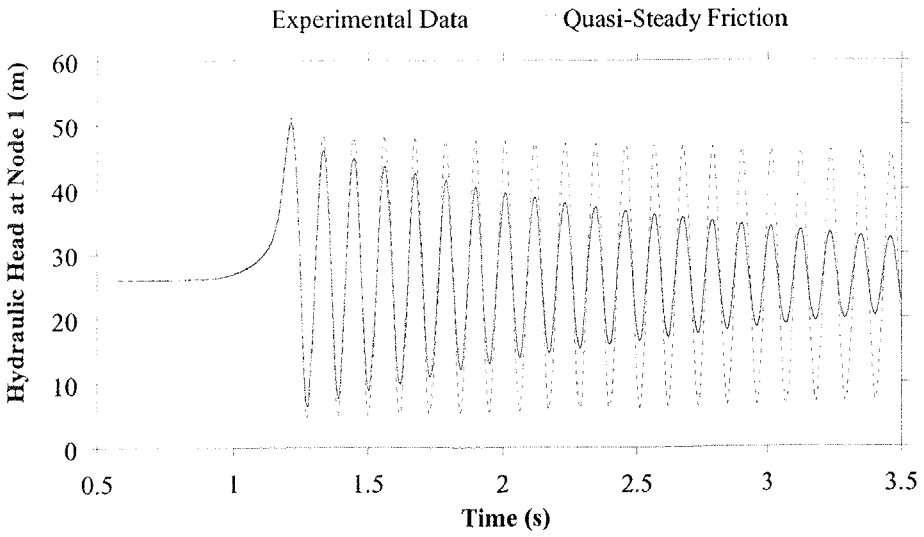

Figure 11.9 Quasi-Steady Friction Model and Experimental Data

The quasi-steady friction model does not correctly predict the damping of the experimental data, suggesting that for closure times as slow as $25L/a$, unsteady friction effects are still predominant. Based on the outcome of modelling fast events, as

described in Section 11.3, the match with the experimental data may be improved with the application of an unsteady friction model. Results for the Brunone *et al.* (1991) model appear in Figure 11.10. The unsteady friction coefficient k_3 was analytically calculated from relationships derived in Chapter 9 (using Eq. 9.6.9) for a Reynolds number of 10,817, $f = 0.0303$ and $k_3 = 0.115$.

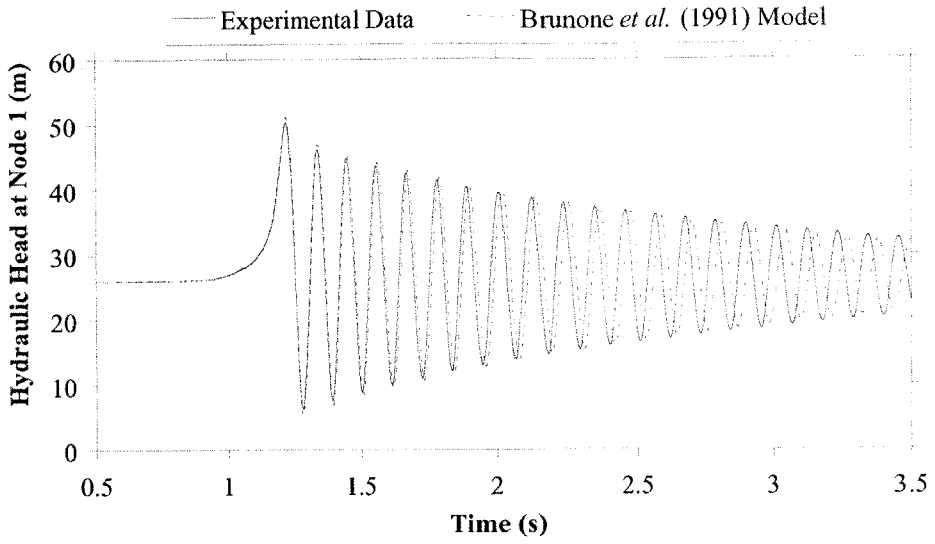

Figure 11.10 Brunone *et al.* (1991) Unsteady Friction Model and Experimental Data

A good match in terms of the shape and damping is produced when using the Brunone *et al.* (1991) model. The phase of the pressure oscillations, however, is not well matched. The Brunone *et al.* (1991) model is a sub-model of the k_A & k_P unsteady friction model. The k_A & k_P model has the ability to control the magnitude and phase of the pressure oscillations independently of each other. Examination of results from the quasi-steady friction model indicates a good match with respect to the phase of the pressure oscillations, suggesting that no phase component is required. Zero phase change is achieved by setting $k_P = 0.0$ and keeping $k_A = 0.029$ (using Eq. 9.3.7, $k_A = k_3$). Figure 11.11 shows results using k_A & k_P unsteady friction model.

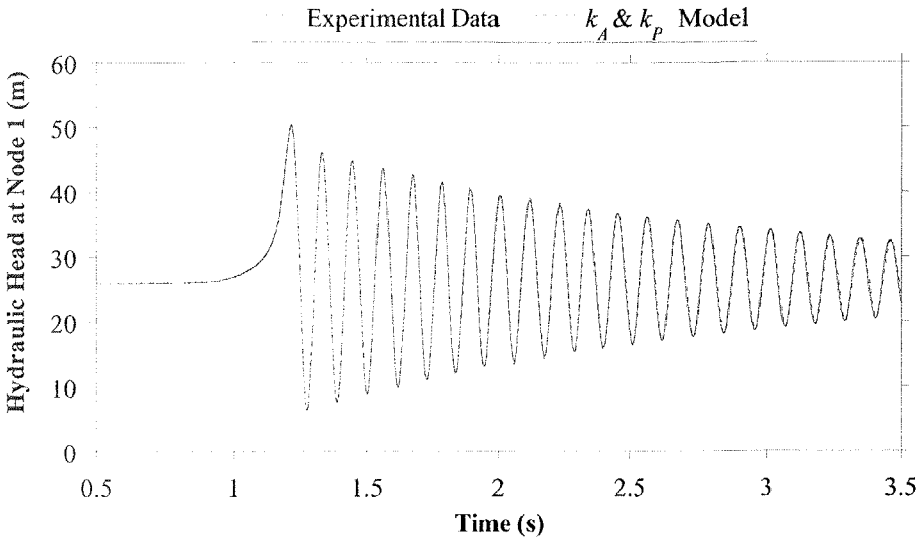

Figure 11.11 Unsteady Friction Model ($k_A = 0.029$, $k_P = 0$) and Experimental Data

The results from the use of the k_A & k_P unsteady friction model are in good agreement with the experimental data. The shape, damping and phase of the experimental data are predicted well. Analysis is performed for the three different slow valve closure times of 0.07, 0.7 and 1.4 s. The coefficient k_P is equal to zero in each case. The coefficient k_A is equal to 0.034, 0.029 and 0.031 respectively for the different valve closure times. The initial velocities for each event were 0.169, 0.493 and 0.320 m/s (corresponding to Reynolds numbers of 3719, 10,817 and 7026). Results are shown in Figures 11.12, 11.13 and 11.14 for nodes 1, 2, 3, and 4.

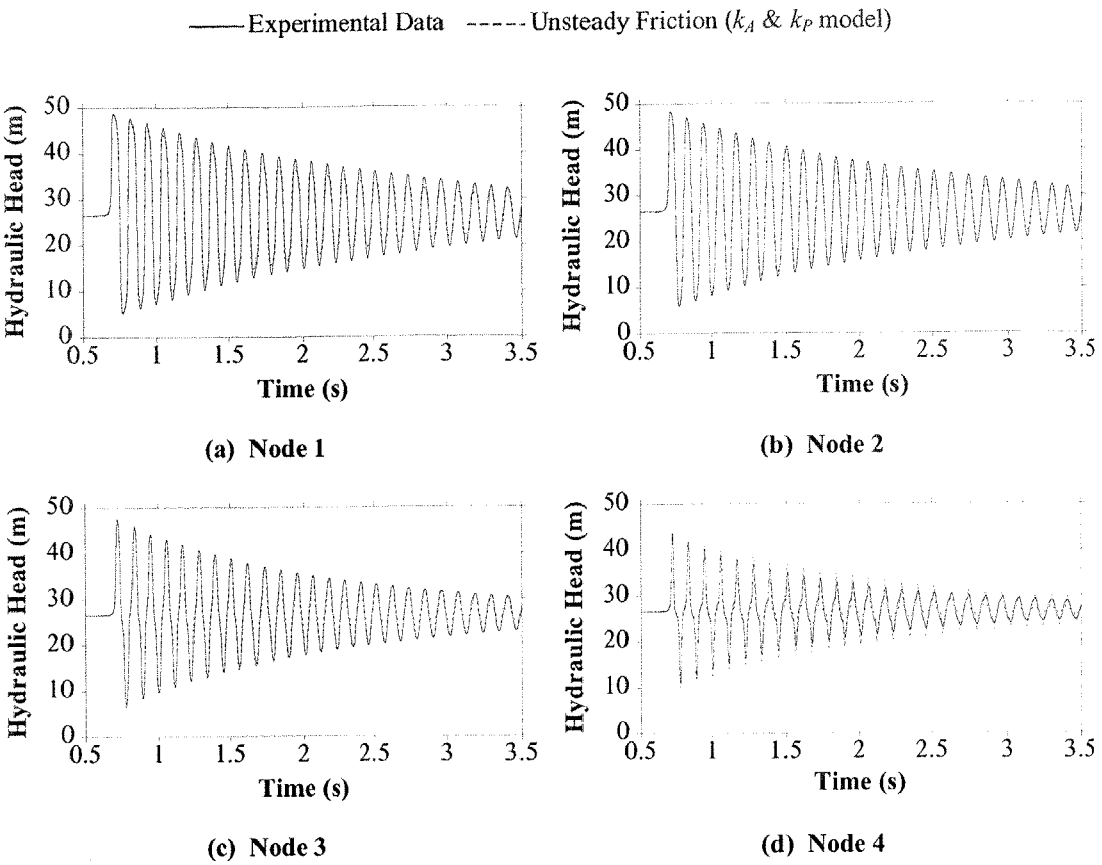

Figure 11.12 Initially Turbulent Slow Event (t_c = 0.07 s, 2.5L/a)

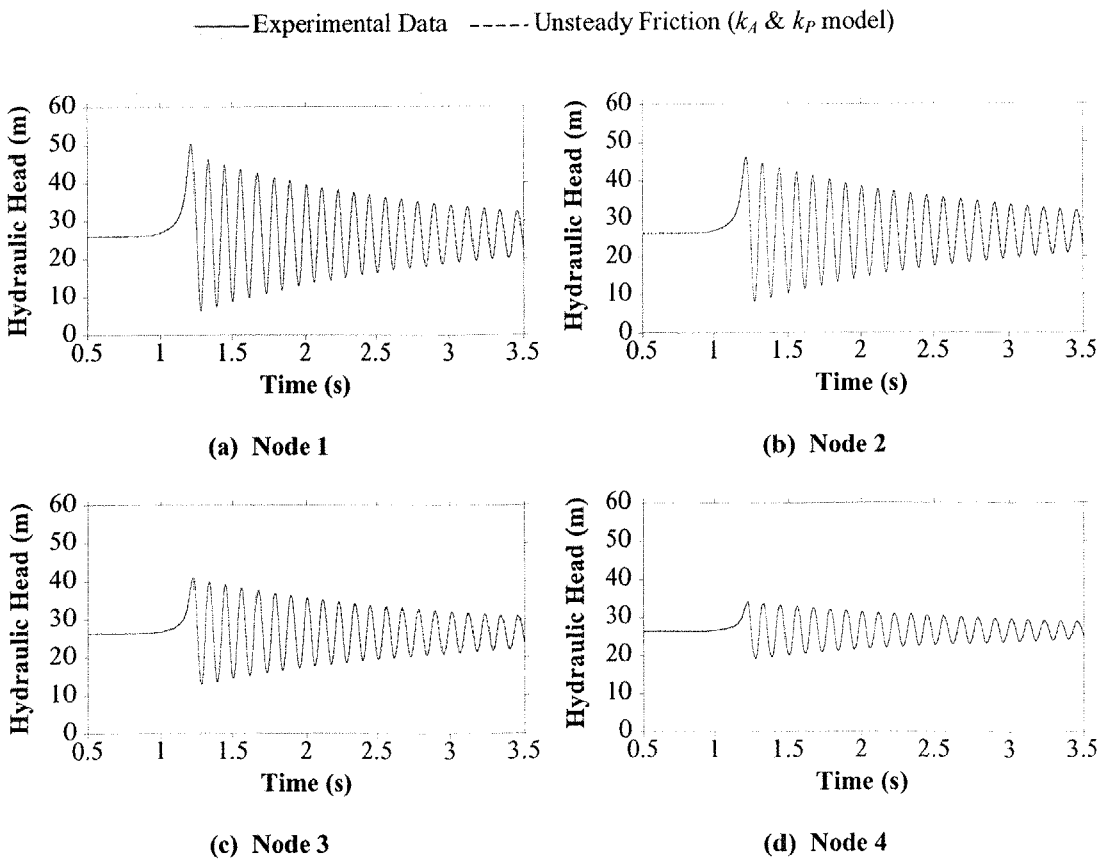

Figure 11.13 Initially Turbulent Slow Event (t_c = 0.7 s, 25 L/a)

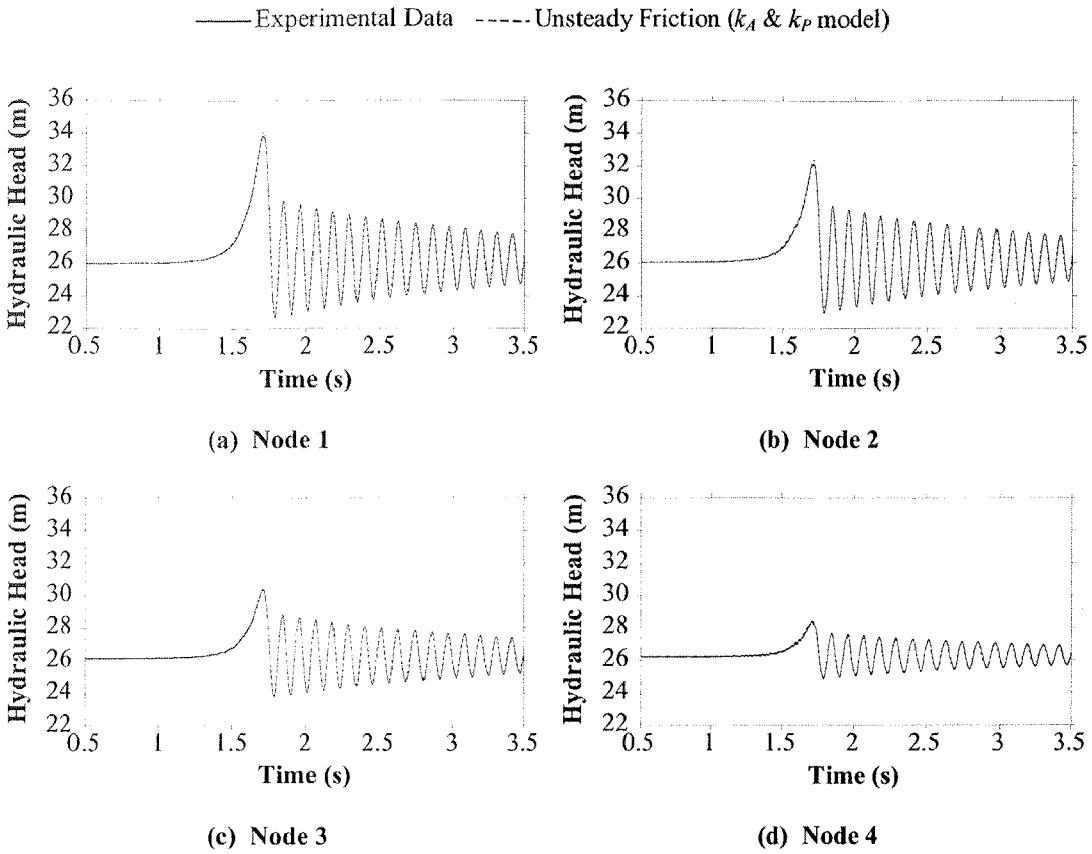

Figure 11.14 Initially Turbulent Slow Event (t_c = 1.4 s, 50L/a)

Good matches between numerical and experimental results are observed for closure times of 0.7 and 1.4 s. The performance of the k_A & k_P model for the closure time of 0.07 s case, however, does have differences in the shape of the response compared to the experimental data. That closure time corresponds to 2.5L/a, which is close to the fast closure time for the pipeline of 2L/a (0.056 s). At nodes 1 and 2 (Figures 11.12(a) and 11.12(b)) the model produces lower magnitude oscillations than the experimental data at node 4 (Figure 11.12(d)) and the magnitude of the pressure oscillations produced by the model are larger than that of the experimental data. The mismatch is probably caused by a transition region between the behaviour exhibited by a fast valve closure event and a slow event. The k_A & k_P model, however, produces adequate results for the 2.5L/a valve closure event.

These experimental results indicate that the behaviour of a slow transient event is different from that of a fast event. A fast event produces a phase change whereas the slow event does not. The behaviour over both fast and slow events (for initially

turbulent flow) is predicted well by the k_A & k_P unsteady friction model, where the coefficients are be summarised as

$$k_A = k_3$$
$$k_P = \begin{cases} (k_3 + k_M) & \text{if} \quad t_c < 2\frac{L}{a} \\ 0 & \text{if} \quad t_c \geq 2\frac{L}{a} \end{cases} \qquad (11.4.1)$$

where k_3 and k_M are calculated from analytic expressions (Eqs. 9.6.9 and 9.6.5) that depend on the Reynolds number of the initial flow and the pipe roughness.

11.5 Verification of Eight Unsteady Flow Events

Traditionally unsteady friction models have been tested for downstream valve closures. Chapter 8 presented eight unsteady flow events that should be adequately modelled by any unsteady friction model. Numerical results in Section 9.2 using the eight unsteady flow events found that the Brunone *et al.* (1991) unsteady friction model was not sufficiently general to reproduce transient damping for six out of the eight unsteady events. A modification was made to the Brunone *et al.* (1991) model to fix this shortcoming. To verify the performance of an unsteady friction model it must be tested against experimental data for each of the eight unsteady events. Actual experimental verification of these events need only be performed for four of the eight events since half are mirror images of the others. The four experimental cases considered are:

(i) downstream valve closure,
(ii) upstream valve closure,
(iii) downstream valve opening and
(iv) upstream valve opening.

All experiments use fast valve closures ($t_c < 2L/a$). The upstream and downstream valve closure tests are shown in Figures 11.15 and 11.16 respectively. Both have an initial flow of 0.3 m/s corresponding to a Reynolds number of 6,584. The unsteady friction coefficients for these tests were $k_A = 0.031$ and $k_P = 0.040$ from Eq. 11.4.1. Results using the quasi-steady model are also presented.

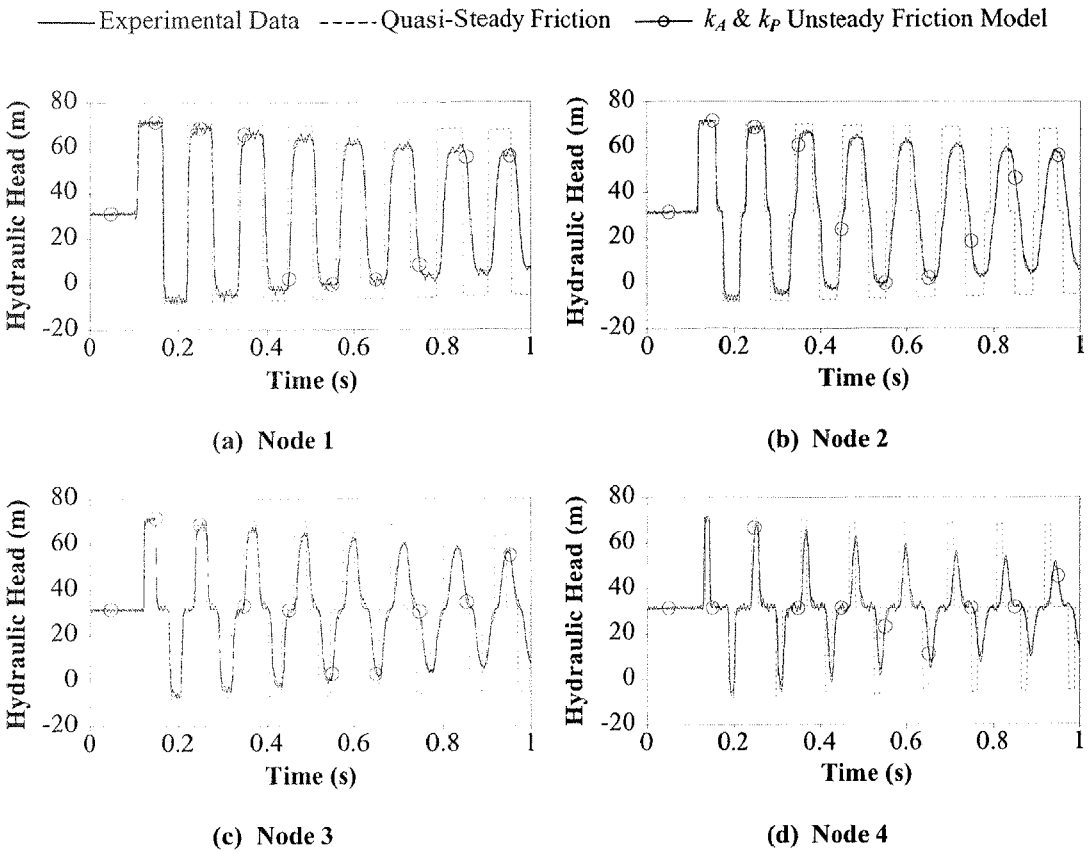

Figure 11.15 Downstream Valve Closure, k_A & k_P Model

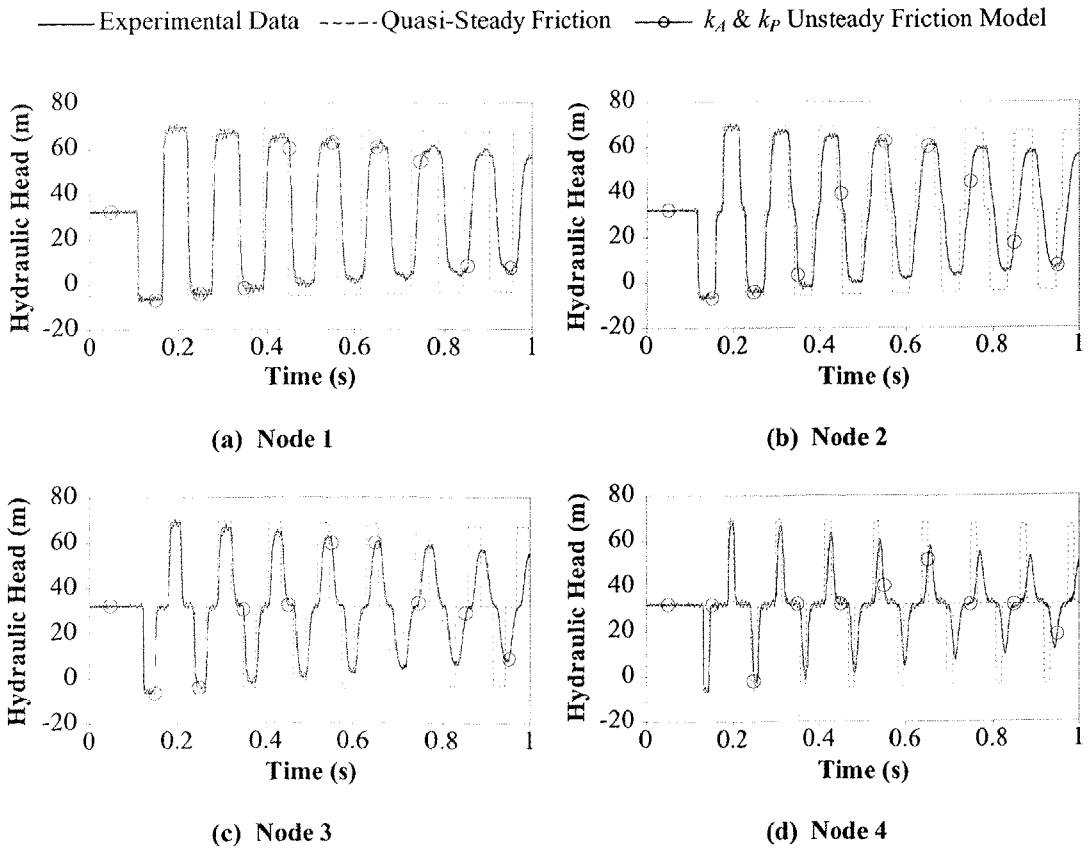

Figure 11.16 Upstream Valve Closure, k_A & k_P Model

Results from the downstream and upstream valve closures show a good match with the experimental data; only small differences are evident.

Now, results for the remaining two unsteady flow event types are presented. Figures 11.17 and 11.18 present results for the downstream and upstream valve openings respectively. Final velocities are 1.36 and 1.35 m/s, corresponding to Reynolds numbers of 29,838 and 29,650 respectively. The unsteady friction coefficients used in the k_A & k_P model are identical, being $k_A = 0.025$ and $k_P = 0.031$ (calculated using Eqs. 9.3.7 and 9.3.8).

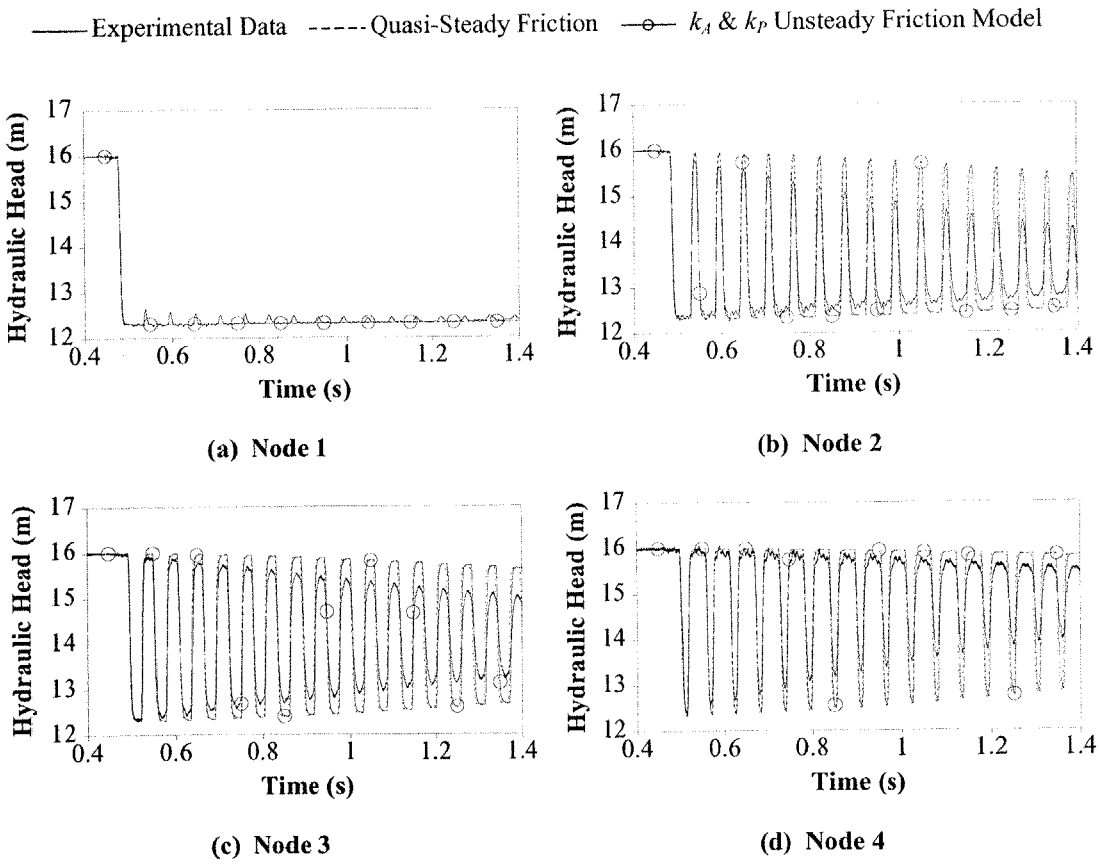

Figure 11.17 Downstream Valve Opening, k_A & k_P Model

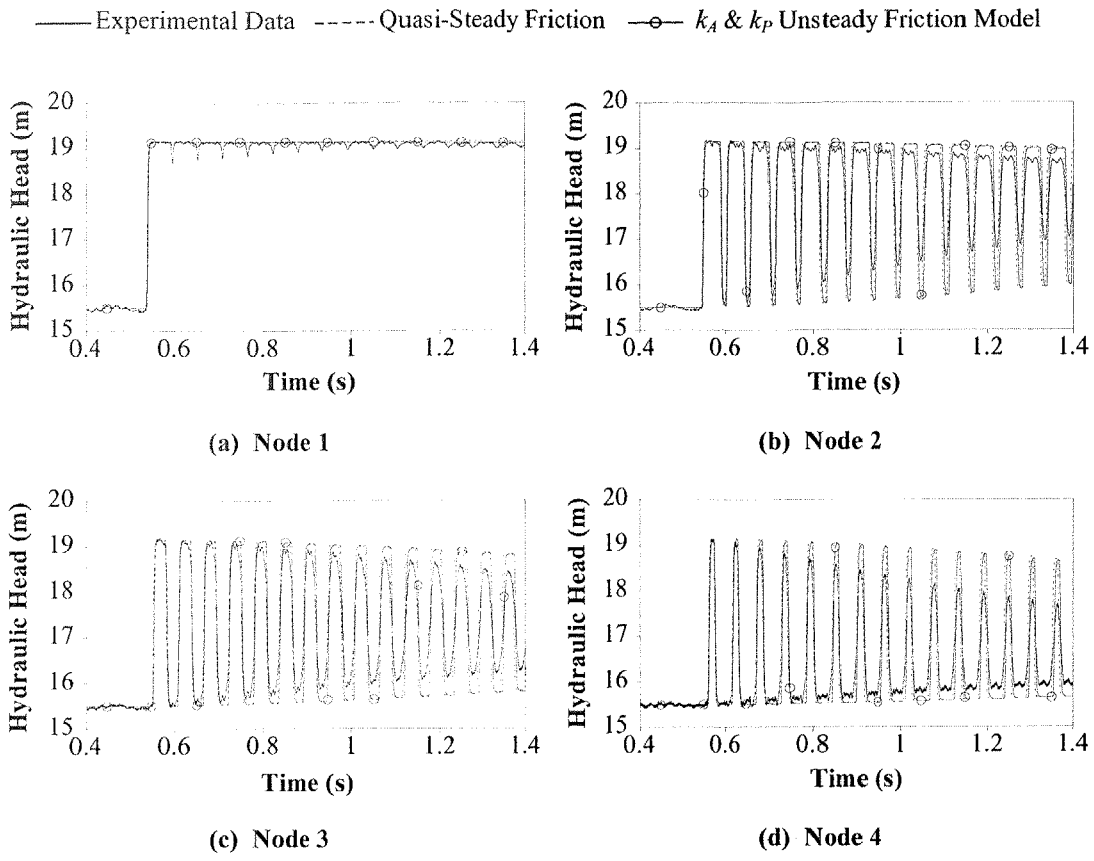

Figure 11.18 Upstream Valve Opening, k_A & k_P Model

Similar results are obtained for both cases. The positioning of the pressure transducer next to the valve causes small peaks in Figures 11.17(a) and 11.18(a). It is actually located a small distance from the valve for practical reasons. That distance causes small pulses to be measured rather than the constant tank pressure. For all positions along the pipeline the phase of the experimental data is well matched by the quasi-steady friction model. The phase change is, however, overestimated by the k_A & k_P model. The damping of the pressure oscillations is not well represented by either the quasi-steady or k_A & k_P unsteady friction models. The overestimation of the phase shift (and no damping) from the k_A & k_P model for the valve opening cases may be explained by investigating the unsteady equation of motion with the k_A & k_P model included,

$$\frac{\partial H}{\partial x}+\frac{1}{g}\frac{dV}{dt}+\frac{fV|V|}{2gD}+\phi_V\frac{k_A}{g}\left|\frac{dV}{dt}\right|+\frac{k_P}{g}\frac{dV}{dt}=0 \quad \text{.....(11.5.1)}$$

where x = distance, t = time, H = pressure head, V = velocity, f = friction factor, g = gravitational acceleration, D = pipe diameter, k_A = unsteady friction coefficient (amplitude component) and k_P = unsteady friction coefficient (phase component). The velocity sign operator ϕ_V is defined as

$$\phi_V = \begin{cases} +1 & \text{if} \quad V \geq 0 \\ -1 & \text{if} \quad V < 0 \end{cases} \qquad \text{.....(11.5.2)}$$

Equivalently

$$\frac{\partial H}{\partial x} + \frac{1}{g}\frac{dV}{dt} + \frac{fV|V|}{2gD} + \phi_A \frac{k_A}{g}\frac{dV}{dt} + \frac{k_P}{g}\frac{dV}{dt} = 0 \qquad \text{.....(11.5.3)}$$

where the velocity sign operator is replaced by an acceleration sign operator ϕ_A defined as

$$\phi_A = \begin{cases} +1 & \text{if} \quad V\dfrac{\partial V}{\partial t} \geq 0 \\ -1 & \text{if} \quad V\dfrac{\partial V}{\partial t} < 0 \end{cases} \qquad \text{.....(11.5.4)}$$

Valve opening events only produce acceleration ($V \times \partial V/\partial t \geq 0$) (Section 9.2); therefore, the acceleration sign operator ϕ_A is always equal to one. Substituting $\phi_A = 1$ into Eq. 11.5.3 results in

$$\frac{\partial H}{\partial x} + \frac{1}{g}\frac{dV}{dt} + \frac{fV|V|}{2gD} + \frac{k_A}{g}\frac{dV}{dt} + \frac{k_P}{g}\frac{dV}{dt} = 0 \qquad \text{.....(11.5.5)}$$

The k_A term is similar to the k_P term (which causes a phase shift in the pressure oscillations, see Appendix B.7 for a mathematical treatment) and produces the same behaviour. The k_A term (for valve opening events) produces an extra phase shift in the pressure oscillations with no damping as shown in Figures 11.17 and 11.18.

Another problem with this type of valve opening event is that flow is being established and would pass through the transition from laminar to turbulent flow, meaning that the Zielke (1968) unsteady friction model may produce better results for valve opening cases, especially since the transition from laminar to turbulent flow may occur at Reynolds numbers higher than those usually specified for laminar flow. Results using the Zielke (1968) model for laminar flow for the eight unsteady flow events appear in Appendix C.5 (Figures C.21 to C.24). These results show that the Zielke (1968) model does not correctly match experimental results for valve closures but does, however, show good matches for the valve opening cases. The failure of the k_A & k_P model to model correctly valve openings limits its range of application, which is evident in the following chapter where no valve openings are used for leak detection studies.

11.6 Verification of Unsteady Friction Damping Factor

Damping from unsteady friction is assumed to be exponential. An analytic exponential damping coefficient (D_U) is derived in Section 9.9 (Eq. 9.9.23). The equation describing the damping of pressure peaks is restated as

$$H_t = H_0 + (H_B - H_0)e^{\left(-D_U \frac{(t-t_B)}{T}\right)} \quad \text{.....(11.6.1)}$$

where H_t = pressure head at time t, H_0 = steady state pressure head, H_B = pressure head at time t_B and T = natural period of the pipeline. D_U was found to be dependent on the unsteady friction coefficients k_A and k_P. Analytic expressions for k_A and k_P are derived in Section 9.6. These expressions for k_A and k_P are dependent on the Reynolds number of the initial flow and the pipe roughness. Both expressions can be used to calculate a theoretical exponential damping coefficient. The verification of exponential damping was tested using a slow valve closure test. The valve closure time was 0.7 s and the initial velocity was 0.427 m/s, which corresponds to a Reynolds number of 9,371. The unsteady friction coefficient k_A is calculated to be 0.0294 using Eqs. 9.3.7 and 9.6.9 (for a slow transient event $k_P = 0$). The exponential damping coefficient is equal to 0.0589 using Eq. 9.9.23. No analytic expression has been proposed for the exponential decay rate due to quasi-steady friction in this thesis. The decay rate for quasi-steady friction has been determined by fitting an exponential decay function to numerically generated quasi-steady friction data. The numerically generated data and fitted decay function are shown in Figure 11.19.

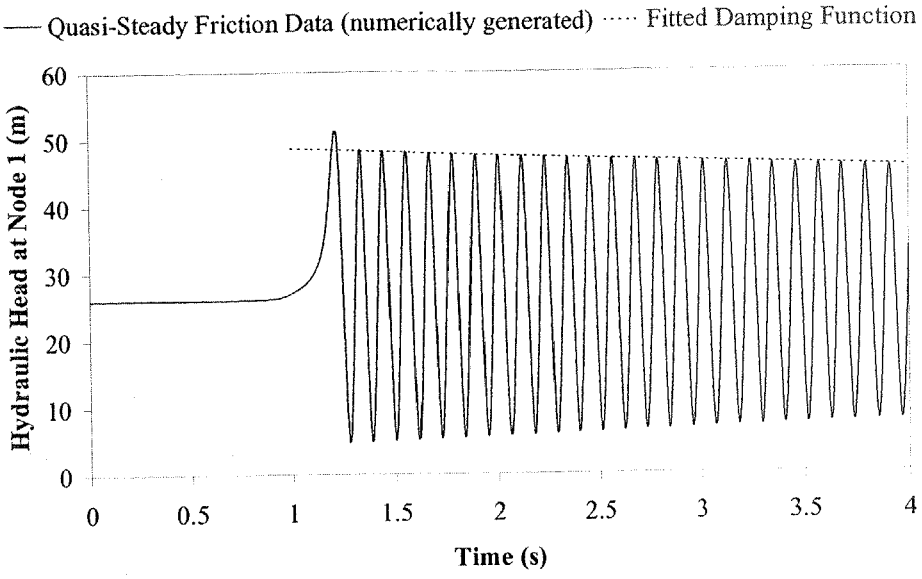

Figure 11.19 Fitted Exponential Damping Function for Quasi-Steady Friction

The decay rate for the quasi-steady friction component of unsteady friction was measured from Figure 11.19 as 0.0057. The total unsteady frictional exponential decay rate is the addition of the quasi-steady and unsteady friction exponential decay rates. The total predicted exponential decay rate is equal to 0.0645. Figure 11.20 shows the experimental data and an exponential curve fitted along the peaks using the predicted exponential decay rate.

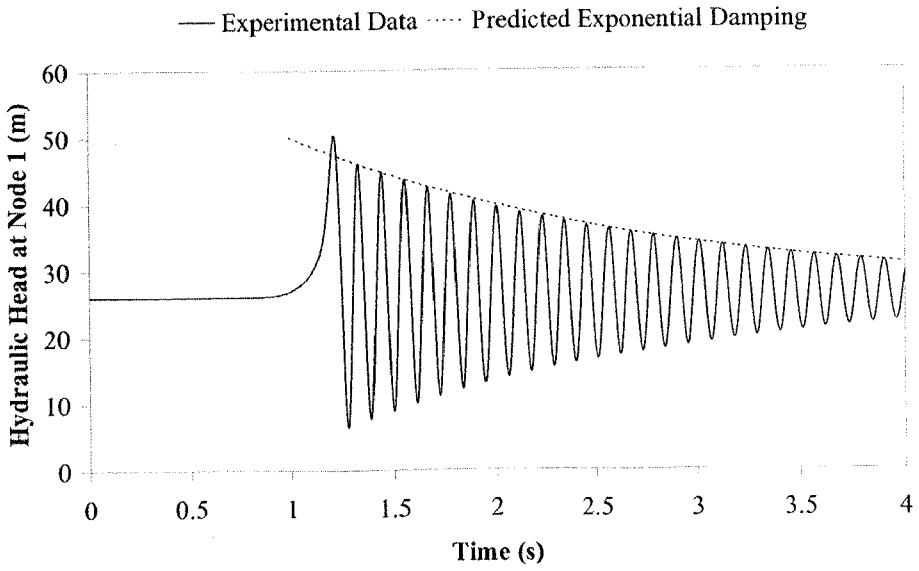

Figure 11.20 Experimental Verification of Exponential Damping Function

A good match is observed between the experimental data and the theoretical exponential damping curve. An exponential damping coefficient, calculated from the experimental data, is equal to 0.0633. The error in the predicted D_U and the experimental D_U was 2.0%. The decay rate of the pressure oscillations could be used to estimate the unsteady friction coefficient from a pressure trace, thus having benefits whereby k_A could be found without having to fit data using a transient solver with an unsteady friction model attached, therefore making the estimation of the unsteady friction coefficient k_A (for slow transient events) fast and easy.

11.7 Verification of Unsteady Friction Coefficients

An important aspect of research presented in this thesis is the analytic relationships derived for the unsteady friction coefficients k_3, k_M, k_A and k_P as presented in Chapter 9. Historically these coefficients have had to be experimentally determined, which in some cases is impossible in existing pipe networks. Previously published data on unsteady friction coefficients are rare. High Reynolds number tests were performed by Shuy and Apelt (1983) for purely accelerating flows (as reported by Vardy and Brown, 1996). Their unsteady friction coefficients combine both k_3 and k_M together. To determine separate k_3 and k_M values, the ratio of the theoretical k_3 to k_M (Eq. 9.6.9 for k_3 and Eq. 9.6.5 for k_M) is used. The original and ratio modified unsteady friction coefficients, shown in Table 11.1, are used for the verification of analytic expressions for k_3, k_M, k_A and k_P derived in Section 9.6.

Table 11.1 Modification of Shuy and Apelt (1983) k_3 Experimental Data

Reynolds Number	Shuy & Apelt (1983)	Theoretical Values		Ratio Modified Shuy & Apelt (1983)	
R	k	k_3	k_M	k_3	k_M
8.0×10^5	0.0245	0.0183	0.0030	0.0211	0.0034
1.3×10^6	0.0216	0.0175	0.0027	0.0187	0.0029
2.0×10^6	0.0194	0.0169	0.0025	0.0169	0.0025

The Shuy and Apelt (1983) experiments have provided data for high Reynolds number flows and the fast valve-closure experiments by Bergant and Simpson (1995) have provided the data for low Reynolds numbers. The latter experiments consisted of

downstream and upstream fast valve closures for velocities of approximately 0.1, 0.2 and 0.3 m/s (corresponding to Reynolds numbers of 2,414, 4,389 and 6,584 respectively). Best fit unsteady friction coefficients (k_3 and k_M) were found from the data using a Levenberg-Marquardt algorithm to minimise the sum of the squares of the differences between experimental and modelled pressure heads at nodes 1, 2, 3 and 4.

The experimentally determined values for the coefficient k_3 are used to verify the expressions relating k_3 to the initial Reynolds number. Previous expressions were produced by Carstens and Roller (1959), Shuy and Apelt (1987) and Vardy and Brown (1996). A smooth pipe expression developed in this thesis is also tested. Figure 11.21 shows the verification for k_3.

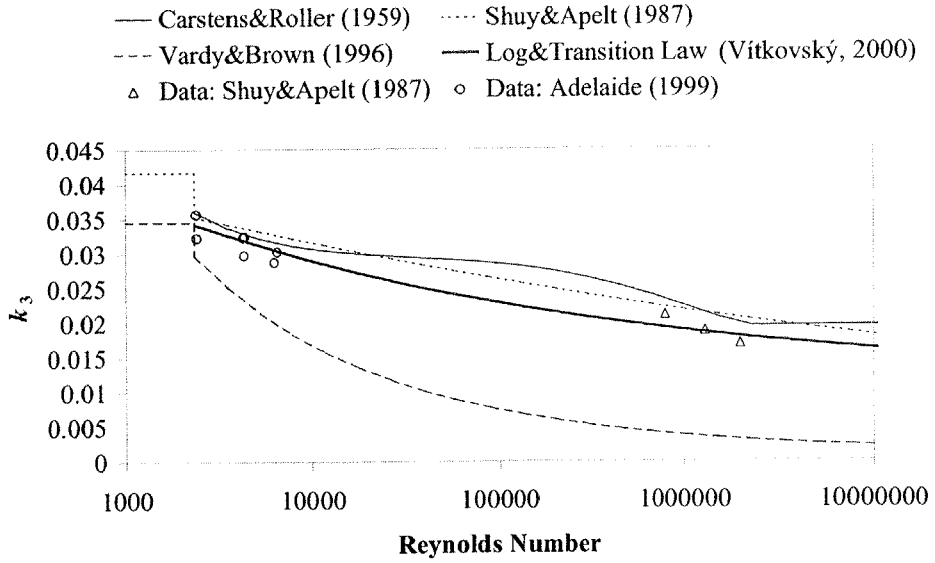

Figure 11.21 Experimental Unsteady Friction Coefficient k_3 Versus Reynolds Number

The proposed smooth pipe relationship—the Vítkovský (2000) line in Figure 11.21—(from Section 9.6) has the best fit to the experimental data compared to the other relationships. The Vardy and Brown (1996) expression performs the worst of all, consistently producing low values of k_3, causing the pressure oscillations to be under damped. A similar graph is created for the momentum correction coefficient k_M. The verification of analytic expressions presented in Section 9.6 using different approximations of the initial velocity profile is shown in Figure 11.22.

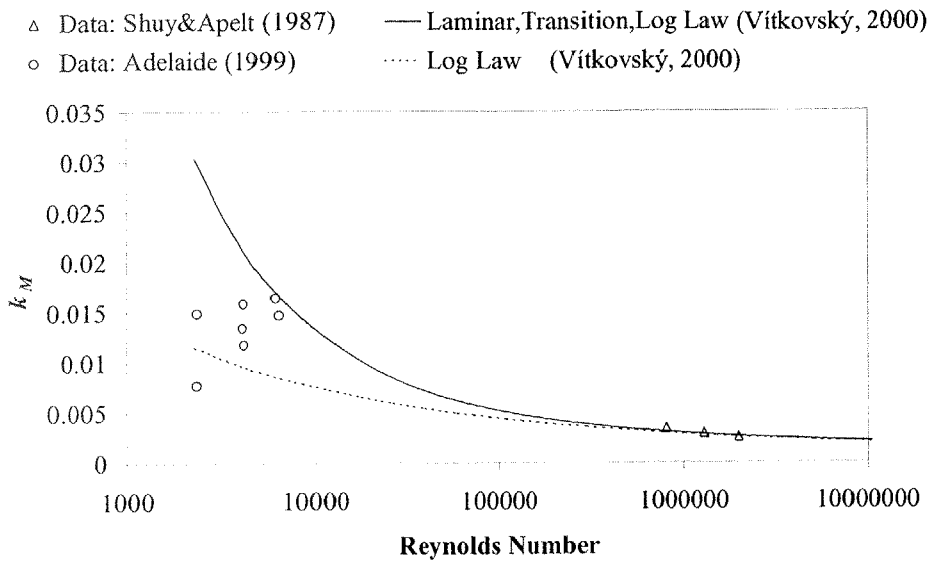

Figure 11.22 Experimental Unsteady Friction Coefficient k_M Versus Reynolds Number

The two expressions developed in this thesis consider the velocity profile modelled by only the log law and by the log law together with transition laws and the viscous sub-layer. The high Reynolds number tests produce a good fit with both curves. The low Reynolds number tests, however, are scattered between the divergence of the two curves. A possible reason is that the viscous sub-layer contains pockets of unstable laminar and turbulent flow. The analysis highlights the problems that can be encountered when dealing with low Reynolds number flows that may be in a transition region.

The same analysis is performed to find the coefficients for the k_A & k_P unsteady friction model. Analytic expressions for the coefficient k_A are presented in Section 9.6 in Eqs. 9.3.7, 9.3.8 and 9.6.9. The most accurate of these use the definition of the initial steady state velocity profile (which depends on the Reynolds number) including the log, transition and viscous sub-layer laws. Comparison with experimental data is shown in Figure 11.23.

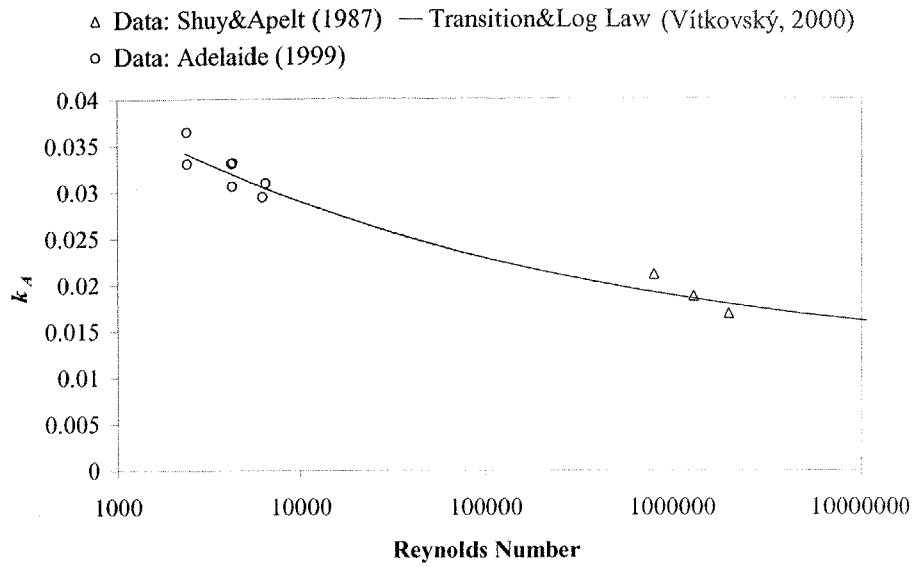

Figure 11.23 Experimental Unsteady Friction Coefficient k_A Versus Reynolds Number

The analytic expression for k_A is a good fit of the experimental data, which is expected because the coefficient k_A is equal to the unsteady friction coefficient k_3 (that also produces a good fit).

The unsteady friction coefficient k_P is the summation of the coefficients k_3 and k_M. Two relationships are tested in a similar way to the results presented above for the k_M coefficient. One relationship uses the logarithmic law only to define the initial turbulent velocity distribution and the other uses a combination of laws for the logarithmic layer, transition region, and viscous sub-layer region in the velocity distribution. Experimental results for the coefficient k_P are shown in Figure 11.24.

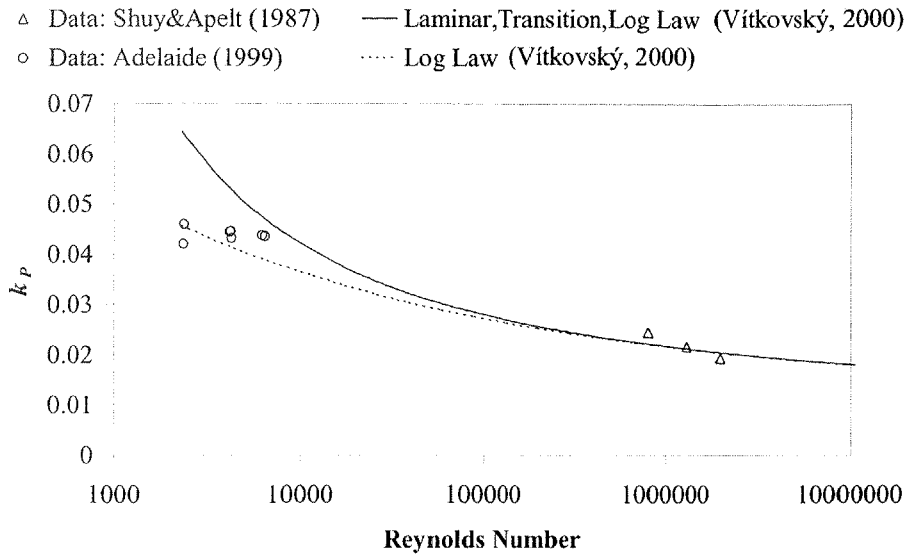

Figure 11.24 Experimental Unsteady Friction Coefficient k_P Versus Reynolds Number

The log law relationship provides the best fit to the experimental data. The fit suggests that there is little need to model the transition and viscous sub-layer regions in the initial velocity distribution.

11.8 Summary

This chapter has presented original work on the modelling of unsteady flow events to account for unsteady friction. Results presented for fast valve closure transient events showed the differences caused by the initial steady state flow being laminar and turbulent. The Zielke (1968) model demonstrated a good fit with the experimental data when the initial flow was laminar. When the initial flow was turbulent, the k_A & k_P numerical model (or the k_3 & k_M sub-model) derived in this thesis showed a good match. The Brunone *et al.* (1991) model produced good matches with regard to the damping in the experimental data but did not predict the phase change correctly. The Brunone *et al.* (1991) and the k_A & k_P models, however, did not predict the correct shape of the pressure oscillations after a fast valve closure when the exact solution was used (the unsteady friction model included in the directional derivatives, in the method of characteristics). Better results were found when using the approximate

implementations of both models (the unsteady friction treated as an addition to steady friction), which was due to diffusion caused by numerical error from the approximation of the derivatives in the unsteady friction models. Different results were observed for an initially turbulent flow subjected to a slow valve closure. The phase change in the pressure oscillations associated with the fast event was not evident for the slow events. The k_A & k_P unsteady friction model is able to predict the slow events due to its ability to control both damping and phase independently. A transition region is theorised for the change from fast to slow valve closures for initially turbulent events. The transition was evident in the experimental data where the valve closure was close to the border of fast and slow valve closure time. Finally, coefficients for the k_A & k_P model are proposed for both fast and slow valve closure events (for an initially turbulent flow).

Experimental results for the eight unsteady flow events previously defined in Section 8.6 are also presented in this chapter. The k_A & k_P numerical model produced a good match for the both the downstream and upstream valve closure cases. The match for the downstream and upstream valve opening cases are similar to the quasi-steady friction model. For the valve opening cases, the k_A & k_P model did not add to the damping of the pressure oscillations (above the quasi-steady damping) and produced an excessive positive phase shift, which limits the validity of the k_A & k_P model. The limitations of the k_A & k_P model affects the type of unsteady event that can be used for verification of the inverse transient method. The Zielke (1968) model for laminar flow produced good results for valve openings.

The exponential nature of the damping of pressure oscillations produced by unsteady friction was experimentally verified. The theoretically derived exponential damping factor was calculated based on relationships derived in Section 9.11. These relationships depend on the unsteady friction coefficient k_3, which was, in turn, calculated using analytic expressions derived in Section 9.7. The theoretical decay matched the decay of the experimental data well, which raises the possibility of an effective way to estimate the unsteady friction coefficient from experimental data by calculating a decay coefficient and then computing an unsteady friction coefficient, thus alleviating the need to use a transient solver and to then fit an unsteady friction model to the data using a minimisation algorithm.

The analytic relationships for k_3, k_M, k_A and k_P for a smooth pipe matched well with experimental data. These relationships predicted dependence on the initial Reynolds number, which is of obvious benefit for engineers where analytic relationships can be used to find unsteady friction coefficients rather than having to determine them experimentally.

Results from this chapter are necessary for the implementation of the inverse transient method for leak detection in the following chapter. A successful application of the inverse transient method for leak detection requires that the pipeline transients can be modelled correctly when there are no leaks.

Chapter 12

Experimental Verification of Leak Detection and Location Methods

12.1 Introduction

This chapter presents one of the first known experimental verifications of the inverse transient method for leak detection and location. The apparatus used to produce the experimental data is described in Chapter 10 (Figure 12.1). Note that the pipe has been divided into 16 reaches for the application of inverse transient analysis.

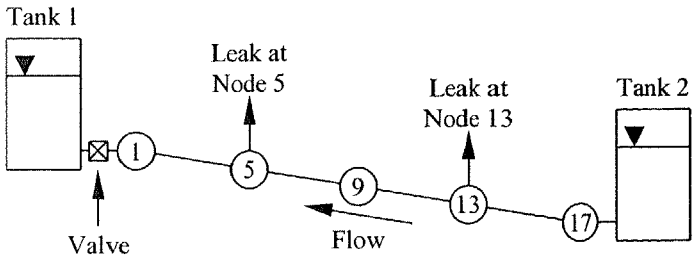

Figure 12.1 Experimental Pipeline Apparatus

As a result of study in the previous chapter on the validity of unsteady friction models, a certain type of transient event has been chosen. Since the k_A & k_P unsteady friction

model was found to produce good results for upstream and downstream valve closures that were slower than $2L/a$, these types of tests are used in this chapter. The different experimental situations are defined by available leak sizes (three sizes equal to 1.0, 1.5 and 2.0 mm), positions at which leakage can occur (two locations at nodes 5 and 13) and different valve closure speeds (fast, medium and slow corresponding to closure times of $2.5L/a$, $25L/a$ and $50L/a$, all of which are slower than $2L/a$). The transient model uses 16 computational reaches in every simulation. Results for leak detection are presented using the inverse transient method and a method that uses information from the first pressure rise after a fast valve closure.

12.2 Initial Investigation of Inverse Transient Analysis

This section presents preliminary investigations into the application of the inverse transient method using experimental data. The various aspects considered are the variation of true leak behaviour with the classical orifice leak relationship (of square root form), the minimisation method used to fit the experimental data, and the effect of unsteady friction on inverse transient results.

12.2.1 Non-Theoretical Leak Relationships

A modelling concern is that the leak equation (the relationship between leak flow and pressure head) is not guaranteed to be of the theoretical orifice-equation form. Thus, an important question is: Does the form of the leak equation have a large effect on modelling and inverse transient results? In field situations, the form of the leak equation will not be known. Theoretically, the orifice equation should model the leak behaviour but, for leaks of different geometries, it may not be a good approximation. In the experimental apparatus used in this thesis, the leaks (especially the larger diameter ones) are not well modelled by the orifice equation. For example, consider the calibration of the 2.0 mm diameter leak in Figure 12.2 (repeated from Chapter 10).

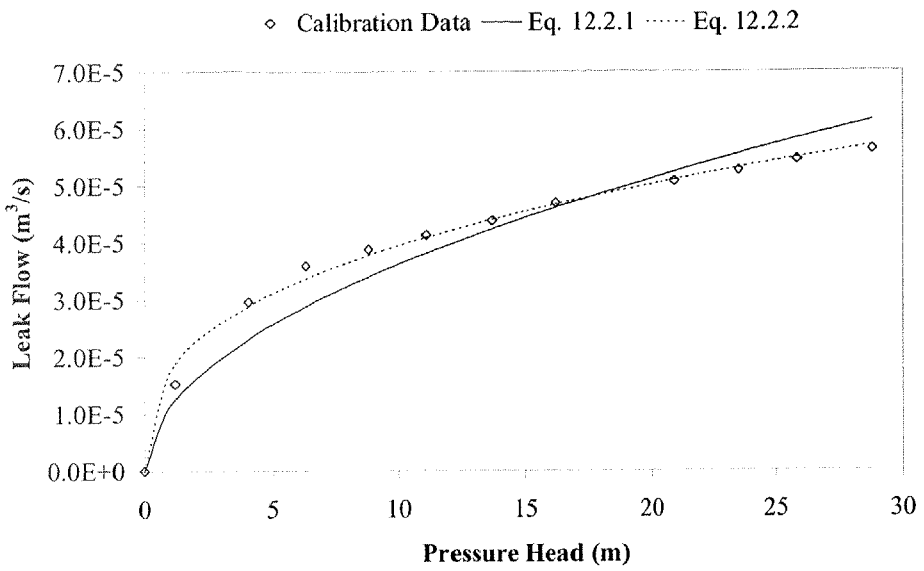

Figure 12.2 Leak Relationship Calibration, 2.0 mm Leak

The orifice equation was fitted to the data (i.e., the coefficient was fitted but the exponent was set to 0.5) using a standard least squares fit and the Levenberg-Marquardt minimisation algorithm. The fitted orifice equation is

$$Q_L = 2.58\times10^{-6}\sqrt{2g}H_L^{0.5} \quad \text{.....(12.2.1)}$$

As observed in Figure 12.2, the orifice equation under-predicts the first portion of the experimental data and over-predicts the second portion, showing a potential for error in modelled results that use this relationship. A better fit can be found by fitting both the coefficient and exponent of the pressure head,

$$Q_L = 4.00\times10^{-6}\sqrt{2g}H_L^{0.347} \quad \text{.....(12.2.2)}$$

The performances of the different fits (Eqs. 12.2.1 and 12.2.2) are tested using a fast transient event (similar to those used for the verification of the inverse transient method). The event is a downstream valve closure with an initial velocity of 0.16 m/s (corresponding to a Reynolds number of 3,511). The pressure head at node 1 is shown in Figure 12.3 using both fitted leak relationships and including the no leak case.

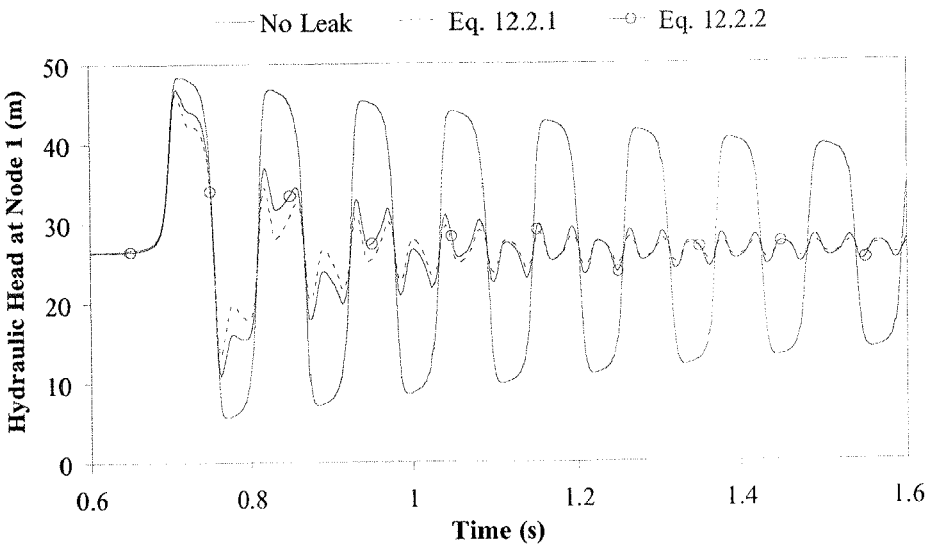

Figure 12.3 Results Using Leak Relationship Eqs. 12.2.1 and 12.2.2

Figure 12.3 shows that Eq. 12.2.1 produces too much damping compared to Eq. 12.2.2, which is because Eq. 12.2.1 over-predicts the quantity of flow between the leak flow and pressure head for high pressures (an artefact of the fit). Since the true relationship is not known, one will have to be assumed, which would typically be the orifice relationship where the exponent of the head at the leak is 0.5. The question now becomes is there a coefficient (i.e., the lumped leak coefficient $C_d A_L$ of the orifice equation) that adequately matches the experimental data? This question is investigated by determining a lumped leak coefficient for a numerical model that uses the theoretical orifice equation (the exponent equal to 0.5) to pressure head data generated by a model that uses the true leak relationship (Eq. 12.2.2), resulting in

$$Q_L = 1.66\times10^{-6}\sqrt{2g}H_L^{0.5} \quad \text{.....(12.2.3)}$$

The lumped leak coefficient after fitting is much smaller (a 36% decrease from 2.58×10^{-6} m^2) than fitting using the experimental leak flow and pressure head measurements. Figure 12.4 shows the pressure head at node 1 when using Eqs. 12.2.2 and 12.2.3.

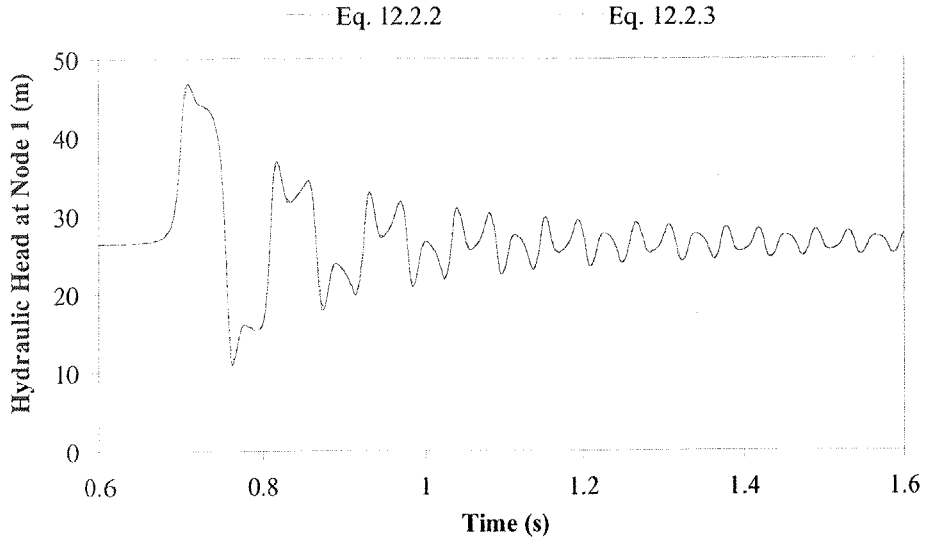

Figure 12.4 Results Using Leak Relationship Eqs. 12.2.2 and 12.2.3

Figure 12.4 shows good agreement between results using the two fitted curves. The lumped leak coefficient for Eq. 12.2.3 (equal to 1.66×10^{-6} m^2) is considered as correct when using the orifice equation in the transient model for the verification of the inverse transient method, given a similar experimental transient event. Different fitted lumped leak coefficients are found for different transient events. The same type of analysis can be applied to the experimental data for the other leak sizes. The resulting lumped leak coefficients are shown in Table 12.1.

Table 12.1 Equivalent Lumped Leak Coefficients

	Lumped Leak Coefficient C_dA_L (m^2)
1.0 mm Leak at Node 5	5.0×10^{-7}
1.5 mm Leak at Node 5	1.1×10^{-6}
2.0 mm Leak at Node 5	1.7×10^{-6}
1.0 mm Leak at Node 13	7.1×10^{-7}

The inverse transient analysis results presented in subsequent sections of this chapter assume that the behaviour of a leak is modelled by the theoretical orifice equation (square root relationship). Therefore, the values of C_dA_L shown in Table 12.1 are considered to be the correct values for each leak size (when checking inverse transient results).

12.2.2 Local Versus Global Minimisation

This section explores the minimisation method used to solve the least squares problem incorporated within the inverse transient analysis algorithm. Liggett and Chen (1994) used the Levenberg-Marquardt algorithm to perform the minimisation. The path to a solution taken by the Levenberg-Marquardt algorithm sometimes produces trial sets of parameters that are negative. These negative parameter values are undesirable (and physically impossible for a leak), meaning that a lumped leak coefficient of zero is a lower bound. It also produces trial sets of parameters that contain lumped leak coefficients that are so large that the leakage is greater than the capacity of the pipeline system, thus setting an upper bound for the lumped leak coefficients. Chen (1995) used a method to constrain the both the friction factors and lumped leak coefficients that checks potential sets of parameters so that if any are outside predefined bounds, those parameters are set to the nearest bound value. Such minimisation constraint interferes with convergence and, in some cases, causes failure. Adding a penalty cost (to the objective function) for sets of parameters that violate the constraints is an alternative that does not interfere with the minimisation algorithm. Another alternative is to minimise the parameters in log space, which allows the algorithm to easily move between different orders of magnitude and does not test negative parameter values. Minimisation in log space is used in the inverse transient method hereafter in this thesis.

The Levenberg-Marquardt algorithm is used to minimise the least squares problem using experimental data for a fast valve closure with a 1.0 mm leak at node 5. Seven possible leak candidates were assumed at nodes 3, 5, 7, 9, 11, 13 and 15. The results of the minimisation are shown in Table 12.3. These results show that leak was incorrectly found at node 3, which is because the Levenberg-Marquardt algorithm only performs a local search. Therefore, it is quite possible that the solution represents a local minimum rather than the global minimum.

There are a few ways to confirm the existence of a minimum. One is if the gradient of the objective function is equal to zero at that point,

$$\nabla E(\mathbf{a}_{\min}) = \frac{\partial E}{\partial a_1}\mathbf{a}_1 + \ldots + \frac{\partial E}{\partial a_7}\mathbf{a}_7 = 0 \quad \text{.....(12.2.4)}$$

where $\mathbf{a}$ = the vector of parameters $\{a_1, \ldots, a_7\}$, which in this case are the lumped leak coefficients at nodes 3, 5, 7, 9, 11, 13 and 15, $\mathbf{a}_{min}$ = the vector of parameters at the suspected minimum and $\mathbf{a}_i$ = a unit vector in the direction of the i^{th} parameter. However satisfying Eq. 12.2.4 does not guarantee that $\mathbf{a}_{min}$ is a minimum, $\mathbf{a}_{min}$ might be a point of inflection. Additional criteria eliminate the existence of an inflection point,

$$\frac{\partial^2 E}{\partial a_i^2} > 0 \quad \text{for} \quad i = 1,\ldots,7 \qquad (12.2.5)$$

Alternatively, a suspected minimum exists if the objective function increases in the neighbourhood of $\mathbf{a}_{min}$,

$$E(\mathbf{a}_{min} + \delta\mathbf{a}) > E(\mathbf{a}_{min}) \qquad (12.2.6)$$

where $\delta\mathbf{a}$ is a small change in the parameters in any direction. These principles are applied to the solution found by the Levenberg-Marquardt algorithm. Table 12.2 shows the partial derivatives of the objective function with respect to each of the leaks. The partial derivatives are not zero suggesting that the Levenberg-Marquardt algorithm solution is not a minimum.

Table 12.2 Properties at the Levenberg-Marquardt Algorithm Solution

Node i	$\partial E/\partial a_i$	$E(\mathbf{a}-\delta a_i)$	$E(\mathbf{a}+\delta a_i)$
3	2.921×10^{10}	2795.791	2791.130
5	1.703×10^{9}	2795.819	2791.103
7	4.893×10^{9}	2795.816	2791.106
9	2.446×10^{10}	2795.796	2791.126
11	4.386×10^{10}	2795.777	2791.145
13	4.634×10^{10}	2795.774	2791.147
15	1.928×10^{10}	2795.801	2791.120

Table 12.2 also shows values of the objective function near the suspected local minimum ($E(\mathbf{a}_{min})$ = 2791.101 m^2). The objective function is calculated for small perturbations (δa_i = $\pm1.0\times10^{-12}$ m^2) in each leak candidate from the suspected minimum. In this case results suggest that the Levenberg-Marquardt solution is a local minimum. To resolve this ambiguity, Figure 12.5 shows a simplified plot of the objective function surface around the suspected minimum (only considering variation in leaks at nodes 4 and 6).

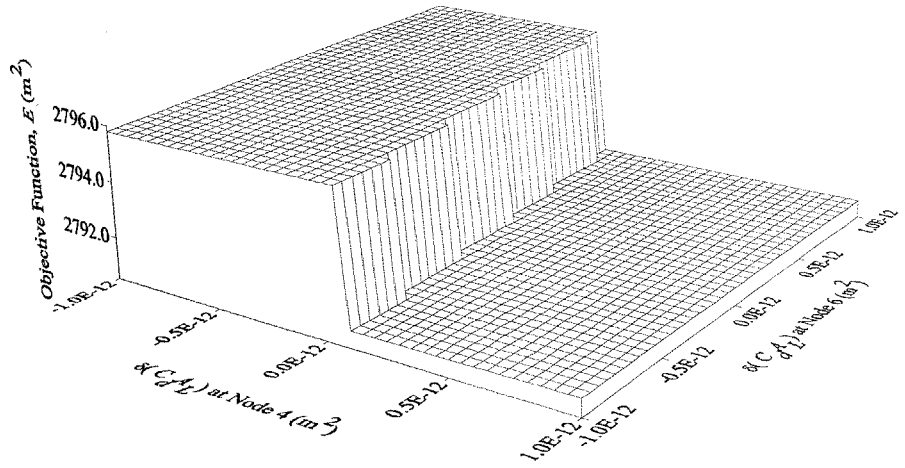

Figure 12.5 Objective Function Surface at Suspected Local Minimum

The plot indicates a cliff in the objective function surface at the suspected minimum. Subsequent analysis shows that the cliff is present in the objective function surface for all leak candidates. In more detail the bottom surface of the cliff slopes downward into the cliff, which causes problems for the Levenberg-Marquardt algorithm. The existence of true local minima (and more cliffs), although not shown in this thesis, has been found for a simple two-leak candidate system for the same transient event.

A minimisation algorithm that provides a better coverage over the search space (a less local, more global search) is the Shuffled Complex Evolution (SCE) algorithm (Duan *et al.*, 1992). The SCE method is based on four main concepts: (1) a combination of deterministic and probabilistic approaches; (2) the systematic evolution of a "complex" of points spanning the parameter space in the direction of global improvement; (3) competitive evolution; and (4) complex shuffling. An initial population of points is randomly sampled from the parameter space. These points are partitioned into a number of complexes that are evolved using competitive evolution techniques in a manner similar to the simplex method. At periodic times during the evolution, the entire set of points are shuffled and reassigned to new complexes, thus enabling information sharing. The competitive evolution ensures that the entire population should move towards the global optimum (given an adequate initial population size). The shuffling allows a more global search and exchange of information about different regions of the search space. The SCE method produced good results for global minimisation for the calibration of conceptual rainfall-runoff models (Duan *et al.*, 1993,

1994; Thyer *et al.*, 1999). The SCE method is also able to bound the parameter search space. Results using the SCE minimisation are also shown in Table 12.3.

Table 12.3 Comparison of Minimisation Algorithm Results

ITA Method	E (m^2)	Lumped Leak Coefficient, $C_d A_L$ (m^2)						
		Node 3	Node 5	Node 7	Node 9	Node 11	Node 13	Node 15
Actual	-	-	**5.0×10^{-7}**	-	-	-	-	-
LVMQ	2791	**4.3×10^{-7}**	2.1×10^{-7}	5.4×10^{-8}	1.1×10^{-8}	1.0×10^{-12}	7.9×10^{-8}	1.0×10^{-12}
SCE	2321	1.1×10^{-7}	**5.1×10^{-7}**	1.4×10^{-12}	2.6×10^{-9}	3.6×10^{-11}	9.9×10^{-8}	6.1×10^{-9}

Largest size leak in bold

Although the SCE method found a leak at the correct position along the pipeline, it also found a possible leak of the same order of magnitude (but smaller) at node 3. The SCE method found a lower objective function (E) value than the Levenberg-Marquardt algorithm (the aim being to minimise the objective function value), indicating that the latter did find a local minimum or a problematic region of the search space.

Another difference between the two methods is speed of computation. The best indicator of the speed of computation is how many function evaluations (transient simulations) are employed by each method. A plot of the convergence of each method is shown in Figure 12.6.

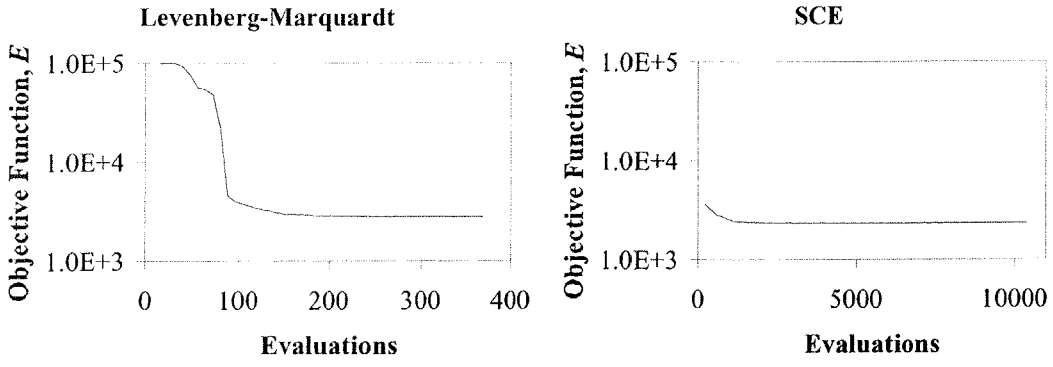

Figure 12.6 Convergence Using Different Minimisation Algorithms

The Levenberg-Marquardt algorithm has an order of magnitude faster convergence than the SCE method, although the SCE method finds a superior solution. These results might also point to the need for a hybrid minimisation method that can exploit the speed

of the Levenberg-Marquardt algorithm and the search space coverage of the SCE method. The SCE method is used for inverse transient analysis hereafter.

12.2.3 Is Unsteady Friction Needed?

The importance of unsteady friction is a modelling concern, given that no completely adequate model for turbulent unsteady friction is valid for all kinds of transient events. Since the effect of leakage is usually larger than the effect of unsteady friction and that unsteady friction, at this moment in time, is not fully understood, a question could be asked: Is unsteady friction modelling needed for leak detection using the inverse transient method? To answer this question, two separate transient events, a fast valve closure and a slow valve closure, are considered. A 1.0 mm leak located at node 5 is used for both events. The inverse transient method is used to fit a transient model to experimental data both including and excluding unsteady friction, the result of which is shown in Figure 12.7.

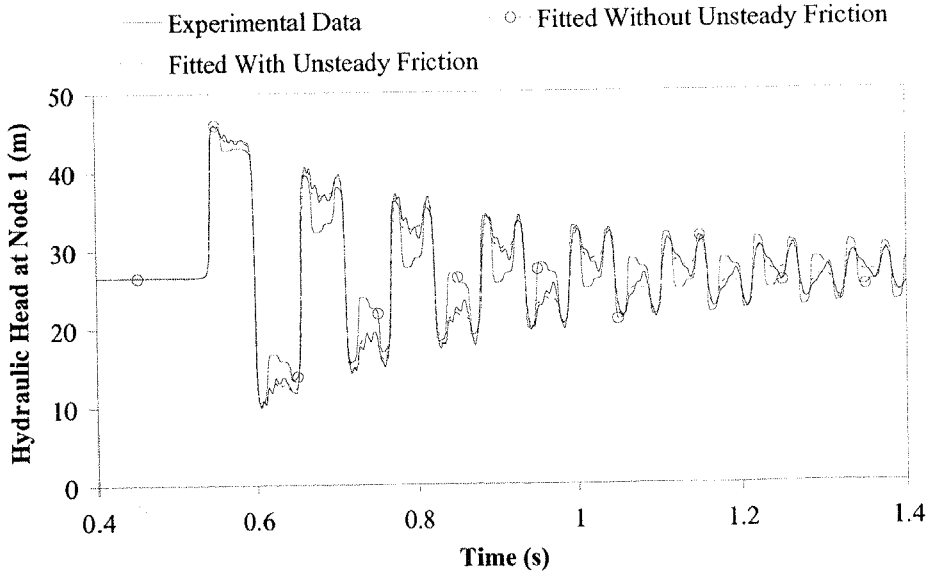

Figure 12.7 Effect of Unsteady Friction on ITA, Fast Valve Closure (t_c = 0.07 s)

The result from the inverse transient method including unsteady friction is C_dA_L = 5.1×10^{-7} m^2 (versus the actual value to 5.0×10^{-7} m^2) at node 5 using k_A = 0.035. The result excluding unsteady friction is C_dA_L = 1.4×10^{-6} m^2 at node 5. The lumped leak coefficients and unsteady friction coefficients are shown in Table 12.4.

Table 12.4 Tabulated Results for Effect of Unsteady Friction (1.0 mm Leak at Node 5, Fast Valve Closure, $t_c = 0.07$ s)

	Lumped Leak Coefficient C_dA_L (m^2)	Unsteady Friction Coefficient k_A
Actual	5.0×10^{-7}	0.035
Fitted Results (Including Unsteady Friction)	5.1×10^{-7}	0.035
Fitted Results (No Unsteady Friction)	1.4×10^{-6}	0.0

Neglecting unsteady friction results in a leak coefficient that is half an order of magnitude too high in this case. Figure 12.7 indicates a worse fit when excluding unsteady friction, suggesting that unsteady friction is important for fast valve closure events. For a slow valve closure the experimental and numerical pressure heads at node 1 are shown in Figure 12.8.

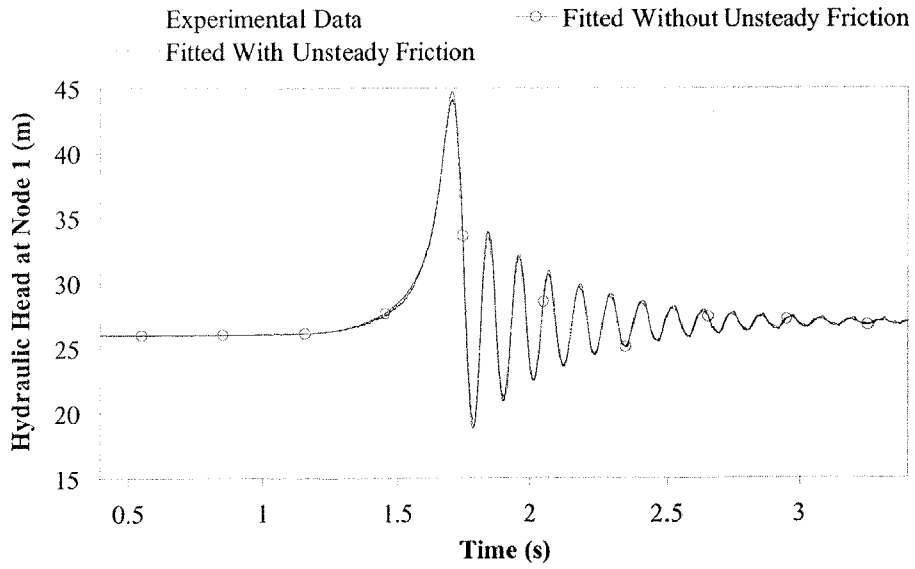

Figure 12.8 Effect of Unsteady Friction on ITA, Slow Valve Closure ($t_c = 1.4$ s)

The results from the inverse transient method for a slow valve closure are $C_dA_L = 4.96\times10^{-7}$ m^2 including unsteady friction ($k_A = 0.028$) and $C_dA_L = 5.52\times10^{-7}$ m^2 excluding unsteady friction. Inverse transient analysis results using a slow valve closure test are shown in Table 12.5.

Table 12.5 Tabulated Results for Effect of Unsteady Friction (1.0 mm Leak at Node 5, Slow Valve Closure, t_c = 1.4 s)

	Lumped Leak Coefficient $C_d A_L$ (m^2)	Unsteady Friction Coefficient k_A
Actual	5.00×10^{-7}	0.028
Fitted Results (Including Unsteady Friction)	4.96×10^{-7}	0.028
Fitted Results (No Unsteady Friction)	5.52×10^{-7}	0.0

In this case, a good fit to the experimental data is found with or without the inclusion of unsteady friction. The lumped leak coefficients in both cases are similar, suggesting that unsteady friction is not as important for slow valve closures as it was for fast valve closures. An unsteady friction model is used in the inverse transient method hereafter.

12.2.4 Inverse Transient Statistics

Two of the most important properties needed to justify a solution from the inverse transient method are the estimated variances in parameters and the goodness-of-fit criterion. Both of these properties need estimates of the standard deviation (or variance) in the measured data. The standard deviation of the measured data was found to increase as the length of cable connecting the pressure transducers to the data acquisition computer increased (see Section 10.4.1). Table 12.6 shows the standard deviation and the variance of the error corresponding to each of the measurement locations.

Table 12.6 Statistics of Measured Pressure Data

Measurement Location	Node 1	Node 5	Node 9	Node 13
Standard Deviation (m)	0.011	0.018	0.025	0.030
Variance (m^2)	0.000121	0.000324	0.000625	0.000900

In this section, the same length of data is used for both fast and slow valve closure events. The length of data is 4.0 s corresponding to 2,287 transient time steps. Measured data are taken at four locations, meaning that the total number of measured data points, M, is equal to 9,148. The same number of parameters (leak candidates) is searched for in each case. The number of parameters, N, is equal to 7 (nodes 3, 5, 7, 9, 11, 13 and 15). Therefore, the number of degrees of freedom is 9,141 ($\nu = M - N$).

A fast valve closure test is first considered to illustrate the estimated variance in parameter errors and the goodness-of-fit criterion. The particular experimental test is for a 2.0 mm leak located at node 5 in the pipeline. The inverse transient results for the test are presented later in Section 12.3.1 when the inverse transient solution is acquired. Plots of the fits of the measured data at each of the measurement locations are shown in Figure 12.9.

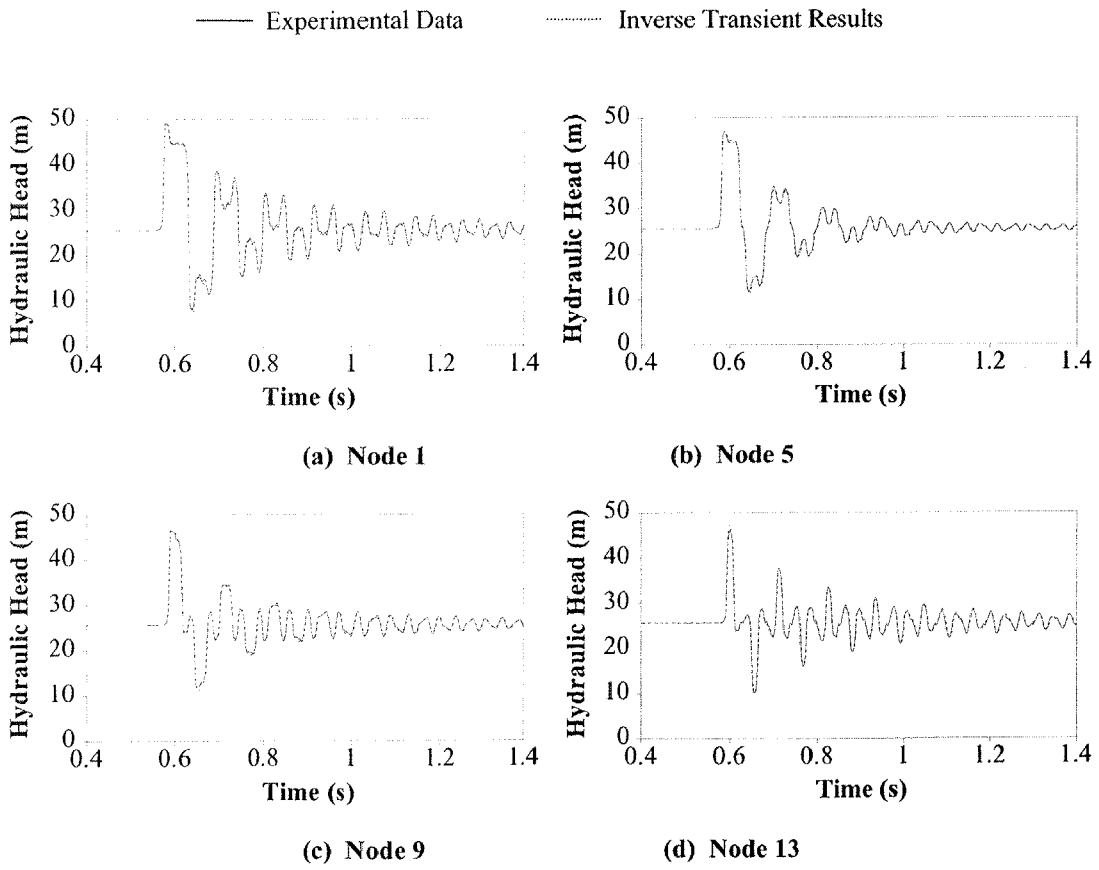

Figure 12.9 Inverse Transient Results
(2.0 mm Leak, Fast Valve Closure, t_c = 0.07 s)

These plots show a good match between the inverse transient results and the measured data. The standard deviation of the predicted error in each of the parameters (C_dA_L for each leak candidate) is estimated using the error in the measured data (see Section 4.7). Table 12.7 shows the predicted standard deviation in the inverse transient results.

Table 12.7 Predicted Statistics in Lumped Leak Coefficients

(2.0 mm Leak, Fast Valve Closure, t_c = 0.07 s)

Location	Node 3	Node 5	Node 7	Node 9	Node 11	Node 13	Node 15
Solution C_dA_L (m^2)	3.2×10^{-11}	1.7×10^{-6}	4.1×10^{-11}	2.9×10^{-9}	5.1×10^{-9}	2.9×10^{-11}	2.6×10^{-7}
St. Dev. C_dA_L (m^2)	1.4×10^{-10}	6.1×10^{-10}	6.4×10^{-10}	1.3×10^{-9}	8.0×10^{-10}	1.1×10^{-9}	1.2×10^{-9}

Table 12.7 shows that, given the error in each of the measurement sites, the expected error in the solution lumped leak coefficients is much smaller than their values. This being a good result since, if the expected error was of the same magnitude as the C_dA_L values, there would be little confidence associated with the inverse transient solution. The goodness-of-fit criterion gives an indication of the applicability of the transient model to model the measured data. The goodness-of-fit criterion is equal to the reduced chi-square statistic (χ_v^2). The chi-square statistic (χ^2) is calculated (see Section 4.8) as 2,166,505. Division by the number of degrees of freedom produces the reduced chi-square statistic, which is equal to 236. A good fit is generally regarded to have a reduced chi-square statistic approximately equal to 1.0. In this case, a value of 236 suggests that the accuracy of the pressure measurements is far greater than the transient model can predict. Therefore, poorer quality pressure transducers could have been used. Also, for the calculation of the expected error in the parameters, the standard deviation of the error in the measured data is not a good representation of the error in the results (given the performance of the model). Assuming a good fit, a better gauge of the error in the measurement data is to calculate the sample standard deviation from the inverse transient results and the experimental data, resulting in a sample variance (s^2) of 0.0605. The sample variance is now used to calculate the expected variance in the inverse transient results, as shown in Table 12.8.

Table 12.8 Predicted Statistics in C_dA_L Using Sampled Variance in Data

(2.0 mm Leak, Fast Valve Closure, t_c = 0.07 s)

Location	Node 3	Node 5	Node 7	Node 9	Node 11	Node 13	Node 15
St. Dev. C_dA_L (m^2)	2.2×10^{-9}	1.1×10^{-8}	1.1×10^{-8}	2.2×10^{-8}	1.3×10^{-8}	1.8×10^{-8}	2.0×10^{-8}

The expected error in the lumped leak coefficients using the sample statistics produces standard deviations that are approximately one order of magnitude larger than those

using the original, measured, statistics. These larger standard deviations are still two orders of magnitude smaller than the actual lumped leak coefficients though.

The same analysis is repeated for a slow valve closure event with a 1.0 mm leak located at node 5. The results from the inverse transient method are shown later in Section 12.3.3. The fit of the model to the measured data at each of the measurement locations is shown in Figure 12.10.

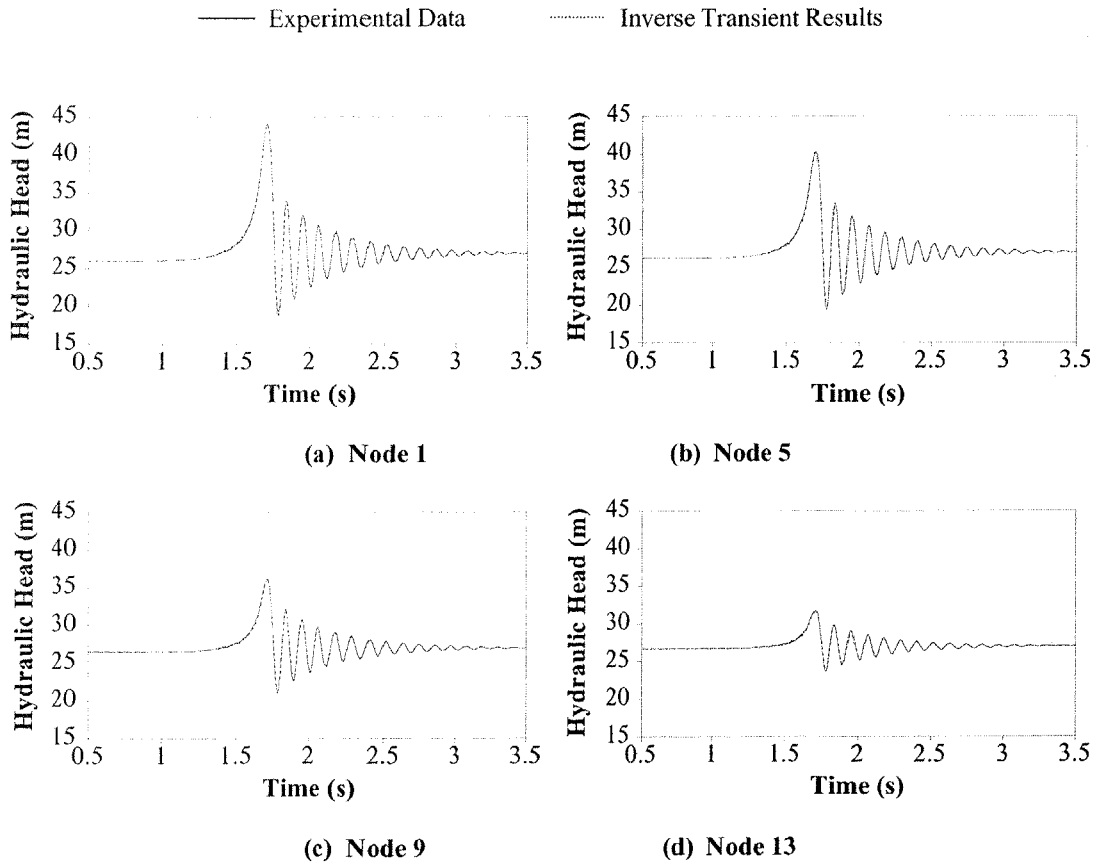

Figure 12.10 Inverse Transient Results
(1.0 mm Leak, Slow Valve Closure, t_c = 1.4 s)

These plots show little difference between the inverse transient results and the measured pressure head data. The predicted error in the lumped leak coefficients and their associated values are shown in Table 12.9.

Table 12.9 Predicted Statistics in Lumped Leak Coefficients

(1.0 mm Leak, Slow Valve Closure, t_c = 1.4 s)

Location	Node 3	Node 5	Node 7	Node 9	Node 11	Node 13	Node 15
Solution C_dA_L (m^2)	5.5×10^{-11}	1.1×10^{-9}	9.9×10^{-11}	5.4×10^{-8}	8.8×10^{-7}	7.5×10^{-7}	9.1×10^{-8}
St. Dev. C_dA_L (m^2)	3.0×10^{-10}	3.7×10^{-10}	3.2×10^{-10}	1.1×10^{-9}	1.9×10^{-9}	1.6×10^{-9}	1.3×10^{-9}

Again, a low standard deviation in the error of the lumped leak coefficients is predicted. The chi-square statistic (χ^2) is 576,582. The reduced chi-square statistic (χ^2_ν) is equal to 63.1 after dividing χ^2 by ν, which is still not close to 1.0 but is about half the size of the corresponding value for the fast valve closure. A better estimation of the error in the data is determined by calculating the sample variance (s^2) from the inverse transient results and the measured data. The value of the sample variance is 0.0149, which is approximately four times smaller than for the fast valve closure. The sample variance in the measured data is then used to calculate the predicted error in the lumped leak coefficients, as shown in Table 12.10.

Table 12.10 Predicted Statistics in C_dA_L Using Sampled Variance in Data

(1.0 mm Leak, Slow Valve Closure, t_c = 1.4 s)

Location	Node 3	Node 5	Node 7	Node 9	Node 11	Node 13	Node 15
St. Dev. C_dA_L (m^2)	2.4×10^{-9}	3.0×10^{-9}	2.6×10^{-9}	9.0×10^{-9}	1.6×10^{-8}	1.4×10^{-8}	1.1×10^{-8}

The standard deviations in the predicted error in lumped leak coefficients are now approximately one order of magnitude larger, suggesting a lower confidence should be associated with inverse transient results using a slow valve closure.

In summary, results suggested that the measured data are far more accurate than the transient model could provide, meaning that the measured variance of the measured data was not a good indication of the effective variance in the data given the accuracy of the transient model. A sample variance (calculated from the inverse transient fit to the measured data) was found to produce more realistic results. The goodness-of-fit for a slow valve closure was better than for a fast transient event. The predicted variance of the error in the parameters was calculated again using the sampled variance. For a fast valve closure, values of the standard deviation of the parameter error were three orders

of magnitude lower than the solution parameter values, suggesting that there is a high confidence in the inverse transient solution. However for a slow valve closure, values of the standard deviation of the parameter error were one order of magnitude (and less) lower than the solution parameter values, suggesting a low confidence in the inverse transient solution.

12.2.5 Leak Sensitivity, Variance, Covariance and Correlation

The previous section showed that the estimated standard deviation of the error in the solution parameters was orders of magnitude greater than the values of the solution parameters for fast valve closures. For slow valve closures, the estimated standard deviation in the solution was of similar magnitude to the values of the solution parameters. This behaviour suggests a low sensitivity of solution parameters and, given the error in the measured data, a low confidence in the inverse transient method for slow valve closures. This section investigates various measures of sensitivity, variance, covariance and correlation for fast and slow valve closure events. The simulations used are based on the fast and slow valve closure tests in the previous sections.

If the objective function is set to zero for the "no-leak" case, the sensitivity of the objective function of the forward transient solution with respect to the leak location is found by considering a similar leak ($C_d A_L = 1.0\times10^{-6}$ m^2) at each of the candidate leak locations. Figure 12.11 shows that the sensitivity of the objective function for a fast valve closure is three orders of magnitude greater than that for a slow valve closure. The sensitivity becomes low for both valve closure rates when the leak is positioned near the constant head tank, because a constant demand (or a leak at a constant head) does produce any effect on the pressure trace.

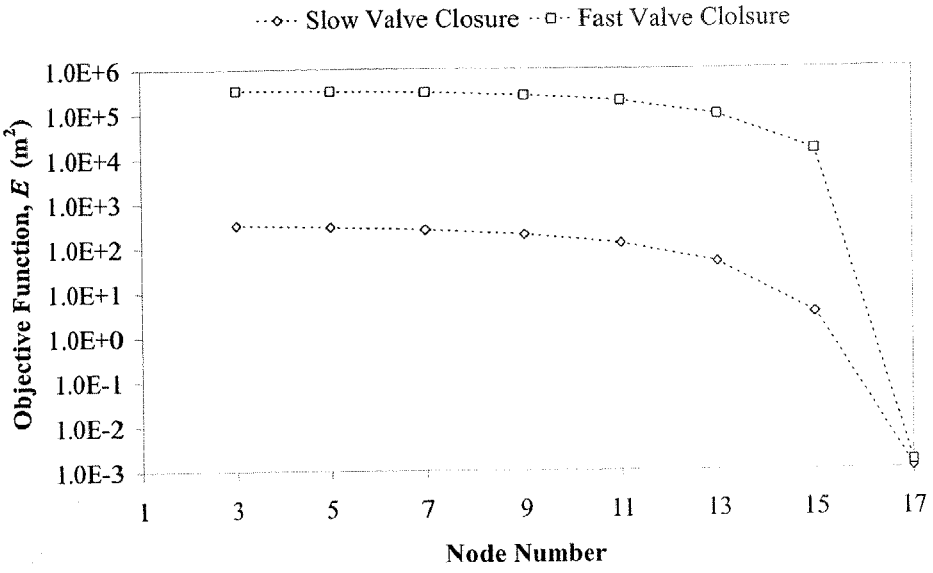

Figure 12.11 Sensitivity of Objective Function Given Leak Location (Forward Transient Solution)

The sensitivity of the objective function for the inverse transient problem is calculated by solving for a single leak located at nodes 3, 5, 7, 9, 11, 13 and 15 one at a time. The measured data is for a leak (C_dA_L = 1.0×10^{-6} m^2) at node 5 with no error for both fast and slow valve closure events. Figure 12.12 shows the sensitivity of the objective function with respect to leak location after applying the inverse transient method.

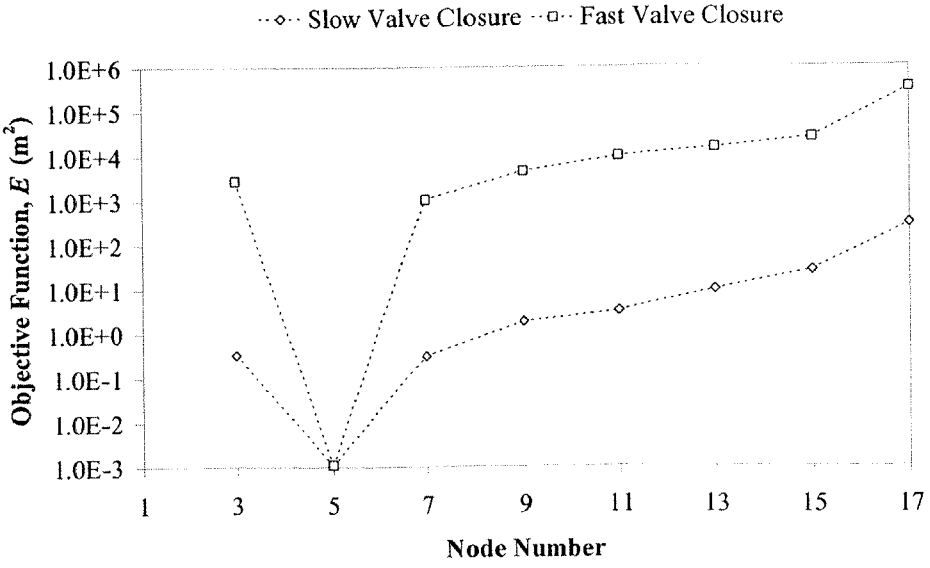

Figure 12.12 Sensitivity of Objective Function Given Leak Location (Inverse Transient Solution)

The sensitivity for the fast valve closure is three orders of magnitude greater than for a slow valve closure, suggesting that inverse transient results using fast valve closures are less likely to be affected by uncertainty in the measured data. Figure 12.13 shows the sensitivity of the solution leak size from the inverse transient method with respect to the leak location. There is little difference between results when using either slow or fast valve closures.

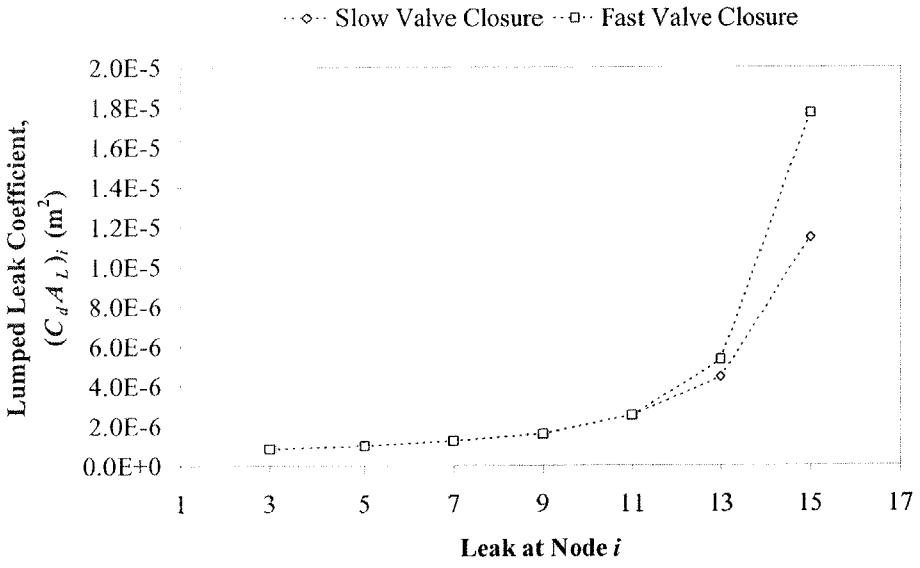

Figure 12.13 Sensitivity of Solved Leak Given Leak Location (Inverse Transient Solution)

The variance, covariance and correlation of solution leak coefficients are considered for fast and slow valve closures based on analysis presented in Section 4.8. The estimated variance in the parameter (a_i) error is related to the variance in the measurement data (H^m) error as

$$\sigma_{a_i}^2 = K_{ii}\sigma_{H^m}^2 \quad \text{.....(12.2.7)}$$

where K_{ii} is an element of the covariance multiplier matrix [K], which is equal to the covariance matrix [C] divided by the variance in the measurement data error, assuming that the variance of the measurement error is equal for each measurement site and that the measurement error is normally distributed. Figure 12.14 shows the variance multiplier for fast and slow valve closure events and indicates that the variance multiplier for the slow valve closure is three orders of magnitude larger than that for the

fast valve closure, suggesting that slow valve closure results are more likely to be degraded by measurement error than those using a fast valve closure.

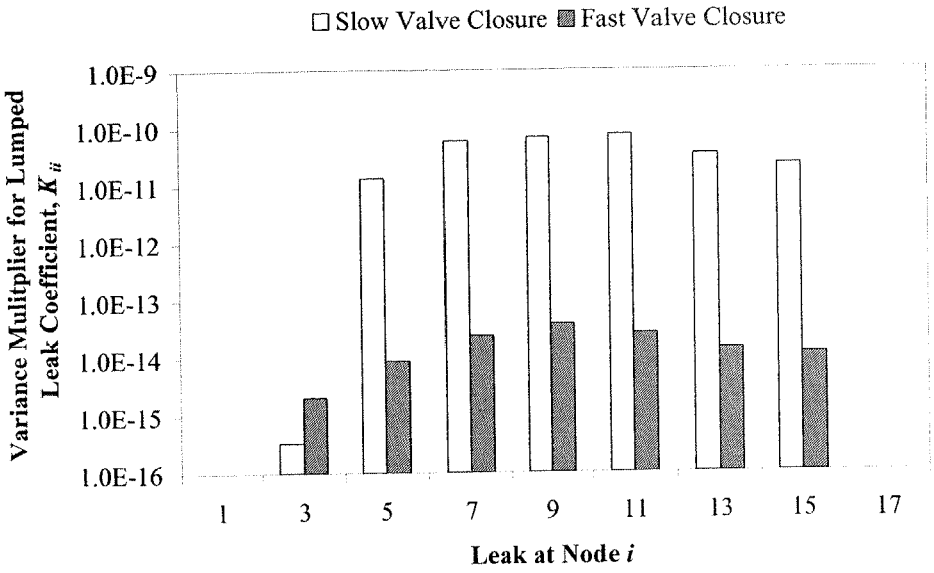

Figure 12.14 Variance Between Leak Candidates at Solution

Similarly, the covariance between two leak coefficients (for parameters a_i and a_j) is related to the variance in the measured data error,

$$\sigma_{a_i a_j} = K_{ij}\sigma^2_{H^m} \quad \text{.....(12.2.8)}$$

Figure 12.15 shows the absolute of the covariance multiplier matrix for the solution parameters from the inverse transient method for both fast and slow valve closures. The absolute is used because the magnitude rather than the sign of the covariance is important. The results show that the covariances, like the variances, for a fast valve closure are much smaller than those for a slow valve closure.

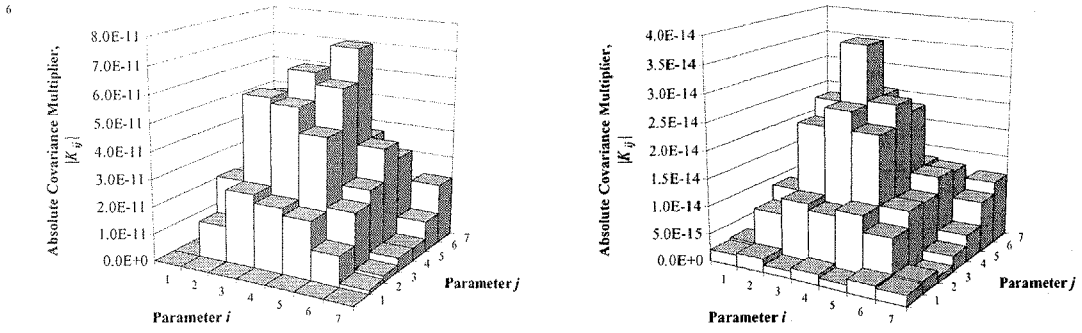

(a) Slow Valve Closure **(b) Fast Valve Closure**

Figure 12.15 Covariance Between Leak Candidates at Solution

The correlation between two parameters can be calculated from each parameter's variance and their covariance or alternatively, if the variance in the measured data error is equal for all measurement sites, using the covariance multiplier matrix $[K]$,

$$\rho_{a_i a_j} = \frac{\sigma_{a_i a_j}}{\sigma_{a_i}\sigma_{a_j}} = \frac{K_{ij}}{\sqrt{K_{ii}K_{jj}}} \qquad \text{.....(12.2.9)}$$

Figure 12.16 shows the absolute correlation between different parameters for both fast and slow valve closures. Again the absolute is used because the magnitude of the correlation is of importance rather than its sign. The results indicate a higher correlation between adjacent parameters (adjacent leaks along the pipeline) for both valve closure rates. For the fast valve closure, a ridge of high correlation exists for symmetrically placed leaks, e.g. between parameters a_1&a_7, a_2&a_6, etc. However, since the absolute correlation between different parameters are all less than one, it is unlikely that a non-unique solution exists for the leak coefficients.

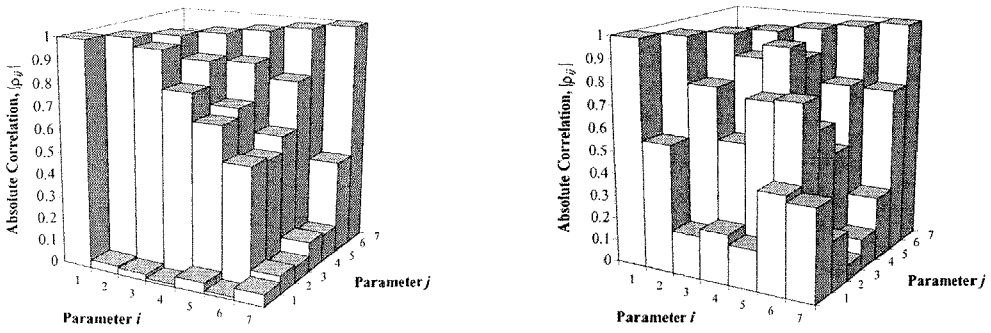

(a) Slow Valve Closure **(b) Fast Valve Closure**

Figure 12.16 Correlation Between Leak Candidates at Solution

12.2.6 Summary of Preliminary Investigation

Results showing various preliminary aspects of leak detection and location for inverse transient analysis were presented in Section 12.2. The calibration of the leakage units performed in Chapter 10 showed that the true leak relationship (between the pressure at the leak and the flow through the leak) was not well represented by the theoretical orifice equation. An equivalent lumped leak coefficient for each of the leak units was calculated for the theoretical orifice relationship. These equivalent lumped leak coefficients are used for the verification of leak detection and location methods in subsequent sections of this chapter. The classical Levenberg-Marquardt minimisation algorithm finds local minima rather than the global minimum. The use of the SCE method improves results (indicating better coverage of the search space); however, the improved results were at the cost of computation speed. An investigation using slow and fast valve closures was performed to determine the importance of unsteady friction on inverse transient analysis results. In the case of fast valve closure, the exclusion of unsteady friction caused large errors in the match between the model and experimental pressure heads. The effect of excluding unsteady friction when using slow transient events is not so large, suggesting that unsteady friction is more important for fast events rather than for slow events, which is to be expected given that it is dependent on the acceleration of the fluid. The goodness-of-fit criterion was used to confirm that the transient model did not produce results that were as accurate as the measured pressures. Thus, improvement in the transient model still needs to occur to better use the measured data. A sample variance was used to predict the variance in the parameter error, all of which were orders of magnitude lower than their corresponding values (indicating good confidence in the solution parameters).

12.3 Experimental Verification of Inverse Transient Analysis

The experimental verification of the inverse transient method is presented in this section. A number of experimental examples, in twelve tests, are analysed to check the effectiveness of the method. Three valve closure rates (fast, medium and slow corresponding to 0.07, 0.7 and 1.4 s respectively) were considered for four different

leak cases. The four different leak cases were a single 1.0, 1.5 and 2.0 mm leak located at node 5 and two 1.0 mm leaks located at nodes 5 and 13. Examples are presented for experimental tests using fast, medium and slow valve closure rates and using single and multiple leaks. The examples presented in this section are for a 1.0 mm leak, results of which are representative of those for the 1.5 and 2.0 mm leaks. Plots of the inverse transient results for all of the twelve tests are presented in Appendix C.8. In each case there are seven leak candidates considered at nodes 3, 5, 7, 9, 11, 13 and 15. The SCE method is used in the application of inverse transient analysis for reasons defined in Section 12.2.2. Comments are made about the inverse transient results through the use of analysis from the fitting of an incorrectly located leak. If an incorrectly placed leak produces a similar fit to a leak placed at the actual location, then the inverse transient solution is insensitive to leak location and, given the uncertainty in the transient model and experimental data, results in poor solutions.

12.3.1 Inverse Transient Analysis of a Fast Valve Closure, Single Leak

The experimental data used in this section were generated using a fast valve closure (time, $t_c = 0.07$ s), which, although named "fast," is not fast in the sense that the closure speed is less than $2L/a$ ($t_c = 0.056$ s). The pipeline contained a single 1.0 mm leak located at node 5 with an actual C_dA_L value of 5.0×10^{-7} m^2. The initial velocity was 0.143 m/s corresponding to a Reynolds number of 3,148. The unsteady friction coefficients used by the k_A & k_P model are $k_A = 0.035$ and $k_P = 0.0$ (calculated using Eqs. 9.6.9 and 10.4.1). Results from the application of the inverse transient method are shown in Table 12.11.

Table 12.11 Inverse Transient Results for a Single Leak, Fast Valve Closure (t_c = 0.07 s)

	Lumped Leak Coefficient, C_dA_L (m^2)						
	Node 3	Node 5	Node 7	Node 9	Node 11	Node 13	Node 15
Actual	-	**5.0×10^{-7}**	-	-	-	-	-
ITA	1.1×10^{-7}	**5.1×10^{-7}**	1.4×10^{-12}	2.6×10^{-9}	3.6×10^{-11}	9.9×10^{-8}	6.1×10^{-9}

Largest size leak in bold

The calculation gives a predominant leak located at node 5, where the actual leak is located. A smaller leak was indicated at node 3, but it is five times smaller than the leak

at node 5. The leaks found at nodes 7, 9, 11, 13 and 15 are negligibly small. Figure 12.17 shows the inverse transient fit at node 1.

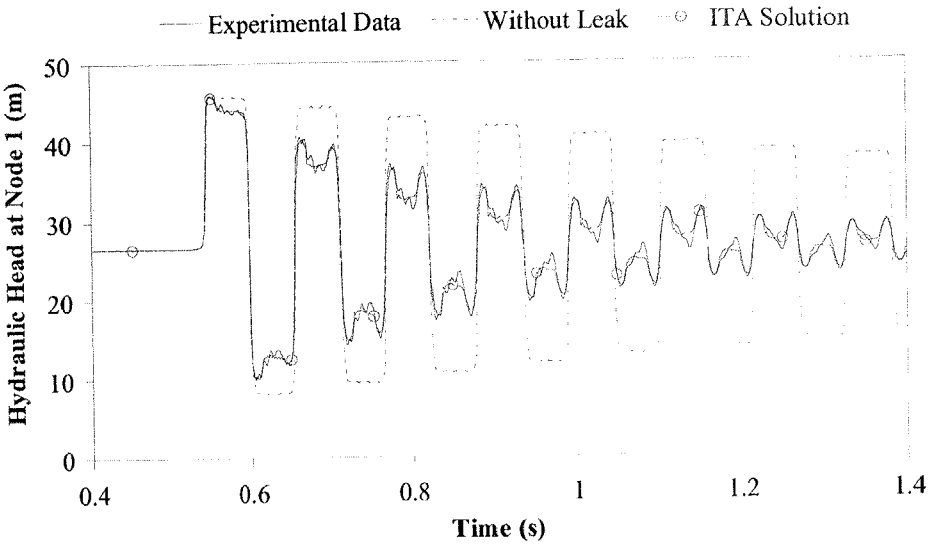

Figure 12.17 ITA Results, Single Leak, Fast Valve Closure (t_c = 0.07 s)

Calculated and experimental heads match well. An example of the sensitivity of the inverse transient solution to the leak location can be made by considering a leak located an incorrect position. In this case, a leak located at node 13 is considered, as shown in Figure 12.18.

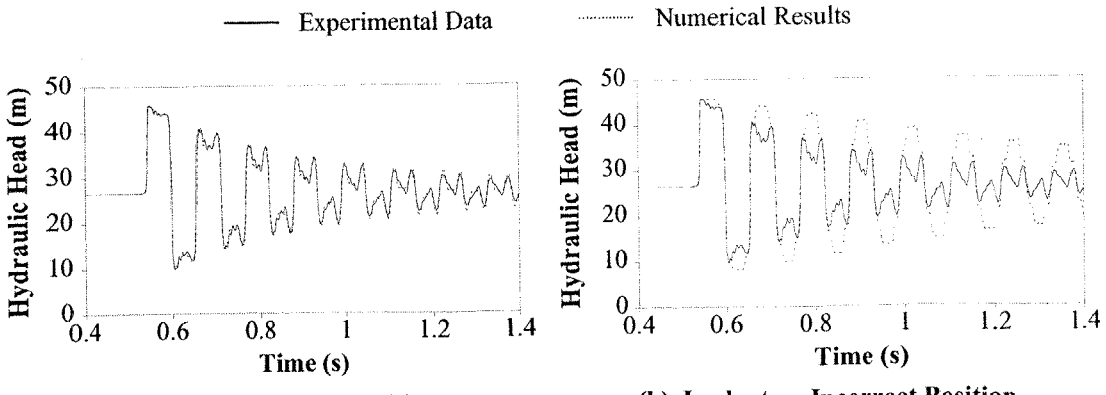

(a) Leak at a Correct Position **(b) Leak at an Incorrect Position**

Figure 12.18 Leak Location Comparison, Single Leak, Fast Valve Closure (t_c = 0.07 s)

Figure 12.18 demonstrates that the inverse transient solution is sensitive to the position of the leak.

12.3.2 Inverse Transient Analysis of a Medium Speed Valve Closure, Single Leak

The experimental data used in this section were generated using a medium speed valve closure ($t_c = 0.7$ s). A single 1.0 mm leak was located in the experimental pipeline at node 5 with an actual C_dA_L value of 5.0×10^{-7} m^2. The initial velocity was 0.360 m/s corresponding to a Reynolds number of 7,901. The unsteady friction coefficients used by the k_A & k_P model are $k_A = 0.030$ and $k_P = 0.0$ (calculated using Eqs. 9.6.9 and 10.4.1). The inverse transient method is applied to the experimental data and the resulting lumped leak coefficients at the candidate nodes are shown in Table 12.13.

Table 12.12 Inverse Transient Results for a Single Leak, Medium Speed Valve Closure (t_c = 0.7 s)

	Lumped Leak Coefficient, C_dA_L (m^2)						
	Node 3	Node 5	Node 7	Node 9	Node 11	Node 13	Node 15
Actual	-	**5.0×10^{-7}**	-	-	-	-	-
ITA	**3.9×10^{-7}**	3.2×10^{-8}	2.0×10^{-10}	1.2×10^{-7}	2.5×10^{-10}	8.8×10^{-12}	5.1×10^{-8}

Largest size leak in bold

The inverse transient method did not find the correct position of the leak. A plot of the fitted pressure head results at node 1 is shown in Figure 12.19.

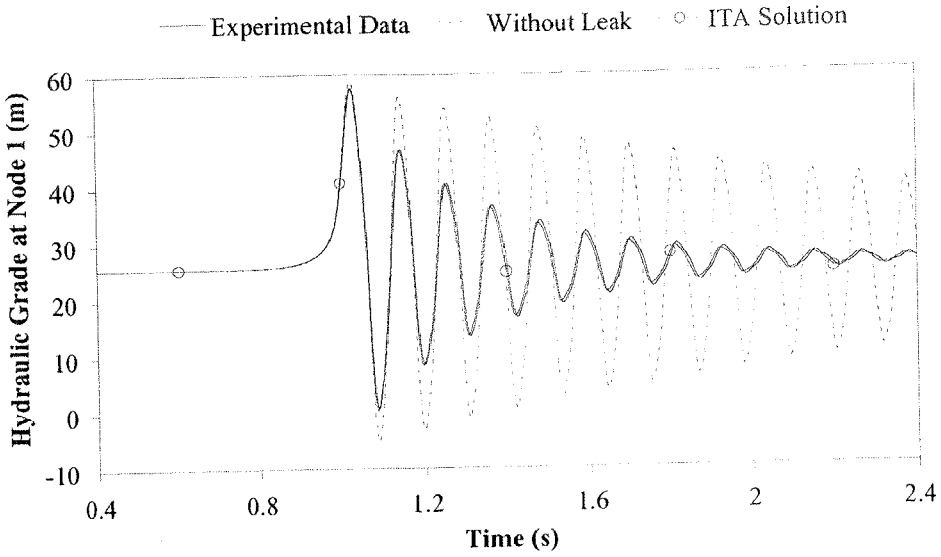

Figure 12.19 ITA Results, Single Leak, Medium Speed Valve Closure (t_c = 0.7 s)

From Figure 12.19 there is a large difference between the pressure head when there are no leaks and when leaks are present. The inverse transient results show a good match with the experimental data. A similar analysis is performed, as shown in the previous section, to indicate if the inverse transient solution is insensitive to the leak location. Leaks occurring at nodes 5 and 13 separately are assumed and the inverse transient method is used to fit a lumped leak coefficient to each leak (one at a time), the results of which are shown in Figure 12.20. The lumped leak coefficient was equal to 5.49×10^{-7} m^2 when the leak was at node 5 and equal to 3.31×10^{-6} m^2 when the leak was at node 13.

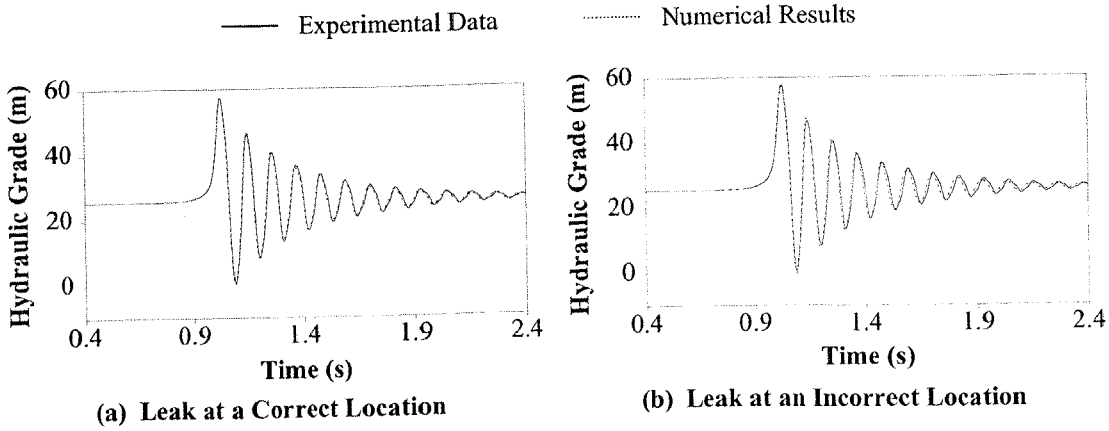

(a) Leak at a Correct Location **(b) Leak at an Incorrect Location**

Figure 12.20 Leak Location Comparison, Single Leak, Medium Speed Valve Closure (t_c = 0.7 s)

In Figure 12.20 a good match is found when assuming leakage at two different positions in the pipeline, which is a rather disturbing result, suggesting that given the insensitivity of the inverse transient solution to the leak location and the presence of measured and model error, a low confidence solution is expected for medium speed valve closure events. Table 12.12 highlights the inverse transient results in which the leak was not found at the correct location.

12.3.3 Inverse Transient Analysis of a Slow Valve Closure, Single Leak

A single 1.0 mm leak is located at node 5 with an actual C_dA_L value of 5.0×10^{-7} m^2 and a slow valve closure (t_c = 1.4 s) is used. The initial velocity is 0.484 m/s corresponding to a Reynolds number of 10,614. The unsteady friction coefficients used are $k_A = 0.029$ and $k_P = 0.0$ (calculated using Eqs. 9.6.9 and 10.4.1). The inverse transient method is applied to the experimental data and the resulting lumped leak coefficients at the candidate nodes are in Table 12.13.

Table 12.13 Inverse Transient Results for a Single Leak, Slow Valve Closure (t_c = 1.4 s)

	Lumped Leak Coefficient, C_dA_L (m^2)						
	Node 3	Node 5	Node 7	Node 9	Node 11	Node 13	Node 15
Actual	-	**5.0×10^{-7}**	-	-	-	-	-
ITA	5.5×10^{-11}	1.1×10^{-9}	9.9×10^{-11}	5.4×10^{-8}	**8.8×10^{-7}**	**7.5×10^{-7}**	9.1×10^{-8}

Largest size leaks in bold

These results show that the inverse transient method did not find the leak at the correct position. The largest leaks are found at nodes 11 and 13. A plot of the fitted pressure head results at node 1 is shown in Figure 12.21.

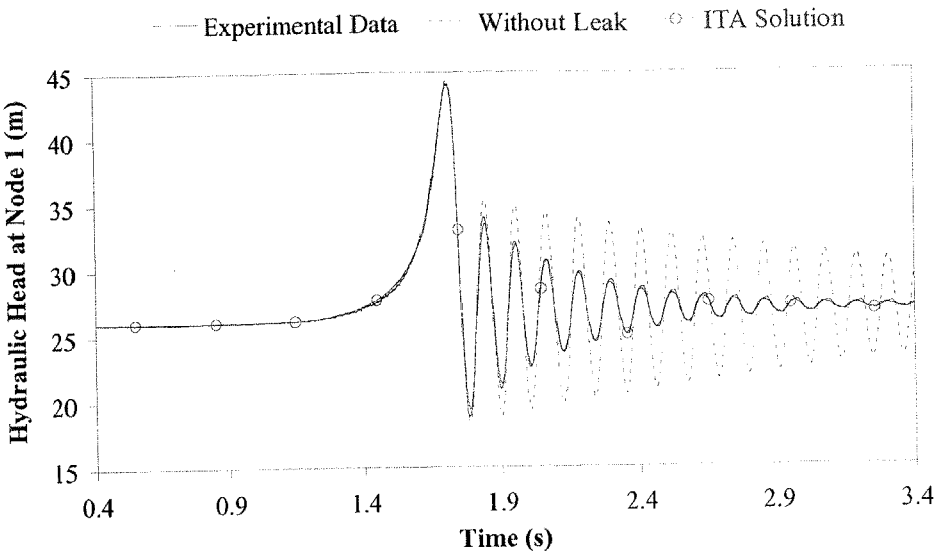

Figure 12.21 ITA Results, Single Leak, Slow Valve Closure (t_c = 1.4 s)

Figure 12.21 shows a large difference between the pressure head when there are no leaks and when leaks are present. The inverse transient results match well with the experimental data. Two inverse transient analyses are performed for single leak candidates at different nodal positions to give an idea of the sensitivity of the inverse transient solution to the leak location. Leaks occurring at nodes 5 and 13 separately are assumed and the inverse transient method is used to fit the lumped leak coefficient of each leak (one at a time). The lumped leak coefficient was equal to 5.0×10^{-7} m^2 when the leak was at node 5 and equal to 2.68×10^{-6} m^2 when the leak was at node 13, the results of which are shown in Figure 12.22.

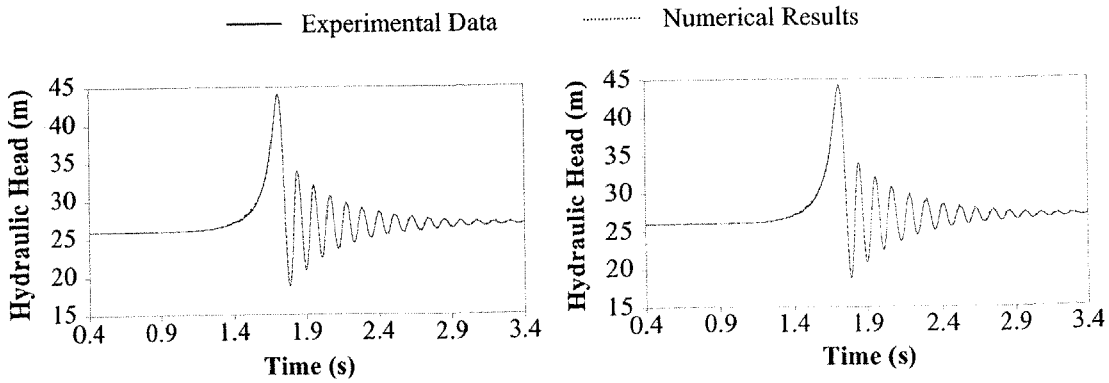

(a) Leak at a Correct Position **(b) Leak at an Incorrect Position**

Figure 12.22 Leak Location Comparison, Single Leak, Slow Valve Closure (t_c = 1.4 s)

The result is similar to analysis presented in the previous section in Figure 12.20 suggesting a low sensitivity in the inverse transient solution to the leak location for slow valve closure events, which is highlighted in the inverse transient results (Table 12.13) where the leak was not found at the correct location. The next sections test how well the inverse transient method deals with multiple leakage.

12.3.4 Inverse Transient Analysis of a Fast Valve Closure, Multiple Leaks

The verification of the inverse transient method for multiple leaks is presented in this section. The experimental apparatus contained two 1.0 mm leaks located at nodes 5 and 13 with actual C_dA_L values of 5.0×10^{-7} and 7.1×10^{-7} m^2 respectively. The transient event was generated by a fast valve closure (closure time, $t_c = 0.07$ s). The initial velocity was 0.138 m/s, corresponding to a Reynolds number of 3,020. The unsteady friction coefficients used are $k_A = 0.035$ and $k_P = 0.0$ (calculated using Eqs. 9.6.9 and 10.4.1). The results from the inverse transient method are shown in Table 12.14.

Table 12.14 Inverse Transient Results for Multiple Leaks, Fast Valve Closure (t_c = 0.07 s)

	Lumped Leak Coefficient, C_dA_L (m^2)						
	Node 3	Node 5	Node 7	Node 9	Node 11	Node 13	Node 15
Actual	-	**5.0×10^{-7}**	-		-	**7.1×10^{-7}**	-
ITA	2.8×10^{-8}	9.8×10^{-12}	1.4×10^{-9}	**9.5×10^{-7}**	7.2×10^{-9}	3.6×10^{-11}	**1.0×10^{-6}**

Largest sizes leaks in bold

The inverse transient method found two incorrect leaks at nodes 11 and 15. A plot of the inverse transient solution and the experimental data is in Figure 12.23.

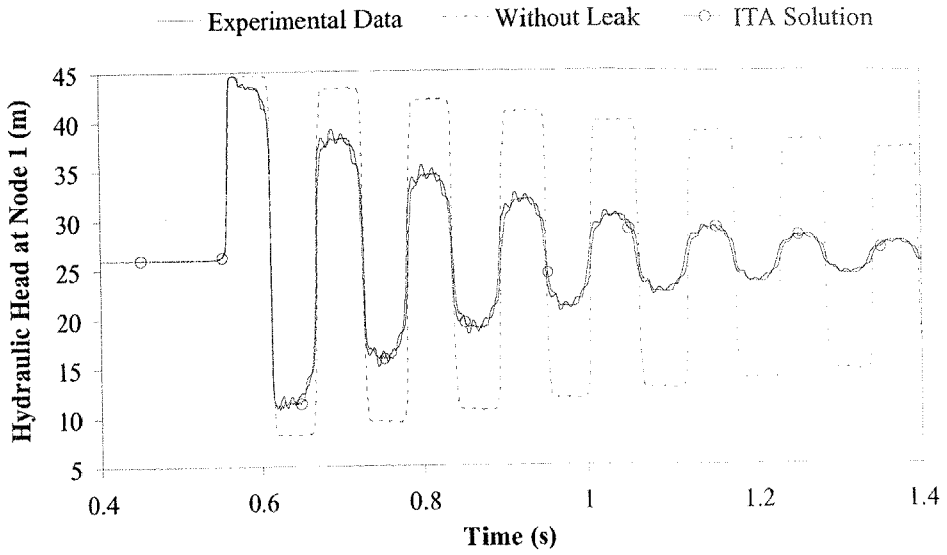

Figure 12.23 ITA Results, Multiple Leakage, Fast Valve Closure (t_c = 0.07 s)

Figure 12.23 shows that the general shape is well produced by the numerical model; however, the period of the pressure oscillations predicted by the numerical model are a little longer than in the experimental data causing a slight mismatch in the phase of the oscillations. Modelling separate leaks at nodes 5 and 13, the results of which are shown in Figure 12.24, tests the sensitivity of multiple leakage.

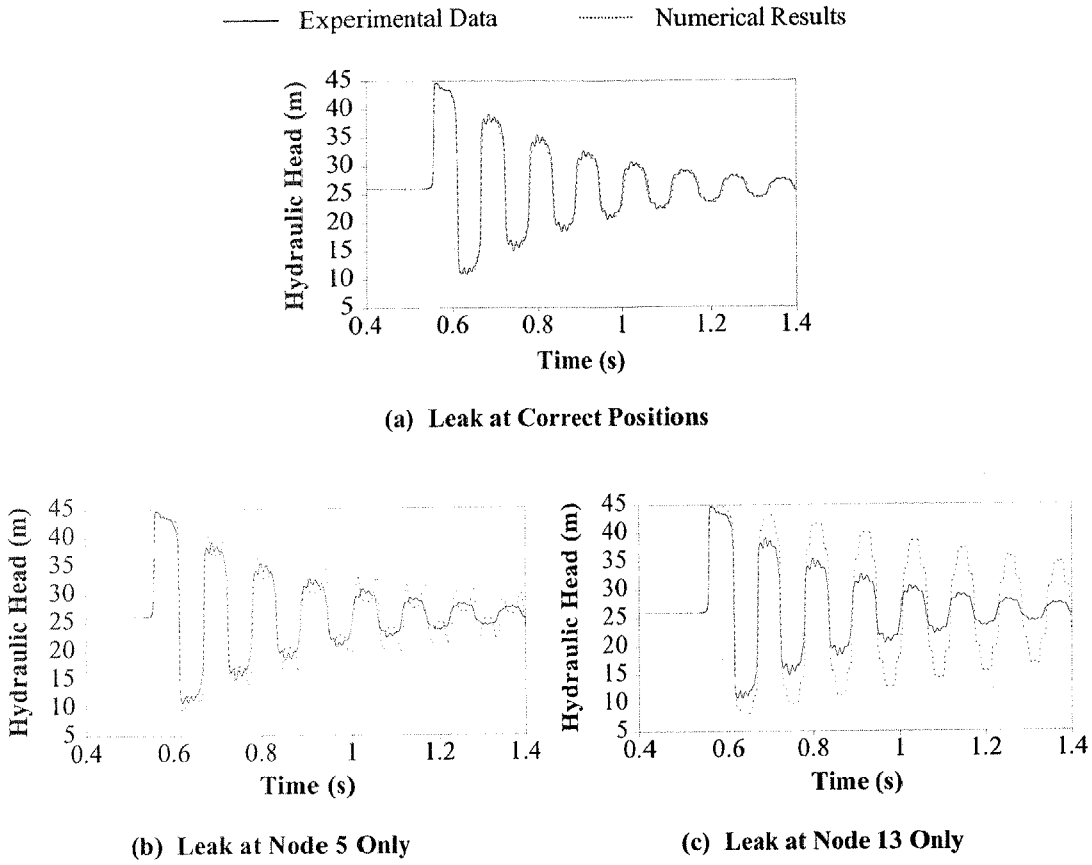

Figure 12.24 Leak Location Comparison, Multiple Leakage, Fast Valve Closure (t_c = 0.07 s)

Figure 12.24 indicates that the inverse transient results are sensitive to multiple leakage along the pipeline. The behaviour of the pressure response for two leaks in the pipeline is different compared to single leaks at different locations along the pipeline. Therefore, the existence of multiple leaks in a pipeline is evident from the inverse transient results although their exact position is not readily determined.

12.3.5 Inverse Transient Analysis of a Medium Speed Valve Closure, Multiple Leaks

Two 1.0 mm leaks, located at nodes 5 and 13, are considered experimentally in this section with actual C_dA_L values of 5.0×10^{-7} and 7.1×10^{-7} m^2 respectively. The transient event is generated using a medium speed valve closure (t_c = 0.7 s). The initial velocity is 0.490 m/s corresponding to a Reynolds number of 10,754. The unsteady friction coefficients used are k_A = 0.029 and k_P = 0.0 (calculated using Eqs. 9.6.9 and 10.4.1). Results from the use of the inverse transient method are shown in Table 12.15.

Table 12.15 Inverse Transient Results for Multiple Leaks, Medium Speed Valve Closure (t_c = 0.7 s)

	Lumped Leak Coefficient, C_dA_L (m^2)						
	Node 3	Node 5	Node 7	Node 9	Node 11	Node 13	Node 15
Actual	-	**5.0×10^{-7}**	-	-	-	**7.1×10^{-7}**	-
ITA	3.8×10^{-10}	5.3×10^{-10}	1.1×10^{-8}	6.8×10^{-12}	1.3×10^{-8}	2.1×10^{-8}	**1.0×10^{-5}**

Largest sizes leak in bold

One dominant leak was found at node 15. All other leaks found along the pipeline are of negligible size. Figure 12.25 shows the fit of the inverse transient method.

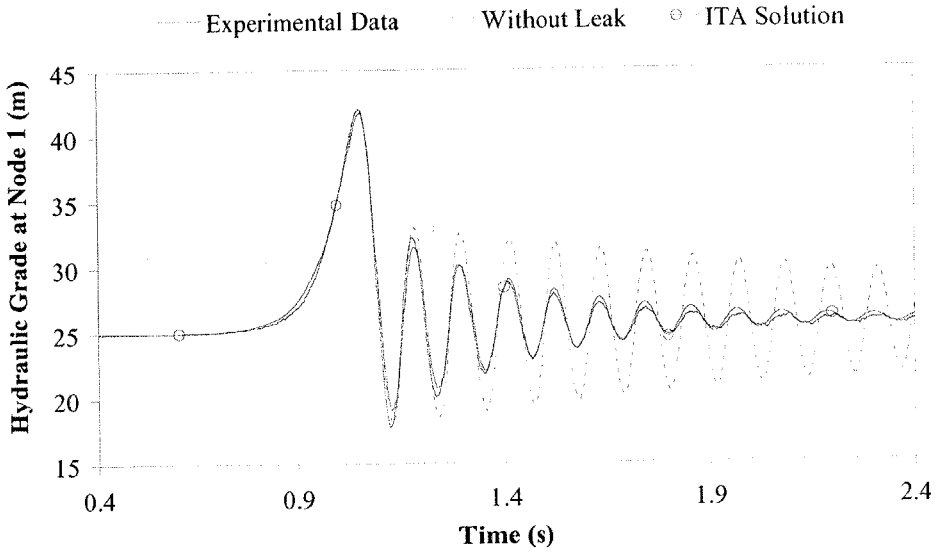

Figure 12.25 ITA Results, Multiple Leakage, Medium Speed Valve Closure (t_c = 0.7 s)

Similar to results observed in Section 12.3.2, the inverse transient results (although incorrect) show a good fit to the experimental data, suggesting that different sized leaks at different locations may predict similar results. Again, the low sensitivity of the inverse transient solution to the leak location is of concern when using medium-speed valve closure events given measurement error.

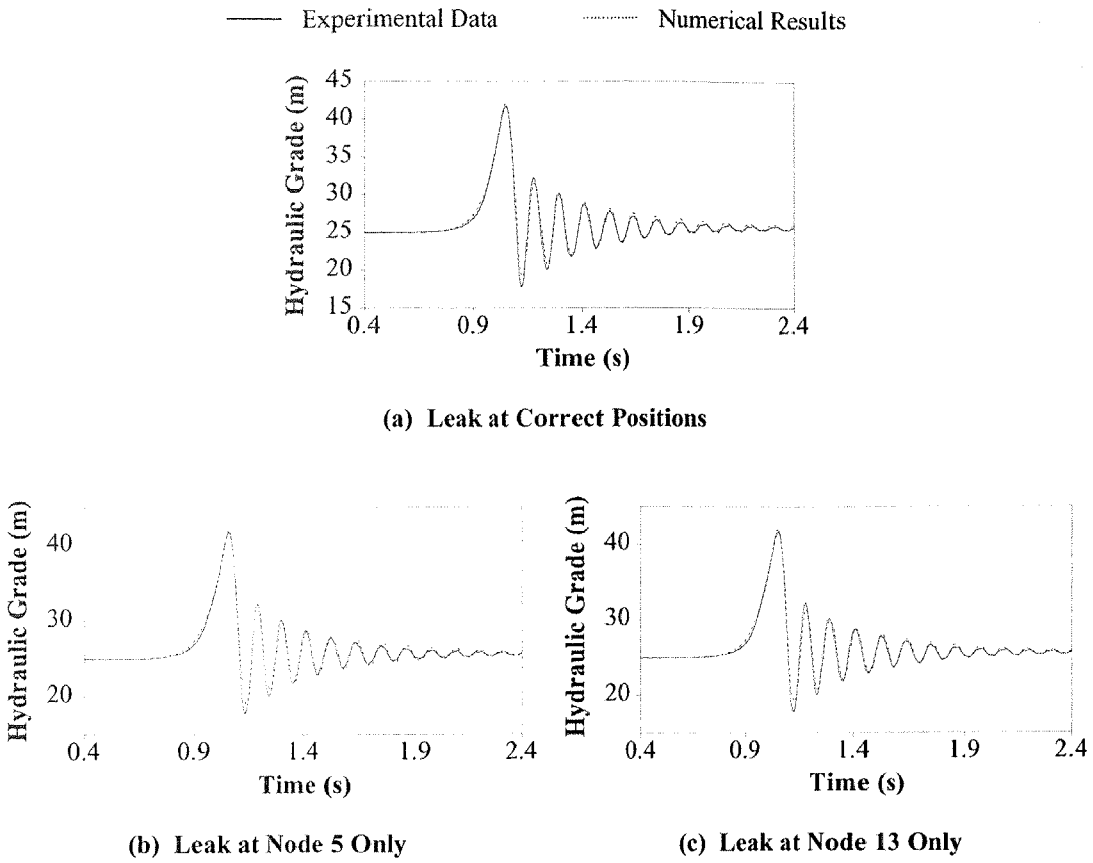

Figure 12.26 Leak Location Comparison, Multiple Leakage, Medium Speed Valve Closure (t_c = 0.7 s)

For inverse transient results assuming a leak only at node 5, the lumped leak coefficient was equal to 5.70×10^{-7} m^2 and for a leak only at node 13 the value was equal to 2.87×10^{-6} m^2. The results for fitting one leak at incorrect locations all show a good match with the experimental data, confirming a low sensitivity in the inverse transient solution to the leak location exists for this speed of valve closure given measurement error.

12.3.6 Inverse Transient Analysis of a Slow Valve Closure, Multiple Leaks

Finally, two 1.0 mm leaks at nodes 5 and 13 are considered experimentally with actual C_dA_L values of 5.0×10^{-7} and 7.1×10^{-7} m^2 respectively. A slow valve closure (t_c = 1.4 s) is used to generate the transient event. The initial velocity is 0.510 m/s, corresponding to a Reynolds number of 11,200. The unsteady friction coefficients used are k_A = 0.029

and $k_P = 0.0$ (calculated using Eqs. 9.6.9 and 10.4.1). Table 12.16 shows the inverse transient results.

Table 12.16 Inverse Transient Results for Multiple Leaks, Slow Valve Closure ($t_c = 1.4$ s)

	Lumped Leak Coefficient, C_dA_L (m^2)						
	Node 3	Node 5	Node 7	Node 9	Node 11	Node 13	Node 15
Actual	-	**5.0×10^{-7}**	-	-	-	**7.1×10^{-7}**	-
ITA	5.8×10^{-12}	6.7×10^{-9}	1.2×10^{-9}	3.7×10^{-11}	**1.8×10^{-6}**	7.3×10^{-10}	1.5×10^{-11}

Largest sizes leak in bold

One dominant leak found at node 11. All other leaks found along the pipeline are of negligible size. These results are comparable with the medium speed valve closure results from the previous section. Figure 12.27 shows a plot of the fit.

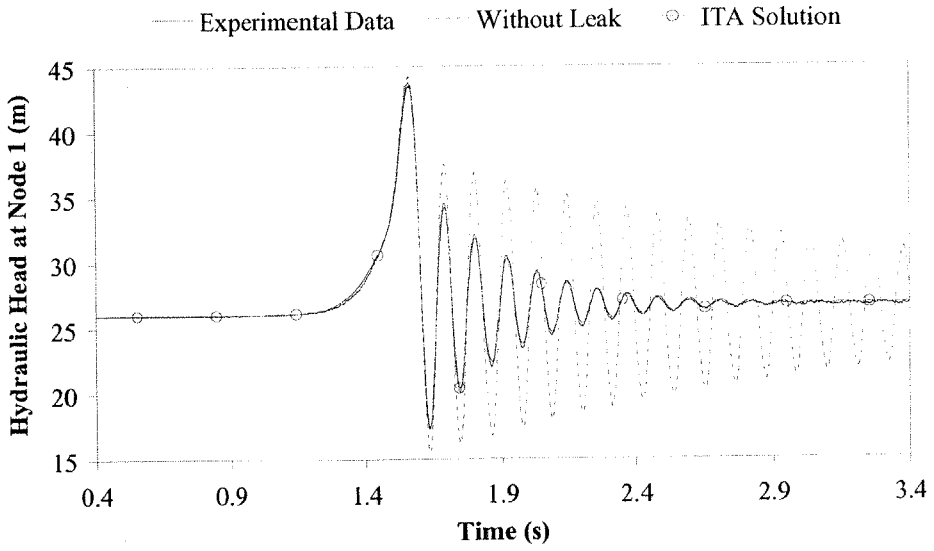

Figure 12.27 ITA Results, Multiple Leakage, Slow Valve Closure ($t_c = 1.4$ s)

Similar to results observed in Section 12.3.3, the inverse transient results (although incorrect) fit the experimental data, suggesting that the different sized leaks at different locations predict similar results.

The sensitivity of the inverse transient solution is now investigated. The inverse transient method is used to fit lumped leak coefficients at incorrect locations to the experimental data, the results of which are shown in Figure 12.28.

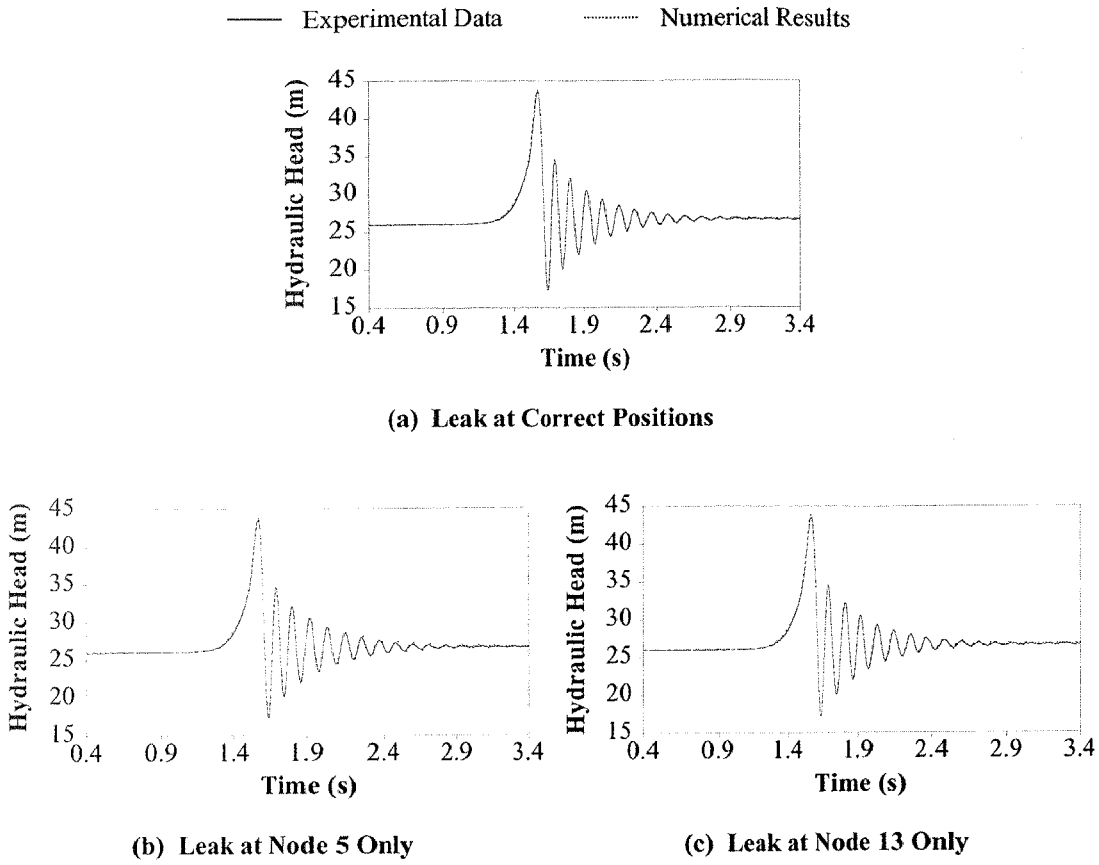

(a) Leak at Correct Positions

(b) Leak at Node 5 Only

(c) Leak at Node 13 Only

Figure 12.28 Leak Location Comparison, Multiple Leakage, Slow Valve Closure (t_c = 1.4 s)

Assuming a leak only at node 5 the lumped leak coefficient was equal to 6.55×10^{-7} m^2 and for a leak only at node 13 the value was calculated to be 3.69×10^{-6} m^2. The results for fitting one leak at incorrect locations both show a good match with the experimental data, confirming observations made for inverse transient results using a slow valve closure and a single leak in Section 12.3.3 where a number of solutions exist given the measurement error and the low sensitivity of the objective function for this speed of valve closure.

12.3.7 Summary of Inverse Transient Analysis Results

The preceding sections graphically show the effect of valve closure speed and presence of multiple leaks on the inverse transient results. A summary of all of the tests is in Table 12.17.

Table 12.17 Summary of Inverse Transient Analysis Results

Test Type	Lumped Leak Coefficient, C_dA_L (m^2)						
	Node 3	Node 5	Node 7	Node 9	Node 11	Node 13	Node 15
	Single 1.0 mm Leak at Node 5						
Actual	-	**5.0×10^{-7}**	-	-	-	-	-
Fast	1.1×10^{-7}	**5.1×10^{-7}**	1.4×10^{-12}	2.6×10^{-9}	3.6×10^{-11}	9.9×10^{-8}	6.1×10^{-9}
Medium	**3.9×10^{-7}**	3.2×10^{-8}	2.0×10^{-10}	1.2×10^{-7}	2.5×10^{-10}	8.8×10^{-12}	5.1×10^{-8}
Slow	5.5×10^{-11}	1.1×10^{-9}	9.9×10^{-11}	5.4×10^{-8}	**8.8×10^{-7}**	7.5×10^{-7}	9.1×10^{-8}
	Single 1.5 mm Leak at Node 5						
Actual	-	**1.1×10^{-6}**	-	-	-	-	-
Fast	1.0×10^{-8}	**7.7×10^{-7}**	3.0×10^{-7}	1.8×10^{-9}	1.3×10^{-7}	1.7×10^{-11}	4.7×10^{-12}
Medium	8.1×10^{-11}	9.3×10^{-7}	8.9×10^{-10}	2.4×10^{-10}	3.9×10^{-12}	**1.1×10^{-6}**	1.2×10^{-8}
Slow	2.8×10^{-9}	3.6×10^{-12}	7.1×10^{-7}	**1.1×10^{-6}**	8.5×10^{-12}	4.1×10^{-9}	2.0×10^{-9}
	Single 2.0 mm Leak at Node 5						
Actual	-	**1.7×10^{-6}**	-	-	-	-	-
Fast	3.2×10^{-11}	**1.7×10^{-6}**	4.1×10^{-11}	2.9×10^{-9}	5.1×10^{-9}	2.9×10^{-11}	2.6×10^{-7}
Medium	6.9×10^{-8}	5.1×10^{-7}	**1.2×10^{-6}**	3.7×10^{-10}	2.4×10^{-10}	6.1×10^{-12}	6.1×10^{-6}
Slow	2.0×10^{-9}	6.2×10^{-7}	1.1×10^{-10}	**1.5×10^{-6}**	8.0×10^{-9}	7.2×10^{-10}	5.3×10^{-9}
	Two 1.0 mm Leaks at Nodes 5 and 13						
Actual	-	**5.0×10^{-7}**	-	-	-	**7.1×10^{-7}**	-
Fast	2.8×10^{-8}	9.8×10^{-12}	1.4×10^{-9}	**9.5×10^{-7}**	7.2×10^{-9}	3.6×10^{-11}	**1.0×10^{-6}**
Medium	3.8×10^{-10}	5.3×10^{-10}	1.1×10^{-8}	6.8×10^{-12}	1.3×10^{-8}	2.1×10^{-8}	**1.0×10^{-5}**
Slow	5.8×10^{-12}	6.7×10^{-9}	1.2×10^{-9}	3.7×10^{-11}	**1.8×10^{-6}**	7.3×10^{-10}	1.5×10^{-11}

Largest size leak(s) in bold

Leaks were located in their correct locations for all single leak cases using a fast valve closure. The location of the leaks, however, was not found at their correct locations for events using medium or slow valve closures. A reason is that a number of similar solutions to the inverse transient problem exist for medium and slow valve closures because of the low sensitivity exhibited by the objective function and the error associated with the measured pressure heads. The low sensitivity and the existence of non-unique inverse transient solutions was demonstrated in Figures 12.20, 12.22, 12.26 and 12.28 whereby differently sized leaks at different locations along the pipeline were found to produce similar pressure responses. This type of behaviour was not seen for the fast valve closure events. For the multiple leak inverse transient results, the same problems with medium and slow valve closure events were found. Due to the problems when finding solutions for the leak size and location for the slower events, the objective of finding two leaks along a pipeline was impossible to meet. The search for multiple leakage using fast valve closure events produced inverse transient results showing single distinct leaks located in the pipeline.

12.4 Leak Detection and Location Problems Using Slow Valve Closure Events

The lack of a correct solution demonstrated by leak detection results using slow valve closures (see Section 12.3.3) provides the basis for a method of summing the effects from a number of small leaks to form one larger, equivalent leak. Fast valve closures produce data that lead to better results in finding locations in contrast to slow closures that produce data to which the calculation is insensitive to leak position. An example of the convergence of the lumped leak coefficients (using the SCE method) using a slow valve closure and a single 1.0 mm leak located at node 5 is shown in Figure 12.29.

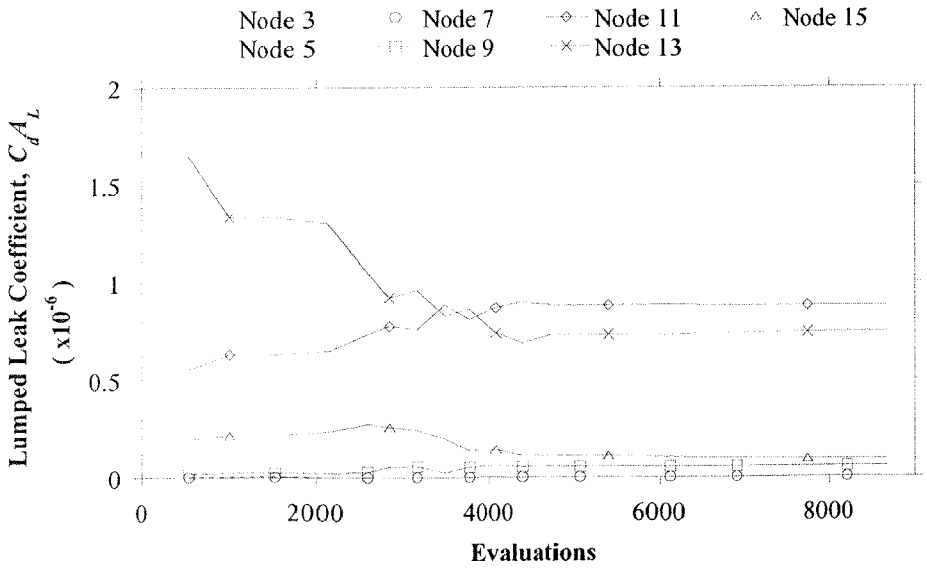

Figure 12.29 Convergence Results for a Slow Valve Closure (t_c = 1.4 s)

The correct leak at node 5 was not found, but rather, two incorrect smaller leaks at nodes 11 and 13 were indicated. Given that a non-unique solution for the leak parameters exists for the example, a better use for the slow valve closure results might be to determine the existence of a leak, rather than to find its location. To test if that use is valid, the effect of a leak at different locations along a pipeline must be investigated. Experimental data for a slow valve closure with a single 1.0 mm leak at node 5 were used. Figure 12.30 is a plot of lumped leak coefficients that produced similar effects, given their position along the pipeline.

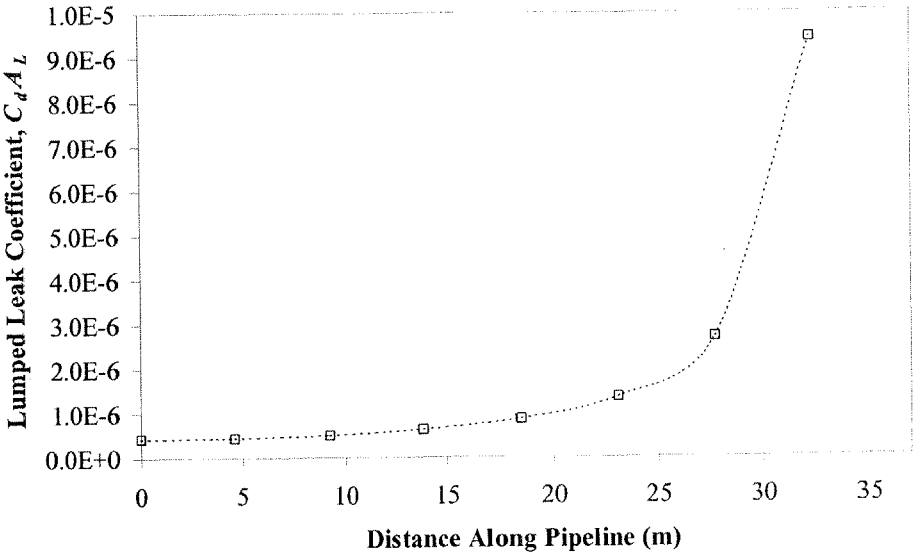

Figure 12.30 Lumped Leak Coefficient Versus Distance Along Pipeline

The curve rises sharply when the leak is positioned near the constant-head tank 2, because leak damping only occurs if the pressure at the leak is allowed to vary. At tank 2 the pressure is constant, resulting in a constant outflow at the leak, which does not add to the complexity of the pressure response signal nor damp the signal. The curve in Figure 12.30 suggests that large lumped leak coefficients found near tank 2 produce a similar effect to moderate lumped leak coefficients nearer to tank 1. A similar plot can be created for the effect of equally sized leaks along the pipeline. Moving an identically sized leak to different locations in the pipeline and calculating its corresponding effect on the pressure oscillations (quantified by a damping coefficient) created Figure 12.31. The results in Figure 12.31 have been normalised by the effect from a leak located at node 5.

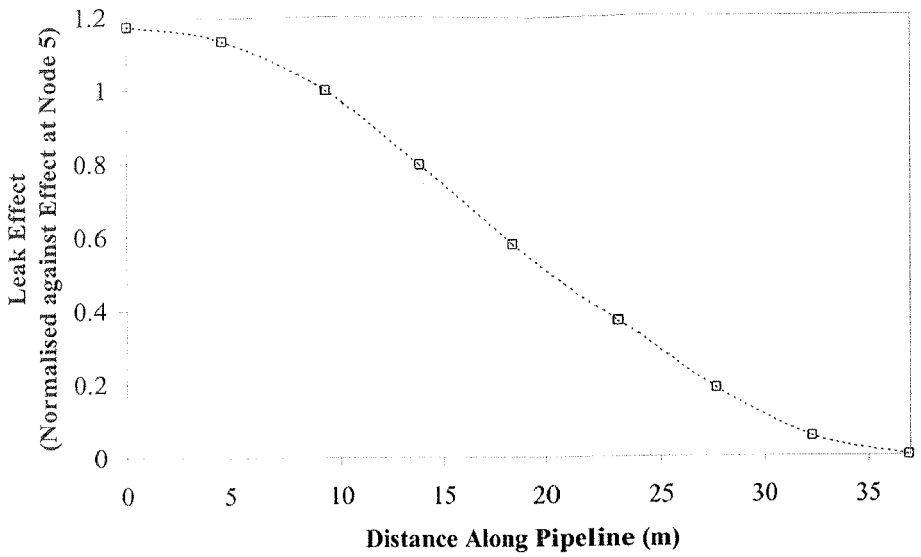

Figure 12.31 Leak Effect Versus Distance Along Pipeline

For equally sized leaks along the pipeline, the effect of a leak near tank 2 is much smaller than the effect of a leak near tank 1. Values from Figure 12.31 can now be used as weights to combine a number of leaks (from the inverse transient method) into one leak at particular position along the pipeline. The summation results in an equivalent lumped leak coefficient for a leak at node 5 (only) of 5.0×10^{-7} m^2, which compares well with results from the determination of the lumped leak coefficient using a fast transient event (5.1×10^{-7} m^2) in the previous section. If the individual lumped leak coefficients were simply summed along the pipeline (without the use of weights from Figure 12.31), the total lumped leak coefficient is equal to 1.8×10^{-6} m^2, overestimating the amount of leakage present in the experimental data. Similar analyses have been performed for all of the tests using medium or slow valve closure, the results of which are shown in Table 12.18.

Table 12.18 Leak Detection Results Using Slow Valve Closures (t_c = 1.4 s)

Test Type	Normalised C_dA_L at Node 5 (m^2)
	Single 1.0 mm Leak at Node 5
Actual	5.0×10^{-7}
Medium	5.4×10^{-7}
Slow	5.0×10^{-7}
	Single 1.5 mm Leak at Node 5
Actual	1.1×10^{-6}
Medium	1.1×10^{-6}
Slow	1.2×10^{-6}
	Single 2.0 mm Leak at Node 5
Actual	1.7×10^{-6}
Medium	1.8×10^{-6}
Slow	1.5×10^{-6}
	Two 1.0 mm Leaks at Nodes 5 and 13
Actual	5.0×10^{-7} at Node 1 and 7.1×10^{-7} at Node 5
Medium	5.5×10^{-7}
Slow	6.5×10^{-7}

These effective lumped leak coefficients at node 5 compare favourably with the lumped leak coefficients found in Section 12.2.1.

The non-unique solutions for leak parameters exhibited by the analysis of slow valve closure events have been used to determine curves that can be used to sum the effect of many leaks along a pipeline. The analysis of slow valve closure events holds promise for the determination of leak existence rather than determination of leak location, leading to a strategy for leak detection where slow events could be used to check whether a leak exists in a pipeline. And if a leak is found to exist, then a fast event can be used to find its magnitude and location.

12.5 A Systematic Levenberg-Marquardt Minimisation Method

In Section 12.2.2, the Levenberg-Marquardt minimisation algorithm was found inadequate for solving the inverse transient problem. The SCE method produced improved results but at higher computational cost. Also, the SCE method is not derivative based, cannot take advantage of information from parameter derivatives, and cannot make use of the fast analytic method for the calculation of the parameter derivatives (see Section 4.4). This section presents a minimisation algorithm that is

based on a systematic approach to the implementation of the Levenberg-Marquardt algorithm.

The systematic Levenberg-Marquardt algorithm (SLVMQ) is based on an observation made in Section 12.2.2 that the Levenberg-Marquardt algorithm was found to become trapped in a local minima when searching for many leaks simultaneously. The Levenberg-Marquardt algorithm requires a good guess if it is to find the actual solution. A better approach for the application of the Levenberg-Marquardt algorithm is to apply it to a smaller number of better located leak candidates (with better initial guesses), which is achieved by the SLVMQ method using "trial" leaks. The SLVMQ method solves the inverse transient problem for trial leaks at all possible locations. The trial leak location with the smallest objective function value is then made a "set" leak and its solution is used as initial guesses for additional runs in which a new trial leak is created. In subsequent runs the inverse transient problem is solved for the set leak and a new trial leak at all possible locations. The best solution is selected and the process is repeated. Figure 12.32 is a flow chart of the application of the SLVMQ method.

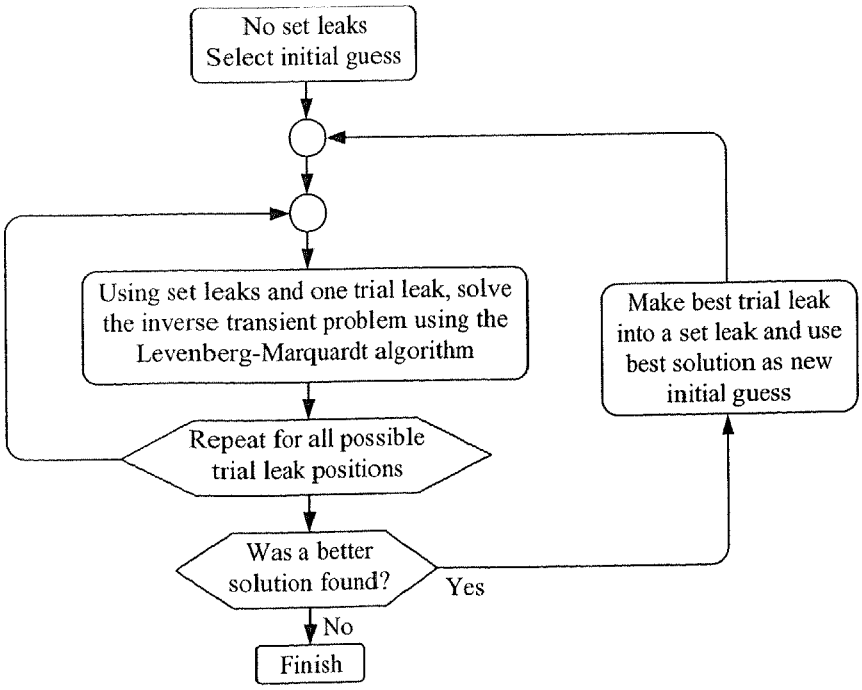

Figure 12.32 Flow Diagram for the SLVMQ Method

The SLVMQ method was tested using data from the experimental pipeline (Figure 12.1). The experimental test data were generated using a fast valve closure (t_c = 0.07 s)

with a single 2.0 mm leak located at node 5. The actual lumped leak coefficient is 1.7×10^{-6} m^2. The number of possible leak locations is 7 at nodes 3, 5, 7, 9, 11, 13 and 15. For the first run of the SLVMQ method, the inverse transient problem is solved using the Levenberg-Marquardt algorithm for one trial leak. The process is repeated for all possible trial leak positions along the pipeline. The initial guess for each trial lumped leak coefficient is zero. The number of Levenberg-Marquardt iterations, objective function value and the size of the trial leak are stored. Table 12.19 contains results for the first trial leak.

Table 12.19 1st Trial Leak, SLVMQ Results (7 Parameters)

Trial Leak Position	Levenberg-Marquardt Iterations	Objective Function E (m^2)	1st Trial Leak C_dA_L (m^2)
Node 3	34	7,268	1.30×10^{-6}
Node 5	**26**	**999**	$\mathbf{1.88\times10^{-6}}$
Node 7	25	5,754	2.16×10^{-6}
Node 9	3	6,920	2.59×10^{-6}
Node 11	99	11,084	4.42×10^{-6}
Node 13	19	16,955	8.76×10^{-6}
Node 15	36	32,229	2.57×10^{-5}

Minimum objective function in bold

A graphical representation of Table 12.19 can be seen in Figure 12.33.

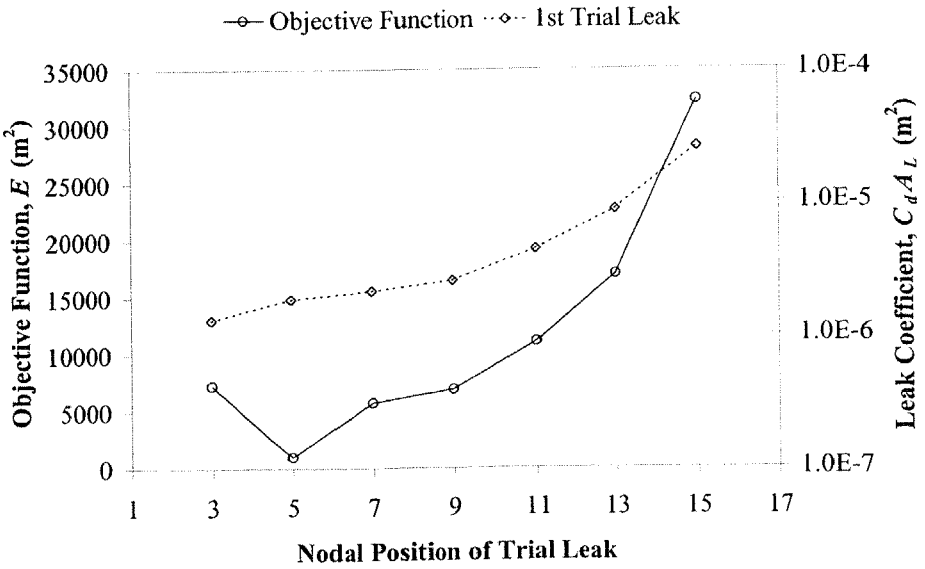

Figure 12.33 1st Trial Leak, SLVMQ Results (7 Parameters)

Table 12.19 shows that the minimum objective function value (best solution) is found when the trial leak is located at node 5, which corresponds to the actual position of the leak.

In the second application the trial leak is set at node 5 and a second trial leak is placed at all possible locations. The initial guess is made equal to the best solution for the first location ($(C_dA_L)_5 = 1.88\times10^{-6}$ m^2 at node 5) with the lumped leak coefficient for the second trial leak equal to zero at all locations. The results are shown in Table 12.20.

Table 12.20 2nd Trial Leak, SLVMQ Results (7 Parameters)

Trial Leak Position	Levenberg-Marquardt Iterations	Objective Function E (m^2)	Leak Coef. C_dA_L (m^2)	
			2nd Trial Leak	Set Leak at Node 5
Node 3	91	765.2	1.26×10^{-7}	1.69×10^{-6}
Node 5	-	*999.4*	-	*1.88×10^{-6}*
Node 7	44	909.1	1.01×10^{-7}	1.82×10^{-6}
Node 9	64	617.3	2.61×10^{-7}	1.58×10^{-6}
Node 11	57	777.1	9.14×10^{-8}	1.77×10^{-6}
Node 13	64	614.9	1.20×10^{-7}	1.75×10^{-6}
Node 15	**61**	**532.3**	**2.90×10^{-7}**	**1.75×10^{-6}**

Minimum objective function in bold, set leak in italics
- trial leak not permitted

A graphical representation of Table 12.20 can be seen in Figure 12.34.

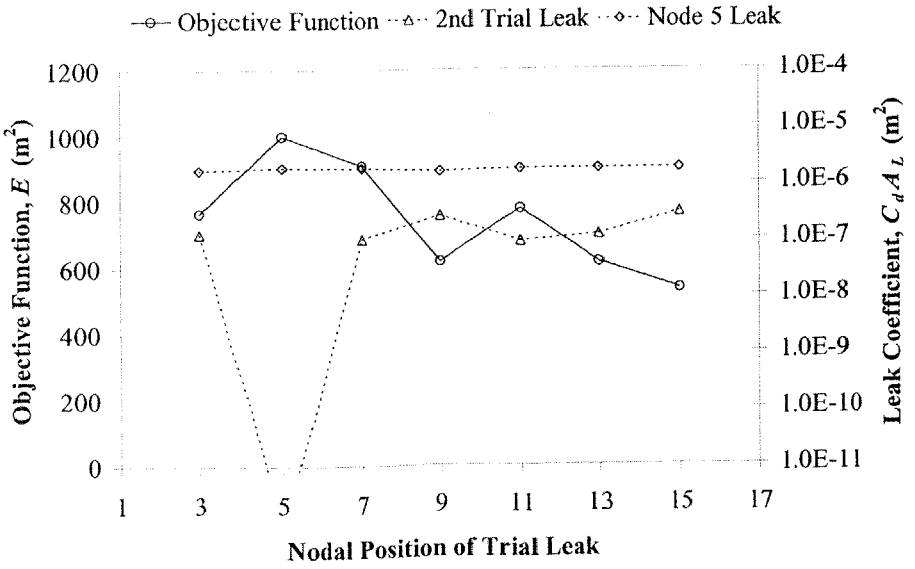

Figure 12.34 2nd Trial Leak, SLVMQ Results (7 Parameters)

The minimum objective function value for the second trial leak is located at node 15. The SLVMQ process is repeated. The second trial leak is set at node 15. The Levenberg-Marquardt algorithm is used to solve the inverse transient problem for the two set leaks and a third trial leak. The initial guesses are $(C_dA_L)_5 = 1.75\times10^{-6}$ m^2 and $(C_dA_L)_{15} = 2.90\times10^{-7}$ m^2. The result for the third trial leak located at all possible locations is shown in Table 12.21.

Table 12.21 3rd Trial Leak, SLVMQ Results (7 Parameters)

Trial Leak Position	Levenberg-Marquardt Iterations	Objective Function E (m^2)	Lumped Leak Coefficient C_dA_L (m^2)		
			3rd Trial Leak	Set Leak at Node 5	Set Leak at Node 15
Node 3	61	532.28	1.0×10^{-12}	1.75×10^{-6}	2.90×10^{-7}
Node 5	-	*532.32*	-	*1.75×10^{-6}*	*2.90×10^{-7}*
Node 7	35	532.17	1.0×10^{-12}	1.75×10^{-6}	2.87×10^{-7}
Node 9	71	531.65	1.0×10^{-12}	1.76×10^{-6}	2.93×10^{-7}
Node 11	**20**	**530.99**	**1.0×10^{-12}**	**1.75×10^{-6}**	**2.94×10^{-7}**
Node 13	30	531.73	1.0×10^{-12}	1.75×10^{-6}	2.95×10^{-7}
Node 15	-	*532.32*	-	*1.75×10^{-6}*	*2.90×10^{-7}*

Minimum objective function in bold, set leaks in italics
- trial leak not permitted

A graphical representation of Table 12.21 can be seen in Figure 12.35.

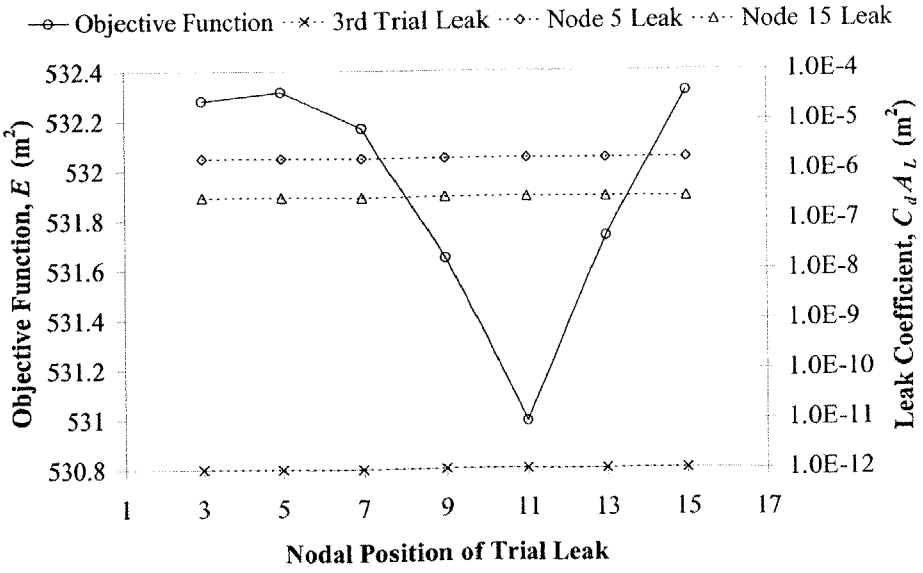

Figure 12.35 3rd Trial Leak, SLVMQ Results (7 Parameters)

The results for the third trial leak do not show a significant improvement in the objective function (improvement only equal to 0.2%). Therefore three trial leaks are

sufficient. The best solution found was $(C_dA_L)_5 = 1.75\times10^{-6}$, $(C_dA_L)_{15} = 2.94\times10^{-7}$ and $(C_dA_L)_{11} = 1.00\times10^{-12}$ m^2. The results from the SLVMQ method are compared with results from the standard Levenberg-Marquardt algorithm (7 unknown leaks) and the SCE method in Table 12.22.

Table 12.22 Comparison of Minimisation Algorithm Results (7 Parameters)

Leak Position	Lumped Leak Coefficient, C_dA_L (m^2)			
	Actual	LVMQ	SCE	SLVMQ
Node 3	-	**1.2×10^{-6}**	3.2×10^{-11}	-
Node 5	**1.7×10^{-6}**	2.1×10^{-7}	**1.7×10^{-6}**	**1.8×10^{-6}**
Node 7	-	5.0×10^{-8}	4.1×10^{-11}	-
Node 9	-	1.0×10^{-12}	2.9×10^{-9}	-
Node 11	-	1.0×10^{-12}	5.1×10^{-9}	1.0×10^{-12}
Node 13	-	1.0×10^{-12}	2.9×10^{-11}	-
Node 15	-	2.4×10^{-7}	2.6×10^{-7}	2.9×10^{-7}
E, (m^2)	-	3,995	533.7	530.9

Largest leak size in bold

The SLVMQ method finds the best solution out of the three minimisation algorithms (although there is only a small difference with the SCE method results).

In the second test of the method the number of possible leak positions (and hence unknown parameters) is increased to 15, at nodes 2, 3, 4, 5, 6, 7, 8, 9, 10, 11, 12, 13, 14, 15 and 16. The inverse transient method was applied to the same experimental data using the SLVMQ, standard Levenberg-Marquardt and SCE methods, the results of which are in Table 12.23.

Table 12.23 Comparison of Minimisation Algorithm Results (15 Parameters)

Leak Position	Lumped Leak Coefficient, $C_d A_L$ (m^2)			
	Actual	LVMQ	SCE	SLVMQ
Node 2	-	1.9×10^{-9}	2.4×10^{-9}	-
Node 3	-	7.1×10^{-8}	4.9×10^{-11}	-
Node 4	-	$\mathbf{2.8\times10^{-7}}$	3.0×10^{-7}	-
Node 5	$\mathbf{1.7\times10^{-6}}$	1.7×10^{-7}	$\mathbf{1.2\times10^{-6}}$	$\mathbf{1.7\times10^{-6}}$
Node 6	-	1.1×10^{-7}	1.3×10^{-7}	-
Node 7	-	1.5×10^{-7}	1.4×10^{-7}	-
Node 8	-	1.1×10^{-11}	7.4×10^{-11}	-
Node 9	-	3.5×10^{-11}	1.3×10^{-9}	-
Node 10	-	6.9×10^{-12}	4.7×10^{-8}	2.4×10^{-8}
Node 11	-	7.5×10^{-12}	1.0×10^{-12}	-
Node 12	-	1.8×10^{-11}	1.6×10^{-9}	-
Node 13	-	2.6×10^{-12}	6.2×10^{-9}	-
Node 14	-	2.6×10^{-12}	8.3×10^{-9}	-
Node 15	-	2.1×10^{-12}	2.3×10^{-11}	-
Node 16	-	1.0×10^{-12}	3.4×10^{-7}	8.9×10^{-7}
E, (m^2)	-	16,015	535.8	434.4

Largest leak size in bold

When the number of unknowns (leak candidates) is increased from 7 to 15, the standard Levenberg-Marquardt method performs the worst and is worse than with 7 possible leaks. The SCE method is better but slightly worse solution than for 7 possible leaks, and the SLVMQ method is best and better than with fewer candidate leaks. The details for the 15 unknowns case using the SLVMQ method are presented in Appendix C.7.

The following analysis investigates the number of evaluations of the transient solver required for the standard Levenberg-Marquardt algorithm, the SCE method and the SLVMQ method. The required number of evaluations of the transient solver for the calculation of the parameter derivatives is

$$E_{DER} = 1 + \xi N_P \quad (12.5.1)$$

where E_{DER} = evaluations of the transient solver for the calculation of the parameter derivatives, ξ = number of evaluations per parameter for the calculation of parameter derivatives and N_P = number of parameters. One evaluation is needed to solve the transient system initially. The constant ξ can be thought of as a measure of the efficiency of the calculation of parameter derivatives. For the divided difference method, the efficiency (ξ) is equal to one. The efficiency of each method of calculation for the parameter derivatives can be approximately determined using the numerical analysis performed in Appendix A. In Appendix A, the calculation of the parameter

derivatives was timed for different calculation methods (restated in Table 12.24). The relationship between the computation times and the number of evaluations of the transient solver is

$$T_{DER} = T_{TS} \times E_{DER} \quad (12.5.2)$$

where T_{DER} = time taken for the calculation of the parameter derivatives and T_{TS} = time taken for the a single calculation of the transient solver. Substituting Eq. 12.6.1 into Eq. 12.6.2 and rearranging for the parameter-derivative computation efficiency produces

$$\xi = \frac{1}{N_P}\left(\frac{T_{DER}}{T_{ST}} - 1\right) \quad (12.5.3)$$

where N_P = the number of parameters. The parameter-derivative computation efficiency (ξ) for each of the methods is presented in Table 12.24.

Table 12.24 Parameter Derivative Calculation Efficiency

Derivative Solution Method	Time (ms)	Efficiency ξ
Forward Solution	2,218	-
Divided Difference	9,597	1.109
Analytic	10,144	1.191
Adjoint	6,375	0.625
Fast Analytic	3,064	0.127

Programming inefficiencies such as the storing and manipulation of large arrays make the efficiency for the divided difference method slightly greater than the theoretical value of one. The total number of evaluations of the transient solver (for minimisation methods that use the Levenberg-Marquardt algorithm) can be written as

$$E_{TOTAL} = I_{LVMQ} \times E_{DER} \quad (12.5.4)$$

where E_{TOTAL} = total number of evaluations of the transient solver and I_{LVMQ} = number of Levenberg-Marquardt algorithm iterations. Eq. 12.6.4 permits comparison of the computational speeds of the standard Levenberg-Marquardt algorithm, SCE method and SLVMQ method using the total number of evaluations of the transient solver performed by each method. The number of evaluations of the transient solver for both the 7 and 15 unknown leak cases for each of the minimisation methods is tabulated in Table 12.25.

Table 12.25 Summary of the Number of Evaluations

Parameter Derivative	Number of Leak Parameters	
Method	7 Parameters	15 Parameters
	Shuffled Complex Evolution	
None	10,165[7]	39,415[15]
	Standard Levenberg-Marquardt	
I_{LVMQ}	166[7]	100[15]
Divided Difference	1,455	1,764
Analytic	1,550	1,887
Adjoint	892	1,038
Fast Analytic	314	291
	Systematic Levenberg-Marquardt	
I_{LVMQ}	242[1], 381[2], 217[3]	506[1], 855[2], 433[3]
Divided Difference	2,675	5,692
Analytic	2,811	5,980
Adjoint	1,874	3,991
Fast Analytic	1,050	2,240

Square brackets denote number of variables used in each minimisation

The standard Levenberg-Marquardt algorithm uses the least number of evaluations of the transient solver; however, it did not find the correct solution. Both the standard Levenberg-Marquardt algorithm and the SLVMQ method are significantly faster than the SCE method. The use of the fast analytic method for the calculation of the parameter derivatives approximately halves the number of evaluations of the transient solver for the SLVMQ method. The reduction is even larger for the standard Levenberg-Marquardt algorithm because it solves for more parameters at one time. The comparative efficiency of the fast analytic method is greater when more parameters are used. The SLVMQ method is faster than the SCE method and finds a better solution.

12.6 Leak Detection and Location Using a First Pressure Rise Method

A simple and effective method that relies on information from the first pressure rise after a valve closure is presented for the detection and location of leaks in a pipeline specific to fast valve closures. The pressure head is recorded at the valve for a period of $2L/a$. The basic mechanics of this method rely on the propagation of the pressure wave created from the valve closure and the reflected pressure relief wave from the leak (as the original pressure wave passes it). The timing of the reflected pressure relief wave and the magnitude of the pressure relief describe the location and magnitude of the leak, respectively. Four different leak configurations were tested: a 1.0 mm leak at node 5, a

1.5 mm leak at node 5, a 2.0 mm leak at node 5 and two 1.0 mm leaks at nodes 5 and 13. The pressure heads measured at node 1 (next to the valve) are shown in Figure 12.36.

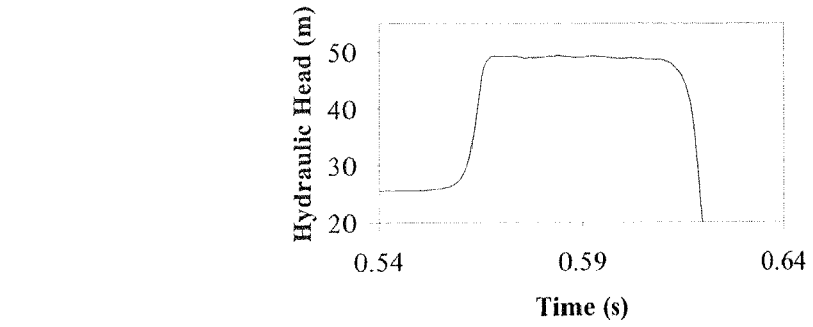

(a) No Leaks

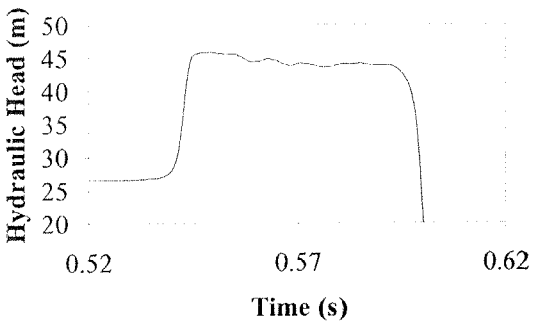

(b) 1.0 mm Leak at Node 5

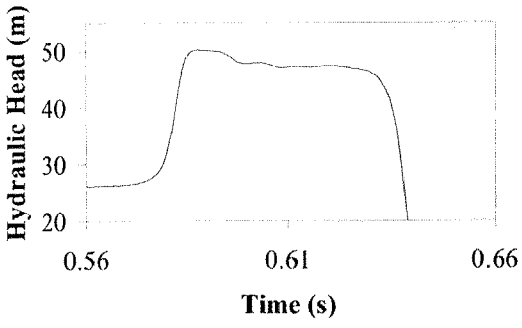

(c) 1.5 mm Leak at Node 5

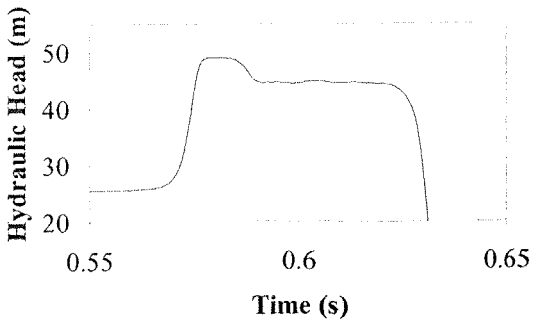

(d) 2.0 mm Leak at Node 5

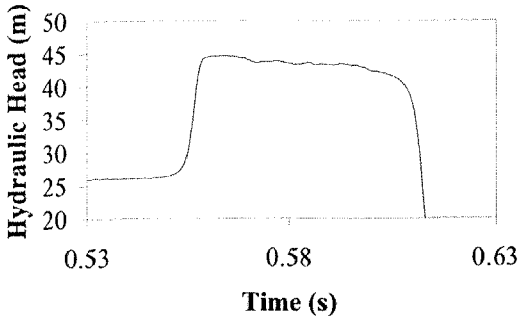

(e) Two 1.0 mm Leaks at Nodes 5 and 13

Figure 12.36 First Pressure Rise, Fast Valve Closure (t_c = 0.07 s)

These plots show irregularities on the first pressure rise when a leak is present, which can be compared to the plot when no leaks are present, as shown in Figure 12.36(a). The characteristics of the first pressure head rise may be described using a theoretical

model (see Appendix C.6 for details). A schematic of a theoretical first pressure head rise at the downstream valve (with leak) is shown in Figure 12.37.

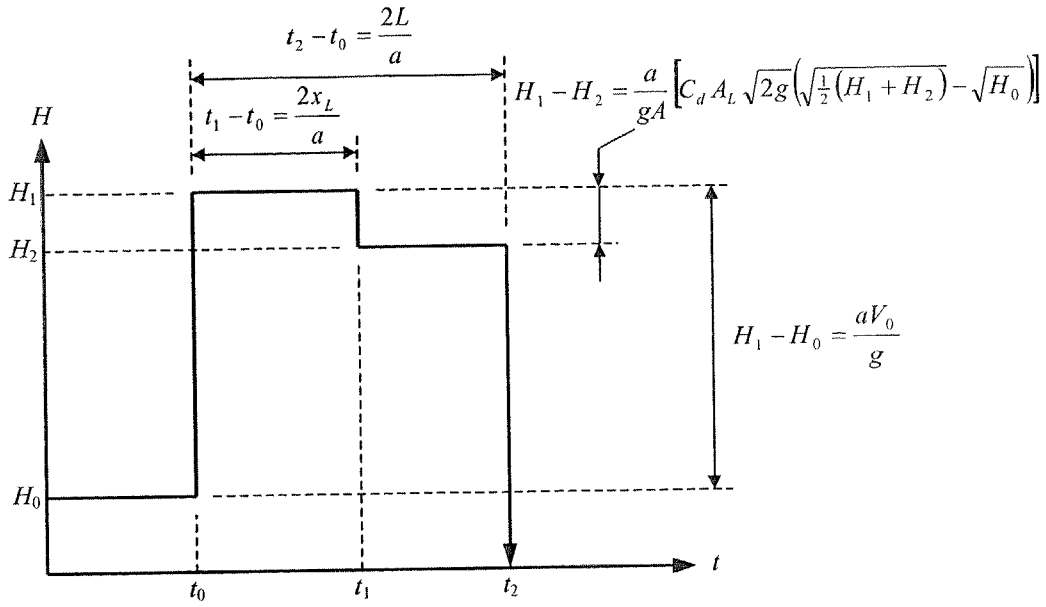

Figure 12.37 First Pressure Rise Behaviour at Valve Due to a Single Leak

The initial pressure rise at time t_0 is equal to the Joukowsky pressure rise. At a time of $t_0 + \frac{1}{2}(t_1 - t_0)$, the pressure wave encounters the leak in the pipeline. The leak provides a small amount of pressure relief. The pressure relief travels in both directions, but of most interest is the propagation back towards the valve. The timing of the returning pressure relief wave defines the position of the leak along the pipeline (x_L) measured from the valve,

$$x_L = \tfrac{1}{2}a(t_1 - t_0) \quad \text{.....(12.6.1)}$$

The magnitude of the returning pressure relief is used to determine the magnitude of the leak ($C_d A_L$). An expression for the lumped leak coefficient is

$$C_d A_L = \frac{A}{a}\sqrt{\frac{g}{2}}\frac{(H_1 - H_2)}{\left(\sqrt{\frac{1}{2}(H_1 + H_2)} - \sqrt{H_0}\right)} \quad \text{.....(12.6.2)}$$

A detailed derivation of both of these relationships is in Appendix C.6.

The analysis of the first pressure rise for one peak can be applied to a two leak case. Figure 12.38 shows the theoretical behaviour of two leaks on the first pressure rise after a fast valve closure.

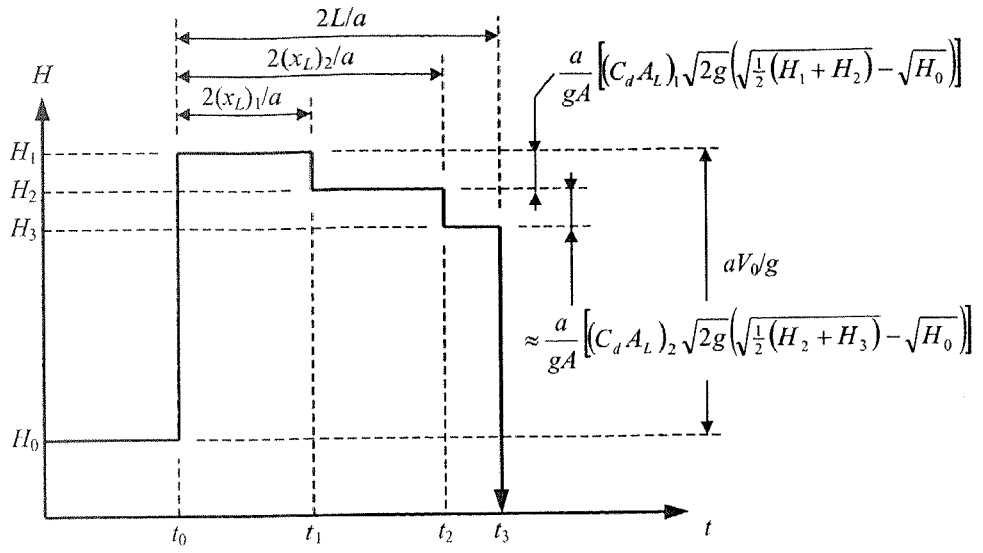

Figure 12.38 First Pressure Rise Behaviour at Valve Due to Two Leaks

Eqs. 12.6.1 and 12.6.2 are applied to the experimental data with results in Table 12.26.

Table 12.26 Leak Detection Results Using Fast Valve Closures (t_c = 0.07 s)

Experimental Configuration	Results	Leak 1		Leak 2	
		x_L (m)	C_dA_L (m^2)	x_L (m)	C_dA_L (m^2)
1.0 mm Leak at Node 5	Actual	9.25	5.0×10^{-7}	-	-
	Fast Transient Method	9.56	5.6×10^{-7}	-	-
1.5 mm Leak at Node 5	Actual	9.25	1.1×10^{-6}	-	-
	Fast Transient Method	9.23	9.8×10^{-7}	-	-
2.0 mm Leak at Node 5	Actual	9.25	1.7×10^{-6}	-	-
	Fast Transient Method	9.23	1.5×10^{-6}	-	-
Two 1.0 mm Leaks at Nodes 1 and 5	Actual	9.25	5.0×10^{-7}	27.75	7.1×10^{-7}
	Fast Transient Method	9.23	5.1×10^{-7}	28.03	5.8×10^{-7}

The true position of the leak for the single leak tests is x_L = 9.25 m. The true positions of the leaks for the multiple leak test are at x_L = 9.25 and 27.75 m. The calculated location using experimental data finds these locations to good accuracy. The solution leak positions and lumped leak coefficients can be verified against the experimental data by transient modelling using their values, the result of which is shown in Figure 12.39.

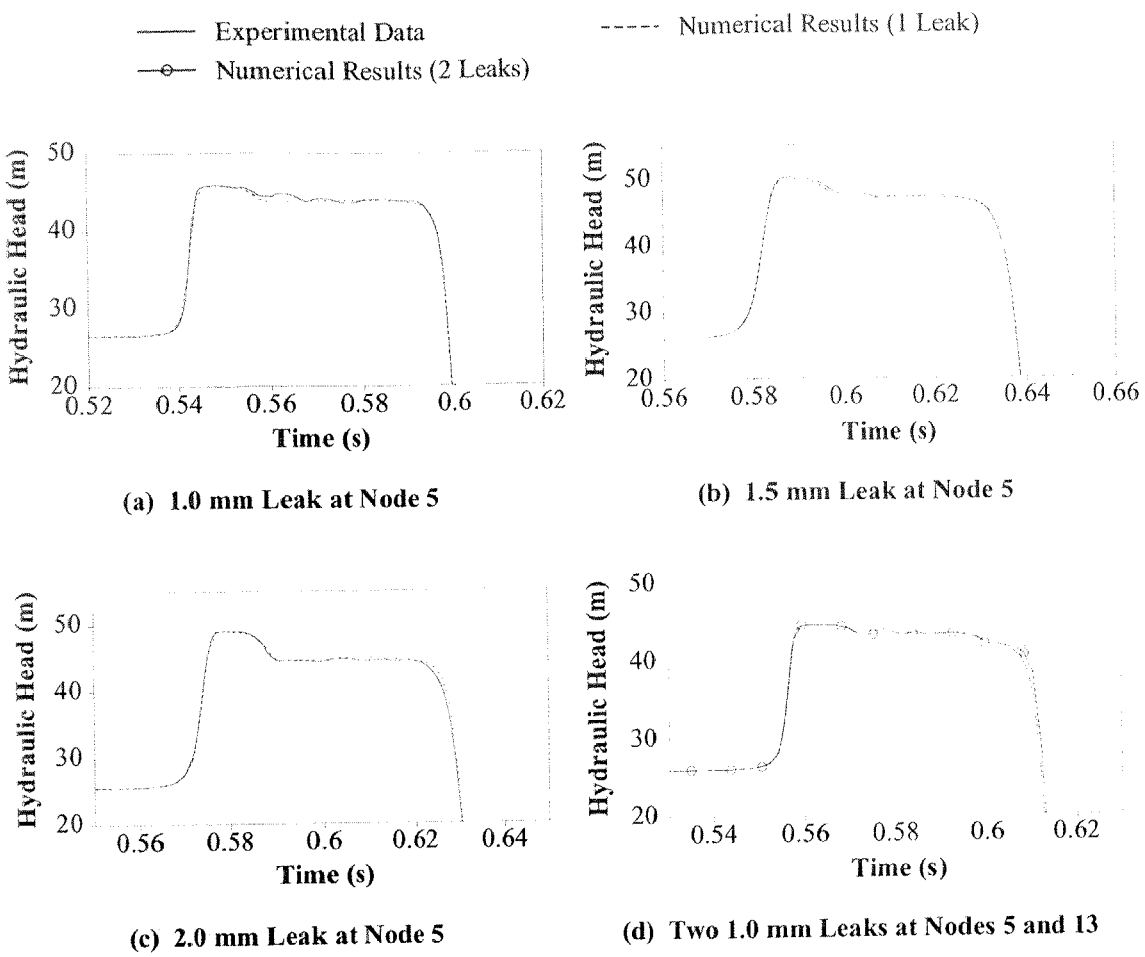

Figure 12.39 First Pressure Rise, Fast Valve Closures (t_c = 0.07 s)

A good match is found between the experimental data and modelled behaviour using the solution parameters. The first pressure rise method is conceptually simple and effective to use and, although this method works well for leakage in a simple pipeline, it is unlikely that such simple relationships could be found for a pipe network. For a network, a transient model could be used to simulate the complex pressure wave propagation and reflections, which would effectively be equivalent to the inverse transient method using measured data only from the initial pressure rise.

12.7 Summary

A preliminary investigation into the effect of non-orifice relationship leakage (which is the case for this study) was conducted. The results suggest that the ideal orifice leak relationship could be used with an altered lumped leak coefficient to produce similar

pressure response characteristics. The altered lumped leak coefficient was determined numerically using a similar valve closure event to those used for the inverse transient verification. Altered lumped leak coefficients were determined for all of the experimental leak sizes and assumed as correct when checking experimental inverse transient results.

A preliminary investigation into the minimisation algorithm used in the inverse transient method found that the Levenberg-Marquardt algorithm became stuck in local minima or difficult objective function topography (very steep multidimensional ridges). A minimisation algorithm called Shuffled Complex Evolution produced better results due a more global and robust search.

Neglecting unsteady friction for slow valve closure events is not that detrimental to the inverse transient method but is detrimental for fast valve closure events, and confirms the need for reliable unsteady friction models for the inverse transient method when considering fast valve closure events.

Results of the inverse transient method applied to an experimental pipeline are presented in this chapter. The inverse transient method was found to be effective for the location and sizing of single leaks when using a fast valve closure event. Results for the medium speed and slow valve closure events were poor because of the insensitivity of the objective function and the error in the measured pressure data, thus decreasing the usefulness of the inverse transient method for these event types. Results for multiple leaks showed similar problems exist as those for slow valve closure events with single leaks. For the medium speed and slow valve closure events, one dominant leak was found rather than the two actual leaks. The inverse transient results for multiple leaks using a fast valve closure could find the existence of two leaks but not their correct positions in the pipeline.

The use of slow valve closure events did not produce good results for the leak detection and location; however, it did produce good results for the determination of the existence of a leak. A numerical relationship between the leak position and the leak magnitude was found and was used to transform the inverse transient results into an equivalent leak at its correct position. The magnitude of the transformed leak correlated well with leak

magnitudes found in Section 12.2.1. Results suggest that once the location of a leak is known, the size of the leak can be found using the numerical relationship determined in Section 12.4 between leak size and location (or vice versa, if the size is known, the location can be found).

A method of leak location and detection using the first pressure rise after a fast valve closure produced good results using experimental data (for multiple leakage as well). A leak detection strategy could be envisioned whereby slow valve closures are used to detect the presence of a leak then, if a leak is detected, a fast valve closure is used to locate and quantify that leak.

In Section 12.5 a systematic Levenberg-Marquardt (SLVMQ) method was derived. The SLVMQ method addresses problems of convergence identified with the standard method of applying the Levenberg-Marquardt algorithm. A better search of the parameter space by the SLVMQ method produced good minimisation results. The SLVMQ method outperformed both the standard Levenberg-Marquardt algorithm and the SCE method. When the number of unknown leak candidates was increased from 7 to 15, the SLVMQ method found an improved solution while both the standard Levenberg-Marquardt algorithm and the SCE method found a worse solution.

Results in this chapter may only be indicative of the pipeline used in the experiments. Perhaps for a different pipeline or pipe network, the slow transient results would work better. The continuing study of the experimental verification of the inverse transient method for different transient events and for different pipe configurations is needed to confirm its usefulness.

Chapter 13

Conclusions and Recommendations

13.1 Conclusions

This thesis presents a comprehensive investigation into inverse transient analysis. The work presented can be classified into three categories: (i) improvements to transient modelling; (ii) improvements to inverse transient analysis; and (iii) experimental verification of transient modelling and inverse transient analysis. Conclusions for each of these three categories are now presented.

13.1.1 Transient Modelling Conclusions

Improvements to transient modelling are very important. The success of the inverse transient method relies on the accuracy of the transient model. Therefore, improvements to the transient model translate into improvements in inverse transient results.

The standard steady state approximation of unsteady pipe friction causes insufficient damping for certain unsteady pipe flow events. The difference between actual and modelled results increase as time progresses. The inverse transient method relies on the transient model to predict transient behaviour for long periods of time. It is therefore

necessary to be able to accurately model transient behaviour for long periods of time (to ensure good inverse transient results). The modelling of unsteady frictional effects improves longer term transient modelling results. Existing acceleration based unsteady friction models were tested and a methodology for unsteady flow classification (into 8 unsteady flow types) is presented. The methodology suggests limitations to the range of application of the original Brunone *et al.* (1991) unsteady friction model. A modification was made leading to a new unsteady friction model (the modified Brunone *et al.* model) that could model more of the 8 unsteady flow events. A number of new acceleration based unsteady friction models were formed from the modified Brunone *et al.* (1991) unsteady friction model. These models included momentum correction factor effects (the k_3 & k_M and k_A & k_P models) and the use of instantaneous Reynolds number dependent unsteady friction coefficients (the variable k_3 and variable k_3 & k_M models). A useful unsteady friction model that was developed is the k_A & k_P unsteady friction model. This model can independently control the frequency and damping of the pressure response for valve closure events. Of great concern is the estimation of the coefficients of these models. Relationships were derived that provide values of these coefficients that are based on the initial steady state velocity distribution.

A solution of the k_A & k_P unsteady friction model was found using a characteristics method. This solution produced different sloped characteristic lines for accelerating and decelerating flows. The solution also suggested that the k_A & k_P unsteady friction model would produce no damping for purely accelerating unsteady flow events (such as flow establishment after a valve opening) or for purely decelerating flows, thus limiting the generality of the k_A & k_P unsteady friction model. A relationship between the exponential damping coefficient of the pressure oscillations after a valve closure to the coefficients of the k_A & k_P model was determined. This relationship is useful for the quick calibration of the unsteady friction coefficients and the k_A & k_P model.

The modelling of leaks and valves in explicit and implicit method of characteristic schemes is presented. The use of an implicit method of characteristics scheme (in a matrix form) showed certain advantages for the simulation of pipe networks. A formulation was presented to model a leak located at a non-nodal position, which is useful for turning the leak location from discrete variable (at nodal positions in a pipeline) into a continuous variable (anywhere along the pipeline).

13.1.2 Inverse Transient Analysis Conclusions

Improvements to the inverse transient method, other than the improvements to the transient model, are presented in this thesis. The improvements pertain to the computation speed of the inverse transient method, accuracy of the final parameters and the minimisation method used.

A number of different minimisation schemes in the application of the inverse transient method were considered. Genetic algorithms were used to enhance the searching capacity of the minimisation algorithm. New crossover and mutation operators were created for continuous variables. The genetic algorithm has a more global search than the standard Levenberg-Marquardt algorithm; however, during the experimental verification of the inverse transient method a minimisation method named the shuffled complex evolution (SCE) method was found to yield superior results. Although the SCE method finds good solutions, it is a rather slow algorithm employing many evaluations of the transient solver. The SCE method does not use derivatives in its search and therefore cannot take advantage of the fast analytic method for the calculation of parameter derivatives. A new method for the application of the Levenberg-Marquardt algorithm, called the systematic Levenberg-Marquardt (SLVMQ) method, was created. The SLVMQ method uses systematic applications of Levenberg-Marquardt algorithm for low numbers of leak candidates. The SLVMQ method outperformed both the standard Levenberg-Marquardt algorithm and the SCE method (even more so for a higher number of unknown leak candidates). Also, the SLVMQ method is a lot more efficient than the SCE method.

The speed of convergence, when using derivative based minimisation techniques, such as the Levenberg-Marquardt algorithm, was also considered. A fast analytic method for the calculation of parameter derivatives shows great potential for speeding up inverse transient analysis, being much faster than the divided difference and adjoint methods. Problems were identified with a previous adjoint formulation. Also, it was found that the initial conditions can bias inverse transient results (and caused a failure to converge in most cases). The use of a steady state solver to calculate the initial conditions

corrected this problem (given that steady state conditions existed before the transient event). The convergence rate was not affected but there was a decrease in the sensitivity of the objective function with respect to the parameters.

Of the most importance is the formation of a method to find measurement site configurations that yield high confidence results. Certain performance indictors were used to gauge the probable outcome of the inverse transient method given a particular configuration of measurement sites. These performance indicators were then used to find optimal measurement site configurations (those sites that minimised the transmission of error from the measured data to the solution parameters) for a specific number of sites in a small example pipe network. The analysis was performed for different numbers of measurement sites creating a Pareto optimal curve showing the trade off between the number of measurement sites and probable inverse transient performance. The Pareto optimal curve can be used by designers to decide upon an adequate number of measurement sites and then to select a configuration that maximises inverse transient performance. The search for optimal measurement site configurations was performed for a larger 51 pipe network. A genetic algorithm was used with new crossover and mutation operators for a combinatorial search. The generic algorithm results were shown to produce measurement site configurations that were more optimal than a number of randomly selected measurement site configurations.

Section 4.8 presented a method for the estimation of the error in the solved parameters (for the inverse transient method) given the error in the measured data. The method was tested using Monte Carlo simulations. The estimated error distribution showed a good match with the Monte Carlo simulation results. The correlation between different inverse transient parameters (only friction factors were used) could be estimated as well. The correlation between some friction factors was high while between others were low, suggesting that some friction factors can be grouped together thus reducing the number of unknowns that are needed to be solved for. The estimates of the error in the parameters were also used to show the effect of the measured pressure data length on the solution parameters. The analysis showed that inverse transient analysis produces much higher precision results than inverse steady state analysis.

13.1.3 Experimental Verification Conclusions

The experimental verification of both the transient model and techniques for the detection and location of leaks was performed using an apparatus consisting of a pipeline positioned between two computer controlled pressure tanks. Different sized leaks could be located at different positions along the pipeline. Transient events were initiated using very fast, fast, medium and slow valve closures.

For accurate simulation of a transient event, the calibration of various elements of the experimental apparatus was required. The pressure transducers, wave speed, steady state friction factor, valve and leak units were calibrated. A fast transient method was used to perform the calibration of the valve, which is considerably quicker than standard steady state methods. The calibration of the leak units produced pressure-flow relationships that were different from the theoretical orifice equation. The simulation of a transient event required smooth inputs for the valve position and/or pressure head (for use in boundary conditions). Various filters were tested to smooth the inputs, the best being a 2^{nd} order Savitsky-Golay smoothing filter. The use of the measured pressure head as a boundary condition was found to produce misleading results, thus, a valve boundary condition was used for subsequent analysis.

The experimental verification of the transient model found that the steady state friction approximation did not produce enough dissipation. Unsteady friction was used to account for this extra dissipation. Experimental verification of unsteady friction models showed different behaviour depending upon the initial state of the flow (laminar or turbulent) for a fast valve closure. The Zielke (1968) model was adequate for the simulation of laminar flow events, while the Brunone *et al.* (1991) model produced good matches for the damping of the pressure response but failed to correctly model the shape of the pressure response. A number of different valve closure rates were tested: very fast, fast, medium and slow (corresponding to valve closure times, t_c, of 0.009, 0.07, 0.7 and 1.4 s respectively). A different behaviour of the pressure response was observed for valve closure times faster or slower than $2L/a$ ($t_c = 0.056$ s). For valve closure speeds faster than $2L/a$, there was a decrease in the frequency of the pressure response compared to those with valve closure times slower than $2L/a$. The behaviour was used to infer k_A & k_P model parameters. The fast valve closure experimental tests

were then used to determine unsteady friction model parameters such as k_3, k_M, k_A and k_P. The experimental tests were used to verify theoretical unsteady friction coefficient relationships. The 8 unsteady flow events were experimentally performed. The Brunone *et al.* (1991) model (and hence the k_A & k_P model) did not predict the extra damping (above the steady state damping) for the valve opening events; however, the Zielke (1968) model did return good matches. A range of applicability for the different unsteady friction models was presented. Also, the experimental verification of the exponential damping rate relationship was presented.

One of the first ever experimental verifications of the inverse transient method was performed in this thesis. During the writing of this thesis a paper was published by Tang *et al.* (2000) showing an experimental result for leak detection using the inverse transient method. Their results showed the presence of a leak, but were inconsistent across a number of tests due to the inability of their transient model to account for the extra dissipation due to unsteady friction. The transient model used in this thesis does include unsteady friction and the leak detection results are consistent for the single leaks of three sizes analysed. Good leak detection and location results were achieved for the single leak, fast valve closure tests. The inverse transient results were worse for the multiple leak case. Results using medium and slow valve closures were found to be unable to determine the leaks size and location simultaneously. The indeterminacy meant that the existence of a leak could be seen but its location could not be determined without knowing its size and vice versa. Numerical relationships were found for the variation of the leak size and location along the pipeline (for a slow valve closure event). The effect of the "non-theoretical" leak pressure-flow relationship had little effect on the determination of the location of the leak for fast valve closure events, rather just on the calculated leak magnitude. A new leak detection and location technique that makes use of first pressure rise data for fast valve closure events was shown to work well for both single and multiple leak cases.

The overall conclusion attained in this thesis is that the analysis of transients in pipelines and pipe networks provide powerful tools for system calibration and leak detection.

13.2 Recommendations for Future Work

The performance of inverse transient analysis depends mainly on the transient modelling accuracy. At the present moment in time, the modelling of unsteady frictional effects is a large unsolved problem faced by researchers. For turbulent flows, there is no true model that is adequate for all unsteady flow cases. It is opinion of the author that unsteady friction models that are based on the instantaneous acceleration alone will never provide a generalised model. Further research into turbulent unsteady frictional effects is a logical step to make, otherwise future experiments (for inverse transient analysis) should be performed using laminar unsteady flows where theoretical relationships are better known.

The effectiveness of the inverse transient method also appears to be dependent on the transient event type, suggesting that research should be directed towards the identification of transient event types or characteristics that maximise the performance of the inverse transient method. A method to achieve this could involve similar analysis presented in Chapter 7 (performance indicators). Furthermore, analysis in Chapter 7 need not only be applied to the inverse transient method. The number and location of measured sites, together with length of data at these sites, is of concern to many different fields that implement parameter estimation or inverse analyses.

It is recommended that a more thorough statistical treatment of the inverse transient method be made, which would bring the method out of the "statistical dark ages", so to speak, and aid the general interpretation and solution of parameters. Types of parameters, other than friction factors and lumped leak coefficients, could also be solved for. These parameters could include the status of valves in a pipe network, diagnosis of pipe blockages, the unsteady calibration of most hydraulic devices and the location of leaks as they occur rather than for existing leaks (a break algorithm).

The inverse transient results presented in Section 12.4 show, for slow valve closure events, an poor solution for the leak size and leak location, which reduces the usefulness of inverse transient analysis (using slow valve closure events) for determining the leak location and size simultaneously. The poor solutions are due to the low sensitivity of the inverse transient method to the leak location and the presence of error in the

measured data and in the transient model. However, if the leak location is known the leak size can be computed and vice-versa. It is proposed that the slow valve closure events presented in Chapter 12 be used to determine the existence of a leak. Once a leak has been detected, another method could be used to find its size or location (perhaps a fast valve closure event). A possible method that could be used to determine the location of a leak based on resonance principles is hypothesised here. A signal could be fed into a pipeline using a computer controlled valve or fluid injection system. A number of different frequency input signals are used and the pressure response measured at some location. When the frequency of the input signal approaches the natural frequency of the pipeline ($a/4L$) an amplification in the pressure response would be observed due to resonance. A similar behaviour might exist for a leak. Once the resonance frequency is found for a leak, the location of the leak is found. Then the inverse transient method could be reapplied to the slow valve closure data and, since the location is known, the size can be determined.

The failure of the standard Levenberg-Marquardt minimisation algorithm for solving the inverse transient problem produced a need for more appropriate minimisation algorithms. The Shuffled Complex Evolution (SCE) algorithm found improved solutions to the inverse transient problem but was computationally expensive. A systematic Levenberg-Marquardt method (SLVMQ) produced better solutions, more efficiently than the SCE method. For large pipe networks the systematic approach to the placement of trial leaks might be achieved through the use of a genetic algorithm similar to that used in Section 7.6. It is the opinion of the author that the failure of the standard Levenberg-Marquardt algorithm was due to the assumption that leak candidates could only exist at certain positions in the pipeline, producing a discrete problem. If the leak position was allowed to vary continuously along the pipeline (rather than at discrete positions), the standard Levenberg-Marquardt algorithm would perform better. The non-nodal leakage formulation (Section 3.10) could be used to achieve this. Although the standard Levenberg-Marquardt algorithm does not find the correct solution for the inverse transient problem presented in this thesis, it is by far the most efficient and fastest algorithm presented.

Although the theoretical behaviour of turbulent unsteady frictional effects is not known for generalised unsteady events, approximate relationships are known for certain event

types. Therefore, inverse transient analysis can still be confidently applied to these types of events. Controlled experimental verification of inverse transient analysis still needs to be applied to pipe networks, and is currently being performed at Adelaide University. Eventually, inverse transient analysis must be used in the field because application is the true nature of engineering. It is expected that field tests will reveal more problems that need to be addressed for the successful implementation of the inverse transient method. In field applications of the inverse transient method there will be many more uncertainties to account for compared to laboratory applications. For example the representation of water demand in the field is more uncertain and, in reality, is not independent of pressure as normally assumed. The effect of uncertainties in the demand and other parameters (other than the uncertainty in the measured head) on the inverse transient method indicates that there is scope for further research.

Bibliography

1. Anderson, A., and Simpson, A.R. (1996). "Genetic Algorithm Optimisation Software in Fortran." *Research Report No. R136*, March, Department of Civil and Environmental Engineering, The University of Adelaide, Australia.
2. Andrés, M. (1995). "Leakage Detection in Practice. Application to the Water Distribution of Valencia." In: *Improving Efficiency and Reliability in Water Distribution Systems*, Water Science and Technology Library, Volume 14, E. Cabrera and A.F. Vela (Editors), Kluwer Academic, Boston, 97-106.
3. Arfaie, M., and Anderson, A. (1991). "Implicit Finite-Differences for Unsteady Pipe Flow." *Mathematical Engineering in Industry*, 3(2), 133-151.
4. Arfaie, M., Suwan, K., and Anderson, A. (1993). "Stability and Accuracy of Pipe Friction Approximations in Method of Characteristics Solutions for Waterhammer." *Mathematical Engineering in Industry*, 4(1), 265-281.
5. Arlt, H. (1983). "Experimentelle Untersuchunge über des instationäre, turbulente Reibungsverhalten bei aufgeprägten Druckimplusen in einer Rohrleitung mit Kreisquerschnitt." *Mitteilungsheft Nr. 102*, Institut für Wasserbau und Wasserwirtschaft, Technische Universität Berlin, Berlin, Germany.
6. Asian Development Bank (1993). *Water Utilities Data Book - Asian Pacific Region*. Manila, Philippines.
7. AWWA Leak Detection and Water Accountability Committee (1996). "Committee Report: Water Accountability." *Journal of the American Water Works Association*, 88(7), July, 108-111.
8. Axworthy, D.H., Ghidaoui, M.S., and McInnis, D.A. (2000). "Extended Thermodynamics Derivation of Energy Dissipation in Unsteady Pipe Flow." *Journal of Hydraulic Engineering*, ASCE, 126(4), April, 276-287.
9. Baghdadi, A.H.A., and Mansy, H.A. (1988). "A Mathematical Model for Leak Location in Pipelines." *Applied Mathematical Modelling*, Vol. 12, February, 25-30.

10. Barenblatt, G.I. (1991). "Scaling Laws (Incomplete Self-Similarity with Respect to Reynolds Numbers) for the Developed Turbulent Flows in Pipes." *Comptes Rendus de l'Académie des Science*, Paris, Série II, Vol. 313, 307-312.

11. Beck, S.B.M, Boucher, R.F., and Haider, H. (1994). "Modelling Water Hammer with Transmission Line Techniques." *IChemE Research Event 1994*, 1994 Symposium, London, January, 1099-1100.

12. Bergant, A., and Simpson, A.R. (1994). "Estimating Unsteady Friction in Transient Cavitating Pipe Flow." *2nd International Conference on Water Pipeline Systems*, Edinburgh, Scotland, May, 3-16.

13. Bergant, A., and Simpson, A.R. (1995). "Water Hammer and Column Separation Measurements in an Experimental Apparatus." *Research No. R128*, June, Department of Civil and Environmental Engineering, The University of Adelaide, Australia.

14. Bergant, A., Simpson, A.R., and Vítkovský, J.P. (1999). "Review of Unsteady Friction Models in Transient Pipe Flow." *9th International Meeting of the Work Group on the Behaviour of Hydraulic Machinery Under Steady Oscillatory Conditions*, IAHR, 7-9 September, Brno, Czech Republic.

15. Betâmio de Almeida, A. (1981). *Regimes Hidráulicos Transitórios em Condutas Elevatórias*. PhD Thesis, Technical University of Lisbon, IST, Portugal.

16. Betâmio de Almeida, A., and Koelle, E. (1992). *Fluid Transients in Pipe Networks*. Computational Mechanics Publications, Southampton, UK.

17. Bhave, P.R. (1988). "Calibrating Water Distribution Network Models." *Journal of Environmental Engineering*, ASCE, 114(1), 120-136.

18. Boulos, P.F., and Wood, D.J. (1990). "Explicit Calculation of Pipe-Network Parameters." *Journal of Hydraulic Engineering*, ASCE, 116(11), 1329-1344.

19. Boyd, I.D., Surry, P.D., Radcliffe, N.J. (1994). "Constrained Gas Network Pipe Sizing with Genetic Algorithms." *Technical Report EPCC-TR94-11*, Edinburgh Parallel Computing Centre.

20. Bratland, O. (1986). "Frequency-Dependent Friction and Radial Kinetic Energy Variation in Transient Pipe Flow." *Proceedings of the 5th International Conference on Pressure Surges*, BHRA, Hannover, Germany, 95-101.

21. Brown, F.T. (1984). "On Weighting Functions for the Simulation of Unsteady Turbulent Flow." *Forum on Unsteady Flow*, ASME, New Orleans, USA, FED-Vol. 15, 26-28.

22. Brunone, B., and Greco M. (1990). "Un modello per la ricostruzione di fenomeni di colpo d'ariete anche in presenza di cavitazione." *Proceedings of the 22nd Italian Congress of Hydraulics and Hydraulic Constructions*, Cosenza, Vol. 4, 147-160.

23. Brunone, B., Golia, U.M., and Greco, M. (1991). "Some Remarks on the Momentum Equations for Fast Transients." *International Meeting on Hydraulic Transients with Column Separation, 9th Round Table*, IAHR, Valencia, Spain, 201-209.

24. Brunone, B., Golia, U.M., and Greco, M. (1995). "Effects of Two-Dimensionality on Pipe Transients Modeling." *Journal of Hydraulic Engineering*, ASCE, 121(12), December, 906-912.

25. Bughazem, M.B., and Anderson, A. (1996). "Problems with Simple Models for Damping in Unsteady Flow." *7th International Conference on Pressure Surges and Transients in Pipelines and Open Channels, BHR Group*, Harrogate, UK, 16-18 April, 537-457.

26. Bughazem, M.B., and Anderson, A. (2000). "Investigation of an Unsteady Friction Model for Waterhammer and Column Separation." *Safe Design and Operation of Industrial Pipe Systems: 8th International Conference on Pressure Surges*, BHR Group, The Hague, The Netherlands, 12-14 April, 483-498.

27. Buthaud, H. (1977). "On the Momentum Correction Factor in Pulsatile Blood Flow." *Journal of Applied Mechanics*, ASME, 44(2), June, 343-344.

28. Campbell, F.C. (1970). "Distribution System Leakage Survey." *Journal of the American Water Works Association*, 62(7), July, 400-402.

29. Carpentier, P., and Cohen, G. (1991). "State Estimation and Leak Detection in Water Distribution Networks." *Civil Engineering Systems*, 8(4), 247-257.

30. Carravetta, A., Golia, U.M., and Greco, M. (1992). "On the Spontaneous Damping of Pressure Oscillations in Water Hammer Transients." *Proceedings of the 23rd Convegno Nazionale di Idraulica e Costruzioni Idrauliche*, Florence, Italy, 4, E.67-79.

31. Carstens, M.R., and Roller, J.E. (1959). "Boundary-Shear Stress in Unsteady Turbulent Pipe Flow." *Journal of the Hydraulics Division*, Proceedings of the ASCE, 95(HY2), 67-81.

32. Cesario, A.L. (1980). "Computer Modelling Programs: Tools for Model Operations." *Journal of the American Water Works Association*, 72(9), September, 508-513.

33. Chaudhry, M.H. (1987). *Applied Hydraulic Transients*. 2nd Edition, Litton Educational Publishing Inc., Van Nostrand Reinhold Co.

34. Chen, C-L. (1991). "Unified Theory on Power Laws for Flow Resistance." *Journal of Hydraulic Engineering*, ASCE, 117(3), March, 370-371.

35. Chen, C-L. (1992). "Momentum and Energy Coefficients Based on Power-Law Velocity Profile." *Journal of Hydraulic Engineering*, ASCE, 118(11), November, 1571-1584.

36. Chen, L. (1995). *Pipe Network Analysis - The Forward and Inverse Problems*. PhD Thesis, August, Cornell University, USA.

37. Cole, S.E. (1979). "Methods of Leak Detection: An Overview." *Journal of the American Water Works Association*, 71(2), February, 73-75.

38. Colebrook, C.F. and White, C.M. (1937). "Experiments with Fluid-Friction in Roughened Pipes." *Proceedings of the Royal Society, London*, Series A, Vol. 161, 367-381.

39. Daily, J.W., Hankey, W.L., Olive, R.W., and Jordaan, J.M. (1956). "Resistance Coefficients for Accelerated and Decelerated Flows Through Smooth Tubes and Orifices." *Transactions of the ASME*, Vol. 78, 1071-1077.

40. Datta, R.S.N., and Sridharan, K. (1994). "Parameter Estimation in Water-Distribution Systems by Least Squares." *Journal of Water Resources Planning and Management*, ASCE, 120(4), 405-422.

41. Davis, L. (1991). *Handbook of Genetic Algorithms*. Van Nostrand Reinhold, New York.

42. Denisov, S.V. (1970). "The Friction Coefficient in Nonstationary Flows." *Inzhenerno-Fizicheskii Zhurnal*, 18(1), January, 118-123.

43. Donachie, R.P. (1974). "Digital Program for Water Network Analysis." *Journal of the Hydraulics Division*, ASCE, 100(3), March, 393-403.

44. Douglas, J.F., Gasiorek, J.M., and Swaffield, J.A. (1985). *Hydraulic Engineering*. 2nd Edition, Longman Scientific & Technical, Longman Group UK Limited.

45. Duan, Q., Sorooshian, S., and Gupta, V. (1992). "Effective and Efficient Global Optimization for Conceptual Rainfall-Runoff Models." *Water Resources Research*, 28(4), April, 1015-1031.

46. Duan, Q., Sorooshian, S., and Gupta, V.K. (1994). "Optimal Use of the SEC-UA Global Optimization Method for Calibrating Watershed Models." *Journal of Hydrology*, Elsevier, Vol. 158, 265-284.

47. Duan, Q.Y., Gupta, V.K, and Sorooshian, S. (1993). "Shuffled Complex Evolution Approach for Effective and Efficient Global Minimization." *Journal of Optimization Theory and Applications*, 76(3), March, 501-521.

48. Eggener, C.L., and Polkowski, L.B. (1976). "Networks Models and the Impact of Modelling Assumptions." *Journal of the American Water Works Association*, 68(4), April, 189-196.

49. Eichinger, P., and Lein, G. (1992). "The Influence of Friction on Unsteady Pipe Flow." *Proceedings of the International Conference on Unsteady Flow and Fluid Transients*, 29 September - 1 October, Durham, United Kingdom, 41-50.

50. Elansary, A.S., Silva, W., and Chaudhry, H.M. (1994). "Numerical and Experimental Investigation of Transient Pipe Flow." *Journal of Hydraulic Research*, 32(5), 689-706.

51. Engelhardt, M.O. (1999). *Development of a Strategy for the Optimum Replacement of Water Mains*. PhD Thesis, Department of Civil and Environmental Engineering, The University of Adelaide, Australia.

52. Fantozzi, M., and Villa, G. (1992). "Organisation of a Systematic Leakage Detection Campaign on Water Supply Network using Computerised Technics - Actual Experiences and Future Development." *Water Supply*, IWSA Regional Conference, Florence, Vol. 10, 149-158.

53. Farmer, E., Kohlrust, R., Myers, G., and Verduzco, G. (1988). "Leak Detection Tool Undergoes Field Tests." *Oil and Gas Journal*, 86(51), December, 48-53.

54. Fox, J.A. (1977). *Hydraulic Analysis of Unsteady Flow in Pipe Networks*. The Macmillan Press Ltd., London, U.K.

55. Fuamba, M., Rahal, H., and Berlamont, J. (1996). "Unsteady Pipe Flow Simulations Using Unsteady Friction Flow Formulae." *7th International*

Conference on Pressure Surges and Fluid Transients in Pipelines and Open Channels, BHR Group, Harrogate, UK, 16-18 April, 313-322.

56. Funk, J.E., and Wood, D.J. (1974). "Frequency Response of Fluid Lines With Turbulent Flow." *Journal of Fluids Engineering*, ASME, December, 365-369.

57. Germanopoulos, G. (1985). "A Technical Node on the Inclusion of Pressure Dependent Demand and Leakage Terms in Water Supply Network Models." *Civil Engineering Systems*, Vol. 2, September, 171-179.

58. Germanopoulos, G. (1995). "Valve Control Regulation for Reducing Leakage." In: *Improving Efficiency and Reliability in Water Distribution Systems*, Water Science and Technology Library, Volume 14, E. Cabrera and A.F. Vela (Editors), Kluwer Academic, Boston, 165-190.

59. Ghidaoui, M.S., Karney, B.W., and McInnis, D.A. (1998). "Energy Estimates for Discretization Errors in Water Hammer Problems." *Journal of Hydraulic Engineering*, ASCE, 124(4), April, 384-393.

60. Gofman, E., and Rodeh, M. (1981). "Loop Equations with Unknown Pipe Characteristics." *Journal of the Hydraulics Division*, ASCE, 100(3), September, 1047-1060.

61. Goldberg, D.E. (1989). *Genetic Algorithms in Search, Optimisation and Machine Learning*. Addison-Wesley Publishing Co., Inc.

62. Goldberg, D.E., and Deb, K. (1991). "A Comparative Analysis of Selection Schemes used in Genetic Algorithms." In: *Foundations of Genetic Algorithms*, G. Rawlins (Editor), Morgan Kaufmann, San Mateo, California.

63. Goldberg, D.E., and Kou, C.H. (1987). "Genetic Algorithms in Pipeline Optimisation." *Journal of Computing in Civil Engineering*, ASCE, 1(2), April, 128-141.

64. Goldberg, D.E., Deb, K., and Clark, J.H. (1992). "Genetic Algorithms, Noise and Sizing of Populations." *Complex Systems*, Vol. 6, 333-362.

65. Goldberg, D.E., Deb, K., and Thierens, D. (1993). "Towards a Better Understanding of Mixing in Genetic Algorithms." *Journal of the Society for Instrumentation and Control Engineers*, 32(1), 10-16.

66. Golia, U.M. (1990). *Sulla valutazione delle forze resistenti nel colpo d'ariete. Pubblicazioni del Dipartimento di Idraulica dell'Università di Napoli*, No. 639, Napoli.

67. Grant, K. (1995). "An Introduction to Genetic Algorithms." *C/C++ Users Journal*, 13(3), March, 45-58.

68. Greco, M. (1990). "Some Recent Findings on Column Separation During Water Hammer." *Excerpta*, Vol. 5, 261-272.

69. Heim, P.M. (1979). "Conducting a Leak Detection Search." *Journal of the American Water Works Association*, 71(2), February, 66-69.

70. Hewitson, C.M. (2000). *Optimisation of Water Distribution Systems using Genetic Algorithms for Hydraulic and Water Quality Issues.* PhD Thesis, Department of Civil and Environmental Engineering, The University of Adelaide, Australia.

71. Hino, M., Sawamoto, M., and Takasu, S. (1977). "Study on the Transition to Turbulence and Frictional Coefficient in an Oscillatory Pipe Flow." *Transactions of the Japanese Society of Civil Engineers*, Vol. 9, 282-284.

72. Holly, F.M., and Preissmann, A. (1977). "Accurate Calculation of Transport in Two Dimensions." *Journal of the Hydraulics Division*, ASCE, 103(11), November, 1259-1277.

73. Hough, J. E. (1988). "Leak Testing of Pipeline Uses Pressure and Acoustic Velocity." *Oil and Gas Journal*, 86(47), November 21, 35-41.

74. Hunter, A. (1996). *Users Manual for SUGAL 2.1.* Internet address: http://www.trajan-software.demon.co.uk/sugal.htm

75. Ivanov, I.S., and Bournaski, E.G. (1983). "An Approximation of the Non-Linear Term in Numerical Solution of Waterhammer Equations by the Method of Characteristics." *20th Congress, International Association for Hydraulic Research*, Vol. 6, Nauka, Moscow, 206-213.

76. Jaeger, C. (1977). *Fluid Transients.* Blackie & Son Limited, Bishopbriggs, Glasgow.

77. Jeppson, R. W. (1976). *Analysis of Flow in Pipe Networks.* Ann Arbor Science Publishers, Inc., Michigan, USA.

78. Jönsson, L. (1995). "Computer and Laboratory Studies of Leak Detection Using Hydraulic Transients." In: *Water Resources Management under Drought or Water Shortage Conditions*, N.T. Tsiourtis (Editor), Balkema, Rotterdam, 119-126.

79. Joukowsky, N. (1900). "Über den hydraulisher Stoß in Wasser-lietungsrohren." *Memoirs de l'Academie Imperiale des Sciences de St Petersburgh.*

80. Kagawa, T., Lee, I., Kitagawa, A., and Takenaka, T. (1983). "High Speed and Accurate Computing Method of Frequency-Dependent Friction in Laminar Pipe Flow for Characteristic Method." *Transactions of the Japanese Society of Mechanical Engineers*, 49(447), 2638-2644.

81. Karney, B.M. (1984). *Analysis of Fluid Transients in Large Distribution Networks*. PhD Thesis, The University of British Columbia, Vancouver, Canada.

82. Karney, B.W. (1990). "Energy Relations in Transient Closed-Conduit Flow." *Journal of Hydraulic Engineering*, ASCE, 116(10), October, 1180-1196.

83. Karney, B.W., and McInnis, D.A. (1990). "Transient Analysis of Water Distribution Systems." *Journal of the American Water Works Association*, 82(7), July, 62-70.

84. Koelle, E., Luvizotto Jr., E., and Andrade, J.G.P. (1996). "Personality Investigation of Hydraulic Networks Using the MOC-Method of Characteristics." *Conference on Pressure Surges and Fluid Transients*, April, BHR Group, 123-138.

85. Kurokawa, J., and Morikawa, M. (1986). "Accelerated and Decelerated Flows in a Circular Pipe." *Bulletin of the Japanese Society of Mechanical Engineers*, 29(249), 758-765.

86. Lambert, A. (1994). "Accounting for Losses: The Bursts and Background Concept." *Water and Environmental Management: Journal of the Chartered Institution of Water and Environmental Management*, 8(2), 205-214.

87. Lansey, K.E. (1988). "A Procedure for Water Distribution Network Calibration Considering Multiple Loading Conditions." *International Symposium on Computer Modelling of Water Distribution Systems*, May, Kentucky, 25-30.

88. Lansey, K.E., Basnet, C. (1991). "Parameter Estimation for Water Distribution Networks." *Journal of Water Resources Planning and Management*, ASCE, 117(1), 126-144.

89. Laverty, G.L. (1979). "Leak Detection: Modern Methods, Cost, and Benefits." *Journal of the American Water Works Association*, 71(2), February, 61-63.

90. Lefebvre, P.J., and White, F.M. (1989). "Experiments on Transition to Turbulence in a Constant-Acceleration Pipe Flow." *Journal of Fluids Engineering*, ASME, Vol. 111, December, 428-438.

91. Letelier, M.F., and Leutheusser, H.J. (1976). "Skin Friction in Unsteady Laminar Pipe Flow." *Journal of the Hydraulics Division*, ASCE, 102(HY1), January, 41-56.

92. Liggett, J.A. (1975). "Numerical Methods of Solution of the Unsteady Flow Equations." In: *Unsteady Flow in Open Channels*, Volume I, K. Mahmood and V. Yevjevich (editors), Water Resources Publications, Fort Collins, Colorado, USA.

93. Liggett, J.A., and Caughey, D.A. (1998). *Fluid Mechanics: An Interactive Text.* CD ROM, American Society of Civil Engineers Press.

94. Liggett, J.A., and Chen L. (1994). "Inverse Transient Analysis in Pipe Networks." *Journal of Hydraulic Engineering*, ASCE, 120(8), 934-955.

95. Liou, C.P. (1994). "Mass Imbalance Error of Waterhammer Equations and Leak Detection." *Journal of Fluids Engineering*, ASME, 116(1), March, 103-108.

96. Liou, J.C.P., and Tian, J. (1995). "Leak Detection - Transient Flow Simulation Approaches." *Journal of Energy Resources Technology*, Vol. 117, September, 243-248.

97. McInnis, D.A. (1992). *Comprehensive Hydraulic Analysis of Complex Pipe Systems.* PhD Thesis, University of Toronto, Canada.

98. McInnis, D.A., and Karney, B.W. (1990). "Application of energy equations in unsteady closed conduit flow." *Proceedings of the Canadian Society of Civil Engineers Annual Conference - First Bi-Annual Environmental Specialty Conference*, Hamilton, Ontario, Canada.

99. McInnis, D.A., and Karney, B.W. (1995). "Field Tests and Demand Models." *Journal of Hydraulic Engineering*, ASCE, 121(3), 218-231.

100. McInnis, D.A., Karney, B.W., and Axworthy, D.H. (1997). "Efficient Valve Representation in Fixed-Grid Characteristics Method." *Journal of Hydraulic Engineering*, ASCE, 123(8), August, 709-718.

101. Murphy, L.J., Dandy, G.C., and Simpson, A.R. (1994). "Optimum Design and Operation of Pumped Water Distribution Systems." *Conference on Hydraulics in Civil Engineering*, February, Institution of Engineers (Australia), Brisbane, Australia.

102. Murphy, L.J., Simpson, A.R., and Dandy, G.C. (1993). "Design of a Pipe Network Using Genetic Algorithms." *WATER*, AWWA, 20(4), August, 40-42.

103. Nash, G.A., and Karney, B.W. (1999). "Efficient Inverse Transient Analysis in Series Pipe Systems." *Journal of Hydraulic Engineering*, ASCE, 125(7), July, 761-764.

104. Nash, J.C., and Walker-Smith, M. (1987). *Nonlinear Parameter Estimation.* Marcel Dekker, Inc.

105. Neuman, S.P. (1973). "Calibration of Distributed Parameter Groundwater Flow Models Viewed as a Multiple-Objective Decision Process under Uncertainty." *Water Resources Research*, 9(4), August, 1006-1021.

106. Ohmi, M., Kyomen, S., and Usui, T. (1985). "Numerical Analysis of Transient Turbulent Flow in a Liquid Line." *Bulletin of the Japanese Society of Mechanical Engineers*, 28(249), 2638-2644.

107. Ormsbee, L.E. (1989). "Implicit Network Calibration." *Journal of Water Resources Planning and Management*, ASCE, 115(2), 243-257.

108. Ormsbee, L.E., and Chase, D.V. (1988). "Hydraulic Network Calibration using Nonlinear Programming." *International Symposium on Computer Modelling of Water Distribution Systems*, May, Kentucky, 31-44.

109. Ormsbee, L.E., and Wood, D.J. (1985). "Explicit Pipe Network Calibration." *Journal of Water Resources Planning and Management*, ASCE, 112(2), 166-182.

110. Pezzinga, G. (1999). "Quasi-2D Model for Unsteady Flow in Pipe Networks." *Journal of Hydraulic Engineering*, ASCE, 125(7), July, 676-685.

111. Press, W.H., Teukolsky, S.A., Vetterling, W.T., and Flannery, B.P. (1992). *Numerical Recipes: The Art of Scientific Computing.* Cambridge University Press, Cambridge, U.K.

112. Propson, T.P. (1972). "Discussion of Unsteady Flow Calculations by Numerical Methods." by V.L. Streeter, *Journal of Basic Engineering*, Transactions of the ASME, Vol. 94, 465-466.

113. Pudar, R.S., and Liggett, J.A. (1992). "Leaks in Pipe Networks." *Journal of Hydraulic Engineering*, ASCE, 118(7), 1031-1046.

114. Raabe, J., and Olbrich, S. (1992). "The Role of Turbulence on Maximum Water Hammer Due to 2D Theory in Axial Symmetric Pipe Flow and Corresponding LD Measurement." *16th Symposium of the IAHR*, Section on Hydraulic Machinery and Cavitation, 14-18 September,Sao Paulo, Brazil.

115. Rahal, C.M., Sterling, M.J.H., and Coulbeck, B. (1980). "Parameter Tuning for Simulation Models of Water Distribution Networks." *Institution of Civil Engineers*, Part 2, Vol. 69, 751-762.

116. Rasmussen, E. (1997). "The Pipes Sound Off." *Civil Engineering: Engineered Design and Construction*, ASCE, June, 52-53.

117. Richardson, J.T., Palmer, M.R., Liepins, G., and Hillard, M. (1989). "Some Guidelines for Genetic Algorithms with Penalty Functions." *Proceedings of the 3rd International Conference on Genetic Algorithms*, Edited by J.D. Schaffer, M. Kaufmann Publishers, San Mateo, California.

118. Rorabaugh, B.C. (1997). *Digital Filter Designer's Handbook (with C++ Algorithms)*. 2nd Edition, S.S. Chapman (Editor), McGraw-Hill, USA.

119. Rouse, H. (1978). *Elementary Mechanics of Fluids*. Dover Publications, Inc., New York, USA.

120. Safwat, H.H., and Polder, J. (1973). "Friction – Frequency Dependence for Oscillatory Flows in Circular Pipe." *Journal of the Hydraulics Division*, ASCE, 99(HY11), November, 1933-1945.

121. Sánchez-Bribiesca, J.L. (1981). "A Finite Difference Method to Evaluate Water Hammer Phenomena." *Journal of Hydrology*, 51(1), 305-311.

122. Savic, D.A., and Walters, G.A. (1995). "Genetic Algorithm Techniques for Calibrating Network Models." *Report No. 95/12*, Centre for Systems and Control Engineering, University of Exeter, Devon, U.K.

123. Schlichting, H. (1955). *Boundary Layer Theory*, McGraw Hill, New York, USA.

124. Shamir, U., and Howard, C.D.D. (1968). "Water Distribution Systems Analysis." *Journal of the Hydraulics Division*, ASCE, 94(1), January, 219-234.

125. Shamir, U., and Howard, C.D.D. (1977). "Engineering Analysis of Water Distribution Systems." *Journal of the American Water Works Association*, 69(9), September, 510-514.

126. Shimada, M. (1988). "Time-Marching Approach for Pipe Steady Flows." *Journal of Hydraulic Engineering*, 114(11), ASCE, November, 1301-1319.

127. Shuy, E.B. (1985). *Friction Loss in Unsteady Laminar and Turbulent Flows in Smooth Round Pipes*. PhD Thesis, The University of Queensland, Australia.

128. Shuy, E.B. (1996). "Wall Shear Stress in Accelerating and Decelerating Turbulent Pipe Flows." *Journal of Hydraulic Research*, IAHR, 34(2), 173-183.

129. Shuy, E.B., and Apelt, C.J. (1983). "Friction Effects in Unsteady Pipe Flows." *Proceedings of the 4th International Conference on Pressure Surges*, Bath UK, 21-23 September, BHRA Fluid Engineering, 147-164.

130. Shuy, E.B., and Apelt, C.J. (1987). "Experimental Studies of Unsteady Wall Shear Stress in Turbulent Flow in Smooth Round Pipes." *Conference on Hydraulics in Civil Engineering 1987*, Melbourne, Australia, 137-341.

131. Sibetheros, I.A., Holley, E.R., and Branski, J.M. (1991). "Spline Interpolations for Water Hammer Analysis." *Journal of Hydraulic Engineering*, ASCE, 117(10), 1332-1351.

132. Silva-Araya, W.F., and Chaudhry, M.H. (1997). "Computation of Energy Dissipation in Transient Flow." *Journal of Hydraulic Engineering*, ASCE, 123(2), February, 108-115.

133. Simpson, A.R., and Bergant, A. (1994). "Developments in Column Separation Experimentation for Pipelines." *Journal of Hydraulic Research*, IAHR, March, 183-194.

134. Simpson, A.R., and Goldberg, D.E. (1994). "Pipeline Optimisation via Genetic Algorithms: from Theory to Practice." *2nd International Conference on Water Pipeline Systems*, Edinburgh, Scotland, May, 309-320.

135. Simpson, A.R., Dandy, G.C., and Murphy, L.J (1994). "Genetic Algorithms Compared to Other Techniques for Pipeline Optimisation." *Journal of Water Resources Planning and Management*, ASCE, 120(4), July/August, 423-443.

136. Simpson, A.R., Murphy, L.J., and Dandy, G.C. (1993). "Pipe Network Optimisation Using Genetic Algorithms." *Water Resources Planning and Management Division Specialty Conference*, ASCE, Seattle, Washington, May.

137. Sou, L., and Wylie, E.B. (1989). "Impulse Response Method for Frequency-Dependent Pipeline Transients." *Journal of Fluids Engineering*, ASME, Vol. 111, December,478-483.

138. Stephenson, D. (1989). *Pipeline Design for Water Engineers*. Elsevier Science Publishers B.V., Amsterdam, the Netherlands.

139. Stoner, M.A. (1970). "Sensitivity Analysis Applied to a Steady State Model of Natural Gas Transportation Systems." *45th Annual Full Meeting of the Society of Petroleum Engineers of AIME*, Houston, Texas, October 4-7.

140. Streeter, V.L. (1942). "The Kinetic Energy and Momentum Correction Factors for Pipes and Open Channels of Great Width." *Civil Engineering*, ASCE, 12(4), 212-213.

141. Streeter, V.L. (1969). "Water Hammer Analysis." *Journal of the Hydraulics Division*, ASCE, 95(HY6), 1959-1972.

142. Streeter, V.L. (1972). "Unsteady Flow Calculations by Numerical Methods." *Journal of Basic Engineering*, Transactions of the ASME, Vol. 94, 457-465.

143. Streeter, V.L., and Lai, C. (1962). "Waterhammer Analysis Including Friction." *Journal of the Hydraulics Division*, ASCE, 88(HY3), May, 79-112.

144. Streeter, V.L., and Wylie, E.B. (1983). *Fluid Mechanics*. McGraw-Hill Book Company.

145. Suzuki, K., Taketomi, T., and Sato, S. (1991). "Improving Zielke's Method of Simulating Frequency-Dependent Friction in Lamina Liquid Pipe Flow." *Journal of Fluids Engineering, Transactions of the ASME*, Vol. 113, 569-573.

146. Sved, G., Schmid, L.J. and Simpson, A.R. (1991). "Minimum Weight Structures Designed by Genetic Algorithms." *Computational Mechanics*, Vol. 1, Cheung, Y.K. *et al.* (Editors), A.A. Balkema, Rotterdam, 317-322.

147. Svingen, B. (1996). *Fluid Structure Interaction in Piping Systems*. PhD Thesis, September, Faculty of Mechanical Engineering, The Norwegian University of Science and Technology, Norway.

148. Swamee, P.K., and Jain, A.K. (1976). "Explicit Equations for Pipe-Flow Problems." *Journal of the Hydraulics Division*, ASCE, 102(HY5), 657-664.

149. Tang, K.W., Brunone, B., Karney, B.W., and Rossetti, A. (2000). "Role and Characterisation of Leaks Under Transient Conditions." *2000 Joint Conference on Water Resources Engineering and Water Resources Planning & Management*, ASCE, July 30-August 2, Minneapolis, USA.

150. Theodoulides, P., Mavroudes, V., and Hurst, C. (1995). "The Leakage Control Policy of Nicosia, Cyprus." *Water Resources Management under Drought or Water Shortage Conditions*, Proceedings of the EWRA 95 Symposium, Nicosia, Cyprus, 14-18 March, 185-189.

151. Thierens, D., and Goldberg, D.E. (1993). "Mixing in Genetic Algorithms." 5^{th} *International Conference on Genetic Algorithms*, Urbana, Illinois, 38-45.

152. Thyer, M., Kuczera, G., and Bates, B.C. (1999). "Probabilistic Optimization for Conceptual Rainfall-Runoff Models: A Comparison of the Shuffled Complex

Evolution and Simulated Annealing Algorithms." *Water Resources Research*, 35(3), March, 767-773.

153. Tijsseling, A.S., and Lavooij, C.S.W. (1990). "Waterhammer with Fluid-Structure Interaction." *Applied Scientific Research*, Vol. 47, 273-285.

154. Trikha, A.K. (1975). "An Efficient Method for Simulating Frequency-Dependent Friction in Transient Liquid Flow." *Journal of Fluids Engineering, Transactions of the ASME*, Vol. 97, 97-105.

155. Tye, I. (2000). *Optimal Design of Stormwater Wetlands.* MSc Thesis, Department of Civil and Environmental Engineering, The University of Adelaide, Australia.

156. Uchida, S. (1956). "The Pulsating Viscous Flow Superposed on the Steady Laminar Motion of Incompressible Fluid in a Circular Pipe." *Zeitschrift für angewandte Mathematik und Physik*, Vol. 7, 403-422.

157. Vardy, A.E. (1992). "Approximating Unsteady Friction at High Reynolds Numbers." *International Conference on Unsteady Flow and Fluid Transients*, Hydraulics Research Wallingford, September 29 - October 1, Durham, England, 21-29.

158. Vardy, A.E., and Brown, J.M. (1996). "On Turbulent, Unsteady, Smooth-Pipe Friction." *Pressure Surges and Fluid Transients*, BHR Group, 289-311.

159. Vardy, A.E., and Hwang, K-L (1991). "A Characteristics Model of Transient Friction in Pipes." *Journal of Hydraulic Research*, 29(5), 669-684.

160. Vardy, A.E., Hwang, K-L, and Brown, J.M. (1993). "A Weighting Function Model of Transient Turbulent Pipe Friction." *Journal of Hydraulic Research*, IAHR, 31(4), 533-548.

161. Vela, A., Pérez, R., and Espert, V. (1991). "Incorporation of Leakages in the Mathematical Model of a Water Distribution Network." *Proceedings of the 2nd International Conference on Computer Methods in Water Resources*, Marrakesh, Morocco, 20-22 February, 245-257.

162. Vela, A.F., Espert, V., and Fuertes, V.S. (1995). "General Overview of Unaccounted for Water in Water Distribution Systems." In: *Improving Efficiency and Reliability in Water Distribution Systems*, Water Science and Technology Library, Volume 14, E. Cabrera and A.F. Vela (Editors), Kluwer Academic, Boston, 61-96.

163. Vennatrø, R. (1996). "Unsteady Friction Pipelines." *18th IAHR Symposium on Hydraulic Machinery and Cavitation*, Valencia, Spain, Vol. 2, 819-826.

164. Verwey, A., and Yu, J.H. (1993). "A Space-Compact High-Order Implicit Scheme for Water Hammer Simulations." *XXVth IAHR Congress*, Vol. 5, August, Tokyo, Japan.

165. Vítkovský, J.P., and Simpson, A.R. (1997). "Calibration and Leak Detection in Pipe Networks Using Inverse Transient Analysis and Genetic Algorithms." *Research Report No. R157*, August, Department of Civil and Environmental Engineering, The University of Adelaide, Australia.

166. Vítkovský, J.P., Simpson, A.R., and Lambert, M.F. (2000). "Leak Detection and Calibration Using Transients and Genetic Algorithms." *Journal of Water Resources Planning and Management*, ASCE, 126(4), July/August, 262-265.

167. Waller, R.O., Hawes, R.D., and Hudson, W.D. (1969). "Joint Discussion: Locating Leaks in Mains and Services." *Journal of the American Water Works Association*, 62(7), July, 403-406.

168. Walski, T.M. (1983). "Technique for Calibrating Network Models." *Journal of Water Resources Planning and Management*, ASCE, 109(4), 360-372.

169. Walski, T.M. (1986). "Case Study: Pipe Network Model Calibration Issues." *Journal of Water Resources Planning and Management*, ASCE, 112(2), 238-249.

170. Wang, G.Z., Fang, C.Z., and Wang K.F. (1991). "State Estimation and Leak Detection and Location in Pipeline." *Proceedings of the 1991 International Conference on Industrial Electronics, Control and Instrumentation*, Kobe, Japan, 28 October - 1 November, 155-160.

171. Watt, C.S., and Boldy, A.P., and Hobbs, J.M. (1980). "Combination of Finite Difference and Finite Element Techniques in Hydraulic Transient Problems." *Proceedings of the 3rd International Conference on Pressure Surges*, Canterbury, England, March 25th-27th, BHRA Fluid Engineering, 43-62.

172. Weil, G.J., Graf, R.J., and Forister, L.M. (1994). "Remote Sensing Pipeline Rehabilitation Methodologies Based upon the Utilisation of Infrared Thermography." In: *Urban Rehabilitation Programs and Techniques*, W.A. Macaitis (Editor), ASCE, 173-181.

173. Weisstein, E. (2000) *Eric Weisstein's World of Mathematics*, Wolfram Research, Internet Address: http://mathworld.wolfram.com

174. Wiggert, D.C. (1968). "Unsteady Flow in Lines with Distributed Leakage." *Journal of the Hydraulics Division*, ASCE, 94(1), January, 143-162.

175. Wood, D.J. (1980). *KYPIPE Users Manual: Computer Analysis of Flow in Pipe Networks Including Extended Period Simulations.* Department of Civil Engineering, University of Kentucky.

176. Wood, D. (1996). *KYPIPE3 Auxiliary Modules.* University of Kentucky, (Frey Water Engineering, Arlington Heights, Illinois), USA.

177. Wood, D.J., and Funk, J.E. (1970). "A Boundary-Layer Theory for Transient Viscous Losses in Turbulent Flow." *Journal of Basic Engineering*, ASME, December, 865-873.

178. Wood, D.J., and Reddy, L.S. (1995). "Using Variable Speed Pumps to Reduce Leakage and Improve Performance." In: *Improving Efficiency and Reliability in Water Distribution Systems*, Water Science and Technology Library, Volume 14, E. Cabrera and A.F. Vela (Editors), Kluwer Academic, Boston, 135-164.

179. Wu, Z-Y. (1994). *Automatic Model Calibration by Simulating Evolution.* MSc Thesis, Hydroinformatics Branch, I.H.E., Delft, The Netherlands.

180. Wylie, E.B. (1983). "The Microcomputer and Pipeline Transients." *Journal of Hydraulic Engineering*, ASCE, 109(12), 1723-1739.

181. Wylie, E.B. (1984). "Fundamental Equations of Waterhammer." *Journal of Hydraulic Engineering*, ASCE, 110(4), 539-542.

182. Wylie, E.B. (1997). "Frictional Effects in Unsteady Turbulent Pipe Flows." *Applied Mechanics Review*, ASME, 50(11), Part 2, November, 241-244.

183. Wylie, E.B. (2000). "Steady State in Hydraulic Systems by Marching Methods" *Safe Design and Operation of Industrial Pipe Systems: 8th International Conference on Pressure Surges*, BHR Group, The Hague, The Netherlands, 12-14 April, 351-361.

184. Wylie, E.B., and Streeter, V.L. (1993). *Fluid Transients in Systems.* Englewood Cliffs, New Jersey, U.S.A.

185. Yang, J.C., and Hsu, E.L. (1990). "Time-Line Interpolation for Solution of the Dispersion Equation." *Journal of Hydraulic Research*, 28(4), 503-523.

186. Yevjevich, V. (1972). *Probability and Statistics in Hydrology.* Water Resources Publications, Fort Collins, Colorado, USA.

187. Young, A.D. (1989). *Boundary Layers.* BSP Professional Books, Blackwell Scientific Publications Ltd., Great Britain.

188. Zielke, W. (1968). "Frequency-Dependent Friction in Transient Pipe Flow." *Journal of Basic Engineering*, ASME, 90(1), 109-115.

Appendix A

Calculation of Parameter, Temporal and Spatial Derivatives for a Simple System

This appendix clarifies new calculation methods for parameter (Section 4.4), temporal and spatial derivatives (both in Section 4.6). The parameter derivatives are used in the Levenberg-Marquardt minimisation method, the temporal and spatial derivatives in MOC grid interpolations and in unsteady friction models. An example network demonstrates these derivative calculation methods. To begin, the forward transient problem is solved. Numerical results show the performance of the different derivative computation methods. All calculations are performed implicitly on a rectangular grid using the method of characteristics and linearisation of friction and leak flow terms.

A.1 Layout of the Simple System

The simple system consists of a pipeline connecting two reservoirs (Figure A.1). There is a single leak midway along the pipeline. The pipeline is similar to the experimental pipeline in the Robin Hydraulics Laboratory at Adelaide University. The pipeline is 37.2 m in length with a diameter of 22.1 mm. The size of the leak, given by the lumped leak coefficient $C_d A_L$, is 6.5×10^{-7} m^2. The head at Tank 1 is 30 m and at Tank 2 is 20 m.

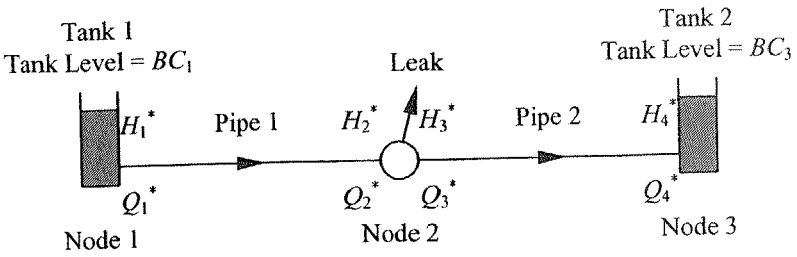

Figure A.1 Simple System with Leakage

There are 8 unknown variables at each time step (all the possible H and Q's are initially designated as unknown variables although some of them may be set to constant values during the transient if they are boundary conditions). These variables are four nodal heads (H_1^*, H_2^*, H_3^* and H_4^*) and four flows (one flow at each end of each pipe section – Q_1^*, Q_2^*, Q_3^* and Q_4^*). Increasing the head at tank 2 from 20m to 30m and then restoring it to its initial value over 0.2 s initiates the transient event. The increase in head may be due to an increase in the water level in the tank or by controlling a valve. The initial flow direction (and definition of positive flow) is from node 1 to node 3. The pipeline is split into two reaches (either side of the leak). The wave speed is 1,319 m/s. Each pipe uses two different friction factors (for illustrative purposes) of value 0.030 and 0.020 for pipe 1 and 2 respectively. The time step used in the analysis is 14 ms.

A.2 Calculation of the Forward Solution for the Simple System

Solution of the forward transient problem calculates the flows and pressure heads throughout the system during a transient event. The implicit forward transient problem defines a simultaneous system of equations for the pressure heads and flows relating conditions at one time step to the next time step. The system of simultaneous equations includes the continuity of flow at nodes, equality of heads at the nodes and the unsteady state governing equations along pipe reaches (solved using the method of characteristics). The solution of the forward transient problem uses a rectangular grid system, which has advantages over diamond grid systems when dealing with complex

pipe networks. The next sections define and solve the forward transient problem for the simple system.

The objective is to develop the following matrix form describing the forward transient problem:

$$[M]\{v^*\}=\{R\} \quad \text{(A.2.1)}$$

where $\{v^*\}$ = the vector of unknown heads and discharges at a particular time step within the transient event, $[M]$ = a coefficient matrix and $\{R\}$ = a right hand side vector. Eq. A.2.1 is a set of simultaneous, linearised equations relating flows and heads from one transient time step to another.

A.2.1 The Simultaneous System

For the example problem, the simultaneous system of nonlinear equations is comprised of four integrated compatibility equations (from the method of characteristics) in the two pipe reaches, two junction equations and two boundary conditions (see Figure A.2). This set of equations defines the calculation of the flows and heads at an unknown time step as a function of the flows and heads at a known time step. The nonlinear terms result from the friction term in the method of characteristics compatibility equations and from the leakage term in the continuity equation. Since the equations are nonlinear, and since the most economical way to solve them is by use of a linear equation solver, they require linearisation. The nonlinearities are then resolved by iteration.

A notation system is introduced to differentiate between variables at different time steps. Figure A.2 shows the notation convention for the simple system at a known time $t = t_0$ and an unknown time step $t = t_0 + \Delta t$. A superscript * on a variable denotes its value at the unknown time step at the current iteration. A superscript $'$ denotes an estimate of the variable from a previous iteration at the unknown time step. A variable with no superscript means that the variable is from the known time step and hence already known.

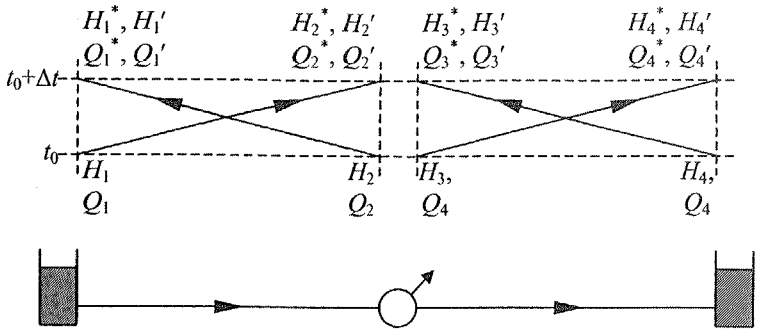

Figure A.2 Characteristic Grid and Notation for Simple System

Now the simultaneous system for the simple system is derived. A head boundary condition at each of the tanks is

$$H_1^* = BC_1 \quad \text{.....(A.2.2)}$$

$$H_4^* = BC_3 \quad \text{.....(A.2.3)}$$

The level of tank 1 changes with time (used to generate the transient event). Thus, the level of tank 1 (BC_1) is specified at each time step. The level of tank 2 is constant and is equal to BC_3. The head at each node, including the leak node, is unique so that

$$H_2^* - H_3^* = 0 \quad \text{.....(A.2.4)}$$

Assuming all nodes are at the same elevation, the leak quantity is

$$Q_L = C_d A_L \sqrt{2gH_L} \quad \text{.....(A.2.5)}$$

where Q_L = the leaking flow, C_d = coefficient of discharge, A_L = the area of the leak and H_L = the head at the leak. Continuity of mass at node 2 is expressed as

$$C_d A_L \sqrt{\frac{2g}{H_2'}} H_2^* - Q_2^* + Q_3^* = 0 \quad \text{.....(A.2.6)}$$

where flows out of the node are assumed to be positive and where the leak equation (Eq. A.2.5) has been linearised by expanding the square root in a series in H_2^* and neglecting all but the linear term. The introduction of a coefficient A_{N2} simplifies the equation of continuity at node 2 as

$$(A_{N2})H_2^* - Q_2^* + Q_3^* = 0 \quad \text{.....(A.2.7)}$$

where A_{N2} is

$$A_{N2} = C_d A_L \sqrt{\frac{2g}{H_2'}} \quad \text{.....(A.2.8)}$$

The integrated compatibility equation along the positive characteristic for pipe 1 is

$$H_2^* = H_1 - \frac{a_{P1}}{gA_{P1}}\left(Q_2^* - Q_1\right) - \frac{\Delta x f_{P1}}{2gD_{P1}A_{P1}^2}\frac{\left(Q_1 + Q_2^*\right)}{2}\frac{|Q_1 + Q_2'|}{2} \quad \text{.....(A.2.9)}$$

in which the pipe friction terms have been linearised and where a_{P1} = the wave speed in pipe 1, A_{P1} = the cross-sectional area of pipe 1, D_{P1} = the diameter of pipe 1, f_{P1} = the friction factor for pipe 1 and Δx = the reach length. Then, Eq. A.2.9 is rearranged, moving all known terms to the right hand side and all unknowns to the left hand side. The subscript P1 refers to the properties of pipe 1 and P2 is for pipe 2. Introduction of coefficients simplify Eq. A.2.9 to

$$H_2^* + \left(B_{P1}^+\right)Q_2^* = C_{P1}^+ \quad \text{.....(A.2.10)}$$

where the coefficients for the positive method of characteristic equation are

$$B_{P1}^+ = \frac{a_{P1}}{gA_{P1}} + \frac{\Delta x f_{P1}|Q_1 + Q_2'|}{8gD_{P1}A_{P1}^2} \quad \text{.....(A.2.11)}$$

$$C_{P1}^+ = H_1 + \left(\frac{a_{P1}}{gA_{P1}} - \frac{\Delta x f_{P1}|Q_1 + Q_2'|}{8gD_{P1}A_{P1}^2}\right)Q_1 \quad \text{.....(A.2.12)}$$

All of the H and Q terms in Eq. A.2.11 and Eq. A.2.12 are either known from the previous time step or known from the previous iteration of the linearised equations. The process is repeated for the integrated compatibility equation along the negative characteristic in pipe 1, as

$$H_1^* = H_2 + \frac{a_{P1}}{gA_{P1}}\left(Q_1^* - Q_2\right) + \frac{\Delta x f_{P1}}{2gD_{P1}A_{P1}^2}\frac{\left(Q_1^* + Q_2\right)}{2}\frac{|Q_1' + Q_2|}{2} \quad \text{.....(A.2.13)}$$

simplified to

$$H_1^* + B\left(C_{P1}^-\right)Q_1^* = C_{P1}^- \quad \text{.....(A.2.14)}$$

where

$$B_{P1}^- = -\frac{a_{P1}}{gA_{P1}} - \frac{\Delta x f_{P1}|Q_1' + Q_2|}{8gD_{P1}A_{P1}^2} \quad \text{.....(A.2.15)}$$

$$C_{P1}^- = H_2 - \left(\frac{a_{P1}}{gA_{P1}} - \frac{\Delta x f_{P1}|Q_1' + Q_2|}{8gD_{P1}A_{P1}^2}\right)Q_2 \quad \text{.....(A.2.16)}$$

Similar equations are developed for pipe 2. First, the integrated compatibility equation along the positive characteristic is

$$H_4^* = H_3 - \frac{a_{P2}}{gA_{P2}}\left(Q_4^* - Q_3\right) - \frac{\Delta x f_{P2}}{2gD_{P2}A_{P2}^2}\frac{\left(Q_3 + Q_4^*\right)}{2}\frac{|Q_3 + Q_4'|}{2} \quad \text{.....(A.2.17)}$$

simplified to

$$H_4^* + \left(B_{P2}^+\right)Q_4^* = C_{P2}^+ \quad \text{.....(A.2.18)}$$

where

$$B_{P2}^+ = \frac{a_{P2}}{gA_{P2}} + \frac{\Delta x f_{P2}|Q_3 + Q_4'|}{8gD_{P2}A_{P2}^2} \quad \text{.....(A.2.19)}$$

$$C_{P2}^+ = H_3 + \left(\frac{a_{P2}}{gA_{P2}} - \frac{\Delta x f_{P2}|Q_3 + Q_4'|}{8gD_{P2}A_{P2}^2}\right)Q_3 \quad \text{.....(A.2.20)}$$

Finally, the integrated compatibility equation along the negative characteristic in pipe 2 is

$$H_3^* = H_4 + \frac{a_{P2}}{gA_{P2}}\left(Q_3^* - Q_4\right) + \frac{\Delta x f_{P2}}{2gD_{P2}A_{P2}^2}\frac{\left(Q_3^* + Q_4\right)}{2}\frac{|Q_4' + Q_3|}{2} \quad \text{.....(A.2.21)}$$

simplified to

$$H_3^* + \left(B_{P2}^-\right)Q_3^* = C_{P2}^- \quad \text{.....(A.2.22)}$$

where

$$B_{P2}^- = -\frac{a_{P2}}{gA_{P2}} - \frac{\Delta x f_{P2}|Q_3' + Q_4|}{8gD_{P2}A_{P2}^2} \quad \text{.....(A.2.23)}$$

$$C_{P2}^- = H_4 - \left(\frac{a_{P2}}{gA_{P2}} - \frac{\Delta x f_{P2}|Q_3' + Q_4|}{8gD_{P2}A_{P2}^2}\right)Q_4 \quad \text{.....(A.2.24)}$$

The set of equations that make up the forward transient problem, given by Eqs. A.2.2 to A.2.24, are repeated for clarity:

$$H_1^* = BC_1$$

$$H_4^* = BC_3$$

$$H_2^* - H_3^* = 0$$

$$(A_{N2})H_2^* - Q_2^* + Q_3^* = 0$$

$$H_2^* + (B^+_{P1})Q_2^* = C^+_{P1}$$

$$H_1^* + (B^-_{P1})Q_1^* = C^-_{P1}$$

$$H_4^* + (B^+_{P2})Q_4^* = C^+_{P2}$$

$$H_3^* + (B^-_{P2})Q_3^* = C^-_{P1}$$

The set of linearised equations for the forward transient problem in matrix form is

$$\begin{bmatrix} 1 & 0 & 0 & 0 & 0 & 0 & 0 & 0 \\ 0 & 0 & 0 & 1 & 0 & 0 & 0 & 0 \\ 0 & 1 & -1 & 0 & 0 & 0 & 0 & 0 \\ 0 & A_{N2} & 0 & 0 & 0 & -1 & 1 & 0 \\ 0 & 1 & 0 & 0 & 0 & B_{P1}^{+} & 0 & 0 \\ 1 & 0 & 0 & 0 & B_{P1}^{-} & 0 & 0 & 0 \\ 0 & 0 & 0 & 1 & 0 & 0 & 0 & B_{P2}^{+} \\ 0 & 0 & 1 & 0 & 0 & 0 & B_{P2}^{-} & 0 \end{bmatrix} \begin{Bmatrix} H_1^* \\ H_2^* \\ H_3^* \\ H_4^* \\ Q_1^* \\ Q_2^* \\ Q_3^* \\ Q_4^* \end{Bmatrix} = \begin{Bmatrix} BC_1 \\ BC_3 \\ 0 \\ 0 \\ C_{P1}^{+} \\ C_{P1}^{-} \\ C_{P2}^{+} \\ C_{P2}^{-} \end{Bmatrix} \quad \text{.....(A.2.25)}$$

Eq. A.2.25 is referred to as the simultaneous system of the forward transient problem. It is written in a condensed form as

$$[M]\{v^*\} = \{R\} \quad \text{.....(A.2.26)}$$

where the coefficient matrix, $[M]$, contains the coefficients of the unknown variables, $\{v^*\}$, and the vector, {R} (sometimes called the right hand side vector) contains the constant terms. The terms denoted by a superscript ' (in Eqs. A.2.6, A.2.7, A.2.11, A.2.17 and A.2.21) are initially unknown and are assumed from the previous time step. Once the simultaneous system is solved for the current time step, the terms denoted by a superscript ' are updated (with the corresponding terms denoted by an asterisk). This process is repeated until further iteration does not change the values of the variables. Typically, three to four iterations produce good convergence. Because small time steps are taken, the values of the variables at the unknown time step are not that different than those at the known time step. Also, the nonlinearities occur only in the friction and leak terms, which do not contain derivatives. Thus, the iteration method finds good answers and a true nonlinear solution method is not necessary.

A.2.2 Numerical Results for the Forward Solution

The solution of the forward transient problem, described for a single time step in Section A.2.1, is applied to the simple system for successive time steps. The results for the heads in the simple system are shown in Figure A.3. The boundary conditions are the heads at nodes 1 and 3.

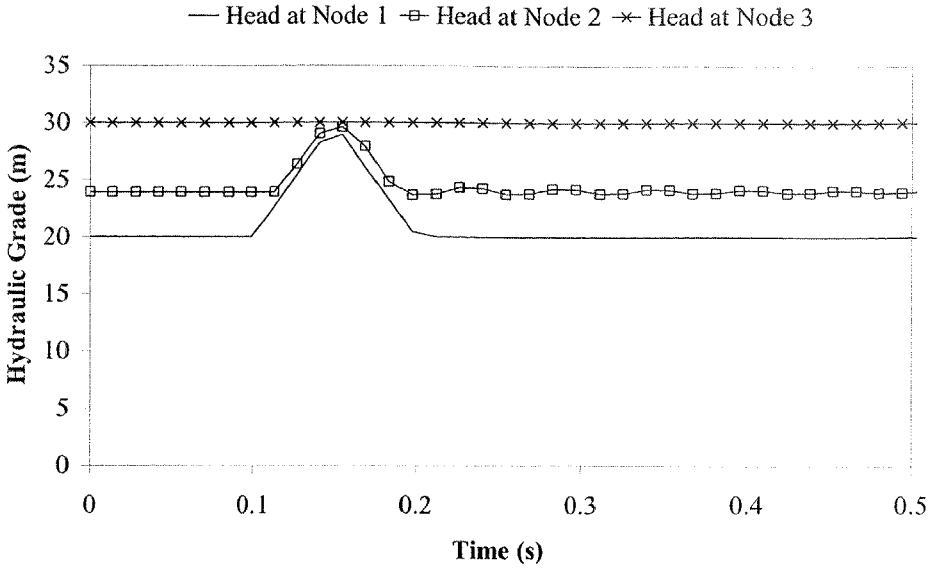

Figure A.3 Hydraulic Grade at Nodes in the Simple System (Computations at Every 14 ms)

A.3 Calculation of Parameter Derivatives for the Simple System

The inverse transient method uses parameter derivatives (partial derivatives with respect to the parameters) for the determination of parameters such as leaks and friction factors. Efficient and fast algorithms such as the Levenberg-Marquardt technique use properties like the Jacobian, gradient and Hessian. Parameter derivatives form these properties. Therefore, fast and accurate calculation of parameter derivatives is essential. The following sections show a number of different parameter derivative calculation methods.

A.3.1 Divided Difference Method for Parameter Derivatives

The divided difference method for the calculation of the parameter derivatives is the simplest. This method requires (N_P + 1) solutions of the forward transient problem for N_P parameters. The forward transient problem is solved using a base set of parameters, then one extra solution for each parameter with a perturbation in that parameter. The divided difference method is a first order approximation of the partial derivative (found

using a Taylor series expansion). The divided difference approximation for the partial derivative of variable ν_j^* with respect to a parameter a_i is

$$\frac{\partial \nu_j^*}{\partial a_i} = \frac{\nu_j^*(\mathbf{a}+\delta a_i) - \nu_j^*(\mathbf{a})}{\delta a_i} \quad \text{(A.3.1)}$$

Decreasing the size of the perturbation, δa_i, increases the accuracy of this method. However, if the perturbation is too small, problems with round-off errors occur, and if it is too large then the derivative is badly approximated.

A.3.2 Adjoint / Analytic Method for Parameter Derivatives

The parameter derivatives may be found using the analytic or adjoint methods (both one and the same, see Sections 4.4.2 and 4.4.3). These methods differentiate the simultaneous system of equations (describing the forward transient problem as shown in Section A.2.1) with respect to each of the parameters. The differentiated system of equations for the forward transient problem is

$$[M]\left\{\frac{\partial \nu^*}{\partial a_i}\right\} = \left\{\frac{\partial R}{\partial a_i}\right\} - \left[\frac{\partial M}{\partial a_i}\right]\{\nu^*\} \quad \text{(A.3.2)}$$

where the matrix $[\partial M/\partial a_i]$ and the vector $\{\partial R/\partial a_i\}$ are the partial derivatives of each element of $[M]$ and $\{R\}$ with respect to each parameter, where a_i may be a lumped leak coefficient or a friction factor. The solution of Eq. A.3.2 for $\{\partial \nu^*/\partial a_i\}$ yields the parameter derivatives for a_i. The method is illustrated by calculation in the simple system. The rows of $[M]$ and $\{R\}$ that correspond to the boundary conditions contain no dependence on any parameters (friction factors or lumped leak coefficients), e.g. Eqs. A.2.2, A.2.3 and A.2.4 for the simple system; therefore, their partial derivatives are equal to zero. The leak continuity equation (Eq. A.2.7) is

$$(A_{N2})H_2^* - Q_2^* + Q_3^* = 0$$

The coefficient A_{N2} that corresponds to the continuity at node 2 (Eq. A.2.8) does contain a dependence on both the leak coefficient and friction factors (through H_2). In the notation used in the following section, although not strict in a mathematical sense, if an equation does not contain a parameter, that parameter is called independent; if an equation does contain that parameter, the parameter is dependent. A_{N2} is

$$A_{N2} = C_d A_L \sqrt{\frac{2g}{H_2'}}$$

Differentiating A_{N2} with respect to an independent parameter (i.e. $a_i = f_{P1}$ or f_{P2}) gives

$$\frac{\partial A_{N2}}{\partial a_i} = -\frac{C_d A_L}{2}\sqrt{\frac{2g}{\left(H_2^*\right)^3}}\frac{\partial H_2'}{\partial a_i} \quad \text{.....(A.3.3)}$$

and differentiating A_{N2} with respect to a dependent parameter (i.e. $a_i = C_d A_L$) gives

$$\frac{\partial A_{N2}}{\partial a_i} = -\frac{C_d A_L}{2}\sqrt{\frac{2g}{\left(H_2^*\right)^3}}\frac{\partial H_2'}{\partial a_i} + \sqrt{\frac{2g}{H_2^*}} \quad \text{.....(A.3.4)}$$

The nonlinear term (H_2' in Eq. A.2.8) is known since the forward transient problem has been solved already for the current time step, thus H_2 is now superscripted with a *. Knowledge of the partial derivative $\partial H_2/\partial a_i$ at the current time step is needed; however, $\partial H_2/\partial a_i$ is not known and therefore $[\partial M/\partial a_i]$ is unknown. This problem is overcome by initially guessing $\partial H_2/\partial a_i$ then updating when new values are computed, forming an iterative process. $\partial H_2/\partial a_i$ behaves like a nonlinear term in the forward transient problem (Eq. A.2.25) so it is superscripted with a $'$ to signify that it must be updated, as shown in Eqs. A.3.3 and A.3.4.

Now, the coefficients of Eq. A.2.25 are considered. All of the coefficients of the unknown head variables have no dependence on the parameters and thus their derivatives are equal to zero (see, for example, Eq. A.2.4). The coefficient in $[M]$ corresponding to the positive characteristic in pipe 1 (Eq. A.2.10) is

$$B_{P1}^+ = \frac{a_{P1}}{gA_{P1}} + \frac{\Delta x f_{P1}\left|Q_1 + Q_2'\right|}{8gD_{P1}A_{P1}^2}$$

Differentiating B_{P1}^+ with respect to an independent parameter (e.g. $C_d A_L$ and f_{P2}) and a dependent parameter (e.g. f_{P1}) results in

$$\frac{\partial B_{P1}^+}{\partial a_i} = \frac{\Delta x f_{P1}\phi_{(Q_1+Q_2')}}{8gD_{P1}A_{P1}^2}\left(\frac{\partial Q_1}{\partial a_i} + \frac{\partial Q_2'}{\partial a_i}\right) \quad \text{.....(A.3.5)}$$

$$\frac{\partial B_{P1}^+}{\partial a_i} = \frac{\Delta x f_{P1}\phi_{(Q_1+Q_2^*)}}{8gD_{P1}A_{P1}^2}\left(\frac{\partial Q_1}{\partial a_i} + \frac{\partial Q_2'}{\partial a_i}\right) + \frac{\Delta x\left|Q_1 + Q_2^*\right|}{8gD_{P1}A_{P1}^2} \quad \text{.....(A.3.6)}$$

A sign operator, named ϕ_x, is defined which returns a value of +1 if the argument x is greater or equal to zero and –1 if less than zero. Thus the sign operator produces a unit

response depending on the sign of its argument. This process is repeated for the negative characteristic in pipe 1. The coefficient from Eq. A.2.15 is

$$B_{P1}^{-} = -\frac{a_{P1}}{gA_{P1}} - \frac{\Delta x f_{P1}|Q_1' + Q_2|}{8gD_{P1}A_{P1}^2}$$

Differentiating Eq. A.2.15 with respect to an independent parameter and dependent parameter respectively produces

$$\frac{\partial B_{P1}^{-}}{\partial a_i} = -\frac{\Delta x f_{P1}\phi_{(Q_1^*+Q_2)}}{8gD_{P1}A_{P1}^2}\left(\frac{\partial Q_1'}{\partial a_i} + \frac{\partial Q_2}{\partial a_i}\right) \quad \text{(A.3.7)}$$

$$\frac{\partial B_{P1}^{-}}{\partial a_i} = -\frac{\Delta x f_{P1}\phi_{(Q_1^*+Q_2)}}{8gD_{P1}A_{P1}^2}\left(\frac{\partial Q_1'}{\partial a_i} + \frac{\partial Q_2}{\partial a_i}\right) - \frac{\Delta x|Q_1^* + Q_2|}{8gD_{P1}A_{P1}^2} \quad \text{(A.3.8)}$$

The differentiation is repeated for pipe 2 where the dependent parameter is the friction in pipe 2. For the positive characteristic in pipe 2 (Eq. A.2.19), the differentiated coefficient for an independent parameter (e.g., C_dA_L and f_{P1}) and dependent parameter (e.g., f_{P2}) are

$$\frac{\partial B_{P2}^{+}}{\partial a_i} = \frac{\Delta x f_{P2}\phi_{(Q_3+Q_4^*)}}{8gD_{P2}A_{P2}^2}\left(\frac{\partial Q_3}{\partial a_i} + \frac{\partial Q_4'}{\partial a_i}\right) \quad \text{(A.3.9)}$$

$$\frac{\partial B_{P2}^{+}}{\partial a_i} = \frac{\Delta x f_{P2}\phi_{(Q_3+Q_4^*)}}{8gD_{P2}A_{P2}^2}\left(\frac{\partial Q_3}{\partial a_i} + \frac{\partial Q_4'}{\partial a_i}\right) + \frac{\Delta x|Q_3 + Q_4^*|}{8gD_{P2}A_{P2}^2} \quad \text{(A.3.10)}$$

For the negative compatibility equation coefficient in pipe 2 (Eq. A.2.23), the differentiated coefficient for an independent parameter and dependent parameter are

$$\frac{\partial B_{P2}^{-}}{\partial a_i} = -\frac{\Delta x f_{P2}\phi_{(Q_3^*+Q_4)}}{8gD_{P2}A_{P2}^2}\left(\frac{\partial Q_3'}{\partial a_i} + \frac{\partial Q_4}{\partial a_i}\right) \quad \text{(A.3.11)}$$

$$\frac{\partial B_{P2}^{-}}{\partial a_i} = -\frac{\Delta x f_{P2}\phi_{(Q_3^*+Q_4)}}{8gD_{P2}A_{P2}^2}\left(\frac{\partial Q_3'}{\partial a_i} + \frac{\partial Q_4}{\partial a_i}\right) - \frac{\Delta x|Q_3^* + Q_4|}{8gD_{P2}A_{P2}^2} \quad \text{(A.3.12)}$$

The total $[\partial M/\partial a_i]$ matrix for the simple system is

$$\left[\frac{\partial M}{\partial a_i}\right]=\begin{bmatrix} 0 & 0 & 0 & 0 & 0 & 0 & 0 & 0 \\ 0 & 0 & 0 & 0 & 0 & 0 & 0 & 0 \\ 0 & 0 & 0 & 0 & 0 & 0 & 0 & 0 \\ 0 & \partial A_{N2}/\partial a_i & 0 & 0 & 0 & 0 & 0 & 0 \\ 0 & 0 & 0 & 0 & 0 & \partial B_{P1}^{+}/\partial a_i & 0 & 0 \\ 0 & 0 & 0 & 0 & \partial B_{P1}^{-}/\partial a_i & 0 & 0 & 0 \\ 0 & 0 & 0 & 0 & 0 & 0 & 0 & \partial B_{P2}^{+}/\partial a_i \\ 0 & 0 & 0 & 0 & 0 & 0 & \partial B_{P2}^{-}/\partial a_i & 0 \end{bmatrix} \quad \text{....(A.3.13)}$$

This matrix is sparse and must be iterated to resolve the terms that contain partial derivatives of variables from the unknown time step. $[\partial M/\partial a_i]$ is different for each parameter.

Like the $[M]$ matrix, the $\{R\}$ vector must also be differentiated with respect to the parameters. Again, the boundary condition terms are not dependent on the parameters and thus their partial derivatives are equal to zero. The elements that correspond to the characteristic equations, however, do have a dependence on the parameters. For the element of $\{R\}$ that corresponds to the positive characteristic in pipe 1 (Eq. A.2.12), its partial derivative with respect to an independent parameter (C_dA_L and f_{P2}) and dependent parameter (f_{P1}) are

$$\frac{\partial C_{P1}^{+}}{\partial a_i}=\frac{\partial H_1}{\partial a_i}+\frac{\partial Q_1}{\partial a_i}\left(\frac{a_{P1}}{gA_{P1}}-\frac{\Delta x f_{P1}\left|Q_1+Q_2^{*}\right|}{8gD_{P1}A_{P1}^{2}}\right)-\frac{Q_1\Delta x f_{P1}\phi_{(Q_1+Q_2^{*})}}{8gD_{P1}A_{P1}^{2}}\left(\frac{\partial Q_1}{\partial a_i}+\frac{\partial Q_2'}{\partial a_i}\right) \quad \text{.....(A.3.14)}$$

$$\frac{\partial C_{P1}^{+}}{\partial a_i}=\frac{\partial H_1}{\partial a_i}+\frac{\partial Q_1}{\partial a_i}\left(\frac{a_{P1}}{gA_{P1}}-\frac{\Delta x f_{P1}\left|Q_1+Q_2^{*}\right|}{8gD_{P1}A_{P1}^{2}}\right)-\frac{Q_1\Delta x f_{P1}\phi_{(Q_1+Q_2^{*})}}{8gD_{P1}A_{P1}^{2}}\left(\frac{\partial Q_1}{\partial a_i}+\frac{\partial Q_2'}{\partial a_i}\right) \quad \text{.....(A.3.15)}$$
$$-\frac{Q_1\Delta x\left|Q_1+Q_2^{*}\right|}{8gD_{P1}A_{P1}^{2}}$$

Note the primed Q terms have been changed to asterisked terms as they are known from the solution of the forward transient problem. The coefficient that is associated with the negative compatibility equation in pipe 1 (Eq. A.2.16) is differentiated with respect to an independent parameter (C_dA_L and f_{P2}) and a dependent parameter (f_{P1}),

$$\frac{\partial C_{P1}^{-}}{\partial a_i}=\frac{\partial H_2}{\partial a_i}-\frac{\partial Q_2}{\partial a_i}\left(\frac{a_{P1}}{gA_{P1}}-\frac{\Delta x f_{P1}\left|Q_1^{*}+Q_2\right|}{8gD_{P1}A_{P1}^{2}}\right)+\frac{Q_2\Delta x f_{P1}\phi_{(Q_1^{*}+Q_2)}}{8gD_{P1}A_{P1}^{2}}\left(\frac{\partial Q_1'}{\partial a_i}+\frac{\partial Q_2}{\partial a_i}\right) \quad \text{.....(A.3.16)}$$

$$\frac{\partial C_{P1}^{-}}{\partial a_i} = \frac{\partial H_2}{\partial a_i} - \frac{\partial Q_2}{\partial a_i}\left(\frac{a_{P1}}{gA_{P1}} - \frac{\Delta x f_{P1}\left|Q_1^* + Q_2\right|}{8gD_{P1}A_{P1}^2}\right) + \frac{Q_2 \Delta x f_{P1}\phi_{(Q_1^*+Q_2)}}{8gD_{P1}A_{P1}^2}\left(\frac{\partial Q_1'}{\partial a_i} + \frac{\partial Q_2}{\partial a_i}\right) \quad \text{..... (A.3.17)}$$
$$+ \frac{Q_2 \Delta x\left|Q_1^* + Q_2\right|}{8gD_{P1}A_{P1}^2}$$

The differentiation is repeated for the coefficient corresponding to the positive compatibility equation in pipe 2 (Eq. A.2.20) with respect to an independent parameter (C_dA_L and f_{P1}) resulting in

$$\frac{\partial C_{P2}^{+}}{\partial a_i} = \frac{\partial H_3}{\partial a_i} + \frac{\partial Q_3}{\partial a_i}\left(\frac{a_{P2}}{gA_{P2}} - \frac{\Delta x f_{P2}\left|Q_3 + Q_4^*\right|}{8gD_{P2}A_{P2}^2}\right) - \frac{Q_3 \Delta x f_{P2}\phi_{(Q_3+Q_4^*)}}{8gD_{P2}A_{P2}^2}\left(\frac{\partial Q_3}{\partial a_i} + \frac{\partial Q_4'}{\partial a_i}\right) \text{.... (A.3.18)}$$

and with respect to a dependent parameter, which in this case is the friction in pipe 2 (f_{P2}),

$$\frac{\partial C_{P2}^{+}}{\partial a_i} = \frac{\partial H_3}{\partial a_i} + \frac{\partial Q_3}{\partial a_i}\left(\frac{a_{P2}}{gA_{P2}} - \frac{\Delta x f_{P2}\left|Q_3 + Q_4^*\right|}{8gD_{P2}A_{P2}^2}\right) - \frac{Q_3 \Delta x f_{P2}\phi_{(Q_3+Q_4^*)}}{8gD_{P2}A_{P2}^2}\left(\frac{\partial Q_3}{\partial a_i} + \frac{\partial Q_4'}{\partial a_i}\right) \quad \text{.... (A.3.19)}$$
$$- \frac{Q_3 \Delta x\left|Q_3 + Q_4^*\right|}{8gD_{P2}A_{P2}^2}$$

Finally, the coefficient of the negative compatibility equation in pipe 2 (Eq. A.2.24) is differentiated with respect to an independent parameter (C_dA_L and f_{P1}) and dependent parameter (f_{P2}) resulting in

$$\frac{\partial C_{P2}^{-}}{\partial a_i} = \frac{\partial H_4}{\partial a_i} - \frac{\partial Q_4}{\partial a_i}\left(\frac{a_{P1}}{gA_{P2}} - \frac{\Delta x f_{P2}\left|Q_3^* + Q_4\right|}{8gD_{P2}A_{P2}^2}\right) + \frac{Q_4 \Delta x f_{P2}\phi_{(Q_3^*+Q_4)}}{8gD_{P2}A_{P2}^2}\left(\frac{\partial Q_3'}{\partial a_i} + \frac{\partial Q_4}{\partial a_i}\right) \text{... (A.3.20)}$$

$$\frac{\partial C_{P2}^{-}}{\partial a_i} = \frac{\partial H_4}{\partial a_i} - \frac{\partial Q_4}{\partial a_i}\left(\frac{a_{P1}}{gA_{P2}} - \frac{\Delta x f_{P2}\left|Q_3^* + Q_4\right|}{8gD_{P2}A_{P2}^2}\right) + \frac{Q_4 \Delta x f_{P2}\phi_{(Q_3^*+Q_4)}}{8gD_{P2}A_{P2}^2}\left(\frac{\partial Q_3'}{\partial a_i} + \frac{\partial Q_4}{\partial a_i}\right) \quad \text{... (A.3.21)}$$
$$+ \frac{Q_4 \Delta x\left|Q_3^* + Q_4\right|}{8gD_{P2}A_{P2}^2}$$

The partial derivative of the vector $\{R\}$ with respect to a parameter a_i can now be formed as

$$\left\{\frac{\partial R}{\partial a_i}\right\} = \begin{Bmatrix} 0 \\ 0 \\ 0 \\ 0 \\ \partial C_{\mathrm{P1}}^{+}/\partial a_i \\ \partial C_{\mathrm{P1}}^{-}/\partial a_i \\ \partial C_{\mathrm{P2}}^{+}/\partial a_i \\ \partial C_{\mathrm{P2}}^{-}/\partial a_i \end{Bmatrix} \quad \text{.....(A.3.22)}$$

Again much like the $[\partial M/\partial a_i]$ matrix, the $\{\partial R/\partial a_i\}$ vector must be updated with new partial derivatives of the variables for the unknown time step. The system of equations (for the parameter derivative) describing the analytic or adjoint methods is restated as

$$[M]\left\{\frac{\partial \nu^*}{\partial a_i}\right\} = \left\{\frac{\partial R}{\partial a_i}\right\} - \left[\frac{\partial M}{\partial a_i}\right]\{\nu^*\} \quad \text{.....(A.3.23)}$$

The simultaneous system lends itself to LU decomposition since the $[M]$ matrix does not change (only the right hand side terms for different parameters changes). Combining the right hand side terms in Eq. A.3.23 produces

$$[M]\left\{\frac{\partial \nu^*}{\partial a_i}\right\} = \{K_{a_i}\} \quad \text{.....(A.3.24)}$$

where

$$\{K_{a_i}\} = \left\{\frac{\partial R}{\partial a_i}\right\} - \left[\frac{\partial M}{\partial a_i}\right]\{\nu^*\} \quad \text{.....(A.3.25)}$$

Furthermore, Eq. A.3.24 is written for all partial derivatives with respect to all parameters as

$$[M]\left[\left\{\frac{\partial \nu^*}{\partial f_{\mathrm{P1}}}\right\} \vdots \left\{\frac{\partial \nu^*}{\partial f_{\mathrm{P2}}}\right\} \vdots \left\{\frac{\partial \nu^*}{\partial (C_d A_L)}\right\}\right] = \left[\{K_{f_{\mathrm{P1}}}\} \vdots \{K_{f_{\mathrm{P2}}}\} \vdots \{K_{C_d A_L}\}\right] \quad \text{.....(A.3.26)}$$

Eq. A.3.26 is written simply as

$$[M]\left[\frac{\partial \nu^*}{\partial a}\right] = [K_a] \quad \text{.....(A.3.27)}$$

Eq. A.3.27 represents a system of equations for the calculation of the partial derivatives for all parameters. The matrix $[K_a]$ still requires iteration because elements of $[\partial \nu^*/\partial a]$ are contained within. Therefore, the parameter derivatives must first be guessed to form the $[\partial M/\partial a_i]$ matrix and $\{\partial R/\partial a_i\}$ vector (and ultimately $[K_a]$). Once the simultaneous system has been solved, the $[\partial M/\partial a_i]$ matrix and $\{\partial R/\partial a_i\}$ vector are updated using the

new values of the current parameter derivatives (an iterative process). The solution is found when there is little change in the parameter derivatives between iterations. Like the solution of the forward transient problem, 3 to 4 iterations are sufficient.

A.3.3 Fast Analytic Method for Parameter Derivatives

This section presents a fast analytic method for the calculation of the parameter derivatives. This method is similar to that used for solving for the variables in the simultaneous system of the forward transient problem. The simultaneous system for the parameter derivatives, using the fast analytic method, is

$$[M_D]\left[\frac{\partial v^*}{\partial a}\right] = [R_D] \quad \text{(A.3.28)}$$

Eq. A.3.28 is different from the simultaneous systems described in the preceding sections. The system of equations is linear for the unknown parameter derivatives, whereas the forward transient problem is nonlinear for the unknown variables. As a consequence, the system of equations does not require iteration, unlike the solutions to the forward transient problem and the analytic/adjoint method for parameter derivatives. To begin, the equations that allow the calculation of the current time step from the previous time step are differentiated with respect to an independent parameter a_i. The derivative of the boundary conditions from the forward solution (Eqs. A.2.2 and A.2.3) is zero because the boundary conditions have no dependence on any of the parameters,

$$\frac{\partial H_1^*}{\partial a_i} = \frac{\partial H_4^*}{\partial a_i} = 0 \quad \text{(A.3.29)}$$

The common head at node 2 (given by Eq. A.2.4) is not a boundary condition and differentiation with respect to a_i produces

$$\frac{\partial H_2^*}{\partial a_i} - \frac{\partial H_3^*}{\partial a_i} = 0 \quad \text{(A.3.30)}$$

The equation of continuity at node 2 for the leak (Eq. A.2.6) is differentiated with respect to an independent parameter resulting in

$$\frac{C_d A_L}{2}\sqrt{\frac{2g}{H_2^*}}\frac{\partial H_2^*}{\partial a_i} - \frac{\partial Q_2^*}{\partial a_i} + \frac{\partial Q_3^*}{\partial a_i} = 0 \quad \text{(A.3.31)}$$

Defining a coefficient D_{N2} simplifies Eq. A.3.31 to the linear expression with respect to the unknown partial derivatives,

$$(D_{N2})\frac{\partial H_2^*}{\partial a_i} - \frac{\partial Q_2^*}{\partial a_i} + \frac{\partial Q_3^*}{\partial a_i} = 0 \quad \text{.....(A.3.32)}$$

where the coefficient D_{N2} is defined as

$$D_{N2} = \frac{C_d A_L}{2}\sqrt{\frac{2g}{H_2^*}} \quad \text{.....(A.3.33)}$$

In this instance, the head at node 2 (H_2) is now known and, rather than being a superscripted prime term that needs updating, is now superscripted with a *. Differentiation of the positive characteristic compatibility equation (Eq. A.2.9) with respect to an independent parameter (Eq. A.3.34) results in

$$\frac{\partial H_2^*}{\partial a_i} = \frac{\partial H_1}{\partial a_i} - \frac{a_{P1}}{gA_{P1}}\left(\frac{\partial Q_2^*}{\partial a_i} - \frac{\partial Q_1}{\partial a_i}\right) - \frac{\Delta x f_{P1}\left|Q_1 + Q_2^*\right|}{4gD_{P1}A_{P1}^2}\left(\frac{\partial Q_1}{\partial a_i} + \frac{\partial Q_2^*}{\partial a_i}\right) \quad \text{.....(A.3.34)}$$

Again, the nonlinear terms have been previously resolved in the forward transient solution; thus the resulting expression for the parameter derivatives is linear. Introduction of some coefficients simplifies Eq. A.3.34 as

$$\frac{\partial H_2^*}{\partial a_i} + (E_{P1}^+)\frac{\partial Q_2^*}{\partial a_i} = F_{P1}^+ \quad \text{.....(A.3.35)}$$

where these coefficients are

$$E_{P1}^+ = \frac{a_{P1}}{gA_{P1}} + \frac{\Delta x f_{P1}\left|Q_1 + Q_2^*\right|}{4gD_{P1}A_{P1}^2} \quad \text{.....(A.3.36)}$$

$$F_{P1}^+ = \frac{\partial H_1}{\partial a_i} + \left(\frac{a_{P1}}{gA_{P1}} - \frac{\Delta x f_{P1}\left|Q_1 + Q_2^*\right|}{4gD_{P1}A_{P1}^2}\right)\frac{\partial Q_1}{\partial a_i} \quad \text{.....(A.3.37)}$$

The same process is repeated for the negative characteristic in pipe 1. The compatibility equation (Eq. A.2.13) is differentiated with respect to an independent parameter forming

$$\frac{\partial H_1^*}{\partial a_i} = \frac{\partial H_2}{\partial a_i} + \frac{a_{P1}}{gA_{P1}}\left(\frac{\partial Q_1^*}{\partial a_i} - \frac{\partial Q_2}{\partial a_i}\right) + \frac{\Delta x f_{P1}\left|Q_1^* + Q_2\right|}{4gD_{P1}A_{P1}^2}\left(\frac{\partial Q_1^*}{\partial a_i} + \frac{\partial Q_2}{\partial a_i}\right) \quad \text{.....(A.3.38)}$$

Coefficients, defined in Eqs. A.3.40 and A.3.41, simplify Eq.3.38 to

$$\frac{\partial H_1^*}{\partial a_i} + (E_{P1}^-)\frac{\partial Q_1^*}{\partial a_i} = F_{P1}^- \quad \text{.....(A.3.39)}$$

where

$$E_{P1}^{-} = -\frac{a_{P1}}{gA_{P1}} - \frac{\Delta x f_{P1}\left|Q_1^* + Q_2\right|}{4gD_{P1}A_{P1}^2} \quad \text{.....(A.3.40)}$$

$$F_{P1}^{-} = \frac{\partial H_2}{\partial a_i} - \left(\frac{a_{P1}}{gA_{P1}} - \frac{\Delta x f_{P1}\left|Q_1^* + Q_2\right|}{4gD_{P1}A_{P1}^2}\right)\frac{\partial Q_2}{\partial a_i} \quad \text{.....(A.3.41)}$$

Again, the process is repeated for the positive characteristic in pipe 2. The compatibility equation (Eq. A.2.17) is differentiated with respect to an independent parameter resulting in

$$\frac{\partial H_4^*}{\partial a_i} = \frac{\partial H_3}{\partial a_i} - \frac{a_{P2}}{gA_{P2}}\left(\frac{\partial Q_4^*}{\partial a_i} - \frac{\partial Q_3}{\partial a_i}\right) - \frac{\Delta x f_{P2}\left|Q_3 + Q_4^*\right|}{4gD_{P2}A_{P2}^2}\left(\frac{\partial Q_3}{\partial a_i} + \frac{\partial Q_4^*}{\partial a_i}\right) \quad \text{.....(A.3.42)}$$

Using coefficients defined in Eqs. A.3.44 and A.3.45, Eq. A.3.42 simplifies to

$$\frac{\partial H_4^*}{\partial a_i} + \left(E_{P2}^{+}\right)\frac{\partial Q_4^*}{\partial a_i} = F_{P2}^{+} \quad \text{.....(A.3.43)}$$

where

$$E_{P2}^{+} = \frac{a_{P2}}{gA_{P2}} + \frac{\Delta x f_{P2}\left|Q_3 + Q_4^*\right|}{4gD_{P2}A_{P2}^2} \quad \text{.....(A.3.44)}$$

$$F_{P2}^{+} = \frac{\partial H_3}{\partial a_i} + \left(\frac{a_{P2}}{gA_{P2}} - \frac{\Delta x f_{P2}\left|Q_3 + Q_4^*\right|}{4gD_{P2}A_{P2}^2}\right)\frac{\partial Q_3}{\partial a_i} \quad \text{.....(A.3.45)}$$

Finally, the negative compatibility equation in pipe 2 (Eq. A.2.21) is differentiated forming

$$\frac{\partial H_3^*}{\partial a_i} = \frac{\partial H_4}{\partial a_i} + \frac{a_{P2}}{gA_{P2}}\left(\frac{\partial Q_3^*}{\partial a_i} - \frac{\partial Q_4}{\partial a_i}\right) + \frac{\Delta x f_{P2}\left|Q_3^* + Q_4\right|}{4gD_{P2}A_{P2}^2}\left(\frac{\partial Q_3^*}{\partial a_i} + \frac{\partial Q_4}{\partial a_i}\right) \quad \text{.....(A.3.46)}$$

Similarly Eq. A.3.46 simplifies to

$$\frac{\partial H_3^*}{\partial a_i} + \left(E_{P2}^{-}\right)\frac{\partial Q_3^*}{\partial a_i} = F_{P2}^{-} \quad \text{.....(A.3.47)}$$

where

$$E_{P2}^{-} = -\frac{a_{P2}}{gA_{P2}} - \frac{\Delta x f_{P2}\left|Q_3^* + Q_4\right|}{4gD_{P2}A_{P2}^2} \quad \text{.....(A.3.48)}$$

$$F_{P2}^{-} = \frac{\partial H_4}{\partial a_i} - \left(\frac{a_{P2}}{gA_{P2}} - \frac{\Delta x f_{P2}\left|Q_3^* + Q_4\right|}{4gD_{P2}A_{P2}^2}\right)\frac{\partial Q_4}{\partial a_i} \quad \text{.....(A.3.49)}$$

Ignoring the coefficients on the left side of Eqs. A.3.35, A.3.39, A.3.44 and A.3.47 for the moment, the coefficients on the right hand sides of the equations are addressed. Collection of the right hand side coefficients forms a right hand side vector with respect to an independent parameter,

$$\{R_{IP}\} = \begin{Bmatrix} 0 \\ 0 \\ 0 \\ 0 \\ F_{P1}^{+} \\ F_{P1}^{-} \\ F_{P2}^{+} \\ F_{P2}^{-} \end{Bmatrix} \quad \text{.....(A.3.50)}$$

This vector is subscripted with *IP* to denote it is with respect to an independent parameter.

Thus far the derivation has been performed with respect to an independent parameter and now is repeated with respect to a dependent parameter. There are no changes in the derivative of the boundary conditions and they remain as given by Eq. A.3.25. The derivative of the continuity equation at node 2 (Eq. A.2.6), now with respect to a dependent parameter, changes to

$$\frac{C_d A_L}{2}\sqrt{\frac{2g}{H_2^*}}\frac{\partial H_2^*}{\partial a_i} + \sqrt{2gH_2^*} - \frac{\partial Q_2^*}{\partial a_i} + \frac{\partial Q_3^*}{\partial a_i} = 0 \quad \text{.....(A.3.51)}$$

The dependent parameter a_i is the lumped leak coefficient $C_d A_L$ at node 2. As in the case of an independent parameter, coefficients simplify to

$$(D_{N2})\frac{\partial H_2^*}{\partial a_i} - \frac{\partial Q_2^*}{\partial a_i} + \frac{\partial Q_3^*}{\partial a_i} = G_{N2} \quad \text{.....(A.3.52)}$$

These coefficients are the same as for the independent parameter case except for a new term that comes from the product rule of differentiation, denoted as the coefficient G where

$$G_{N2} = -\sqrt{2gH_2^*} \quad \text{.....(A.3.53)}$$

Differentiation of the positive characteristic compatibility equation for pipe 1 (Eq. A.2.9) with respect to a dependent parameter results in

$$\frac{\partial H_2^*}{\partial a_i} = \frac{\partial H_1}{\partial a_i} - \frac{a_{P1}}{gA_{P1}}\left(\frac{\partial Q_2^*}{\partial a_i} - \frac{\partial Q_1}{\partial a_i}\right) - \frac{\Delta x f_{P1}\left|Q_1 + Q_2^*\right|}{4gD_{P1}A_{P1}^2}\left(\frac{\partial Q_1}{\partial a_i} + \frac{\partial Q_2^*}{\partial a_i}\right) - \frac{\Delta x\left|Q_1 + Q_2^*\right|}{8gD_{P1}A_{P1}^2}\left(Q_1 + Q_2^*\right) \quad \text{.....(A.3.54)}$$

The dependent parameter in this case is the friction factor in pipe 1 (f_{P1}). Writing Eq. A.3.54 in a simplified form produces

$$\frac{\partial H_2^*}{\partial a_i} + \left(E_{P1}^+\right)\frac{\partial Q_2^*}{\partial a_i} = F_{P1}^+ + G_{P1}^+ \quad \text{.....(A.3.55)}$$

The coefficients E, and F in Eq. A.3.55 are the same as for an independent parameter. The extra term, G^+_{P1}, from the product rule is

$$G_{P1}^+ = -\frac{\Delta x\left|Q_1 + Q_2^*\right|}{8gD_{P1}A_{P1}^2}\left(Q_1 + Q_2^*\right) \quad \text{.....(A.3.56)}$$

Differentiation of the negative compatibility equation in pipe 1 (Eq. A.2.16) with respect to a dependent parameter (f_{P1}) results in

$$\frac{\partial H_1^*}{\partial a_i} = \frac{\partial H_2}{\partial a_i} + \frac{a_{P1}}{gA_{P1}}\left(\frac{\partial Q_1^*}{\partial a_i} - \frac{\partial Q_2}{\partial a_i}\right) + \frac{\Delta x f_{P1}\left|Q_1^* + Q_2\right|}{4gD_{P1}A_{P1}^2}\left(\frac{\partial Q_1^*}{\partial a_i} + \frac{\partial Q_2}{\partial a_i}\right) + \frac{\Delta x\left|Q_1^* + Q_2\right|}{8gD_{P1}A_{P1}^2}\left(Q_1^* + Q_2\right) \quad \text{.....(A.3.57)}$$

The introduction of coefficients E, F and G simplifies Eq. A.3.57 to

$$\frac{\partial H_1^*}{\partial a_i} + \left(E_{P1}^-\right)\frac{\partial Q_1^*}{\partial a_i} = F_{P1}^- + G_{P1}^- \quad \text{.....(A.3.58)}$$

where E and F were defined in Eqs. A.3.40 and A.3.41 and

$$G_{P1}^- = +\frac{\Delta x\left|Q_1^* + Q_2\right|}{8gD_{P1}A_{P1}^2}\left(Q_1^* + Q_2\right) \quad \text{.....(A.3.59)}$$

Repeating for pipe 2, the dependent parameter is the friction in pipe 2 (f_{P2}). Differentiation of the positive characteristic compatibility equation for pipe 2 (Eq. A.2.17) forms

$$\frac{\partial H_4^*}{\partial a_i} = \frac{\partial H_3}{\partial a_i} - \frac{a_{P2}}{gA_{P2}}\left(\frac{\partial Q_4^*}{\partial a_i} - \frac{\partial Q_3}{\partial a_i}\right) - \frac{\Delta x f_{P2}\left|Q_3 + Q_4^*\right|}{4gD_{P2}A_{P2}^2}\left(\frac{\partial Q_3}{\partial a_i} + \frac{\partial Q_4^*}{\partial a_i}\right) - \frac{\Delta x\left|Q_3 + Q_4^*\right|}{8gD_{P2}A_{P2}^2}\left(Q_3 + Q_4^*\right) \quad \text{.....(A.3.60)}$$

simplified to

$$\frac{\partial H_4^*}{\partial a_i}+\left(E_{P2}^+\right)\frac{\partial Q_4^*}{\partial a_i}=F_{P2}^+ +G_{P2}^+ \quad \text{.....(A.3.61)}$$

where

$$G_{P2}^+ =-\frac{\Delta x\left|Q_3+Q_4^*\right|}{8gD_{P2}A_{P2}^2}\left(Q_3+Q_4^*\right) \quad \text{.....(A.3.62)}$$

Apart from the new coefficient G, the other coefficients (E and F) are the same as for the independent parameter cases (Eqs. A.3.44 and A.3.45).

Finally, the negative characteristic compatibility equation in pipe 2 (Eq. A.2.21) is differentiated with respect to a dependent parameter (f_{P2}),

$$\begin{aligned}\frac{\partial H_3^*}{\partial a_i}=\frac{\partial H_4}{\partial a_i}+\frac{a_{P2}}{gA_{P2}}\left(\frac{\partial Q_3^*}{\partial a_i}-\frac{\partial Q_4}{\partial a_i}\right)+\frac{\Delta x f_{P2}\left|Q_3^*+Q_4\right|}{4gD_{P2}A_{P2}^2}\left(\frac{\partial Q_3^*}{\partial a_i}+\frac{\partial Q_4}{\partial a_i}\right)\\ +\frac{\Delta x\left|Q_3^*+Q_4\right|}{8gD_{P2}A_{P2}^2}\left(Q_3^*+Q_4\right)\end{aligned} \quad \text{.....(A.3.63)}$$

simplified to

$$\frac{\partial H_3^*}{\partial a_i}+\left(E_{P2}^-\right)\frac{\partial Q_3^*}{\partial a_i}=F_{P2}^- +G_{P2}^- \quad \text{.....(A.3.64)}$$

where

$$G_{P2}^- =\frac{\Delta x\left|Q_3^*+Q_4\right|}{8gD_{P2}A_{P2}^2}\left(Q_3^*+Q_4\right) \quad \text{.....(A.3.65)}$$

The other coefficients E and F are the same as for the independent parameter case (Eqs. A.3.48 and A.3.49). All of the new G terms come from the product rule when the continuity at node 2 equation and each of the 4 integrated compatibility equations are differentiated with respect to a dependent parameter. Collecting the G terms forms the right hand side dependent parameter vector (subscript *DP*),

$$\{R_{DP}\}=\begin{Bmatrix}0\\0\\0\\G_{N2}\\G_{P1}^{+}\\G_{P1}^{-}\\G_{P2}^{+}\\G_{P2}^{-}\end{Bmatrix} \quad \text{(A.3.66)}$$

Essentially, these extra terms form the simultaneous system for the derivatives with respect to each parameter. The definition of a matrix $[g_a]$ shows which equations (rows in the $[M]$ matrix and $\{R\}$ vector) have a dependence on each parameter $\{a\}$. The matrix $[g_a]$ has rows corresponding to the equations and columns corresponding to the parameters. For the example system,

$$[g_a]=\begin{bmatrix}0&0&0\\0&0&0\\0&0&0\\0&0&1\\1&0&0\\1&0&0\\0&1&0\\0&1&0\end{bmatrix} \quad \text{(A.3.67)}$$

An operator,

$$[R_{DP}]_{i,j} = [g_a]_{i,j}\{R_{DP}\}_j \quad \text{(A.3.68)}$$

and the dependent parameter vector $\{R_{DP}\}$ form the dependent parameter matrix $[R_{DP}]$. Eq. A.3.68 works on single elements of the $\{R_{DP}\}$ vector and the $[g_a]$ matrix for parameter i and row j (corresponding to the equations in the simultaneous system). For the example system, the matrix $[R_{DP}]$ is

$$[R_{DP}]=\begin{bmatrix}0&0&0\\0&0&0\\0&0&0\\0&0&G_{N2}\\G_{P1}^{+}&0&0\\G_{P1}^{-}&0&0\\0&G_{P2}^{+}&0\\0&G_{P2}^{-}&0\end{bmatrix} \quad \text{(A.3.69)}$$

The independent parameter vector (Eqs. A.3.66) and the dependent parameter matrix (Eq. A.3.69) combine to form a total right hand side matrix $[R_D]$,

$$[R_D]=[\{R_{IP}\}\vdots\{R_{IP}\}\vdots\{R_{IP}\}]+[R_{DP}] \quad \text{.....(A.3.70)}$$

Upon determining $[R_D]$, the total simultaneous system for all derivatives can be defined as

$$[M_D]\left[\frac{\partial \nu^*}{\partial a}\right]=[R_D] \quad \text{.....(A.3.71)}$$

where the matrix of the unknown parameter derivatives for the simple system is

$$\left[\frac{\partial \nu^*}{\partial a}\right]=\begin{bmatrix} \partial H_1^*/\partial f_{P1} & \partial H_1^*/\partial f_{P2} & \partial H_1^*/\partial(C_d A_L) \\ \partial H_2^*/\partial f_{P1} & \partial H_2^*/\partial f_{P2} & \partial H_2^*/\partial(C_d A_L) \\ \partial H_3^*/\partial f_{P1} & \partial H_3^*/\partial f_{P2} & \partial H_3^*/\partial(C_d A_L) \\ \partial H_4^*/\partial f_{P1} & \partial H_4^*/\partial f_{P2} & \partial H_4^*/\partial(C_d A_L) \\ \partial Q_1^*/\partial f_{P1} & \partial Q_1^*/\partial f_{P2} & \partial Q_1^*/\partial(C_d A_L) \\ \partial Q_2^*/\partial f_{P1} & \partial Q_2^*/\partial f_{P2} & \partial Q_2^*/\partial(C_d A_L) \\ \partial Q_3^*/\partial f_{P1} & \partial Q_3^*/\partial f_{P2} & \partial Q_3^*/\partial(C_d A_L) \\ \partial Q_4^*/\partial f_{P1} & \partial Q_4^*/\partial f_{P2} & \partial Q_4^*/\partial(C_d A_L) \end{bmatrix} \quad \text{.....(A.3.72)}$$

The common coefficient matrix $[M_D]$ that contains all of the left-hand side coefficients is

$$[M_D]=\begin{bmatrix} 1 & 0 & 0 & 0 & 0 & 0 & 0 & 0 \\ 0 & 0 & 0 & 1 & 0 & 0 & 0 & 0 \\ 0 & 1 & -1 & 0 & 0 & 0 & 0 & 0 \\ 0 & D_{N2} & 0 & 0 & 0 & -1 & 1 & 0 \\ 0 & 1 & 0 & 0 & 0 & E_{P1}^+ & 0 & 0 \\ 1 & 0 & 0 & 0 & E_{P1}^- & 0 & 0 & 0 \\ 0 & 0 & 0 & 1 & 0 & 0 & 0 & E_{P2}^+ \\ 0 & 0 & 1 & 0 & 0 & 0 & E_{P2}^- & 0 \end{bmatrix} \quad \text{.....(A.3.73)}$$

Importantly, the $[M_D]$ matrix does not change when differentiating with respect to an independent or a dependent parameter (or any parameter). The simultaneous system for the derivatives, as given by Eq. A.3.71, is linear with respect to the calculation of the parameter derivatives and requires no iteration. The fast analytic method is a significant outcome of this thesis research as it provides a method of improving the computational speed for the inverse transient method. The fast analytic method may be applied in a stepwise fashion or over the whole transient simulation period. The boundary conditions for the simultaneous system of equations are equal to zero. The initial

conditions are the derivatives of the variables with respect to the parameters at time step zero and can be found from a steady state solver.

A.3.4 Numerical Results for the Parameter Derivatives

The simple system, shown in Figure A.1, was used to test how fast each method (divided difference, analytic/adjoint and fast analytic) would perform in computing the parameter derivatives. An overall simulation time of 10,000 time steps provided a measurable time. The same linear solver was used for each method, which was a LU decomposition followed by a back substitution(s). LU decomposition is fast compared to inverting and multiplying a matrix for solution. Care was taken to not include extra or redundant computer code for any method so that the comparisons in speed would not be biased. Table A.1 shows the time taken for each method to solve for the derivatives over the 10,000 time steps (a total simulation time of 140 seconds) for the simple system. The fastest performer was the fast analytic method, which uses the least linear solver calls because it does not have to iterate to compute the parameter derivatives. The fast analytic method is only a little slower than the forward solution.

Table A.1 Calculation Time for the Jacobian of the Simple System

Method	Time Taken (ms)
Forward Solution Only	2,218
Divided Difference Method	9,597
Adjoint Method or Analytic Method (with storing of $[M]^{-1}$)	6,325
Fast Analytic Method	3,064

The inverse of the $[M]$ matrix was stored for the adjoint method, since doing this is the same as solving for the adjoint variables. Figure A.4 shows a plot of the parameter derivatives for the simple system for the first 0.5 seconds of the transient event. There are no detectable differences seen between the three schemes.

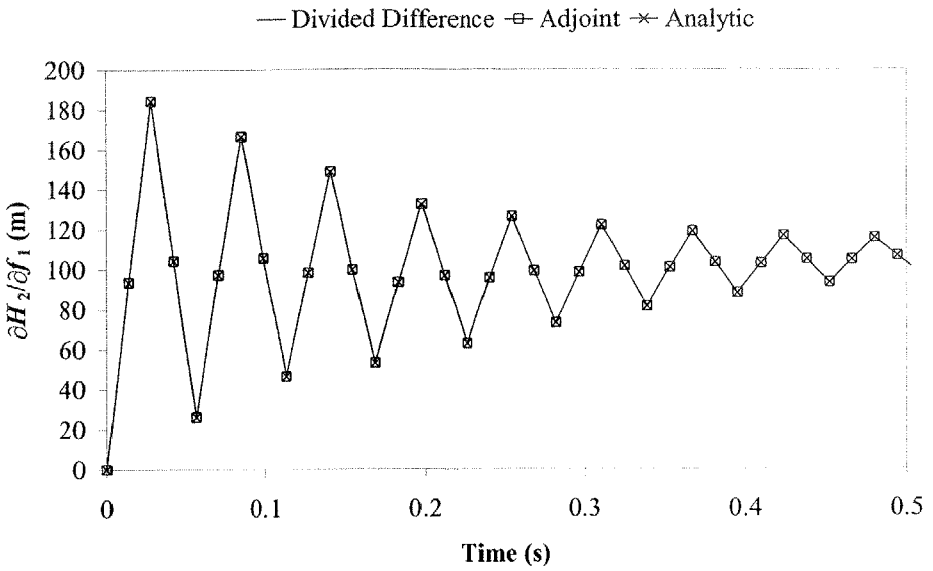

Figure A.4 Calculation of $\partial H_2/\partial f_1$ Using Different Methods for the Simple System (Computations Every 14 ms)

The fast analytic and adjoint methods produce the best results (results are identical). As expected, the divided difference method produces error because it is an approximation of the parameter derivatives (from using a perturbation in the parameter). Figure A.5 shows the error when the other methods are compared to the fast analytic method. The error in the divided difference method is relatively small.

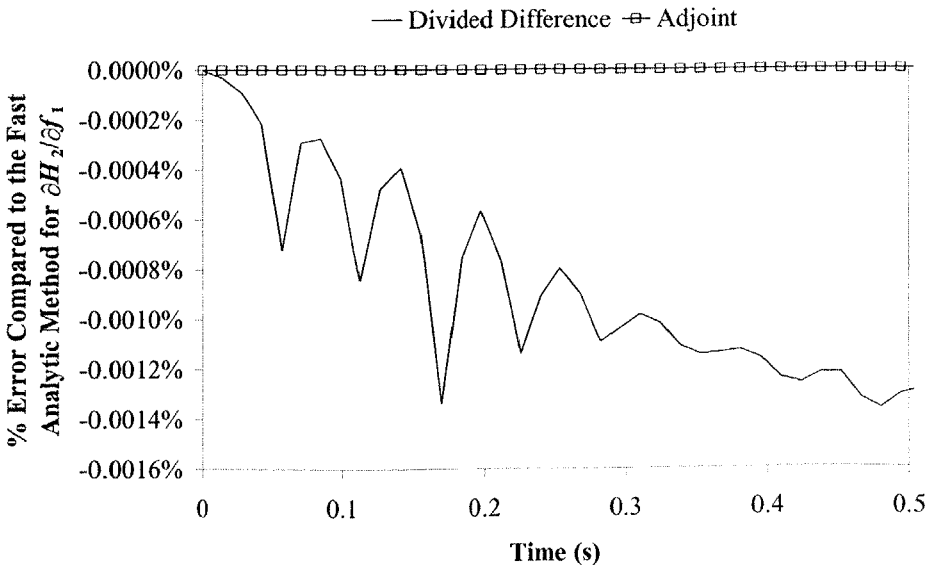

Figure A.5 Comparative Error in $\partial H_2/\partial f_1$ for the Simple System

Because there are only small differences in results between the three different parameter derivative computation methods, the time taken for calculation is the basis for selection of the best method. The fast analytic method is twice as fast as the adjoint/analytic method and three times as fast as the divided difference method. For larger problems and problems requiring long simulation times, the fast analytic method outperforms the other methods by larger margins, thus making the fast analytic method a superior choice for the calculation of parameter derivatives.

A.4 Calculation of Temporal Derivatives for the Simple System

Typically, the temporal derivatives are found using a divided difference method. The characteristic grid spacing restricts the step size of the divided difference method. This restriction can cause errors in the values of the temporal derivatives. Temporal derivatives are needed for unsteady friction models and high order compact timeline interpolation schemes. The calculation of temporal derivatives for the simple system in Figure A.1 can be formulated in a similar way to the fast analytic method for the parameter derivatives (as derived in Section A.3.3). The following section shows the formulation of a set of simultaneous equations for analytic temporal derivatives using the simple system, as given by

$$[M_T]\left\{\frac{\partial v^*}{\partial t}\right\} = \{R_T\} \quad \text{.....(A.4.1)}$$

Numerical results show the comparison this method to the divided difference method for the computation of the temporal derivatives.

A.4.1 Divided Difference Method for Temporal Derivatives

The divided difference method for the temporal derivatives requires one solution of the forward transient problem. The perturbation Δt is the time difference between two time steps. The divided difference approximation for the partial derivative of variable v_j^* with respect to time is

$$\frac{\partial v_j^*}{\partial t} = \frac{v_j^* - v_j}{\Delta t} \quad \text{.....(A.4.2)}$$

An increase in the density of the method-of-characteristics grid increases the accuracy of this method, but also increases the computation time for the forward transient solution.

A.4.2 Analytic Method for Temporal Derivatives

The derivation of the analytic method for finding temporal derivatives is split into two parts. The first part deals with boundary conditions and junction equations. The second deals with the method-of-characteristics compatibility equations. To begin, the boundary conditions (Eqs. A.2.2 and A.2.3) are differentiated with respect to time forming

$$\frac{\partial H_1^*}{\partial t} = \frac{\partial (BC_1)}{\partial t} \quad \text{.....(A.4.3)}$$

$$\frac{\partial H_4^*}{\partial t} = \frac{\partial (BC_3)}{\partial t} \quad \text{.....(A.4.4)}$$

Differentiation of the equation describing the head equality at node 2 (Eq. A.2.4) with respect to time produces

$$\frac{\partial H_2^*}{\partial t} - \frac{\partial H_3^*}{\partial t} = 0 \quad \text{.....(A.4.5)}$$

Finally, differentiating the continuity equation at node 2 containing the leak with respect to time gives

$$\frac{C_d A_L}{2}\sqrt{\frac{2g}{H_2^*}}\frac{\partial H_2^*}{\partial t} - \frac{\partial Q_2^*}{\partial t} + \frac{\partial Q_3^*}{\partial t} = 0 \quad \text{.....(A.4.6)}$$

The primed terms in Eq. A.2.6 have been replaced by asterisked terms since the H and Q values are known from the forward transient solution. The definition of a coefficient A_{N2} is

$$A_{N2} = \frac{C_d A_L}{2}\sqrt{\frac{2g}{H_2^*}} \quad \text{.....(A.4.7)}$$

which simplifies Eq. A.4.6 to a linear expression in the partial derivatives,

$$(A_{N2})\frac{\partial H_2^*}{\partial t} - \frac{\partial Q_2^*}{\partial t} + \frac{\partial Q_3^*}{\partial t} = 0 \quad \text{.....(A.4.8)}$$

The governing unsteady equations (equations of motion and continuity) can be directly differentiated with respect to time. This pair of equations are solved using the method of characteristics (much in the same way as the un-differentiated equations were) forming two compatibility equations valid along the positive and negative characteristic lines (see Section 4.6). The positive characteristic compatibility equation for pipe 1 is

$$\frac{\partial H_2^*}{\partial t} = \frac{\partial H_1}{\partial t} - \frac{a_{P1}}{gA_{P1}}\left(\frac{\partial Q_2^*}{\partial t} - \frac{\partial Q_1}{\partial t}\right) - \frac{\Delta x f_{P1}\left|Q_1 + Q_2^*\right|}{4gD_{P1}A_{P1}^2}\left(\frac{\partial Q_1}{\partial t} + \frac{\partial Q_2^*}{\partial t}\right) \quad \text{.....(A.4.9)}$$

Introduction of coefficients B and C simplify Eq. A.4.9 to

$$\frac{\partial H_2^*}{\partial t} + \left(B_{P1}^+\right)\frac{\partial Q_2^*}{\partial t} = C_{P1}^+ \quad \text{.....(A.4.10)}$$

where Eqs. A.4.11 and A.4.12 define the coefficients B and C respectively.

$$B_{P1}^+ = \frac{a_{P1}}{gA_{P1}} + \frac{\Delta x f_{P1}\left|Q_1 + Q_2^*\right|}{4gD_{P1}A_{P1}^2} \quad \text{.....(A.4.11)}$$

$$C_{P1}^+ = \frac{\partial H_1}{\partial t} + \left(\frac{a_{P1}}{gA_{P1}} - \frac{\Delta x f_{P1}\left|Q_1 + Q_2^*\right|}{4gD_{P1}A_{P1}^2}\right)\frac{\partial Q_1}{\partial t} \quad \text{.....(A.4.12)}$$

The superscript on B and C denotes to which characteristic it belongs and the subscript denotes to which pipe it belongs. Repeating the differentiation for the negative characteristic compatibility equation for pipe 1 (Eq. A.2.13) results in

$$\frac{\partial H_1^*}{\partial t} = \frac{\partial H_2}{\partial t} + \frac{a_{P1}}{gA_{P1}}\left(\frac{\partial Q_1^*}{\partial t} - \frac{\partial Q_2}{\partial t}\right) + \frac{\Delta x f_{P1}\left|Q_1^* + Q_2\right|}{4gD_{P1}A_{P1}^2}\left(\frac{\partial Q_1^*}{\partial t} + \frac{\partial Q_2}{\partial t}\right) \quad \text{.....(A.4.13)}$$

simplified to

$$\frac{\partial H_1^*}{\partial t} + \left(B_{P1}^-\right)\frac{\partial Q_1^*}{\partial t} = C_{P1}^- \quad \text{.....(A.4.14)}$$

where

$$B_{P1}^- = -\frac{a_{P1}}{gA_{P1}} - \frac{\Delta x f_{P1}\left|Q_1^* + Q_2\right|}{4gD_{P1}A_{P1}^2} \quad \text{.....(A.4.15)}$$

$$C_{P1}^- = \frac{\partial H_2}{\partial t} - \left(\frac{a_{P1}}{gA_{P1}} - \frac{\Delta x f_{P1}\left|Q_1^* + Q_2\right|}{4gD_{P1}A_{P1}^2}\right)\frac{\partial Q_2}{\partial t} \quad \text{.....(A.4.16)}$$

The differentiated positive characteristic compatibility equation for pipe 2 (Eq. A.2.17) with respect to time is

$$\frac{\partial H_4^*}{\partial t} = \frac{\partial H_3}{\partial t} - \frac{a_{P2}}{gA_{P2}}\left(\frac{\partial Q_4^*}{\partial t} - \frac{\partial Q_3}{\partial t}\right) - \frac{\Delta x f_{P2}\left|Q_3 + Q_4^*\right|}{4gD_{P2}A_{P2}^2}\left(\frac{\partial Q_3}{\partial t} + \frac{\partial Q_4^*}{\partial t}\right) \quad \text{.....(A.4.17)}$$

simplified to

$$\frac{\partial H_4^*}{\partial t} + \left(B_{P2}^+\right)\frac{\partial Q_4^*}{\partial t} = C_{P2}^+ \quad \text{.....(A.4.18)}$$

where

$$B_{P2}^+ = \frac{a_{P2}}{gA_{P2}} + \frac{\Delta x f_{P2}\left|Q_3 + Q_4^*\right|}{4gD_{P2}A_{P2}^2} \quad \text{.....(A.4.19)}$$

$$C_{P2}^+ = \frac{\partial H_3}{\partial t} + \left(\frac{a_{P2}}{gA_{P2}} - \frac{\Delta x f_{P2}\left|Q_3 + Q_4^*\right|}{4gD_{P2}A_{P2}^2}\right)\frac{\partial Q_3}{\partial t} \quad \text{.....(A.4.20)}$$

Finally, differentiating the negative characteristic compatibility equation for pipe 2 (Eq. A.2.16) with respect to time gives

$$\frac{\partial H_3^*}{\partial t} = \frac{\partial H_4}{\partial t} + \frac{a_{P2}}{gA_{P2}}\left(\frac{\partial Q_3^*}{\partial t} - \frac{\partial Q_4}{\partial t}\right) + \frac{\Delta x f_{P2}\left|Q_3^* + Q_4\right|}{4gD_{P2}A_{P2}^2}\left(\frac{\partial Q_3^*}{\partial t} + \frac{\partial Q_4}{\partial t}\right) \quad \text{.....(A.4.21)}$$

simplified to

$$\frac{\partial H_3^*}{\partial t} + \left(B_{P2}^-\right)\frac{\partial Q_3^*}{\partial t} = C_{P2}^- \quad \text{.....(A.4.22)}$$

where

$$B_{P2}^- = -\frac{a_{P2}}{gA_{P2}} - \frac{\Delta x f_{P2}\left|Q_3^* + Q_4\right|}{4gD_{P2}A_{P2}^2} \quad \text{.....(A.4.23)}$$

$$C_{P2}^- = \frac{\partial H_4}{\partial t} - \left(\frac{a_{P2}}{gA_{P2}} - \frac{\Delta x f_{P2}\left|Q_3^* + Q_4\right|}{4gD_{P2}A_{P2}^2}\right)\frac{\partial Q_4}{\partial t} \quad \text{.....(A.4.24)}$$

Collection of Eqs. A.4.3 to A.4.24 forms a set of linear equations, the solution of which are the partial derivatives of Q and H with respect to time,

$$\begin{bmatrix} 1 & 0 & 0 & 0 & 0 & 0 & 0 & 0 \\ 0 & 0 & 0 & 1 & 0 & 0 & 0 & 0 \\ 0 & 1 & -1 & 0 & 0 & 0 & 0 & 0 \\ 0 & A_{N2} & 0 & 0 & 0 & -1 & 1 & 0 \\ 0 & 1 & 0 & 0 & 0 & B_{P1}^+ & 0 & 0 \\ 1 & 0 & 0 & 0 & B_{P1}^- & 0 & 0 & 0 \\ 0 & 0 & 0 & 1 & 0 & 0 & 0 & B_{P2}^+ \\ 0 & 0 & 1 & 0 & 0 & 0 & B_{P2}^- & 0 \end{bmatrix} \begin{Bmatrix} \partial H_1^*/\partial t \\ \partial H_2^*/\partial t \\ \partial H_3^*/\partial t \\ \partial H_4^*/\partial t \\ \partial Q_1^*/\partial t \\ \partial Q_2^*/\partial t \\ \partial Q_3^*/\partial t \\ \partial Q_4^*/\partial t \end{Bmatrix} = \begin{Bmatrix} \partial(BC_1)/\partial t \\ \partial(BC_3)/\partial t \\ 0 \\ A_{N2} \\ C_{P1}^+ \\ C_{P1}^- \\ C_{P2}^+ \\ C_{P2}^- \end{Bmatrix} \quad \text{.....(A.4.25)}$$

or

$$[M_T]\left\{\frac{\partial v^*}{\partial t}\right\} = \{R_T\} \quad \text{(A.4.26)}$$

Solution of this set of linear equations gives temporal derivatives for all heads and flows for the current time step. Note that none of the elements of the $[M_T]$ matrix depend on the unknown temporal derivatives and, as the system of equations is linear, can be solved in one sweep of the LU decomposition method.

A.4.3 Numerical Results for the Computation of the Temporal Derivatives

The previous section showed an analytic method for the calculation the temporal derivatives of the heads and flows for the simple system. This section compares the numerical results from both the analytic and divided difference methods. The comparison of the relative computation times use a total time of simulation of 140 seconds corresponding to 10,000 time steps. The time taken for the calculation of the forward transient solution is included in results since each method requires this computation. Table A.2 shows the computation time taken for each method.

Table A.2 Calculation Time of Temporal Derivatives for the Simple System

Method	Time Taken (ms)
Forward Solution Only	2,215
Divided Difference Method	2,345
Analytic Method	2,755

All methods show a similar magnitude of speed, although the divided difference method is the quickest, being only a little slower than the forward solution. The divided difference method's accuracy is limited by the discretisation of the characteristic grid. In contrast, the divided difference method for parameter derivatives is not restricted by the MOC grid (the perturbation in a parameter is not a function of the grid discretisation) and, therefore, produces far better solutions than for temporal derivatives. Figure A.6 shows a plot of the temporal derivatives using both methods of the head at node 2.

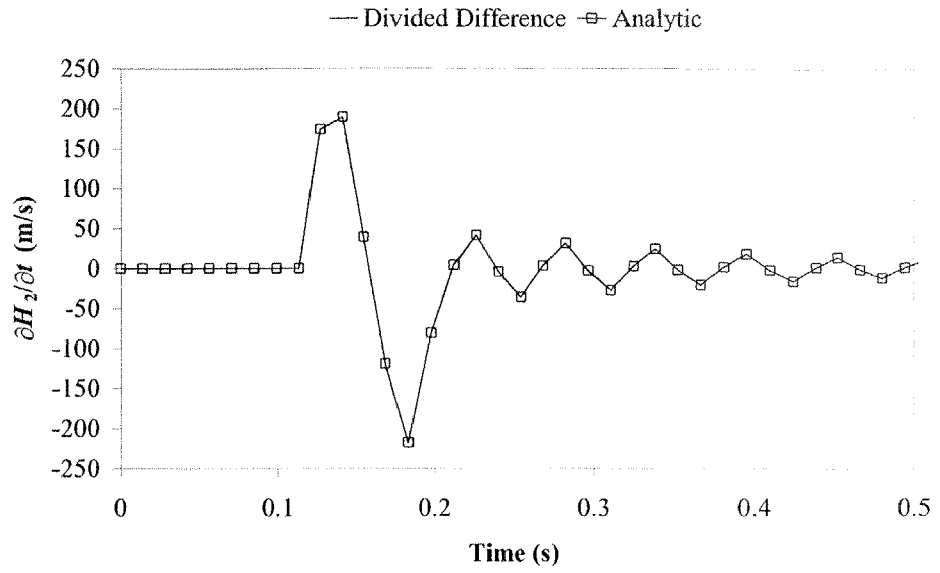

Figure A.6 Calculation of $\partial H_2/\partial t$ Using Different Methods for the Simple System

Both of the temporal derivative calculation methods show similar results. Assuming that the analytic method produces more accurate results than the divided difference method, Figure A.7 shows a plot of the error difference between the two methods. The large errors shown in the later portion of Figure A.7 are misleading and arise from derivative values that are close to zero.

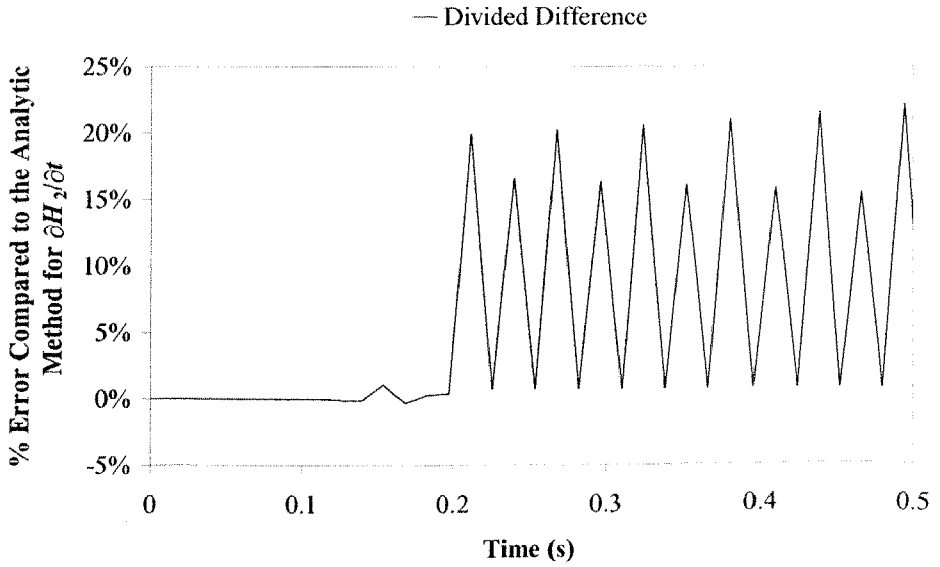

Figure A.7 Comparative Error in $\partial H_2/\partial t$ for the Simple System

The coefficient matrix $[M_T]$ is identical to $[M_D]$ used in the calculation of parameter derivatives using the fast analytic method. Temporal derivatives are formed from differentiation with respect to time, which in this case is similar to an independent parameter. Therefore, the temporal derivatives may be found during the calculation of the parameter derivatives, saving an additional LU decomposition, by adding the temporal-derivative-right-hand-side vector $\{R_T\}$ to the total parameter-derivative matrix $[R_D]$ and the temporal-derivative vector $\{\partial v^*/\partial t\}$ to the parameter-derivative matrix $[\partial v^*/\partial a]$.

A.5 Calculation of Spatial Derivatives for the Simple System

The spatial derivatives of the heads and flows are used in compact spaceline interpolation schemes and unsteady friction models. Divided difference methods (typically used) do not produce accurate spatial derivatives. This section presents two analytic methods for the computation of spatial derivatives. The first is similar to the analytic method for temporal derivatives and the other converts temporal derivatives into spatial derivatives using the governing unsteady equations. Numerical results present the application of the divided difference method and the two analytic methods for the computation of spatial derivatives in the simple system.

A.5.1 Divided Difference Method for Spatial Derivatives

The determination of the spatial derivatives using the divided difference method requires one solution of the forward transient problem. Eq. A.5.1 shows the divided difference approximation for the partial derivative of variable v_j^* with respect to distance. The perturbation in space (Δx) is the computational reach length (between adjacent nodes) from the method of characteristics grid.

$$\frac{\partial v_j^*}{\partial x} = \frac{v_j^* - v_{j-1}^*}{\Delta x} \quad \text{.....(A.5.1)}$$

An increase in the discretisation of the method of characteristics grid increases the accuracy of this method, although it also increases the computation time for the forward transient solution.

A.5.2 Analytic Method for Spatial Derivatives

The formulation for analytic spatial derivatives (like its temporal counterpart) is split into two parts. The first part considers the boundary conditions and the continuity of flow at the leak at node 2, and the second, the method of characteristics compatibility equations for each pipe. The spatial derivative boundary conditions and junction equations are found by first differentiating them with respect to time and then converting these temporal derivatives into spatial derivatives using the governing unsteady equations. The boundary condition at node 1 is shown in Eq. A.2.2. For determination of the spatial derivative boundary condition; the boundary condition at node 1 (Eq. A.2.2) is differentiated with respect to time as is shown in Eq. A.4.3. The unsteady equation of continuity (a governing equation) is stated as

$$\frac{\partial H}{\partial t}+\frac{a^2}{gA}\frac{\partial Q}{\partial x}=0 \qquad \text{(A.5.2)}$$

Substitution of the $\partial H/\partial t$ boundary condition (Eq. A.4.3) into the equation of continuity (Eq. A.5.2) forms a $\partial Q/\partial x$ boundary condition,

$$\frac{\partial Q_1^*}{\partial x}=-\frac{gA_{P1}}{a_{P1}^2}\frac{\partial H_1^*}{\partial t}=A_{N1} \qquad \text{(A.5.3)}$$

The right hand side of Eq. A.5.3 contains only known terms. A coefficient A_{N1} represents these terms, where A_{N1} is defined as

$$A_{N1}=-\frac{gA_{P1}}{a_{P1}^2}\frac{\partial(BC_1)}{\partial t} \qquad \text{(A.5.4)}$$

Like the boundary condition at node 1, the spatial derivative boundary condition at node 3 is formed by differentiating the head boundary condition (A.2.3) with respect to time then applying the unsteady equation of continuity (A.5.2) forming

$$\frac{\partial Q_4^*}{\partial x}=-\frac{gA_{P2}}{a_{P2}^2}\frac{\partial H_4^*}{\partial t}=A_{N3} \qquad \text{(A.5.5)}$$

The right hand side of Eq. A.5.5 only contains known terms. A coefficient A_{N3} represents these terms, where A_{N3} is defined as

$$A_{N3} = -\frac{gA_{P2}}{a_{P2}^2}\frac{\partial(BC_3)}{\partial t} \quad \text{(A.5.6)}$$

Two relationships apply at node 2: the equality of heads and the continuity of flow. First considering the equality of heads at node 2 (Eq. A.2.4), differentiation with respect to time (previously found in Eq. A.4.5) and conversion to spatial flow derivatives (using the unsteady equation of continuity Eq. A.5.7) forms

$$-\frac{gA_{P1}}{a_{P1}^2}\frac{\partial Q_2^*}{\partial x} + \frac{gA_{P2}}{a_{P2}^2}\frac{\partial Q_3^*}{\partial x} = 0 \quad \text{(A.5.7)}$$

Introduction of coefficients B_{P1} and B_{P2} simplifies Eq. A.5.7 to

$$(B_{P1})\frac{\partial Q_2^*}{\partial x} + (B_{P2})\frac{\partial Q_3^*}{\partial x} = 0 \quad \text{(A.5.8)}$$

where the coefficients B_{P1} and B_{P2} are defined as

$$B_{P1} = -\frac{gA_{P1}}{a_{P1}^2} \quad \text{(A.5.9)}$$

$$B_{P2} = \frac{gA_{P2}}{a_{P2}^2} \quad \text{(A.5.10)}$$

Calculation of the spatial derivative of the continuity of flows at node 2 requires the unsteady equation of motion,

$$\frac{\partial H}{\partial x} + \frac{1}{gA}\frac{\partial Q}{\partial t} + \frac{fQ|Q|}{2gDA^2} = 0 \quad \text{(A.5.11)}$$

Differentiation of the continuity of flow at node 2 (Eq. A.2.6) with respect to time (previously found in Eq. A.4.6) and using the unsteady equation of motion to convert the temporal derivatives into spatial derivatives produces

$$-\frac{C_d A_L}{2}\sqrt{\frac{2g}{H_2^*}}\frac{a_{P1}^2}{gA_{P1}}\frac{\partial Q_2^*}{\partial x} + gA_{P1}\frac{\partial H_2^*}{\partial x} + \frac{f_{P1}Q_2^*|Q_2^*|}{2D_{P1}A_{P1}} - gA_{P2}\frac{\partial H_3^*}{\partial x} - \frac{f_{P2}Q_3^*|Q_3^*|}{2D_{P2}A_{P2}} = 0 \quad \text{(A.5.12)}$$

Ignoring the leak term, the continuity of flow around node 2 becomes a continuity of weighted spatial head derivatives. Introduction of coefficients C_{N2}, D_{N2}, E_{N2} and F_{N2} simplifies A.5.12 to

$$(C_{N2})\frac{\partial Q_2^*}{\partial x} + (D_{N2})\frac{\partial H_2^*}{\partial x} + (E_{N2})\frac{\partial H_3^*}{\partial x} = (F_{N2}) \quad \text{(A.5.13)}$$

where the coefficients in Eq. A.5.13 are defined as

$$C_{N2} = -\frac{C_d A_L}{2}\sqrt{\frac{2g}{H_2^*}}\frac{a_{P1}^2}{gA_{P1}} \quad \text{(A.5.14)}$$

$$D_{N2} = gA_{P1} \quad \text{.....(A.5.15)}$$

$$E_{N2} = -gA_{P1} \quad \text{.....(A.5.16)}$$

$$F_{N2} = -\frac{f_{P1}Q_2^*|Q_2^*|}{2D_{P1}A_{P1}} + \frac{f_{P2}Q_3^*|Q_3^*|}{2D_{P2}A_{P2}} \quad \text{.....(A.5.17)}$$

Differentiation of the unsteady equations of continuity and motion with respect to space and their subsequent solution using the method of characteristics produces two spatial-derivative compatibility equations valid along the C^+ and C^- characteristic lines (details shown in Section 8.5). The positive characteristic spatial derivative compatibility equation for pipe 1 is

$$\frac{\partial H_2^*}{\partial x} = \frac{\partial H_1}{\partial x} - \frac{a_{P1}}{gA_{P1}}\left(\frac{\partial Q_2^*}{\partial x} - \frac{\partial Q_1}{\partial x}\right) - \frac{\Delta x f_{P1}|Q_1 + Q_2^*|}{4gD_{P1}A_{P1}^2}\left(\frac{\partial Q_1}{\partial x} + \frac{\partial Q_2^*}{\partial x}\right) \quad \text{.....(A.5.18)}$$

Substitution of known terms with coefficients G and I gives

$$\frac{\partial H_2^*}{\partial x} + \left(G_{P1}^+\right)\frac{\partial Q_2^*}{\partial x} = I_{P1}^+ \quad \text{.....(A.5.19)}$$

The coefficients G and I are given a superscript denoting the characteristic line and a subscript denoting the pipe number. The coefficients for Eq. A.5.19 are

$$G_{P1}^+ = \frac{a_{P1}}{gA_{P1}} + \frac{\Delta x f_{P1}|Q_1 + Q_2^*|}{4gD_{P1}A_{P1}^2} \quad \text{.....(A.5.20)}$$

$$I_{P1}^+ = \frac{\partial H_1}{\partial x} + \left(\frac{a_{P1}}{gA_{P1}} - \frac{\Delta x f_{P1}|Q_1 + Q_2^*|}{4gD_{P1}A_{P1}^2}\right)\frac{\partial Q_1}{\partial x} \quad \text{.....(A.5.21)}$$

Repeating for the negative characteristic in pipe 1, the spatial derivative compatibility equation is

$$\frac{\partial H_1^*}{\partial x} = \frac{\partial H_2}{\partial x} + \frac{a_{P1}}{gA_{P1}}\left(\frac{\partial Q_1^*}{\partial x} - \frac{\partial Q_2}{\partial x}\right) + \frac{\Delta x f_{P1}|Q_1^* + Q_2|}{4gD_{P1}A_{P1}^2}\left(\frac{\partial Q_1^*}{\partial x} + \frac{\partial Q_2}{\partial x}\right) \quad \text{.....(A.5.22)}$$

simplified to

$$\frac{\partial H_1^*}{\partial x} + \left(G_{P1}^-\right)\frac{\partial Q_1^*}{\partial x} = I_{P1}^- \quad \text{.....(A.5.23)}$$

where

$$G_{P1}^- = -\frac{a_{P1}}{gA_{P1}} - \frac{\Delta x f_{P1}|Q_1^* + Q_2|}{4gD_{P1}A_{P1}^2} \quad \text{.....(A.5.24)}$$

$$I_{P1}^{-} = \frac{\partial H_2}{\partial x} - \left(\frac{a_{P1}}{gA_{P1}} - \frac{\Delta x f_{P1} \left| Q_1^* + Q_2 \right|}{4gD_{P1}A_{P1}^2} \right) \frac{\partial Q_2}{\partial x} \quad \text{.....(A.5.25)}$$

Considering the positive characteristic for pipe 2, the spatial derivative compatibility equation is

$$\frac{\partial H_4^*}{\partial x} = \frac{\partial H_3}{\partial x} - \frac{a_{P2}}{gA_{P2}} \left(\frac{\partial Q_4^*}{\partial x} - \frac{\partial Q_3}{\partial x} \right) - \frac{\Delta x f_{P2} \left| Q_3 + Q_4^* \right|}{4gD_{P2}A_{P2}^2} \left(\frac{\partial Q_3}{\partial x} + \frac{\partial Q_4^*}{\partial x} \right) \quad \text{.....(A.5.26)}$$

simplified to

$$\frac{\partial H_4^*}{\partial x} + \left(G_{P2}^{+} \right) \frac{\partial Q_4^*}{\partial x} = I_{P2}^{+} \quad \text{.....(A.5.27)}$$

where

$$G_{P2}^{+} = \frac{a_{P2}}{gA_{P2}} + \frac{\Delta x f_{P2} \left| Q_3 + Q_4^* \right|}{4gD_{P2}A_{P2}^2} \quad \text{.....(A.5.28)}$$

$$I_{P2}^{+} = \frac{\partial H_3}{\partial x} + \left(\frac{a_{P2}}{gA_{P2}} - \frac{\Delta x f_{P2} \left| Q_3 + Q_4^* \right|}{4gD_{P2}A_{P2}^2} \right) \frac{\partial Q_3}{\partial x} \quad \text{.....(A.5.29)}$$

Finally, the spatial derivative compatibility equation in pipe 2 for the negative characteristic is

$$\frac{\partial H_3^*}{\partial x} = \frac{\partial H_4}{\partial x} + \frac{a_{P2}}{gA_{P2}} \left(\frac{\partial Q_3^*}{\partial x} - \frac{\partial Q_4}{\partial x} \right) + \frac{\Delta x f_{P2} \left| Q_3^* + Q_4 \right|}{4gD_{P2}A_{P2}^2} \left(\frac{\partial Q_3^*}{\partial x} + \frac{\partial Q_4}{\partial x} \right) \quad \text{.....(A.5.30)}$$

simplified to

$$\frac{\partial H_3^*}{\partial x} + \left(G_{P2}^{-} \right) \frac{\partial Q_3^*}{\partial x} = I_{P2}^{-} \quad \text{.....(A.5.31)}$$

where

$$G_{P2}^{-} = -\frac{a_{P2}}{gA_{P2}} - \frac{\Delta x f_{P2} \left| Q_3^* + Q_4 \right|}{4gD_{P2}A_{P2}^2} \quad \text{.....(A.5.32)}$$

$$I_{P2}^{-} = \frac{\partial H_4}{\partial x} - \left(\frac{a_{P2}}{gA_{P2}} - \frac{\Delta x f_{P2} \left| Q_3^* + Q_4 \right|}{4gD_{P2}A_{P2}^2} \right) \frac{\partial Q_4}{\partial x} \quad \text{.....(A.5.33)}$$

Eqs. A.5.3 to A.5.33 form a set of simultaneous linear equations for the spatial derivatives of all heads and flows for the current time step. A summary of the equations is

$$\partial Q_1^* / \partial x = A_{N1}$$

$$\partial Q_4^* / \partial x = A_{N3}$$

$$(B_{P1})\partial Q_2^*/\partial x + (B_{P2})\partial Q_3^*/\partial x = 0$$

$$(C_{N2})\partial Q_2^*/\partial x + (D_{N2})\partial H_2^*/\partial x + (E_{N2})\partial H_3^*/\partial x = F_{N2}$$

$$\partial H_2^*/\partial x + (G^+_{P1})\partial Q_2^*/\partial x = \Gamma^+_{P1}$$

$$\partial H_1^*/\partial x + (G^-_{P1})\partial Q_1^*/\partial x = \Gamma^-_{P1}$$

$$\partial H_4^*/\partial x + (G^+_{P2})\partial Q_4^*/\partial x = \Gamma^+_{P2}$$

$$\partial H_3^*/\partial x + (G^-_{P2})\partial Q_3^*/\partial x = \Gamma^-_{P2}$$

The simultaneous system of equations for the spatial derivatives, written in a matrix form, is

$$\begin{bmatrix} 0 & 0 & 0 & 0 & 1 & 0 & 0 & 0 \\ 0 & 0 & 0 & 0 & 0 & 0 & 0 & 1 \\ 0 & 0 & 0 & 0 & 0 & B_{P1} & B_{P2} & 0 \\ 0 & D_{N2} & E_{N2} & 0 & 0 & C_{N2} & 0 & 0 \\ 0 & 1 & 0 & 0 & 0 & G^+_{P1} & 0 & 0 \\ 1 & 0 & 0 & 0 & G^-_{P1} & 0 & 0 & 0 \\ 0 & 0 & 0 & 1 & 0 & 0 & 0 & G^+_{P2} \\ 0 & 0 & 1 & 0 & 0 & 0 & G^-_{P2} & 0 \end{bmatrix} \begin{Bmatrix} \partial H_1^*/\partial x \\ \partial H_2^*/\partial x \\ \partial H_3^*/\partial x \\ \partial H_4^*/\partial x \\ \partial Q_1^*/\partial x \\ \partial Q_2^*/\partial x \\ \partial Q_3^*/\partial x \\ \partial Q_4^*/\partial x \end{Bmatrix} = \begin{Bmatrix} A_{N1} \\ A_{N3} \\ 0 \\ F_{N2} \\ I^+_{P1} \\ I^-_{P1} \\ I^+_{P2} \\ I^-_{P2} \end{Bmatrix} \quad \text{.....(A.5.34)}$$

Writing Eq. A.5.34 in an abbreviated form produces

$$[M_X]\left\{\frac{\partial v^*}{\partial x}\right\} = \{R_X\} \quad \text{.....(A.5.35)}$$

where $[M_X]$ is a matrix of coefficients and $\{R_X\}$ is a vector containing known right hand side terms. Solving Eq. A.5.35 for $\{\partial v^*/\partial x\}$ gives the spatial derivatives of the heads and flows for the current time step. Unlike the analytic method for the calculation of the temporal derivatives, the analytic method for the calculation of the spatial derivatives does not share a common coefficient matrix with the fast analytic parameter derivative method (i.e. $[M_T] = [M_D]$, $[M_X] \neq [M_D]$), and thus cannot be included in the calculation of parameter derivatives to save computation time. As shown in this section, the spatial derivative boundary conditions and junction equations cannot be simply determined by differentiation with respect to space, e.g. the equality of heads at node 2 is $H_2 = H_3$ and for the temporal derivatives $\frac{\partial H_2}{\partial t} = \frac{\partial H_3}{\partial t}$, but for the spatial derivatives $\frac{\partial H_2}{\partial x} \neq \frac{\partial H_3}{\partial x}$.

A.5.3 Temporal Conversion Method for Spatial Derivatives

An alternative formulation for the calculation of the spatial derivatives is to determine the temporal derivatives for all variables and then convert them into spatial derivatives using the governing unsteady equations (without setting up a simultaneous system of equations for the spatial derivatives). The unsteady equation of motion converts the temporal derivatives of the flow into spatial derivatives of the head as shown below for the simple system:

$$\frac{\partial H_1^*}{\partial x} = -\frac{1}{gA_{P1}}\left(\frac{\partial Q_1^*}{\partial t} + \frac{f_{P1}Q_1^*\left|Q_1^*\right|}{2D_{P1}A_{P1}}\right) \quad \text{(A.5.36)}$$

$$\frac{\partial H_2^*}{\partial x} = -\frac{1}{gA_{P1}}\left(\frac{\partial Q_2^*}{\partial t} + \frac{f_{P1}Q_2^*\left|Q_2^*\right|}{2D_{P1}A_{P1}}\right) \quad \text{(A.5.37)}$$

$$\frac{\partial H_3^*}{\partial x} = -\frac{1}{gA_{P2}}\left(\frac{\partial Q_3^*}{\partial t} + \frac{f_{P2}Q_3^*\left|Q_3^*\right|}{2D_{P2}A_{P2}}\right) \quad \text{(A.5.38)}$$

$$\frac{\partial H_4^*}{\partial x} = -\frac{1}{gA_{P2}}\left(\frac{\partial Q_4^*}{\partial t} + \frac{f_{P2}Q_4^*\left|Q_4^*\right|}{2D_{P2}A_{P2}}\right) \quad \text{(A.5.39)}$$

The flows in the friction terms of Eq. A.5.36 to A.5.39 are known from the solution to the forward transient problem. The unsteady equation of continuity converts the temporal derivatives of the heads into spatial derivatives of the flows at the same corresponding location,

$$\frac{\partial Q_1^*}{\partial x} = -\frac{gA_{P1}}{a_{P1}^2}\frac{\partial H_1^*}{\partial t} \quad \text{(A.5.40)}$$

$$\frac{\partial Q_2^*}{\partial x} = -\frac{gA_{P1}}{a_{P1}^2}\frac{\partial H_2^*}{\partial t} \quad \text{(A.5.41)}$$

$$\frac{\partial Q_3^*}{\partial x} = -\frac{gA_{P2}}{a_{P2}^2}\frac{\partial H_3^*}{\partial t} \quad \text{(A.5.42)}$$

$$\frac{\partial Q_4^*}{\partial x} = -\frac{gA_{P2}}{a_{P2}^2}\frac{\partial H_4^*}{\partial t} \quad \text{(A.5.43)}$$

A.5.4 Numerical Results for the Spatial Derivatives

This section presents the numerical calculation of the spatial derivatives for all heads and flows in the simple system (Figure A.1) using the divided difference, analytic and temporal conversion methods. Ten thousand transient time steps ensure a significant time of calculation. Table A.3 shows the time taken for the calculation of the spatial derivatives using each method.

Table A.3 Calculation Time of Spatial Derivatives for the Simple System

Method	Time Taken (ms)
Forward Solution Only	2,215
Divided Difference Method	2,231
Analytic Method	2,779
Temporal Conversion Method	2,796

The fastest spatial derivative calculation method is the divided difference method. Although speed of computation is highly desired, the divided difference method produces low accuracy spatial derivatives. Figure A.8 shows the spatial derivative of the head at node 2 for the divided difference, analytic and temporal conversion methods for the simple system.

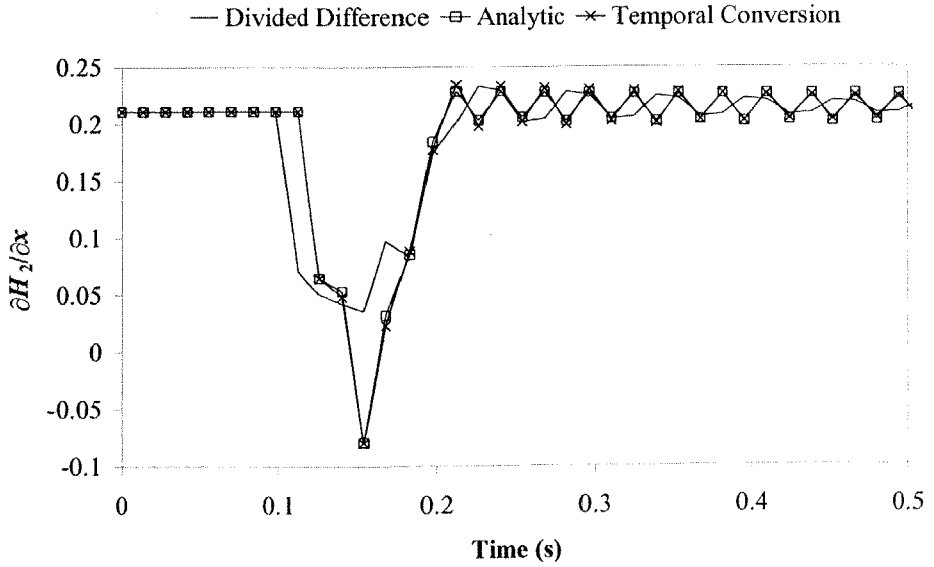

Figure A.8 Calculation of $\partial H_2/\partial x$ Using Different Methods for the Simple System

Figure A.8 shows a good agreement between the spatial derivatives from the analytic and temporal conversion methods. The divided difference method, however, shows significantly different spatial derivatives. Assuming that the most accurate method is the analytic method, Figure A.9 shows the error in the spatial derivatives compared to the analytic method.

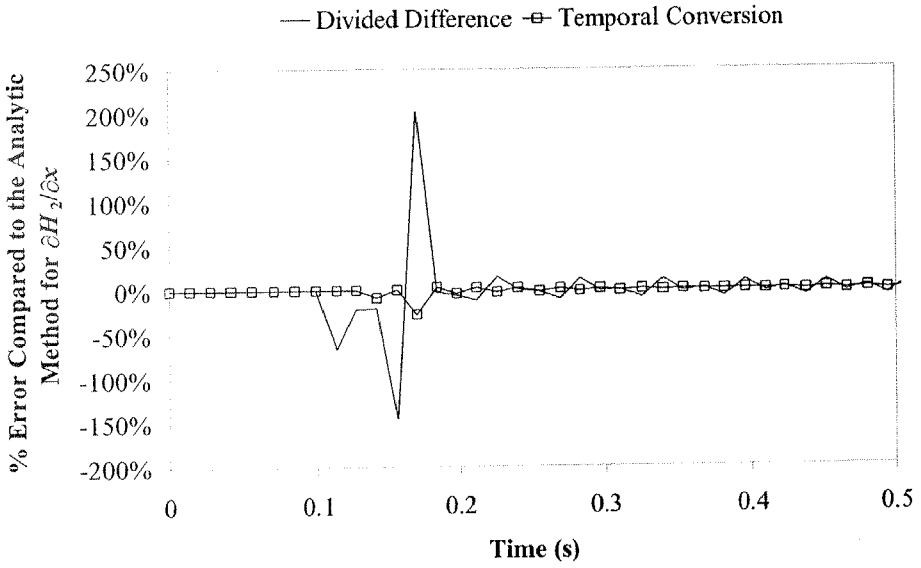

Figure A.9 Comparative Error in $\partial H_2/\partial x$ for the Simple System

Figure A.9 shows the minimal difference between the temporal correction method and the analytic method and a large error in the divided difference method results.

A.6 Summary of Results for the Simple System

This appendix illustrates different methods for the calculation of parameter, temporal and spatial derivatives of head and flow. Numerical tests of each method's performance use the simple system of Figure A.1. The simple system consists of a pipeline between two tanks with different water elevation. A leak exists at the centre of the pipeline. Expressions for the various derivatives were determined in this appendix and results presented.

A.6.1 Parameter Derivatives

The parameter derivatives were found using three methods: the divided difference method, analytic method (equivalent to the adjoint method), and the fast analytic method. The newly proposed fast analytic method was considerably faster than the other methods, including the adjoint method. The fast analytic method's speed is due to its linearity in the parameter derivatives and thus does not require iteration (to resolve derivative terms in $[\partial M/\partial a_i]$ and $\{\partial R/\partial a_i\}$ of the current time step). Both the analytic (and hence adjoint) and fast analytic methods reduce the number of matrix solver calls by using LU decomposition (since parts of the simultaneous system for the parameter derivatives remain unchanged irrespective of which parameter is considered). All methods considered for the calculation of the parameter derivatives produce results of similar accuracy, although the fast analytic and analytic (and hence adjoint) methods produce the most accurate results.

A.6.2 Temporal Derivatives

Two methods were used to calculate the temporal derivatives: the divided difference method and an analytic method. Both methods showed little difference in accuracy and computational speed, although the divided difference method was slightly faster. However, the speed of the analytic method could be improved by incorporating it into the fast analytic method for the parameter derivatives, thus saving time on matrix computations. The accuracy of the analytic method is expected to be better than the divided difference method for problems where coarse grids are used.

A.6.3 Spatial Derivatives

Three methods were used to find the spatial derivatives of the heads and flows: the divided difference method, the analytic method, and the temporal conversion method. The analytic and temporal conversion methods are newly proposed in this thesis. The spatial derivatives were calculated most accurately by the analytic and temporal correction methods, whereas the divided difference method showed large errors (due to

the grid being too coarse in space). The computational speed of each method was similar. The temporal conversion method is much simpler than the analytic method, which has more difficult boundary conditions and junction equations.

Appendix B

Unsteady Friction Models and Derivations

This appendix contains additional information needed for Chapters 8 and 9 that contains work on unsteady state friction. A detailed graphical description of the 8 unsteady flow events, derivations of the unsteady equations of motion and energy including α and β corrections, additional derivation for the calculation of the unsteady friction coefficients k_1, k_3 and k_M are presented. Derivations for the inclusion of the k_A & k_P unsteady friction model in the method of characteristics are also included.

B.1 Implementation of the Brunone *et al.* (1991) Unsteady Friction Model

There are different ways to implement the Brunone *et al.* (1991) unsteady friction model in the method of characteristics. They are the unsteady friction model (1) "treated as an addition to steady friction" and (2) "included in the directional derivatives" (in the method of characteristics). The inclusion of unsteady friction in the directional derivatives is described in Section 8.4. The object of this section is to explore the problems when implementing the Brunone *et al.* (1991) model treated as an addition to steady friction. Other issues addressed in this section are use of the rectangular and trapezoidal rules for unsteady friction integration, the use of diamond and rectangular grid types and the stability of the unsteady friction model.

B.1.1 Unsteady Friction Integration Using the Rectangular and Trapezoidal Rules

The rectangular and trapezoidal rules for integration are used in this section to evaluate the integral of the unsteady friction term along the characteristic line. The use of the rectangular rule does not require information about conditions at the same time level for which a solution is being determined. In contrast, the trapezoidal rule does require information about conditions at the same time level and generally requires more iteration to solve the same problem, thus resulting in the rectangular rule being faster but the method is not without its drawbacks. When using the rectangular rule, properties such as friction, which are dependent on conditions at either end of a characteristic line, must be approximated so that they are only dependent on known conditions at the base of the characteristic line. Doing this leads to inaccuracies. One aim of this section is to investigate the differences in results due to making this approximation and illustrate the importance of the approach when modelling unsteady friction.

Traditionally, the governing equations are solved using the method of characteristics (MOC). A detailed account of this procedure applied to transient pipeline flow is found in Chapter 3. The two compatibility equations, from the MOC, are valid along characteristic lines defined by $dx/dt = +a$ and $dx/dt = -a$ respectively. These compatibility equations contain the steady and unsteady friction terms and are integrated along the characteristic lines. The steady and unsteady friction terms may be evaluated numerically using the rectangular rule or a more accurate method, such as the trapezoidal rule.

The steady state friction term depends on conditions along the characteristic line. As the variation of the friction factor and the velocity along the characteristic line are not known approximations are needed. Wylie and Streeter (1993) and Propson (1972) have previously investigated approximations of this variation. Obviously, a more accurate approximation of the steady state friction term is preferred.

The Brunone *et al.* (1991) unsteady friction model requires values of the local temporal ($\partial V/\partial t$) and convective acceleration ($\partial V/\partial x$) as shown in the equation of motion

$$\frac{\partial H}{\partial x}+\frac{1}{g}\frac{\partial V}{\partial t}+\frac{fV|V|}{2gD}+\frac{k_3}{g}\left(\frac{\partial V}{\partial t}-a\frac{\partial V}{\partial x}\right)=0 \quad \text{..... (B.1.1)}$$

Consider the positive characteristic compatibility equation after applying the method of characteristics but before integration

$$dH+\frac{a}{g}dV+\frac{fV|V|}{2gD}dx+\frac{k_3}{g}\left(\frac{\partial V}{\partial t}-a\frac{\partial V}{\partial x}\right)dx=0 \quad \text{..... (B.1.2)}$$

The integration of Eq. B.1.2 along the characteristic line $dx/dt = a$ from a point A to a point P results in

$$(H_P-H_A)+\frac{a}{g}(V_P-V_A)+\int_A^P\frac{fV|V|}{2gD}dx+\int_A^P\frac{k_3}{g}\left(\frac{\partial V}{\partial t}-a\frac{\partial V}{\partial x}\right)dx=0 \quad \text{..... (B.1.3)}$$

where the integrals of the friction terms are not evaluated. If the rectangular rule of integration is used the result is

$$(H_P-H_A)+\frac{a}{g}(V_P-V_A)+\frac{fV_A|V_A|}{2gD}\Delta x+\frac{k_3}{g}\left(\frac{\partial V_A}{\partial t}-a\frac{\partial V_A}{\partial x}\right)\Delta x=0 \quad \text{..... (B.1.4)}$$

However, if the trapezoidal rule of integration is used the result will be

$$\begin{aligned}&(H_P-H_A)+\frac{a}{g}(V_P-V_A)+\frac{f}{2gD}\frac{\left(V_A|V_A|+V_P|V_P|\right)}{2}\Delta x\\&+\frac{k_3}{g}\left[\frac{1}{2}\left(\frac{\partial V_A}{\partial t}+\frac{\partial V_P}{\partial t}\right)-\frac{a}{2}\left(\frac{\partial V_A}{\partial x}+\frac{\partial V_P}{\partial x}\right)\right]\Delta x=0\end{aligned} \quad \text{..... (B.1.5)}$$

The calculation of the partial derivatives in the unsteady friction term is required at the base of the characteristic line (point A) when using the rectangular rule and at both ends (points A and P) of the characteristic line when using the trapezoidal rule. Both Eqs. B.1.4 and B.1.5 may be written as

$$(H_P-H_A)+\frac{a}{g}(V_P-V_A)+\frac{f(V|V|)_+}{2gD}\Delta x+\frac{k_3}{g}\left[\left(\frac{\partial V}{\partial t}\right)_+-a\left(\frac{\partial V}{\partial x}\right)_+\right]\Delta x=0 \quad \text{..... (B.1.6)}$$

where $(V|V|)_+$, $(\partial V/\partial t)_+$ and $(\partial V/\partial x)_+$ represents evaluation by either the rectangular or trapezoidal rules for the positive characteristic. Figure B.1 shows each method for computing the temporal and convective derivatives for use in both the rectangular and trapezoidal rules of integration. The points circled with a dashed line are interpolated for a diamond grid scheme. If a rectangular grid scheme is used the points circled with a dashed line would be available directly without interpolation.

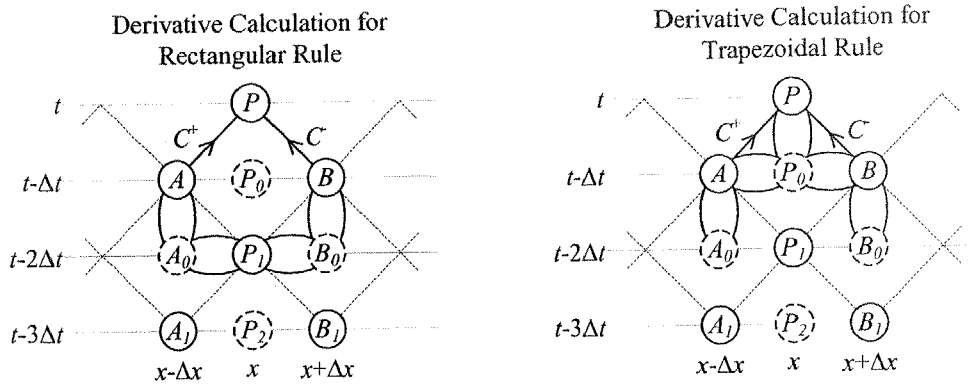

Figure B.1 Derivative Calculation Using Rectangular and Trapezoidal Rules on a Diamond Grid

In Figure B.1 consider the calculation of head and velocity at point P at time step t for a diamond grid. All head and velocity values for previous time steps have been previously calculated and are known. When using the rectangular rule, the temporal accelerations are found between points A and A_0 for the positive characteristic and between points B and B_0 for the negative characteristic.

$$\frac{\partial V_{A,A_0}}{\partial t} = \frac{V_A - V_{A_0}}{\Delta t} \quad \text{and} \quad \frac{\partial V_{B,B_0}}{\partial t} = \frac{V_B - V_{B_0}}{\Delta t} \qquad \text{(B.1.7)}$$

The convective accelerations are found between points P_1 and A_0 for the positive characteristic and points B_0 and P_1 for the negative characteristic.

$$\frac{\partial V_{P_1,A_0}}{\partial x} = \frac{V_{P_1} - V_{A_0}}{\Delta x} \quad \text{and} \quad \frac{\partial V_{B_0,P_1}}{\partial x} = \frac{V_{B_0} - V_{P_1}}{\Delta x} \qquad \text{(B.1.8)}$$

The behaviour of the temporal and convective accelerations along the characteristic lines (A to P and B to P) are approximated by conditions at the base of the characteristics. Thus, when using the rectangular rule, the estimation of the temporal and convective derivatives on a diamond grid is

$$\left(\frac{\partial V}{\partial t}\right)_+ = \frac{\partial V_{A,A_0}}{\partial t}, \left(\frac{\partial V}{\partial t}\right)_- = \frac{\partial V_{B,B_0}}{\partial t}, \left(\frac{\partial V}{\partial x}\right)_+ = \frac{\partial V_{P_1,A_0}}{\partial x} \text{ and } \left(\frac{\partial V}{\partial x}\right)_- = \frac{\partial V_{P_1,B_0}}{\partial x} \qquad \text{(B.1.9)}$$

When using the trapezoidal rule, the temporal accelerations at the base of the characteristic are found identically to those when using the rectangular rule (Eqs. B.1.7 to B.1.9). The temporal accelerations at the top of the characteristic (for both the positive and negative characteristics) are found between points P and P_0.

$$\frac{\partial V_{P,P_0}}{\partial t} = \frac{V_P - V_{P_0}}{\Delta t} \qquad \text{(B.1.10)}$$

The convective accelerations are found between points P_0 and A for the positive characteristic and points B and P_0 for the negative characteristic.

$$\frac{\partial V_{P_0,A}}{\partial x} = \frac{V_{P_0} - V_A}{\Delta x} \quad \text{and} \quad \frac{\partial V_{B,P_0}}{\partial x} = \frac{V_B - V_{P_0}}{\Delta x} \qquad \text{(B.1.11)}$$

The behaviour of the temporal and convective accelerations along the characteristic line are approximated by conditions at each end of the characteristics as

$$\left(\frac{\partial V}{\partial t}\right)_+ = \frac{1}{2}\left(\frac{\partial V_{A,A_0}}{\partial t} + \frac{\partial V_{P,P_0}}{\partial t}\right) \quad \text{and} \quad \left(\frac{\partial V}{\partial t}\right)_- = \frac{1}{2}\left(\frac{\partial V_{B,B_0}}{\partial t} + \frac{\partial V_{P,P_0}}{\partial t}\right) \qquad \text{(B.1.12)}$$

The convective accelerations, however, are based on conditions at the base of the characteristics,

$$\left(\frac{\partial V}{\partial x}\right)_+ = \frac{\partial V_{P_0,A}}{\partial x} \quad \text{and} \quad \left(\frac{\partial V}{\partial x}\right)_- = \frac{\partial V_{B,P_0}}{\partial x} \qquad \text{(B.1.13)}$$

The convective accelerations are based on conditions at the base of the characteristic because the calculation of the convective acceleration at the top of the characteristic would require interpolations outside of the domain of influence of point P. A similar formulation can be made for the derivatives on a rectangular grid system. It is important for the rectangular rule scheme that the derivatives do not use any information outside the computational reach that is at section $x - 2\Delta x$ or section $x + 2\Delta x$, which is important for implementation in networked piping systems and near boundary conditions where derivatives across computational reaches cannot be formed.

Numerical testing of rectangular and trapezoidal rule schemes is performed on a reservoir-pipeline-valve system. The system consists of a 37.2 m long copper pipeline with a 22 mm diameter. The initial flow in the pipeline has a Reynolds number of 5,600. The valve is closed such that a fast valve closure was achieved (time of closure, $t_c < 2L/a$). The head used for comparisons between the two schemes is next to the valve and denoted H_V. Figure B.2 shows an absence of any differences between the observed head when using the rectangular and trapezoidal rules. The similarity in the results suggests that the higher order trapezoidal rule approximation of the integral of the unsteady friction term is not required, rather the rectangular rule is sufficient.

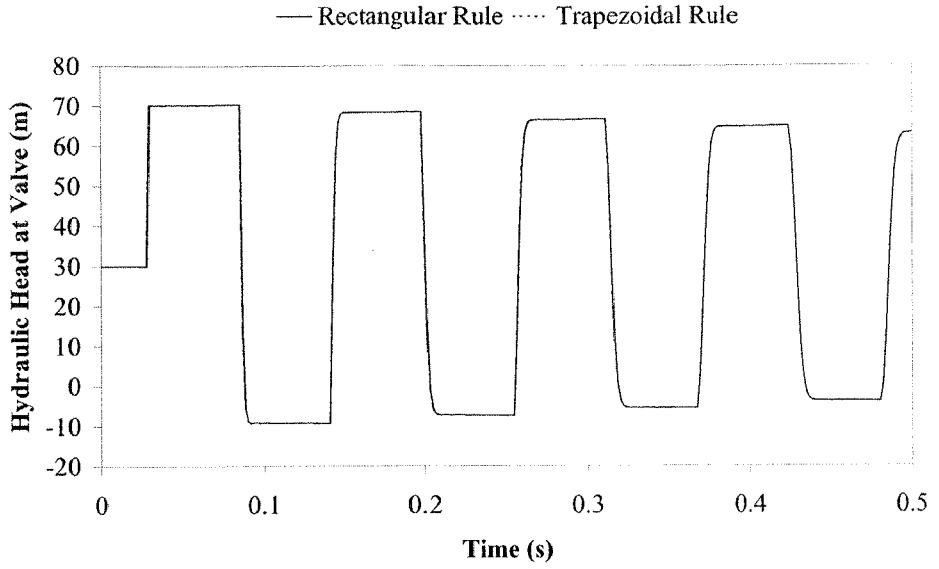

Figure B.2 Results Using the Rectangular and Trapezoidal Rules on a Diamond Grid ($n = 16$)

B.1.2 Implementation on Rectangular and Diamond MOC Grids

There are two types of characteristic grids that may be used when setting up a MOC scheme. The two grid types are a diamond shaped grid and a rectangular shaped grid, both of which are shown in Figure B.3.

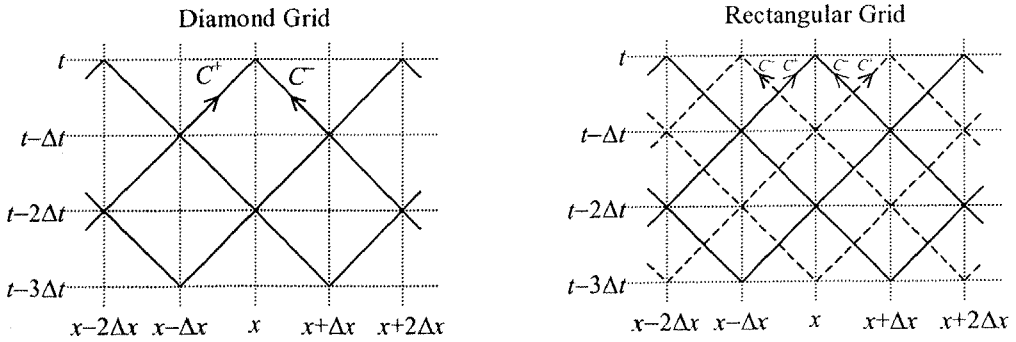

Figure B.3 Rectangular and Diamond MOC Grids

The rectangular grid system is really two diamond grids superimposed on top of each other. For standard transient analysis, including steady state friction, the two grids do not interact with each other; however, when including unsteady friction the calculation of the partial derivatives can cause interaction between the two grids. The effect of the

different grid types when including unsteady friction is tested for the identical pipeline and transient event as used by Section B.1.1, and the results of which are shown in Figure B.4. Both the diamond and rectangular grid systems divide the pipeline into 16 computational reaches.

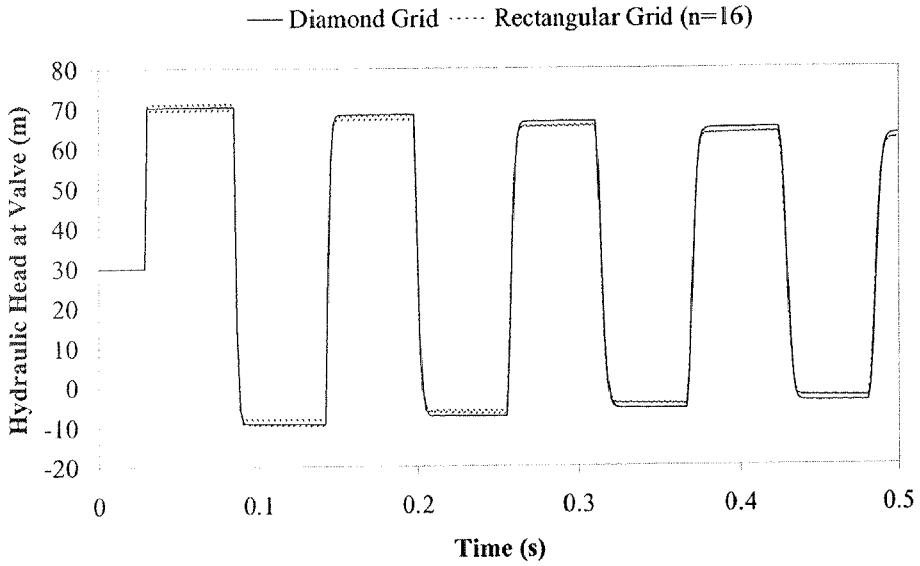

Figure B.4 Results Using Diamond and Rectangular Grid Systems (n = 16)

An oscillation in the head (that becomes smaller as time progresses) is observed in Figure B.4 for the rectangular grid system. In addition, the rectangular grid system produces slightly more damping than the diamond grid system. The tying together of the two separate grids causes the oscillation by the calculation of the derivatives used in the unsteady friction model. The two grids are subjected to slightly different boundary conditions and are incompatible when they interact with each other. The number of computational reaches, n, was increased from 16 to 32 to test whether a finer grid would decrease the oscillation (Figure B.5).

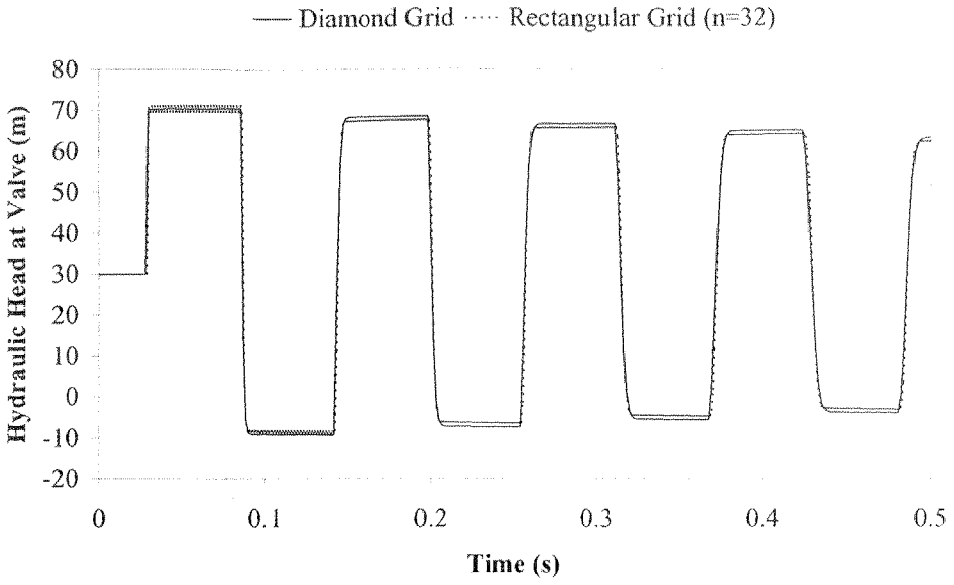

Figure B.5 Results Using Diamond and Rectangular Grid Systems (n = 32)

Figure B.5 shows that using a finer grid does make the resulting head variation smoother, however, the slight increase in damping (when using the rectangular grid system) is still present. The results in this section suggest that when using a rectangular grid system, the separate grids should not be allowed interact with each other and unsteady friction schemes (and other phenomena) should be defined on one grid only.

B.1.3 Bergant and Simpson's (1994) Implementation

Bergant and Simpson (1994) undertook the validation of a number of different unsteady state friction models on an experimental pipeline under both cavitating and non-cavitating flow conditions. The models considered were: no friction, steady state friction, quasi-steady state friction, Zielke (1968) unsteady state friction, Hino *et al.* (1977) unsteady state friction, and Brunone *et al.* (1991) unsteady state friction. The performance of most of these models were poor except for the Zielke (1968) model and Brunone *et al.* (1991) model of which the Brunone *et al.* (1991) model yielded the best matches. After a closer inspection of the method used (and code) to find the spatial derivatives there seemed to be an error in a relationship used to approximate the spatial derivative used in the Brunone *et al.* (1991) unsteady state friction term. To understand the error it is necessary to show how partial derivatives are found numerically.

Consider a function f that is dependent on two variables x and y. The partial derivative $\partial f/\partial x$ may be calculated using a first order divided difference method,

$$\frac{\partial f}{\partial x} = \frac{f(x+h,y)-f(x,y)}{h} \quad \text{(B.1.14)}$$

where h = an appropriately sized perturbation in x. If this derivative is to be calculated on a diamond grid system and within a computation unit, the flow (or velocity) is required at an undetermined point (see points A_0 and B_0 in Figure B.1). In a paper on transient cavitation, Wylie (1984) describes an approximation to find an undetermined point in terms of a weighting factor, ψ, which taken in the time direction is

$$Q_{t-2\Delta t} = \psi Q_{t-\Delta t} + (1-\psi)Q_{t-3\Delta t} \quad \text{(B.1.15)}$$

Weighting factor values used by Bergant and Simpson (1994) were 1.0 for spatial derivatives and 0.5 for time derivatives of the flow. Figure B.6 shows the result of using these values on the characteristic grid, where points A_0 and B_0 are to be determined.

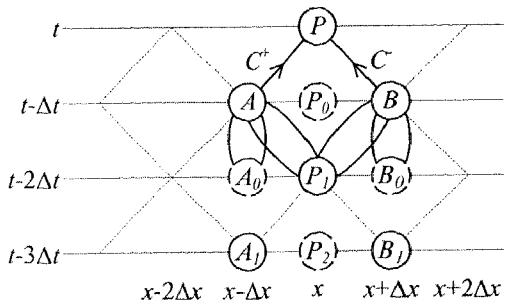

Figure B.6 Partial Derivatives in an Explicit MOC Grid, ψ = 1.0

Figure B.6 shows (with rings) where the derivatives are taken for spatial and temporal cases and, for ψ = 1.0, looks like an 'M' shaped configuration. The spatial partial derivatives are displayed as the inner sloping rings. These partial derivatives originally were meant to be taken between points P_1&A_0 and B_0&P_1 but using Eq. B.1.15 with ψ = 1.0 they are effectively taken between points P_1&A and B&P_1 (along the characteristic lines). This violates the definition of a partial derivative since the variable of time is not being held constant. To add to this, numerical experiments, details of which are not shown here, demonstrate that $\frac{\partial V^+}{\partial x} \approx -\frac{\partial V^-}{\partial x}$ (when calculated across the characteristic line) and subsequently these terms cancel each other out during the MOC computation. Therefore, the Brunone *et al.* (1991) unsteady state friction method used

in the Bergant and Simpson (1994) paper is actually a variant of a Carstens and Roller (1959)-type method.

The correct Wylie (1984) weighting function value (even though the partial derivatives are in the space direction) is to use $\psi = 0.5$. Figure B.7 represents the use of $\psi = 0.5$. The weighting function produces an effective linear interpolation between points $A\&A_1$ for point A_0 and $B\&B_1$ for point B_0, resulting in a 'U' configuration, which is contained within a computational unit.

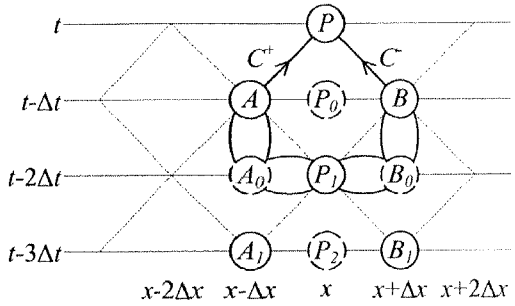

Figure B.7 Partial Derivatives in an Explicit MOC Grid, $\psi = 0.5$

This section casts doubt on the results presented in Bergant and Simpson (1994) for the implementation of the Brunone *et al.* (1991) unsteady state friction model.

B.1.4 Internal Consistency of the Brunone et al. (1991) Unsteady Friction Model

The internal consistency of the Brunone *et al.* (1991) unsteady friction model is investigated using a simple pipeline. The transient event used is a fast downstream valve closure (identical to previous sections). The number of reaches, *n*, are increased from 1 to 16 while keeping the Courant number at equality, which is equivalent to decreasing the pipe reach lengths from 37.2 m to 2.325 m. Figure B.8 shows the effect of different numbers of reaches.

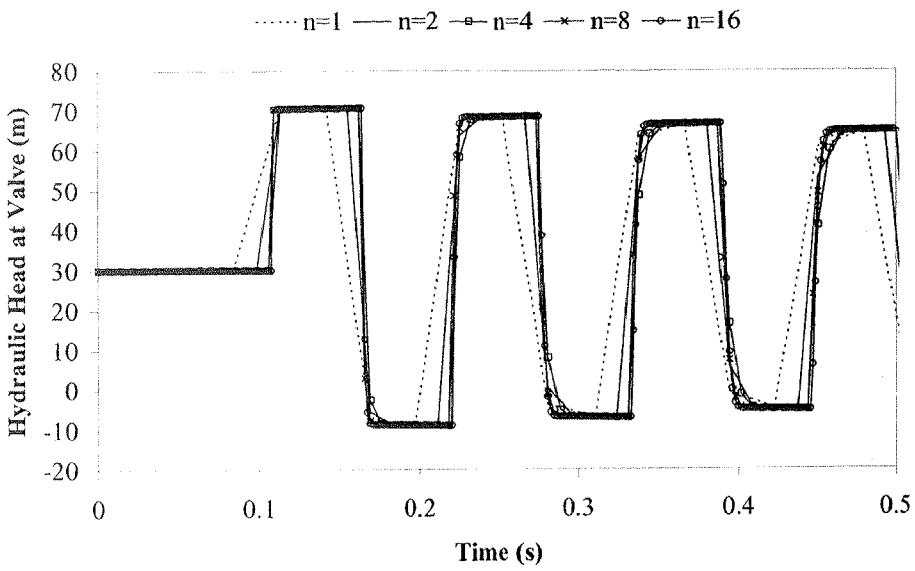

Figure B.8 Internal Consistency of the Brunone *et al.* (1991) Unsteady Friction Model

Figure B.8 shows that for numbers of reaches larger than four the results are similar. Analysis with 32 computational reaches produced indistinguishable results from the 16 reach result, thus suggesting that the Brunone *et al.* (1991) unsteady friction scheme is internally consistent for 4 or more internal reaches (for this specific problem). The number of computational reaches has no effect on the magnitude of the pressure oscillations, also suggesting that there is an accuracy criteria below which the characteristic grid is too coarse for successful unsteady friction implementation (the MOC grid does not accurately approximate finite differences).

B.1.5 Summary of Implementation Procedures

This section provides methods for the successful implementation of the Brunone *et al.* (1991) unsteady friction model treated as an addition to steady friction. Topics investigated include rectangular and trapezoidal rule integration schemes, different grid types, past implementations and internal consistency analysis. Bughazem and Anderson (1996) produce results showing that the Brunone *et al.* (1991) unsteady friction model is unstable for different numbers of computational reaches. Their result is inconsistent compared with results from Section B.1.4.

B.2 Diagrams for 8 Simple Unsteady Flow Events

The 8 unsteady flow events were previously defined in Chapter 9, however it is useful to explain how the pressure and flow changes during each event (in a qualitative way). Figures B.9 to B.16 show the variation of pressure and flow for the different periods during each event. Each of these cases uses a frictionless pipeline between two reservoirs and a valve to initiate the transient event. The original hydraulic grade line is the dashed line.

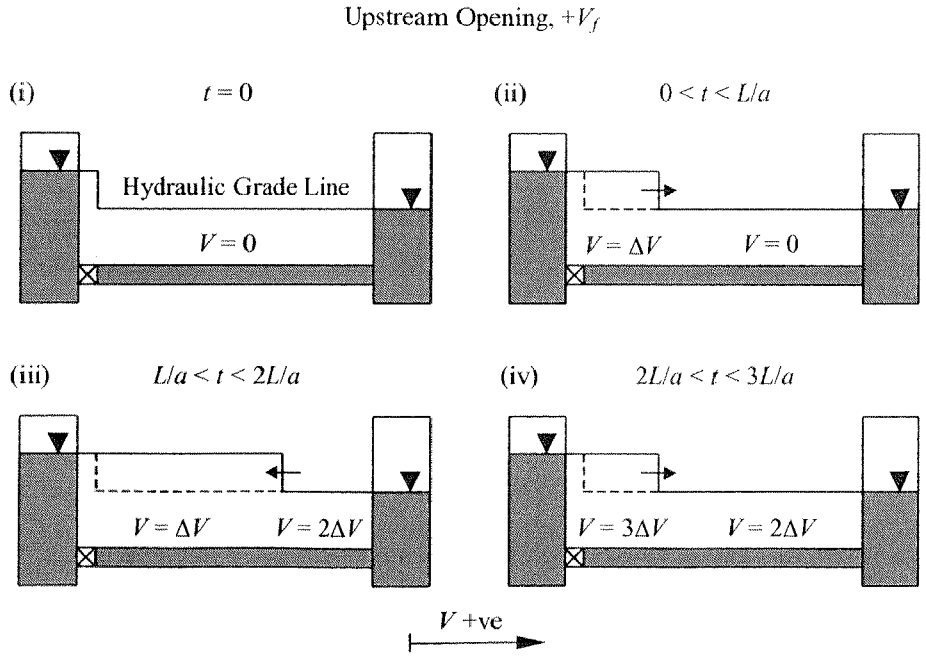

Figure B.9 Simple Flow Event (A)

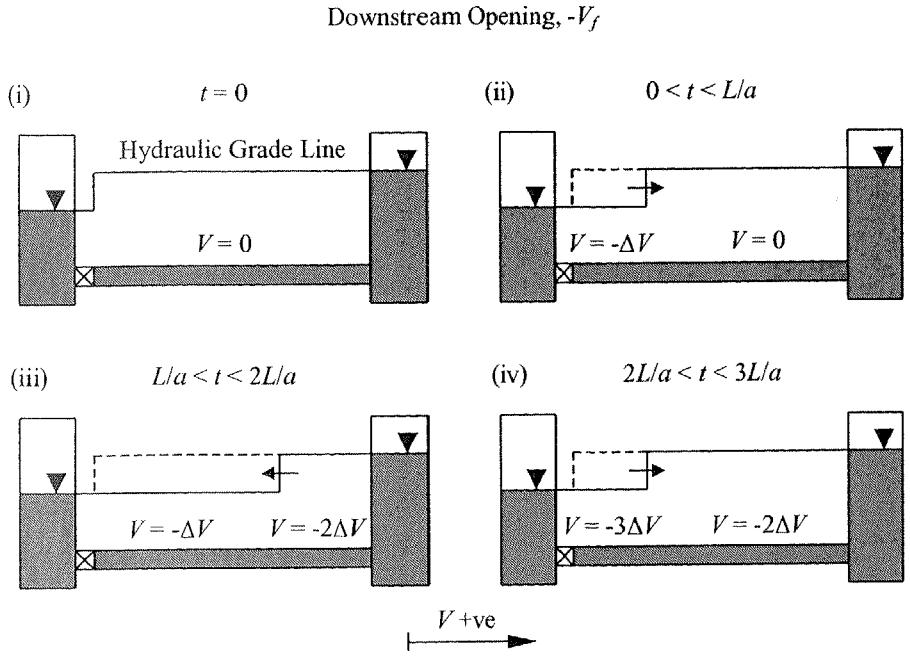

Figure B.10 Simple Flow Event (B)

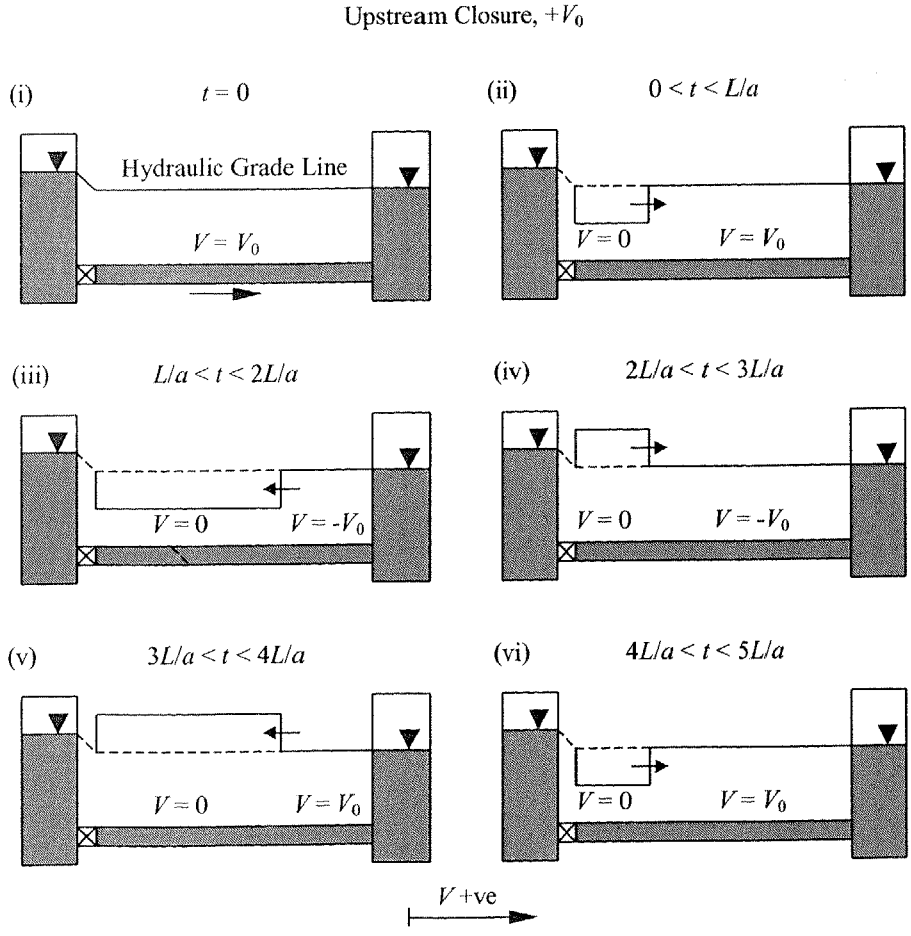

Figure B.11 Simple Flow Event (C)

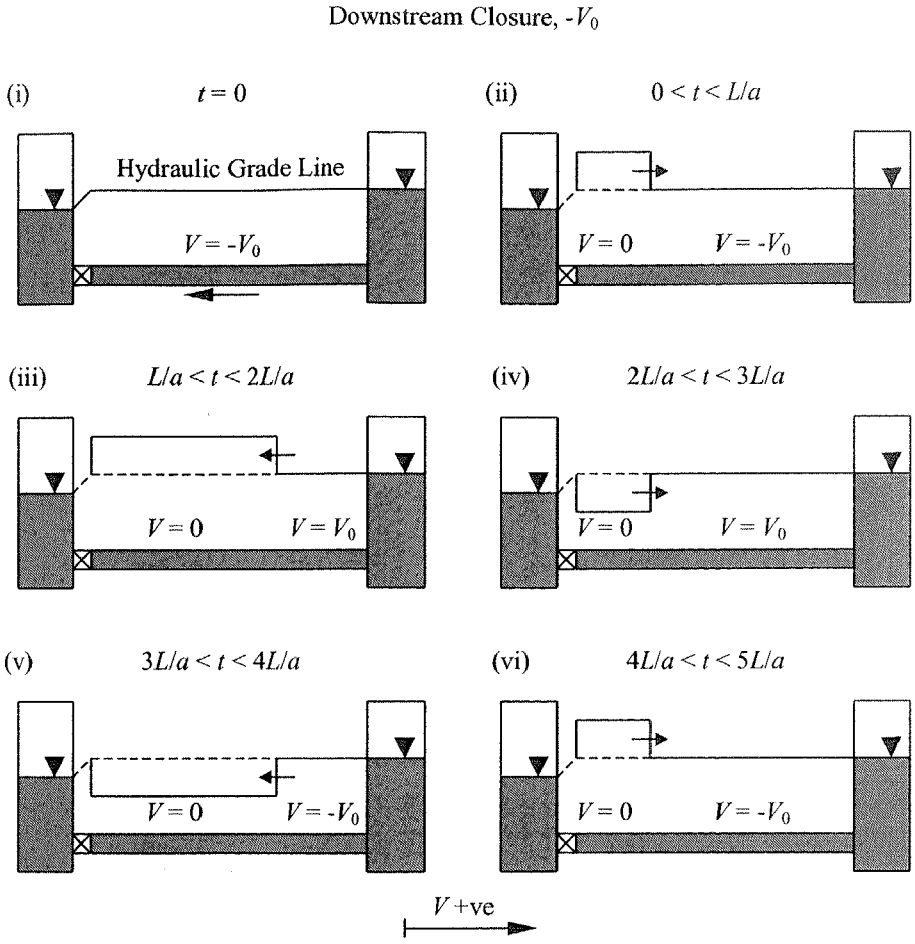

Figure B.12 Simple Flow Event (D)

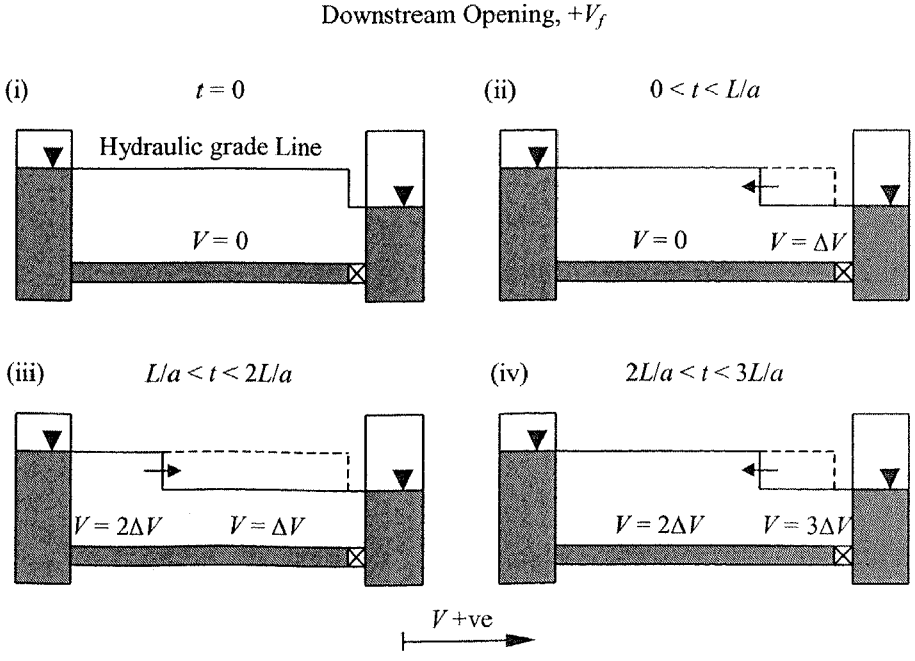

Figure B.13 Simple Flow Event (E)

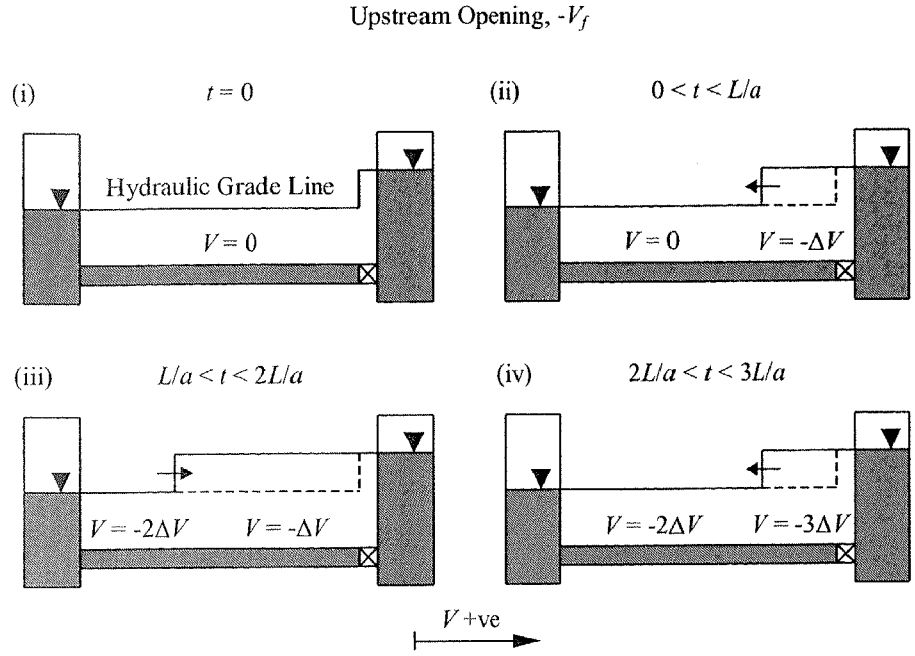

Figure B.14 Simple Flow Event (F)

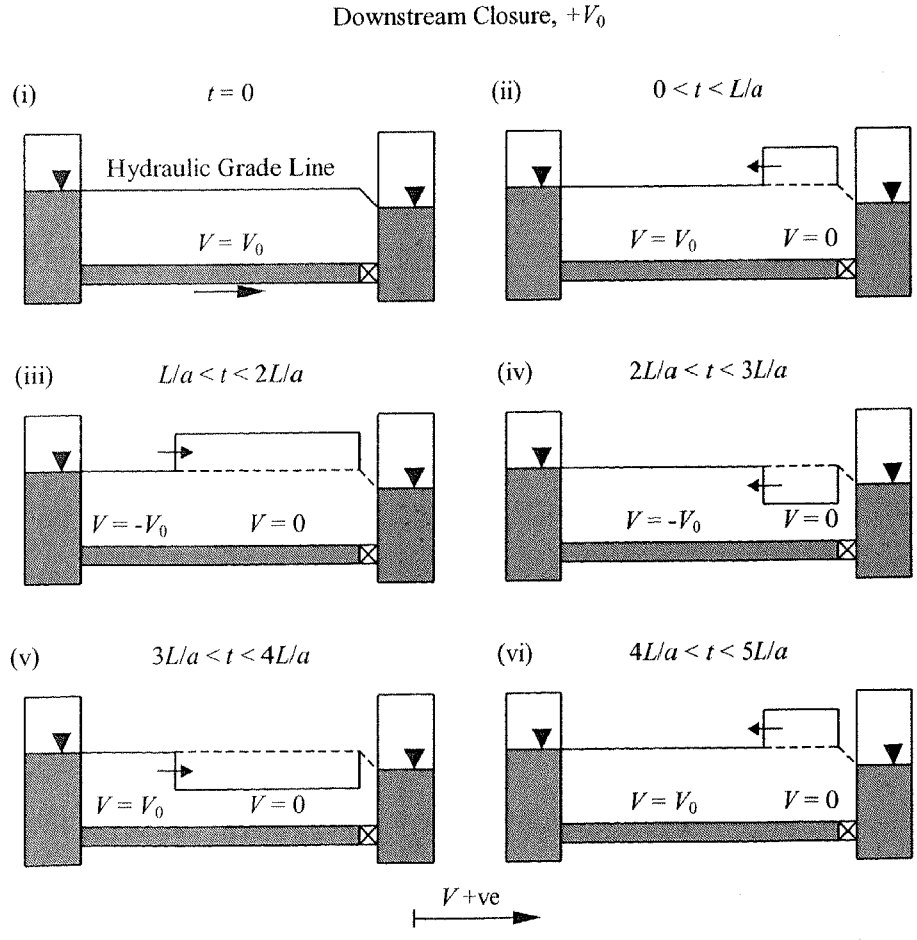

Figure B.15 Simple Flow Event (G)

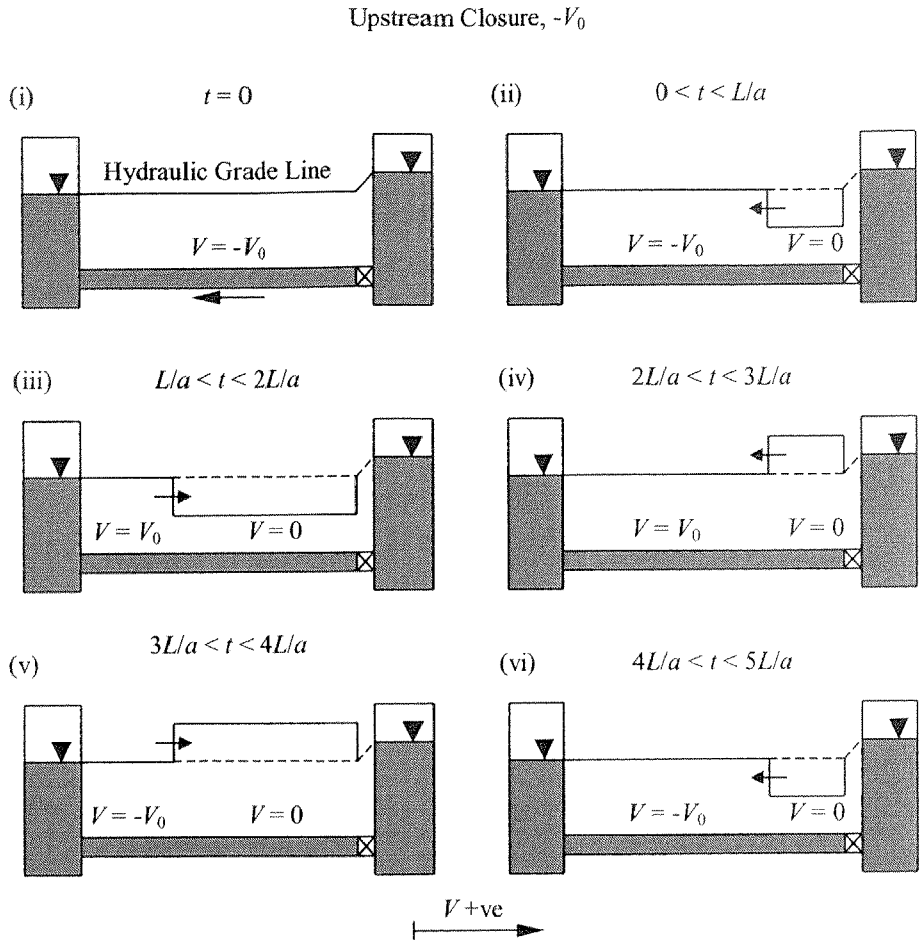

Figure B.16 Simple Flow Event (H)

B.3 Derivation of Equation of Motion (Momentum) Including β Correction

The derivation of the momentum equation including β correction begins similarly to the derivation of the equation of motion without β correction (shown in Chapter 3). Reynolds transport theorem is used with the extensive property being the system momentum, implying conservation of linear-momentum. The introduction of the momentum into Reynolds transport theorem gives

$$\sum \mathbf{F} = \frac{\partial}{\partial t}\int_{CS} \rho v d\vartheta + \int_{CS} \rho \mathbf{v}\mathbf{v} \cdot d\mathbf{A} \quad \text{.....(B.3.1)}$$

It is useful to deal with each side of Eq. B.3.1 separately. First the left-hand side of the equation is dealt with. The left-hand side is equal to the sum of the forces acting of the control volume. These forces are identified by the examination of a free body diagram of the control volume (see Section 3.2.2). The left-hand side is

$$LHS = pA - \left[pA + \frac{\partial(pA)}{\partial x}\delta x \right] + p\frac{\partial A}{\partial x} - \rho g A \frac{\partial z}{\partial x}\delta x - \tau_0 \pi D \delta x \quad \text{..... (B.3.2)}$$

Eq. B.3.2 is simplified by expanding the partial derivative producing the final left-hand side expression

$$LHS = -A\frac{\partial p}{\partial x}\delta x - \rho g A \frac{\partial z}{\partial x}\delta x - \tau_0 \pi D \delta x \quad \text{..... (B.3.3)}$$

Now the right hand side of Eq. B.3.1 is examined. First, the right-hand side is transformed to pipe flow properties (such as area) and the control surface term is dealt with.

$$RHS = \frac{\partial}{\partial t}\int_A \rho v \delta x dA + \left(\int_A \rho v^2 dA + \frac{\partial}{\partial x}\int_A \rho v^2 dA \delta x \right) - \int_A \rho v^2 dA \quad \text{..... (B.3.4)}$$

Simplification of Eq. B.3.4 forms

$$RHS = \frac{\partial}{\partial t}\int_A \rho v \delta x dA + \frac{\partial}{\partial x}\int_A \rho v^2 dA \delta x \quad \text{..... (B.3.5)}$$

The integrals are evaluated using the definitions of the average velocity, $AV = \int_A v dA$, and the definition of the momentum correction factor, $\beta AV^2 = \int_A v^2 dA$.

$$RHS = \frac{\partial(\rho AV\delta x)}{\partial t} + \frac{\partial(\rho \beta AV^2)}{\partial x}\delta x \quad \text{..... (B.3.6)}$$

The linear-momentum equation now includes the momentum correction factor and this implies that there is a velocity profile effect present. The partial derivatives in the right-hand side are partially expanded producing

$$RHS = \rho A\frac{\partial V}{\partial t}\delta x + V\frac{\partial(\rho A)}{\partial t}\delta x + \rho AV\frac{\partial(\beta V)}{\partial x}\delta x + \beta V\frac{\partial(\rho AV)}{\partial x}\delta x \quad \text{..... (B.3.7)}$$

Rearranging and collecting some terms yields

$$RHS = \rho A\frac{\partial V}{\partial t}\delta x + \rho AV\frac{\partial(\beta V)}{\partial x}\delta x + V\left[\frac{\partial(\rho A)}{\partial t} + \frac{\partial(\rho AV)}{\partial x}\right]\delta x + (\beta - 1)V\frac{\partial(\rho AV)}{\partial x}\delta x \quad \text{..... (B.3.8)}$$

The bracketed term is the continuity equation (equal to zero) and is cancelled out, transforming the relationship into a non-conservative form.

$$RHS = \rho A\frac{\partial V}{\partial t}\delta x + \rho AV\frac{\partial(\beta V)}{\partial x}\delta x + (\beta - 1)V\frac{\partial(\rho AV)}{\partial x}\delta x \quad \text{..... (B.3.9)}$$

The final term in Eq. B.3.9 is typically small compared to the other terms and is neglected.

$$RHS = \rho A \frac{\partial V}{\partial t} \delta x + \rho A V \frac{\partial (\beta V)}{\partial x} \delta x \quad \text{.....(B.3.10)}$$

Finally the partial derivative is fully expanded producing

$$RHS = \rho A \frac{\partial V}{\partial t} \delta x + \rho \beta A V \frac{\partial V}{\partial x} \delta x + \rho A V^2 \frac{\partial \beta}{\partial x} \delta x \quad \text{.....(B.3.11)}$$

At this point both the left-hand side (Eq. B.3.3) and right-hand side (Eq. B.3.11) are recombined to form

$$-A \frac{\partial p}{\partial x} \delta x - \rho g A \frac{\partial z}{\partial x} \delta x - \tau_0 \pi D \delta x = \rho A \frac{\partial V}{\partial t} \delta x + \rho \beta A V \frac{\partial V}{\partial x} \delta x + \rho A V^2 \frac{\partial \beta}{\partial x} \delta x \quad \text{.....(B.3.12)}$$

Moving the left-hand side terms to the right hand side and dividing by $g\rho A \delta x$ produces

$$0 = \frac{1}{g} \frac{\partial V}{\partial t} + \frac{\beta V}{g} \frac{\partial V}{\partial x} + \frac{V^2}{g} \frac{\partial \beta}{\partial x} + \frac{1}{g\rho} \frac{\partial p}{\partial x} + \frac{\partial z}{\partial x} + \frac{\tau_0 \pi D}{\rho g A} \quad \text{.....(B.3.13)}$$

Substituting the hydraulic head for the pressure and elevation makes a simplification. The definition of the hydraulic head is

$$H = \frac{p}{g\rho} + z \quad \text{.....(B.3.14)}$$

Differentiation with respect to the distance along the pipe section, x, forms

$$\frac{\partial H}{\partial x} = \frac{1}{g\rho} \frac{\partial p}{\partial x} + \frac{\partial z}{\partial x} \quad \text{.....(B.3.15)}$$

Substitution of Eq. B.3.15 into Eq. B.3.13 produces

$$0 = \frac{1}{g} \frac{\partial V}{\partial t} + \frac{\beta V}{g} \frac{\partial V}{\partial x} + \frac{V^2}{g} \frac{\partial \beta}{\partial x} + \frac{\partial H}{\partial x} + \frac{\tau_0 \pi D}{\rho g A} \quad \text{.....(B.3.16)}$$

Expressing the steady friction in terms of the unit head loss per unit length J results in

$$0 = \frac{1}{g} \frac{\partial V}{\partial t} + \frac{\beta V}{g} \frac{\partial V}{\partial x} + \frac{V^2}{g} \frac{\partial \beta}{\partial x} + \frac{\partial H}{\partial x} + J \quad \text{.....(B.3.17)}$$

Eq B.3.17 is the equation of motion with β correction included. The standard equation (without β effects) is found by setting β to 1 (with the partial derivative of β equalling zero).

B.4 Derivation of Equation of Motion (Energy) Including α and β Corrections

The derivation of the unsteady energy equation starts with Reynolds transport theorem where the extensive fluid property is energy. Doing this exacts the conservation of energy and produces a scalar relationship (as compared to the momentum equation, which is a vector relationship). The internal energy per unit mass, e, is introduced into Reynolds transport theorem,

$$\frac{\delta Q_H}{\delta t} - \frac{\delta W}{\delta t} = \frac{\partial}{\partial t}\int_{C\vartheta} \rho e d\vartheta + \int_{CS} \rho e \mathbf{v} \cdot d\mathbf{A} \quad \text{..... (B.4.1)}$$

where Q_H is the heat energy and W is the work done by the system. Similar to the derivation of the equation of motion including β corrections, Eq. B.4.1 is split into two and each half is dealt with separately. The left-hand side is the work done and heat flow to the control surface. The work done by the system on its surroundings is composed of two parts. The first is the work done by the pressure forces on the moving boundary, W_{pr}, and the other is shaft work, W_S.

$$\delta W = \delta W_{pr} + \delta W_S \quad \text{..... (B.4.2)}$$

The shaft work is equal to zero therefore the work done is only dependent on W_{pr}. The work done by the pressure on the control surface is

$$\delta W_{pr} = \delta t \int_{CS} p\mathbf{v} \cdot d\mathbf{A} \quad \text{..... (B.4.3)}$$

Dividing both sides of Eq. B.4.3 by the change in time results in the rate of work done by the pressure on the control surface.

$$\frac{\delta W_{pr}}{\delta t} = \int_{CS} p\mathbf{v} \cdot d\mathbf{A} \quad \text{..... (B.4.4)}$$

The integral over the control surface is determined by examining the integral at each end of the pipe section and including the work done due to force of the pressure on the changing area along the pipe section.

$$\frac{\delta W_{pr}}{\delta t} = \left[\left(\int_A pvdA + \frac{\partial}{\partial x}\int_A pvdA\delta x\right) - \int_A pvdA\right] - p\frac{\partial(AV)}{\partial x}\delta x \quad \text{..... (B.4.5)}$$

Eq. B.4.5 simplifies to

$$\frac{\delta W_{pr}}{\delta t} = \frac{\partial}{\partial x}\int_A pvdA\delta x - p\frac{\partial(AV)}{\partial x}\delta x \quad \text{..... (B.4.6)}$$

Evaluation of the integral expression in Eq. B.4.6 forms

$$\frac{\delta W_{pr}}{\delta t} = \frac{\partial(pAV)}{\partial x}\delta x - p\frac{\partial(AV)}{\partial x}\delta x \quad \text{.....(B.4.7)}$$

Partial expansion of the first partial derivative term in Eq. B.4.7 produces

$$\frac{\delta W_{pr}}{\delta t} = p\frac{\partial(AV)}{\partial x}\delta x + AV\frac{\partial p}{\partial x}\delta x - p\frac{\partial(AV)}{\partial x}\delta x \quad \text{.....(B.4.8)}$$

Finally, the rate of work done by the pressure on the control surface is

$$\frac{\delta W_{pr}}{\delta t} = AV\frac{\partial p}{\partial x}\delta x \quad \text{.....(B.4.9)}$$

Therefore, the left-hand side of Eq. B.4.1 is

$$LHS = \frac{\delta Q_H}{\delta t} - AV\frac{\partial p}{\partial x}\delta x \quad \text{.....(B.4.10)}$$

Now the right-hand side of Eq. B.4.1 is dealt with. The internal energy per unit mass, e, is a combination of potential energy, kinetic energy and intrinsic energy. The intrinsic energy per unit mass, u, is due to molecular spacing and forces (dependent upon p, ρ or T).

$$e = gz + \tfrac{1}{2}V^2 + u \quad \text{.....(B.4.11)}$$

Substitution of the internal energy into the right-hand side of Eq. B.4.1 produces

$$RHS = \frac{\partial}{\partial t}\int_{CV}\left(\rho gz + \tfrac{1}{2}\rho v^2 + \rho u\right)d\vartheta + \int_{CS}\left(\rho gz + \tfrac{1}{2}\rho v^2 + \rho u\right)\mathbf{v}\cdot d\mathbf{A} \quad \text{.....(B.4.12)}$$

Similar to other derivations, the evaluation of the integral over the control surface is achieved by examining the integral at either end of the pipe section.

$$\begin{aligned} RHS = {} & \frac{\partial}{\partial t}\int_A\left(\rho gz + \tfrac{1}{2}\rho v^2 + \rho u\right)\delta x dA + \int_A\left(\rho gz + \tfrac{1}{2}\rho v^2 + \rho u\right)v dA \\ & + \frac{\partial}{\partial x}\int_A\left(\rho gz + \tfrac{1}{2}\rho v^2 + \rho u\right)v dA\delta x - \int_A\left(\rho gz + \tfrac{1}{2}\rho v^2 + \rho u\right)v dA \end{aligned} \quad \text{.....(B.4.13)}$$

Simplification of Eq. B.4.13 leaves only integral expressions that are evaluated over the pipe cross-sectional area.

$$RHS = \frac{\partial}{\partial t}\int_A\left(\rho gz + \tfrac{1}{2}\rho v^2 + \rho u\right)\delta x dA + \frac{\partial}{\partial x}\int_A\left(\rho gz + \tfrac{1}{2}\rho v^2 + \rho u\right)v dA\delta x \quad \text{.....(B.4.14)}$$

Evaluation of the integrals in Eq. B.4.14 and introducing the average velocity, V, momentum correction factor, β, and kinetic energy correction factor, α, gives

$$\begin{aligned} RHS = {} & gz\frac{\partial(\rho A\delta x)}{\partial t} + \frac{1}{2}\frac{\partial(\rho\beta AV^2\delta x)}{\partial t} + \frac{\partial(\rho uA\delta x)}{\partial t} + g\frac{\partial(\rho AVz)}{\partial x}\delta x \\ & + \frac{1}{2}\frac{\partial(\rho\alpha AV^3)}{\partial x}\delta x + \frac{\partial(\rho uAV)}{\partial x}\delta x \end{aligned} \quad \text{.....(B.4.15)}$$

where the kinetic energy correction factor is defined as $\alpha AV^3 = \int_A v^3 dA$. The convective partial derivative containing the elevation z in Eq. B.4.15 is partially expanded and the terms multiplied by gz are grouped as

$$RHS = gz\left[\frac{\partial(\rho A)}{\partial t} + \frac{\partial(\rho AV)}{\partial x}\right]\delta x + g\rho AV\frac{\partial z}{\partial x}\delta x + \frac{1}{2}\frac{\partial(\rho\beta AV^2)}{\partial t}\delta x + \frac{1}{2}\frac{\partial(\rho\alpha AV^3)}{\partial x}\delta x + \frac{\partial(\rho uA)}{\partial t}\delta x + \frac{\partial(\rho uAV)}{\partial x}\delta x \quad \text{..... (B.4.16)}$$

The bracketed term is the continuity equation and is equal to zero. The energy equation is now in a non-conservative form. Partial expansion of the partial derivatives containing the momentum and kinetic energy correction factors produces

$$RHS = g\rho AV\frac{\partial z}{\partial x}\delta x + \frac{\rho A}{2}\frac{\partial(\beta V^2)}{\partial t}\delta x + \frac{\beta V^2}{2}\frac{\partial(\rho A)}{\partial t}\delta x + \frac{\rho AV}{2}\frac{\partial(\alpha V^2)}{\partial x}\delta x + \frac{\alpha V^2}{2}\frac{\partial(\rho AV)}{\partial x}\delta x + \frac{\partial(\rho uA)}{\partial t}\delta x + \frac{\partial(\rho uAV)}{\partial x}\delta x \quad \text{.... (B.4.17)}$$

Rearranging forms

$$RHS = g\rho AV\frac{\partial z}{\partial x}\delta x + \frac{\rho A}{2}\frac{\partial(\beta V^2)}{\partial t}\delta x + \frac{\rho AV}{2}\frac{\partial(\alpha V^2)}{\partial x}\delta x + \frac{\beta V^2}{2}\left[\frac{\partial(\rho A)}{\partial t} + \frac{\partial(\rho AV)}{\partial x}\right]\delta x + \frac{(\alpha-\beta)V^2}{2}\frac{\partial(\rho AV)}{\partial x}\delta x + \frac{\partial(\rho uA)}{\partial t}\delta x + \frac{\partial(\rho uAV)}{\partial x}\delta x \quad \text{..... (B.4.18)}$$

The bracketed term multiplied by $\beta V^2/2$ is the continuity equation, which is equal to zero. The term containing $(\alpha - \beta)$ is small compared to the other terms and is dropped forming

$$RHS = g\rho AV\frac{\partial z}{\partial x}\delta x + \frac{\rho A}{2}\frac{\partial(\beta V^2)}{\partial t}\delta x + \frac{\rho AV}{2}\frac{\partial(\alpha V^2)}{\partial x}\delta x + \frac{\partial(\rho uA)}{\partial t}\delta x + \frac{\partial(\rho uAV)}{\partial x}\delta x \quad \text{..... (B.4.19)}$$

Now the intrinsic energy terms are partially expanded.

$$RHS = g\rho AV\frac{\partial z}{\partial x}\delta x + \frac{\rho A}{2}\frac{\partial(\beta V^2)}{\partial t}\delta x + \frac{\rho AV}{2}\frac{\partial(\alpha V^2)}{\partial x}\delta x + \rho A\frac{\partial u}{\partial t}\delta x + u\frac{\partial(\rho A)}{\partial t}\delta x + \rho AV\frac{\partial u}{\partial x}\delta x + u\frac{\partial(\rho AV)}{\partial x}\delta x \quad \text{..... (B.4.20)}$$

Rearranging Eq. B.4.20 forms

$$RHS = g\rho AV\frac{\partial z}{\partial x}\delta x + \frac{\rho A}{2}\frac{\partial\left(\beta V^2\right)}{\partial t}\delta x + \frac{\rho AV}{2}\frac{\partial\left(\alpha V^2\right)}{\partial x}\delta x + u\left[\frac{\partial(\rho A)}{\partial t} + \frac{\partial(\rho AV)}{\partial x}\right]\delta x + \rho A\left(\frac{\partial u}{\partial t} + V\frac{\partial u}{\partial x}\right)\delta x \quad \text{.....(B.4.21)}$$

The bracketed term multiplied by u is the continuity equation and is equal to zero. The left over terms containing the intrinsic energy are recombined to form the total derivative of the intrinsic energy with respect to time,

$$RHS = g\rho AV\frac{\partial z}{\partial x}\delta x + \frac{\rho A}{2}\frac{\partial\left(\beta V^2\right)}{\partial t}\delta x + \frac{\rho AV}{2}\frac{\partial\left(\alpha V^2\right)}{\partial x}\delta x + \rho A\frac{du}{dt}\delta x \quad \text{.....(B.4.22)}$$

Equating the left-hand side expression (Eq. B.4.10) with the right-hand side expression (Eq. B.4.22) forms

$$\frac{\delta Q_H}{\delta t} - AV\frac{\partial p}{\partial x}\delta x = g\rho AV\frac{\partial z}{\partial x}\delta x + \frac{\rho A}{2}\frac{\partial\left(\beta V^2\right)}{\partial t}\delta x + \frac{\rho AV}{2}\frac{\partial\left(\alpha V^2\right)}{\partial x}\delta x + \rho A\frac{du}{dt}\delta x \quad \text{...(B.4.23)}$$

Moving the terms on the left-hand side of Eq. B.4.23 to the right-hand side and grouping the partial derivatives of the pressure and elevation with respect to space together forms

$$0 = \frac{\rho A}{2}\frac{\partial\left(\beta V^2\right)}{\partial t}\delta x + \frac{\rho AV}{2}\frac{\partial\left(\alpha V^2\right)}{\partial x}\delta x + g\rho AV\left(\frac{1}{g\rho}\frac{\partial p}{\partial x} + \frac{\partial z}{\partial x}\right)\delta x + \rho A\frac{du}{dt}\delta x - \frac{\delta Q_H}{\delta t} \quad \text{.....(B.4.24)}$$

The hydraulic head is the addition of the pressure head and the elevation head,

$$H = \frac{p}{g\rho} + z \quad \text{.....(B.4.25)}$$

Differentiation of Eq. B.4.25 with respect to the distance along the pipe, x, produces

$$\frac{\partial H}{\partial x} = \frac{1}{g\rho}\frac{\partial p}{\partial x} + \frac{\partial z}{\partial x} \quad \text{.....(B.4.26)}$$

Substitution of Eq. B.4.26 into Eq. B.4.26 produces

$$0 = \frac{\rho A}{2}\frac{\partial\left(\beta V^2\right)}{\partial t}\delta x + \frac{\rho AV}{2}\frac{\partial\left(\alpha V^2\right)}{\partial x}\delta x + g\rho AV\frac{\partial H}{\partial x}\delta x + \rho A\frac{du}{dt}\delta x - \frac{\delta Q_H}{\delta t} \quad \text{.....(B.4.27)}$$

At this point the intrinsic energy, u, is re-examined. The exact value of the intrinsic energy is not known, however, the change in the intrinsic energy may be determined. The change in the intrinsic energy, du, is equal to energy due to the shear of the pipe wall on the fluid divided by the mass of the control volume, where this change in the intrinsic energy is converted to heat energy. The change in heat energy is small and is

neglected. In lumping the intrinsic energy and heat energy together (Liggett and Caughey, 1998), an expression for the change in the lumped intrinsic and heat energy is

$$\rho A\delta x\frac{du}{dt}-\frac{\delta Q_H}{\delta t}=\tau_0\pi D\delta xV \quad \text{..... (B.4.28)}$$

Substitution of Eq. B.4.28 into Eq. B.4.27 forms

$$0=\frac{\rho A}{2}\frac{\partial\left(\beta V^2\right)}{\partial t}\delta x+\frac{\rho AV}{2}\frac{\partial\left(\alpha V^2\right)}{\partial x}\delta x+g\rho AV\frac{\partial H}{\partial x}\delta x+\tau_0\pi D\delta xV \quad \text{..... (B.4.29)}$$

Expansion of all partial derivatives gives

$$\begin{aligned}0=\rho\beta AV\frac{\partial V}{\partial t}\delta x+\frac{\rho AV^2}{2}\frac{\partial\beta}{\partial t}\delta x+\rho\alpha AV\frac{\partial V}{\partial x}\delta x+\frac{\rho AV^2}{2}\frac{\partial\alpha}{\partial x}\delta x\\+g\rho AV\frac{\partial H}{\partial x}\delta x+\tau_0\pi DV\delta x\end{aligned} \quad \text{..... (B.4.30)}$$

Division by $\rho gAV\delta x$, which is common to most of the terms, greatly simplifies Eq. B.4.30 to

$$0=\frac{\beta}{g}\frac{\partial V}{\partial t}+\frac{V}{2g}\frac{\partial\beta}{\partial t}+\frac{\alpha V}{g}\frac{\partial V}{\partial x}+\frac{V}{2g}\frac{\partial\alpha}{\partial x}+\frac{\partial H}{\partial x}+\frac{\tau_0\pi D}{g\rho A} \quad \text{..... (B.4.31)}$$

Expressing the steady friction in terms of the unit head loss per unit length, J, the unsteady energy equation including α and β corrections is

$$0=\frac{\beta}{g}\frac{\partial V}{\partial t}+\frac{V}{2g}\frac{\partial\beta}{\partial t}+\frac{\alpha V}{g}\frac{\partial V}{\partial x}+\frac{V^2}{2g}\frac{\partial\alpha}{\partial x}+\frac{\partial H}{\partial x}+J \quad \text{..... (B.4.32)}$$

B.5 Solution of the k_A & k_P Unsteady Friction Model Treated as an Addition to Steady Friction

The k_A & k_P unsteady friction model can be solved with the equations of motion and continuity in two different ways. They are the unsteady friction model (1) treated as an addition to steady friction and (2) included in the directional derivatives (in the method of characteristics). This section performs the method of characteristics on the governing unsteady equations with the k_A & k_P model treated as an addition to steady friction. The equation of motion including the k_A & k_P unsteady friction model is

$$L_1=\frac{\partial H}{\partial x}+\frac{1}{g}\frac{dV}{dt}+\frac{fV|V|}{2gD}+\frac{k_P}{g}\frac{dV}{dt}+\phi_V\frac{k_A}{g}\left|\frac{dV}{dt}\right|=0 \quad \text{..... (B.5.1)}$$

where the velocity sign operator is defined as

$$\phi_V = \begin{cases} +1 & \text{if} \quad V \geq 0 \\ -1 & \text{if} \quad V < 0 \end{cases} \quad \text{.....(B.5.2)}$$

The equation of continuity is equal to L_2,

$$L_2 = \frac{dH}{dt} + \frac{a^2}{g}\frac{\partial V}{\partial x} = 0 \quad \text{.....(B.5.3)}$$

Using the method of characteristics, a linear combination of the two partial differential equations is made using a constant, λ.

$$L = L_1 + \lambda L_2 = 0 \quad \text{.....(B.5.4)}$$

Substitution of Eqs. B.5.1 and B.5.3 into Eq. B.5.4 forms

$$L = \frac{\partial H}{\partial x} + \frac{1}{g}\frac{dV}{dt} + \frac{fV|V|}{2gD} + \frac{k_P}{g}\frac{dV}{dt} + \phi_V \frac{k_A}{g}\left|\frac{dV}{dt}\right| + \lambda\frac{dH}{dt} + \frac{\lambda a^2}{g}\frac{\partial V}{\partial x} = 0 \quad \text{.....(B.5.5)}$$

The full derivatives are decomposed into their partial constituents except for the k_A & k_P unsteady friction model. Collecting all of the partial derivatives of the head together and all of the partial derivative of the velocity together, except those relating to the k_A & k_P unsteady friction model, results in

$$L = \left(\lambda\frac{\partial H}{\partial t} + \lambda V\frac{\partial H}{\partial x} + \frac{\partial H}{\partial x}\right) + \left(\frac{1}{g}\frac{\partial V}{\partial t} + \frac{V}{g}\frac{\partial V}{\partial x} + \frac{\lambda a^2}{g}\frac{\partial V}{\partial x}\right) + \frac{fV|V|}{2gD} + \frac{k_P}{g}\frac{dV}{dt} + \phi_V\frac{k_A}{g}\left|\frac{dV}{dt}\right| \quad \text{.....(B.5.6)}$$

A common factor of λ is taken outside of the grouped head terms; likewise, a common factor of $1/g$ is taken out of the grouped velocity terms forming

$$L = \lambda\left[\frac{\partial H}{\partial t} + \left(V + \frac{1}{\lambda}\right)\frac{\partial H}{\partial x}\right] + \frac{1}{g}\left[\frac{\partial V}{\partial t} + \left(V + \lambda a^2\right)\frac{\partial V}{\partial x}\right] + \frac{fV|V|}{2gD} + \frac{k_P}{g}\frac{dV}{dt} + \phi_V\frac{k_A}{g}\left|\frac{dV}{dt}\right| \quad \text{.....(B.5.7)}$$

The partial derivative terms in the square brackets in Eq. B.5.7 are made into directional derivatives (i.e., $d/dt = \partial/\partial t + dx/dt \times \partial/\partial x$) along a line of slope

$$\frac{dx}{dt} = V + \frac{1}{\lambda} = V + \lambda a^2 \quad \text{.....(B.5.8)}$$

A solution to B.5.8 for the factor λ is

$$\lambda = \pm\frac{1}{a} \quad \text{.....(B.5.9)}$$

Therefore dx/dt is

$$\frac{dx}{dt} = V \pm a \quad \text{(B.5.10)}$$

In water hammer, the velocity V is small compared to the wave speed a (by a couple of magnitudes), therefore dx/dt is

$$\frac{dx}{dt} = \pm a \quad \text{(B.5.11)}$$

Using the solution for λ and forming the directional derivatives, Eq. B.5.7 becomes

$$\pm\frac{1}{a}\frac{dH}{dt} + \frac{1}{g}\frac{dV}{dt} + \frac{fV|V|}{2gD} + \frac{k_P}{g}\frac{dV}{dt} + \phi_V \frac{k_A}{g}\left|\frac{dV}{dt}\right| = 0 \quad \text{(B.5.12)}$$

Eq. B.5.12, representing two equations that are valid along $dx/dt = +a$ and $dx/dt = -a$ (the positive and negative characteristic lines) is named a compatibility equation. Multiplying the first two terms in Eq. B.5.12 by $\pm adt$ and the rest of the terms are multiplied by $\pm dx$ results in

$$dH \pm \frac{a}{g}dV \pm \frac{fV|V|}{2gD}dx \pm \frac{k_P}{g}\frac{dV}{dt}dx \pm \phi_V \frac{k_A}{g}\left|\frac{dV}{dt}\right|dx = 0 \quad \text{(B.5.13)}$$

Writing Eq. B.5.13 for positive (C^+) and negative characteristic (C^-) lines gives

C^+:
$$dH + \frac{a}{g}dV + \frac{fV|V|}{2gD}dx + \frac{k_P}{g}\frac{dV}{dt}dx + \phi_V \frac{k_A}{g}\left|\frac{dV}{dt}\right|dx = 0 \quad \text{(B.5.14)}$$

C^-:
$$dH - \frac{a}{g}dV - \frac{fV|V|}{2gD}dx - \frac{k_P}{g}\frac{dV}{dt}dx - \phi_V \frac{k_A}{g}\left|\frac{dV}{dt}\right|dx = 0 \quad \text{(B.5.15)}$$

The compatibility equations can be used to calculate values of head and velocity at a current time from conditions at a previous time. The calculation is performed on a characteristic grid. Figure B.17 shows a section of a characteristic grid that will be used for the explicit calculation of conditions at a current time (point P) from conditions at a previous time step (points A and B). The C^+ and C^- characteristic lines (with slopes defined in Eq. B.5.11) in Figure B.17 shown where each respective compatibility equation is valid.

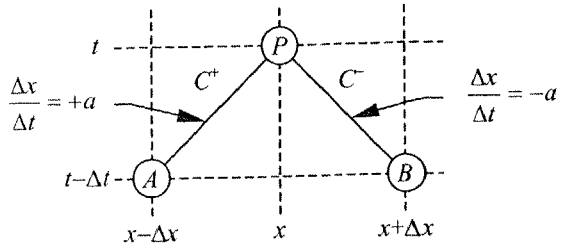

Figure B.17 Characteristic Grid, Numerical Evaluation of both the k_A & k_P Terms

Relationships between points P, A and B are formed by integrating the compatibility equations along each characteristic line, resulting in

$$C^+: \quad \int_A^P dH + \int_A^P \frac{a}{g} dV + \int_A^P \frac{fV|V|}{2gD} dx + \int_A^P \frac{k_P}{g} \frac{dV}{dt} dx + \int_A^P \phi_V \frac{k_A}{g} \left| \frac{dV}{dt} \right| dx = 0 \quad \text{.....(B.5.16)}$$

$$C^-: \quad \int_B^P dH - \int_B^P \frac{a}{g} dV - \int_B^P \frac{fV|V|}{2gD} dx - \int_B^P \frac{k_P}{g} \frac{dV}{dt} dx - \int_B^P \phi_V \frac{k_A}{g} \left| \frac{dV}{dt} \right| dx = 0 \quad \text{.....(B.5.17)}$$

The evaluation of the first two integral terms in Eqs. B.5.16 and B.5.17 is straightforward. The friction terms, however, must be integrated using approximate methods. There are two ways to achieve this integration. The first is to use the rectangular rule of numerical integration. The integral is based on values of V and dV/dt at the base of the characteristic line. The integrated compatibility equations are

$$C^+: \quad (H_P - H_A) + \frac{a}{g}(V_P - V_A) + \frac{fV_A|V_A|}{2gD}\Delta x + \frac{k_P}{g}\frac{dV_A}{dt}\Delta x + \phi_V^+ \frac{k_A}{g}\left|\frac{dV_A}{dt}\right|\Delta x = 0 \quad \text{.....(B.5.18)}$$

$$C^-: \quad (H_P - H_B) - \frac{a}{g}(V_P - V_B) - \frac{fV_B|V_B|}{2gD}\Delta x - \frac{k_P}{g}\frac{dV_B}{dt}\Delta x - \phi_V^- \frac{k_A}{g}\left|\frac{dV_B}{dt}\right|\Delta x = 0 \quad \text{.....(B.5.19)}$$

where the velocity sign operators for each integrated compatibility equation are now defined as

$$\phi_V^+ = \begin{cases} +1 & \text{if} \quad V_A \geq 0 \\ -1 & \text{if} \quad V_A < 0 \end{cases} \quad \& \quad \phi_V^- = \begin{cases} +1 & \text{if} \quad V_B \geq 0 \\ -1 & \text{if} \quad V_B < 0 \end{cases} \quad \text{.....(B.5.20)}$$

A better approximation of the integrals of the friction terms is to use the trapezoidal rule of integration. The integrated compatibility equations using the trapezoidal rule are

$$C^+: \quad (H_P - H_A) + \frac{a}{g}(V_P - V_A) + \frac{f\Delta x}{2gD}\frac{(V_A + V_P)}{2}\frac{|V_A + V_P|}{2} + \frac{k_P}{2g}\left(\frac{dV_A}{dt} + \frac{dV_P}{dt}\right)\Delta x + \phi_V^+ \frac{k_A}{2g}\left|\frac{dV_A}{dt} + \frac{dV_P}{dt}\right|\Delta x = 0 \quad \text{.....(B.5.21)}$$

$$C^-: \quad (H_P - H_B) - \frac{a}{g}(V_P - V_B) - \frac{f\Delta x}{2gD}\frac{(V_B + V_P)}{2}\frac{|V_B + V_P|}{2} - \frac{k_P}{2g}\left(\frac{dV_B}{dt} + \frac{dV_P}{dt}\right)\Delta x - \phi_V^- \frac{k_A}{2g}\left|\frac{dV_B}{dt} + \frac{dV_P}{dt}\right|\Delta x = 0 \quad \text{.....(B.5.22)}$$

where the velocity sign operators for each integrated compatibility equation are defined as

$$\phi_V^+ = \begin{cases} +1 & \text{if} \quad V_A + V_P \geq 0 \\ -1 & \text{if} \quad V_A + V_P < 0 \end{cases} \quad \& \quad \phi_V^- = \begin{cases} +1 & \text{if} \quad V_B + V_P \geq 0 \\ -1 & \text{if} \quad V_B + V_P < 0 \end{cases} \qquad \text{..... (B.5.23)}$$

These equations use conditions at both ends of each characteristic line (points *A*, *B* and *P*). Since the conditions at point *P* are not known before the compatibility equations are solved, they must be solved in an iterative manner.

B.6 Solution of the k_A & k_P Unsteady Friction Model, the k_P Term Included in the Directional Derivatives Only

This section performs the method of characteristics on the governing unsteady equations including the k_A & k_P unsteady friction model in the directional derivatives (in the method of characteristics). The equation of motion including the k_A & k_P unsteady friction model is

$$L_1 = \frac{\partial H}{\partial x} + \frac{1}{g}\frac{dV}{dt} + \frac{fV|V|}{2gD} + \frac{k_P}{g}\frac{dV}{dt} + \phi_V \frac{k_A}{g}\left|\frac{dV}{dt}\right| = 0 \qquad \text{..... (B.6.1)}$$

where the velocity sign operator is defined as

$$\phi_V = \begin{cases} +1 & \text{if} \quad V \geq 0 \\ -1 & \text{if} \quad V < 0 \end{cases} \qquad \text{..... (B.6.2)}$$

In this case, the phase component of the k_A & k_P unsteady friction model is included with the other dV/dt acceleration term. The amplitude component is, however, kept separate mainly due to its difficult nature (taking its sign from the velocity rather than dV/dt). Therefore Eq. B.6.1 becomes

$$L_1 = \frac{\partial H}{\partial x} + \frac{(1+k_P)}{g}\frac{dV}{dt} + \frac{fV|V|}{2gD} + \phi_V \frac{k_A}{g}\left|\frac{dV}{dt}\right| = 0 \qquad \text{..... (B.6.3)}$$

The equation of continuity, equal to L_2, is

$$L_2 = \frac{dH}{dt} + \frac{a^2}{g}\frac{\partial V}{\partial x} = 0 \qquad \text{..... (B.6.4)}$$

The two partial differential equations are linearly combined through the use of a constant, λ, as

$$L = L_1 + \lambda L_2 = 0 \quad \text{.....(B.6.5)}$$

Substitution of Eqs. B.6.3 and B.6.4 into Eq. B.6.5 forms

$$L = \frac{\partial H}{\partial x} + \frac{(1+k_P)}{g}\frac{dV}{dt} + \frac{fV|V|}{2gD} + \phi_V \frac{k_A}{g}\left|\frac{dV}{dt}\right| + \lambda\frac{dH}{dt} + \frac{\lambda a^2}{g}\frac{\partial V}{\partial x} = 0 \quad \text{.....(B.6.6)}$$

Decomposing the total derivatives into their partial constituents except for the k_A term and collecting all of the partial derivatives of the head together and all of the partial derivative of the velocity together except those relating to the k_A terms, results in

$$L = \left[\lambda\frac{\partial H}{\partial t} + \lambda V\frac{\partial H}{\partial x} + \frac{\partial H}{\partial x}\right] + \left[\frac{(1+k_P)}{g}\frac{\partial V}{\partial t} + \frac{(1+k_P)V}{g}\frac{\partial V}{\partial x} + \frac{\lambda a^2}{g}\frac{\partial V}{\partial x}\right] + \frac{fV|V|}{2gD} + \phi_V\frac{k_A}{g}\left|\frac{dV}{dt}\right| \quad \text{.....(B.6.7)}$$

A common factor of λ is taken outside of the grouped head terms and, likewise, a common factor of $(1 + k_P)/g$ is taken out of the grouped velocity terms, producing

$$L = \lambda\left[\frac{\partial H}{\partial t} + \left(V + \frac{1}{\lambda}\right)\frac{\partial H}{\partial x}\right] + \frac{(1+k_P)}{g}\left[\frac{\partial V}{\partial t} + \left(V + \frac{\lambda a^2}{1+k_P}\right)\frac{\partial V}{\partial x}\right] + \frac{fV|V|}{2gD} + \phi_V\frac{k_A}{g}\left|\frac{dV}{dt}\right| \quad \text{.....(B.6.8)}$$

The partial derivative terms in the square brackets (in Eq. B.6.8) are formed into directional derivatives (i.e., $d/dt = \partial/\partial t + dx/dt \times \partial/\partial x$) along a line of slope

$$\frac{dx}{dt} = V + \frac{1}{\lambda} = V + \frac{\lambda a^2}{1+k_P} \quad \text{.....(B.6.9)}$$

A solution to B.6.9 for the factor λ is

$$\lambda = \pm\frac{\sqrt{1+k_P}}{a} \quad \text{.....(B.6.10)}$$

Given λ, then dx/dt is

$$\frac{dx}{dt} = V \pm \frac{a}{\sqrt{1+k_P}} \quad \text{.....(B.6.11)}$$

In water hammer, the velocity V small compared to the wave speed a (typically two or three orders of magnitude smaller), therefore dx/dt may be approximated as

$$\frac{dx}{dt} = \pm\frac{a}{\sqrt{1+k_P}} \quad \text{.....(B.6.12)}$$

Now Eq. B.6.12 includes the phase coefficient k_P as compared to B.5.11, which does not. Using the solution for λ and forming the directional derivatives, Eq. B.6.8 becomes

$$\pm\frac{\sqrt{1+k_P}}{a}\frac{dH}{dt}+\frac{(1+k_P)}{g}\frac{dV}{dt}+\frac{fV|V|}{2gD}+\phi_V\frac{k_A}{g}\left|\frac{dV}{dt}\right|=0 \quad \text{..... (B.6.13)}$$

Eq. B.6.13 is really two compatibility equations each valid along characteristic lines of slopes shown in Eq. B.6.12. Multiplication of the first two terms in Eq. B.6.13 by $\pm a dt/\sqrt{1+k_P}$ and the rest of the terms by $\pm dx$ gives

$$dH\pm\frac{a\sqrt{1+k_P}}{g}dV\pm\frac{fV|V|}{2gD}dx\pm\phi_V\frac{k_A}{g}\left|\frac{dV}{dt}\right|dx=0 \quad \text{..... (B.6.14)}$$

Eq. B.6.14 is written for the positive (C^+) and negative (C^-) characteristics along the lines $dx/dt = a/\sqrt{1+k_P}$ and $dx/dt = -a/\sqrt{1+k_P}$ respectively,

C^+:
$$dH+\frac{a\sqrt{1+k_P}}{g}dV+\frac{fV|V|}{2gD}dx+\phi_V\frac{k_A}{g}\left|\frac{dV}{dt}\right|dx=0 \quad \text{..... (B.6.15)}$$

C^-:
$$dH-\frac{a\sqrt{1+k_P}}{g}dV-\frac{fV|V|}{2gD}dx-\phi_V\frac{k_A}{g}\left|\frac{dV}{dt}\right|dx=0 \quad \text{..... (B.6.16)}$$

The compatibility equations can be used to calculate values of head and velocity at a current time from conditions at a previous time. This calculation is performed on a characteristic grid. Figure B.18 shows a section of a characteristic grid that will be used for the explicit calculation of conditions at a current time (point P) from conditions at a previous time step (points A and B). The C^+ and C^- characteristic lines (with slopes defined in Eq. B.6.12) are shown where each respective compatibility equation is valid.

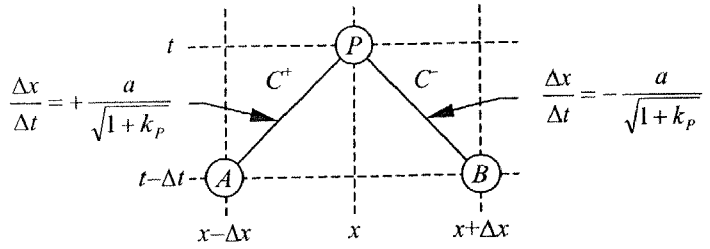

Figure B.18 Characteristic Grid, Numerical Evaluation of the k_A Term Only

The relationships between points P, A and B, formed by integrating the compatibility equations along each characteristic line, are

C^+:
$$\int_A^P dH+\int_A^P\frac{a\sqrt{1+k_P}}{g}dV+\int_A^P\frac{fV|V|}{2gD}dx+\int_A^P\phi_V\frac{k_A}{g}\left|\frac{dV}{dt}\right|dx=0 \quad \text{..... (B.6.17)}$$

$$C^-: \qquad \int_B^P dH - \int_B^P \frac{a\sqrt{1+k_P}}{g} dV - \int_B^P \frac{fV|V|}{2gD} dx - \int_B^P \phi_V \frac{k_A}{g} \left| \frac{dV}{dt} \right| dx = 0 \quad \text{.....(B.6.18)}$$

The evaluation of the first two integral terms in Eqs. B.6.17 and B.6.18 is straightforward. The friction terms, however, must be integrated using approximate methods. There are two ways to achieve the integration, the first of which is the rectangular rule. The application of the rectangular rule of integration to Eqs. B.6.17 and B.6.18 produces

$$C^+: \qquad (H_P - H_A) + \frac{a\sqrt{1+k_P}}{g}(V_P - V_A) + \frac{fV_A|V_A|}{2gD}\Delta x + \phi_V^+ \frac{k_A}{g}\left|\frac{dV_A}{dt}\right|\Delta x = 0 \quad \text{.....(B.6.19)}$$

$$C^-: \qquad (H_P - H_B) - \frac{a\sqrt{1+k_P}}{g}(V_P - V_B) - \frac{fV_B|V_B|}{2gD}\Delta x - \phi_V^- \frac{k_A}{g}\left|\frac{dV_B}{dt}\right|\Delta x = 0 \quad \text{.....(B.6.20)}$$

where the velocity sign operators for each integrated compatibility equation are now defined as

$$\phi_V^+ = \begin{cases} +1 & \text{if} \quad V_A \geq 0 \\ -1 & \text{if} \quad V_A < 0 \end{cases} \quad \& \quad \phi_V^- = \begin{cases} +1 & \text{if} \quad V_B \geq 0 \\ -1 & \text{if} \quad V_B < 0 \end{cases} \quad \text{.....(B.6.21)}$$

The friction terms only use conditions at the base of the characteristic line. A better approximation of the integrals of the friction terms is to use the trapezoidal rule of integration. The integrated compatibility equations using the trapezoidal rule are

$$C^+: \qquad \begin{aligned} &(H_P - H_A) + \frac{a\sqrt{1+k_P}}{g}(V_P - V_A) + \frac{f\Delta x}{2gD}\frac{(V_A + V_P)}{2}\frac{|V_A + V_P|}{2} \\ &+ \phi_V^+ \frac{k_A}{2g}\left|\frac{dV_A}{dt} + \frac{dV_P}{dt}\right|\Delta x = 0 \end{aligned} \quad \text{.....(B.6.22)}$$

$$C^-: \qquad \begin{aligned} &(H_P - H_B) - \frac{a\sqrt{1+k_P}}{g}(V_P - V_B) - \frac{f\Delta x}{2gD}\frac{(V_B + V_P)}{2}\frac{|V_B + V_P|}{2} \\ &- \phi_V^- \frac{k_A}{2g}\left|\frac{dV_B}{dt} + \frac{dV_P}{dt}\right|\Delta x = 0 \end{aligned} \quad \text{.....(B.6.23)}$$

where the velocity sign operators for each integrated compatibility equation are defined as

$$\phi_V^+ = \begin{cases} +1 & \text{if} \quad V_A + V_P \geq 0 \\ -1 & \text{if} \quad V_A + V_P < 0 \end{cases} \quad \& \quad \phi_V^- = \begin{cases} +1 & \text{if} \quad V_B + V_P \geq 0 \\ -1 & \text{if} \quad V_B + V_P < 0 \end{cases} \quad \text{.....(B.6.24)}$$

Eqs. B.6.22 and B.6.23, however, use conditions at both ends of each characteristic line (points *A*, *B* and *P*). The conditions at point *P* are not known before the compatibility equations are solved and thus must be solved in an iterative manner.

B.7 Solution of the k_A & k_P Model Included in the Directional Derivatives

This section performs the method of characteristics on the governing unsteady equations including the k_A & k_P unsteady friction model in the direction derivatives (in the method of characteristics). The equation of motion including the k_A & k_P unsteady friction model is

$$L_1 = \frac{\partial H}{\partial x} + \frac{1}{g}\frac{dV}{dt} + \frac{fV|V|}{2gD} + \frac{k_P}{g}\frac{dV}{dt} + \phi_V \frac{k_A}{g}\left|\frac{dV}{dt}\right| = 0 \quad \text{(B.7.1)}$$

where the velocity sign operator is defined as

$$\phi_V = \begin{cases} +1 & \text{if} \quad V \geq 0 \\ -1 & \text{if} \quad V < 0 \end{cases} \quad \text{(B.7.2)}$$

For the full inclusion of the k_A & k_P unsteady friction model in the method of characteristics, the equation of motion (Eq. B.7.1) is rewritten in an equivalent form. The modulus sign from the acceleration term dV/dt, which is multiplied by k_A, is eliminated using an acceleration sign operator ϕ_A,

$$L_1 = \frac{\partial H}{\partial x} + \frac{1}{g}\frac{dV}{dt} + \frac{fV|V|}{2gD} + \frac{k_P}{g}\frac{dV}{dt} + \phi_A \frac{k_A}{g}\frac{dV}{dt} = 0 \quad \text{(B.7.3)}$$

where the acceleration sign operator is defined as

$$\phi_A = \begin{cases} +1 & \text{if} \quad V\dfrac{dV}{dt} \geq 0 \\ -1 & \text{if} \quad V\dfrac{dV}{dt} < 0 \end{cases} \quad \text{(B.7.4)}$$

Collecting all of the dV/dt terms in Eq. B.7.3 forms

$$L_1 = \frac{\partial H}{\partial x} + \frac{\left(1 + k_P + \phi_A k_A\right)}{g}\frac{dV}{dt} + \frac{fV|V|}{2gD} = 0 \quad \text{(B.7.5)}$$

The equation of continuity, equal to L_2, is

$$L_2 = \frac{dH}{dt} + \frac{a^2}{g}\frac{\partial V}{\partial x} = 0 \quad \text{(B.7.6)}$$

A linear combination of Eqs. B.7.5 and B.7.6, using a multiplier λ, is

$$L = L_1 + \lambda L_2 = 0 \quad \text{(B.7.7)}$$

Substitution of the right-hand sides of Eqs. B.7.5 and B.7.6 into Eq. B.7.7 forms

$$L=\frac{\partial H}{\partial x}+\frac{\left(1+k_P+\phi_A k_A\right)}{g}\frac{dV}{dt}+\frac{fV|V|}{2gD}+\lambda\frac{dH}{dt}+\frac{\lambda a^2}{g}\frac{\partial V}{\partial x}=0 \quad \text{.....(B.7.8)}$$

The full derivatives are then decomposed into their partial constituents. Rearrangements are made that collect all of the partial derivatives of the hydraulic grade together and all of the partial derivative of the velocity together. The result of doing this is shown in Eq. B.7.9.

$$L=\left[\lambda\frac{\partial H}{\partial t}+\lambda V\frac{\partial H}{\partial x}+\frac{\partial H}{\partial x}\right]+\left[\frac{\left(1+k_P+\phi_A k_A\right)}{g}\frac{\partial V}{\partial t}+\frac{\left(1+k_P+\phi_A k_A\right)V}{g}\frac{\partial V}{\partial x}+\frac{\lambda a^2}{g}\frac{\partial V}{\partial x}\right]+\frac{fV|V|}{2gD} \quad \text{...(B.7.9)}$$

Taking a common factor of λ outside of the grouped head terms and, likewise, a common factor of $(1 + k_P + \phi_A k_A)/g$ out of the grouped velocity terms gives

$$L=\lambda\left[\frac{\partial H}{\partial t}+\left(V+\frac{1}{\lambda}\right)\frac{\partial H}{\partial x}\right]+\frac{\left(1+k_P+\phi_A k_A\right)}{g}\left[\frac{\partial V}{\partial t}+\left(V+\frac{\lambda a^2}{1+k_P+\phi_A k_A}\right)\frac{\partial V}{\partial x}\right]+\frac{fV|V|}{2gD} \quad \text{.....(B.7.10)}$$

The partial derivative terms in the square brackets (in Eq. B.7.10) are formed into directional derivatives (i.e., $d/dt = \partial/\partial t + dx/dt \times \partial/\partial x$) along a line of slope

$$\frac{dx}{dt}=V+\frac{1}{\lambda}=V+\frac{\lambda a^2}{1+k_P+\phi_A k_A} \quad \text{.....(B.7.11)}$$

A solution to B.7.11 for the factor λ is

$$\lambda=\pm\frac{\sqrt{1+k_P+\phi_A k_A}}{a} \quad \text{.....(B.7.12)}$$

Therefore dx/dt must be

$$\frac{dx}{dt}=V\pm\frac{a}{\sqrt{1+k_P+\phi_A k_A}} \quad \text{.....(B.7.13)}$$

In water hammer, the velocity V is small compared to the wave speed a (typically two to three orders of magnitude smaller), therefore V is neglected giving

$$\frac{dx}{dt}=\pm\frac{a}{\sqrt{1+k_P+\phi_A k_A}} \quad \text{.....(B.7.14)}$$

Now dx/dt includes both the k_P and k_A coefficients, as compared to Eqs. B.5.11 and B.6.12 both of which do not. Eq. B.7.14 suggests that the slope of the characteristic

lines depends on whether the fluid is accelerating or decelerating. Using the solution for λ and forming the directional derivatives, Eq. B.7.10 becomes

$$\pm\frac{\sqrt{1+k_P+\phi_A k_A}}{a}\frac{dH}{dt}+\frac{1+k_P+\phi_A k_A}{g}\frac{dV}{dt}+\frac{fV|V|}{2gD}=0 \quad \text{..... (B.7.15)}$$

Multiplication of the first two terms in Eq. B.7.15 by $\pm a dt/\sqrt{1+k_P+\phi_A k_A}$ and the rest of the terms by $\pm dx$ produces

$$dH\pm\frac{a\sqrt{1+k_P+\phi_A k_A}}{g}dV\pm\frac{fV|V|}{2gD}dx=0 \quad \text{..... (B.7.16)}$$

Writing Eq. B.7.16 for the positive (C^+) and negative (C^-) characteristics along the lines $dx/dt = a/\sqrt{1+k_P+\phi_A k_A}$ and $dx/dt = -a/\sqrt{1+k_P+\phi_A k_A}$ respectively, gives

C^+:
$$dH+\frac{a\sqrt{1+k_P+\phi_A^+ k_A}}{g}dV+\frac{fV|V|}{2gD}dx=0 \quad \text{..... (B.7.17)}$$

C^-:
$$dH-\frac{a\sqrt{1+k_P+\phi_A^- k_A}}{g}dV-\frac{fV|V|}{2gD}dx=0 \quad \text{..... (B.7.18)}$$

The compatibility equations can be used to calculate values of head and velocity at a current time from conditions at a previous time. The calculation is performed on a characteristic grid. Figure B.19 shows a section of a characteristic grid for the explicit calculation of conditions at a current time (point P) from conditions at a previous time step (points A and B). The C^+ and C^- characteristic lines (with slopes defined in Eq. B.7.14) are shown where each respective compatibility equation is valid.

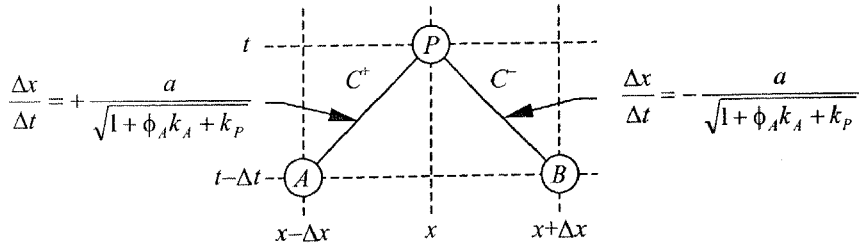

Figure B.19 Characteristic Grid, k_A & k_P Model Fully Included in MOC

The relationships between points P, A and B are formed by integrating the compatibility equations along each characteristic line,

C^+:
$$\int_A^P dH+\int_A^P\frac{a\sqrt{1+k_P+\phi_A^+ k_A}}{g}dV+\int_A^P\frac{fV|V|}{2gD}dx=0 \quad \text{..... (B.7.19)}$$

$$C^-: \qquad \int_B^P dH - \int_B^P \frac{a\sqrt{1+k_P+\phi_A^- k_A}}{g} dV - \int_B^P \frac{fV|V|}{2gD} dx = 0 \qquad \text{.....(B.7.20)}$$

The evaluation of the first two integral terms in Eqs. B.7.19 and B.7.20 is straightforward. The steady state friction term, however, must be integrated using approximate methods. There are two ways to do this: the rectangular and trapezoidal rules of integration. Evaluation of the integral terms in Eqs. B.7.19 and B.7.20, using the rectangular rule for the friction term, gives

$$C^+: \qquad (H_P - H_A) + \frac{a\sqrt{1+k_P+\phi_A^+ k_A}}{g}(V_P - V_A) + \frac{fV_A|V_A|}{2gD}\Delta x = 0 \qquad \text{.....(B.7.21)}$$

$$C^-: \qquad (H_P - H_B) - \frac{a\sqrt{1+k_P+\phi_A^- k_A}}{g}(V_P - V_B) - \frac{fV_B|V_B|}{2gD}\Delta x = 0 \qquad \text{.....(B.7.22)}$$

where the acceleration sign operators for each integrated compatibility equation are now defined as

$$\phi_A^+ = \begin{cases} +1 & \text{if} \quad |V_P| \geq |V_A| \\ -1 & \text{if} \quad |V_P| < |V_A| \end{cases} \quad \& \quad \phi_A^- = \begin{cases} +1 & \text{if} \quad |V_P| \geq |V_B| \\ -1 & \text{if} \quad |V_P| < |V_B| \end{cases} \qquad \text{.....(B.7.23)}$$

Care must be taken when using Eqs. B.7.21, B.7.22 and B.7.23 to determine conditions at point P with regards to the sign operator. Since conditions at point P are unknown, it is initially not known whether the flow is accelerating or decelerating between points A and P (C^+) or B and P (C^-). A solution is to initially assume that the flow is accelerating, solve for conditions at point P, and then check if the assumption was correct. If the assumption was incorrect, the calculation is performed for decelerating flow.

A better approximation of the integral of the steady state friction term is to use the trapezoidal rule of integration. The integrated compatibility equations, using the trapezoidal rule, are

$$C^+: \quad (H_P - H_A) + \frac{a\sqrt{1+k_P+\phi_A^+ k_A}}{g}(V_P - V_A) + \frac{f\Delta x}{2gD}\frac{(V_A+V_P)}{2}\frac{|V_A+V_P|}{2} = 0 \qquad \text{.....(B.7.24)}$$

$$C^-: \quad (H_P - H_B) - \frac{a\sqrt{1+k_P+\phi_A^- k_A}}{g}(V_P - V_B) - \frac{f\Delta x}{2gD}\frac{(V_B+V_P)}{2}\frac{|V_B+V_P|}{2} = 0 \qquad \text{.....(B.7.25)}$$

The friction term in Eqs. B.7.24 and B.7.25 use conditions at both ends of each characteristic line (points A, B and P); therefore the integrated compatibility equations must be solved in an iterative manner.

B.8 Supplement to the Derivation of k_1

The content of this section pertains to the derivation of an expression for the Carstens and Roller's unsteady friction coefficient k_1. From Section 9.5 the relationship between k_1 and function F_3 was determined to be

$$k_1 = 4F_3\big|_{r=r_0} \quad \text{(B.8.1)}$$

The function F_3 can be expanded to be in terms of earlier functions F_1 and F_2.

$$k_1 = 4\left[F_1 - \frac{r}{r_0}F_2\big|_{r=0}\right]_{r=r_0} \quad \text{(B.8.2)}$$

Eq. B.8.2 is taken at the boundary $r = r_0$ (pipe wall). Enforcing this action simplifies the relationship. The relationship is now comprised of two pieces, one to be evaluated at the centre of the pipeline and the other at the boundary of the pipeline.

$$k_1 = 4\left(F_1\big|_{r=r_0} - F_2\big|_{r=0}\right) \quad \text{(B.8.3)}$$

These two parts are solved separately. The first part is the evaluation of F_1 at the pipe wall. The equation for F_1 is

$$F_1 = \frac{r}{2r_0} - \frac{1}{r_0 r}\int_0^r rg_v.dr \quad \text{(B.8.4)}$$

The evaluation of the integral term at $r = r_0$ is made easier by revisiting how the velocity distribution function, g_v, is found. Eq. B.8.5 shows how the average velocity V is calculated from the radial velocity v.

$$\pi r_0^2 V = \int_0^{r_0} 2\pi rv.dr \quad \text{(B.8.5)}$$

Rearrangement of Eq. B.8.5 forms

$$\frac{r_0^2}{2} = \int_0^{r_0} rg_v.dr \quad \text{(B.8.6)}$$

The integral term on the right hand side of Eq. B.8.6 is the same as the integral term in Eq. B.8.4. Substitution of Eq. B.8.6 into Eq. B.8.4 and the subsequent evaluation at $r = r_0$ results in

$$F_1\big|_{r=r_0} = 0 \quad \text{(B.8.7)}$$

Therefore, the first part of Eq. B.8.3 is equal to zero. The second part of Eq. B.8.3 is the calculation of F_2 at $r = 0$. The expression for F_2 is

$$F_2 = \frac{1}{2} - g_v + \frac{1}{r^2}\int_0^r r g_v . dr \quad \text{(B.8.8)}$$

The function F_2 is evaluated at the centre of the pipe ($r = 0$), which is achieved by taking the limit of F_2 as r approaches 0,

$$F_2\big|_{r=0} = \frac{1}{2} - g_v\big|_{r=0} + \lim_{r\to 0}\frac{1}{r^2}\int_0^r r g_v . dr \quad \text{(B.8.9)}$$

The integral is simplified in the limit by noting that at the centre of the pipe the derivative of the velocity distribution function, g_v, is zero.

$$\left.\frac{\partial g_v}{\partial r}\right|_{r=0} = 0 \quad \text{(B.8.10)}$$

Eq. B.8.10 allows the integral to be simplified by imagining that g_v is a constant in the limit $r \to 0$,

$$F_2\big|_{r=0} = \frac{1}{2} - g_v\big|_{r=0} + \lim_{r\to 0}\frac{1}{r^2} g_v \int_0^r r . dr \quad \text{(B.8.11)}$$

The evaluation of the integral and the cancellation of the r^2 terms in the limit $r \to 0$ produces

$$F_2\big|_{r=0} = \frac{1}{2} - g_v\big|_{r=0} + \lim_{r\to 0}\frac{1}{r^2} g_v \frac{r^2}{2} \quad \text{(B.8.12)}$$

Evaluation of the limit $r \to 0$ results in

$$F_2\big|_{r=0} = \tfrac{1}{2}\left(1 - g_v\big|_{r=0}\right) \quad \text{(B.8.13)}$$

Now the F_1 and F_2 components (Eqs. B.8.7 and B.8.13 respectively) are substituted into Eq. B.8.3 producing

$$k_1 = 2\left(g_v\big|_{r=0} - 1\right) \quad \text{(B.8.14)}$$

Eq. B.8.14 is an expression for the unsteady friction coefficient k_1 that depends on the velocity distribution function g_v evaluated at the centre of the pipe. Writing Eq. B.8.14 in terms of the Brunone *et al.* (1991) unsteady friction coefficient k_3 gives

$$k_3 = \tfrac{1}{2}\left(g_v\big|_{r=0} - 1\right) \quad \text{(B.8.15)}$$

B.9 Universal Velocity Distributions

For both the evaluation of the momentum correction factor and the unsteady friction factor, the velocity profile in a pipe must be known. Historically there are two representations of the velocity profile, the first is a power law relationship and the second is a logarithmic law relationship. The logarithmic law relationship is widely regarded as more accurate; however, recent research suggests that power law does a better job than the logarithmic law for the core regions of flow (Barenblatt, 1991).

B.9.1 Log Law of Velocity Distribution

The logarithmic law of velocity distribution is the best and arguably most accurate set of laws that describe the velocity distribution for turbulent flows. Schlichting (1955) gave a detailed account of the laws that describe the velocity distribution. A couple of useful properties are required; the first of which is called the friction velocity,

$$v_* = \sqrt{\frac{\tau_0}{\rho}} \quad \text{(B.9.1)}$$

where τ_0 = the boundary shear stress and ρ = the density. The friction velocity is a convenient abbreviation of a term that occurs often in the analysis. The second useful property is the dimensionless axial velocity in the direction of the pipe flow,

$$\phi = \frac{v}{v_*} \quad \text{(B.9.2)}$$

where v = the axial velocity. The final useful property is the dimensionless distance from the pipe wall,

$$\eta = \frac{y v_*}{\nu} \quad \text{(B.9.3)}$$

where ν = kinematic viscosity and y = distance from the pipe wall. The velocity distribution for pipe flow can be split into two zones: the viscous sub-layer and the log layer. For the viscous sub-layer the relationship between the dimensionless axial velocity and the dimensionless distance from the pipe wall is

$$\phi = \eta \quad \text{(B.9.4)}$$

For a smooth pipe, the log layer (or the fully turbulent layer) relationship is

$$\phi = A\ln(\eta) + B \quad \text{(B.9.5)}$$

The coefficients A and B have been experimentally determined as 2.5 and 5.5 respectively. The coefficient A is equal to $1/\kappa$ where κ is the von Kármán universal constant ($\kappa = 0.4$ experimentally derived). There are different internal regions in steady turbulent flow velocity profile. The extent of the internal regions is approximately defined as

$$\begin{array}{ll} \eta < 5 & \text{viscous sub - layer region} \\ 5 < \eta < 70 & \text{transition region} \\ \eta > 70 & \text{turbulent region} \end{array} \quad \text{(B.9.6)}$$

The different velocity profile regions are better demonstrated through the use of an example. Figure B.20 shows the velocity distribution for a smooth pipe at a Reynolds number of 5,000.

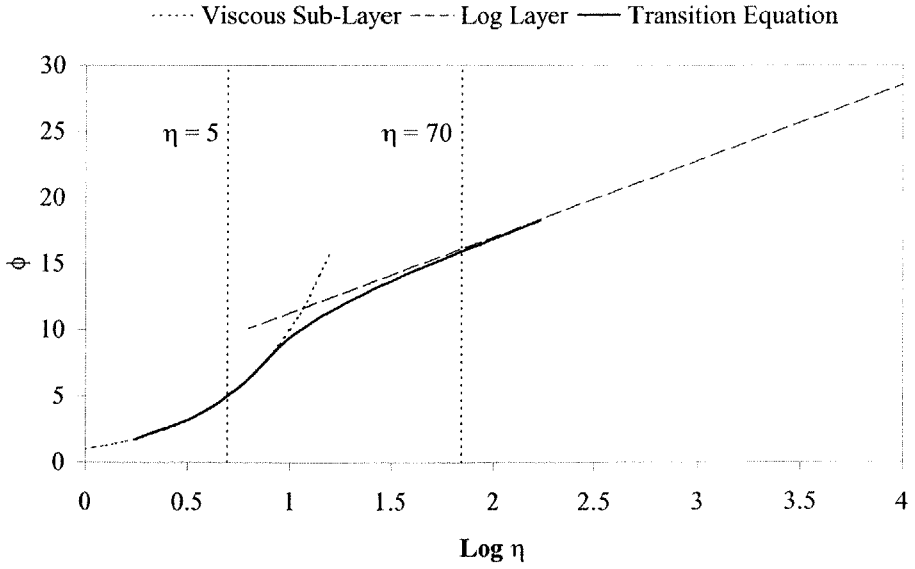

Figure B.20 Velocity Distribution for a Smooth Pipe

Although the relationship for the velocity profile for the viscous sub-layer (Eq. B.9.4) and the log layer (Eq. B.9.5) have been defined there is still the problem of the calculation of the transition region between the two regions. Young (1989) deals with the transition region by defining a viscous sub-layer distance, η_l,

$$\eta_l = A\ln(A) + B \quad \text{(B.9.7)}$$

Eq. B.9.4 is used for dimensionless distances from the wall smaller than η_l. For distances greater than η_l (both in the transition and fully turbulent friction regions), the velocity distribution is

$$\phi = A\ln(\eta - \eta_l + A) + B \quad \text{(B.9.8)}$$

The logarithmic law equations may be further expanded for rough pipes. A new variable is utilised for rough pipes and is related to the sand grain roughness height k_S.

$$\eta_R = \frac{k_S v_*}{\nu} \quad \text{(B.9.9)}$$

The relative sand grain roughness, k_S/r_0, is equal to twice the relative roughness used for commercially rough pipes, ε/D, (Schlichting, 1955). Similar to the different regions for the pipe friction, there are different regimes for different degrees of roughness. These regimes are

$$\begin{array}{ll} \eta_R < 5 & \text{hydraulically smooth regime} \\ 5 < \eta_R < 70 & \text{transition regime} \\ \eta_R > 70 & \text{completely rough regime} \end{array} \quad \text{(B.9.10)}$$

Colebrook-White (1937) developed an expression relating the Darcy-Weisbach friction factor to the Reynolds number and the relative pipe roughness,

$$\frac{1}{\sqrt{f}} = 1.74 - 2\log\left(\frac{k_S}{r_0} + \frac{18.7}{\mathbf{R}\sqrt{f}}\right) \quad \text{(B.9.11)}$$

The Colebrook-White equation (Eq. B.9.11) can be used to produce a general relationship for the whole region from hydraulically smooth to completely rough. A roughness coefficient C_R is introduced to define the B term (from the log law) for a rough pipe. Schlichting (1955) found C_R to be dependent on the relative sand grain roughness and the Darcy-Weisbach friction factor, f,

$$C_R = \sqrt{\frac{8}{f}} + 3.75 - A\ln\left(\frac{r_0}{k_S}\right) \quad \text{(B.9.12)}$$

For completely turbulent flows C_R was experimentally determined as 8.5. To extend the smooth pipe log law to rough pipes causes the coefficient B becomes dependent on the roughness (and is subscripted with $_R$). The rough pipe coefficient B_R is

$$B_R = C_R - A\ln(\eta_R) \quad \text{(B.9.13)}$$

The rough pipe logarithmic law of velocity distribution for turbulent flows is

$$\phi = A\ln(\eta) + B_R \quad \text{(B.9.14)}$$

where the roughness manifests itself as an extra integration constant and thus only effects the coefficient B_R. Similar to the smooth pipe relationships, an extra relationship is needed for the laminar-turbulent transition region. For the calculation of the rough pipe velocity distribution the viscous sub-layer equation does not change, i.e. Eq. B.9.4 is still valid. The viscous sub-layer distance, however, does change for different roughness pipes. The rough pipe viscous sub-layer distance η_{IR} is

$$\eta_{IR} = A\ln(A) + B_R \quad \text{(B.9.15)}$$

For distances greater than the rough pipe viscous sub-layer distance, the transition relationship is used in a similar way as for the smooth pipe case,

$$\phi = A\ln(\eta - \eta_{IR} + A) + B_R \quad \text{(B.9.16)}$$

Figure B.21 shows the velocity distribution for a rough pipe with a relative roughness of 0.01. As the roughness becomes smaller the turbulent portion of the curve moves downwards, parallel to the smooth pipe curve.

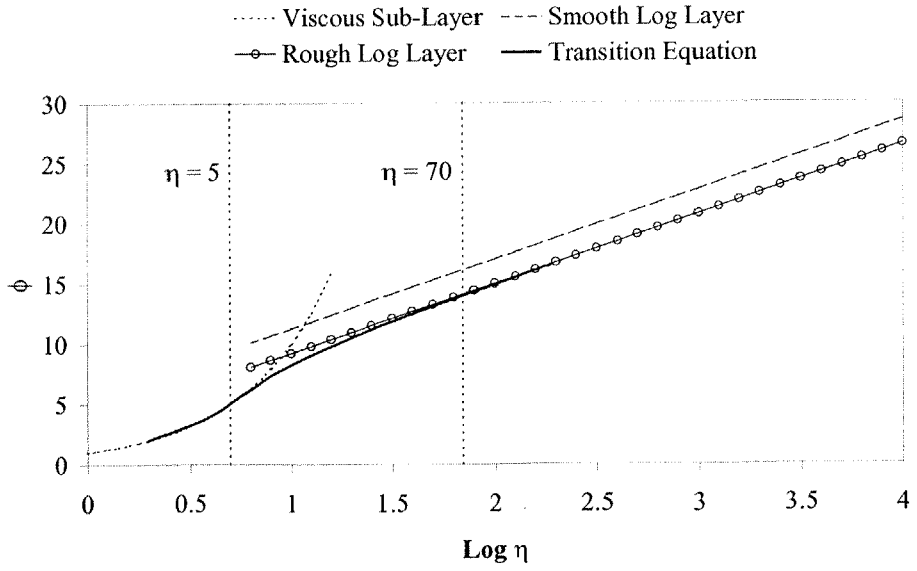

Figure B.21 Velocity Distribution for a Rough Pipe ($\varepsilon/D = 0.01$)

There is a third layer called the defect layer for very high Reynolds number flows at greater distances from the pipe wall, which is described by the law of the wake. However, the logarithmic law of the wall provides a good approximation of the defect layer in the absence of a pressure gradient across the boundary layer (Young, 1989).

Finally, the velocity distribution function g_v is found by rearranging Eqs. B.9.1 and B.9.2 and inserting the relationship between the boundary shear stress and the Darcy-Weisbach friction factor ($\tau_0 = \rho f V^2/8$), resulting in

$$g_v = \frac{v}{V} = \phi\sqrt{\frac{f}{8}} \quad \text{..... (B.9.17)}$$

B.9.2 Power Law of Velocity Distribution

An alternative way to define the velocity distribution in a pipe is to use a power law. Historically, power laws were used before logarithmic laws as an empirically derived law from experimental data. The power law relationship (Schlichting, 1955) is

$$g_v = \frac{v}{V} = \frac{(2n+1)(n+1)}{2n^2}\left(\frac{y}{r_0}\right)^{\frac{1}{n}} \quad \text{..... (B.9.18)}$$

The power law exponent, n, is a function of the Reynolds number. Schlichting (1955) tabulated experimental results (for smooth pipes) for n as previously shown in Table 8.3. A simple function is fitted to Schlichting's data based solely on the Reynolds number of the flow,

$$n = 0.4799(\text{Log}_{10}\mathbf{R})^3 - 36.5305(\text{Log}_{10}\mathbf{R})^2 + 29.967(\text{Log}_{10}\mathbf{R}) - 39.652 \text{ ..... (B.9.19)}$$

Eq. B.9.19 is valid for turbulent flows up to a Reynolds number of 2×10^6 after which n is equal to 10. Figure B.22 shows a plot of the fitted relationship for the Reynolds number and the power law exponent n (Eq. B.9.19) and data from Schlichting (1955).

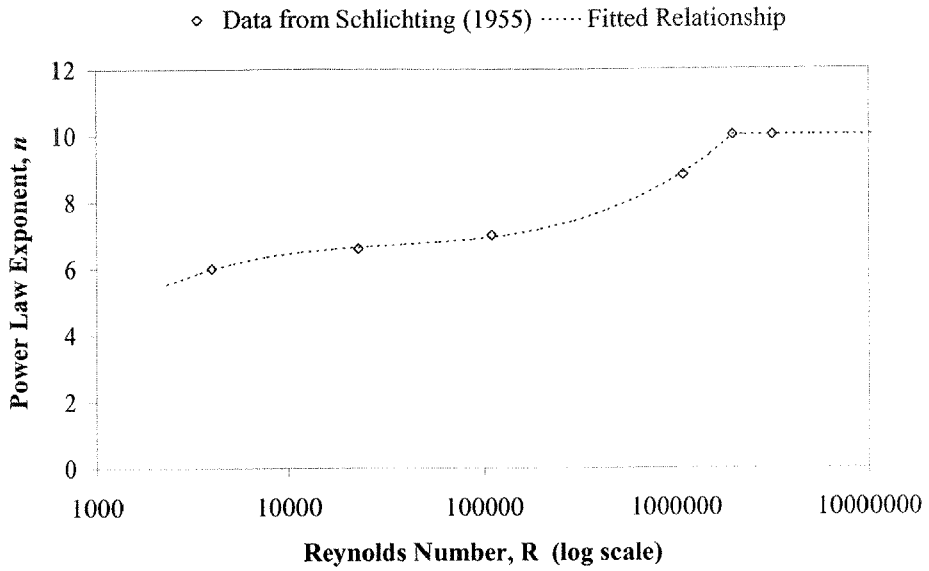

Figure B.22 Fitted Relationship for the Power Law Exponent *n*

Using the logarithmic law, Chen (1991) showed the dependence of n on the Darcy-Weisbach friction factor,

$$n = \kappa\sqrt{\frac{8}{f}} \qquad \text{(B.9.20)}$$

Eq. B.9.20 is a useful relationship because it shows the dependence of the Reynolds number on n and the effect of roughness as well (through f). Chen (1991) proposed an alternative relationship for smooth pipes,

$$n = \ln\left(\frac{9\mathbf{R}}{2e^{1.5}}\sqrt{\frac{f}{8}}\right) \qquad \text{(B.9.21)}$$

Also, Chen (1991) extended Eq. B.9.21 for fully turbulent rough pipes, resulting in an expression for n that only depends on the relative roughness,

$$n = \ln\left(\frac{30}{e^{1.5}}\frac{r_0}{k_S}\right) \qquad \text{(B.9.22)}$$

Barenblatt (1991) proposed that the use of power laws for describing the inner turbulent layer of flow in a pipe, which correlates better with experimental data than logarithmic laws do.

B.10 Determination of the Momentum Correction Factor

The momentum correction factor for steady flow is dependent on the Reynolds number of the flow and the relative roughness. Streeter (1942) was the first to investigate the relationship between the momentum correction factor and the Reynolds number for smooth pipes. The momentum correction factor using the power law of velocity distribution Chen (1992) is

$$\beta = \frac{(n+1)(2n+1)^2}{4n^2(n+2)} \quad \text{(B.10.1)}$$

Chen (1992) determined the momentum correction factor using the logarithmic law of velocity distribution as

$$\beta = 1 + \frac{5f}{32\kappa^2} \quad \text{(B.10.2)}$$

Eq. B.10.2 is a function of the Darcy-Weisbach friction factor and is thus dependent on the Reynolds number of the flow and the relative roughness of the pipe.

The behaviour of the momentum correction factor in unsteady pulsatile blood flow was investigated by Buthaud (1977) who showed that values of $\beta = \infty$ were theoretically predicted. The high momentum correction factors applied at the reversal of the flow. Buthaud (1977) suggested that, in reality, the momentum correction factor was much lower, exhibiting less variation than was theoretically predicted. Buthaud (1977) suggests a different definition of the momentum correction factor be used for unsteady flow. The Buthaud (1977) modified momentum correction factor β_1 is

$$\beta_1 = \frac{1}{A\hat{V}^2}\int_A v^2 dA \quad \text{(B.10.3)}$$

where A = the cross-sectional pipe area, v = axial velocity at different radial positions and $\hat{V}$ = average velocity computed from the absolute axial velocity as

$$\hat{V} = \frac{1}{A}\int_A |v| dA \quad \text{(B.10.4)}$$

Due to the modulus sign in Eq. B.10.4, $\hat{V}$ is always larger than zero ensuring that Eq. B.10.3 is never undefined.

B.11 Derivation of k_3 Based on the Smooth Pipe Logarithmic Law with Transition Formulae

The formulation for k_3 based on the smooth pipe logarithmic law including the transition region formulae begins from the relationship between k_3 and velocity distribution function is

$$k_3 = \tfrac{1}{8} g_v\big|_{r=0} - \tfrac{1}{8} \quad \text{.....(B.11.1)}$$

Substitution of the relationship for the velocity distribution based on the logarithmic laws (Eq. B.9.17) into Eq. B.11.1 forms

$$k_3 = \frac{1}{8}\phi\big|_{r=0}\sqrt{\frac{f}{8}} - \frac{1}{8} \quad \text{.....(B.11.2)}$$

The dimensionless velocity function (ϕ), evaluated at the centre of the pipe and including the transition formulae (Eq. B.9.8), is substituted in Eq. B.11.2 producing

$$k_3 = \sqrt{\frac{f}{512}}\left[A\ln\left(\eta\big|_{r=0} - \eta_l + A\right) + B\right] - \frac{1}{8} \quad \text{.....(B.11.3)}$$

Substitution of the dimensionless thickness of the viscous sub-layer η_l (Eq. B.9.7) needed for the transition formulae into Eq. B.11.3 forms

$$k_3 = \sqrt{\frac{f}{512}}\left[A\ln\left(\eta\big|_{r=0} - A\ln(A) - B + A\right) + B\right] - \frac{1}{8} \quad \text{.....(B.11.4)}$$

Using the dimensionless distance η (Eq. B.9.3), evaluated at the centre of the pipe, in Eq. B.11.4 gives

$$k_3 = \sqrt{\frac{f}{512}}\left[A\ln\left(\frac{r_0 v_*}{\nu} - A\ln(A) - B + A\right) + B\right] - \frac{1}{8} \quad \text{.....(B.11.5)}$$

Substitution of the relationship for friction velocity (Eq. B.9.2) into Eq. B.11.5 and replacement of the pipe radius (r_0) with the pipe diameter (D) forms

$$k_3 = \sqrt{\frac{f}{512}}\left[A\ln\left(\frac{D}{2\nu}\sqrt{\frac{\tau_0}{\rho}} - A\ln(A) - B + A\right) + B\right] - \frac{1}{8} \quad \text{.....(B.11.6)}$$

Substitution of the friction factor (f) for the boundary shear stress (τ_0) using the relationship $\tau_0 = fV^2\rho/8$ leaves an expression only dependent on the Darcy-Weisbach friction factor,

$$k_3 = \sqrt{\frac{f}{512}}\left[A\ln\left(\frac{DV}{2\nu}\sqrt{\frac{f}{8}} - A\ln(A) - B + A\right) + B\right] - \frac{1}{8} \quad \text{.....(B.11.7)}$$

Finally, introduction of the Reynolds number ($\mathbf{R} = VD/\nu$) produces the final expression for k_3 using the smooth pipe logarithmic laws including the transition formulae,

$$k_3 = \sqrt{\frac{f}{512}}\left[A\ln\left(\mathbf{R}\sqrt{\frac{f}{32}} - A\ln(A) - B + A\right) + B\right] - \frac{1}{8} \quad \text{(B.11.8)}$$

B.12 Derivation of k_3 Based on the Smooth Pipe Logarithmic Law Only

An expression for the unsteady friction coefficient k_3 is derived using the smooth pipe logarithmic laws only. The transition formulae are neglected because the velocity distribution function is evaluated at the centre of the pipe where the behaviour is not influenced by the transition between the log layer and the viscous sub-layer. The derivation begins with the relationship between k_3 and velocity distribution function,

$$k_3 = \tfrac{1}{8} g_v\big|_{r=0} - \tfrac{1}{8} \quad \text{(B.12.1)}$$

Substitution of the relationship for the velocity distribution based on the logarithmic laws (Eq. B.9.17) into Eq. B.12.1 forms

$$k_3 = \frac{1}{8}\phi\big|_{r=0}\sqrt{\frac{f}{8}} - \frac{1}{8} \quad \text{(B.12.2)}$$

Using the dimensionless velocity function (ϕ), evaluated at the centre of the pipe and not including the transition formulae (Eq. B.9.5), Eq. B.12.2 becomes

$$k_3 = \sqrt{\frac{f}{512}}\left[A\ln\left(\eta\big|_{r=0}\right) + B\right] - \frac{1}{8} \quad \text{(B.12.3)}$$

Substitution of the dimensionless distance η (Eq. B.9.3), evaluated at the centre of the pipe, into Eq. B.12.3 gives

$$k_3 = \sqrt{\frac{f}{512}}\left[A\ln\left(\frac{r_0 v_*}{\nu}\right) + B\right] - \frac{1}{8} \quad \text{(B.12.4)}$$

Using the friction velocity relationship (Eq. B.9.2), Eq. B.12.4 becomes

$$k_3 = \sqrt{\frac{f}{512}}\left[A\ln\left(\frac{D}{2\nu}\sqrt{\frac{\tau_0}{\rho}}\right) + B\right] - \frac{1}{8} \quad \text{(B.12.5)}$$

Substitution of the friction factor (f) for the boundary shear stress (τ_0), using the relationship $\tau_0 = fV^2\rho/8$, leaves an expression only dependent on the friction factor,

$$k_3 = \sqrt{\frac{f}{512}}\left[A\ln\left(\frac{DV}{2\nu}\sqrt{\frac{f}{8}}\right)+B\right]-\frac{1}{8} \quad \text{.....(B.12.6)}$$

Introduction of the Reynolds number ($\mathbf{R} = VD/\nu$) into Eq. B.12.6 produces

$$k_3 = \sqrt{\frac{f}{512}}\left[A\ln\left(\mathbf{R}\sqrt{\frac{f}{32}}\right)+B\right]-\frac{1}{8} \quad \text{.....(B.12.7)}$$

Using the Colebrook-White equation, Eq. B.12.7 is further simplified. The Colebrook-White equation is

$$\frac{1}{\sqrt{f}} = 1.74 - 2\log\left(\frac{18.7}{\mathbf{R}\sqrt{f}}\right) \quad \text{.....(B.12.8)}$$

The term $\mathbf{R}\sqrt{f}$ is common to both Eq. B.12.7 and the Colebrook-White equation (Eq. B.12.8). Rearrangement of the Colebrook-White equation into a more useful form gives

$$\ln\left(\mathbf{R}\sqrt{\frac{f}{32}}\right) = \frac{\ln(10)}{2}\left(\frac{1}{\sqrt{f}}-1.74\right)+\ln\left(\frac{18.7}{\sqrt{32}}\right) \quad \text{.....(B.12.9)}$$

Substitution of Eq. B.12.9 into Eq. B.12.7 results in a relationship for k_3 that is only in terms of the friction factor f,

$$k_3 = \sqrt{\frac{f}{512}}\left[A\left(\frac{\ln(10)}{2}\left(\frac{1}{\sqrt{f}}-1.74\right)+\ln\left(\frac{18.7}{\sqrt{32}}\right)\right)+B\right]-\frac{1}{8} \quad \text{.....(B.12.10)}$$

Simplification of Eq. B.12.10 forms an expression relating the unsteady friction coefficient (k_3) to the Darcy-Weisbach friction factor (f) using the logarithmic law of velocity distribution.

$$k_3 = 0.1539\sqrt{f} + 2.201\times10^{-3} \quad \text{.....(B.12.11)}$$

B.13 Derivation of k_3 Based on the Rough Pipe Logarithmic Law with Transition Formulae

The derivation for k_3 based on the rough pipe logarithmic law including the transition region formulae begins from the relationship between k_3 and velocity distribution function,

$$k_3 = \tfrac{1}{8}g_v\big|_{r=0} - \tfrac{1}{8} \quad \text{.....(B.13.1)}$$

Insertion of the relationship for the velocity distribution based on the logarithmic laws (Eq. B.9.17) into Eq. B.13.1 forms

$$k_3 = \frac{1}{8}\phi\big|_{r=0}\sqrt{\frac{f}{8}} - \frac{1}{8} \quad \text{(B.13.2)}$$

Substitution of the dimensionless velocity function (ϕ), evaluated at the centre of the pipe and including the transition formulae (Eq. B.9.16), into Eq. B.13.2 gives

$$k_3 = \sqrt{\frac{f}{512}}\left[A\ln\left(\eta\big|_{r=0} - \eta_{IR} + A\right) + B_R\right] - \frac{1}{8} \quad \text{(B.13.3)}$$

Substitution of the dimensionless thickness of the rough pipe viscous sub-layer η_I (Eq. B.9.15), needed for the transition formulae, Eq. B.13.3 produces

$$k_3 = \sqrt{\frac{f}{512}}\left[A\ln\left(\eta\big|_{r=0} - A\ln(A) - B_R + A\right) + B_R\right] - \frac{1}{8} \quad \text{(B.13.4)}$$

Evaluation of the dimensionless distance η (Eq. B.9.3) at the centre of the pipe yields

$$k_3 = \sqrt{\frac{f}{512}}\left[A\ln\left(\frac{r_0 v_*}{\nu} - A\ln(A) - B_R + A\right) + B_R\right] - \frac{1}{8} \quad \text{(B.13.5)}$$

Substitution of the relationship for friction velocity (Eq. B.9.2) into Eq. B.13.5 and replacing the pipe radius (r_0) with the pipe diameter (D) forms

$$k_3 = \sqrt{\frac{f}{512}}\left[A\ln\left(\frac{D}{2\nu}\sqrt{\frac{\tau_0}{\rho}} - A\ln(A) - B_R + A\right) + B_R\right] - \frac{1}{8} \quad \text{(B.13.6)}$$

Introduction of the friction factor (f) for the boundary shear stress (τ_0), using the relationship $\tau_0 = fV^2\rho/8$, leaves an expression that is only dependent on the Darcy-Weisbach friction factor,

$$k_3 = \sqrt{\frac{f}{512}}\left[A\ln\left(\frac{DV}{2\nu}\sqrt{\frac{f}{8}} - A\ln(A) - B_R + A\right) + B_R\right] - \frac{1}{8} \quad \text{(B.13.7)}$$

Finally, replacement of VD/ν with the Reynolds number (**R**) results in an expression for k_3 using the rough pipe logarithmic laws including the transition formulae,

$$k_3 = \sqrt{\frac{f}{512}}\left[A\ln\left(\mathbf{R}\sqrt{\frac{f}{32}} - A\ln(A) - B_R + A\right) + B_R\right] - \frac{1}{8} \quad \text{(B.13.8)}$$

B.14 Derivation of k_3 Based on the Rough Pipe Logarithmic Law Only

An expression for the unsteady friction coefficient k_3 is derived using the rough pipe logarithmic laws only. The transition formulae may be neglected because the velocity distribution function is evaluated at the centre of the pipe where the behaviour is not influenced by the transition between the log layer and the viscous sub-layer. Consider the relationship between k_3 and velocity distribution function,

$$k_3 = \tfrac{1}{8} g_v\big|_{r=0} - \tfrac{1}{8} \quad \text{.....(B.14.1)}$$

Substitution of the relationship for the velocity distribution based on the logarithmic laws (Eq. B.9.17) into Eq. B.14.1 forms

$$k_3 = \frac{1}{8}\phi\big|_{r=0}\sqrt{\frac{f}{8}} - \frac{1}{8} \quad \text{.....(B.14.2)}$$

Inserting the dimensionless velocity function (ϕ), evaluated at the centre of the pipe and not including the transition formulae (Eq. B.9.14), into Eq. B.14.2 gives

$$k_3 = \sqrt{\frac{f}{512}}\left[A\ln\left(\eta\big|_{r=0}\right) + B_R\right] - \frac{1}{8} \quad \text{.....(B.14.3)}$$

Introduction of the definition of the dimensionless distance η (Eq. B.9.3) evaluated at the centre of the pipe into Eq. B.14.3 results in

$$k_3 = \sqrt{\frac{f}{512}}\left[A\ln\left(\frac{r_0 v_*}{\nu}\right) + B_R\right] - \frac{1}{8} \quad \text{.....(B.14.4)}$$

Substitution of the relationship for friction velocity (Eq. B.9.2) into Eq. B.14.4 forms

$$k_3 = \sqrt{\frac{f}{512}}\left[A\ln\left(\frac{D}{2\nu}\sqrt{\frac{\tau_0}{\rho}}\right) + B_R\right] - \frac{1}{8} \quad \text{.....(B.14.5)}$$

Replacement of the friction factor (f) by the boundary shear stress (τ_0), using the relationship $\tau_0 = fV^2\rho/8$, leaves an expression only dependent on the friction factor,

$$k_3 = \sqrt{\frac{f}{512}}\left[A\ln\left(\frac{DV}{2\nu}\sqrt{\frac{f}{8}}\right) + B_R\right] - \frac{1}{8} \quad \text{.....(B.14.6)}$$

Replacement of VD/ν with the Reynolds number (**R**) yields

$$k_3 = \sqrt{\frac{f}{512}}\left[A\ln\left(\mathbf{R}\sqrt{\frac{f}{32}}\right) + B_R\right] - \frac{1}{8} \quad \text{.....(B.14.7)}$$

B_R was previously defined in Eq. B.9.14 and is repeated as

$$B_R = C_R - A\ln(\eta_R) \quad \text{(B.14.8)}$$

Substitution of C_R (defined in Eq. B.9.12), that originally came from the Colebrook-White equation, into Eq. B.14.8 gives

$$B_R = \sqrt{\frac{8}{f}} + 3.75 - A\ln\left(\frac{r_0}{k_S}\right) - A\ln(\eta_R) \quad \text{(B.14.9)}$$

Using the definition of dimensionless distance parameter η_R (Eq. B.9.9), which depends on the roughness height, Eq. B.14.9 becomes

$$B_R = \sqrt{\frac{8}{f}} + 3.75 - A\ln\left(\frac{r_0}{k_S}\right) - A\ln\left(\frac{k_S v_*}{\nu}\right) \quad \text{(B.14.10)}$$

Substitution of the relationship for friction velocity (Eq. B.9.2) into Eq. B.14.10 forms

$$B_R = \sqrt{\frac{8}{f}} + 3.75 - A\ln\left(\frac{r_0}{k_S}\right) - A\ln\left(\frac{k_S}{r_0}\frac{r_0}{\nu}\sqrt{\frac{\tau_0}{\rho}}\right) \quad \text{(B.14.11)}$$

Using $\tau_0 = fV^2\rho/8$, the friction factor (f) replaces the boundary shear stress (τ_0),

$$B_R = \sqrt{\frac{8}{f}} + 3.75 - A\ln\left(\frac{r_0}{k_S}\right) - A\ln\left(\frac{k_S}{r_0}\frac{VD}{2\nu}\sqrt{\frac{f}{8}}\right) \quad \text{(B.14.12)}$$

Using $\mathbf{R} = VD/\nu$, the Reynolds number is introduced forming

$$B_R = \sqrt{\frac{8}{f}} + 3.75 - A\ln\left(\frac{r_0}{k_S}\right) - A\ln\left(\frac{k_S}{r_0}\mathbf{R}\sqrt{\frac{f}{32}}\right) \quad \text{(B.14.13)}$$

Separation of the relative roughness height from the second logarithmic term gives

$$B_R = \sqrt{\frac{8}{f}} + 3.75 - A\ln\left(\frac{r_0}{k_S}\right) - A\ln\left(\mathbf{R}\sqrt{\frac{f}{32}}\right) + A\ln\left(\frac{r_0}{k_S}\right) \quad \text{(B.14.14)}$$

Cancellation of the terms containing the relative roughness heights leaves a simplified relationship for the coefficient B_R,

$$B_R = \sqrt{\frac{8}{f}} + 3.75 - A\ln\left(\mathbf{R}\sqrt{\frac{f}{32}}\right) \quad \text{(B.14.15)}$$

Substitution of B_R (Eq. B.14.15) into the equation for k_3 (Eq. B.14.7) produces

$$k_3 = \sqrt{\frac{f}{512}}\left[A\ln\left(\mathbf{R}\sqrt{\frac{f}{32}}\right) + \sqrt{\frac{8}{f}} + 3.75 - A\ln\left(\mathbf{R}\sqrt{\frac{f}{32}}\right)\right] - \frac{1}{8} \quad \text{(B.14.16)}$$

The logarithmic terms containing the Reynolds number cancel out leaving an expression for k_3 that is only dependent on the friction factor f,

$$k_3 = \sqrt{\frac{f}{512}}\left(\sqrt{\frac{8}{f}} + 3.75\right) - \frac{1}{8} \quad \text{(B.14.17)}$$

After further simplification, the final expression for k_3 using the rough pipe logarithmic law is

$$k_3 = 3.75\sqrt{\frac{f}{512}} \quad \text{(B.14.18)}$$

B.15 Derivation of k_3 Based on the Power Law

As an alternative to the logarithmic laws, an expression for the unsteady friction coefficient k_3 can be found using the power law of velocity distribution. The derivation begins with the relationship between k_3 and velocity distribution function,

$$k_3 = \tfrac{1}{8} g_v\big|_{r=0} - \tfrac{1}{8} \quad \text{(B.15.1)}$$

Insertion of the relationship for the velocity distribution based on the power law (Eq. B.9.18) into Eq. B.15.1 forms

$$k_3 = \frac{1}{8}\left[\frac{(2n+1)(n+1)}{2n^2}\left(\frac{y|_{r=0}}{r_0}\right)^n - 1\right] \quad \text{(B.15.2)}$$

The exponent n can be found for smooth and rough pipes (see Section B.9.2). The variable y, which is the distance from the pipe wall, is evaluated at centreline of the pipeline, therefore the ratio y/r_0 is one and Eq. B.15.2 becomes

$$k_3 = \frac{1}{8}\left(\frac{(2n+1)(n+1)}{2n^2} - 1\right) \quad \text{(B.15.3)}$$

Simplification of Eq. B.15.3 forms a relationship for k_3, which is dependent only on the power law exponent n,

$$k_3 = \frac{3n+1}{16n^2} \quad \text{(B.15.4)}$$

B.16 Derivation of k_M Based on Logarithmic and Power Laws

In this section the unsteady coefficient k_M is determined using both the logarithmic and the power laws of velocity distribution. The unsteady coefficient k_M is related to the momentum correction factor β (Section 9.2) as

$$k_M = ¼(\beta - 1) \quad \text{(B.16.1)}$$

First the derivation for k_M using the logarithmic law is examined. Chen (1992) developed an expression for β based on the log law (Eq. B.10.2). Substitution of Eq. B.10.2 into Eq. B.16.1 forms

$$k_M = \frac{1}{4}\left(\frac{5f}{32\kappa^2}+1\right)-\frac{1}{4} \quad \text{(B.16.2)}$$

Upon simplification, an expression for the unsteady coefficient k_M is produced that is dependent on the friction factor and von Kármán's constant ($\kappa = 0.40$).

$$k_M = \frac{5f}{128\kappa^2} \quad \text{(B.16.3)}$$

Now the power law of velocity distribution is considered. Chen (1992) also determined an expression for β (Eq. B.10.1) in terms of the power exponent n. Substitution of Eq. B.10.1 into (Eq. B.16.1) results in

$$k_M = \left(\frac{(n+1)(2n+1)^2}{16n^2(n+2)}\right)-\frac{1}{4} \quad \text{(B.16.4)}$$

The simplification of Eq. B.16.4 forms an expression for the unsteady coefficient k_M that is only dependent on the exponent of the power law equation (n).

$$k_M = \frac{5n+1}{16n^2(n+2)} \quad \text{(B.16.5)}$$

Values for n are discussed in Section 9.6.2.

Appendix C

Additional Experimental Data and Analysis

This appendix contains additional experimental data and analysis for Chapters 10, 11 and 12. All of the transducer calibration curves and additional leak calibration plots are presented. Verification results for different unsteady friction models are presented along with the performance of the Zielke (1968) unsteady friction model over the eight unsteady flow events.

C.1 Transducer Calibration Curves

Previously in Section 10.4.1, one calibration curve for a transducer located at node 1 in the experimental pipeline was shown. The complete set of curves is presented in this section. Calibration curves for transducers located at nodes 1, 2, 3, 4, and 5 in the experimental pipeline are shown in Figures C.1, C.2, C.3, C.4 and C.5 respectively.

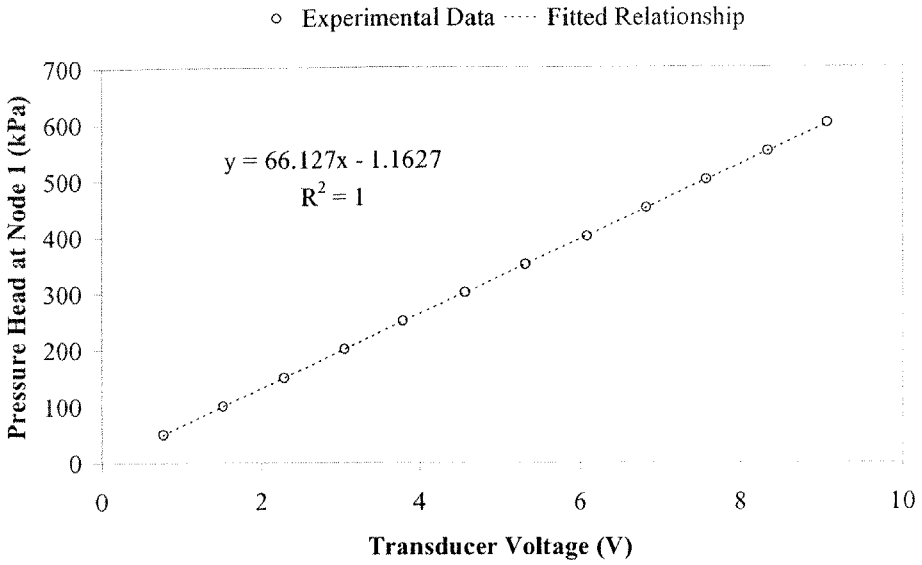

Figure C.1 Calibration of Node 1 Pressure Transducer

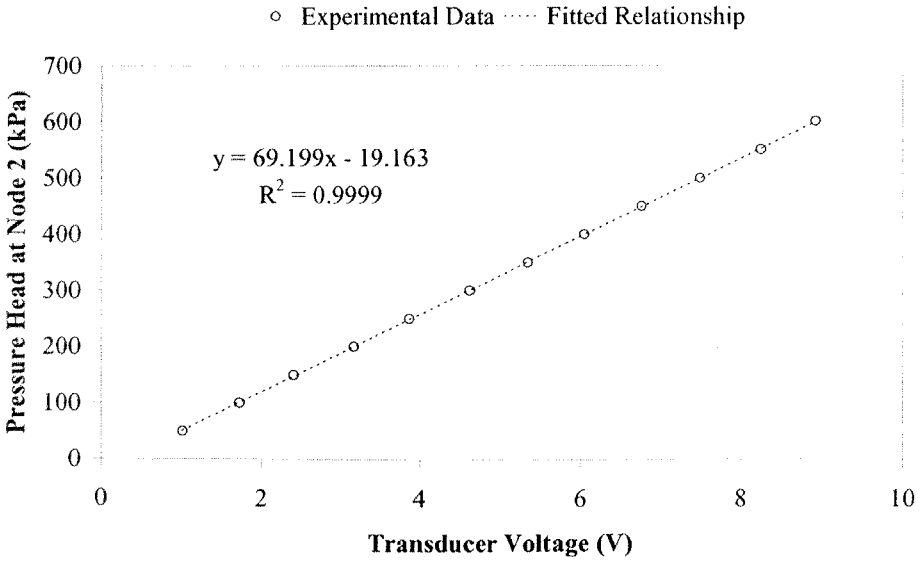

Figure C.2 Calibration of Node 2 Pressure Transducer

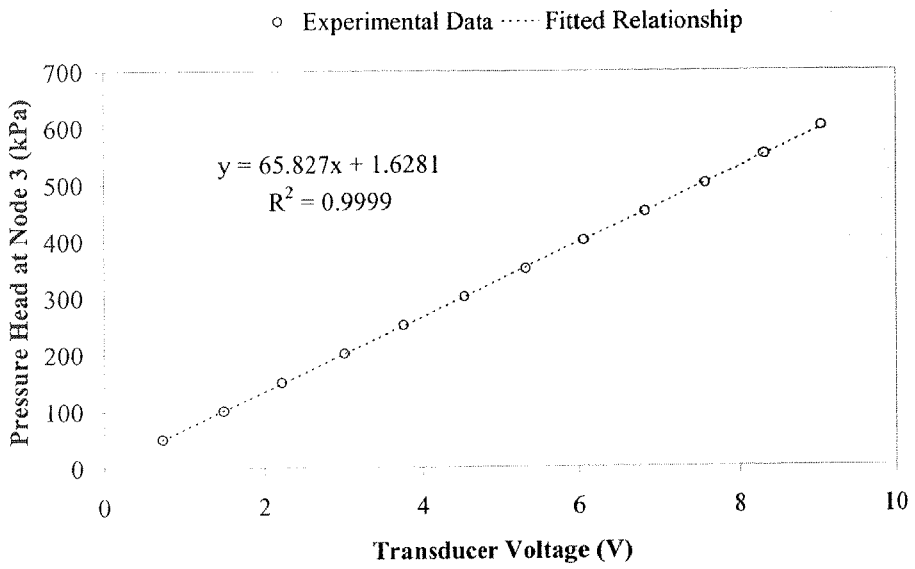

Figure C.3 Calibration of Node 3 Pressure Transducer

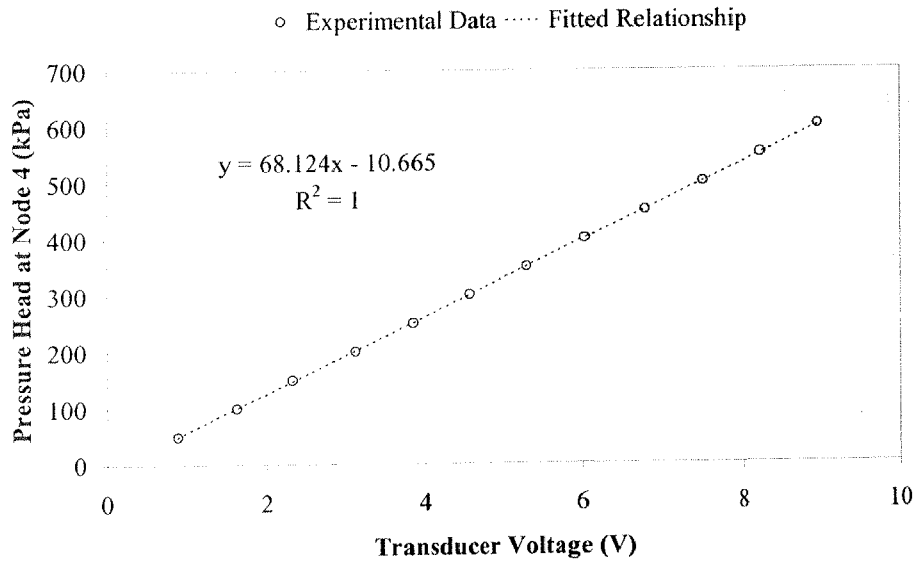

Figure C.4 Calibration of Node 4 Pressure Transducer

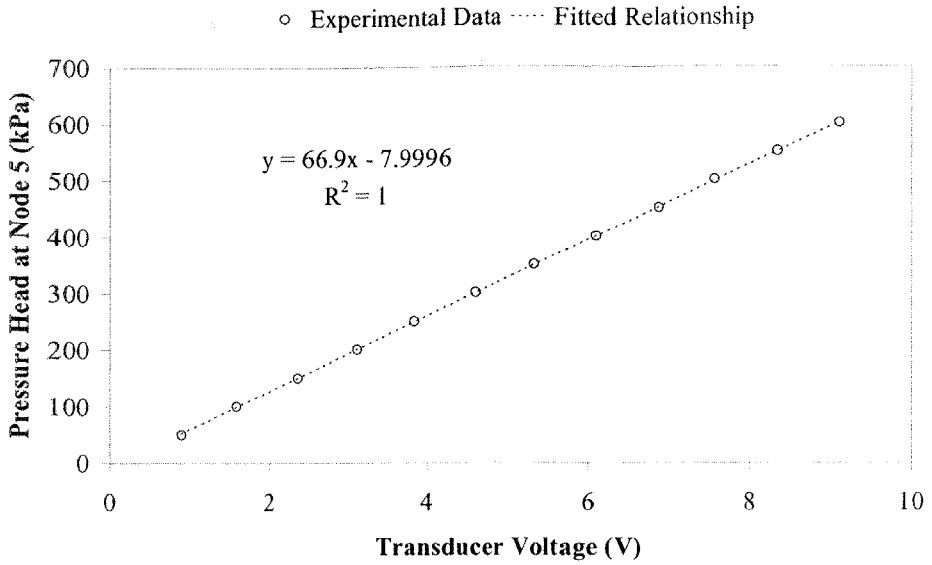

Figure C.5 Calibration of Node 5 Pressure Transducer

C.2 Leak Calibration Curves

Section 10.4.5 presented various calibration curves for the four different leakage units. Other calibrations for these curves are presented in this section. The relationship between the leak flow and the pressure at the leak is assumed to be square root in nature,

$$Q_L = C_d A_L \sqrt{2gH_L} \quad \text{.....(C.2.1)}$$

Using a least squares approach, the coefficient of discharge from Eq. C.2.1 can be found from experimental calibration data, the result of which is two-fold. The first result is the determination of C_d (over a range of pressures) that can is used to verify inverse transient analysis results from Chapter 12. The second is to gauge how well the leak relationship (Eq. C.2.1) models the steady state leakage. The first of the four leakage blocks tested was the 1.0 mm (#1) leak, results for the fitted leak relationship (including the value C_d) are shown in Figure C.6. These results show that Eq. C.2.1 is a reasonable approximation of the leak behaviour. A more detailed analysis of the effect of the approximate fitted leak equation is shown in Section 12.2.1.

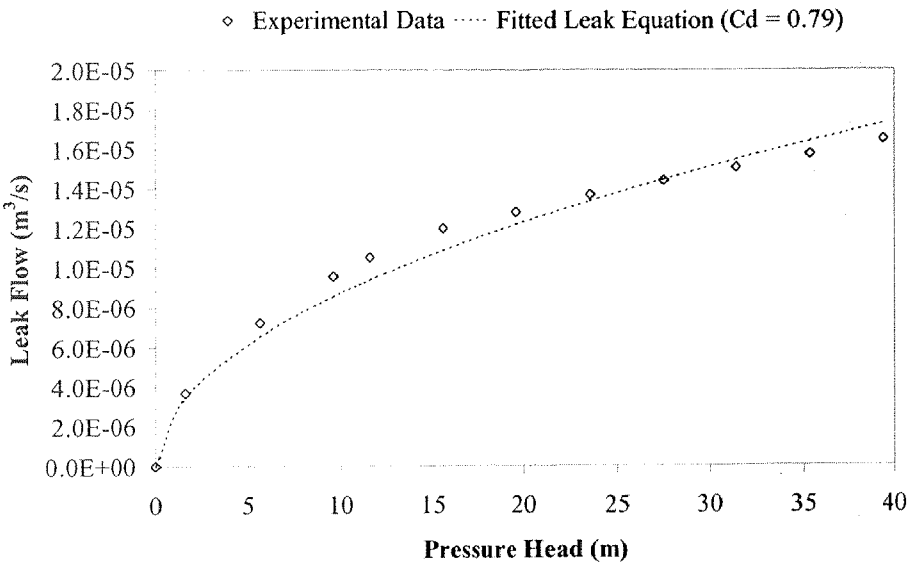

Figure C.6 Fitted Leak Function for 1.0 mm Leak (#1)

The same analysis is performed for the other 1.0 mm (#2) leak. Figure C.7 shows a good fit using Eq. C.2.1.

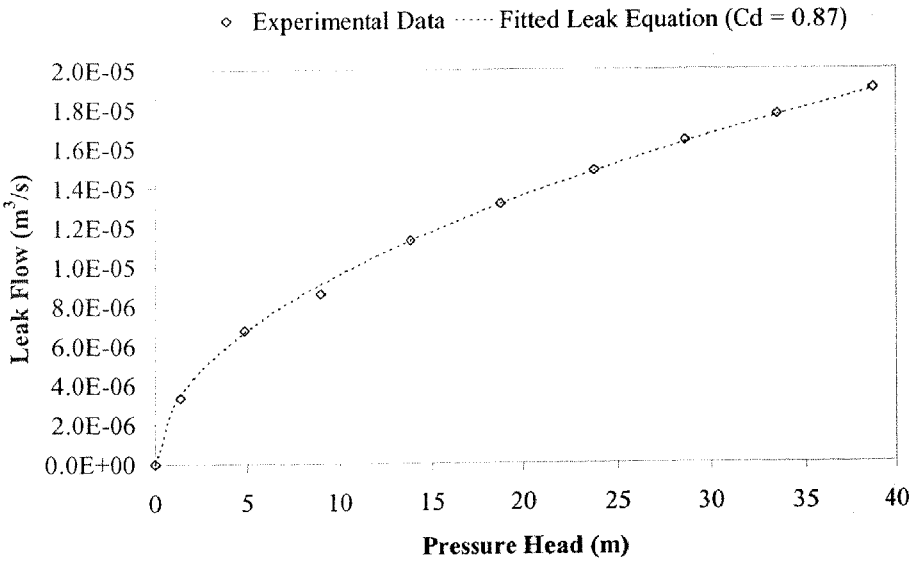

Figure C.7 Fitted Leak Function for 1.0 mm Leak (#2)

The result of the fitting Eq. C.2.1 for the 1.5 mm leakage unit is shown in Figure C.8. This result is satisfactory except that the slope of the higher-pressure tests does not match the fitted relationship, suggesting that for even higher pressures, the leak equation would not be a good approximation of the behaviour of the 1.5 mm leak.

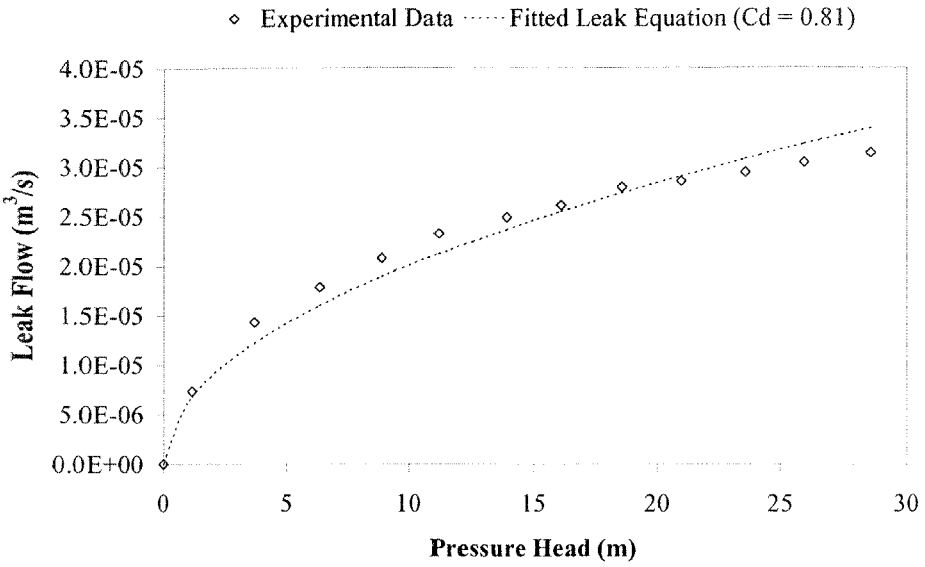

Figure C.8 Fitted Leak Function for 1.5 mm Leak

Results for the 2.0 mm leak are shown in Figure C.9. These results are similar to the pervious results from the 1.5 mm leak. The leak equation does not quite represent the experimental data for high pressures or low pressures. A reason is that, in reality, the approximation that C_d is constant is incorrect. The coefficient of discharge is Reynolds number dependent; suggesting that results using the inverse transient method may produce inconsistent lumped leak areas for the large leak diameter units.

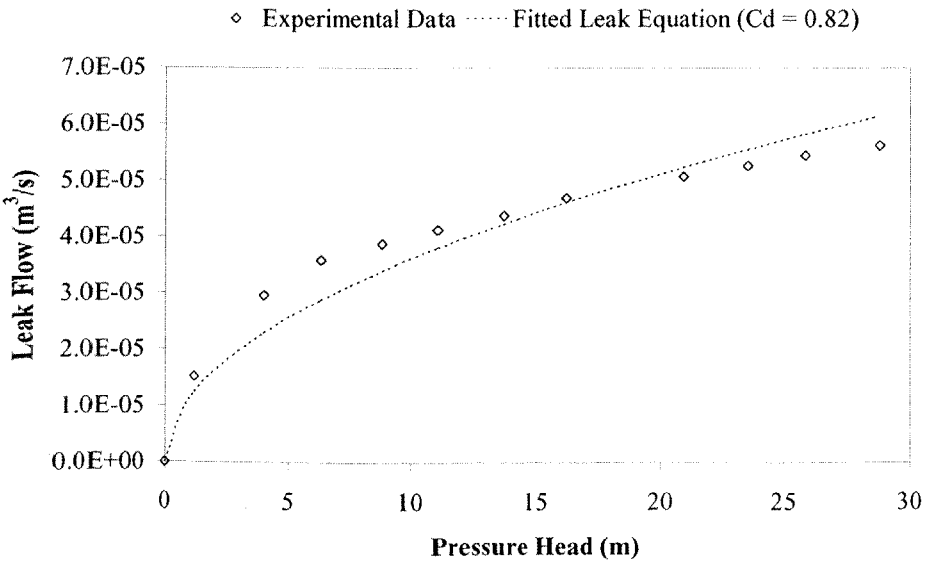

Figure C.9 Fitted Leak Function for 2 mm Leak

All of the fitted relationships are plotted together to show the relative magnitudes of the curves for each of the four different leakage units, as shown in Figure C.10. As expected, the two leakage units that have the same size leak diameters produce similar curves.

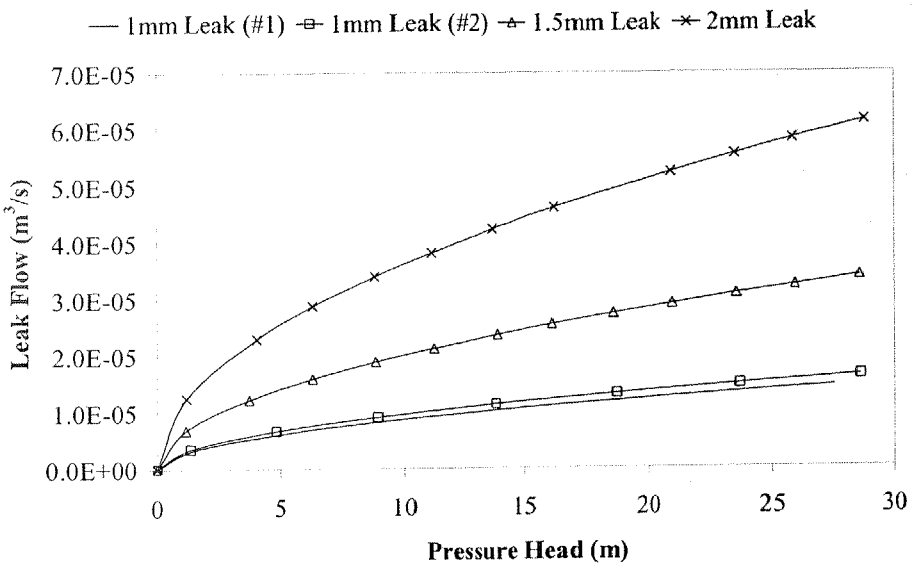

Figure C.10 Fitted Leak Functions for All Leaks

C.3 Effects of Incorrect Filtering

A number of different filtering methods were discussed in Section 10.5. Some effects of incorrect filtering are easy to observe from modelled data whereas others are more difficult to observe. Under-filtering produces data that still contains undesirable noise (that was trying to be filtered out). Over-filtering can affect the general trend of the data through smoothing of both the signal and the noise (when only noise was to be eliminated). Good filtering (also called a sufficient level of filtering) is defined as the elimination of the noise in the data leaving only the true signal. This section presents problems that have occurred when using incorrectly filtered data (both over and under filtered examples) that are to be input into a transient model. In this study, data can be input into a transient model two ways. The first way is as a pressure in a known pressure boundary condition. The second way is as a valve position in a variable

position valve boundary condition. The effects of incorrect filtering are presented using these two ways that data can be input into a transient model.

If the head at a known pressure head boundary condition is used as input, the original data may contain random error. If the data are not filtered, the random error in the data will be transmitted to other locations in the pipeline through the transient model, an example of which is shown in Figure C.11. In this example, the pipeline is the same as experimental pipeline as described earlier in Chapter 10. The transient model uses two head boundary conditions at either end of the pipeline. Steady state conditions are modelled. A small randomly distributed (Gaussian) error is introduced into the head boundary condition data at node 1. As the results show, the error has been transmitted to node 2 and amplified as well. In this case there was no filtering of the boundary condition data and shows that under-filtering can cause massive errors to occur in simulation results, which is remedied by filtering a sufficient level (where only the noise is removed and the signal remains).

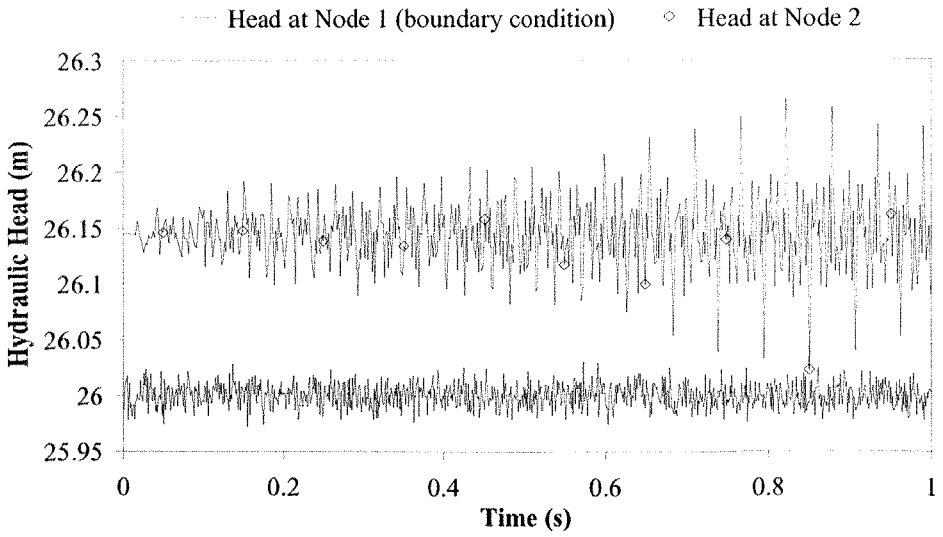

Figure C.11 Amplification of Noise from Head Boundary Condition

There are two possible problems that can occur when filtering valve position data. These problems occur from either under-filtering or over-filtering of data. Under-filtering data can be demonstrated through the use of a slow valve closure. In fact, the effects of under-filtering valve position data are more prevalent in slower valve closure

tests because more time is being spent in the highly sensitive, nearly closed region. The slow valve closure used in this example is for a valve closure time of 1.0 s. The initial velocity for this example is 0.32 m/s corresponding to a Reynolds number of 7,026. The valve position data during this event are shown in Figure C.12. The data were sampled at 2,000 Hz. To test the difference between under-filtering data and good filtering of data, two sets of data are shown. The first is non-filtered data and the other is data that has been filtered using a moving average (window size of 111 points). As can be observed, there is little observable difference between the two curves.

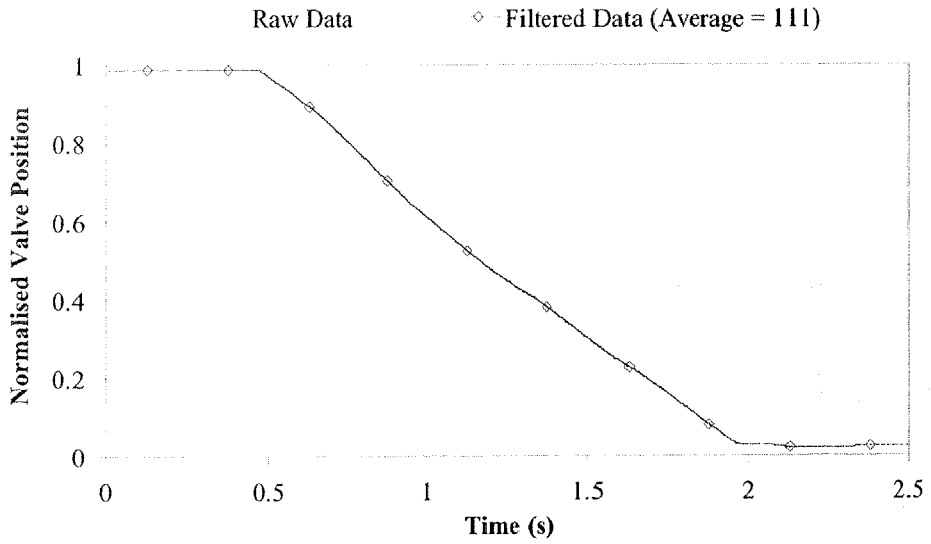

Figure C.12 Raw and Smoothed Valve Data

Numerical simulation results using these two differently filtered sets of data are shown in Figure C.13. The results show that even though there seems to be little difference between the valve position curves, the behaviour of the simulation results are a lot better when using filtered data. The error (when using the raw data) is most evident when the valve is ¾ to fully closed.

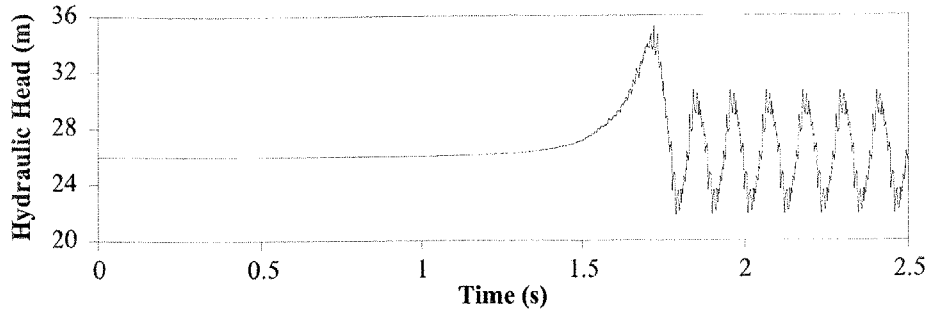

(a) Analysis Using Raw Valve Data

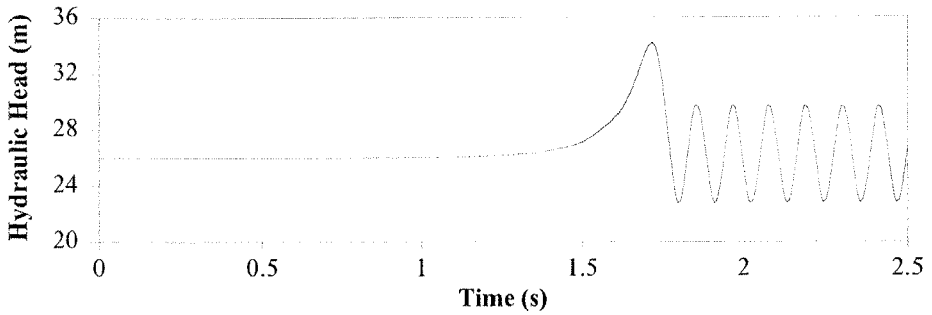

(b) Analysis Using Filtered Valve Position Data (Average = 111)

Figure C.13 Head at Valve Using Raw and Filtered Valve Data

Another form of error is observed when over-filtering is used. Different degrees of filtering are sufficient for different types of events. In the previous example, using a moving average (window size of 111 points) produced good results for a transient event initiated by a 1.5 s valve closure. In this case, the same degree of filtering is applied to a faster valve closure (approximately 0.1 s closure time). The initial velocity is 0.17 m/s corresponding to a Reynolds number of 3,754. Figure C.14 shows the results of over-filtering on the valve position data.

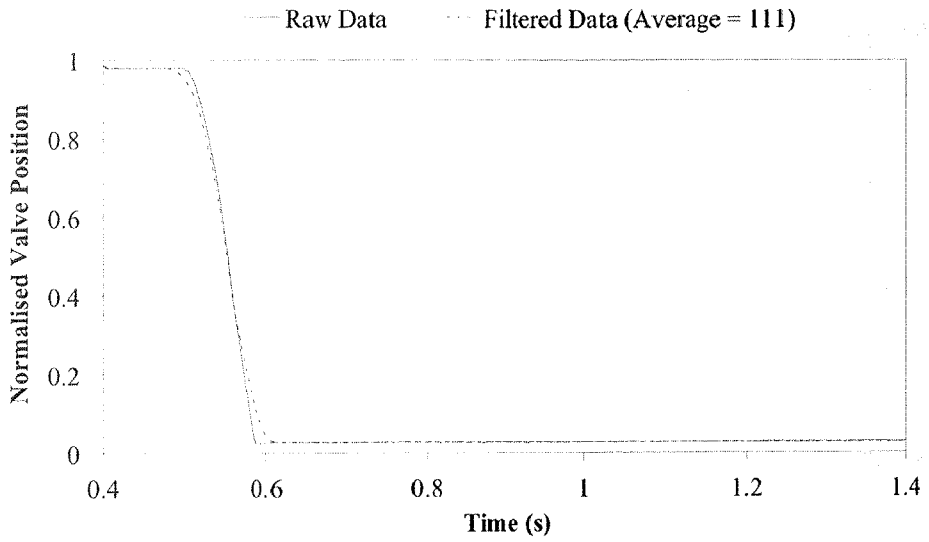

Figure C.14 Raw and Smoothed Valve Data

Figure C.14 shows that the moving average filter smooths some the features of the actual curve, the results of which are evident in the simulated pressures at the valve using filtered and non-filtered valve position data (Figure C.15). The over-filtering, in this case, causes a shift in the pressure oscillations, which could be detrimental to calibration techniques where curve matching is needed.

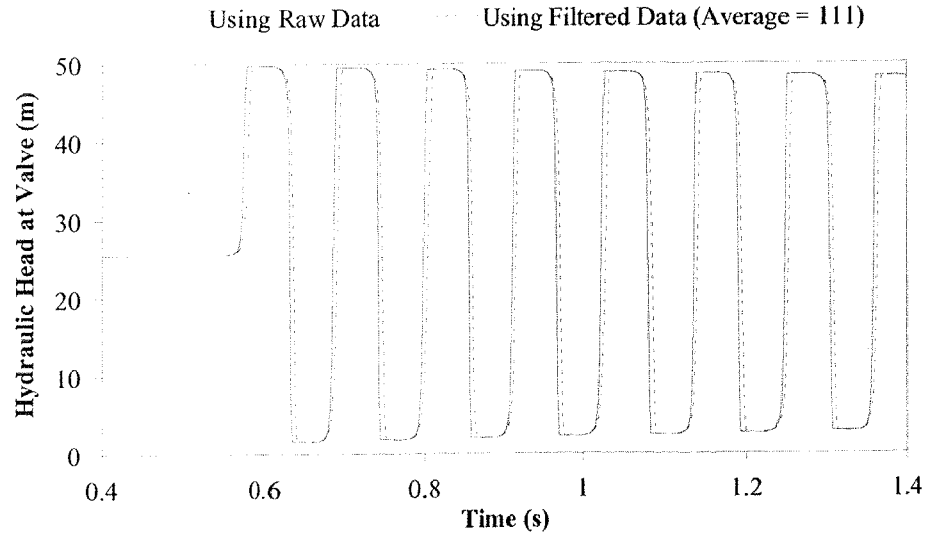

Figure C.15 Head at Valve Using Raw and Smoothed Valve Data

This section has presented results for different types of filters and problems that can occur through under- and over-filtering, and forms a basis for the treatment of input data used in the experimental verification Chapters 11 and 12.

C.4 Verification of Additional Unsteady Friction Models

A number of different unsteady friction models were discussed in Section 8.2. The performance of each of these against initially turbulent flows for valve closure tests is presented in this section. The experimental data were collected from an event with an initial velocity of 0.3 m/s (Reynolds number of 6,584). All modelled results shown in this section use 16 computational reaches (N) and any derivatives needed for unsteady friction models are calculated using an approximate divided difference scheme. The Golia (1990) unsteady friction model produces results that are equivalent (in most respects) to the Brunone *et al.* (1991) unsteady friction model. Figure C.16 shows results for the Brunone *et al.* (1991) model, which shows a good match with a small error in the phase of the pressure oscillations.

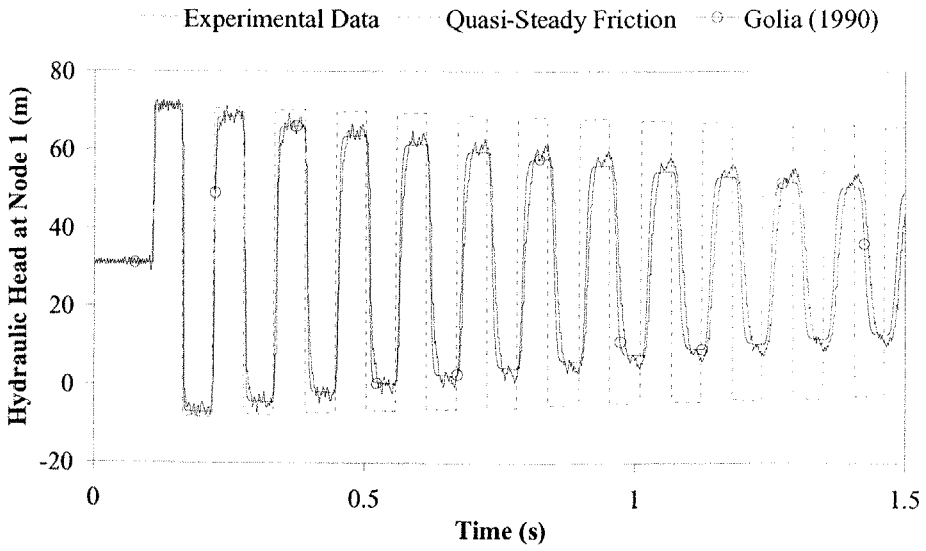

Figure C.16 Golia (1990) Unsteady Friction Model

Results using the Hino *et al.* (1977) unsteady friction model are shown in Figure C.17. These plots show that the Hino *et al.* (1977) model fails to produce enough damping

and no change in the phase of the pressure oscillations. The Hino *et al.* (1977) model was initially derived for oscillating flow in a U-tube.

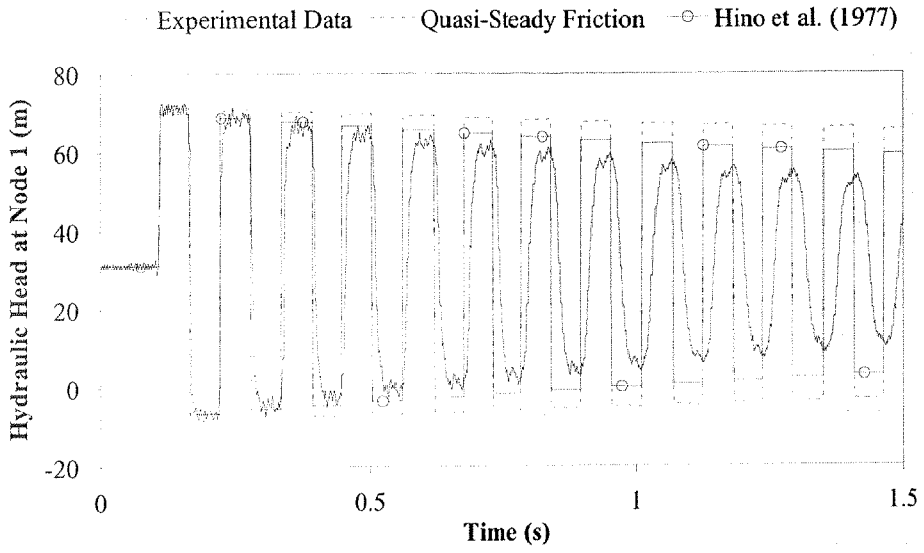

Figure C.17 Hino *et al.* (1977) Unsteady Friction Model

The next three models are laminar flow models. It is proposed that these models may still be valid for low Reynolds number turbulent flows. The first to be tested is the Zielke (1968) unsteady friction model, the results of which are shown in Figure C.18. These results show that the Zielke (1968) model produces similar damping of the pressure oscillations but fails to produce the shape and change in phase of the oscillations observed in the experimental data.

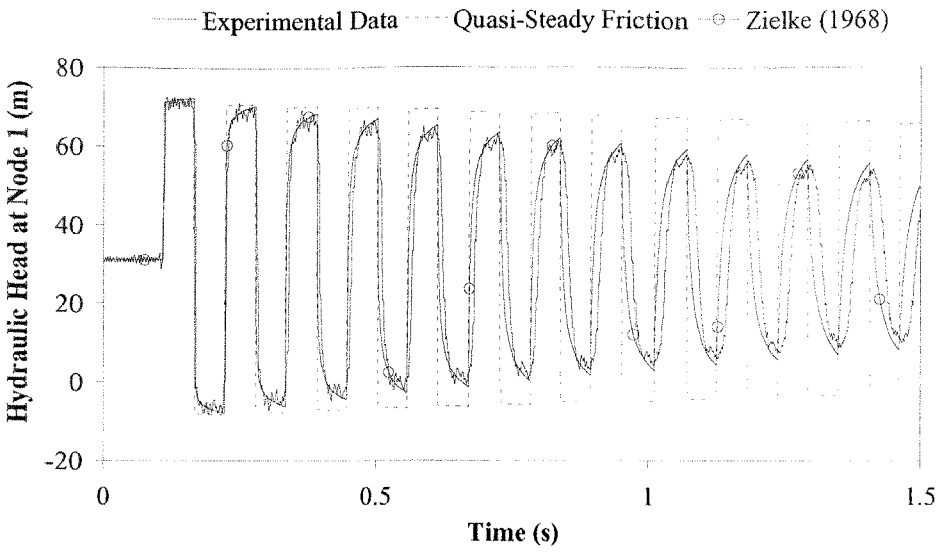

Figure C.18 Zielke (1968) Unsteady Friction Model

The Trikha (1975) unsteady friction model should produce exactly the same results as the Zielke (1968) model. The Zielke (1968) model is computationally slow as shown in Table C.1. By making some approximations Trikha (1975) produced a faster model, the result of its use is shown in Figure C.19. These results are similar to the pervious results for the Zielke (1968) model. The Trikha (1975) model, however, does produce a smaller amount of damping than the Zielke (1968) model, suggesting that the approximations made to create the Trikha (1975) model do have an effect on the modelled results.

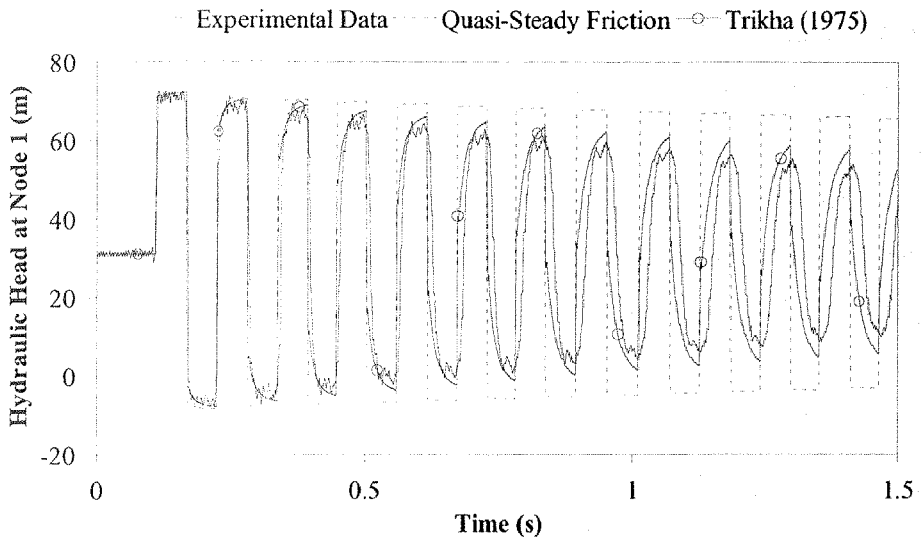

Figure C.19 Trikha (1975) Unsteady Friction Model

The final unsteady friction model considered here is the Kagawa *et al.* (1983) unsteady friction model. Similar to the Trikha (1975) model, the Kagawa *et al.* (1983) model attempts to produce the Zielke (1968) behaviour much more efficiently (with less computation time). Kagawa *et al.* (1983) achieved a higher efficiency by storing some extra variables; results for their model are shown in Figure C.20. The results produced using the Kagawa *et al.* (1983) unsteady friction model show a good agreement with those using the Zielke (1968) model.

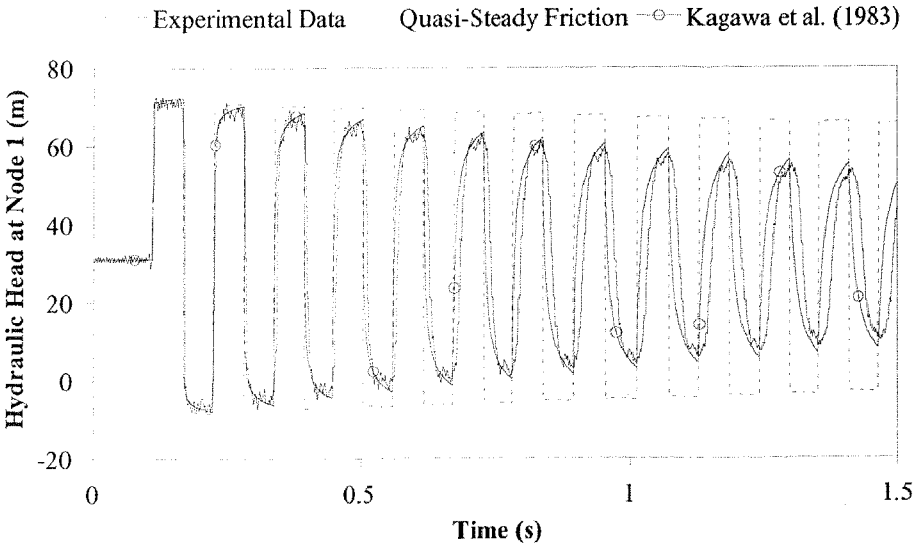

Figure C.20 Kagawa *et al.* (1983) Unsteady Friction Model

The computation time for each unsteady friction model has been recorded. The time can be used to compare the efficiency of the calculation of unsteady friction in the various models. The computation times for each unsteady friction formulation are shown in Table C.1. The computation time from the quasi-steady friction model is the fastest because no unsteady friction model is present. The times for the Hino *et al.* (1977), Golia (1990), and Brunone *et al.* (1991) unsteady friction models are similar.

Table C.1 Computation Times for Unsteady Friction Models

Unsteady Friction Model	Computation Time (s)
Quasi-Steady	0.44
Hino (1977)	0.61
Golia (1990)	0.48
Brunone *et al.* (1991)	0.50
Zielke (1968)	183.06
Trikha (1975)	0.64
Kagawa *et al.* (1983)	1.45

The main reason for recording the computations times is to test the computational efficiency of the three laminar unsteady friction models. It has been previously stated that the Zielke (1968) model is slow to compute, mainly because it uses a weighted sum of past velocity changes that reaches back to the initial conditions. For long simulation times the Zielke (1968) model becomes very slow indeed, as shown in Table C.1. The Trikha (1975) and Kagawa *et al.* (1983) models attempt to speed up computation. The Trikha (1975) model is the fastest out of the two models with the Kagawa *et al.* (1983) model being a little more than twice as slow; however, the Kagawa *et al.* (1983) model produces behaviour that more closely resembles the Zielke (1968) model, thus introducing a trade-off between the accuracy of the model and the speed of computation.

C.5 Verification of 8 Unsteady Flow Events Using the Zielke (1968) Model

Section 11.5 investigates the performance of the k_A & k_P unsteady friction model for the 8 unsteady flow events. These 8 events (reduced to 4 due to mirror equivalence) were conducted experimentally to produce data that could be used to test an unsteady fiction

model's validity over a range of events. The tests consisted of downstream and upstream valve closures and downstream and upstream valve openings. The k_A & k_P unsteady friction model was found to accurately model the valve closure tests but not the valve opening tests. It is proposed that since the initial flow for the valve opening must pass through the laminar flow region, the Zielke (1968) unsteady friction model might reproduce the experimental results better. Thus, the Zielke (1968) unsteady friction model has been tested against the different event types. The results for the downstream and upstream valve closures are shown in Figures C.21 and C.22 respectively. The initial velocity in each case is 0.3 m/s, which corresponds to a Reynolds number of 6,584.

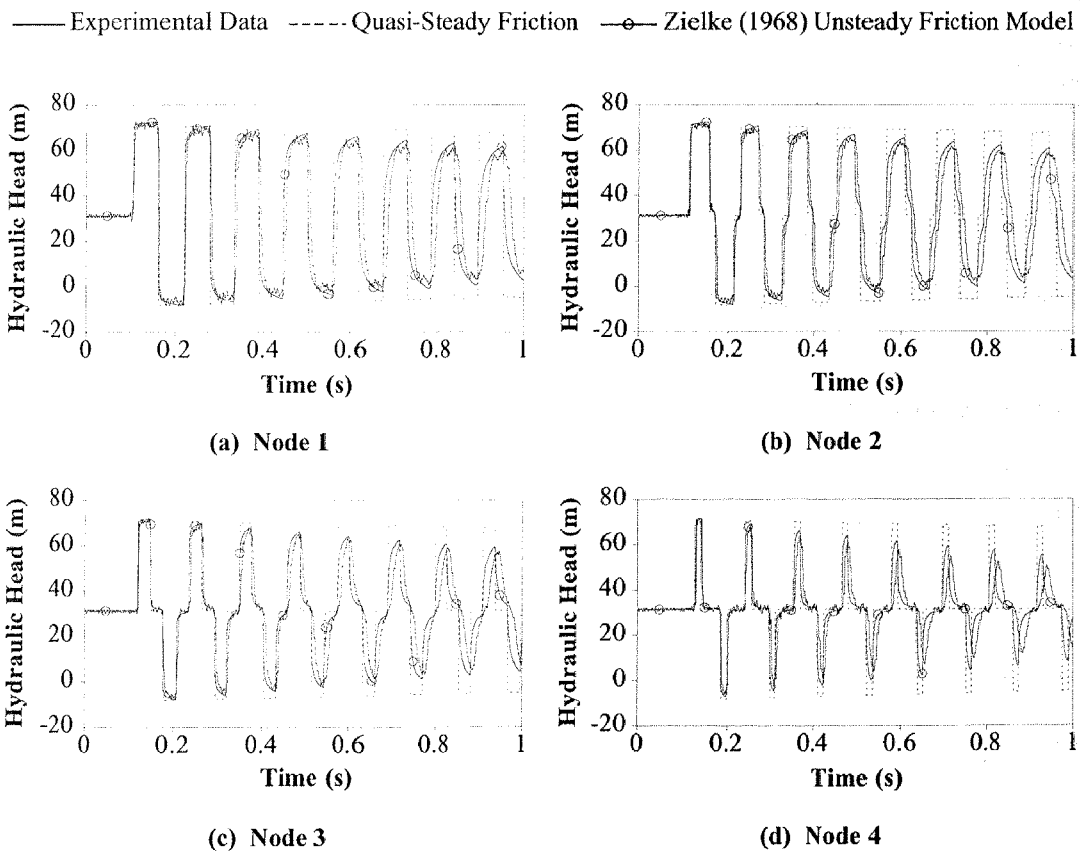

Figure C.21 Downstream Valve Closure, Zielke (1968) Model

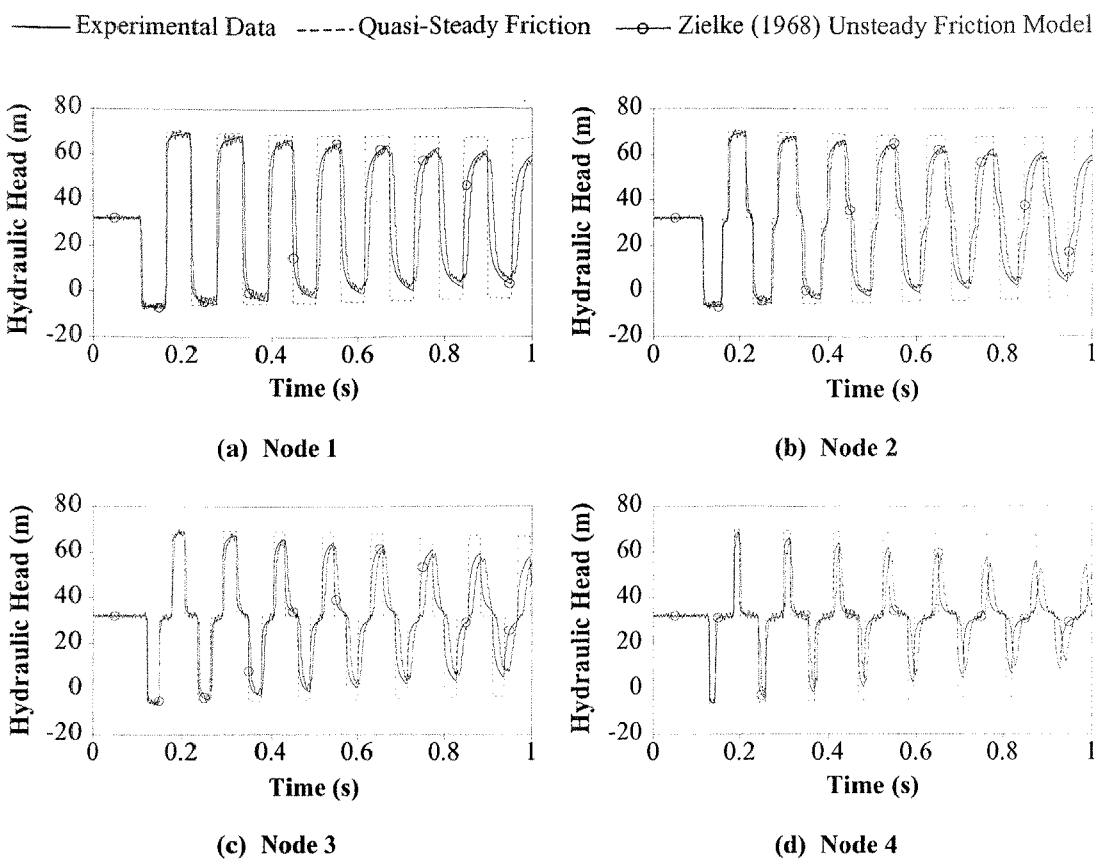

Figure C.22 Upstream Valve Closure, Zielke (1968) Unsteady Friction Model

The results show that the Zielke model does not accurately predict transient behaviour for valve closures, which is expected because the initial flow is turbulent in each case. The initial flow for a valve opening, however, is not turbulent. The final velocities for the downstream and upstream valve openings are 1.36 and 1.35 m/s (corresponding to Reynolds number of 29,838 and 29,650) respectively. The results using the Zielke unsteady friction model are shown in Figures C.23 and C.24 for the downstream and upstream valve openings respectively.

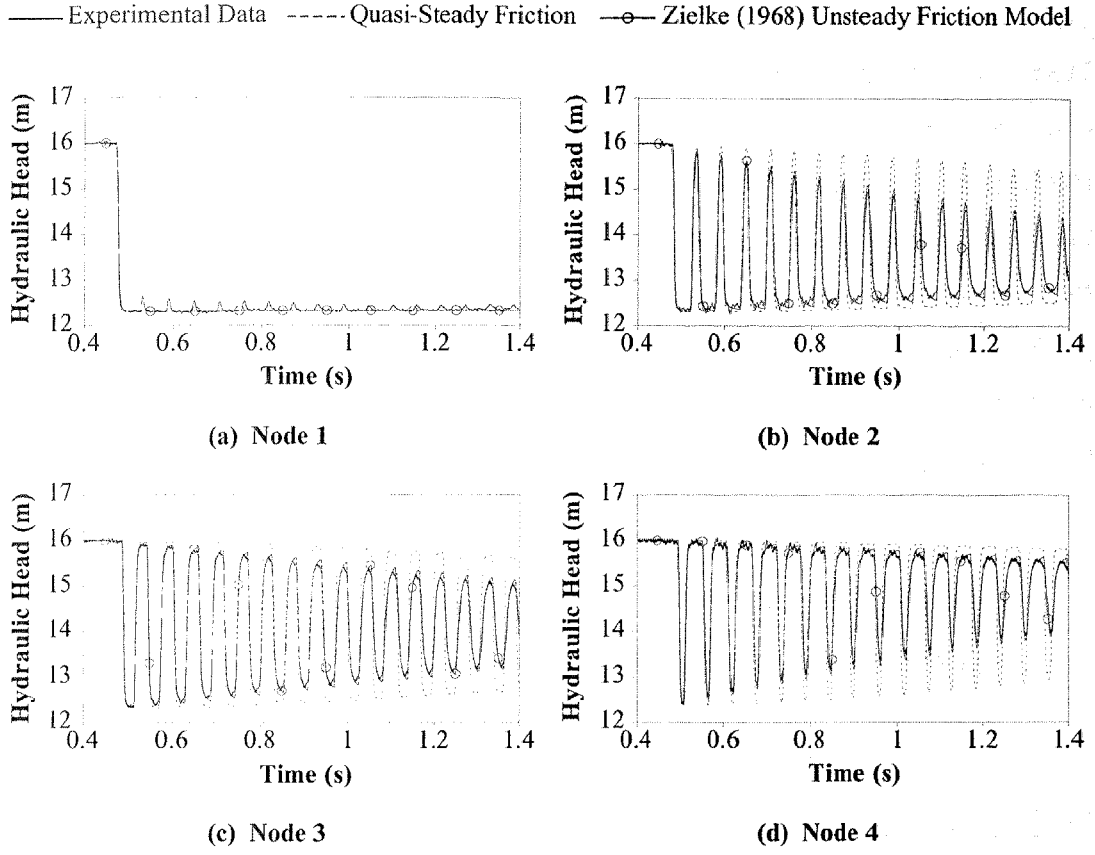

Figure C.23 Downstream Valve Opening, Zielke (1968) Unsteady Friction Model

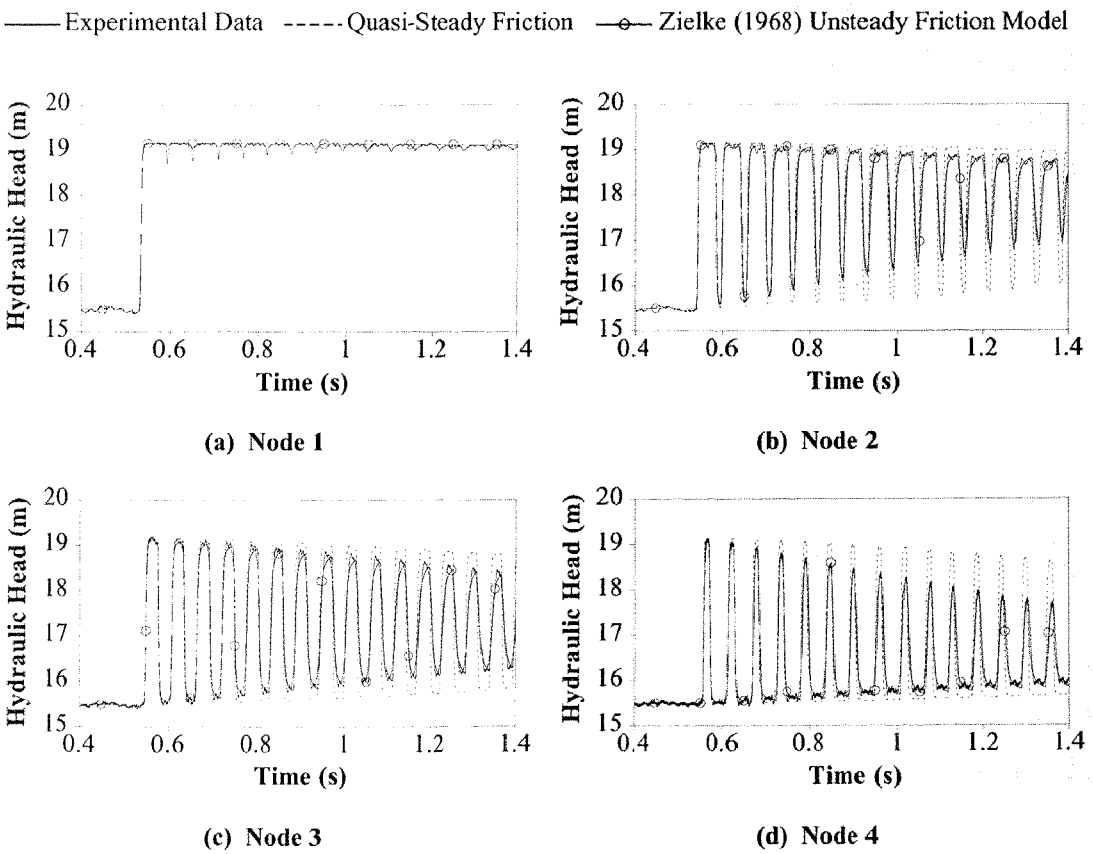

Figure C.24 Upstream Valve Opening, Zielke (1968) Unsteady Friction Model

These results show a good match between the experimental data and the Zielke (1968) unsteady friction model. The phase and damping of the pressure oscillations are well predicted by the Zielke (1968) model. There are only small differences in the shape of the peaks and troughs of the pressure oscillations. Even though the final state of the fluid in each opening case is turbulent, the laminar flow unsteady friction model produces good results. These results, together with those from Section 11.5, show that the k_A & k_P model is valid for initially turbulent flow valve closures and the Zielke (1968) model is valid for valve openings whose final flows are turbulent.

C.6 Derivation of First Pressure Rise Leak Detection Formulae

The detection and location of leakage in a pipeline may be achieved through the observation of the pressure head variation, a special case of which is for fast valve closure events. In this case, the behaviour of the first pressure head rise can be used to find both the location and magnitude of any leaks that are present along a pipeline. This section derives relationships that can be used to do just this. The derivation is facilitated through the use of an example pipeline, a layout of which is shown in Figure C.25.

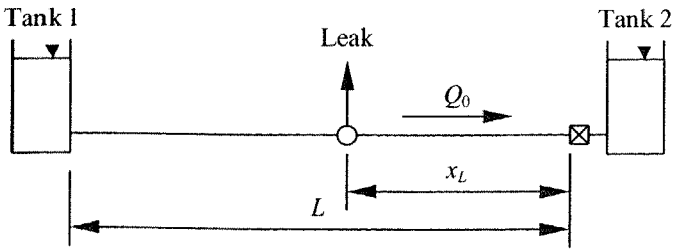

Figure C.25 Layout of Example Pipeline

The example pipeline consists of a pipe of length L connecting two tanks. A leak is located at a distance of x_L from Tank 2. The initial head in the pipeline is H_0 and the initial flow in the pipeline (travelling from left to right) is equal to Q_0. A transient event is initiated by the instantaneous closure of the valve located next to Tank 2. The pipeline is assumed to be frictionless, which can be justified since steady friction and

unsteady frictional effects are not significant for the first pressure head rise. Characteristic lines are drawn tracing the propagation of pressure waves after the transient event has been initialised, as shown in Figure C.26.

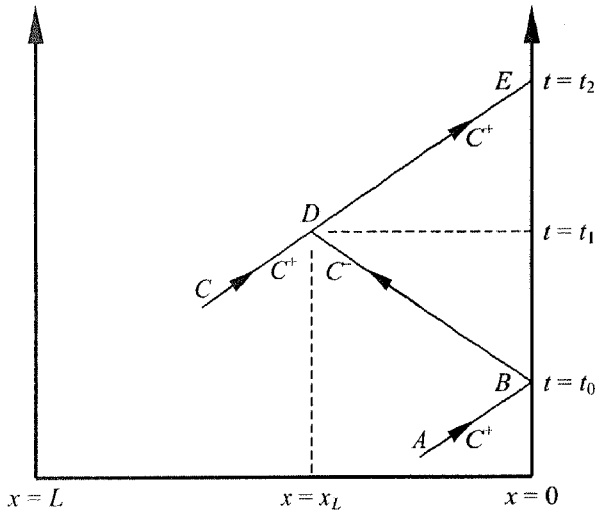

Figure C.26 Characteristic Grid for Example Pipeline

The transient event is initiated at a time of t_0, corresponding to point B on the characteristic grid. Steady state initial conditions exist at points A and C. Point D is defined as when the disturbance (caused by valve closure at point B) first arrives at the leak. Finally, point E is defined as when the return wave from the leak first returns to the valve. The objective of the following derivation is to find relationships for the leak location (x_L) and the leak size ($C_d A_L$) that are dependent on observable quantities. It is preferable that these quantities be pressures because they are more readily available than flows. The conditions (pressure head and flow) at point A are the initial steady pressure head and flow,

$$H_A = H_0 \quad \text{(C.6.1)}$$

$$Q_A = Q_0 \quad \text{(C.6.2)}$$

At point B, the valve next to Tank 2 closes instantaneously. Therefore, the flow at point B is zero. The pressure head at point B is determined using the C^+ compatibility equation,

$$H_B = H_0 + BQ_0 \quad \text{(C.6.3)}$$

$$Q_B = 0 \quad \text{(C.6.4)}$$

where B is the characteristic impedance, defined as

$$B = \frac{a}{gA} \quad \text{(C.6.5)}$$

The calculation of the pressure head and flow at point D requires the known conditions at points B and C. The conditions at point B were previously stated and the conditions at point C are the initial steady state conditions. The flow at point C is equated by observing the continuity of flow around the leak.

$$H_C = H_0 \quad \text{(C.6.6)}$$

$$Q_C = Q_0 + C_d A_L \sqrt{2gH_0} \quad \text{(C.6.7)}$$

The unknowns to be solved for at point D are the pressure head H_D and the flows on either side of the leak (denoted Q_D^+ and Q_D^- corresponding to the C^+ and C^- characteristic lines). These conditions occur at the leak, which is at a distance of x_L from the valve at Tank 2 and at a time of t_1. Conditions at point D are determined by considering the continuity of flow (including the leak flow) and the two compatibility equations. The conditions at points C and B are required for the C^+ and C^- compatibility equations respectively. Solving for the unknowns at point D gives

$$H_D = H_B - \tfrac{1}{2} B C_d A_L \sqrt{2g}\left(\sqrt{H_D} - \sqrt{H_0}\right) \quad \text{(C.6.8)}$$

$$Q_D^+ = \tfrac{1}{2} C_d A_L \sqrt{2g}\left(\sqrt{H_D} + \sqrt{H_0}\right) \quad \text{(C.6.9)}$$

$$Q_D^- = -\tfrac{1}{2} C_d A_L \sqrt{2g}\left(\sqrt{H_D} - \sqrt{H_0}\right) \quad \text{(C.6.10)}$$

Finally, the conditions at point E are considered. Conditions at point E occur when the return wave from the leak first arrives at the valve (at a time of t_2). Since the valve is closed, the flow at point E is equal to zero. The C^+ compatibility equation is used to solve for the head at point E (H_E) using Q_E and conditions at point D,

$$H_E = H_D - \tfrac{1}{2} B C_d A_L \sqrt{2g}\left(\sqrt{H_D} - \sqrt{H_0}\right) \quad \text{(C.6.11)}$$

$$Q_E = 0 \quad \text{(C.6.12)}$$

The objective of the derivation is to develop relationships for $C_d A_L$ and x_L that are dependent on pressure heads only (unsteady flows are not an easily measurable property). Furthermore, pressure measurements are generally not available at points C and D therefore any relationship must not depend on conditions at these points. The measurable pressure heads (that can be used to form relationships for $C_d A_L$ and x_L) are H_0, H_B and H_E. Unfortunately, the steady state flow (Q_0) and the head at the leak (H_D) are present in the expressions for H_B and H_E (Eqs. C.6.3 and C.6.11 respectively). This problem is solved by carefully choosing linear combinations of the expressions for the

pressure heads. The first useful combination is the subtraction of Eq. C.6.8 from Eq. C.6.11, resulting in an expression for the head at the leak (H_D) that is only in terms of the heads at the valve (H_B and H_E),

$$H_D = \tfrac{1}{2}\left(H_B + H_E\right) \quad \text{(C.6.13)}$$

The second useful combination is the addition of Eq. C.6.8 to Eq. C.6.11, resulting in

$$H_E = H_B - BC_d A_L \sqrt{2g}\left(\sqrt{H_D} - \sqrt{H_0}\right) \quad \text{(C.6.14)}$$

Eq. C.6.14 only contains the pressure heads H_0, H_B, H_D and H_E. The pressure head at the leak is eliminated through the substitution of Eq. C.6.13 producing

$$H_E = H_B - BC_d A_L \sqrt{2g}\left(\sqrt{\tfrac{1}{2}\left(H_B + H_E\right)} - \sqrt{H_0}\right) \quad \text{(C.6.15)}$$

Now Eq. C.6.15 contains the lumped leak coefficient (C_dA_L) and measurable pressure heads. Rearranging Eq. C.6.15 and substituting Eq. C.6.5 for the characteristic impedance forms an expression for the lumped leak coefficient that is only in terms of pressure heads that are measured at the valve.

$$C_d A_L = \frac{A}{a}\sqrt{\frac{g}{2}}\frac{\left(H_B - H_E\right)}{\left[\sqrt{\tfrac{1}{2}\left(H_B + H_E\right)} + \sqrt{H_0}\right]} \quad \text{(C.6.16)}$$

Eq. C.6.16 provides a relationship that estimates the magnitude of a leak in the pipeline. The location of the leak (x_L) is determined from the timing of the pressure relief from the leak. The wave speed is used to turn the time into a location,

$$x_L = \tfrac{1}{2}a\left(t_2 - t_0\right) \quad \text{(C.6.17)}$$

The measurable pressure heads and the timing of the pressure relief can be visualised on a diagram of the pressure head experienced at the valve over a time period of $2L/a$, a plot of which is shown in Figure C.27.

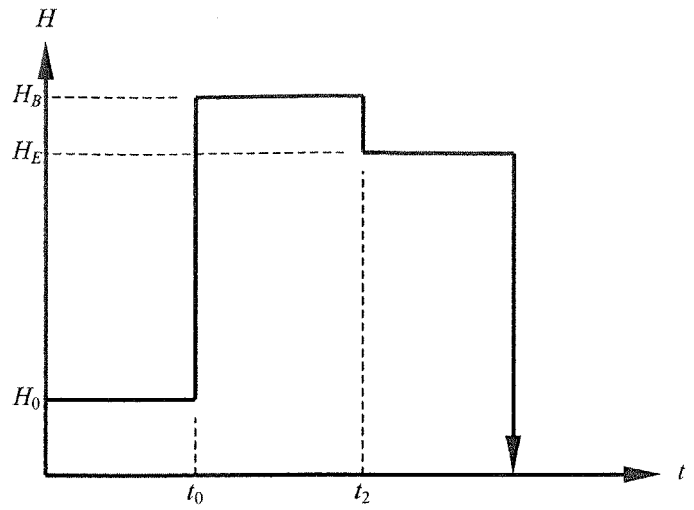

Figure C.27 First Pressure Head Rise Behaviour at Valve

This section presents a method that can be used to calculate the magnitude and location of a leak in a pipeline. Properties of the first pressure rise due to a fast valve closure and its subsequent interaction with a leak provides a basis for this method. Experimental results using the first pressure rise method are shown in Chapter 12.

C.7 Additional Results for a Systematic Levenberg-Marquardt Minimisation Method

Section 12.5 presented inverse transient results using a systematic Levenberg-Marquardt (SLVMQ) minimisation method. Results were presented for leak detection at 7 possible leak locations and 15 possible leak locations. Details of the 7 possible leak location case were presented in Section 12.5 however details for the 15 possible leak location case were not. This section presents the details of the 15 possible leak location case for the SLVMQ algorithm. The actual leak location is at node 5 and the actual C_dA_L is equal to 1.7×10^{-6} m^2. Table C.2 shows results for the first trial leak at the 15 possible leak locations.

Table C.2 1st Trial Leak, SLVMQ Results (15 Parameters)

Trial Leak Position	Levenberg-Marquardt Iterations	Objective Function E (m^2)	1st Trial Leak C_dA_L (m^2)
Node 2	5	6007	1.34×10^{-6}
Node 3	34	7268	1.30×10^{-6}
Node 4	73	7329	1.79×10^{-6}
Node 5	**26**	**999**	**1.88×10^{-6}**
Node 6	41	15961	2.05×10^{-6}
Node 7	25	5754	2.16×10^{-6}
Node 8	39	5129	2.11×10^{-6}
Node 9	3	6920	2.59×10^{-6}
Node 10	41	9763	3.33×10^{-6}
Node 11	99	11084	4.42×10^{-6}
Node 12	30	14278	5.88×10^{-6}
Node 13	19	16955	8.76×10^{-6}
Node 14	30	20984	1.40×10^{-5}
Node 15	36	32229	2.57×10^{-5}
Node 16	5	70978	5.86×10^{-5}

Minimum objective function in bold

A graphic representation of Table C.2 is shown in Figure C.28.

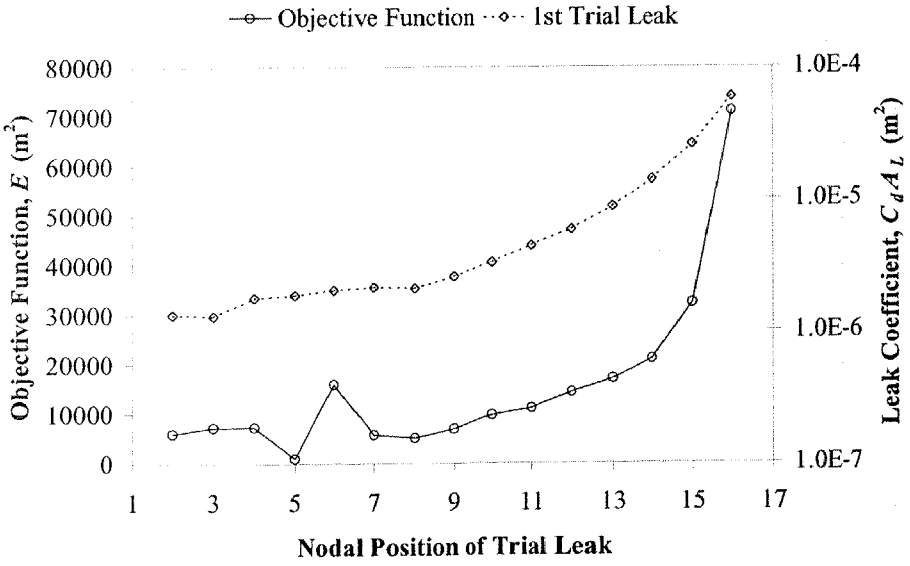

Figure C.28 1st Trial Leak, SLVMQ Results (15 Parameters)

The best inverse transient solution (with the lowest objective function value) was found at node 5, the actual location of the leak. The best trial leak location is now set and a second trial leak is used. The initial guess for the next set of Levenberg-Marquardt runs is $C_dA_L = 1.88\times10^{-6}$ m^2 for the set leak at node 5 and $C_dA_L = 0.0$ m^2 for the second trial

leak. The inverse transient method is applied for all remaining positions that the second trial leak can occur at, the results of which are shown in Table C.3.

Table C.3 2nd Trial Leak, SLVMQ Results (15 Parameters)

Trial Leak Position	Levenberg-Marquardt Iterations	Objective Function E (m^2)	Leak Coef. C_dA_L (m^2)	
			2nd Trial Leak	Set Leak at Node 5
Node 2	54	649.6	1.42×10^{-7}	1.62×10^{-6}
Node 3	91	765.2	1.26×10^{-7}	1.69×10^{-6}
Node 4	56	998.6	2.71×10^{-10}	1.86×10^{-6}
Node 5	-	*999.4*	-	*1.88×10^{-6}*
Node 6	34	999.1	4.34×10^{-9}	1.88×10^{-6}
Node 7	44	909.1	1.01×10^{-7}	1.82×10^{-6}
Node 8	55	717.2	2.66×10^{-7}	1.61×10^{-6}
Node 9	64	617.3	2.61×10^{-7}	1.58×10^{-6}
Node 10	71	753.8	1.10×10^{-7}	1.76×10^{-6}
Node 11	57	777.1	9.14×10^{-8}	1.77×10^{-6}
Node 12	57	709.2	8.71×10^{-8}	1.77×10^{-6}
Node 13	64	614.9	1.20×10^{-7}	1.75×10^{-6}
Node 14	57	616.1	1.49×10^{-7}	1.76×10^{-6}
Node 15	80	532.4	2.91×10^{-7}	1.75×10^{-6}
Node 16	**71**	**442.1**	**9.91×10^{-7}**	**1.76×10^{-6}**

Minimum objective function in bold, set leak in italics
- trial leak not permitted

A graphical representation of Table C.3 is shown in Figure C.29.

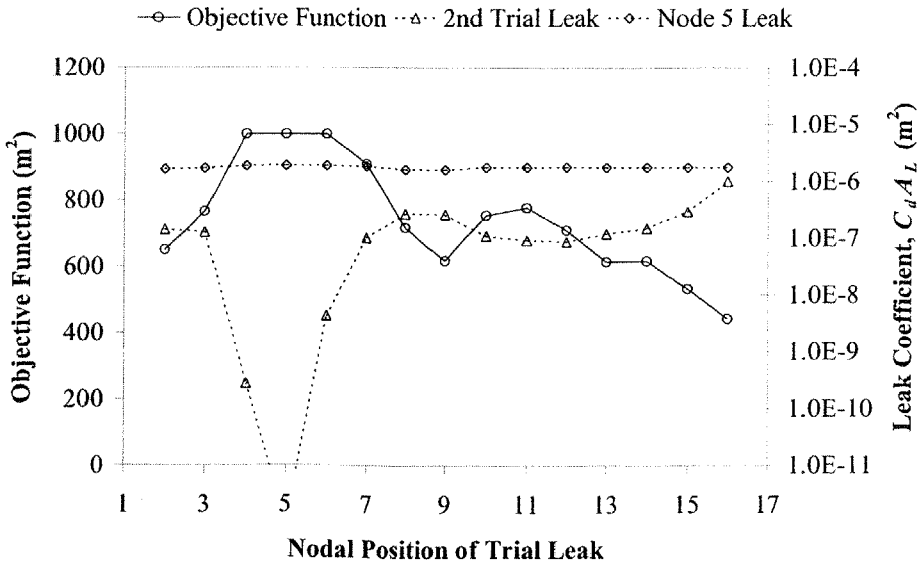

Figure C.29 2nd Trial Leak, SLVMQ Results (15 Parameters)

The best inverse transient solution (with the lowest objective function value) for the second trial leak was found at node 16. The best trial leak location is now set and a third trial leak is used. The initial guess for the next set of Levenberg-Marquardt runs is $C_dA_L = 1.76\times10^{-6}$ and $C_dA_L = 9.91\times10^{-7}$ m^2 for the set leaks at nodes 5 and 16, respectively, and C_dA_L = 0.0 m^2 for the third trial leak. The inverse transient method is applied for all remaining positions that the third trial leak can occur at, the results of which are shown in Table C.4.

Table C.4 3rd Trial Leak, SLVMQ Results (15 Parameters)

Trial Leak Position	Levenberg-Marquardt Iterations	Objective Function E (m^2)	Lumped Leak Coefficient C_dA_L (m^2)		
			3rd Trial Leak	Set Leak at Node 5	Set Leak at Node 16
Node 2	69	442.07	6.84×10^{-11}	1.76×10^{-6}	9.91×10^{-7}
Node 3	21	442.08	6.84×10^{-11}	1.76×10^{-6}	9.91×10^{-7}
Node 4	63	442.09	6.83×10^{-11}	1.76×10^{-6}	9.91×10^{-7}
Node 5	-	*442.10*	-	*1.76×10^{-6}*	*9.91×10^{-7}*
Node 6	*	442.10	0.0	1.76×10^{-6}	9.91×10^{-7}
Node 7	*	442.10	0.0	1.76×10^{-6}	9.91×10^{-7}
Node 8	100	442.09	1.00×10^{-12}	1.75×10^{-6}	9.92×10^{-7}
Node 9	28	442.10	2.72×10^{-10}	1.76×10^{-6}	9.91×10^{-7}
Node 10	**40**	**434.43**	**2.40×10^{-8}**	**1.74×10^{-6}**	**8.87×10^{-7}**
Node 11	43	434.50	2.10×10^{-8}	1.74×10^{-6}	8.71×10^{-7}
Node 12	39	439.30	7.12×10^{-9}	1.75×10^{-6}	9.43×10^{-7}
Node 13	30	441.48	1.08×10^{-8}	1.75×10^{-6}	9.18×10^{-7}
Node 14	*	442.10	0.0	1.76×10^{-6}	9.91×10^{-7}
Node 15	*	442.10	0.0	1.76×10^{-6}	9.91×10^{-7}
Node 16	-	*442.10*	-	*1.76×10^{-6}*	*9.91×10^{-7}*

Minimum objective function in bold, set leaks in italics
* no improvement for trial leak, - trial leak not permitted

A graphical representation of Table C.4 is shown in Figure C.30.

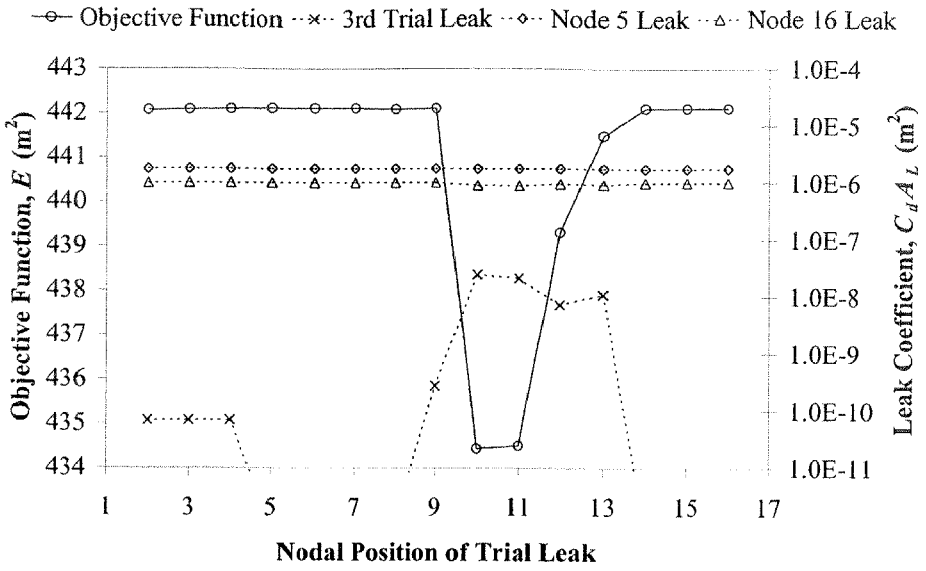

Figure C.30 3rd Trial Leak, SLVMQ Results (15 Parameters)

The best inverse transient solution after three iterations of the systematic Levenberg-Marquardt method is $C_dA_L = 1.74\times10^{-6}$ m^2 at node 5, $C_dA_L = 2.40\times10^{-8}$ m^2 at node 10 and $C_dA_L = 8.87\times10^{-7}$ m^2 at node 16. The solution compares favourably with actual sizes and locations of the leak.

C.8 Additional Experimental Verification of Inverse Transient Analysis

Verification of the inverse transient method using experimental data was performed in Section 12.3. The results presented in Section 12.3 were sufficient but incomplete. One leak size (1.0 mm) was presented out of the three possible leak sizes (1.0, 1.5 and 2.0 mm). The inverse transient analysis results for all of the experimental tests are presented in this section. Inverse transient results for slow, medium and fast valve closure experimental tests with a 1.0 mm leak at node 5 are tabulated in Table C.5. Plots of the pressure head at node 1 for the experimental data and inverse transient results are shown in Figures C.31, C.32 and C.33 for valve closure speeds of fast, medium and slow respectively.

Table C.5 Inverse Transient Analysis Results (1.0 mm Leak at Node 5)

Test Type	Lumped Leak Coefficient, C_dA_L (m^2)						
	Node 3	Node 5	Node 7	Node 9	Node 11	Node 13	Node 15
Actual	-	**5.0×10^{-7}**	-	-	-	-	-
Fast	1.1×10^{-7}	**5.1×10^{-7}**	1.4×10^{-12}	2.6×10^{-9}	3.6×10^{-11}	9.9×10^{-8}	6.1×10^{-9}
Medium	**3.9×10^{-7}**	3.2×10^{-8}	2.0×10^{-10}	1.2×10^{-7}	2.5×10^{-10}	8.8×10^{-12}	5.1×10^{-8}
Slow	5.5×10^{-11}	1.1×10^{-9}	9.9×10^{-11}	5.4×10^{-8}	**8.8×10^{-7}**	7.5×10^{-7}	9.1×10^{-8}

Largest size leak in bold

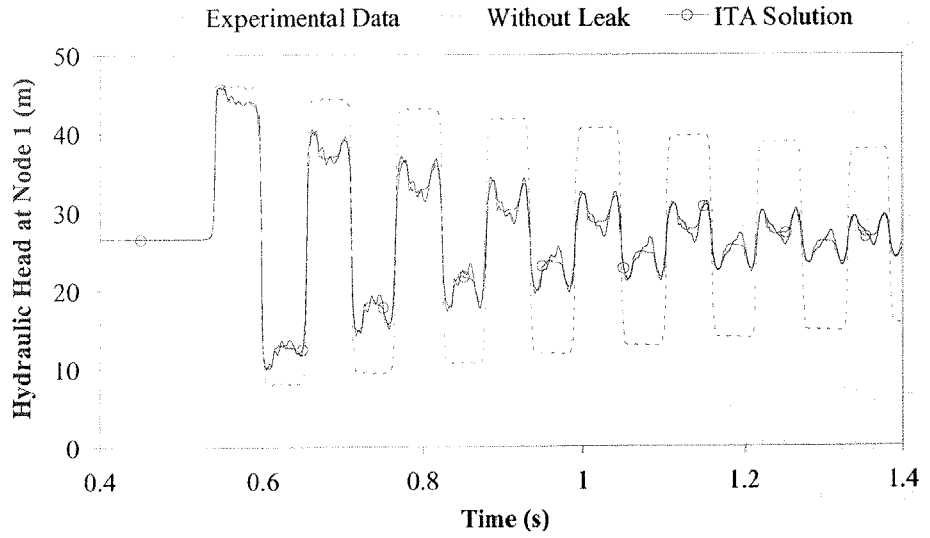

Figure C.31 Fast Valve Closure (t_c = 0.07 s), 1.0 mm Leak at Node 5

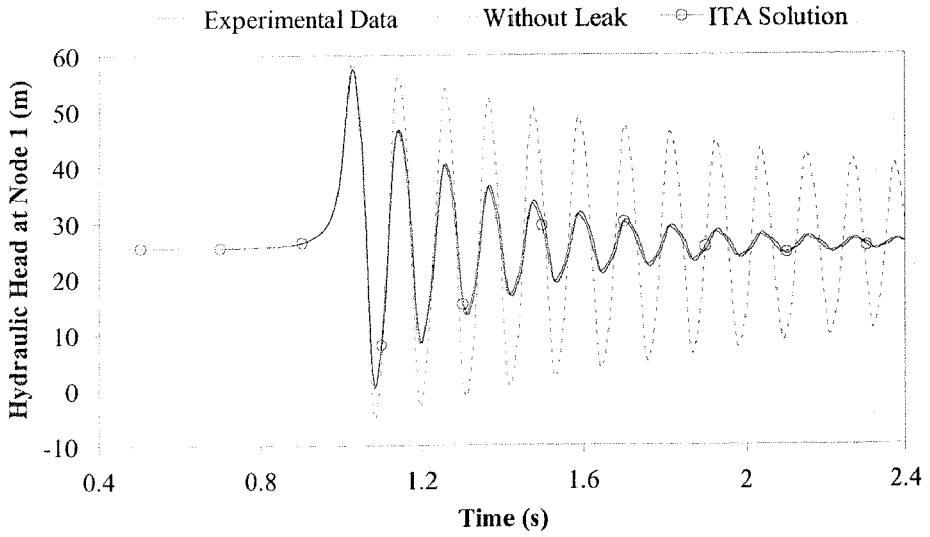

Figure C.32 Medium Speed Valve Closure (t_c = 0.7 s), 1.0 mm Leak at Node 5

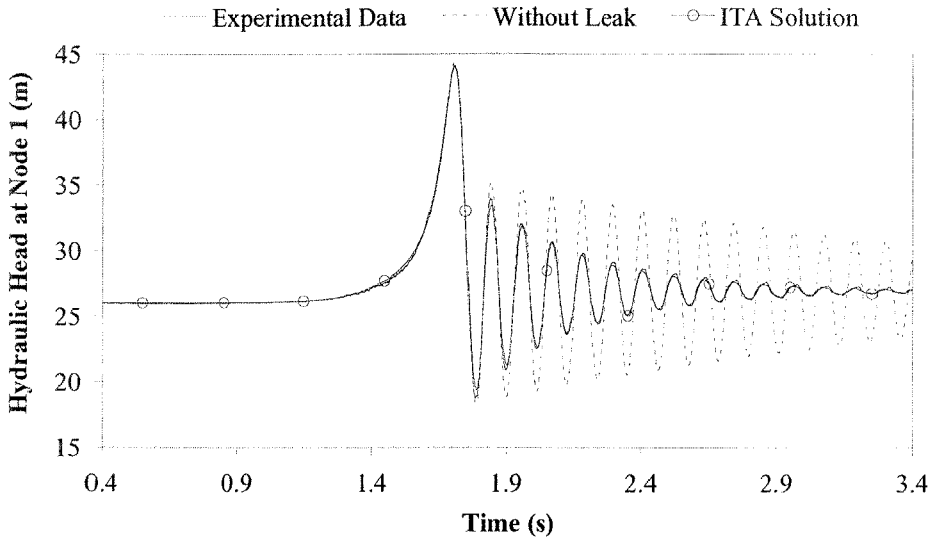

Figure C.33 Slow Valve Closure (t_c = 1.4 s), 1.0 mm Leak at Node 5

Inverse transient results for slow, medium and fast valve closure experimental tests with a 1.5 mm leak at node 5 are tabulated in Table C.6. Plots of the pressure head at node 1 for the experimental data and inverse transient results are shown in Figures C.34, C.35 and C.36, and for valve closure speeds of fast, medium and slow respectively.

Table C.6 Inverse Transient Analysis Results (1.5 mm Leak at Node 5)

Test Type	Lumped Leak Coefficient, C_dA_L (m^2)						
	Node 3	Node 5	Node 7	Node 9	Node 11	Node 13	Node 15
Actual	-	**1.1×10^{-6}**	-	-	-	-	-
Fast	1.0×10^{-8}	**7.7×10^{-7}**	3.0×10^{-7}	1.8×10^{-9}	1.3×10^{-7}	1.7×10^{-11}	4.7×10^{-12}
Medium	8.1×10^{-11}	9.3×10^{-7}	8.9×10^{-10}	2.4×10^{-10}	3.9×10^{-12}	**1.1×10^{-6}**	1.2×10^{-8}
Slow	2.8×10^{-9}	3.6×10^{-12}	7.1×10^{-7}	**1.1×10^{-6}**	8.5×10^{-12}	4.1×10^{-9}	2.0×10^{-9}

Largest size leak in bold

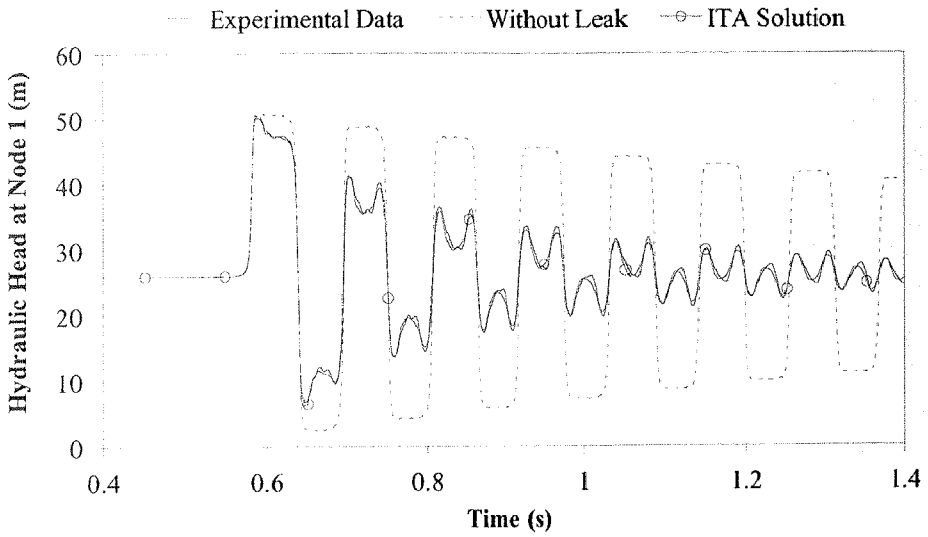

Figure C.34 Fast Valve Closure (t_c = 0.07 s), 1.5 mm Leak at Node 5

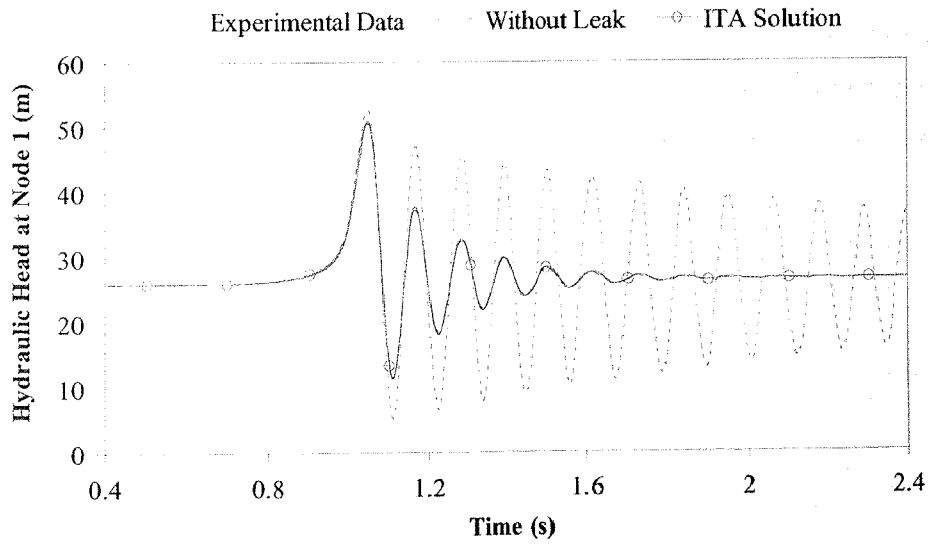

Figure C.35 Medium Speed Valve Closure (t_c = 0.7 s), 1.5 mm Leak at Node 5

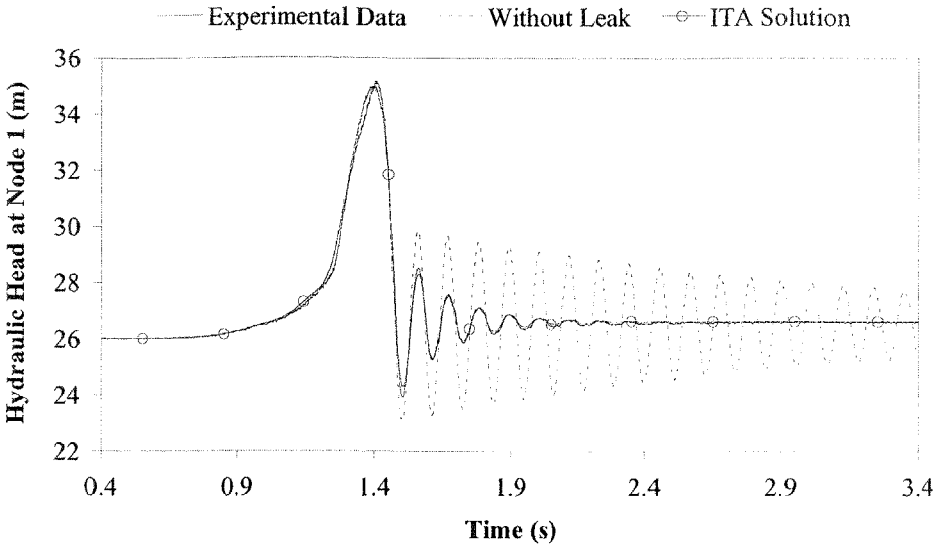

Figure C.36 Slow Valve Closure (t_c = 1.4 s), 1.5 mm Leak at Node 5

Inverse transient results for slow, medium and fast valve closure experimental tests with a 2.0 mm leak at node 5 are tabulated in Table C.7. Plots of the pressure head at node 1 for the experimental data and inverse transient results are shown in Figures C.37, C.38 and C.39 for valve closure speeds of fast, medium and slow respectively.

Table C.7 Inverse Transient Analysis Results (2.0 mm Leak at Node 5)

Test Type	Lumped Leak Coefficient, C_dA_L (m^2)						
	Node 3	Node 5	Node 7	Node 9	Node 11	Node 13	Node 15
Actual	-	**1.7×10^{-6}**	-	-	-	-	-
Fast	3.2×10^{-11}	**1.7×10^{-6}**	4.1×10^{-11}	2.9×10^{-9}	5.1×10^{-9}	2.9×10^{-11}	2.6×10^{-7}
Medium	6.9×10^{-8}	5.1×10^{-7}	**1.2×10^{-6}**	3.7×10^{-10}	2.4×10^{-10}	6.1×10^{-12}	6.1×10^{-6}
Slow	2.0×10^{-9}	6.2×10^{-7}	1.1×10^{-10}	**1.5×10^{-6}**	8.0×10^{-9}	7.2×10^{-10}	5.3×10^{-9}

Largest size leak in bold

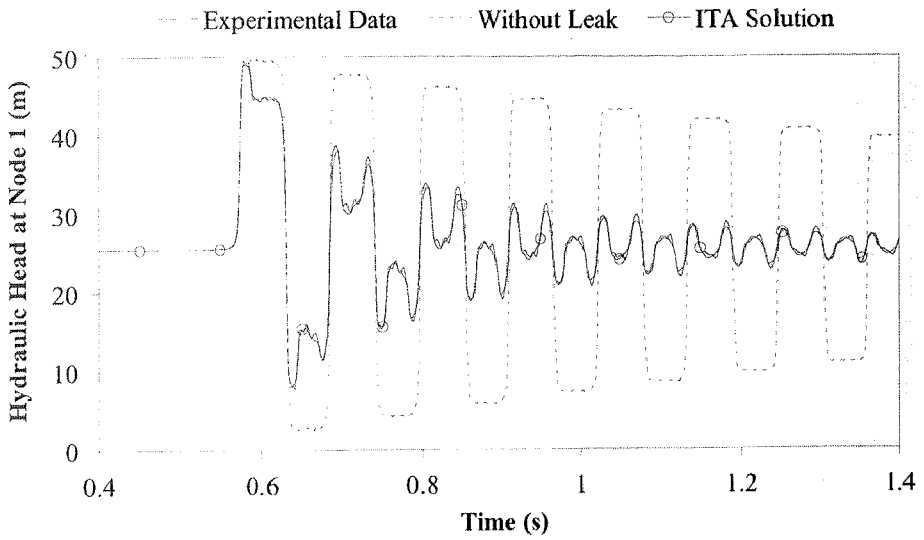

Figure C.37 Fast Valve Closure ($t_c = 0.07$ s), 2.0 mm Leak at Node 5

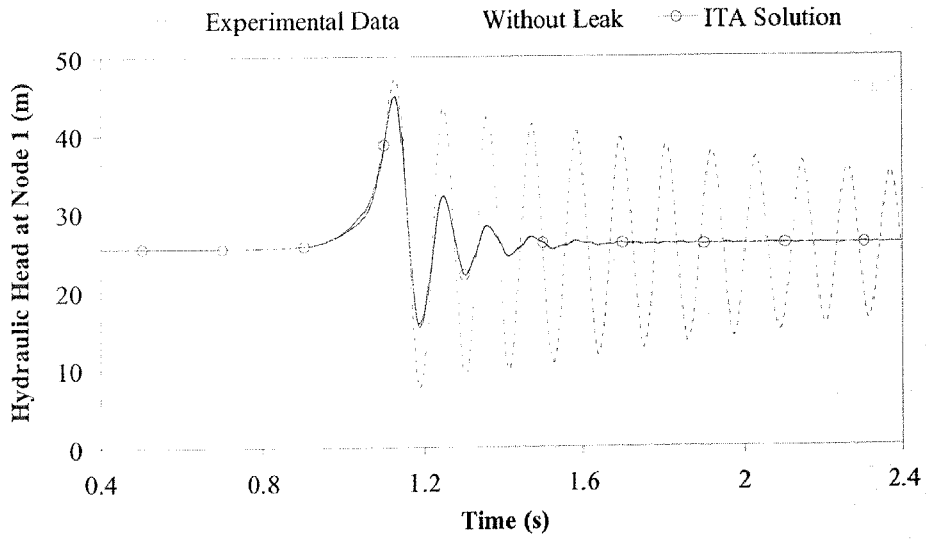

Figure C.38 Medium Speed Valve Closure ($t_c = 0.7$ s), 2.0 mm Leak at Node 5

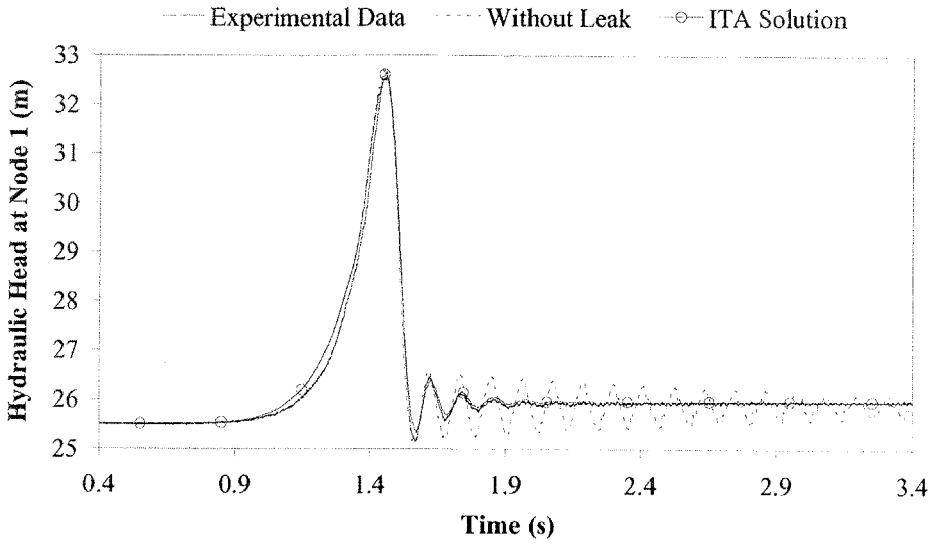

Figure C.39 Slow Valve Closure (t_c = 1.4 s), 2.0 mm Leak at Node 5

Inverse transient results for slow, medium and fast valve closure experimental tests with two 1.0 mm leaks at nodes 5 and 13 are tabulated in Table C.8. Plots of the pressure head at node 1 for the experimental data and inverse transient results are shown in Figures C.40, C.41 and C.42 for valve closure speeds of fast, medium and slow respectively.

Table C.8 Inverse Transient Analysis Results

(Two 1.0 mm Leaks at Nodes 5 and 13)

Test Type	Lumped Leak Coefficient, C_dA_L (m^2)						
	Node 3	Node 5	Node 7	Node 9	Node 11	Node 13	Node 15
Actual	-	**5.0×10^{-7}**	-	-	-	**7.1×10^{-7}**	-
Fast	2.8×10^{-8}	9.8×10^{-12}	1.4×10^{-9}	**9.5×10^{-7}**	7.2×10^{-9}	3.6×10^{-11}	**1.0×10^{-6}**
Medium	3.8×10^{-10}	5.3×10^{-10}	1.1×10^{-8}	6.8×10^{-12}	1.3×10^{-8}	2.1×10^{-8}	**1.0×10^{-5}**
Slow	5.8×10^{-12}	6.7×10^{-9}	1.2×10^{-9}	3.7×10^{-11}	**1.8×10^{-6}**	7.3×10^{-10}	1.5×10^{-11}

Largest size leak(s) in bold

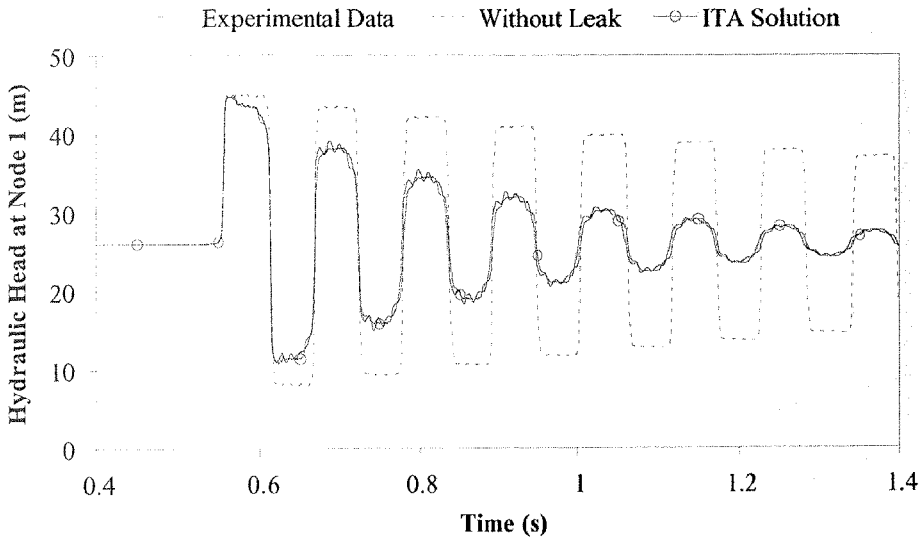

Figure C.40 Fast Valve Closure (t_c = 0.07 s), Two 1.0 mm Leaks at Nodes 5 and 13

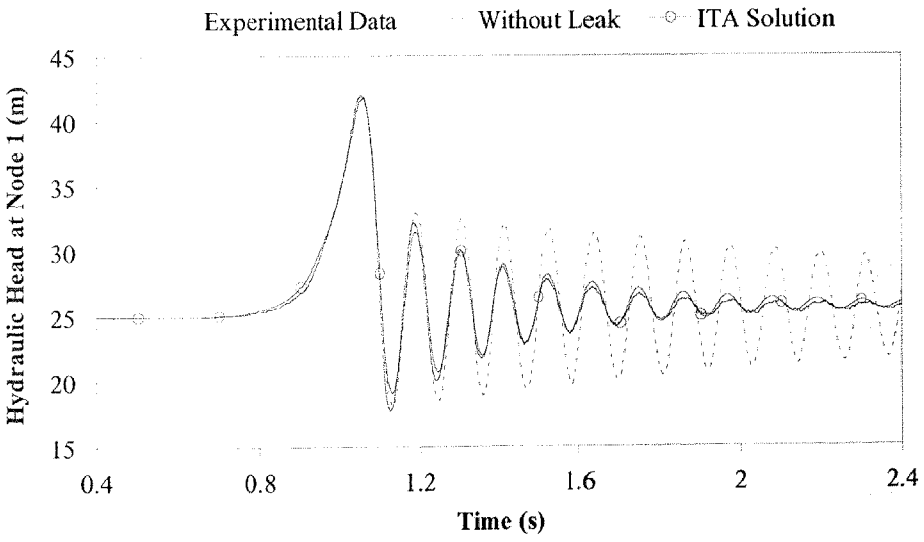

Figure C.41 Medium Speed Valve Closure (t_c = 0.7 s), Two 1.0 mm Leaks at Nodes 5 and 13

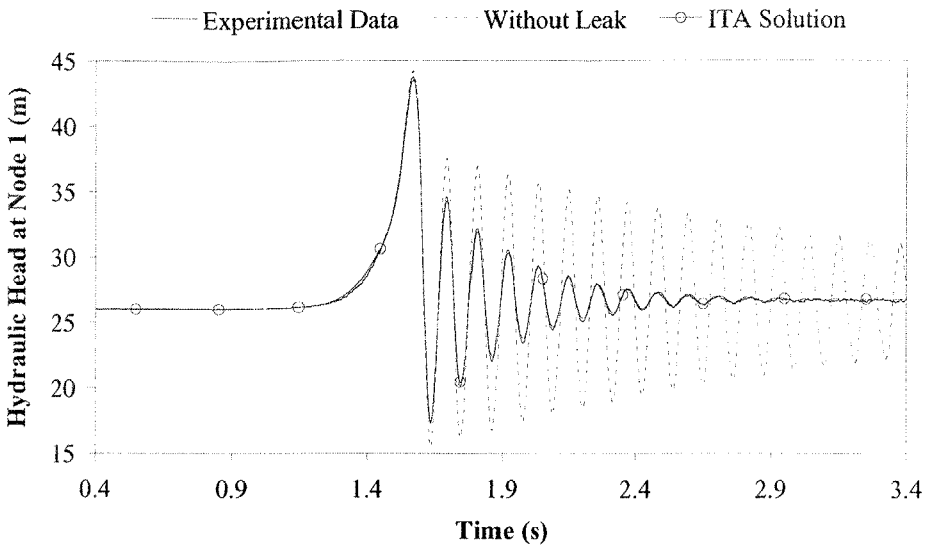

Figure C.42 Slow Valve Closure (t_c = 1.4 s), Two 1.0 mm Leaks at Nodes 5 and 13

Appendix D

Additional Material for Chapters 5, 6 and 7

This Appendix contains additional material for Chapters 5, 6 and 7.

D.1 Selection of Performance Indictor Parameters

A number of performance indicators are defined in Chapter 7. The performance indicators that depend on partial derivatives (all, except for the Monte Carlo simulations) are subject to the problems associated with the divided difference method for finding derivatives. There are two sources of error. If the perturbation, h, is too large, the divided difference method will not yield a good approximation of the partial derivative. On the other hand, if the perturbation is too small, machine errors (from using finite word length) can contaminate calculations to an extent where the answer is unusable. The correct size is found somewhere between these two extremes. It occurs where there is no change in the partial derivative with small changes in the perturbation.

The most important partial derivatives are those of pressure with respect to each of the parameters (lumped leak coefficients and friction factors), $\partial H/\partial a$. The $\partial H/\partial a$ is used by the performance indicators **SE**, **SH** and **SV**. Elements of the performance indicator vectors **SE**, **SH** and **SV** for the j^{th} parameter are

$$\mathbf{SE}_j = \left| \sum_{i=1}^{M} \left(\left(H_i^m - H_i \right) \frac{\partial H_i}{\partial a_j} \right) \right|^{-1} \quad \text{.....(D.1.1)}$$

$$\mathbf{SH}_j = \left(\sum_{i=1}^{N_{MN}} \sum_{l=1}^{N_{TS}} \left| \frac{\partial H_{i,l}}{\partial a_j} \right| \right)^{-1} \quad \text{.....(D.1.2)}$$

$$\mathbf{SV}_j = \sqrt{\left([\alpha']^{-1} \right)_{j,j}} \quad \text{and} \quad \alpha'_{j,k} = \sum_{i=1}^{M} \left(\frac{\partial H_i}{\partial a_j} \frac{\partial H_i}{\partial a_k} \right) \quad \text{.....(D.1.3)}$$

where $a_j = j^{\text{th}}$ parameter, $H_i = i^{\text{th}}$ modelled pressure data point, $H_i^m = i^{\text{th}}$ measured pressure data point and M = total number of measured pressure data points. The $\partial H/\partial a$ partial derivative is common to the performance indicators **SH**, **SE** and **SV** in Eqs. D.1.1, D.1.2 and D.1.3; hence, it is important to find the correct magnitude of the perturbation (h) needed to calculate this partial derivative. Figure D.1 shows stable values of the performance indicator **SH** when the perturbation is smaller than 0.001 and suggests that values of the perturbation larger than 0.001 do not yield an accurate approximation of the partial derivatives of pressure with respect to the parameters (the derivative approximation becomes too coarse). The parameters used in Chapter 6 are friction factors, the correct perturbation size for other parameters, such as lumped leak coefficients, will be different. Also, the perturbation size is dependent on the transient event type. Typically an adequate parameter perturbation size is approximately three to six orders of magnitude smaller than the parameter's value.

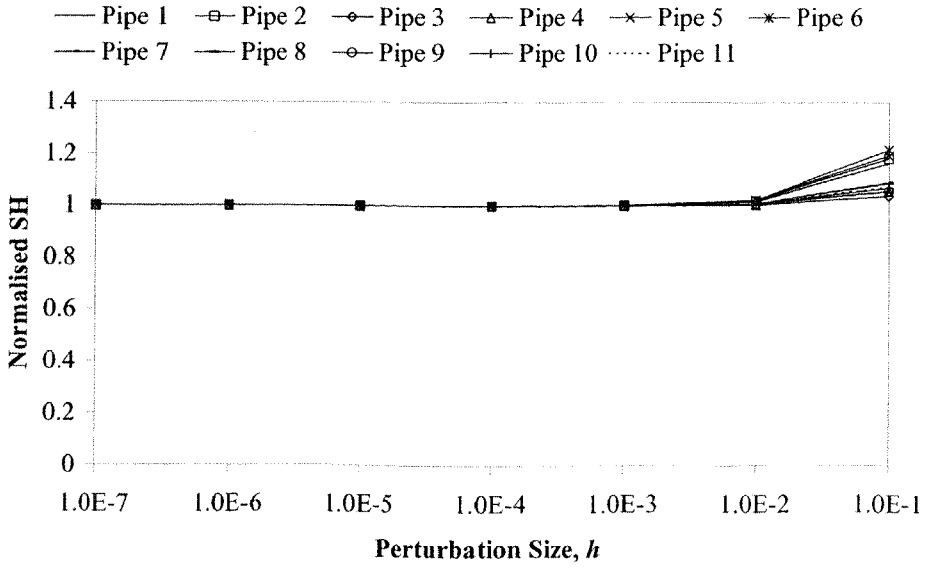

Figure D.1 Normalised SH Versus Perturbation Size, *h*

The parameters for the inverse solution based performance indicators are now addressed. Figures D.2, D.3 and D.4 show the behaviour of the different partial derivatives of the parameters with respect to the measured pressures as they change with different sizes of perturbations. The effect of the perturbation size (h) on the inverse solution based parameter $\mathbf{SAH_1}$ is shown in Figure D.2. An element of the $\mathbf{SAH_1}$ performance indicator vector corresponding to the j^{th} parameter is

$$(\mathbf{SAH}_1)_j = \sum_{i=1}^{N_{MS}} \sum_{l=1}^{N_{TS}} \left| \frac{\partial a_j}{\partial H_{i,l}^m} \right| \quad \text{.....(D.1.4)}$$

where N_{MS} = number of measurement sites and N_{TS} = number of transient time steps. This indicator is undefined for perturbations greater than 0.1 m and is considered stable for values less than 1.0×10^{-7} m (the partial derivative is well approximated). $\mathbf{SAH_1}$ is undefined for large perturbations because there is too much error for the inverse transient method to successfully find any parameters.

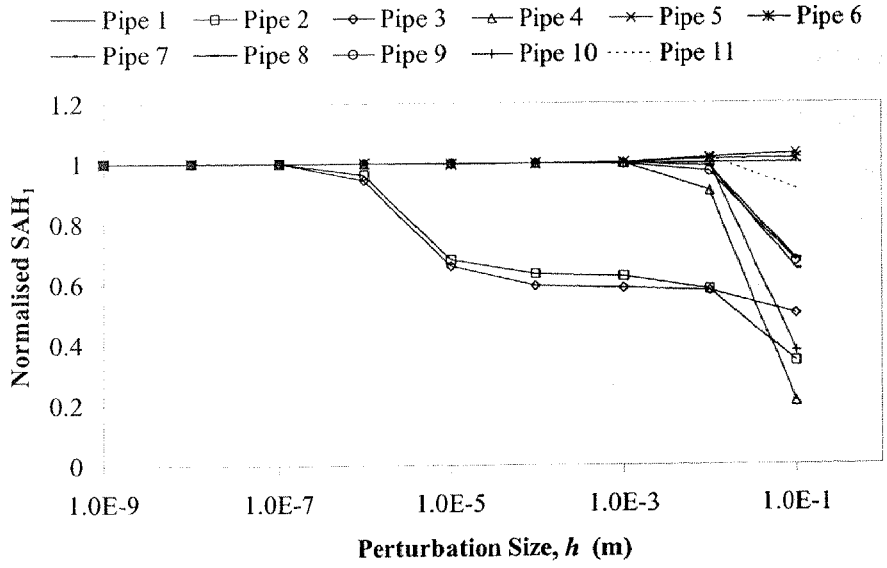

Figure D.2 Normalised $\mathbf{SAH_1}$ Versus Perturbation Size, h

The $\mathbf{SAH_2}$ performance indicator shares the same characteristics as the $\mathbf{SAH_1}$ indicator. An element of the $\mathbf{SAH_2}$ performance indicator vector corresponding to the j^{th} parameter is

$$(\mathbf{SAH}_2)_j = \sum_{i=1}^{N_{MS}} \left| \frac{\partial a_j}{\partial H_i^m} \right| \quad \text{.....(D.1.5)}$$

The $\mathbf{SAH_2}$ indicator is undefined for total perturbation values greater than 0.01 m (the inverse transient method fails) and stable for values less than 0.0001 m.

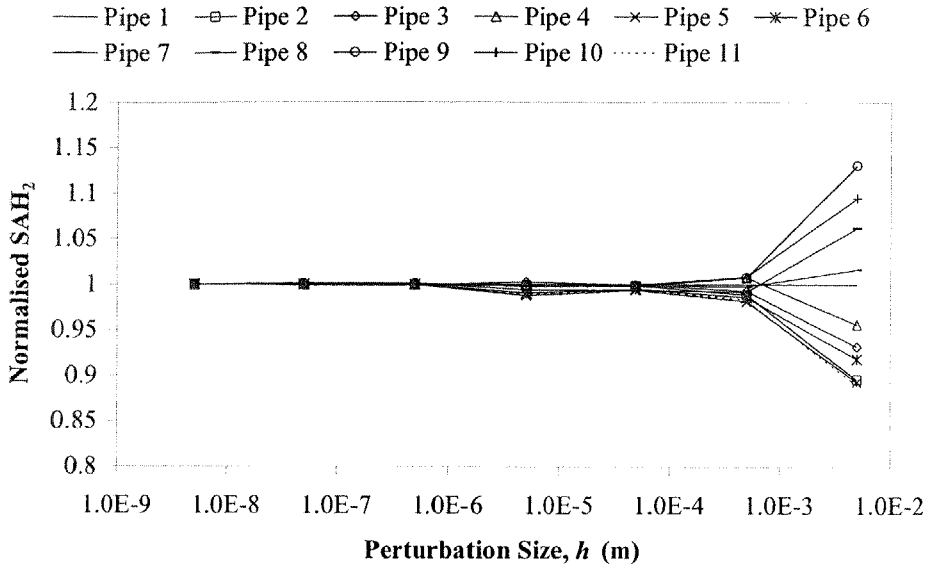

Figure D.3 Normalised $\mathbf{SAH_2}$ Versus Perturbation Size, *h*

The $\mathbf{SAH_3}$ indicator is far more tolerant than the last two performance indicators. An element corresponding to the j^{th} parameter of the $\mathbf{SAH_3}$ performance indicator vector is

$$\left(\mathbf{SAH}_3\right)_j = \left|\frac{\partial a_j}{\partial H^m}\right| \qquad \text{.....(D.1.6)}$$

$\mathbf{SAH_3}$ still exhibits much the same behaviour as the last two indicators. In this case, the relationship becomes undefined for total perturbations greater than 1.0 m and stable for total perturbations less than 0.0001 m.

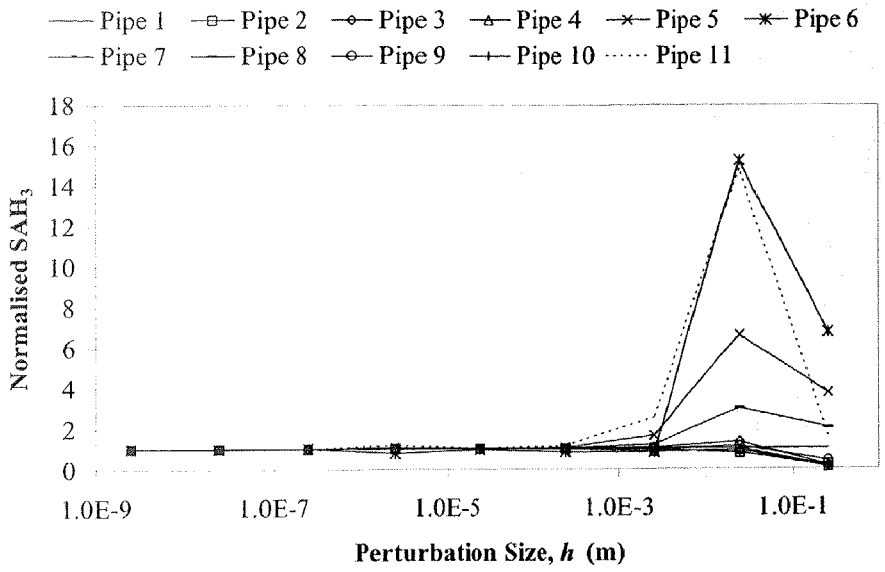

Figure D.4 Normalised SAH_3 Versus Perturbation Size, *h*

There are two parameters that describe the implementation of Monte Carlo simulations. These parameters are the number of simulations and the standard deviation of the introduced errors. The first to be examined is the number of simulations. Ideally the number of simulations should be as high as possible; a greater number of simulations produces a better estimation of the distribution of the error for each parameter. In Figure D.5 a sufficient number of Monte Carlo simulations is achieved when the average is stable (approaches horizontal). For low numbers of Monte Carlo simulations the behaviour of the average error is unstable, generally suggesting that if the number of simulations is below approximately 50 they do not give a good representation of the true parameter error. The number of simulations needed for a good Monte Carlo Simulation was set at 10,000; however, for application to the inverse transient method such a large number is impractical. A Monte Carlo simulation size of 200 simulations has been used for the remainder of this study. It is noted that the minimum number of simulations is problem dependent.

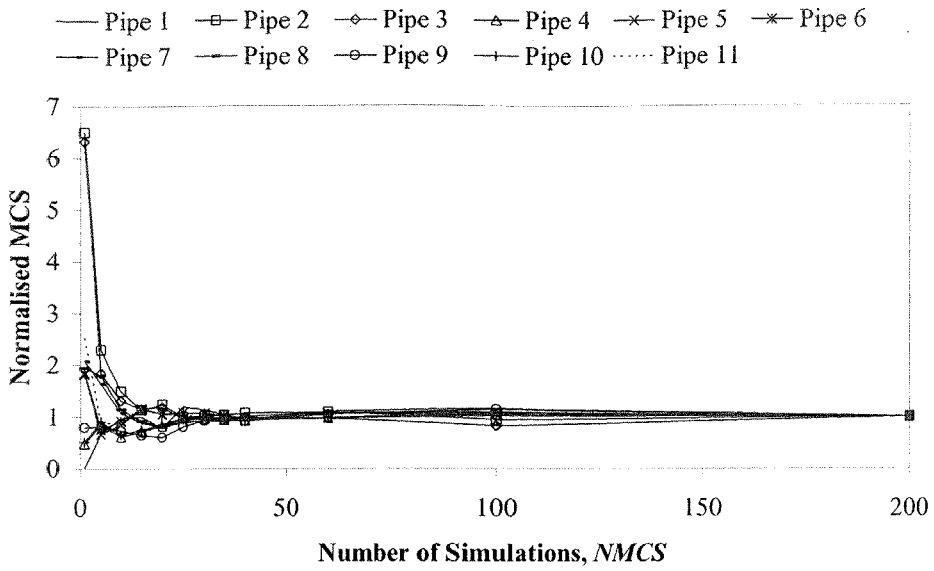

Figure D.5 Normalised MCS Versus Number of Monte Carlo Simulations

The second parameter used in Monte Carlo simulations is the introduced error in the data (in this case pressure data). The error in the pressure data is assumed to be normally distributed. If the introduced error is too large, the inverse transient method might not work, and if it is too low, the errors will have no effect producing a poor distribution curve for the Monte Carlo simulations. Figure D.6 shows the effect of changing the standard deviation of the introduced error in the data on the total error in the parameters after 200 Monte Carlo simulations.

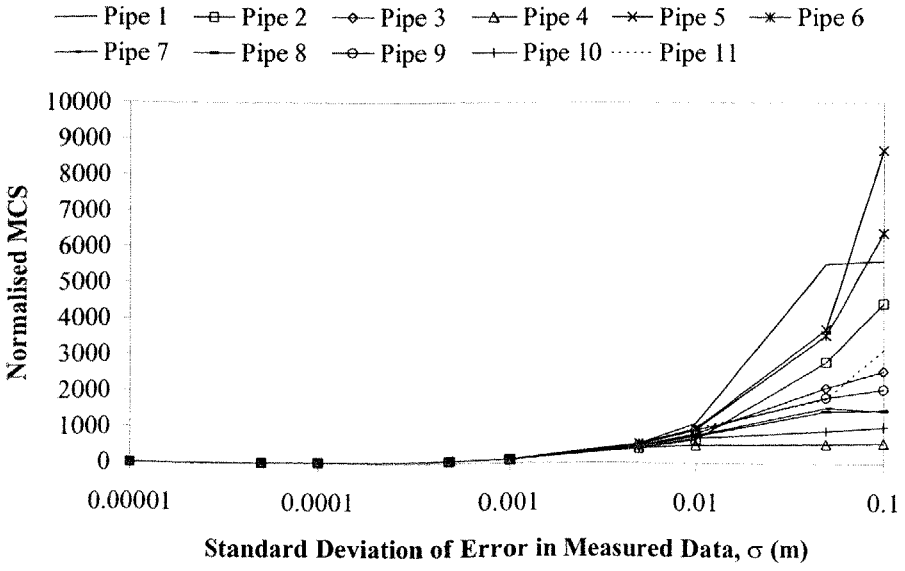

Figure D.6 Normalised MCS Versus Error in Measured Data, σ

It is hard to draw any conclusions from this figure. A better way to interpret the behaviour of Monte Carlo simulations with varying errors in data is to normalise the total error in parameters. That total error is normalised by dividing it by the standard deviation of the introduced error in the pressure data. Recalling the derivation of the estimated variance from Section 4.8, the relationship is restated in a simplified form for a constant measurement data error,

$$\sigma^2_{a_j} = K\sigma^2_{H^m} \quad \text{(D.1.7)}$$

where $\sigma^2_{a_j}$ = variance in the parameter a_j, $\sigma^2_{H^m}$ = the variance in the measured data H^m and K is a constant dependent on the inverse of the Hessian of the objective function E. Eq. D.1.7 suggests that, if all other conditions are kept constant, the estimated standard deviation of the error in the parameters is linearly dependent on the standard deviation of the errors in the pressure data (for small sized errors). Given this relationship, the normalised total error in parameters should be constant for moderately sized errors in the pressure data as shown in Figure D.7.

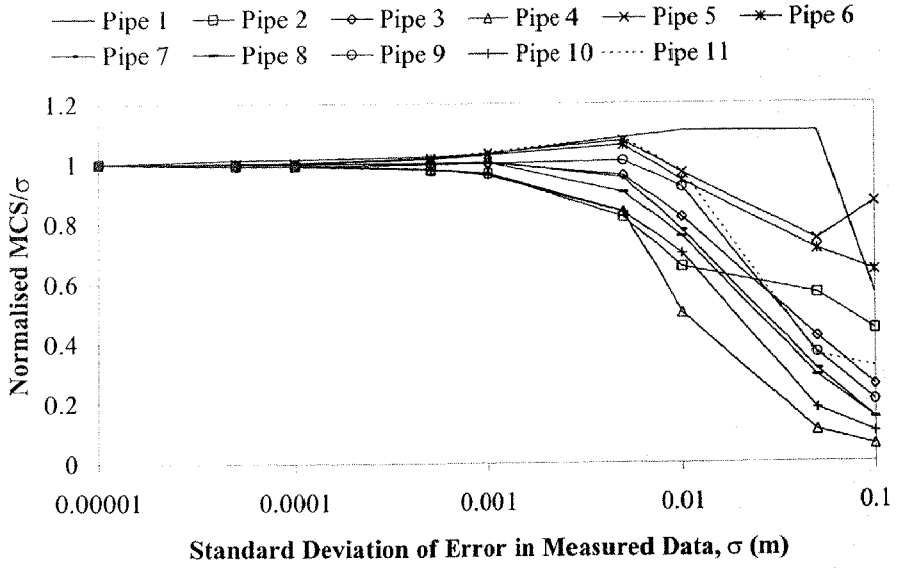

Figure D.7 Normalised MCS/σ Versus Error in Measured Data, σ

The normalised total error in the parameters is constant for standard deviations in the pressure data smaller than approximately 0.001. This point is of great interest because it shows one of the limits below which the formulation for the estimation of parameter variances (shown in Section 4.7) is not valid.

D.2 Measured Pressure Head Data Used in Chapter 5

Chapter 5 presented work about the effect of incorrect initial conditions on the inverse transient method. Two different cases studies were used to highlight the effects of using incorrect initial conditions. Sections D.2.1 and D.2.2 present the measured pressure head data for an example pipeline and for the network used in Chen (1995) respectively.

D.2.1 Data for Example Pipeline

The data used in the application of the inverse transient method in the example pipeline are shown in Table D.1. Two hundred and eighty three time steps of pressure head data at nodes 5, 9 and 13 were used as measured data. The time step (Δt) for the measured pressure head data was 1.762×10^{-3} s.

Table D.1 Measured Pressure Head Data for the Example Pipeline

Time Step	Measured Pressure (m)			Time Step	Measured Pressure (m)			Time Step	Measured Pressure (m)		
	Node 5	Node 9	Node 13		Node 5	Node 9	Node 13		Node 5	Node 9	Node 13
0	22.445	24.963	27.482	100	25.934	27.155	28.447	200	22.429	25.085	27.119
1	22.445	24.963	27.482	101	25.562	26.798	27.905	201	22.410	25.086	26.942
2	22.445	24.963	27.482	102	25.208	26.414	27.533	202	22.442	24.921	27.078
3	22.445	24.963	27.482	103	24.853	26.030	27.161	203	22.473	24.697	27.213
4	22.445	24.963	27.482	104	24.498	25.646	26.790	204	22.504	24.473	27.348
5	22.445	24.963	27.482	105	24.143	25.267	26.453	205	22.526	24.272	27.433
6	22.445	24.963	27.482	106	23.787	24.896	26.705	206	22.384	24.438	27.411
7	22.445	24.963	27.482	107	23.431	24.525	26.957	207	22.192	24.604	27.382
8	22.445	24.963	27.482	108	23.075	24.155	27.208	208	22.000	24.770	27.352
9	22.445	24.963	27.482	109	22.715	23.821	27.365	209	21.827	24.875	27.327
10	22.445	24.963	27.482	110	22.348	24.095	27.364	210	21.955	24.875	27.358
11	22.445	24.963	27.482	111	21.982	24.370	27.363	211	22.084	24.876	27.390
12	22.445	24.963	27.482	112	21.616	24.644	27.361	212	22.213	24.876	27.421
13	22.445	24.963	27.482	113	21.284	24.817	27.361	213	22.293	24.877	27.441
14	22.445	24.963	27.482	114	21.525	24.817	27.385	214	22.418	24.872	27.463
15	22.445	24.963	27.482	115	21.767	24.817	27.410	215	22.589	24.868	27.493
16	22.445	24.963	27.482	116	22.008	24.817	27.435	216	22.759	24.864	27.523
17	22.445	24.963	27.482	117	22.157	24.816	27.451	217	22.914	24.859	27.549
18	22.445	24.963	27.482	118	22.396	24.810	27.452	218	22.795	25.005	27.513
19	22.445	24.963	27.482	119	22.721	24.804	27.454	219	22.677	25.204	27.478
20	22.445	24.963	27.482	120	23.045	24.798	27.455	220	22.559	25.402	27.442
21	22.445	24.963	27.482	121	23.338	24.792	27.455	221	22.484	25.580	27.418
22	22.445	24.963	27.482	122	23.119	25.030	27.424	222	22.511	25.432	27.542
23	22.445	24.963	27.482	123	22.899	25.354	27.394	223	22.546	25.283	27.709
24	22.445	24.963	27.482	124	22.679	25.677	27.364	224	22.582	25.135	27.876
25	22.445	24.963	27.482	125	22.541	25.969	27.341	225	22.613	25.042	28.028
26	22.445	24.963	27.482	126	22.554	25.726	27.577	226	22.578	25.046	27.916
27	22.445	24.963	27.482	127	22.572	25.484	27.897	227	22.543	25.053	27.803
28	22.445	24.963	27.482	128	22.589	25.241	28.216	228	22.508	25.059	27.691
29	22.445	24.963	27.482	129	22.604	25.089	28.506	229	22.486	25.065	27.622
30	22.445	24.963	27.482	130	22.570	25.100	28.295	230	22.467	25.065	27.505
31	22.445	24.963	27.482	131	22.537	25.116	28.084	231	22.442	25.065	27.346
32	22.445	24.963	27.482	132	22.503	25.132	27.874	232	22.416	25.065	27.188
33	22.445	24.963	27.482	133	22.481	25.147	27.744	233	22.394	25.066	27.044
34	22.445	24.963	27.482	134	22.480	25.144	27.524	234	22.425	24.927	27.155
35	22.445	24.963	27.482	135	22.480	25.140	27.225	235	22.456	24.738	27.266
36	22.445	24.963	27.482	136	22.480	25.136	26.925	236	22.487	24.549	27.376
37	22.445	24.963	27.482	137	22.481	25.136	26.655	237	22.508	24.378	27.446
38	22.445	24.963	27.482	138	22.507	24.905	26.859	238	22.393	24.519	27.422
39	22.445	24.963	27.482	139	22.533	24.592	27.063	239	22.237	24.660	27.391
40	22.445	24.963	27.482	140	22.560	24.279	27.267	240	22.082	24.800	27.360
41	22.445	24.963	27.482	141	22.579	23.997	27.395	241	21.942	24.888	27.332
42	22.445	24.963	27.482	142	22.362	24.229	27.383	242	22.046	24.889	27.362
43	22.445	24.963	27.482	143	22.067	24.461	27.367	243	22.151	24.889	27.393
44	22.445	24.963	27.482	144	21.773	24.693	27.351	244	22.256	24.890	27.423
45	22.445	24.963	27.482	145	21.506	24.840	27.337	245	22.321	24.891	27.443
46	22.445	24.963	27.482	146	21.702	24.840	27.367	246	22.423	24.887	27.466
47	22.445	24.963	27.482	147	21.897	24.840	27.396	247	22.561	24.883	27.498
48	22.445	24.963	27.482	148	22.092	24.840	27.426	248	22.700	24.879	27.529

49	22.445	24.963	27.482
50	22.445	24.963	27.482
51	22.445	24.963	27.482
52	22.445	24.963	27.482
53	22.445	24.963	27.482
54	22.445	24.963	27.482
55	22.445	24.963	27.482
56	22.445	24.963	27.482
57	22.445	24.963	27.482
58	22.445	24.963	27.482
59	22.445	24.963	27.482
60	22.445	24.963	27.482
61	22.568	24.963	27.482
62	22.901	24.963	27.482
63	23.234	24.963	27.482
64	23.567	24.963	27.482
65	23.901	25.086	27.482
66	24.234	25.416	27.482
67	24.567	25.747	27.482
68	24.901	26.077	27.482
69	25.240	26.408	27.603
70	25.590	26.738	27.931
71	25.941	27.069	28.259
72	26.291	27.400	28.587
73	26.641	27.737	28.915
74	26.991	28.085	29.243
75	27.341	28.432	29.571
76	27.691	28.780	29.900
77	28.042	29.127	30.115
78	28.393	29.475	30.137
79	28.744	29.822	30.159
80	29.095	30.170	30.181
81	29.446	30.399	30.203
82	29.797	30.427	30.224
83	30.148	30.455	30.246
84	30.499	30.483	30.267
85	30.737	30.510	30.283
86	30.784	30.538	30.289
87	30.830	30.565	30.295
88	30.877	30.593	30.301
89	30.885	30.619	30.307
90	30.261	30.644	30.313
91	29.636	30.669	30.319
92	29.012	30.694	30.325
93	28.489	30.681	30.336
94	28.136	30.040	30.354
95	27.783	29.399	30.373
96	27.430	28.758	30.392
97	27.077	28.223	30.373
98	26.696	27.867	29.731
99	26.315	27.511	29.089
149	22.213	24.840	27.445
150	22.405	24.834	27.457
151	22.666	24.829	27.472
152	22.927	24.823	27.488
153	23.164	24.818	27.502
154	22.985	25.021	27.467
155	22.807	25.296	27.433
156	22.628	25.570	27.398
157	22.516	25.818	27.374
158	22.537	25.612	27.563
159	22.565	25.406	27.821
160	22.592	25.200	28.078
161	22.617	25.071	28.310
162	22.581	25.079	28.140
163	22.545	25.091	27.969
164	22.508	25.103	27.799
165	22.485	25.114	27.694
166	22.475	25.112	27.516
167	22.462	25.110	27.275
168	22.449	25.108	27.033
169	22.438	25.109	26.815
170	22.468	24.914	26.981
171	22.498	24.649	27.147
172	22.528	24.384	27.313
173	22.549	24.146	27.417
174	22.374	24.342	27.398
175	22.136	24.539	27.373
176	21.899	24.735	27.349
177	21.684	24.859	27.327
178	21.842	24.859	27.359
179	22.001	24.859	27.390
180	22.159	24.860	27.422
181	22.257	24.860	27.442
182	22.412	24.855	27.460
183	22.623	24.850	27.485
184	22.834	24.845	27.510
185	23.024	24.840	27.531
186	22.879	25.012	27.495
187	22.734	25.246	27.459
188	22.589	25.479	27.423
189	22.498	25.690	27.399
190	22.523	25.515	27.552
191	22.556	25.340	27.759
192	22.589	25.165	27.966
193	22.618	25.055	28.153
194	22.582	25.061	28.015
195	22.546	25.070	27.877
196	22.510	25.079	27.739
197	22.487	25.087	27.654
198	22.471	25.086	27.510
199	22.450	25.085	27.315
249	22.825	24.876	27.558
250	22.728	24.999	27.523
251	22.631	25.168	27.489
252	22.535	25.336	27.455
253	22.474	25.487	27.433
254	22.500	25.361	27.533
255	22.536	25.235	27.669
256	22.572	25.109	27.804
257	22.604	25.030	27.926
258	22.571	25.034	27.835
259	22.538	25.038	27.744
260	22.505	25.043	27.652
261	22.484	25.047	27.596
262	22.464	25.047	27.501
263	22.437	25.048	27.372
264	22.409	25.049	27.243
265	22.385	25.050	27.126
266	22.415	24.932	27.217
267	22.444	24.772	27.308
268	22.474	24.613	27.398
269	22.494	24.469	27.455
270	22.401	24.587	27.432
271	22.274	24.706	27.400
272	22.148	24.825	27.369
273	22.034	24.900	27.341
274	22.120	24.900	27.369
275	22.205	24.901	27.398
276	22.291	24.902	27.427
277	22.344	24.903	27.445
278	22.427	24.899	27.468
279	22.540	24.896	27.500
280	22.652	24.892	27.532
281	22.754	24.889	27.561
282	22.675	24.994	27.529
283	22.595	25.137	27.497

D.2.2 Data for the Chen (1995) Network

The data used in the application of the inverse transient method in the pipe network used by Chen (1995) are shown in Table D.2. One hundred and seventy two time steps of pressure head data at nodes 3 and 5 were used as measured data. The time step (Δt) for the measured pressure head data was 0.1173 s.

Table D.2 Measured Pressure Head Data for the Chen (1995) Network

Time Step	Pressure (m)		Time Step	Pressure (m)		Time Step	Pressure (m)		Time Step	Pressure (m)	
	Node 3	Node 5		Node 3	Node 5		Node 3	Node 5		Node 3	Node 5
0	29.467	29.302	48	34.128	36.643	96	31.182	30.503	144	25.019	21.913
1	29.467	29.302	49	34.387	37.129	97	30.856	29.806	145	25.655	22.843
2	29.467	29.302	50	34.615	37.588	98	30.368	29.140	146	26.048	23.764
3	29.467	29.302	51	34.824	37.949	99	29.906	28.364	147	26.292	24.546
4	29.467	29.302	52	35.094	38.184	100	29.375	27.511	148	26.582	25.167
5	29.467	29.302	53	35.342	38.363	101	28.770	26.755	149	26.858	25.819
6	29.467	29.302	54	35.597	38.462	102	28.213	26.227	150	27.112	26.456
7	29.467	29.302	55	35.834	38.487	103	27.753	25.746	151	27.461	27.006
8	29.467	29.302	56	36.119	38.444	104	27.189	25.229	152	27.667	27.537
9	29.467	29.302	57	36.431	38.405	105	26.414	24.654	153	27.787	28.006
10	29.467	29.302	58	36.574	38.395	106	25.569	24.113	154	27.963	28.404
11	29.467	29.302	59	36.644	38.402	107	24.989	23.644	155	28.232	28.738
12	29.467	29.302	60	36.724	38.397	108	24.537	23.245	156	28.761	29.143
13	29.467	29.302	61	36.793	38.481	109	23.958	22.934	157	29.487	29.702
14	29.467	29.302	62	36.820	38.572	110	23.400	22.583	158	30.176	30.200
15	29.467	29.302	63	36.841	38.650	111	22.984	22.011	159	30.801	30.622
16	29.467	29.302	64	36.825	38.759	112	22.599	21.362	160	31.273	31.127
17	29.467	29.302	65	36.802	38.952	113	22.198	20.578	161	31.664	31.727
18	29.467	29.302	66	36.747	39.202	114	21.943	19.792	162	32.298	32.266
19	29.467	29.302	67	36.528	39.446	115	21.916	19.090	163	32.976	32.738
20	29.467	29.302	68	36.394	39.645	116	21.908	18.419	164	33.465	33.156
21	29.467	29.302	69	36.312	39.707	117	21.717	17.762	165	33.791	33.458
22	29.467	29.302	70	36.220	39.679	118	21.357	17.091	166	33.854	33.680
23	29.467	29.467	71	36.104	39.525	119	21.161	16.488	167	33.808	33.835
24	29.467	29.694	72	35.996	39.306	120	21.041	16.065	168	33.710	33.991
25	29.467	29.922	73	35.899	39.031	121	20.810	15.891	169	33.566	34.182
26	29.467	30.150	74	35.787	38.695	122	20.590	15.772	170	33.544	34.278
27	29.467	30.378	75	35.634	38.297	123	20.458	15.749	171	33.496	34.163
28	29.650	30.607	76	35.467	37.875	124	20.361	15.848	172	33.243	34.111
29	29.903	30.835	77	35.456	37.449	125	20.219	16.069			
30	30.156	31.146	78	35.405	37.100	126	19.973	16.337			
31	30.409	31.488	79	35.301	36.788	127	19.840	16.567			
32	30.663	31.830	80	35.145	36.487	128	19.925	16.775			
33	30.917	32.098	81	35.002	36.241	129	19.883	17.022			
34	31.172	32.340	82	34.805	36.052	130	19.819	17.232			
35	31.508	32.581	83	34.665	35.897	131	19.879	17.406			
36	31.929	32.822	84	34.532	35.773	132	19.983	17.613			
37	32.372	33.031	85	34.390	35.680	133	20.091	17.833			
38	32.594	33.227	86	34.179	35.621	134	20.211	17.888			
39	32.788	33.401	87	33.786	35.491	135	20.372	17.812			
40	33.003	33.548	88	33.400	35.229	136	20.840	17.730			
41	33.218	33.758	89	33.027	34.983	137	21.335	17.800			
42	33.386	34.081	90	32.743	34.735	138	21.704	18.160			
43	33.564	34.430	91	32.526	34.366	139	22.189	18.602			
44	33.742	34.871	92	32.330	33.676	140	22.758	19.130			
45	33.854	35.328	93	31.988	32.882	141	23.277	19.756			
46	33.873	35.766	94	31.655	32.075	142	23.817	20.414			
47	33.909	36.202	95	31.382	31.275	143	24.402	21.093			

D.3 Measured Pressure Head Data Used in Chapter 6

Chapter 6 presented a study on the use of genetic algorithms as the minimisation algorithm in the inverse transient method. The small example network was used for the study. Two different sets of measured data were used. The first set of measurement data was used for friction factor calibration only and contains no leakage (Section D.3.1). The second set of measured pressure data was used for both leak detection and calibration and contained a leak at node 2 (Section D.3.2).

D.3.1 Data for Small Example Network (No Leak)

The data used for the calibration of the small network using inverse transient analysis and genetic algorithms are shown in Table D.3. Seventy time steps of pressure head measurement at nodes 2, 3, 4, 5, 6 and 7 were used as measured data (node 1 was a reservoir). The time step (Δt) for the measured pressure head data was 0.5789 s.

Table D.3 Measured Pressure Data for the Small Example Network (No Leak)

Time Step	Measured Pressure Head (m)					
	Node 2	Node 3	Node 4	Node 5	Node 6	Node 7
0	28.732	28.968	27.483	28.739	28.848	28.979
1	28.731	28.968	27.483	28.717	28.859	28.990
2	28.689	28.962	27.459	28.705	28.837	28.973
3	28.741	28.927	27.407	28.729	28.794	28.936
4	28.769	28.952	29.099	28.693	28.805	28.909
5	29.487	28.968	32.063	29.353	28.778	28.950
6	31.064	29.649	33.206	30.654	29.479	29.064
7	32.493	31.120	33.338	31.976	30.834	30.472
8	33.294	32.529	35.104	33.102	32.867	33.094
9	33.858	33.366	37.034	34.848	35.345	35.255
10	34.752	34.239	37.746	37.054	37.321	36.378
11	36.393	35.559	39.070	38.027	38.322	37.281
12	38.011	36.494	41.095	38.180	38.203	38.255
13	38.424	36.598	41.683	38.872	38.166	38.080
14	37.680	36.167	40.917	39.412	38.730	37.479
15	36.595	35.684	40.253	38.326	38.862	37.836
16	35.749	35.216	38.960	36.682	37.730	37.765
17	34.829	34.418	37.244	35.849	35.768	35.826
18	34.119	33.034	33.075	34.872	33.961	33.286
19	31.651	31.710	27.963	31.605	32.432	31.711
20	27.651	29.438	24.923	27.809	29.448	30.783
21	24.088	26.404	22.139	24.823	26.292	27.212
22	21.964	23.624	18.551	22.504	22.556	22.222
23	21.160	21.950	16.792	19.095	18.437	18.634
24	20.747	20.835	16.049	15.998	15.050	17.015
25	19.065	19.934	14.202	15.867	14.031	16.072
26	17.348	19.629	13.037	16.910	16.332	16.140
27	17.831	20.157	14.068	17.334	18.861	19.053
28	20.339	22.274	15.987	18.579	20.141	21.867
29	23.493	24.929	18.568	22.249	21.415	22.743
30	26.374	26.589	23.308	25.877	24.415	24.282
31	29.005	27.919	27.086	28.166	28.555	28.021
32	30.046	30.555	27.199	30.424	31.851	32.047
33	30.427	32.893	26.648	32.656	33.968	34.750
34	31.177	32.980	28.973	33.538	35.540	35.515
35	32.019	31.930	32.033	33.589	35.301	34.482
36	32.912	31.826	32.852	33.127	32.901	32.233
37	33.135	31.993	31.509	32.036	30.116	30.685
38	31.075	30.922	29.862	30.335	29.544	30.215
39	28.221	28.668	27.461	28.920	30.228	29.855
40	26.145	27.432	24.855	27.555	29.447	28.864
41	25.567	27.449	23.793	26.165	26.441	27.192
42	26.253	26.848	24.379	24.842	23.887	25.058
43	26.947	25.430	24.781	24.390	23.173	23.376
44	26.292	25.268	24.451	24.690	23.672	23.133
45	25.025	26.315	23.713	24.958	24.526	25.076
46	24.946	26.901	23.049	25.326	26.208	27.585
47	26.148	27.226	24.047	26.525	28.284	28.271
48	28.071	28.163	27.053	28.378	28.706	27.981

49	30.350	29.562	29.801	29.701	28.188	28.431
50	31.706	30.652	30.437	30.619	29.243	30.048
51	31.367	31.218	30.014	31.507	32.178	31.932
52	30.548	31.380	29.939	32.296	34.252	33.488
53	30.272	31.619	30.319	32.687	33.936	34.011
54	31.187	31.819	30.505	32.365	32.622	32.956
55	32.317	31.392	30.720	31.423	31.355	31.140
56	31.843	30.415	30.726	30.663	29.945	29.756
57	29.672	29.550	29.304	29.924	29.074	29.185
58	27.620	28.789	26.434	28.573	29.016	29.328
59	26.548	28.024	24.462	26.903	28.810	28.953
60	26.267	27.222	24.543	26.158	27.013	27.300
61	26.665	26.633	25.441	26.043	24.733	25.189
62	27.283	26.490	25.643	25.690	23.980	24.197
63	27.047	26.674	25.032	25.292	24.883	25.075
64	26.186	26.898	24.214	25.719	26.266	26.817
65	25.761	27.336	24.378	26.875	27.630	28.043
66	26.731	28.066	25.889	27.894	28.625	28.531
67	29.035	28.855	27.688	28.552	28.847	28.769
68	30.870	29.722	29.139	29.514	28.730	29.111
69	31.060	30.508	30.150	30.758	29.651	29.877
70	30.457	30.759	30.157	31.417	31.709	31.361

D.3.2 Data for Small Example Network (With Leak)

The data used for leak detection and calibration of the small network using inverse transient analysis and genetic algorithms are shown in Table D.4. Seventy time steps of pressure head data at nodes 2, 3, and 6 were used as measured data (node 1 was a reservoir). The time step (Δt) for the measured pressure head data was 0.5789 s.

Table D.4 Measured Pressure Data for the Small Example Network (With Leak)

Time Step	Measured Pressure (m)			Time Step	Measured Pressure (m)			Time Step	Measured Pressure (m)		
	Node 2	Node 3	Node 6		Node 2	Node 3	Node 6		Node 2	Node 3	Node 6
0	28.574	28.832	28.703	25	19.325	20.244	14.638	50	30.805	30.088	28.813
1	28.568	28.832	28.714	26	17.605	19.879	16.754	51	30.583	30.517	31.280
2	28.525	28.824	28.691	27	18.030	20.322	19.001	52	29.948	30.648	32.941
3	28.583	28.785	28.643	28	20.368	22.280	20.067	53	29.738	30.872	32.578
4	28.611	28.815	28.654	29	23.246	24.743	21.232	54	30.497	31.087	31.587
5	29.306	28.831	28.623	30	25.805	26.251	24.114	55	31.418	30.780	30.777
6	30.841	29.499	29.330	31	28.212	27.431	28.026	56	31.049	29.993	29.700
7	32.243	30.947	30.687	32	29.252	29.901	31.032	57	29.357	29.329	28.928
8	33.035	32.343	32.687	33	29.729	32.154	32.913	58	27.843	28.789	28.876
9	33.612	33.169	35.105	34	30.529	32.259	34.382	59	27.103	28.224	28.804
10	34.517	34.026	37.031	35	31.349	31.266	34.271	60	26.845	27.581	27.408
11	36.133	35.338	38.030	36	32.163	31.242	32.195	61	27.019	27.116	25.629
12	37.708	36.273	37.943	37	32.438	31.534	29.753	62	27.454	27.005	25.117
13	38.122	36.381	37.932	38	30.732	30.642	29.356	63	27.315	27.122	25.826
14	37.445	35.974	38.501	39	28.323	28.637	30.085	64	26.684	27.260	26.732
15	36.464	35.540	38.632	40	26.561	27.625	29.465	65	26.341	27.582	27.642
16	35.723	35.130	37.538	41	26.087	27.765	26.827	66	27.029	28.120	28.436
17	34.872	34.402	35.688	42	26.664	27.267	24.678	67	28.709	28.673	28.683
18	34.179	33.102	34.046	43	27.221	25.949	24.175	68	30.017	29.309	28.572
19	31.778	31.847	32.668	44	26.618	25.770	24.577	69	30.123	29.919	29.209
20	27.935	29.641	29.764	45	25.510	26.698	25.115	70	29.738	30.086	30.727
21	24.534	26.697	26.624	46	25.445	27.154	26.412				
22	22.507	23.997	22.928	47	26.420	27.323	28.209				
23	21.662	22.342	18.912	48	27.892	28.060	28.554				
24	21.095	21.199	15.646	49	29.669	29.224	27.997				

D.4 Measured Pressure Head Used in Chapter 7

Chapter 7 presented research on the optimal location of measurement sites, optimal number of measurement sites and the length of measured data. Two different sized pipe networks were used in Chapter 7 for the optimal location and number of measurement sites. Sections D.4.1 and D.4.2 present the measured pressure head data for a small example pipe network and for the 51 pipe network respectively.

D.4.1 Data for the Small Example Network

The transient event for the small example pipe network was initiated by a reduction of demand at node 4 from 58 L/s to 28 L/s in a period of 8 seconds followed by an increase in the demand to its original value in a subsequent 10 seconds (Figure D.8).

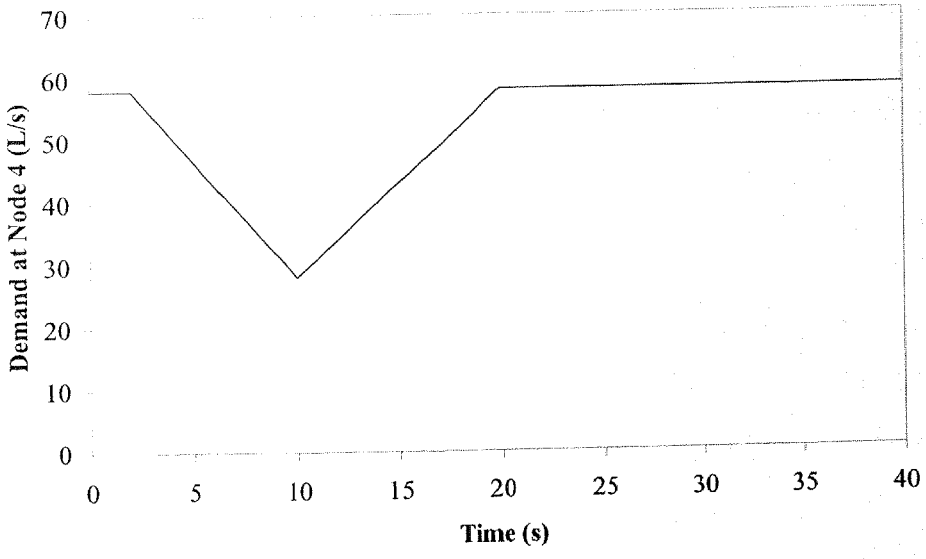

Figure D.8 Transient Event Initiation: Demand at Node 4

The data used in the application of the inverse transient method for the small example pipe network are shown in Table D.5. Seventy time steps of pressure head data at nodes 2, 3, 4, 5, 6 and 7 were used as measured data (node 1 was a reservoir). The time step (Δt) for the measured pressure head data was 0.5789 s.

Table D.5 Measured Pressure Head Data for the 51 Pipe Network

Time Step	Measured Pressure Head (m)					
	Node 2	Node 3	Node 4	Node 5	Node 6	Node 7
0	29.050	29.225	27.797	29.050	29.142	29.234
1	29.050	29.225	27.797	29.050	29.142	29.234
2	29.050	29.225	27.797	29.050	29.142	29.234
3	29.050	29.225	27.797	29.050	29.142	29.234
4	29.050	29.225	29.391	29.050	29.142	29.234
5	29.829	29.225	32.313	29.671	29.142	29.234
6	31.574	29.922	33.573	31.126	29.760	29.644
7	32.492	31.719	34.062	32.372	31.617	31.481
8	32.528	33.035	35.136	33.653	34.073	34.325
9	33.456	33.357	36.117	35.474	36.340	35.853
10	34.988	34.219	37.935	36.588	37.240	35.954
11	35.972	35.305	39.736	36.839	36.203	36.343
12	36.034	35.295	39.319	36.998	35.947	36.435
13	34.935	34.402	37.905	36.519	37.225	35.973
14	33.486	33.416	36.873	35.311	36.543	35.816
15	32.962	32.911	35.740	34.054	33.916	34.360
16	32.947	32.282	35.095	32.752	31.891	31.601
17	32.172	30.753	35.003	31.565	30.450	30.416
18	30.776	29.808	29.992	30.843	30.097	30.392
19	28.220	30.259	22.855	28.944	30.783	30.225
20	25.335	28.895	21.914	26.191	29.075	29.744
21	25.366	25.401	23.258	25.147	25.176	26.044
22	26.651	24.409	23.091	24.022	22.145	20.922
23	25.489	25.396	21.845	21.870	19.790	21.175
24	23.020	24.842	18.637	21.591	20.906	23.922
25	22.160	23.839	17.042	22.797	25.698	23.862
26	23.894	24.501	20.418	23.600	25.733	24.460
27	27.127	27.023	24.371	24.971	22.376	25.519
28	29.299	29.151	25.511	27.143	24.761	25.287
29	28.805	28.677	25.829	28.820	30.021	28.679
30	27.422	28.844	25.765	29.863	32.703	33.204
31	28.490	31.391	24.995	30.578	33.032	32.423
32	31.106	31.736	26.685	30.521	30.310	30.320
33	31.054	29.467	29.819	29.758	27.834	29.477
34	28.550	28.305	27.236	28.826	28.932	27.906
35	26.297	28.052	21.736	26.925	28.893	28.081
36	24.958	27.216	22.343	24.725	26.088	28.184
37	25.952	25.744	25.382	24.912	24.040	24.138
38	28.116	25.114	25.956	25.692	22.977	21.825
39	27.461	26.840	25.911	24.999	23.480	25.235
40	25.795	28.445	24.029	26.184	27.237	28.555
41	26.874	28.125	23.599	28.921	31.225	29.521
42	29.477	28.913	29.174	29.857	31.186	30.482
43	32.031	31.467	33.072	31.083	29.125	30.644
44	33.305	32.660	31.397	32.985	30.543	30.827
45	31.524	31.836	30.750	32.719	34.662	33.662
46	29.434	31.084	30.357	32.300	35.812	35.489
47	30.442	31.590	28.514	32.467	33.135	32.658

48	31.935	31.537	30.051	30.566	29.344	29.513
49	30.744	29.291	31.433	28.818	26.975	28.506
50	27.994	27.384	27.054	28.533	27.986	27.398
51	25.903	27.531	22.729	26.629	28.947	27.614
52	25.571	27.524	23.037	24.886	26.265	28.186
53	26.898	26.617	25.182	25.924	24.149	25.031
54	28.332	26.202	27.211	26.577	24.698	23.150
55	28.120	27.168	27.189	26.230	25.572	26.805
56	26.989	29.086	24.674	27.673	28.319	29.664
57	27.609	29.689	25.002	29.563	31.737	30.096
58	30.109	29.267	29.907	30.290	31.325	31.185
59	32.087	30.828	32.763	31.468	29.748	30.685
60	32.430	32.573	31.123	32.466	30.830	30.374
61	31.051	31.569	29.677	31.780	33.076	33.407
62	29.178	30.357	29.233	31.364	34.340	34.082
63	29.531	30.568	28.380	31.413	32.373	30.830
64	31.089	30.368	29.206	29.640	27.934	29.025
65	30.175	29.167	29.819	27.972	26.322	27.993
66	27.532	27.562	26.479	28.070	28.029	26.807
67	26.021	26.883	23.380	26.909	28.545	27.964
68	26.150	27.701	23.986	25.376	26.849	28.263
69	27.566	27.803	25.603	26.592	25.111	25.519
70	28.880	26.919	27.607	27.577	25.269	24.944

D.4.2 Data for the 51 Pipe Network

A 51 pipe network was utilised in Section 7.6 to find optimal measurement site configurations. The network consisted of 51 pipes and 35 nodes. Three tanks supply the network and most nodes have constant demands. The definition of properties needed to describe the fluid and the network appear here. The fluid properties of the water flowing through the network are a density of 1000.0 kg/m^3 and bulk modulus of elasticity of 2.2×10^9 Pa. The pipe network properties can vary between different pipes but some are common for all pipes. The common properties are a pipe wall thickness of 0.0254 m and a Young's modulus of elasticity of the pipe walls of 2.07×10^{11} Pa. The properties that are different for each pipe (length, friction factor and diameter) are shown in Table D.6.

Table D.6 Pipe Data for the 51 Pipe Network

Pipe ID	Length (m)	Friction Factor, f	Diameter (m)	Pipe ID	Length (m)	Friction Factor, f	Diameter (m)
1	870	0.0247	1.524	27	934.3	0.04	0.9144
2	450	0.0248	0.6096	28	885	0.0268	0.6096
3	460	0.0274	0.4572	29	885	0.0298	0.4572
4	895	0.0289	0.3048	30	905	0.0355	0.6096
5	457.2	0.0338	0.3048	31	885	0.04	0.6096
6	467.2	0.04	0.3048	32	885	0.0393	0.3048
7	457.2	0.0243	0.6096	33	905	0.0337	0.6096
8	457.2	0.0276	0.4572	34	457.2	0.0345	0.3048
9	467.2	0.0356	0.3048	35	457.2	0.04	0.3048
10	450	0.04	0.3048	36	905	0.0357	0.3048
11	450	0.0198	0.3048	37	885	0.0308	0.3048
12	460	0.0392	0.4572	38	450	0.0314	0.3048
13	450	0.0298	0.4572	39	460	0.0352	0.3048
14	450	0.034	0.4572	40	895	0.0286	0.6096
15	467.2	0.0262	0.6096	41	885	0.0385	0.4572
16	457.2	0.0289	0.6096	42	905	0.0298	0.6096
17	457.2	0.0341	0.3048	43	885	0.032	0.3048
18	934.4	0.0357	0.3048	44	457.2	0.0313	0.3048
19	914.4	0.04	0.3048	45	905	0.0319	0.3048
20	914.4	0.0362	0.6096	46	450	0.0296	0.6096
21	467.2	0.0162	0.4572	47	885	0.0298	0.6096
22	457.2	0.0298	0.4572	48	905	0.0261	0.6096
23	914.4	0.034	0.3048	49	450	0.0269	0.4572
24	934.4	0.0322	0.3048	50	450	0.0315	0.4572
25	457.2	0.032	0.3048	51	994.96	0.0279	0.9144
26	457.2	0.04	0.3048				

The wave speed was calculated for each pipe using

$$a = \sqrt{\frac{K/\rho}{1+\frac{K}{E}\frac{D}{e}}} \quad \text{.....(D.4.1)}$$

where a = wave speed, K = bulk modulus of elasticity of the water, ρ = density of the water, E = Young's modulus of elasticity of the pipe wall, D = pipe diameter and e = thickness of the pipe wall. The minimum Courant number is equal to 0.408. This value is too small for accurate calculation and, therefore, some of the pipes were divided into computational sections to increase the minimum Courant number. Pipes 1, 4, 18, 19, 20, 23, 24, 27, 28, 29, 30, 31, 32, 33, 36, 37, 40, 41, 42, 43, 45, 47, 48 and 51 were cut in half resulting in a 75 pipe, 59 node discretised pipe network. The new minimum Courant number for the discretised pipe network is 0.803. A compact cubic timeline interpolation is used in the transient model. The node data for the pipe network (tank

heads and demands) are shown in Table D.7. The elevations of all the nodes in the network are equal to zero.

Table D.7 Node Data for the 51 Pipe Network

Node ID	Tank Head (m)	Demand (m^3/s)	Node ID	Tank Head (m)	Demand (m^3/s)
1	132.4	-	19	-	0.08495
2	-	-	20	-	-
3	-	0.05663	21	121.92	-
4	-	0.08495	22	-	0.05663
5	-	0.07079	23	-	0.08495
6	-	0.11327	24	-	0.05663
7	-	0.04248	25	-	0.08495
8	-	0.05663	26	-	0.05663
9	-	0.11327	27	-	0.14159
10	-	0.11327	28	-	0.02832
11	-	0.11327	29	-	0.05663
12	-	0.05663	30	-	0.08495
13	-	0.05663	31	-	-
14		0.08495	32	-	0.05663
15	-	0.11327	33	-	0.08495
16	-	-	34	-	0.08495
17	-	0.11327	35	121.4	-
18	-	-			

The total simulation time for the transient event is 40.0 s. The transient event is initiated by instantaneously decreasing the demand at node 7 from 0.04248 m^3/s to zero at a time of 1.0 s, where it remains for the rest of the transient event (Figure D.9). All other tank heads and demands are kept constant throughout the transient event.

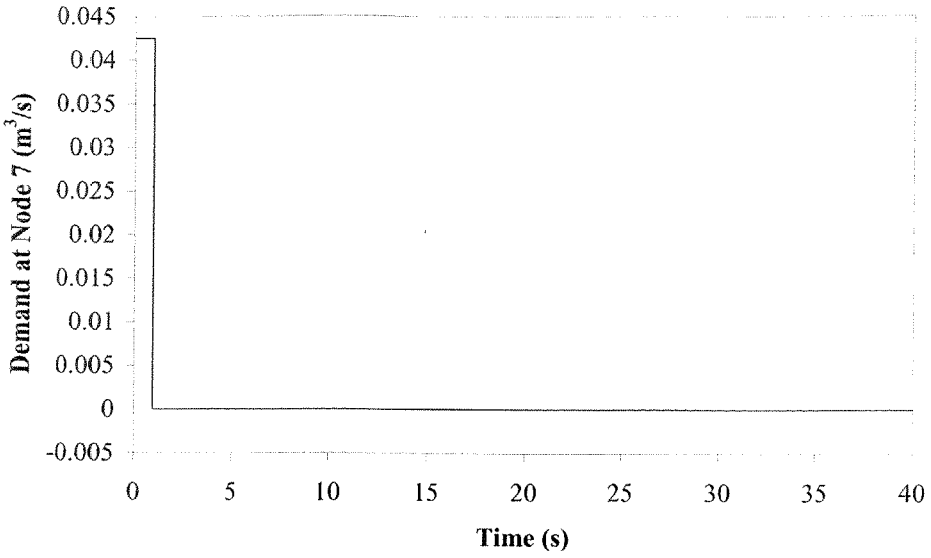

Figure D.9 Transient Event Initiation: Demand at Node 7

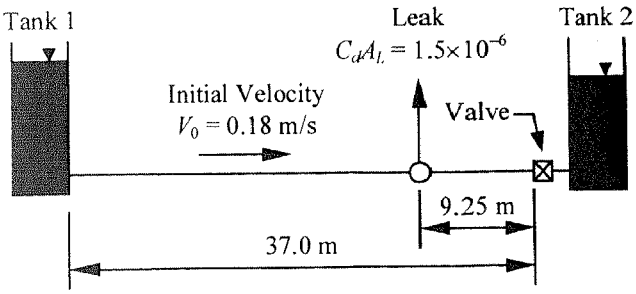

Experimental Pipeline

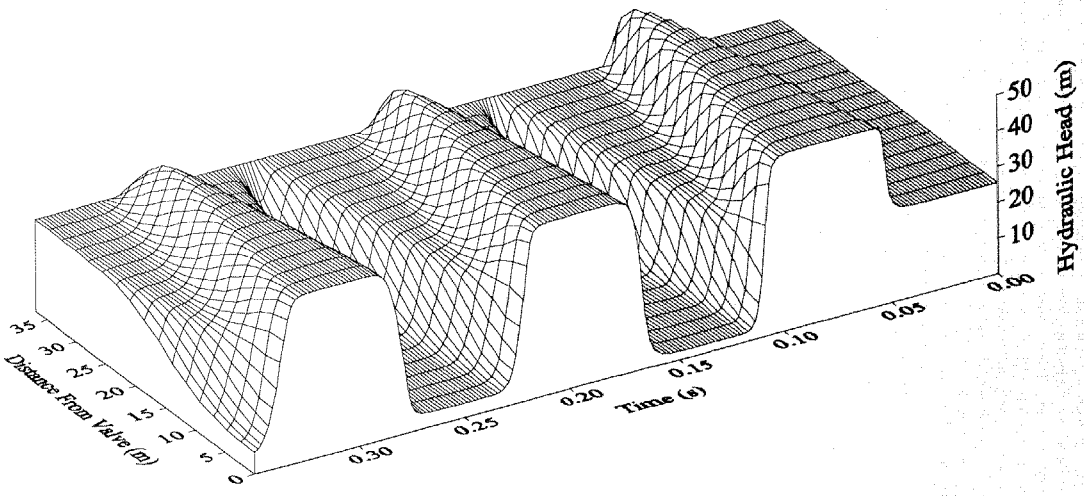

Transient Response: Fast Valve Closure, Without Leak

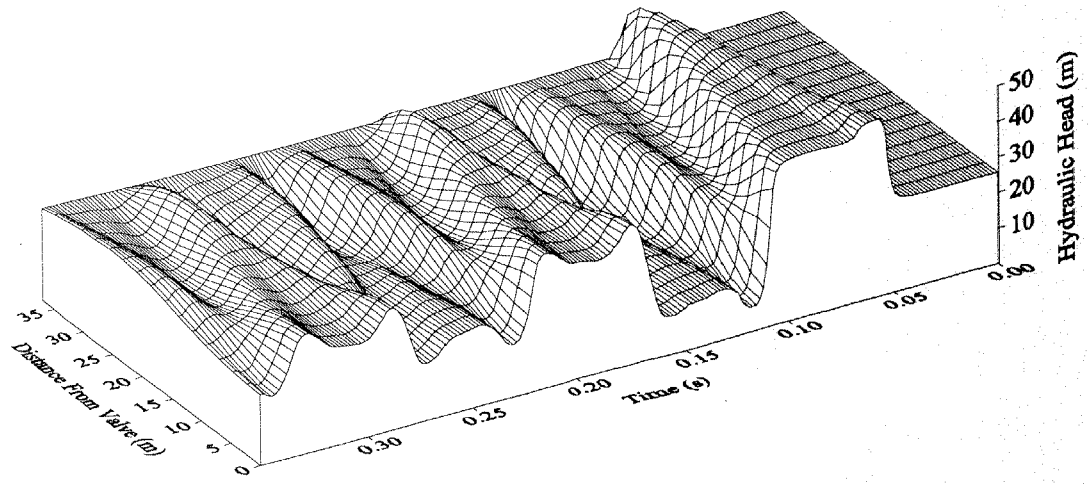

Transient Response: Fast Valve Closure, With Leak